



# **Electron Tube Design**

**Electron Tube Division  
RADIO CORPORATION OF AMERICA  
Harrison, New Jersey**

Privately issued by  
ELECTRON TUBE DIVISION  
Radio Corporation of America  
for use by its employees and for restricted  
distribution.

First Printing, 1962

Printed in U.S.A.

# FOREWORD

The fifty-three articles in this book were written by RCA engineers and scientists to acquaint RCA tube engineers, particularly those of limited tube experience, with the terminology, objectives, problems, and techniques peculiar to electron tubes. The articles are intended to provide the basic principles underlying the design, manufacture, and application of the many present-day varieties of tubes.

Because this book is a compilation of articles by authors, each writing more or less independently, duplication will be encountered. In this kind of material, however, duplication is desirable. First, some duplication is necessary to help keep individual articles complete in themselves; second, some repetition may assist the reader in acquiring information faster; and, most important, different treatments of similar subjects illustrate how tube design is affected by the different design objectives and the different environments of individual authors.

In general, the treatment is non-mathematical and free of detailed descriptions which often are subject to change. For more detailed treatment, the reader is referred to the references and bibliography at the end of most articles. References to published material list the publications; those to unpublished information show a code, the key to which is available to authorized persons through RCA Electron Tube Division librarians.

Because the preparation of these articles extended over several years, some authors are no longer associated with the design activities which they discuss. In such cases, however, the authors' names are shown in the article captions with the locations where the preparation of the articles took place. Most articles involved the cooperation of associates of the authors. These contributions are gratefully acknowledged by the authors.

This book is the result of a strong management desire, supported by the Engineering Education Committees at Harrison and Lancaster, to bring the original Vacuum Tube Design book up to date. It was recognized that the earlier book had played a very important role in the orientation, training, and development of RCA tube-design engineers, that a revised edition would supplement and strengthen the programs conducted by the education committees, and that engineering supervision would benefit greatly if new engineers had access to basic tube-design know-how written by RCA authorities.

An early step in implementing the program for the revised book was the formation by Dr. G. R. Shaw, then chief engineer of the Electron Tube Division, of a steering committee under the chairmanship of J. F. Hirlinger. From the first, this committee worked closely with the education committees, who had the responsibility of choosing subject matter, selecting and appointing authors, and guiding and encouraging authors in the completion of their assignments.

Much progress was made, but a greater and more concerted effort was needed to carry the program through to prompt completion. As a result, R. S. Burnap, Manager of Commercial Engineering, on his retirement, was appointed a consultant to the RCA Electron Tube Division with his most important and essentially full-time assignment the completion of the Electron Tube Design book. With the establishment of new schedules and through the special efforts of committee members, authors, and reviewers to complete their commitments, the job was finished.

The names of contributing committee members during the preparation of the book, together with the names of those who reviewed or edited articles follow. The contributions of these people and of the men who carried the heaviest load, the authors, are hereby acknowledged with the sincerest of thanks.

R. S. Burnap

*Consultant to the Electron  
Tube Division*

## ENGINEERING EDUCATION COMMITTEES

### Harrison

T. M. Cunningham	Chairman (1)
W. Zvonik	Chairman (2)
H. Waltke	Chairman (3)
J. J. Thompson	Chairman (4)
J. J. Thompson	Vice Chairman (1)
R. Rauth	Vice Chairman (2)
D. Gardam	Training Representative (1)
P. Theall	Training Representative (2)

### Lancaster

L. B. Headrick	Chairman (1)
G. G. Thomas	Chairman (2)
R. E. Slough, Jr.	Training Representative (1)
J. L. Hopkins	Training Representative (2)

## BOOK COMMITTEES

### Harrison

T. M. Cunningham	Chairman (1)
J. J. Thompson	Chairman (2)
J. Gutowski	Vice Chairman (1)
R. J. Nelson	Vice Chairman (2)
R. Lambdin	
O. H. Schade, Jr.	
L. Scholz	

### Lancaster

A. Nekut*	Chairman (1)
M. Lemeshka*	Co-Chairman
M. Petrisek*	Chairman (2)
W. N. Parker*	
A. C. Grimm	
H. A. Kaufman	
A. L. Lucarelli	
H. C. Moodey	
Y. W. Uyeda	
R. H. Zachariason	

\*Member of original planning group.

## TECHNICAL REVIEW COMMITTEES

### Harrison

Same personnel as Book Committee

### Lancaster

R. H. Zachariason	Chairman
M. V. Hoover	
W. N. Parker	
D. D. Van Ormer	

## STEERING COMMITTEE

J. F. Hirlinger, Chairman	Harrison	C. A. Meyer	Harrison
R. S. Burnap	Harrison	A. G. Nekut (1)	Lancaster
R. L. Klem (1)	Harrison	W. N. Parker (2)	Lancaster
T. M. Cunningham (2)	Harrison	G. R. Shaw	Harrison
M. B. Lemeshka (1)	Lancaster	H. T. Swanson (1)	Lancaster
M. Petrisek (2)	Lancaster	C. W. Thierfelder (2)	Marion

(1) First member; (2) Succeeding member

## REVIEWERS AND EDITORS

H. Baum	W. F. Griffin	M. B. Knight	A. M. Morrell	C. P. Smith
B. Becker	M. Grimes	R. W. Lambdin	G. A. Morton	J. W. Smith
M. Berg	A. C. Grimm	C. T. Lattimer	L. S. Nergaard	W. A. Smith
F. G. Block	J. Gutowski	W. F. Lawrence	R. G. Neuhauser	C. H. Thomas
B. B. Brown	C. P. Hadley	E. A. Lederer	W. N. Parker	J. J. Thompson
R. S. Burnap	A. E. Hardy	R. L. Leigh	F. Paschke	A. Trax
T. M. Cunningham	W. A. Harris	J. T. Mark	H. J. Prager	J. C. Turnbull
S. B. Deal	M. D. Harsh	E. M. McElwee	O. H. Schade, Sr.	S. Umbreit
R. W. Engstrom	L. B. Headrick	C. H. Meltzer	O. H. Schade, Jr.	D. H. Van Ormer
D. W. Epstein	T. J. Henry	P. A. Metzger	L. C. Scholz	F. S. Veith
F. G. Foerster	C. W. Horsting	C. A. Meyer	F. Scott	P. Weimer
N. S. Freedman	R. B. Janes	B. Miller	B. Sheren	M. R. Weingarten
J. Gallup	M. Jinetopoulos	C. D. Mitchell	R. Shrader	J. F. Wilhelm
L. P. Garner	H. Johnson	J. Monagle	A. L. Smith	R. H. Zachariason
		H. C. Moodey		

## PRODUCTION COORDINATOR - B. A. Pierz

# CONTENTS

Article Title	Author	Page
<b>Emitters and Photoconductors</b>		
Fundamentals of Electron Emission	L. S. Nergaard	1
Oxide-Coated Emitters	C. P. Hadley	28
Electron-Emission Coating for the Oxide Cathode	C. H. Meltzer & E. G. Widell	37
Nickel Base Metal for the Oxide Cathode	C. H. Meltzer & E. G. Widell	64
The Interface and Other Oxide-Cathode Impedances	E. J. Hannig	77
Tungsten, Thoriated-Tungsten, and Thoria Emitters	W. E. Harbaugh	90
Photoelectric and Secondary-Electron Emission	A. H. Sommer	99
Photoconductors for Camera Tubes	C. W. Rector	108
<b>Phosphors</b>		
Cathodoluminescent Materials	R. N. Summergrad	128
Application and Colorimetry of Phosphor Screens	A. E. Hardy	138
Manufacture of Cathodoluminescent Materials	J. A. Markoski	153
<b>Space Current</b>		
Calculation of Fields and Currents	L. C. Scholz	159
Space Current Flow	M. V. Hoover	202
<b>General Design Considerations for Receiving Tubes</b>		
Heaters	A. G. F. Dingwall	216
Heat Transfer in Receiving Tubes	O. H. Schade, Jr.	244
Contact Potential and Grid Currents	E. R. Schrader	266
A New Approach to the Calculation of Electron-Tube Characteristics	O. H. Schade, Sr.	278
<b>Metals, Metallurgy, and Metal Fabrication</b>		
Metals and Metallurgy	C. W. Horsting, et al	315
The Metallic State	C. W. Horsting	
Metals for Electron Tubes	J. J. Carrona	
Testing of Metals	C. H. Li	
Cathode Materials for Receiving Tubes	L. S. Solet	
Plate Materials (Metals)	H. G. Scheible & T. A. Sternberg	
Grids and Leads	A. J. Stoeckert	
Metal-to-Metal Joining	E. S. Thall	
Joining Metals to Glasses and Ceramics	K. Strater	
Systematic Charts of the Properties of Electron Tube Metals	S. Y. Husni	

# CONTENTS (Cont'd)

Article Title	Author	Page
Metals for Vacuum Tube Construction	P.D. Strubhar	370
Principles of Metal Forming	L.S. Sloane	377
Processes Used in Metal Parts Fabrication and Finishing	H.A. Kauffman	385
Insulators, Envelope Materials, and Seals		
Glass for Receiving Tubes	J. Gallup	392
Glass and Its Properties and Seals	J.C. Turnbull & G.E. Eiwen	406
Ceramics	W.F. Lawrence	433
Ceramics and Ceramic-to-Metal Seals	M. Berg	452
Design of Mica Spacers	M. Bondy & M. Jinetopoulos	465
Parts Cleaning, Coating, and Basing		
Parts Cleaning and Processing	F.I. Scott	472
Coatings, Bases, and Basing Cements	L.P. Fox	481
Exhaust and Finishing		
High-Vacuum Technology and Equipment	W.G. Henderson & A.L. Lucarelli	485
Exhaust of Receiving-Type Tubes	C.J. Pearce	506
Getters	C.H. Thomas	519
Aging and Stabilization	G. Wolfe	526
Design, Processing, and Application of Receiving-Type Tubes and Picture Tubes		
Diodes	A.P. Kauzmann	537
Small-Signal Radio-Frequency Amplifier Tubes	W.A. Harris	577
Design of Intermediate-Frequency Amplifier Tubes	M.B. Knight	599
Design of Converter and Mixer Tubes	T.J. Henry	607
Design of AM and FM Detector Tubes	T.J. Henry	622
Vacuum-Tube Oscillators	W.E. Babcock	637
Beam Power Tube Design Considerations	O.H. Schade, Jr.	656
Audio Output, Vertical-Deflection, and Horizontal-Deflection Tubes for Receiving Applications	M. Bondy	669
Black-and-White Picture Tubes	Thierfelder, et al	682
Color Picture Tube Design and Processing	H.C. Moodey & A.M. Morrell	709

## CONTENTS (Cont'd)

Article Title	Author	Page
Circuit Troubles Caused by Unusual Tube Effects	W.E. Babcock	736

### Design, Processing, and Application of Industrial-Type Tubes

Some Factors Affecting the Design and Application of Small Power Tubes	J.W. Gaylord	743
Large-Power-Tube Design, Processing, and Testing	W.P. Bennett	763
Gas Tube Design	H.H. Wittenberg	792
Design and Processing of Oscillograph Tubes	E.M. Smith	818
Phototube Design	J.L. Weaver	826
Camera Tube Design and Processing	B.H. Vine	838
Image-Converter Tubes	R.G. Stoudenheimer	848
Design and Processing of Storage Tubes	M.D. Harsh	862
Design and Processing of Microwave Magnetrons	F.E. Vaccaro & D.E. Nelson	876
Traveling-Wave Tube Design	E.E. Bliss	898

# Fundamentals of Electron Emission

L. S. Nergaard

Princeton

## ELEMENTARY CONSIDERATIONS

In the preparation of this article on electron emission, two courses seemed open: (1) to give brief descriptions of the various emission mechanisms and then to present a substantial amount of data relating to these mechanisms, or (2) to give a more detailed elementary exposition of the physical phenomena involved and then to illustrate them in some detail with a particular example, the oxide cathode. The latter alternative seemed preferable because a comprehensive literature survey can make boring reading and, more important, it was believed that an elementary discussion of the physical phenomena involved in electron emission would prepare the way for a study of the vast literature on the subject and, at the very least, provide a lexicon for the reading of this literature. Accordingly, the second course was adopted.

In the subsequent discussion, the viewpoint will be quite elementary and even mechanistic where possible. To this writer, barium oxide on a cathode is not a white coating of "gunk" prepared by a complicated bit of witchcraft. The writer has no complaint with witchcraft but he regards the end result in this case as a collection of crystallites, each containing an orderly array of very tangible spherical barium and oxygen ions stacked alternately. It is just this kind of mental imagery that the writer hopes to convey so that atoms, ions, and other elementary particles will have the reality of the balls on a pool table. Then the interactions of particles are easy to visualize and to remember. As long as the behavior conforms to classical mechanics, visualization is easy, but difficulties arise when quantum effects enter and particles display wavelike properties. These difficulties may be surmounted for the most part by considering electrons and photons as short wave trains ("wave-packets") and invoking the familiar concepts of physical optics. The quantum effects which are of concern are: (1) the dual nature of particles, (2) the quantization of energy, and (3) quantum statistics.

## The Dual Nature of Particles

The wave theory of light, which accounts for the numerous interference effects observed in optics and radio propagation, was firmly entrenched when Planck showed that the spectral distribution of radiation from a black body can be accounted for by assuming that radiation occurs in energy particles (quanta) of size  $h\nu$ ,

where  $h$  is a constant (Planck's constant) and  $\nu$  is the frequency of the light. When it was shown that the photoelectric threshold for metals is given by

$$h\nu_0 = \phi \quad (1)$$

where  $\nu_0$  is the lowest light frequency at which photo-emission occurs and  $\phi$  is the work function of the metal, the evidence for quanta was overwhelming. Because both the wave characteristics and particle characteristics are required to encompass optical phenomena, the particles ("photons") may be thought of as wave trains characterized by a frequency, yet localized in space so that they are in a sense particles. As noted above, the energy of a photon is

$$E = h\nu \quad (2)$$

The momentum  $p$  of a photon is equal to its energy divided by its velocity (the velocity of light  $c$ ), or

$$p = \frac{h}{c} = \frac{h}{\lambda} \quad (3)$$

where  $\lambda$  is the wave length

This value for the momentum was precisely demonstrated by A. H. Compton in 1922.

In 1924, deBroglie suggested that electrons, which are normally considered particles, might also display wave properties. He associated a wave length

$$\lambda = \frac{h}{p} \quad (4)$$

with the electrons. This relation is the same as that found for photons. In 1925, Walter Elsasser suggested that electrons should display diffraction phenomena. Diffraction effects in accord with the above relation were found in 1927 by Davisson and Germer and by G. P. Thomson.\*\* Thus both electrons and photons can be visualized as wave trains.

\*See Mott, N. F., and R. W. Gurney, Electronic Process in Ionic Crystals, Oxford University Press, London, 1950.

\*\*The electron wave length can be written  $\lambda \approx (1.1 \times 10^{-7})/V^{1/2}$  cm where  $V$  is the energy of the electron in volts. Hence, an 100-volt electron has a wave length of about  $10^{-8}$  cm, or about a lattice spacing for a metal. It is this short wave length that gives the electron microscope its high resolution.

## Quantization of Energy

The possible energy states of a system are discrete. The energy losses and gains of a system correspond to transitions between the discrete states and, thus, are also discrete. This discreteness of the energy states may be regarded as a consequence of the wave nature of particles. (See Appendix A.) In some systems, the energy states are so closely spaced that the thermal energy  $kT$  ( $k$  = Boltzmann's constant,  $T$  = absolute temperature) of the particles constituting the system can cause transitions between states. In such systems, the states may be regarded as a continuous band of states.

## Quantum Statistics

In describing the equilibrium distribution of particles among possible energy states, two kinds of statistics are possible: Fermi-Dirac statistics and Bose-Einstein statistics.

**Fermi-Dirac Statistics.** These statistics, which apply to atoms, ions, and electrons, state that the probability that a state of energy be occupied by a particle is given by the expression

$$\frac{1}{1 + \exp [(\epsilon - \epsilon_F)/kT]} \quad (5)$$

where  $\epsilon$  is the state of energy of the electron, and  $\epsilon_F$  is the Fermi-energy, the energy at which the probability of occupancy is one-half. In Appendix B it is shown that transitions in a system obeying Fermi-Dirac statistics may be regarded as bimolecular and that, except for electrons, each state may be occupied by only one particle; in the case of electrons, each state may be occupied by two electrons if their spins are oppositely directed.

**Bose-Einstein Statistics.** These statistics apply to photons and phonons (the energy quanta of lattice vibrations) and state that the probability that a state of energy  $\epsilon$  be occupied may be expressed as

$$\frac{1}{\exp (\epsilon/kT) - 1} \quad (6)$$

We will have no need for the Bose-Einstein statistics.

The subsequent discussion will consist of a brief introduction to solid-state physics and will lay the ground work for the discussion of electron-emission processes. The emission processes involved in thermionic emission, field emission, photo-emission, and secondary emission will then be outlined. Finally, the physics of the oxide cathode will be discussed in some detail. The oxide cathode is the bread and butter of the tube industry and particular attention to this emitter is well justified.

## ELEMENTARY SOLID-STATE PHYSICS\*

If all that an emitter did was to emit electrons co-

\*The following books on solid-state physics are standard: Kittel is the latest and, in some ways, the most readable; Seitz, F., *The Modern Theory of Solids*, McGraw-Hill, New York, 1940; Mott, N. F., and R. W. Gurney, *Electronic Process in Ionic Crystals*, Oxford University Press, London, 1950; Kittel, C., *Introduction to Solid State Physics*, Wiley and Sons, New York, 1956.

piously, life would be simple. However, such is not the case; an electron emitter also emits atoms and molecules as well, and may absorb atoms and molecules from ambient gases. The emission and absorption of atoms and molecules changes the constitution of the emitter and alters its emitting properties. Therefore, it is necessary to consider some properties of solids other than their electron-emitting properties if the behavior of emitters is to be understood.

## Some Properties of Solids

A solid is an assemblage of atoms or ions. The parent atoms can be thought of as almost rigid spheres each consisting of a positively charged nucleus surrounded by electrons. Outside of this core of nucleus and electrons are a few electrons (the valence electrons) which determine the chemical properties of the atoms. The total charge carried by the core electrons and the valence electrons is equal to the nuclear charge so that the net charge on an atom is zero. When atoms are packed together that may share electrons, i. e., the valence electrons of one atom may spend part of the time on neighboring atoms. When this sharing occurs, the crystal is said to be covalently bound. Germanium and silicon are examples of covalent crystals. Another possibility exists when a crystal contains atoms of two or more kinds. Then, the valence electrons of one constituent may transfer to atoms of another constituent to form positive and negative ions; the ions are held together by coulomb forces. Such crystals are called ionic crystals. The alkali-halides, such as NaCl, are examples of ionic crystals. In either event, the crystal can be regarded as made up of stacked spheres. Fig. 1 shows a two-dimensional model of a crystal; each ball bearing represents an ion or an atom. This model gives an effective visualization of how a crystal is constituted and illustrates several of the defects that occur in real crystals. A lattice vacancy is obvious and the slip plane of a dislocation due to the non-uniform strain on the boundary is quite visible. Fig. 2 shows the effect of an "impurity" (an oversize atom) on the crystal. Notice that the crystal makes room for the impurity by leaving vacancies.

How well the packed-sphere model is borne out in real crystals is shown by the fact that Goldschmidt was able to select a set of numbers, one assigned to each ion, such that the sums of the numbers associated with any pair of ions gave the lattice spacing of the crystal formed from the ions.\* These numbers are called ionic radii and range from 0.07 Å for  $F^{7-}$  to 2.94 Å for  $Sn^{4+}$ .

Although the atoms are almost rigid, they still can move somewhat and they do move with an energy of motion that depends on the temperature. The energy stored in atomic or ionic motion is responsible, in large part, for the specific heat of solids; the remainder of the specific heat is due to the heat motion of electrons.

Some effects of this heat motion are illustrated in

\*Tables of ionic radii are to be found in Seitz, F., *The Modern Theory of Solids*, McGraw-Hill, New York, 1940

Fig. 3. This is an energy diagram in which the energy of a particle is shown vertically and its position horizontally. The binding energy of the atoms is shown by the periodic curve; it shows the potential energy that must be surmounted for an atom to jump from a normal lattice site, near a minimum, to an adjacent lattice site. Such a jump can occur when: (1) an atom picks up enough thermal energy to surmount the potential hill and (2) an adjacent lattice site is vacant. This jump process is the vacancy mechanism for self-diffusion and the energy  $\epsilon_D$  is the activation energy for self-diffusion. Notice that where the crystal terminates on the right, there is a potential barrier of height  $\Delta H$ . When a surface atom picks up enough thermal energy to surmount this hill it is "free" and can escape from the solid. The value  $\Delta H$ , then, is the heat of sublimation.

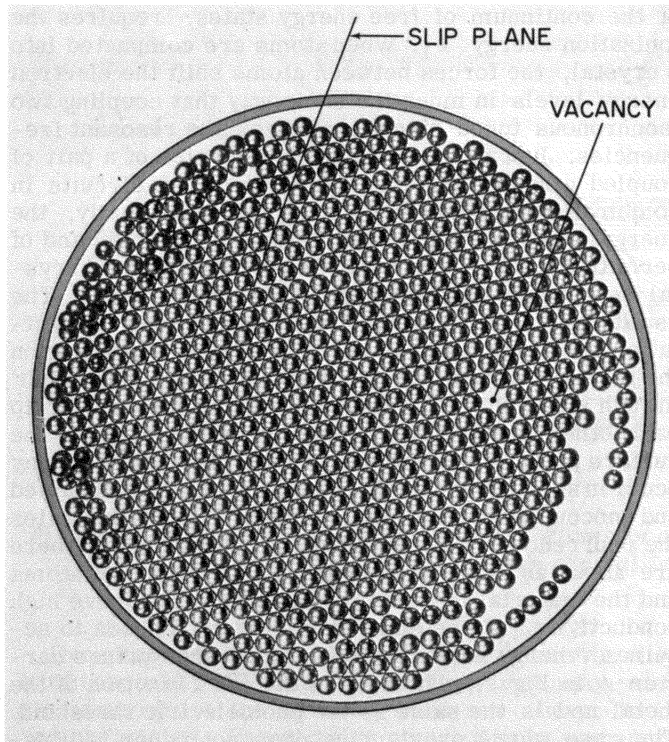


Figure 1. Ball-Bearing Model of a Two-Dimensional Crystal with Several Common Crystal Defects – Vacancies and Dislocations

In ionic crystals, where the binding energy is coulombic, an applied electric field tilts the energy level diagram as shown in Fig. 4. Then, the probability of a negative ion acquiring enough thermal energy to surmount the hill on the right is greater than the probability of getting enough energy to surmount the hill on the left. Consequently, if there are vacancies in the negative lattice, negative ions will drift to the right. Similarly, positive ions will drift to the left. These processes constitute electrolysis. The activation energy for electrolysis differs by very little from that for diffusion and in practice is the same.

The evaporation process mentioned above has its counterpart in absorption. This counterpart must exist or all solids would evaporate away in time – some in a very short time. The fact is that solids are in equilib-

rium with their surroundings. Such an equilibrium is illustrated in Fig. 5. The figure shows schematically a solid having  $N$  sites that a particular constituent can occupy,  $n_S$  of which are occupied. Also shown is the vapor phase which has  $N_C$  sites for the same constituent, of which  $n_V$  are occupied. The rate at which particles move from the solid to the vapor phase and from the vapor to the solid phase is discussed in Appendix B; the equilibrium formula is found to be (in the notation of Fig. 5)

$$n_S N_C W_{12} = n_V (N - n_S) W_{21} \quad (7)$$

where  $W_{12}$  is the probability that the constituent of concern moves from state 1 to state 2 in unit time (see Appendix B)

$$\frac{W_{21}}{W_{12}} = \exp (-\Delta H/kT) \quad (8)$$

and

$\Delta H$  = the latent heat of sublimation.

It frequently happens that

$$n_S \ll N \quad (9)$$

then

$$n_V = n_S \frac{N_C}{N} \exp (-\Delta H/kT) \quad (10)$$

Eq. (10) says that the number of particles in the vapor phase is directly proportional to the number in the solid phase and that their ratio is determined very sensitively by the latent heat of sublimation  $\Delta H$ ; conversely, to maintain a certain constituent in a solid phase, a certain vapor pressure of this constituent must be maintained about it. When the latent heat is high, the required pressure may be very small indeed but is still finite.

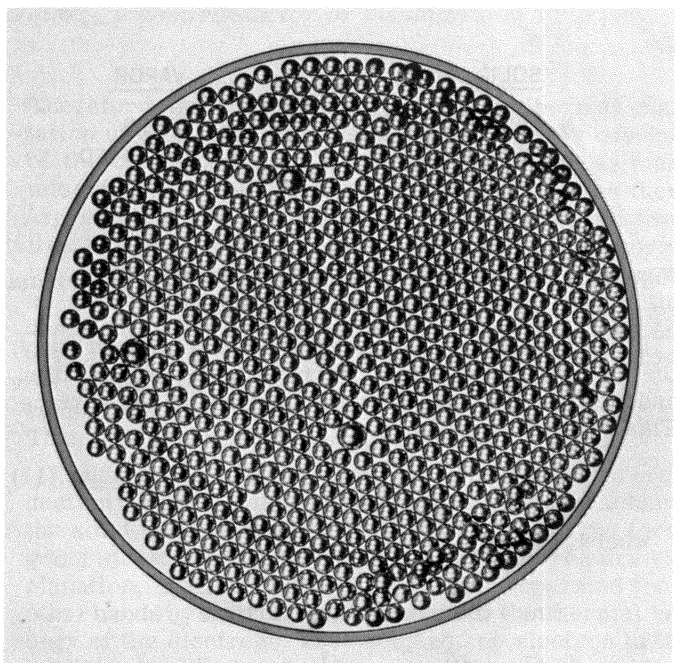


Figure 2. Ball-Bearing Model of a Two-Dimensional Crystal with Impurities (Over-size Balls). (Note that the crystal accommodates the impurities by forming vacancies and dislocations)

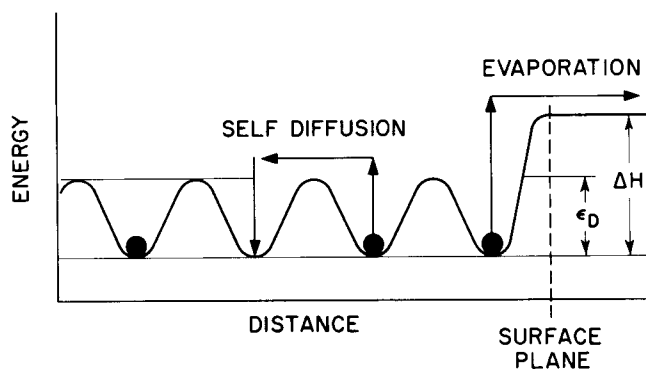


Figure 3. The Energy of an Atom as a Function of Distance Through a Crystal

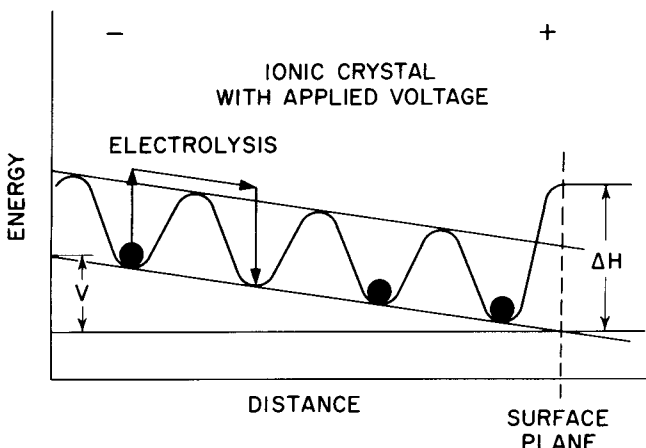


Figure 4. The Periodic Electric Field with a Voltage Applied to an Ionic Crystal

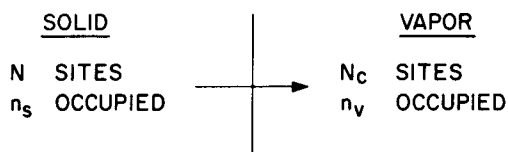


Figure 5. Solid-Vapor Relationships in the Equilibrium Between a Solid and a "Vacuum"

If the ambient vapor is continuously pumped away, the "saturated emission" current is the product of  $n_v$  and the mean thermal velocity is normal to the surface. This velocity is given by

$$\bar{v}_n = \frac{1}{4} \bar{v} \quad (11)$$

where  $\bar{v} = \sqrt{\frac{8 kT}{\pi m}}$

$m$  = the mass of the particle

$(\bar{v}_n \sim 10^7 \text{ cm sec}^{-1} \text{ at room temperature})$

Thus the particle current density, i.e., the rate of evaporation per square centimeter, is given by

$$j_p = n_v \bar{v}_n \quad (12)$$

## Electronic Properties of Solids

Band Structure. The discussion so far has related to the atomic constituents of solids. It is now pertinent to consider the behavior of electrons within the atoms or ions that constitute the solid.

As has been noted earlier, an atom in free space consists of a compact nucleus carrying an integral number of positive electronic charges surrounded by an equal number of electrons. To free each electron from the nuclear field requires a specific amount of energy. This situation is illustrated in Fig. 6 which shows the energy-level diagram of a valence electron of a simple atom. The energy level of the electron is shown as at 1 in the figure, together with an excitation level for this electron at  $1e$ . To raise the electron into the bottom of the continuum of free energy states, requires the ionization energy  $\epsilon_1$ . When atoms are compacted into a crystal, the forces between atoms shift the electron energy levels in much the same way that coupling two isochronous tuned circuits changes the resonant frequencies. Just as the resonant frequencies of a pair of coupled circuits must be ascribed to the circuits in combination and not to each circuit individually, the energy levels of the atoms "split" to form a band of permitted levels which must be associated with the crystal as a whole instead of with individual atoms. The "splitting" of the uppermost atomic level and its excitation level may occur in one of two ways depending on the atoms involved. First, the "splitting" may occur in such a way that the resultant bands of levels overlap each other and the free electron continuum above the surface potential barrier or second, the splitting may occur in such a way that the resultant bands of occupied and unoccupied levels do not overlap. Fig. 7 illustrates the occurrence of such overlapping. In this case, there are about as many free electrons as there are atoms and the material is metallic. Such materials have high conductivity. To be emitted, an electron needs to acquire an energy sufficient to surmount the surface barrier  $\phi$  in Fig. 7, where  $\phi$  is the work function of the metal and is the same as the photoelectric threshold. The case where overlapping does not occur is illustrated in Fig. 8. In this case, there is a region of width  $\epsilon_g$  which cannot be occupied by electrons; this region is called the "forbidden gap." Materials with a gap between the occupied and free electron bands are semiconductors or insulators. To obtain conductivity, electrons must be thermally excited so that their energy is high enough to enable them to cross the gap into free electron levels.

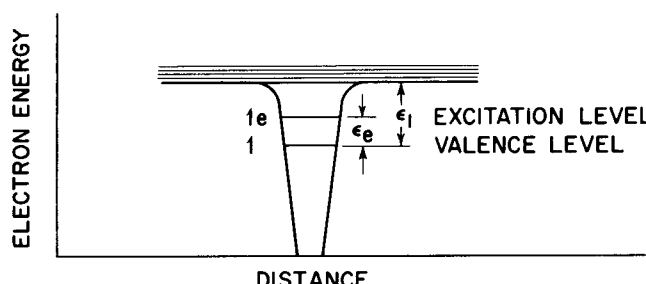


Figure 6. Energy-Level Diagram of a Simple Atom Containing Two Electrons

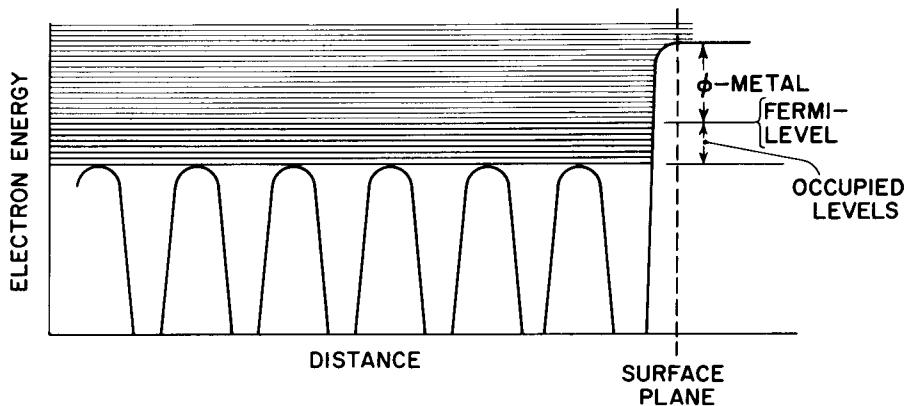


Figure 7. "Splitting" of energy levels of atoms in a crystal to form bands. If the bands overlap, as in this figure, the crystal is metallic.

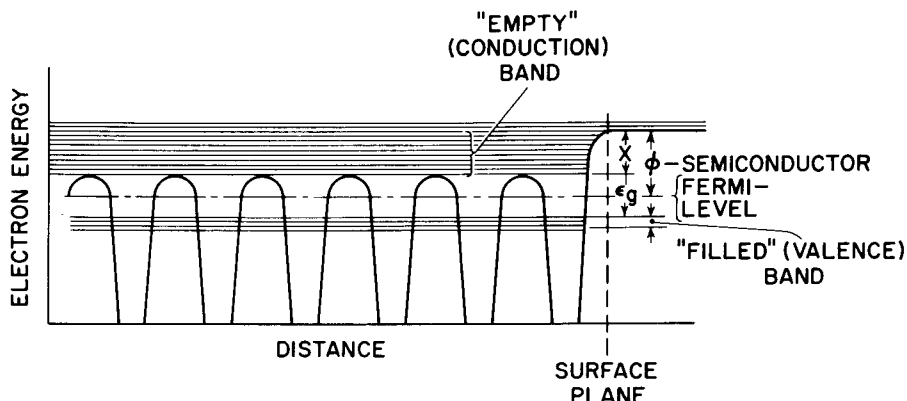


Figure 8. "Splitting" of energy levels of atoms in a crystal to form bands. If the bands do not overlap, a forbidden gap forms and the crystal is, therefore, a semiconductor or insulator.

Except at absolute zero temperature, where the filled band is actually full and the free states are empty, some electrons from the "filled" band are always in the "empty" states. To avoid this contradictory nomenclature, it is advisable to introduce other terms for these bands at this point. Because the filled band is occupied by valence electrons, it is called the valence band. Because electrons in the free states can conduct, this band of states is called the conduction band. It now remains to compute how many electrons from the valence band are to be found in the conduction band at any temperature. The conduction band has  $N_c$  states that may be occupied. Because the density of states in the valence band is so high, it may be regarded as also having  $N_c$  states which may be occupied. Suppose  $n$  electrons from the valence band are in the conduction band. The equilibrium number of such electrons is given by

$$(N_c - n)^2 W_{12} = n^2 W_{21} \quad (13)$$

Because  $n \ll N_c$  for all reasonable temperatures

$$n = N_c \left( \frac{W_{12}}{W_{21}} \right)^{\frac{1}{2}} = N_c \exp(-\epsilon_g/2kT) \quad (14)$$

where  $\epsilon_g$  is the band-gap energy

Therefore, the activation energy for the thermal excitation of electrons into the conduction band is one-half of the bandgap energy. Because there are as many missing electrons ("holes") in the filled band as there are electrons in the conduction band, the Fermi level lies half-way between bands. The semiconductor or insulator is then said to be "intrinsic." To evaporate, an electron in the free energy states (the conduction band) must acquire an additional energy  $X$ . This energy is equal to the energy difference between the lowest conduction band levels (the only ones occupied at reasonable temperatures) and the surface barrier. Thus, the thermionic work function is  $X + \epsilon_g/2$ .

Conductivity. If there are no electrons in the conduction band of a solid, or no holes in the valence band, the solid is non-conducting. The first part of the foregoing statement is obvious, the latter may require explanation. If all of the levels of a band, separated from other bands by substantially more than the thermal energy of the electrons, are occupied, no electron in the band can be accelerated. Acceleration would result in an increase in energy, and there are no empty energy states into which the electron can move. Hence, solids with large band-gaps are insulators. Electrons in the conduction band of a solid have many unoccupied states

into which they can move, so they can be accelerated. Similarly, holes in the valence band open up energy states into which electrons can move, thus permitting acceleration. Whenever an electron moves into an unoccupied state in the valence band, it leaves a "hole" behind just as do atoms in vacancy diffusion. It is convenient to think of the hole rather than the electrons as moving. The hole then acts like a positive charge. In summary, both conduction electrons and valence-band holes can act as charge carriers; the former are negative (n-type), the latter are positive (p-type).

Both electrons and holes move with thermal velocities, velocities of the order of  $10^7$  cm per sec. In so doing, they collide with lattice atoms or impurities now and then. If the average distance between collisions is  $L$ , the average time between collisions is

$$\tau = \frac{L}{\bar{v}} \quad (15)$$

where  $\bar{v}$  is the thermal velocity, as previously defined

In the presence of an electric field  $E$ , an electron or hole, starting from rest, moves a distance  $s = (q/2m)Et$  in a time  $t$ . When  $t = \tau$  the electron makes a collision and must start from rest again.

Hence

$$L = \frac{1}{2} \frac{q}{m} E \tau^2 \quad (16)$$

And the average drift velocity due to the field is

$$v = \frac{L}{\tau} = \frac{1}{2} \frac{q}{m} E \tau = \frac{1}{2} \frac{q}{m} \frac{L}{\bar{v}} E \quad (17)$$

This equation is not exact because some electrons have a remanent forward component of velocity after a collision and others moving at angles to the field are scattered forward. A more refined computation taking these effects into account leads to

$$v = \frac{8}{\pi} \frac{q}{m} \frac{L}{\bar{v}} E \quad (18)$$

instead of Eq. (17).

In both computations, it has been assumed that  $v$  is small compared to  $\bar{v}$  so that the collision time is determined by the thermal velocity. This assumption is valid for all the usual applied voltages. The ratio of drift velocity to field is called the mobility  $\mu$ , where

$$\mu = \frac{8}{\pi} \frac{q}{m} \frac{L}{\bar{v}} \quad (19)$$

where Eq. (18) has been used instead of the less exact Eq. (17).

Note that in many solids, the apparent mass of electrons and holes is not the free-space mass of electrons. Due to the periodic fields they see in crystals, their masses may be as small as a few per cent of the free-electron mass and theoretically may become negative in certain instances. These apparent or effective masses, as they are called, are usually denoted by  $m^*$ .

The conductivity, then, is the product of the number of carriers, the charge they carry, and the mobility, or

$$\sigma = nq\mu \quad (20)$$

Diffusion. The diffusion of electrons or holes — or atoms, ions, or molecules, for that matter — occurs when their density varies from point to point. This variation in density gives rise to a current in the absence of an electric field and is important in many semiconductor devices, including transistors. To illustrate the formation of such a current, consider a plane normal to a one-dimensional distribution of electrons, as shown in Fig. 9. All of the electrons with velocity directed to the right, in a column of length  $L$  and unit-area cross section on the left of the reference plane, will, on the average, cross the reference plane in a time  $\tau$  without making a collision. Similarly, the electrons with velocity directed to the left in a similar column on the right will move to the left. The average density of electrons on the left is  $[n - (dn/dx)(L/2)]$ ; the density on the right is  $[n + (dn/dx)(L/2)]$ .

Hence, the net rate of flow to the right is

$$j_D = (n - \frac{dn}{dx} \frac{L}{2}) \frac{L}{\tau} - (n + \frac{dn}{dx} \frac{L}{2}) \frac{L}{\tau} = - \frac{L^2}{\tau} \frac{dn}{dx} \quad (21)$$

or

$$j_D = - \bar{v} L \frac{dn}{dx} \quad (22)$$

Now  $j_D$  is the diffusion current density and, by definition, the diffusion constant is

$$D = \bar{v} L \quad (23)$$

The relation between the mobility and the diffusion constant is

$$\frac{\mu}{D} = \frac{8}{\pi} \frac{qL}{m\bar{v}} \frac{1}{\bar{v}L} = \frac{q}{kT} \quad (24)$$

This expression is the Einstein relation.

In a region where positive charges, such as holes, are non-uniformly distributed in the  $x$ -direction, and a field is applied in the  $x$ -direction the net current density is

$$j = ne \mu E - De \frac{dn}{dx} \quad (25)$$

If the current is made zero, the equation is easily integrable because  $-\int E dx = V$ , the voltage drop.

The result is

$$n = n_0 \exp(-eV/kT) \quad (26)$$

where  $n_0$  is the density when  $V = 0$ .

This expression is the well-known Boltzmann equation.

Donors, Acceptors, and Traps. So far, it has been assumed that the crystals have been free from defects and have contained no foreign atoms. If this assumption were true, semiconductors and insulators would have little utility — transistors would be impossible

and the oxide cathode would not exist. Fortunately, it is possible to introduce foreign atoms, ions, and vacancies into solids to make them useful. In a covalent crystal, the substitution of a fraction of atoms having one more electron than the host-crystal atoms provides electron "donors." These atoms produce energy levels that lie in the forbidden gap near the conduction band, and are therefore easily ionized. A conventional energy-level diagram with donor levels is shown in Fig. 10. In this figure, the horizontal lines of Fig. 8, indicating the energy levels that constitute the valence and conduction bands, are omitted and only the uppermost state of the valence band and the lowest state of the conduction band are shown. The potential barrier at the surface is indicated by a step. The energy levels introduced by the donors are shown by the dotted horizontal line, dotted to indicate that the donors are localized and do not give rise to a band that extends throughout the crystal. Similarly, the substitution of atoms having one less valence electron than the host atoms of a covalent crystal produces "acceptor levels" near the valence band, levels which by accepting electrons from the valence band thus produce holes in the valence band. Donors can be produced in ionic crystals by substituting ions of higher valence than the negative constituent ions of the crystal, or of lower valence than the positive constituent ions of the crystal. Conversely, acceptors can be produced by substituting ions of lower valence than the negative constituent ions of the crystal, or of higher valence than the positive constituent ions. Vacancies in the negative lattice of ionic crystals also provide donors; such donors are known as F-centers. Positive ion vacancies yield acceptors and are known as V-centers. To maintain charge neutrality of the crystal, the vacancies must be occupied by as many electrons as constituted the net negative charge of the ion removed.

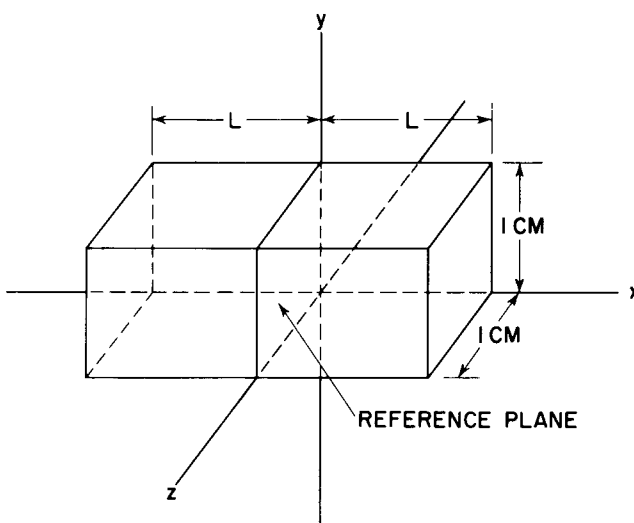


Figure 9. Column for the Computation of a Diffusion Current

Because donor centers and acceptor centers lie in the forbidden gap, they require less thermal energy for ionization than does excitation from the valence

band to the conduction band.\* The number of electrons excited to the conduction band from donors of density  $N_D$  lying at an energy  $\epsilon_D$  below the conduction band is easily computed, by use of the by-now familiar formalism for computing equilibrium distributions. The resulting equation is

$$(N_D - n) N_C W_{12} = n^2 W_{21} \quad (27)$$

where  $n$  is the density of ionized donors, i.e. the number of electrons in the conduction band.

The solution of this quadratic equation is

$$n = \frac{N_C}{2} \exp(-\epsilon_D/kT) \sqrt{1 + \frac{4N_D}{N_C} \exp(\epsilon_D/kT) - 1} \quad (28)$$

When

$$N_D \ll N_C \exp(-\epsilon_D/kT) \quad (29)$$

All of the donors are ionized, and

$$n = N_D \quad (30)$$

When

$$N_D \gg N_C \exp(-\epsilon_D/kT) \quad (31)$$

Only a fraction of the donors are ionized, and

$$n = \sqrt{N_D N_C} \exp(-\epsilon_D/kT) \quad (32)$$

and the activation energy is one-half the difference in energy between the donors and the edge of the conduction band. Fig. 11 is a plot of Eq. (28) for the particular case  $(N_C/2)\exp(-\epsilon_D/kT) = 10^{10}$  and shows the change from full ionization to partial ionization as the density of donors is increased.

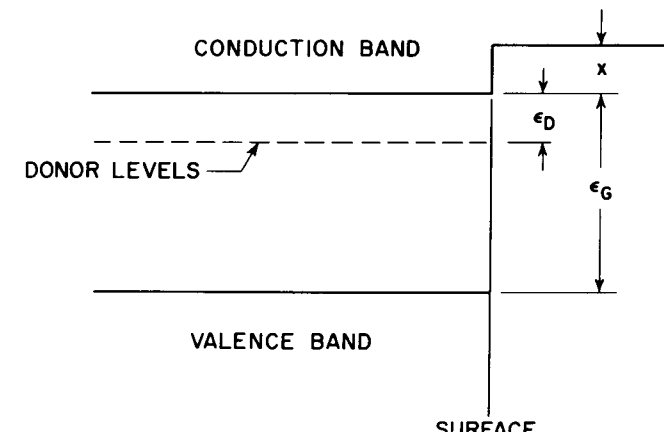


Figure 10. Conventional Energy-Level Diagram for a Solid

\*It is assumed that the energy levels of other donors and of the valence band lie far enough below the energy levels of the donors considered so that these "other donors" and the valence band do not contribute significantly to the occupation of the conduction band.

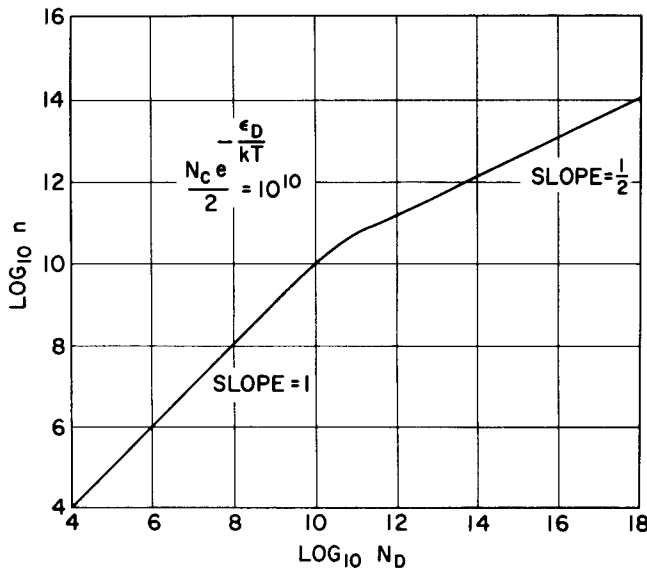


Figure 11. The Density of Electrons  $n$  in the Conduction Band of a Solid as a Function of the Donor Density  $N_D$  When  $N_c e \epsilon_D / kT = 2 \times 10^{10}$

The "doping" atoms normally used in germanium and silicon have such low activation energies that Eq. (29) is satisfied, and all of the donors and acceptors are ionized at room temperature. However, the donors in BaO lie far enough below the conduction band so that Eq. (31) is satisfied, even at the temperatures at which oxide cathodes are operated (1000 to 1100 K). As a result, the oxide cathode requires a high density of donors to provide useful conductivity and emission. These requirements will be discussed in detail later.

Donor and acceptor levels are not the only levels produced by foreign atoms, introduced by intent or accidentally. Unfortunately, foreign atoms may produce levels known as "trapping levels." These are levels in the forbidden gap, unoccupied at zero temperature, which drain electrons from the conduction band, either directly or by emptying donors lying above them. They are particularly pernicious in photoconducting devices. When electrons are excited from the valence band to the conduction band by incident light, many are trapped by these levels. This trapping reduces the photoconductivity and, what is worse, these traps empty very slowly so that electrons dribble back into the conduction band from the traps for a long time after the light has been shut off. This dribbling back results in a very slow decay in the photoconductivity. At present, trapping levels set a definite (and embarrassingly low) limit to the speed of response of photoconductive devices.

Other foreign atoms form recombination centers. These centers trap electrons (or holes). Having done so, they then trap holes (or electrons) which recombine with the charge already trapped, thus destroying electrons and holes in pairs. Such centers may limit the equilibrium densities of electrons and holes obtainable and, therefore, the recombination through centers rather than direct recombination may limit conductivity.

## Conclusion

This section has skinned the aspects of solid-state

physics that pertain to electron emission; the viewpoint has been elementary, some would say naive. However, the intent has been to outline the basic phenomena involved in emission problems and to introduce the jargon that will be encountered in the literature on the subject, without at the same time burdening the reader with mathematical rigor.

## EMISSION MECHANISMS

This section will be devoted to an outline of the various schemes by which electrons are persuaded to leave their natural habitat in solids so that they may be exploited in an environment free from the lattice and impurity collisions that impede their motions in solids. Only the basic mechanisms will be considered and no attempt will be made to detail the artifices used to exploit the various mechanisms.

### Thermionic Emission

Thermionic emission is simply the thermal evaporation of electrons from a solid. Hence, Eq. (12), derived in the preceding section, may be used to write down the evaporation current density

$$j_p = n_v \bar{v}_n \quad (12)$$

This equation gives the particle current. To obtain the electron current, Eq. (12) must be multiplied by the electron charge  $q$ , thus

$$j_e = n_v q \bar{v}_n \quad (33)$$

For a semiconductor, the number of electrons  $N_v$  in the vapor phase is related to the number of electrons in the conduction band by Eq. (10)

$$n_v = n_s \frac{N_c}{N} \exp(-\Delta H/kT) \quad (10)$$

For electrons, the latent heat  $\Delta H$  is the product of the electron charge  $q$  and the electron affinity  $X^*$ ; the number of possible sites  $N$  for electrons in the conduction band is  $N_c$ ; and the number of occupied sites  $n_s$  is the number of electrons in the conduction band  $n$ . Hence, Eq. (10) reduces to

$$n_v = n \exp(-qX/kT) \quad (34)$$

To obtain the emission formula, it remains to express  $n$  in terms of donor density in the semiconductor. Eq. (32) gives the required relation for the semiconductors used as thermionic emitters

$$n = \sqrt{N_D N_c} \exp(-\epsilon_D/2kT) \quad (32)$$

Combining Eq. (33), (34), and (32)

$$j_e = e \bar{v}_n \sqrt{N_c N_D} \exp\left[\frac{-q(X + \epsilon_D/2)}{kT}\right]$$

or

\*In emission problems, it is customary to express  $X$ , and  $\epsilon_D$ , and  $\phi$  in terms of electric potential, i.e., electron volts; this convention will be used henceforth.

$$j_e = AT^2 \sqrt{\frac{N_D}{N_c}} \exp\left[\frac{-q(X + \epsilon_D/2)}{kT}\right] \quad (35)$$

where  $A = \frac{4\pi k^2 m q}{h^3}$

In practical units, the value of A is the familiar

$$A = 120 \text{ amperes cm}^{-2} \text{ deg}^{-2}$$

Note that the work function is the sum of the electron affinity X and one-half the energy gap between the donors and the edge of the conduction band.

For metals where the valence band overlaps the conduction band (see Fig. 7), the solid may be regarded as an intrinsic semiconductor (one having no donors, acceptors or traps) with zero bandgap. Then, Eq. (14) with  $\epsilon_g$  set equal to zero is applicable, i.e.,  $n = N_c$ . Using this value for the electron density in the conduction band is tantamount to setting  $N_D = N_c$ , and  $\epsilon_D = 0$  in Eq. (35).

Thus for a metal

$$j_e = AT^2 \exp(-q\phi/kT) \quad (37)$$

where X of Eq. (35) has been replaced by  $\phi$ , the usual symbol for the work function of a metal.

The work functions of metals are usually high (of the order of 4.5 electron volts) so they are ordinarily used only in high-power transmitting tubes where their thermal stability and insensitivity to ambient gases make them desirable.

The work function of a metal can be reduced by building a dipole layer on the cathode surface. Fig. 12 is an energy-level diagram showing a dipole layer consisting of a monolayer of oxygen, on the metal surface, covered by a monolayer of some low-work-function metal, such as cesium or barium. The oxygen underlayer binds the low-work-function metal to the base metal so that the evaporation rate of the low-work-function metal is greatly reduced. Unfortunately, the evaporation rate is still appreciable. Furthermore, the dipole layer is easily removed by ion bombardment, so that any gas in the tube has a serious effect on such an emitter. To mitigate these difficulties, A. W. Hull invented the "dispenser cathode" in which a reservoir of active material replenishes the dipole layer as it is lost by evaporation or bombardment. More recently the dispenser cathode has received much attention. The Lemmens ("L") and Katz ("M-K") cathodes are examples of the dispenser cathode. In some of these cathodes, alkaline earth oxides and a reducing agent are stored in a reservoir. The reducing agent reacts with the oxides to produce free metals which proceed to the emitting surface through a porous plug by Knudsen flow through the pores or by surface diffusion. If the reducing agent reacts rapidly, the porosity of the plug controls the rate of replenishment; if the reducing agent reacts slowly, the rate of reaction controls the rate of replenishment. In other versions, alkaline earth compounds (oxides, silicates, and aluminates are used) are compacted with finely divided metal powder to form the emitter. These

cathodes are mechanically stable and can be made with precision. Because any loss of dipole layer is replenished, they can be operated at temperatures at which they yield emissions of the order of amperes per  $\text{cm}^2$ .

The measurement of the work function of an emitter is by no means simple. Part of the difficulty arises from the fact that the work function is lowered by an electron-accelerating field at the emitter surface. This effect is known as the Schottky effect.<sup>1</sup> It arises because an electron leaving the surface sees its image in the surface. Thus, in the case of a metal, the force on an electron is

$$F = \frac{q^2}{(2x)^2} - qE \quad (38)$$

where x is the electron's distance from the surface, and E is the applied field. At some distance l from the surface, the force becomes zero and the electron can be regarded as free. This distance is obtained by setting  $F = 0$ . Thus,

$$l = \frac{1}{2} \sqrt{\frac{q}{E}} \quad (39)$$

The work required to remove an electron from the surface is

$$W = \int_0^l \left[ \frac{q^2}{(2x)^2} - qE \right] dx$$

Examination of this equation shows that something is wrong because the integral is infinite. The difficulty is that the image force cannot vary as  $x^{-2}$  down to atomic distances; somewhere near the surface, the image force must change in a manner which keeps the force finite. Schottky ingeniously bypassed the difficulty by dividing up the integral as follows

$$W = \int_0^\infty qf(x) dx - \int_1^\infty \frac{q^2}{(2x)^2} dx - \int_0^l qE dx$$

where  $f(x)$  represents the image force near the surface and behaves as  $q/(2x)^2$  remote from the surface. Integration then gives

$$W = \int_0^\infty qf(x) dx - \frac{q^2}{4l} - qEl \quad (40)$$

Eliminating l by use of Eq. (39) gives

$$W = \int_0^\infty qf(x) dx = q \sqrt{qE}$$

In the absence of field, W must be just  $q\phi$ , where  $\phi$  is the work function. Therefore,

$$W = q[\phi - \sqrt{qE}] \quad (41)$$

In practical units, this relation is

$$W = q[\phi - 3.72 \times 10^{-4} \sqrt{E}]$$

where E is in volts  $\text{cm}^{-1}$

The result shows that the work function is reduced by an electric field and that the equation for the emission of a metal in the presence of a field should be

$$j_e = AT^2 \exp\left[-\frac{q}{kT}(\phi - \sqrt{qE})\right] \quad (42)$$

This equation may be written

$$j_e = j_0 \exp\left[\frac{q}{kT} \sqrt{qE}\right] \quad (43)$$

where  $j_0$  is known as the field-free emission

A plot of the logarithm of  $j_e$  versus the square root of the field should yield a straight line with a zero-field intercept of  $\ln j_0$ . To determine the work function of a metal, it is the logarithm of  $j_0 T^{-2}$  that should be plotted against  $T^{-1}$  to make a so-called Richardson plot. Then, the slope of the line will be  $\phi$  and the intercept will be  $A$ .

For semiconductors, the simple image-force representation is not adequate because the density of electrons is usually so low that the field of the external electron extends a considerable distance into the solid — a Debye length.<sup>2</sup> To complicate matters further, the dielectric constant of semiconductors usually differs substantially from unity. The treatment of a problem of this complexity is beyond the scope of a simple exposition such as this. It will only be noted that Schottky plots and Richardson plots made from the zero-current intercepts obtained on semi-conducting cathodes must be treated with great reserve.

When data for Schottky plots are taken with great precision, it is found that the resulting curve shows periodic deviations from the straight line computed above.<sup>3, 4</sup> These deviations are due to the wavelike nature of the electrons. As the field at the surface increases, the potential barrier keeping electrons in the solid becomes narrower and it acts like a "quarter-wave plate" in optics so that, depending on their velocity (wave length), some electrons are more easily transmitted and others are more completely reflected. The net effect of summing over-all velocities is the periodic variation in emission. The effect is very small, but in the hands of Coomes and his co-workers it has provided a powerful tool for studying the nature of surfaces.

Because of the great difficulty in determining true

work functions, W. S. Nottingham has suggested that the Richardson equation

$$j_e = AT^2 \exp(-q\phi/kT) \quad (37)$$

be written for all thermionic emitters and that  $A$  and  $\phi$  be starred ( $A^*$ ,  $\phi^*$ ) to indicate that they are not true values of the thermionic constants. He proposed the name "work factor" for  $\phi^*$ . This proposal has the merit of providing a basis for the comparison of cathodes without raising the many questions involved in interpreting the constants in fundamental terms.

## Field Emission<sup>5, 6</sup>

Field emission results from the wavelike nature of electrons. It is the periodic deviation from the Schottky line effect carried to the extreme where most of emitted electrons "tunnel" through, rather than moving over the potential barrier. Because the computation of the field-emission formula is complex and laborious, the derivation will not be reproduced here. A computation that illuminates the physical mechanism involved and displays the general functional form of the emission equation will suffice.

Fig. 13 is an electron-energy diagram of a metal with a strong field at the surface. As before,  $\phi$  is the work function and  $\eta$  is the width of the occupied levels. The potential outside of the surface is

$$V = \phi - Ex \quad (44)$$

where  $E$  is the electric field

The triangular area labeled  $A$  is the potential barrier through which the field-emission electrons must penetrate. Also shown is the curve of the distribution of electrons in the various energy states. Notice that there are practically no electrons where the barrier is thin; therefore, most of the emitted electrons must penetrate the barrier where its thickness is

$$S = \frac{\phi}{E} \quad (45)$$

The equation of an electron wave (as in Appendix A) is

$$\psi = \exp(\pm i \frac{2\pi x}{\lambda}) \quad (46)$$

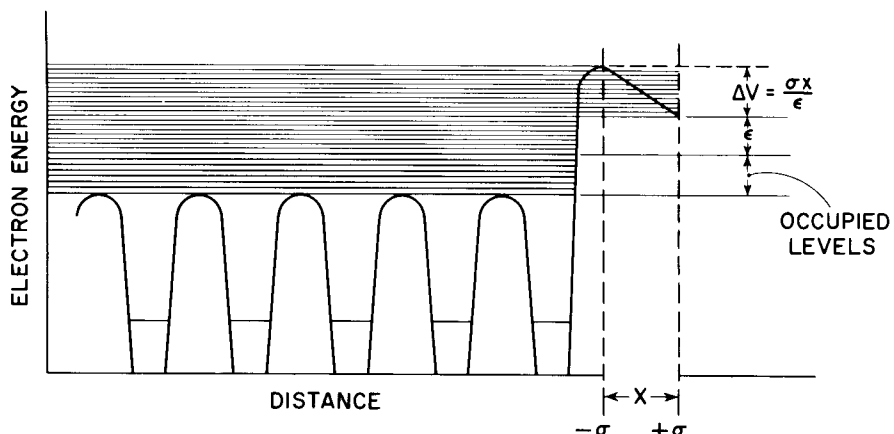


Figure 12. Energy-Level Diagram Showing Reduction of the Work Function of a Metal by Building a Dipole Layer on the Cathode Surface

where

$$\frac{2\pi}{\lambda} = \frac{p}{\hbar}$$

(See App. A, Eq. 4)

and the momentum  $p$  is  $\sqrt{2m(\epsilon - U)}$

The total energy  $\epsilon$  of the electrons at top of the occupied levels (Fermi Sea) is zero.

The average potential energy through the potential barrier is

$$U = \frac{p\phi}{2} \quad (47)$$

Therefore, the momentum is

$$p = \sqrt{-m\phi} \quad (48)$$

$$= i\sqrt{mq\phi}$$

And the propagation constant is

$$\frac{2\pi}{\lambda} = i\sqrt{\frac{mq\phi}{\hbar}} \quad (49)$$

Hence, the wave function is

$$\psi = \exp\left(-\frac{\sqrt{mq\phi}}{\hbar}x\right) \quad (50)$$

The electron density is a maximum on the left and drops off to the right, so it is clear that the negative sign is pertinent to this case. Thus

$$\psi = \exp\left(-\frac{\sqrt{mq\phi}}{\hbar}x\right) \quad (51)$$

Hence, the density of "free" electrons at  $x = s$  is

$$\psi\psi^* = \exp\left(-2\sqrt{\frac{mq\phi}{\hbar}}\frac{\phi}{E}\right) \equiv \exp\left(-C\frac{\phi^{3/2}}{E}\right) \quad (52)$$

This calculation has been very rough; it yields the form of the exponential factor in the emission equation and that is about all. The complete emission formula in practical units is

$$J = 6.2 \times 10^6 \left(\frac{\eta}{\phi}\right)^{1/2} \frac{E^2}{\eta + \phi} \exp\left(-6.84 \times 10^7 \frac{\phi^{3/2}}{E}\right) \quad (53)$$

For the refractory metals,  $\phi$  is about 4.5 electron volts and  $\eta$  is about 10 volts. With  $\phi = 4.5$  electron volts, the exponential is approximately

$$e^{-\left(\frac{6.5 \times 10^8}{E}\right)} \sim 10^{-\left(\frac{2.8 \times 10^8}{E}\right)}$$

Hence, a field of about  $1.3 \times 10^7$  volts per centimeter is required to obtain an emission current of an ampere per square centimeter. Because the emission varies so rapidly with field, a very slight increase in field will run the current into thousands of amperes per square centimeter. However, such field strengths can be obtained only with very sharp points and the heating of these points at the high current densities obtained gives rise to surface diffusion of the atoms of the metal. The surface diffusion tends to lower the surface energy of the solid and rounds off the point so that the field decreases, and with it, the emission. Hence, only the

most refractory metals have found use as field emitters and these, chiefly in field-emission microscopes. An attempt has been made to use germanium as a field-emitter in a surface study; however, the point deformed badly and, on the whole, little was learned.

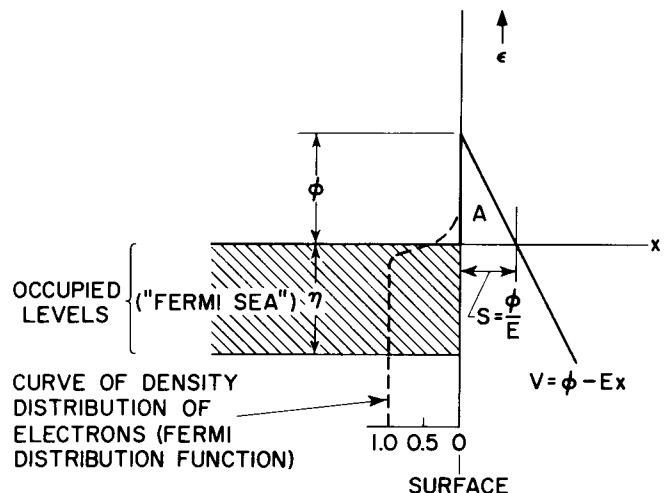


Figure 13. Energy-Level Diagram of a Metal with an Intense Electric Field at the Surface so that Field Emission Occurs

### Photoemission<sup>7, 8</sup>

Photoemission is the ejection of electrons from a solid by photons. The first question to be answered is, what electrons? A consideration of the results of a head-on collision between a photon and a free electron will elucidate the problem. The energy transferred from a particle of mass  $m_1$  and energy  $\epsilon_1$  to a second particle of mass  $m_2$ , at rest initially (keeping in mind conservation of energy and momentum) is

$$\epsilon_2 = \epsilon_1 \frac{4m_1 m_2}{(m_1 + m_2)^2} \quad (54)$$

Suppose the first particle is a photon and the second is an electron. The phenomenon involved is Compton scattering, but to avoid the complications of a relativistic computation a heuristic approach which leads to the correct answer will be used.

As noted earlier, the momentum of a photon is

$$p = \frac{h\nu}{c} \quad (3)$$

If the energy  $h\nu$  is written as

$$h\nu = \frac{p^2}{2m^*} \quad (55)$$

where  $p$  is the momentum and  $m^*$  is the apparent mass

The apparent mass is

$$m^* = \frac{h\nu}{2C^2} \quad (56)$$

This mass is very small; if the energy is one electron volt, the mass is  $m^* \sim 10^{-33}$  gram.

Because this mass is small compared to the mass of

an electron, Eq. (54) may be written

$$\epsilon_2 = \epsilon_1 4 \frac{m_1}{m_2} = \epsilon_1 4 \frac{m^*}{m_2} \quad (57)$$

or

$$\epsilon_2 = \epsilon_1 2 \frac{h\nu}{m_2 c^2} \quad (58)$$

This is the maximum energy transfer in a Compton encounter. If  $h\nu$  is expressed in electron volts, Eq. (58) becomes

$$\epsilon_2 = 10^{-5} h\nu \epsilon_1 \quad (59)$$

Hence, a photon in the visible region of the spectrum, say a 2-volt photon, can transfer only a  $2 \times 10^{-5}$  fraction of its energy to an electron.\* This energy is far from enough to overcome the work function of any material. It now seems clear that a direct encounter between a photon and an electron cannot cause photoemission and that a "three-body" collision is necessary. i. e., the photoelectron must be at least partially "bound" so that neighboring electrons, atoms, or the lattice as a whole can take part, and the stringent momentum conservation requirement encountered in the free-electron collision can thus be relaxed.

In metals, photoelectrons come from the top of the Fermi sea. Thus, the photoelectric threshold occurs at

$$h\nu = q\phi \quad (60)$$

where  $\phi$  is the work function

When  $h\nu$  exceeds  $q\phi$ , the ejected electrons have a maximum kinetic energy of

$$1/2 mv^2 = h\nu - q\phi \quad (61)$$

This is the Einstein equation which, when verified experimentally, clinched the particle concept of light. Because the emitted electrons do not all come from the same depth in the Fermi sea, the curve of yield vs. energy  $h\nu$  has a tail that makes the exact determination of  $\phi$  from photoelectric measurements difficult. This difficulty was obviated by R. W. Fowler who computed the "straggling" effect and arrived at a universal curve that makes possible the determination of  $\phi$

Fowler's formula is given by

$$\ln \frac{I}{T^2} = B + \ln \left[ \frac{h(\nu - \nu_0)}{kT} \right] \quad (62)$$

where

$I$  = the photoelectric current

$B$  = a constant

$T$  = the emitter temperature

\*Similar considerations apply to "electron sputtering." The ratio of electron-mass to atom-mass is of about the same order of magnitude as that above. It seems likely that in "electron sputtering" the incident electron interacts with another electron in an atom or ion, then excites it to a higher electronic state for which the binding energy of the atom or ion to the host crystal is small with the result that the atom or ion departs via dissociation.

$h$  = Planck's constant

$k$  = Boltzmann's constant

$\nu$  = the frequency of the incident light

$\nu_0$  = the frequency of the light when  $h\nu = q\phi$

and

$$f(x) = \begin{cases} e^x - \frac{e^{2x}}{2^2} + \frac{e^{3x}}{3^2} + \dots, & x \leq 0 \\ \frac{\pi^2}{6} + \frac{x^2}{2} - (e^{-x} - \frac{e^{-2x}}{2^2} + \frac{e^{-3x}}{3^2} + \dots), & x \geq 0 \end{cases}$$

The use of the so-called Fowler plot is shown in Fig. 14. The curves labeled  $T_1$  and  $T_2$  are "experimental" curves taken at temperatures  $T_1$  and  $T_2$ , respectively. These are matched to the universal curve by translating them horizontally and vertically. The required horizontal translation gives  $q\phi/kT$  from which  $\phi$  may be computed; the required vertical translation gives the constant  $B$ .

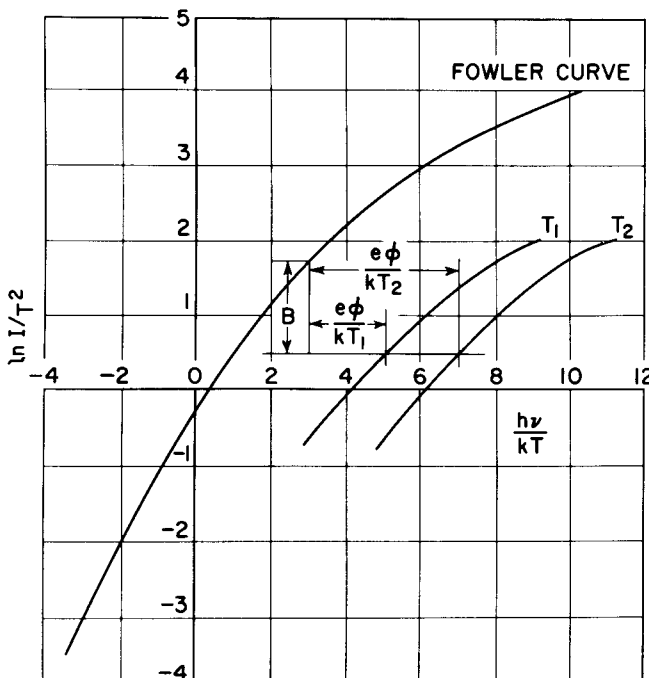


Figure 14. The "Fowler Curve" for Photoelectric Emission and an Example of How the Work Function of a Metal is Determined by Matching Experimental Curves to the Fowler Curve

In semiconductors and insulators, photoelectrons may be obtained from the donor levels and from the valence band. In the former case, a peak, centered at  $\epsilon_D + X$ , is found when the yield is plotted against the energy of the incident photon.\* In the latter case, the yield increases for photon energies exceeding the threshold value of  $\epsilon_g + X$ . Again the yield curve has a "tail" near the threshold. Attempts to determine the true threshold by matching the Fowler curve have met with varying degrees of success; it is not yet clear that a curve based on a metallic model will fit a semiconductor.

\*As before,  $\epsilon_D$  is the depth of the donors below the edge of the conduction band,  $X$  is the electron affinity, and  $\epsilon_g$  is the band-gap energy.

Fig. 15 shows curves of the photoemission of BaO in the inactive state and in a thermionically active state.<sup>9</sup> The effect of the donors produced by activation is apparent in the substantial "tail" on the "active" curve that extends to much lower photon energies than in the inactive case. This tail may be resolved into peaks indicating a set of donor levels at about 2.3 ev below the conduction band and a second set of donor levels at about 1.4 ev below the conduction band. For comparison, Fig. 16 shows the corresponding curves of photoconduction. These curves are displaced from the photoemission curves by  $h\nu \sim 0.5$  ev. In photoconduction electrons need only be excited to the conduction band whereas in photoemission they must be excited over the surface barrier. Hence, the displacement between the photoemission and photoconductivity curves must be equal to the electron affinity, i.e.,  $X \sim 0.5$  ev in the case of BaO.

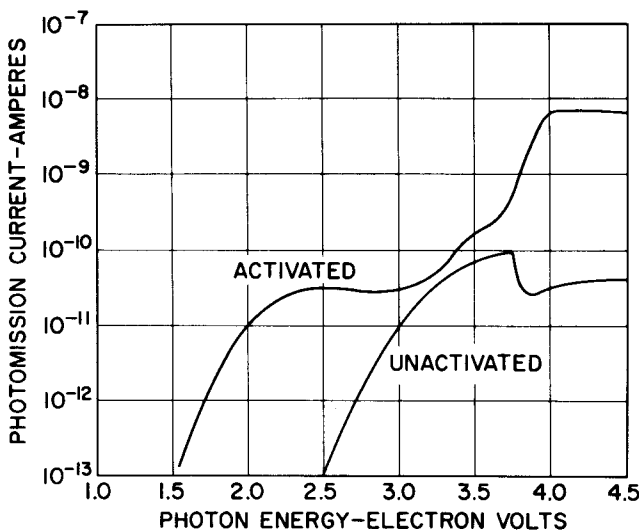


Figure 15. The Photoemission Current vs. Photon Energy for Activated and Unactivated BaO

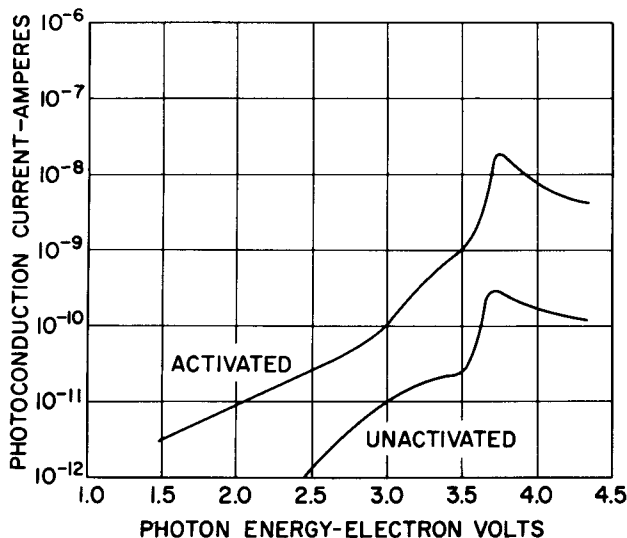


Figure 16. The Photoconduction Current vs. Photon Energy for Activated and Unactivated BaO

The photoelectric yield of metals may be quite high. Hughes and DuBridge cite values of 1 electron for every 14 photons for potassium, and 1 electron for every 4 photons for gold. The usual yield in television pick-up tubes is about 1 electron for every 100 photons.

### Secondary Emission<sup>10, 11</sup>

Secondary emission is the ejection of electrons from a solid by electrons impinging on the solid. The theory of secondary emission is in an unhappy state – no theory fits the experimental results in detail. To illustrate some of the physical notions involved, and to point up some of the features common to all present theories, the theory of Bruining will be discussed.

The first problem is that of computing the energy loss of the impinging electron as it moves into the solid. At the energies required for secondary emission, the electron wave length is so small that the chance of a head-on collision with any other electron in the solid is trivial. Hence the encounter of the oncoming electron with any other electron is fleeting. The momentum transferred to the secondary electron may be written

$$\Delta p = \bar{F}t \quad (63)$$

where  $\bar{F}$  is the average force felt during the encounter time  $t$ , in other words  $\bar{F}t$  is the impulse.

Now  $t$  depends on the range  $l$  of the force  $\bar{F}$  and the velocity of the primary electron

$$v = \sqrt{\frac{2qV}{m}} \quad (64)$$

where  $V$  is the energy in electron volts.

Therefore

$$\Delta p = \frac{\bar{F}l}{\sqrt{\frac{2qV}{m}}} \quad (65)$$

The energy imparted to the secondary electron is

$$\Delta \epsilon = \frac{(\Delta p)^2}{2m} = \frac{(\bar{F}l)^2}{2m \frac{2qV}{m}} \quad (66)$$

This is also the loss of energy of the primary electron. If there are  $n$  encounters per centimeter of path, the energy of the primary electron decreases as

$$\frac{\partial \epsilon}{\partial x} = -n \frac{(\bar{F}l)^2}{2m \frac{2qV}{m}} \quad (67)$$

If the energy  $\epsilon$  is expressed in terms of  $V$

$$\frac{\partial V}{\partial x} = -n \frac{(\bar{F}l)^2}{2mq \frac{2qV}{m}} \equiv -\frac{a}{2V} \quad (68)$$

Integrating yields

$$V^2 - V_0^2 = -ax \quad (69)$$

or

$$V = \sqrt{V_0^2 - ax} \quad (70)$$

where  $V_0$  is the energy of the electron at the entrance surface of the solid

This equation is the Whiddington Law for the loss of energy of an electron moving into a solid.

Terrill has found that for many metals

$$\frac{a}{\gamma} \sim 0.4 \times 10^{12} \text{ volts}^2 \text{ cm}^{-1} \quad (71)$$

where  $\gamma$  is the density of the metal relative to the density of water.

Bruining then writes the contribution to the secondary-emission current  $di_s$  of an element  $dx$  at a distance  $x$  below the surface as

$$di_s = \beta i_r e^{-\alpha x} \frac{d(qV)}{dx} dx \quad (72)$$

where

$\beta$  = a constant

$i_r$  = the primary constant

The "Attenuation factor" for secondary electrons is  $e^{-\alpha x}$ . This attenuation factor accounts for the fact that some of the secondary electrons moving toward the surface are scattered and do not reach the surface.\*

The energy given to secondaries in the interval  $dx$  is  $\frac{d(qV)}{dx} dx$ . The total secondary current is then

$$i_s = \beta i_r \int_0^{x=V_0^2/a} e^{-\alpha x} \frac{d(qV)}{dx} dx \quad (73)$$

This equation may be simplified by the substitution

$$y = -\sqrt{\frac{\alpha}{a}} V \quad (74)$$

It then becomes

$$i_s = \beta i_r q \sqrt{\frac{a}{\alpha}} e^{-r^2} \int_0^r e^{y^2} dy \quad (75)$$

where

$$r = \sqrt{\frac{\alpha}{a}} V_0 \quad (76)$$

This equation has a maximum for

$$V_0 = 0.92 \sqrt{\frac{a}{\alpha}} \quad (77)$$

However, like all other theoretical expressions for secondary emission, when the theoretical maximum is fitted to the maximum of an experimental curve, the rest of the curve fails to fit. Therefore, nothing is to be gained by further discussion of the theory.

Experimentally, the energy distribution of secondary electrons is as shown in Fig. 17. Most of the secondary electrons have an energy of less than 10 electron volts, as shown by the peak on the left. The peak

on the right, centered on the primary energy, results from reflected electrons.

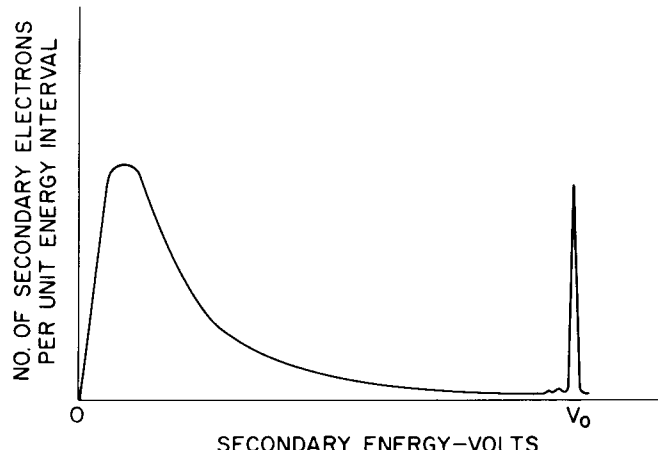


Figure 17. Typical Energy Distribution Curve of Secondary Electrons

The secondary emission ratio  $\delta$ , the number of secondary electrons divided by the number of primary electrons, of a number of metals is shown approximately in Fig. 18. In every case, the maximum yield occurs at about 600 electron volts.

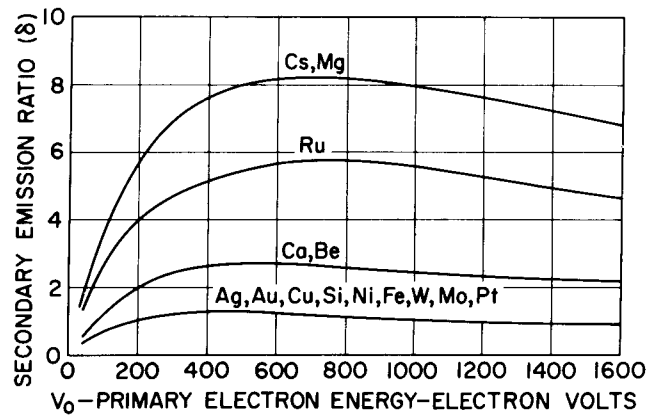


Figure 18. Secondary-Emission Yield vs. Primary-Electron Energy (The curves are approximate and are intended to show only the general behavior and magnitude of the yield of the metals listed)

Compound materials have been found that have yields higher than those of the pure metals. For example, cesium-on-oxygen-on-silver gives a yield of  $\delta = 8$  to 11, and magnesium-on-oxygen-on-silver gives a yield of  $\delta = 8$ . The latter emitter has prompted a study at the University of Minnesota of the secondary-emitting properties of single crystals of magnesium oxide. Recently, Lye at Minnesota has measured the secondary yield from the surface of a single crystal of  $MgO$  prepared by cleaving the crystal in a vacuum of  $10^{-8}$  mm of Hg. He obtained an initial yield of  $\delta = 24$ ; the yield dropped with time and electron bombardment.

Some insulating secondary emitters, notably  $MgO$  films, display the Malter effect, the emission of elec-

\*This factor is used in all secondary-emission theories.

trons for an extended period after the primary beam has been shut off. This phenomenon is believed to result from the charging up of a thin insulating surface layer. Such a charging up produces a field high enough to produce field emission. To illustrate this, suppose that a layer one atom thick were charged to a potential of 1 volt. Then, the field would be approximately  $10^8$  volts per centimeter. This value is high enough to give a very high initial field-emission current.

It may have been noted that there are some "wrinkles" in the curve immediately to the left of the  $V_0$  peak in Fig. 17. In examining these wrinkles critically and in further experiments on the penetration by electrons of thin metallic films, it has been found that there are discrete energy losses by the primary electrons. Ruthemann and Lang have studied this behavior in detail.<sup>12, 13</sup> Pines and Bohm have advanced the theory that these discrete energy losses result from the collective behavior of the electrons in the metal.<sup>14, 15</sup> The mechanism they envisage is plasma oscillation, a behavior found by Langmuir and Tonks in gas discharges.<sup>1</sup> The computation of the characteristic absorption energy proceeds as follows: Suppose the density of electrons in the Fermi sea is  $n$ . Now consider a slab of thickness  $dx$ , as in Fig. 19. Suppose the electrons immediately to the left of the slab are displaced to right by an amount  $\xi$  and those at the right displaced by an amount  $\xi + \frac{d\xi}{dx} dx$ . Then, the net charge moved into the slab is

$$\rho dx = qn \xi - qn \left( \xi + \frac{d\xi}{dx} \right) dx = -qn \left( \frac{d\xi}{dx} \right) dx \quad (78)$$

where  $\rho$  is the charge density. Hence,  $\rho = -qn \frac{d\xi}{dx}$ .

By the Gauss theorem, the divergence of the field  $E$  is  $\partial E / \partial x = \rho / \epsilon = -(qn / \epsilon) (\partial \xi / \partial x)$ , where  $\epsilon$  here denotes the dielectric constant. Integration yields  $E = (-qn / \epsilon) \xi$ . The integration constant has been set to zero, because the field vanishes when there is no displacement.

The equation of motion of an electron then is

$$\frac{d^2\xi}{dt^2} = \frac{q}{m} E = - \frac{q^2 n}{m} \xi \quad (79)$$

This equation is that of a simple harmonic motion with an angular frequency

$$\omega_p = \sqrt{\frac{nq^2}{m\epsilon}} \quad (80)$$

This frequency is the so-called plasma frequency. According to Pines and Bohm, electrons should lose energy in discrete amounts, which Pines calls plasmons, and of magnitude

$$\Delta E = \hbar \omega_p \quad (81)$$

For the case of aluminum, the discrete losses are about 15 electron volts. To see how the theory hangs together, it is interesting to compute the electron density corresponding to this energy loss of 15 electron volts.

Setting

$$E = \hbar \omega = qV \quad (82)$$

with  $V = 15 qV$  gives

$$\omega_p \sim 2 \times 10^{16} \quad (83)$$

From Eq. (80)

$$n = \frac{\omega_p^2 m \epsilon}{q^2} \sim 10^{23} \quad (84)$$

This value is of the right order of magnitude for the density of electrons in the conduction band of a metal. This result does not mean that the theory is correct; the fact is that the theory is the subject of much controversy. Many feel that collisions of the electrons with lattice atoms will provide such strong damping that free oscillation cannot take place. Stern glass, who has done much work on the contribution of inner-shell electrons to secondary emission, has suggested that the discrete losses are in fact due to the excitation of electrons from an inner shell and are indicative of the discrete level from which they came.<sup>16</sup> The resolution of this problem is not yet at hand.

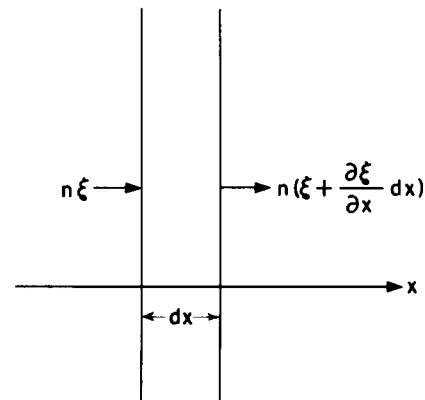


Figure 19. Charge Displacement in an Electron Plasma

## THE PHYSICS OF THE OXIDE CATHODE\*

### Emission-Current Density

The ability of the oxide cathode to emit at current levels of 50-100 amperes  $\text{cm}^{-2}$  for microsecond periods seemed remarkable at one time. In the light of modern solid-state theory, it does not seem as remarkable. In the previous chapter, the emission equation for a semiconducting cathode was found to be

$$j_e = AT^2 \sqrt{\frac{N_D}{N_c}} \exp \left[ -\frac{q}{kT} \left( X + \frac{\epsilon_D}{2} \right) \right] \quad (35)$$

\*Recent research on oxide cathodes is summarized in a chapter entitled "Electron and Ion Motion" by the present writer, in *Halbleiter, III*, edited by W. Schottky, Vieweg and Sohn, Braunschweig. This paper contains an extensive bibliography of oxide cathode work, past and present.

At 1000 K,  $N_c$  is about  $10^{19}$  for electrons. It should be possible to produce donors to about 1 part in  $10^5$ , i. e.,  $N_D = 10^{18}$ . If these donors lie 1.4 electron volts below the conduction band, as DeVore found in BaO, then, with  $X = 0.5$  electron volts, the current density at 1000K should be

$$j_e \sim 40 \text{ amperes cm}^{-2} \quad (85)$$

This current density was obtained by Nergaard and Matheson in pulsed diodes.<sup>17</sup> This current density, however, cannot be maintained indefinitely. Ten years ago, the usual explanation of this phenomenon was that the cathode was deactivated by "poisoning." The writer found it difficult to accept this explanation; he had activated many oxide cathodes by drawing current for extended periods, not by shutting it off, yet under pulse conditions the cathode was supposed to be able to reactivate spontaneously in a few milliseconds in the absence of current.

In 1931, Becker and Sears had shown that oxide cathodes could be activated, at least temporarily, by passing current through them in the back direction.<sup>18</sup> They attributed this phenomenon to an electrolysis of what would now be called donors. (They called it Ba.) In 1945, Sproull published the results of his work on the pulse decay of the oxide cathode, and put forward the hypothesis that pulse decay was due to an electrolytic depletion of a dipole layer on the surface of the cathode.<sup>19</sup> These models, involving electrolysis, appealed to the writer and were developed and extended in a series of studies by the writer and his co-workers (R. M. Matheson, R. H. Plumlee, and H. B. DeVore) to give a coherent model of oxide-cathode behavior.

#### Model of the Oxide Cathode

The model conceives of the oxide cathode as consisting of a semiconducting host material (BaO or a combination of alkaline-earth oxides) containing mobile donors produced by any of a variety of chemical reduction processes. The mobility of the donors permits them to electrolyze and diffuse at the normal operating temperature of the cathode. Not only are the donors mobile, but other constituents of the cathode, such as  $\text{CO}_2$ ,  $\text{O}_2$ ,  $\text{H}_2$ ,  $\text{H}_2\text{O}$ , or their dissociation products, are mobile as well. This may seem to lead to a very complex model of the cathode; however, the model is no more complex than the cathode itself and it is the complexity of the cathode that makes it the ubiquitous emitter that it is.

To give a coherent account of the implications of the mobile-donor model,<sup>20</sup> its principal consequences will be outlined first; then these consequences will be illustrated by experimental data. In brief these consequences are:

1. When no current is flowing, the donors are uniformly distributed throughout the cathode; when current is drawn, the donors electrolyze towards the base metal. This flow sets up a donor density gradient so that back-diffusion of donors occurs. When the current is constant, electrolysis is everywhere balanced by back-diffusion. The donors do not plate

out at the base metal, because of their low solubility in the metal.

2. The resistance of the cathode is a function of the average current. The average current determines the distribution of donors which determine the resistivity. Because donors are depleted from the region of the emitting surface, the voltage drop near the surface is high; because donors accumulate towards the base metal, the voltage drop near the base metal is low. The net effect is that the resistance of the coating rises with the current through it.

3. At modest current levels, a diode may show marked departures from the Child-Langmuir law without being emission limited. This departure is due to the cathode-resistance voltage drop, which reduces the voltage across the vacuum diode. The increase of cathode resistance with life may, in fact, determine the useful life of a tube.

4. At very high current levels, donor depletion reduces the electron density at the emitting surface to the point that emission limitation sets in. It then becomes apparent that the work function depends on the average current.

5. If a pulse is applied to a diode, the initial current will be high but, as the donors redistribute and the resistance of the cathode rises, the current will decay correspondingly. The initial current in a second pulse will depend on the extent of the electrolysis during the first pulse (i. e., on the current density and pulse length) and on the time between pulses during which the donors can diffuse towards the zero-current uniform distribution.

6. If donors are produced at the cathode surface during current flow, the donors flow through the surface-depletion layer into the bulk of the cathode and, in so doing, reduce the resistance of the depletion layer and greatly enhance the electron current. Subsequent to donor production, the conductance of the cathode is increased in proportion to the number of donors added.

7. The electrolysis of oxygen ions in the cathodes increases the oxygen-ion density at the surface and thus enhances the evaporation of oxygen. This electrolysis is a reduction process in which the external power supply that produces the current acts as a reducing agent. It is the mechanism that permits the activation of cathodes on passive base metals, and the mechanism by which a cathode maintains its activity for thousands of hours in the presence of residual oxygen in tubes.

8. Other constituents of the cathode also electrolyze. Among those studies are  $\text{CO}_2$ ,  $\text{H}_2$ , and  $\text{H}_2\text{O}$ . Particularly interesting is the case of  $\text{H}_2\text{O}$ ; it is found that  $\text{H}_2\text{O}$  is absorbed by the cathode when oxygen is eliminated. This effect suggests that the donor in the cathode is actually  $\text{Ba}^{++}(\text{OHe})^{--}$  and that it is the spare electron ( $e$ ) that is easily ionized to provide conductivity. Then, donor electrolysis occurs by proton ( $\text{H}^+$ ) transfer, and the rapid decay of current

under pulse conditions is easily accounted for.

These items do not exhaust the numerous aspects of the oxide cathode that might be discussed in terms of the present model. However, they illustrate the features pertinent to the activation and life of cathodes and to the limitations of a cathode in practical use.

### Cathode Conductivity

In considering cathode conductivity, it is well to start with consideration of the conductance of a cathode in the absence of current in order to have a reference base.

The conductivity is

$$\sigma = nq\mu \quad (20)$$

To obtain the conductance per unit area, it is merely necessary to divide by the thickness of the cathode  $d$ , thus

$$g = \frac{nq\mu}{d} \quad (86)$$

The thickness  $d$  is about  $10^{-2}$  centimeter, and  $\mu$  has been measured by Pell to be about 10. It remains to determine  $n$  from Eq. (31), using DeVore's value for  $\epsilon_D$ , i.e.,  $\epsilon_D = 1.4$  electron volts. Then, with  $N_D = 10^{18}$ , as before,

$$n = \sqrt{N_c N_D} \exp(\epsilon_D/2kT) 10^{15} \text{ cm}^{-3} \quad (87)$$

and

$$g \sim 10^{-1} \text{ mho cm}^{-2} \quad (88)$$

In other words, the resistance of a unit area of the cathode with no current is about 10 ohms. When current is drawn this resistance rises very markedly, and at high currents the heating due to cathode resistance becomes very large.

In practical cathodes, this problem is ameliorated by making cathodes porous.<sup>21, 22</sup> Part of the conduction then occurs through the pores where the mean-free-path of electrons is large. To illustrate the order of magnitude of pore conductivity:

Eq. (34) gives the density of the electrons in the pores

$$n_v = n \exp(-qX/kT) \quad (34)$$

With  $n \sim 10^{15} \text{ cm}^{-3}$ , as above, and  $X = 0.5 \text{ ev}$ ,

$$n_v \sim 3 \times 10^{12} \quad (89)$$

The mobility is

$$\mu = \frac{8}{\pi} \frac{qL}{m\bar{v}} \quad (19)$$

With  $L \sim 10^{-3} \text{ cm}$

$$\mu \sim 10^4 \quad (89)$$

Then,  $g \sim 5 \times 10^{-1} \text{ mho cm}^{-2}$ , i.e., the pores have a

conductivity about 5 times as large as that of a solid coating.

In cathodes made by coating silicon-bearing nickel, there is another resistance to be concerned about, namely interface resistance.<sup>23, 24</sup> Interface resistance arises from the diffusion of silicon out of the nickel and the subsequent reaction with  $\text{BaO}$  to form barium orthosilicate ( $2\text{BaO} \cdot \text{SiO}_2$ ), which is an insulator. Depending on the thickness of the layer and on its activation (it is an impurity semiconductor), the resistance of the layer may range from a fraction of an ohm to thousands of ohms. The presence of interface resistance is easily detected because, in its presence, the current displays a decay with a time constant of about 1 microsecond. Because the decay of current due to donor depletion has a time constant of the order of a millisecond, the separation of interface resistance from bulk resistance is easy. When both are present, a diode has an equivalent circuit shown in Fig. 20. This circuit is valid at a given average current level; if the current level is changed, the circuit constants must also be changed.  $R_1$  represents the initial sum of interface resistance and bulk resistance.  $C_2$  with  $R_1$  gives a time constant of about a microsecond and, thus, accounts for the interface decay.  $R_1$  is usually about 5 times  $R_0$  in the milliamperes plate-current range.  $R_1$  and  $R_0$ , together with  $C_1$ , have a time constant of about 1 millisecond, which corresponds to depletion decay. The latter decay is very embarrassing in dc oscilloscopes, because at an average current of 25 ma  $\text{cm}^{-2}$  the decay may amount to 5 per cent.

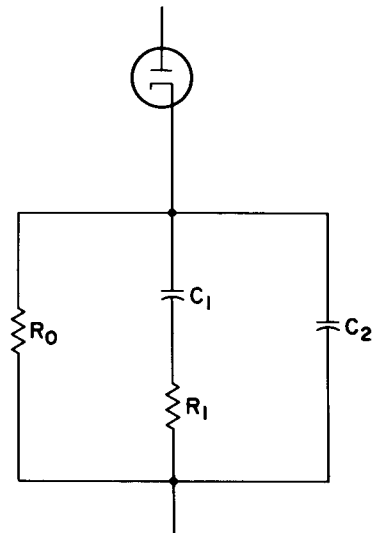


Figure 20. The Small-Signal Equivalent Circuit of a Diode with a Given Direct Current

The effect of cathode resistance on the current-voltage characteristic of a diode is illustrated in Fig. 21, which was drawn from data of Eisenstein.<sup>25</sup> To obtain these curves, Eisenstein measured the velocity distribution of electrons emerging from an aperture in the anode of a diode having an oxide cathode. The retarding potential required to stop electrons is equal to the potential drop in vacuum through which the electrons have fallen. Hence, the applied voltage minus the stop-

ping voltage is the potential drop through the cathode. The lower curve is the measured diode characteristic. The upper solid curve is the diode characteristic corrected for the cathode voltage drop. The dotted curve is the computed perveance line. It appears that the current is, in fact, space-charge limited and that the diode characteristic is deformed by the cathode voltage drop, which is 275 volts at an applied voltage of about 1500 volts.

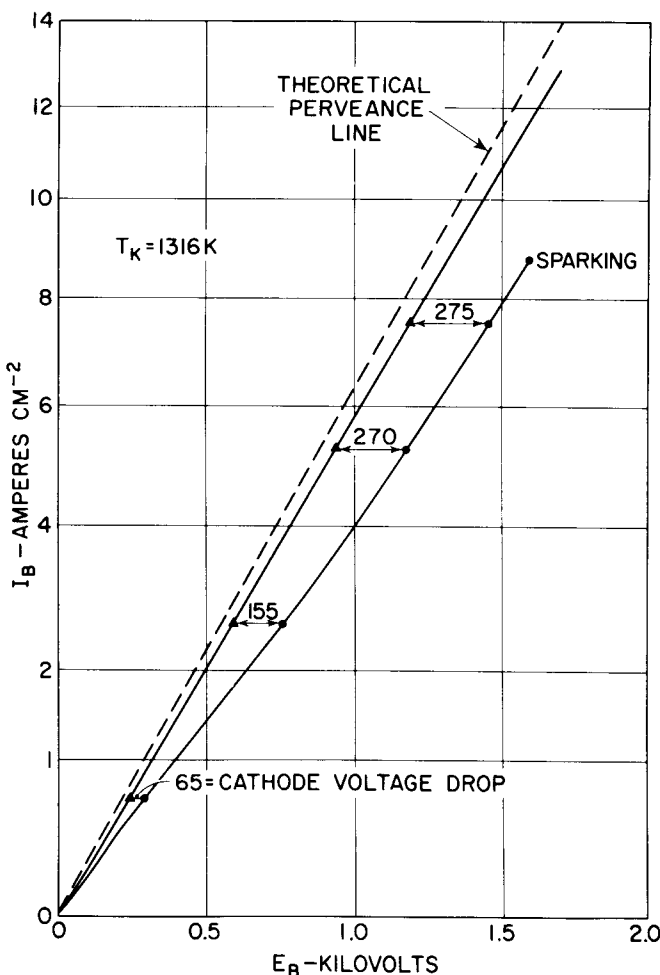


Figure 21. The Effect of Cathode Resistance on a Diode Characteristic (after Eisenstein)

The effect of cathode resistance on tube life is illustrated in Fig. 22. The data pertain to eight tubes and have been averaged for each point on the curves. The curve labeled  $I/I_0$  is the ratio of emission to the emission at the beginning of life, both measured in a factory emission test set. The curve labeled  $P/P_0$  is the ratio of power output into a standard load to the power output at the beginning of life. If it is supposed that the drops in emission and power output are due to an increase of cathode resistance, it is possible to compute the change in cathode resistance with life from the  $I/I_0$  curve and then compute a  $P/P_0$  curve for comparison with the experimental curve. The resistance change was computed from:

$$R_K = \frac{I_0^{2/3} - I^{2/3}}{\alpha^{2/3} I} \quad (90)$$

where  $R_K$  is the cathode resistance and  $\alpha$  is the perveance of the tube. Because the cathode resistance acts as a negative feedback resistor, it reduces the apparent transconductance  $g_m$  according to the relation

$$\frac{g_m}{g_{mo}} = \frac{1}{1 + g_{mo} R_K} \quad (91)$$

where  $g_{mo}$  is the true transconductance of the triode. Finally, the ratio of power output to initial power output is

$$\frac{P}{P_0} \sim \left( \frac{g_m}{g_{mo}} \right)^2 \quad (92)$$

When this computation was carried out, the computed values of  $P/P_0$  were in agreement with the measured values. At the end of life, the cathode resistances of the tubes were measured and found to agree with the resistance computed from  $I/I_0$ . Finally, an attempt to measure emission was made. When the cathode resistance was corrected for, there was no evidence of emission limitation up to an ampere per  $\text{cm}^2$ . It appears that these tubes failed solely because of an increase of cathode resistance with life. It also appears that the factory test set did not measure actual emission; it measured a current limited by cathode resistance.

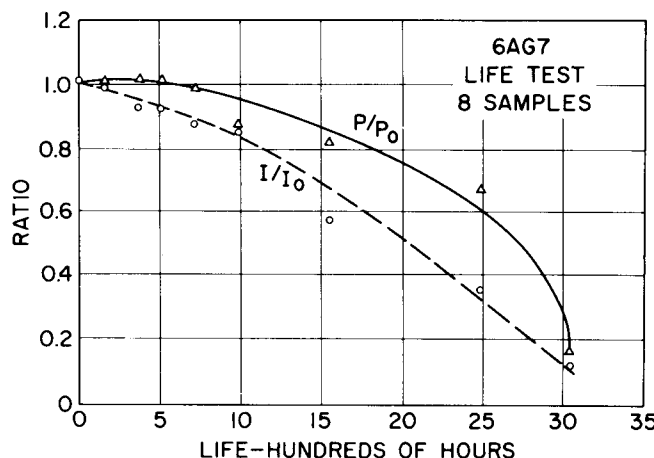


Figure 22. The Effect of Cathode Resistance on Tube Life

### Pulse Operation of Oxide Cathodes

The work function of an oxide cathode is a function of the average current through the cathode. This relationship is illustrated in Fig. 23, which shows a set of Schottky plots obtained by operating the cathode at the average plate currents designated by  $I_{DC}$  in the figure and then delineating the Schottky curves with a short pulse. The zero-voltage intercepts of these curves are the field-free emissions, and are a measure of the work function. As the average current is increased from  $3.5 \times 10^{-6}$  to  $13.2 \times 10^{-3}$  amperes, the work function increases by about 0.11 electron volts.

Because the pulse operation of oxide cathodes is of importance in radar application, it is worth examining

the pulse behavior in a little detail.<sup>20</sup> The complete decay of cathode current is shown in Fig. 24. Although this tube was capable of an initial pulse emission of 40 amperes  $\text{cm}^{-2}$ , a measurement at this current level could not be made because the anode would have melted; hence, a low initial current was used. Note that the time constant is of the order of a millisecond and decay is almost complete in one second.

That the resistance of the cathode changes during pulse decay is shown in Fig. 25. This series of curves

was obtained by interrupting the anode voltage for a few microseconds during a 145-microsecond pulse and measuring the current voltage characteristic during re-application of the voltage. Notice that the departures from linearity of these curves start at very low voltages. If decay were due to emission limitation only, the curves should coincide in the low-current region and then break off abruptly at saturation. The early departure, which increases with elapsed time, shows that the internal resistance of the cathode increases during decay. After the long pulse, the E-I characteristics

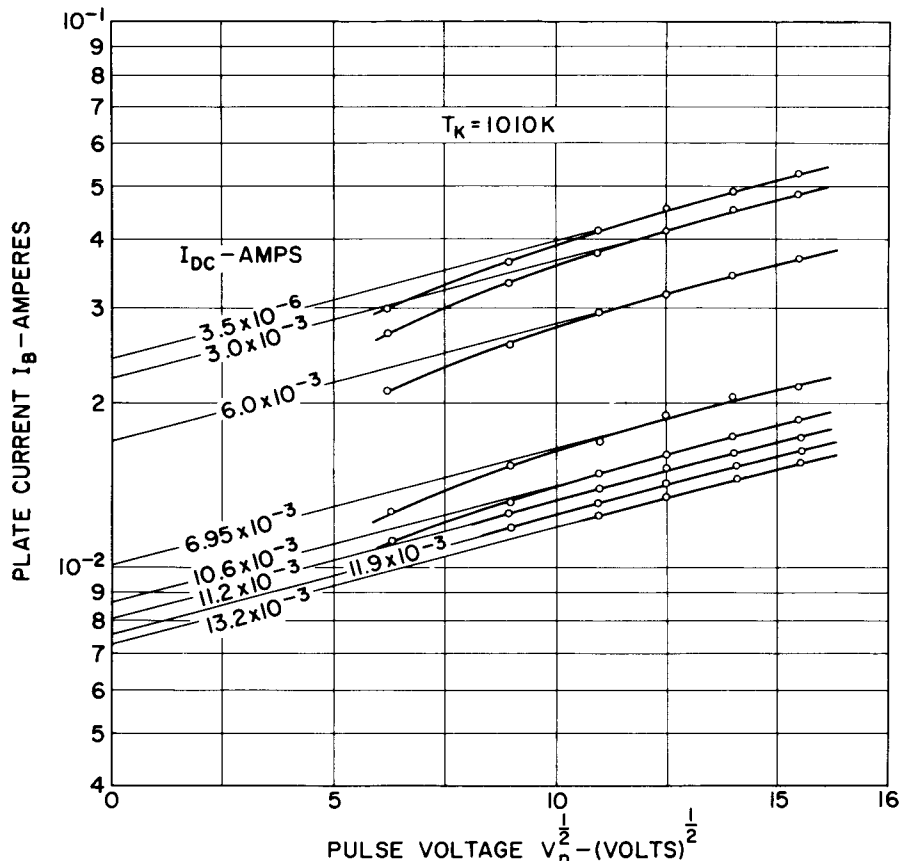


Figure 23. Schottky Curves Showing the Effect of Average Current on the Work Function of an Oxide Cathode

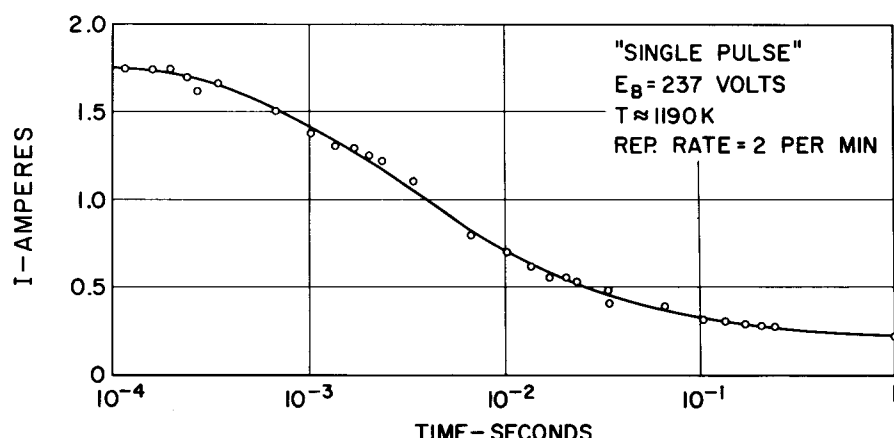


Figure 24. The Decay of the Current from an Oxide Cathode During a One-Second Pulse

were sampled with short pulses during recovery. Under these conditions, the curves of Fig. 25 are retraced in reverse order. Fig. 26 shows how the current decays and recovers during and after the 155-microsecond pulse. The variation of peak pulse current with duty is shown in Fig. 27. Notice that the peak pulse and dc emissions approach one another as the cathode temperature is reduced. This result is to be expected; as the temperature is lowered, so is the donor mobility, and at low-enough temperatures the donors will be "frozen in," and no pulse decay will occur.

### Donors and Their Formation

The subsequent discussion relates to what the donors in the oxide cathode are, and how they are formed. The high diffusion rate of donors required to account for pulse decay suggested that they were F-centers—oxygen vacancies occupied by two electrons. To obtain data on this possibility, cathodes were activated at the receiving end of R. H. Plumlee's 60-degree mass spectrometer using the analyzer as a pure and controllable

source of the reducing metals, Ba, Ca, Sr, and Mg.<sup>26</sup> Fig. 28 shows a typical result of depositing one of these metals (Ba) on an inactive cathode. When deposition starts, the electron current  $I$  rises markedly; when deposition stops, the electron current falls to an asymptotic value higher than the initial current. The rise during deposition is due to donors migrating through the depletion layer. The donors move slowly compared to the electrons, so that the electron current rises markedly in order to maintain space-charge neutrality. The effect is somewhat analogous to the gas amplification that occurs in a gas-filled photocell. The shape and magnitude of the deposition curves are independent of the metal used. Mg has an ionic radius of 0.78 Å., Ba has an ionic radius of 1.43 Å. Therefore, if the metals actually moved into the cathode, Mg should move very much more rapidly than Ba. That it does not suggests that neither is the donor, but that all of these reducing metals produce something else—perhaps F-centers—that does move into the cathode. The increase in emission subsequent to deposition is proportional to the amount of metal deposited and is independent of

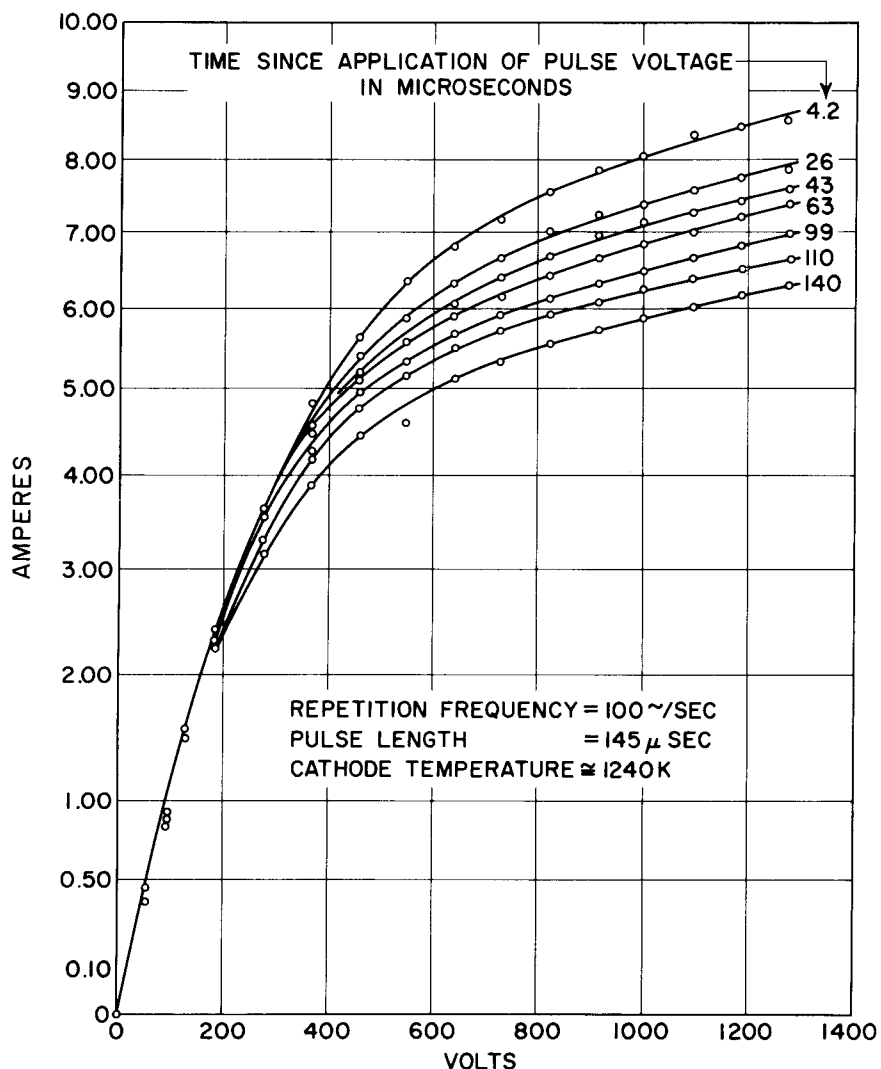


Figure 25. Current-Voltage Characteristics of a Diode as a Function of Elapsed Time During a 145-Microsecond Pulse

which metal is used. This result is shown in Fig. 29 in which  $\Delta I/I_0$  is the fractional increase in emission and  $N$  is the number of monolayers of metal deposited. In computing  $N$  from the measured ion current and time of deposition, it was assumed that the actual cathode area was the projected area.

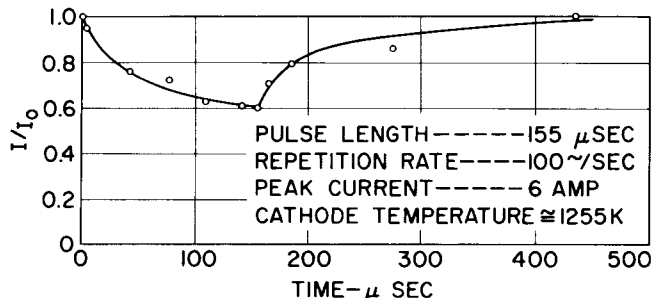


Figure 26. The Decay and Recovery of the Pulsed Emission of an Oxide Cathode (The available current during recovery was measured with a short sampling pulse)

As was noted in an earlier section, the amount of anything in a solid is related to the amount of the same thing in the gas phase by the relation

$$n_v = n_s \frac{N_c}{N} \exp(-\Delta H/kT) \quad (10)$$

To study how the constituents of an oxide cathode are related to the gas-phase constituents of a vacuum tube, Plumlee installed a diode at the source end in his mass spectrometer.<sup>27</sup> The anode of the diode was apertured so he could examine the evaporation products of the cathode. The pressure in the spectrometer was less than  $10^{-7}$  mm of Hg. (If this value seems like a good vacuum, recall that at this pressure about  $3 \times 10^{-2}$  monolayers of atoms are deposited on the cathode sur-

face from the gas phase every second. If these atoms did not re-evaporate, they would increase the thickness of the cathode about 2 mils in 1000 hours.)

The equilibrium pressure of oxygen in contact with an oxide cathode proved of particular interest. It was found that the rate of evaporation of neutral  $O_2$  was proportional to the voltage applied to the diode. Becker had observed this behavior in 1929. Fig. 30 shows the results of Plumlee's measurements. The voltage-dependent evolution of  $O_2$  becomes less and less as the cathode activates (the state of activity is noted in the figure.) As was pointed out earlier in this section, the enhanced evaporation results from the electrolysis of oxygen ions to the surface. When oxygen evaporates, donors are formed. Because elimination of oxygen may seem tantamount to producing excess "free" barium, this experiment might be interpreted to show that the donors are barium atoms, a view widely held in the past. Recent experiments of Timmer at Cornell University show that this view is untenable.<sup>28</sup> Timmer has measured the Ba vapor pressure required to maintain excess Ba in  $BaO$ . His measurements show that in order to maintain the density of excess Ba in the cathode necessary to make the cathode active, a Ba vapor pressure of  $10^{-6}$  mm of Hg is required. Hence, in any tube pumped to  $10^{-7}$  mm of Hg or better, the donors cannot be free barium. A possible alternative will be discussed later.

Because the  $CO_2$  peak observed in these measurements was larger than the  $O_2$ ,  $H_2$ , and  $H_2O$  peaks, the behavior of  $CO_2$  was examined in somewhat more detail than the other peaks. Fig. 31 shows the behavior of the  $CO_2$  peak as a function of time when the anode is turned on and off. When the anode voltage is turned on,  $CO_2$  electrolyzes to the surface, enhances the evaporation rate, and the vapor pressure of  $CO_2$  rises until the gas-phase thermal current of  $CO_2$  to the surface just balances the

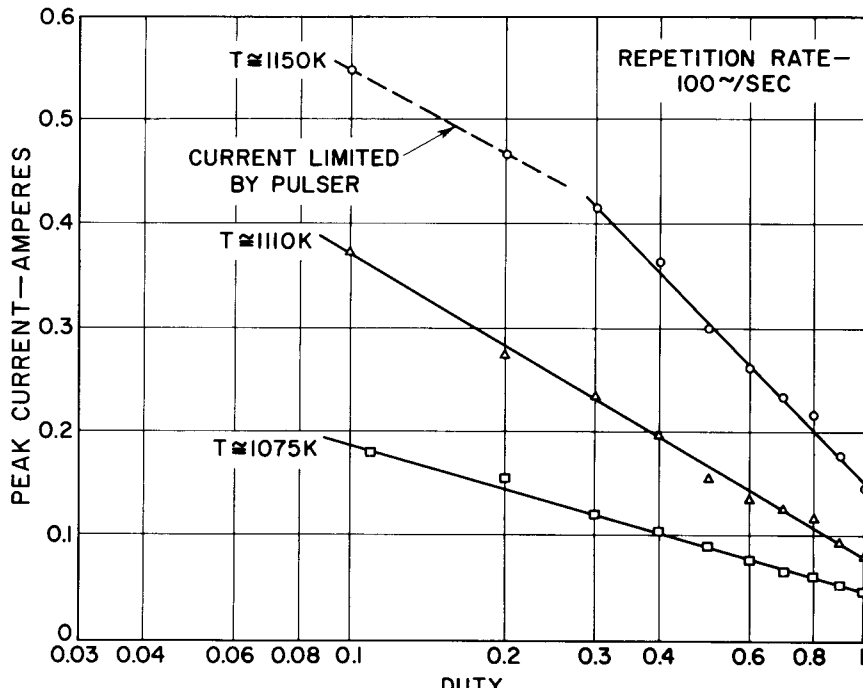
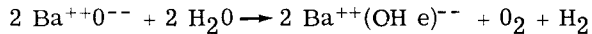


Figure 27. Peak Pulse Current vs. Duty for an Oxide Cathode

enhanced evaporation rate. Then, the peak height becomes constant. When the anode voltage is turned off, the evaporation rate drops and the cathode "soaks up"  $\text{CO}_2$  until the initial situation is restored.

The  $\text{H}_2$  (neutral) peak behaves in the same way. The water peak proved the exception — its behavior was the reverse of that of  $\text{O}_2$ ,  $\text{H}_2$ , and  $\text{CO}_2$ . This behavior is shown in Fig. 32. Aside from the spikes, which have yet to be explained, the general behavior shows that the cathode absorbs  $\text{H}_2\text{O}$  when anode voltage is applied. It was some time before an explanation of this behavior was found and a new class of donors had to be "invented" before the explanation would hang together. The "invention" and explanation is Plumlee's.<sup>29, 30</sup> It can be summed up by the chemical equation



Thus, water (in small amounts) reacts with  $\text{BaO}$  to form a donor with the concurrent release of  $\text{O}_2$  and  $\text{H}_2$ , and the behavior of  $\text{O}_2$ ,  $\text{H}_2$ , and  $\text{H}_2\text{O}$  is tied together. The hydrogen nucleus (a proton) carries a positive charge;

therefore, it should electrolyze into the cathode on application of voltage in the forward direction of the diode. Furthermore, every oxygen ion in the lattice is a possible site for the proton. On this account alone the diffusion rate should be about 5 to 6 orders of magnitude faster than any vacancy diffusion mechanism. The activation energy for the diffusion of protons in ice has been measured and found to be about 0.25 electron volts. This agrees with the measurements of the "activation energy for pulse decay" (0.25 to 0.4 electron volts.) The diffusion rate of protons in  $\text{BaO}$  has been computed roughly, assuming that every oxygen ion is a possible site and that the activation energy is 0.25 electron volts. The result agrees with the diffusion rate required to account for pulse decay. Thus, Plumlee's hypothesis ties together a variety of phenomena qualitatively and, from present indication, quantitatively.

The oxide cathode is not yet completely understood. However, considerable progress has been made since World War II and the vast accumulation of knowledge of the oxide cathode in the fifty odd years since its discovery in 1904 is taking on a unity and coherence that

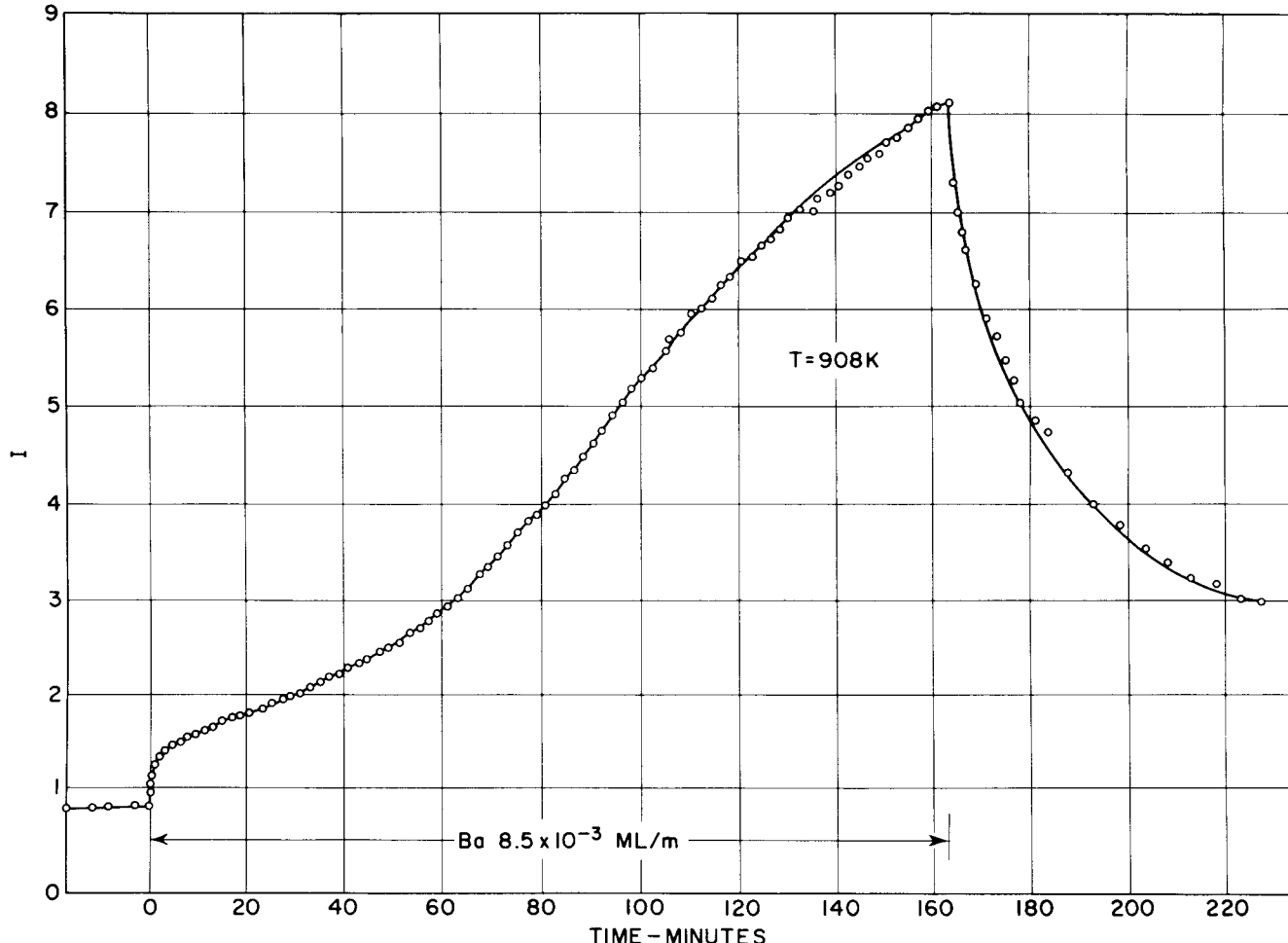


Figure 28. The Current Response of a Diode when Ba is Deposited on the Oxide Cathode. (The deposition rate is  $8.5 \times 10^{-3}$  monolayers per minute, computed on the assumption that the cathode is a smooth  $\text{BaO}$  crystal face.)

promises a complete understanding in the foreseeable future.

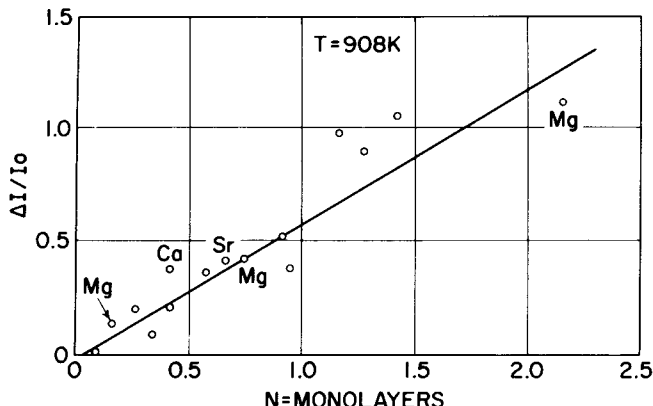


Figure 29. The Fractional Change in Activity of an Oxide Cathode as a Function of the Number of Monolayers of Reducing Metal Deposited (The unmarked points are for Ba)

#### APPENDIX A. THE "WAVE EQUATION" FOR ELECTRONS, AND THE DENSITY OF STATES

##### The Wave Equation

The simplest wave equation that can be written mathematically is the one-dimensional wave progressing in the x-direction.

$$\psi = \exp(-i \frac{2\pi x}{\lambda}) \quad (A1)$$

This function satisfies the differential equation

$$\frac{d^2\psi}{dx^2} + \left(\frac{2\pi^2}{\lambda}\right) \psi = 0 \quad (A2)$$

If  $\lambda$  is expressed in terms of De Broglie's relation

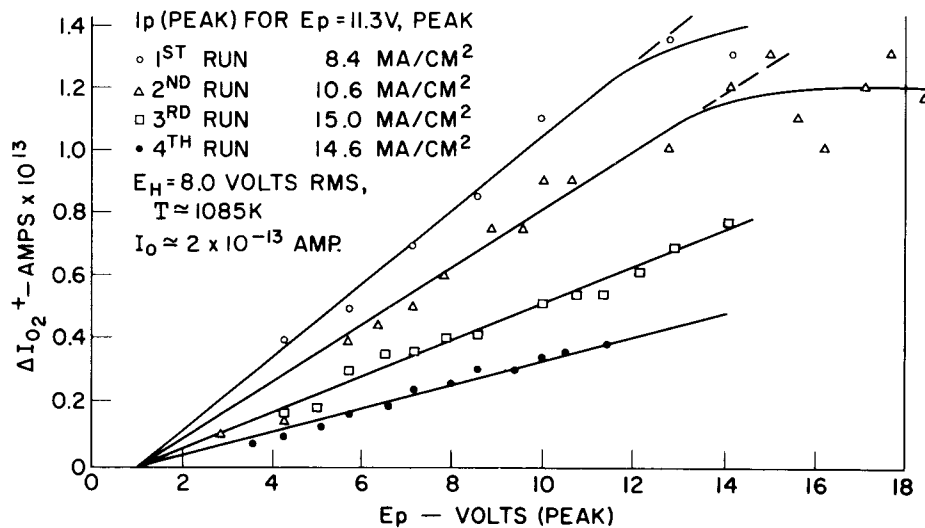


Figure 30. Oxygen Evolution from a BaO Cathode as a Function of Diode Voltage and Cathode Activity (The state of cathode activity for each run is noted in the table)

$$\lambda = \frac{h}{p} \quad (A3)$$

the propagation constant becomes

$$\frac{2\pi}{\lambda} = \frac{2\pi p}{h} = \frac{p}{\hbar} \quad (A4)$$

$$\text{where } \hbar = h/2\pi$$

Now express the momentum  $p$  in terms of the total energy  $\epsilon$  and the potential energy  $U$ :

$$\frac{p^2}{2m} = \epsilon - U \quad (A5)$$

When the appropriate substitutions are made, the wave equation becomes

$$\frac{\partial^2 \psi}{\partial x^2} + \frac{2m}{\hbar^2} (\epsilon - U) \psi = 0 \quad (A6)$$

This is the one-dimensional form of Schrodinger's wave equation. The above manipulation must not be regarded as a derivation of Schrodinger's equation. It is no more possible to derive this equation from first principles than it is to derive Newton's Laws from them. Schrodinger's equation should be regarded as an empirical formula, summing up the experience of the time, fortified by the vast number of predictions made from it which have been experimentally confirmed. Like Newton's laws, it has its weaknesses and fails to predict the relativistic effects now accounted for by its generalization, the Dirac wave equation.

The wave function  $\psi(x)$  is interpreted as a quantity such that  $\psi(x) \psi^*(x) dx$  is the probability that the electron will be found in the interval between  $x$  and  $x + dx$  ( $\psi^*$  is the complex conjugate of  $\psi$ ).

##### A Simple Case of Quantization

Consider an electron in a one-dimensional potential

well such that  $U = 0$  when  $0 \leq x \leq a$ , and  $U = \infty$  outside of the well. Inside the well the wave equation is

$$\frac{\partial^2 \psi}{\partial x^2} + \frac{2m}{\hbar^2} \epsilon \psi = 0 \quad (A7)$$

And its solution is

$$\psi = A \cos \alpha x + B \sin \alpha x \quad (A8)$$

Where

$$\alpha^2 = \frac{2m}{\hbar^2} \epsilon \quad (A9)$$

Because the electron is inside the well and the wave function must be continuous at the boundary between in-

side and outside,  $\psi$  must vanish at the edges of the well, i. e.,  $A = 0$ ,  $\alpha = \frac{n\pi}{a}$ ,  $n = 1, 2, 3, \dots$

Therefore,

$$\epsilon = \frac{\pi^2}{2m} \left( \frac{n\pi}{a} \right)^2 = \frac{1}{8m} \left( \frac{nh}{a} \right)^2 \quad (A10)$$

and the possible energy states are discrete. The corresponding classical momenta are

$$p = \pm \sqrt{2m\epsilon} = \pm \frac{nh}{2a} \quad (A11)$$

and are also discrete

### The Density of States for a Free Electron

In the subsequent discussion of the distribution of

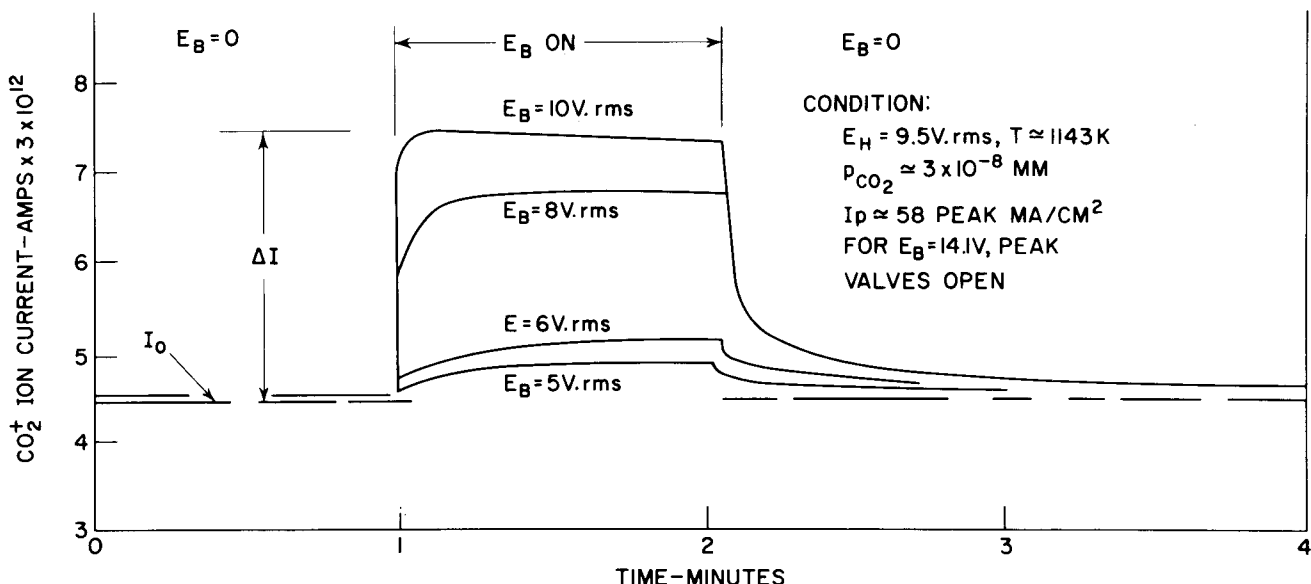


Figure 31. Carbon-Dioxide Evolution of a BaO Cathode as a Function of Time and Anode Voltage

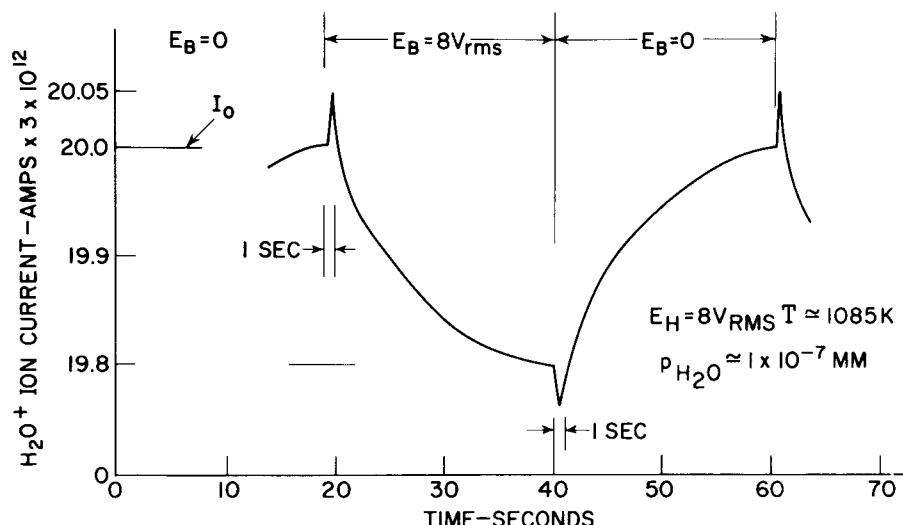


Figure 32. Water Evolution of a BaO Cathode as a Function of Time and Anode Voltage

"free" electrons among possible energy states, the density of states, i. e., the number of states in a given energy interval, must be known. This value may be obtained from the results of Eq. (A11) above.

If the size of the well— $a$  in Eq. (A10)—is increased, the difference in energy between discrete states diminishes and ultimately becomes less than  $kT$ , the thermal energy of the electrons, and the electrons become "free." Then the number of states in the momentum interval  $\Delta p$  is

$$\Delta n = \frac{\Delta p}{h} a \quad (A12)$$

The factor  $1/2$  in Eq. (A11) must be dropped in the enumeration because both plus and minus  $p$  correspond to the same energy. For the case of a three-dimensional box of dimensions  $abc$ , the relation corresponding to Eq. (A12) is seen to be

$$\Delta n = \frac{\Delta p_x \Delta p_y \Delta p_z abc}{h^3} \quad (A12a)$$

where  $p_x$ ,  $p_y$ , and  $p_z$  are the  $x$ ,  $y$ , and  $z$  components of the momentum

Thus, the number of states per unit volume of space is the volume in momentum-phase space  $\Delta p_x$ ,  $\Delta p_y$ ,  $\Delta p_z$  divided by  $h^3$ . In other words, each state occupies a volume  $h^3$  in phase space.

To compute the number of states in an energy interval, it is convenient to write Eq. (A12a) in spherical coordinates. The volume in a spherical shell of thickness  $dp$  and radius  $p$  is

$$dV_p = 4\pi p^2 dp \quad (A13)$$

In terms of energy, this equation becomes

$$dV_p = 2\pi (2m)^{3/2} \epsilon^{1/2} d\epsilon \quad (A14)$$

Then, the number of states in the energy interval between  $\epsilon$  and  $(\epsilon + d\epsilon)$  is

$$dN = \frac{2\pi (2m)^{3/2}}{h^3} \epsilon^{1/2} d\epsilon \quad (A15)$$

which is the required relation.

## APPENDIX B. FERMI-DIRAC STATISTICS

### The Transitions Between Two "States"

Consider a group of  $N_1$  states lying in an energy band not exceeding  $kT$  ( $k$  is Boltzmann's constant) in width centered at an energy  $\epsilon_1$  and a second similar band of  $N_2$  states centered on an energy  $\epsilon_2$ . Then the number of states occupied in the first band is the number of states multiplied by the probability of occupancy

$$n_1 = N_1 \left[ \exp \left( \frac{\epsilon_1 - \epsilon_F}{kT} \right) + 1 \right]^{-1} \quad (B1)$$

Similarly, the number of occupied states in the second

band is

$$n_2 = N_2 \left[ \exp \left( \frac{\epsilon_2 - \epsilon_F}{kT} \right) + 1 \right]^{-1} \quad (B2)$$

Eliminating  $\epsilon_F$  between the two equations, yields

$$n_1 (N_2 - n_2) e^{-\epsilon_2/kT} = n_2 (N_1 - n_1) e^{-1/kT} \quad (B3)$$

By multiplying through by a constant, this expression may be written

$$n_1 (N_2 - n_2) W_{12} = n_2 (N_1 - n_1) W_{21} \quad (B4)$$

This equation admits of a simple interpretation in terms of a bimolecular reaction:  $n_1$  is the number of particles in the  $N_1$  states, i. e., the number of particles available for transitions to the  $N_2$  states;  $(N_2 - n_2)$  is the number of unoccupied states to which transitions can be made;  $W_{12}$  is a rate-constant such that  $N_1(N_2 - n_2) W_{12}$  is the rate at which particles make transitions from the  $N_1$  states to the  $N_2$  states. Then Eq. (B4) merely states that under equilibrium conditions there is no net exchange of particles between the states. The statistics yield no information on the magnitudes of  $W_{12}$  and  $W_{21}$  but state that their ratio is

$$\frac{W_{21}}{W_{12}} = \exp \left[ -(\epsilon_1 - \epsilon_2)/kT \right] \quad (B5)$$

The interpretation outlined above provides a simple and direct way of writing the equilibrium conditions for a system obeying Fermi-Dirac statistics.

### Transitions to "Free" Energy States

Frequently it is necessary to consider transitions to the conduction band in a solid or transitions from a solid phase to a vapor phase. The electrons in a conduction band or the atoms or molecules in a vapor phase are essentially free, in that they may occupy states in a distribution of energy levels whose separation is small compared to  $kT$ . It is convenient to consider that all of the free electrons have one energy. The question then is what value to assign  $N_2$  in Eq. (B4) when  $N_2$  represents the number of "free" states. The value may be obtained as follows.

Eq. (A15) gives the number of levels available in the energy interval  $d\epsilon$  at energy  $\epsilon$ .

$$dN = \frac{2\pi (2m)^{3/2}}{h^3} \epsilon^{1/2} d\epsilon \quad (B6)$$

The probability of occupancy is given by Eq. (B1). Hence, the number of particles in the interval  $d\epsilon$  is

$$dn = 2\pi \frac{(2m)^{3/2}}{h^3} \frac{\epsilon^{1/2} d\epsilon}{\exp \frac{(\epsilon - \epsilon_F)}{kT} + 1} \quad (B7)$$

The total number of particles is obtained by integrating  $\epsilon$  from 0 to  $\infty$ . The integration is simple if  $e^{[(\epsilon - \epsilon_F)/kT]} \gg 1$ , which is true in most problems of concern. It should be noted that the energy is being meas-

ured from the lowest level among the free states and that  $\epsilon_F$  must be negative for this inequality to hold. When the inequality does hold, Eq. (B2) may be approximated by

$$dn = 2\pi \frac{(2m)^{3/2}}{h^3} \exp \frac{(\epsilon - \epsilon_F)}{kT} \epsilon^{1/2} d\epsilon$$

Integration yields

$$n = N_c \exp \left( \frac{\epsilon_F}{kT} \right) \quad (B8)$$

where

$$N_c = \left( \frac{2\pi m}{h^2} \right)^{3/2} \quad (B9)$$

Thus, for transitions from states  $N_1$ , lying at an energy  $|\epsilon_1|$  below the free states, to the free states, Eq. (B4) may be written

$$n_1 (N_c - n_1) W_{12} = n_1 (N_1 - n_1) W_{21} \quad (B10)$$

When  $n_1 \ll N_c$ , then  $n_1 N_c W_{12} = n_1 (N_1 - n_1) W_{21}$  where

$$\frac{W_{21}}{W_{12}} = \exp \left( - \frac{|\epsilon_1|}{kT} \right) \quad (B11)$$

Studies of the magnetic properties of electrons reveal that they have a magnetic moment as though their charge were spinning about an axis and that if two electrons have their spins oppositely directed, both may occupy one energy state. Hence, for electrons

$$N_c = 2 \left( \frac{2\pi m}{h^2} \right)^{3/2} \quad (B12)$$

## LIST OF SYMBOLS

- A = Richardson constant
- a = a distance
- a = a constant =  $n(\bar{F}l)^2/2qV$
- B = a constant
- b = a distance
- C = a capacitance
- c = a distance
- c = the velocity of light
- D = diffusion constant
- d = thickness
- E = electric field strength
- e = base of Naperian logarithms
- exp = exponential function
- F = force
- f(x) = function of x
- g = conductance per unit area
- $g_m$  = "apparent" transconductance (mutual conductance)
- $g_{mo}$  = "true" transconductance
- $\Delta H$  = heat of sublimation
- h = Planck's constant
- $i/h$  =  $h/2\pi$  (also written  $\hbar$ )
- I = current
- $I_0$  = initial current
- i =  $\sqrt{-1}$

- $i_s$  = secondary - emission current
- $i_r$  = primary current
- j = current density
- $j_D$  = diffusion current density
- $j_e$  = electron-emission current density
- $j_o$  = field-free-emission current density
- k = Boltzmann's constant
- L = mean free path
- l = a length
- m = particle mass
- $m^*$  = effective mass
- N = Density of states; density of sites available to a constituent
- $N_c$  = "density of states" in the conduction band of a solid or in the vapor phase
- $N_D$  = donor density
- n = particle density
- $n_o$  = particle density in a reference state
- $n_s$  = particle density in a solid
- $n_v$  = particle density in a vapor
- P = power output
- $P_0$  = initial power output
- p = momentum
- q = electronic charge
- $R_k$  = cathode resistance
- s = distance
- T = absolute temperature
- t = time
- U = potential energy
- V = voltage; energy in electron volts
- v = velocity; drift velocity
- $\bar{v}$  = mean thermal velocity
- $\bar{v}_n$  = mean thermal velocity normal to a surface
- W = work
- $W_{mn}$  = transition probability from state m to state n per unit time
- x = distance
- $\alpha$  = perveance; attenuation constant
- $\beta$  = a constant
- $\gamma$  = density relative to density of water
- $\delta$  = secondary emission ratio
- $\epsilon$  = energy
- $\epsilon_D$  = activation energy for self-diffusion; energy gap between donors and conduction band
- $\epsilon_F$  = Fermi energy
- $\epsilon_g$  = band-gap energy
- $\eta$  = depth of Fermi sea
- $\lambda$  = wave length
- $\mu$  = mobility
- $\nu$  = frequency
- $\nu_0$  = threshold frequency for photoemission
- $\xi$  = a displacement from equilibrium position
- $\rho$  = charge density
- $\sim$  = approximately equal to
- $\sigma$  = conductivity
- $\tau$  = mean collision time
- $\phi$  = work function
- $x$  = electron affinity
- $\psi$  = a wave function
- $\psi^*$  = its complex conjugate
- $\omega$  = frequency  $\times 2\pi$
- $\omega_p$  = plasma frequency  $\times 2\pi$

## REFERENCES

1. Compton, K. T., and I. Langmuir, "Electrical Discharges in Gases," Rev. Mod. Phys., Vol. 2, p. 123, April 1930
2. PB 119240, Library of Congress, Washington 25, D. C.
3. Seifert, R. L. E., and T. E. Phipps, Phys. Rev., Vol. 53, p. 443, 1938; Vol. 56, p. 652, 1939
4. Munich, La Berge, and Coomes, Phys. Rev., Vol. 80, p. 887, 1950
5. Fowler, R. H., and L. Nordheim, Roy. Soc. Proc. A, Vol. 119, p. 173, 1928
6. Stern, T. E., B. S. Gossling, and R. H. Fowler, Roy. Soc. Proc., Vol. 124, p. 699, July 1, 1929
7. Hughes, A. L., and L. A. Dubridge, Photoelectric Phenomena, McGraw-Hill, New York, 1932
8. Zworykin, V. K., and E. G. Ramberg, Photoelectricity, Wiley and Sons, New York, 1949
9. De Vore, H. B., Phys. Rev., Vol. 83, p. 805, August 15, 1951
10. Kollath, R., Physik. Zeits., Vol. 38, p. 202, 1937
11. McKay, K. G., "Secondary Emission," a chapter in Advances in Electronics I, edited by L. Marton, Academic Press, New York, 1948
12. Ruthemann, G., Naturwissenschaften, Vol. 29, p. 648, 1941; Vol. 30, p. 145, 1942
13. Lang, W., Optik, Vol. 3, p. 233, 1948
14. Pines, D., and D. Bohm, Phys. Rev., Vol. 85, p. 338, 1952; Vol. 92, p. 608, 1953
15. Pines, D., Rev. Mod. Phys., Vol. 28, p. 184, 1956
16. Sternglass, E. J., Bulletin of Am. Phys. Soc., Series II, Vol. 1, No. 6, p. 801, June 21, 1956
17. Matheson, R. M., and L. S. Nergaard, Jour. Appl. Phys., Vol. 23, p. 869, 1952
18. Becker, J. A., and R. W. Sears, Phys. Rev., Vol. 38, p. 2193, 1931
19. Sproull, R. L., Phys. Rev., Vol. 67, p. 166, 1945
20. Nergaard, L. S., RCA Review, Vol. 13, p. 464, 1952
21. Loosjes, R., and H. J. Vink, Philips Res. Rpt., Vol. 4, p. 449, 1949
22. Forman, R., Phys. Rev., Vol. 96, p. 1479, 1954
23. Eisenstein, A., Jour. Appl. Phys., Vol. 20, p. 776, 1949
24. Nergaard, L. S., and R. M. Matheson, RCA Review, Vol. 15, p. 225, 1954
25. Eisenstein, A., Jour. Appl. Phys., Vol. 20, p. 776, 1949
26. Plumlee, R. H., R. M. Matheson, and L. S. Nergaard, RCA Review, Vol. 18, p. 385, 1957
27. Plumlee, R. H., RCA Review, Vol. 17, p. 190, 1956
28. Timmer, C., Jour. Appl. Phys., Vol. 28, p. 495, 1957
29. Plumlee, R. H., Jour. Appl. Phys., Vol. 27, p. 659, 1956
30. Plumlee, R. H., RCA Review, Vol. 17, p. 231, 1956

# Oxide-Coated Emitters

C. P. Hadley

Lancaster

In 1903, Wehnelt<sup>1, 2, 3</sup> reported that the alkaline-earth oxides are efficient thermionic emitters of electrons. Over the fifty-odd years since this discovery, the oxide-coated cathode has been the subject of intensive investigation, and many workers have contributed to a better comprehension of its operation. Particularly rapid advances in understanding have occurred since the advent of the theory of semiconductors.<sup>4</sup> As a result, the phenomenon of thermionic emission from the oxide-coated cathode is now understood in principle but, in spite of extensive work, by no means in detail.

With regard to commercial use, the oxide-coated cathode is by far the leading thermionic emitter. In spite of its susceptibility to poisoning, ion bombardment, and damage by high voltages, its advantages of low cost, low temperature of operation, and relatively high current density have led to its use in an overwhelming majority of tubes requiring a copious supply of electrons. In recent years, several new emitters have appeared, such as the Philips L-cathode and the molded-nickel cathode. Although these types are finding uses in special applications, they have given no indication of monopolizing the field of thermionic emission. Indeed, no serious challenge has even been made to the supremacy of the oxide-coated cathode, nor is there any evidence that any successful challenge is imminent.

## GENERAL DESCRIPTION

The typical oxide-coated cathode, shown in Fig. 1, consists of a solid solution of barium, strontium, and calcium oxides supported on a metallic base. The most useful base metals are various alloys of nickel. The cathode may be directly or indirectly heated. Typical operating temperatures range between 1000 K and 1100 K; 1075 K (brightness) is common in commercial cathode-ray tubes. The electron emission available under constant voltage conditions may be as high as 0.5 ampere per square centimeter, although 0.1 ampere per square centimeter is a more conservative value for long-life operation. Under microsecond pulse conditions, a current density of 10 to 50 amperes per square centimeter is not unusual. A typical oxide-coated cathode is made as follows: The coating material, composed of alkaline earth carbonates suspended in organic liquids in which a binder is dissolved, is applied to a nickel sleeve by spraying. After the cathode is mounted and placed in the envelope, several distinct processing steps are required for proper emission. These are:

(1) evacuation of the envelope including baking; (2) burn-out of the binder; (3) decomposition of the carbonates to oxides (frequently called breakdown); and (4) activation (also known as aging).

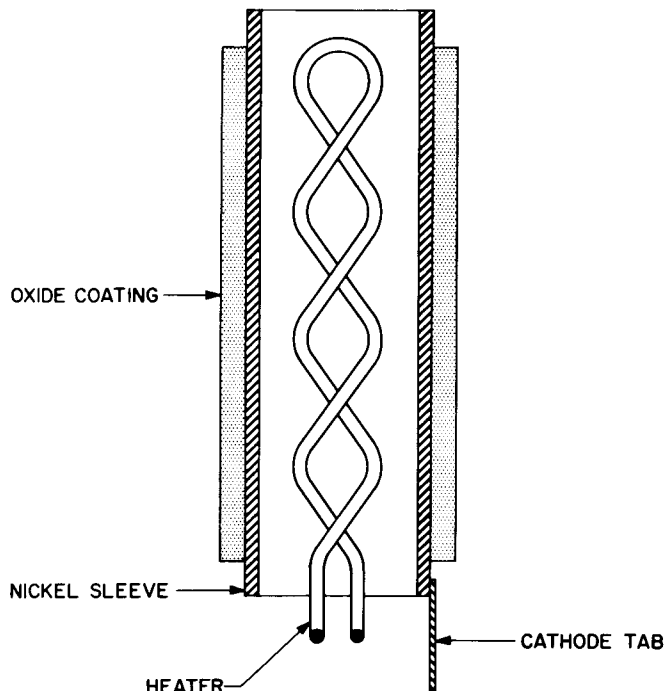
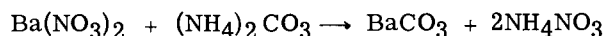
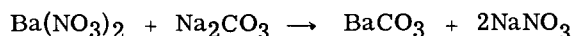


Figure 1. Cross Section of Indirectly Heated Oxide-Coated Cathode

## THE CATHODE COATING

The carbonates for the cathode coating are usually precipitated from a water solution of the nitrates. Typical reactions are:



The first reaction produces a sodium-precipitated carbonate which is used in the majority of sprays. It has been often said, although not fully substantiated, that residual sodium which remains after washing of the carbonate is helpful in cathode activation. However, recent practice tends toward the use of the ammonium-

precipitated carbonates, which can be more readily cleaned of residual impurities.

A typical carbonate (RCA C-175) contains coprecipitated barium, strontium, and calcium carbonates in the molecular percentages of 49, 44, and 7 per cent, respectively. A typical cathode spray (RCA C-185) contains the same carbonate mixture and a binder of nitrocellulose, alcohol, diatol, and diethyl oxalate. In the preparation of the spray, the carbonate is thoroughly dried and then ball-milled with the binder.

The cathode coating is applied to the nickel sleeve by spraying. The coating may be a few thousandths of an inch thick and have a weight of 6 to 8 milligrams for each square centimeter of cathode area.

Various cathode sprays are used depending on the intended applications. The molecular ratio of the carbonates may be changed, for example, to obtain various emission levels. This effect was first shown by Benjamin and Rooksby<sup>14</sup>. Their data, repeated in Fig. 2, show that maximum initial emission is usually obtained with low percentages (20 to 30 per cent) of BaO. More recent results by C.H. Meltzer, show a much broader region of maximum initial emission. (See his chapter entitled, "The Oxide Coated Cathode.") Other workers have further increased initial emission by adding 5 per cent of CaO to the coating. Factors other than initial emission are involved, however, and the proportions used in any cathode spray are a compromise. Operating life, for example, is prolonged by an increase in barium content; whereas grid emission is decreased with an increase in calcium content; the cathode spray (C-185) described above, represents a suitable compromise for general use. Examples of cathode sprays for various applications are given below.

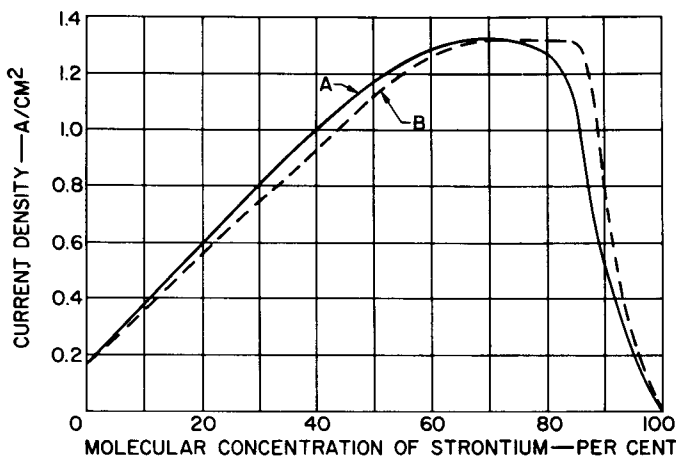


Figure 2. Dependence of Emission on Proportions of Barium Oxide and Strontium Oxide. Curve A: carbonate content before heat treatment; curve B, oxide content after activation<sup>14</sup>

1. For general use, when emission must be obtained readily and applied voltages are not too high, a spray which produces a fluffy coating (fast-drying) is desired; C-185, described above, is suitable.
2. The cathodes of tubes operating at high plate voltages require a smooth, dense coating. Such a coating

is achieved by use of slow-drying solvents, such as amy1 acetate, and carbonates having a small particle size. This last requirement can be satisfied with a mixture of singly precipitated barium carbonate and strontium carbonate.

3. If the structure of the tube is such that the grid runs hot, thermionic emission from the grid may be a problem. This grid emission may be decreased by decreasing the barium evaporation from the cathode, a result which is achieved by increasing the calcium content of the spray. Molecular concentrations of  $\text{CaCO}_3$  as high as 20 per cent are occasionally used.

### THE BASE MATERIAL

The functions of the metallic base are to support the cathode coating, to conduct heat and current to the coating, and to provide reducing agents for activation of the cathode. The last function, that of activation, will be explained in detail later. The essential point to be made here is that adequate emission is obtained only by virtue of activating centers within the coating, and that these centers are produced by a chemical reduction of the alkaline-earth oxides. The needed reducing agents may migrate to the cathode from remote parts of the tube, but the heat source of reducing materials is the metal sleeve which itself contains small quantities of impurities as alloys. The most common of the base metals is nickel alloyed with small amounts of silicon, magnesium, or carbon. The various cathode nickels have been arbitrarily classified as active, normal, or passive, depending on the quantity and character of the reducing agents present. The analysis of three typical alloys is given in Table I.

Table I

Material	Cathode Alloys (all values in per cent)		
	Active-599	Normal-220	Passive-499
Nickel and cobalt	99.0 min.	99.2 min.	99.8 min.
Silicon	0.15-0.25	0.01-0.05	0.01 max.
Magnesium	Present	0.01-0.1	0.005 max.
Carbon	0.04 max.	0.04 max.	0.05 max.
Copper	0.02 max.	0.2 max.	0.1 max.
Iron	0.02 max.	0.2 max.	0.1 max.
Manganese	0.2 max.	0.2 max.	0.002 max.
Sulfur	0.008 max.	0.008 max.	0.005 max.
Titanium	--	--	0.005 max.

The advantage of the active alloy is the ease with which emission is obtained, even under poor conditions of vacuum and cleanliness. There are, however, disadvantages which make the use of such an alloy undesirable except where necessary: (1) the cathode coating tends to peel from the base metal; (2) an interface material forms between the oxide and the base metal. When 599 alloy is used as the base, the interface material is barium orthosilicate ( $\text{Ba}_2\text{SiO}_4$ ). The  $\text{Ba}_2\text{SiO}_4$  interface is a poor electrical conductor, especially if current is not being drawn through it continuously, and, therefore, acts as a degenerative resistance in series with the cathode. The interface resistance is particularly undesirable in tubes designed for computer applications,

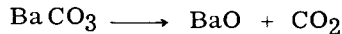
because such tubes may be cut off for a large proportion of the operating time.

Normal and passive alloys do not usually show interface resistance, and have less tendency to peel than the active alloys. Normal and passive cathodes are somewhat difficult to activate and should not be used when vacuum conditions are poor. Improved techniques of tube manufacture, however, make the use of active alloys unnecessary; modern tendency is toward the use of the purer nickels as base materials.

## DECOMPOSITION OF BINDER AND CARBONATES

A vacuum bake is included early in the processing of a tube containing an oxide-coated cathode. If the bake is at more than about 275°C, the nitrocellulose binder is burned out. Following the vacuum bake, the coating is usually somewhat yellow or brown in color because of carbon left behind from the binder. If a Lucite binder is used, the binder sublimes without residue.

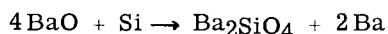
After the bake, heating current is applied to the cathode to decompose the carbonates. A typical reaction is:



Some of the carbon dioxide reacts with the residual carbon from the binder to form carbon monoxide, and the cathode coating turns pure white. Both the carbon dioxide and carbon monoxide are pumped from the tube. The rate at which the breakdown occurs depends on the cathode temperature. Fig. 3 gives curves<sup>5</sup> of the vapor pressure of carbon dioxide during the decomposition as a function of the temperature for  $\text{CaCO}_3$ ,  $\text{SrCO}_3$ , and  $\text{BaCO}_3$ . The barium carbonate is the most stable of the three compounds, and requires a temperature in excess of 1200 K for breakdown to occur in a reasonable time. A typical breakdown temperature would be 1250 K, and, for a small tube, the breakdown would be complete in 30 to 120 seconds. The breakdown is usually monitored with an ionization gauge; the completion of the reaction is indicated by a rapid fall in pressure.

## ACTIVATION

After the breakdown is complete, the cathode is activated by further heat treatment at temperatures near 1250 K. As explained previously, activation is essentially a chemical reduction of the cathode coating. There are three mechanisms by which such reduction may occur: (1) by dissociation of the oxide by ion bombardment, (2) by electrolysis of the oxide by passage of current, and (3) by chemical reduction by reducing agents. Chemical reduction is a very important mechanism and will be explained in some detail. The essential reaction involved is the reduction of barium oxide. One typical reaction is given below:



For a suitable reaction to occur, the reducing agent must satisfy the following requirements:

1. The reducing agent must be present in an available form. If the silicon or magnesium is in the cath-

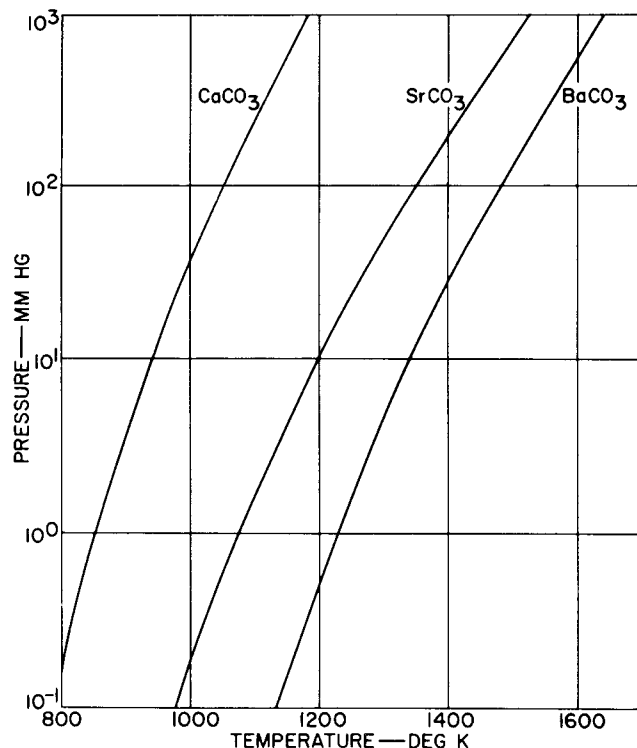


Figure 3. Vapor Pressure of Carbon Dioxide During the Breakdown Reaction

ode nickel as a compound of oxygen or sulfur (usually as inclusions at metal grain boundaries), for example, it will be bound too firmly to its anion to react with the barium oxide.

2. The reducing agent must be protected during the breakdown, otherwise it will react with carbon dioxide and be made unavailable. (If the reducer is alloyed with the nickel base, this requirement, as well as that of 1 above, is fulfilled.)
3. The reducer must diffuse through the base metal readily enough to be available for reaction.
4. The reduction must take place rapidly enough to be useful. Table II, devised by Rittner,<sup>6</sup> gives the equilibrium pressure of barium at 1000 K during the reaction between barium oxide and various elements. This equilibrium pressure is a measure of the rapidity with which the reaction progresses; i. e., the greater the equilibrium pressure, the more rapid the reaction. Although, of course, reducing agents other than those listed in Table II exist, they are either nearly inert, as far as the reduction of  $\text{BaO}$  is concerned, or are so active that the pressure of  $\text{Ba}$  produced is essentially that of  $\text{Ba}$  vapor in equilibrium with solid  $\text{Ba}$ .

As a rough rule of thumb, barium pressures no greater than  $10^{-10}$  to  $10^{-11}$  mm of mercury can be tolerated for cathodes of reasonable life. Thus, according to Table II, any cathode base composed entirely of a material more active than molybdenum would lead to excessive barium evaporation and a heavy interface.

If the reducing agent is included as an alloy of the base metal (for example, as silicon in nickel), the rate of reaction is reduced by two factors: (1) the presence of

the reducing agent as a compound (in the example, silicon would be present as  $\text{Ni}_3\text{Si}$ ), and (2) the absence of a saturated solution of the reducer. Rittner<sup>6</sup> outlines the method of accounting for these factors and gives as an example the equilibrium pressure of barium over the reaction of  $\text{BaO}$  with 0.1 per cent (by weight) of silicon in nickel. At 1000 K, this equilibrium pressure is approximately  $10^{-6}$  millimeters of mercury, a pressure which would be maintained only a short time during the initial operation of the cathode.

Table II  
Reduction of Barium Oxide

Reducing Agent	Pressure of Barium (gas) mm. Hg
Thermal Disassociation	$8 \times 10^{-16}$
Tin (Sn)	$4 \times 10^{-15}$
Iron (Fe)	$8 \times 10^{-15}$
Vanadium (V)	$9 \times 10^{-13}$
Zinc (Zn)	$2 \times 10^{-12}$
Gallium (Ga)	$4 \times 10^{-12}$
Molybdenum (Mo)	$6 \times 10^{-12}$
Chromium (Cr)	$4 \times 10^{-10}$
Tungsten (W)	$2 \times 10^{-9}$
Columbium (Cb)	$2 \times 10^{-9}$
Boron (B)	$1 \times 10^{-8}$
Manganese (Mn)	$1 \times 10^{-8}$
Tantalum (Ta)	$1 \times 10^{-8}$
Carbon (C)	$4 \times 10^{-6}$
Titanium (Ti)	$7 \times 10^{-6}$
Cesium (Ce)	$2 \times 10^{-4}$
Barium (Ba(s) + Ba(g))	$1 \times 10^{-2}$

### MECHANISM OF OPERATION

Early workers on the oxide cathode recognized that high emission was associated with the presence of excess barium.<sup>7</sup> It was believed that the excess metal formed a dipole layer on the surface of the oxide and, thus, reduced the work function. More recent work has emphasized the semiconductor nature of the cathode, and has associated the principal activating centers with oxygen deficiencies.<sup>8</sup> Still more recently, Plumlee<sup>9</sup> has indicated that the activating centers may be more complex, possibly involving the  $\text{OH}^-$  radical. Experimental measurements of the energy of the various levels of the band structure of  $\text{BaO}$  have yielded a variety of results. Nergaard<sup>10</sup> has summarized them as follows (see Fig. 4):

1. Band gap: about 5 electron volts.
2. Electron affinity: about 0.5 electron volt.
3. Valence-band exciton states: about 1.2 electron volts below the conduction band.
4. Impurity levels: 3.5, 2.4, 2.0, 1.4, and 0.8 electron volts below the conduction band. (The levels at 1.4 and 2.4 electron volts are probably most certain.)

The two important electrical characteristics of the cathode are its thermionic emission and its conductivity. These characteristics may readily be calculated<sup>11</sup>. The

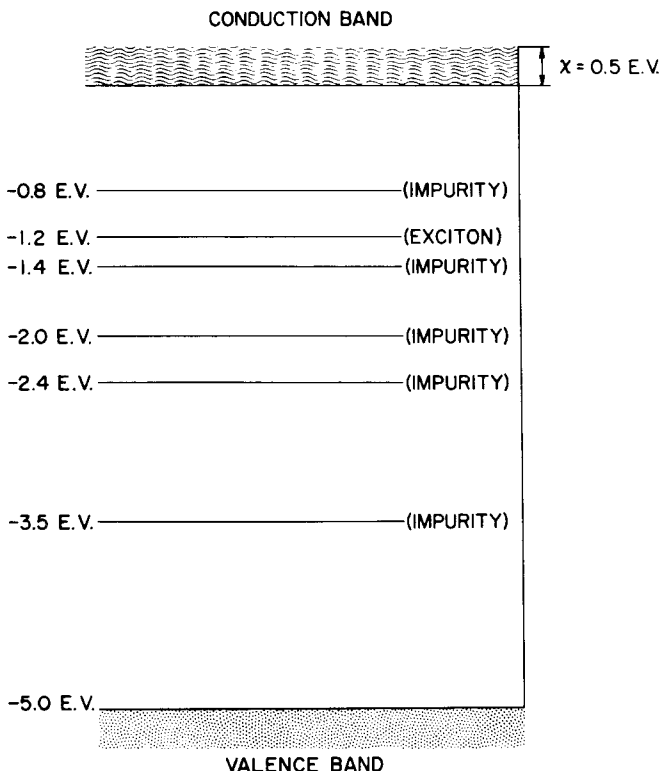


Figure 4. Energy-Level Structure of Oxide Cathode<sup>10</sup>

density of electrons in the conduction band  $n_c$  is given by

$$n_c = N_c e^{q \xi / kT} \quad , \quad N_c = \frac{2}{h^3} (2 \pi m k T)^{3/2} \quad (1)$$

Here  $N_c$  represents the density of available states in the conduction band,  $\xi$  is the energy of the Fermi level (measured from the bottom of the conduction band)  $q$  is the electron charge,  $k$  is Boltzmann's constant,  $T$  is the absolute temperature,  $h$  is Planck's constant, and  $m$  is the mass of the electron. The energy of the Fermi level  $\xi$  may be calculated from the expression

$$n_c + \sum_i \frac{N_i}{1 + e^{q(E_i - \xi) / kT}} = \sum_i n_{oi} \quad (2)$$

where  $N_i$  is the density of states in the forbidden band at the energy  $E_i$ , and  $n_{oi}$  is the density of electrons in the  $i^{\text{th}}$  state at a temperature of absolute zero.

The conductivity of the coating  $\sigma$  is given by

$$\sigma = n_c q \mu \quad (2)$$

and thermionic emission current density is

$$j_0 = n_c q \sqrt{\frac{kT}{2 \pi m}} e^{-q \chi / kT} \quad (3)$$

In the above expressions,  $\mu$  is the electron mobility, and  $\chi$  is the electron affinity.

The problem in making any calculations is to determine the proper model to use. The experimentally de-

terminated model of energy levels described above is complicated; and, in any event, the density of the various levels is not well known. A simplified model of barium oxide which explains many, although not all, of the experimental results, is as follows: As stated previously, the band-gap is about 5 electron volts and the electron affinity about 0.5 electron volts. It is assumed that only one activation level, a donor level, is important and that it is located at about 1.4 electron volts below the conduction band. In the notation being used,  $\chi = 0.5$  electron volts,  $E_i = E_b = -1.4$  electron-volts, and the density of the activation levels is given by  $N_i = N_b$ . With these assumptions, the emission and conductivity equations become:

$$j_o = \left[ \frac{qk^{5/4}(8\pi m)^{1/4}}{h^{3/2}} \sqrt{N_b} \right] T^{5/4} e^{-q\phi_0/kT} \quad (4)$$

$$\sigma = \left[ \frac{\sqrt{2}}{h^{3/2}} (2\pi mk)^{3/4} \mu q\sqrt{N_b} \right] T^{3/4} e^{qE_b/2kT} \quad (5)*$$

$\phi_0$ , the work-function, is given by  $\phi_0 = \chi - E_b/2$

Similar equations containing slightly different band-structure values apply to a triple-oxide cathode. Typical constants for such a cathode are:

$$\phi_0 = 1 \text{ electron volt}$$

$$N_b = 10^{23} \text{ levels/cubic meter}$$

$$j_o = 20 \text{ amperes/square centimeter}$$

$$\sigma = 10^{-2} \text{ mhos/centimeter}$$

The current density given above is well in excess of the emission usually drawn, and applies more correctly to pulsed emission. The reason that dc emission is lower than pulsed emission by at least two orders of magnitude is ascribed by Nergaard<sup>8</sup> to the mobility of the donors. According to this picture, donor levels which are ionized by thermal excitation of electrons to the conduction band experience a force away from the cathode surface when current is drawn. The result is that  $N_b$  of Eqs. (4) and (5) becomes quite small near the emitting surface, and the cathode conductivity becomes low in this region.

Another factor of importance in the operation of the cathode is the interface resistance. As described previously, cathode nickels which contain silicon lead to the formation of an interface compound. A sketch of such a situation is shown in Fig. 5. The interface material is itself a semi-conductor and exhibits a conductivity of the sort expressed by Eq. (5). A typical interface layer may be of the order of  $10^{-3}$  centimeters in thickness and may, if well-activated, exhibit a conductivity at 1000 K of about  $10^{-6}$  mhos/centimeter<sup>12</sup>. In some cases, the resistivity may be much higher. For example, the resistance of the interface tends to

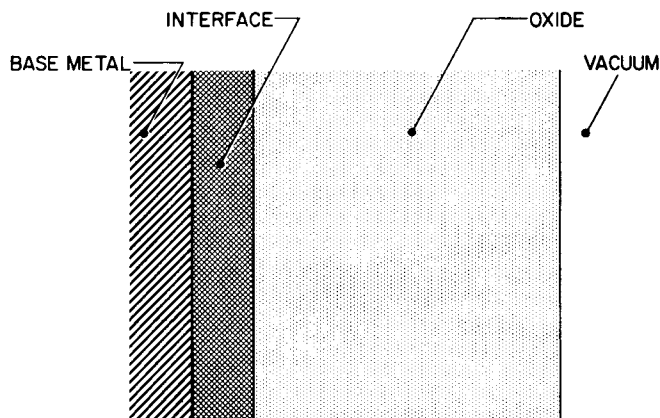


Figure 5. Diagram of Oxide Cathode with Interface<sup>12</sup>

be higher if current is not drawn continuously from the cathode.

## THE MEASUREMENT OF THERMIONIC EMISSION

A measurement of the thermionic emission must be made on each manufactured tube which contains an oxide-coated cathode; such measurement is by no means straightforward. Indeed, most so-called "emission" measurements are relative determinations, the results of which depend on many factors other than the condition of the cathode. Such factors include tube geometry and cleanliness of collecting electrodes.

The most practical method of making a true measurement of the thermionic emission of an oxide-coated cathode is to connect the tube involved as a diode. In the elementary theory usually given for the current-voltage characteristics of a diode, two regions are recognized. For the lower voltages, the current is said to be space-charge limited, and the current varies as the  $3/2$  power of the voltage. For higher voltages, the emission is said to be temperature limited and is essentially constant. On the basis of this simple theory, a satisfactory emission measurement can be made by the application of a collection voltage which is sufficiently high to reach the saturation region.

Unfortunately, a number of additional effects occur which are of importance and which complicate the measurement considerably. These additional effects, listed below, are described in detail later.

1. The initial velocities of the emitted electrons alter the simple space-charge theory.
2. The application of a high collection field lowers the surface barrier over which the electrons must pass to be emitted and thus eliminates a true temperature saturation.
3. The electrical resistance of the cathode coating causes a voltage drop during emission measurement. As a result, the actual voltage difference between the cathode surface and the anode is less than the applied voltage.
4. The cathode may be poisoned during testing. Cathode poisoning raises the cathode surface barrier and decreases emission.

\*Under some circumstances the current may be carried as a flow of space charge through the pores of the cathode coating. In such cases, Eq. (5) does not apply.<sup>15</sup>

5. Because of the difference in work functions of the cathode and anode, a contact difference in potential acts in series with the tube.  
 6. Some types of cathodes (oxide-coated cathodes in particular) give a higher emission for microsecond pulses than they do for steady-stage voltage conditions.

In the previous section (Mechanism of Operation), the thermionic emission equation for the oxide cathode was derived. Any proper measurement of emission must be characteristic only of the cathode material and hence must be some form of evaluation of Eq. (4). The experimental measurement, therefore, must duplicate the assumptions under which the emission equation was derived. It is not profitable to list all of the assumptions here, because most of them are well-enough satisfied in ordinary procedure. Two of the assumptions, however, necessitate special precautions. These precautions are:

1. The cathode condition ( $N_b$  and  $\phi_0$ ) must remain constant during a measurement.
2. The electrons being measured must not escape over a barrier either greater or less than  $\chi$ . This implies that the electric field at the surface of the cathode must be zero.

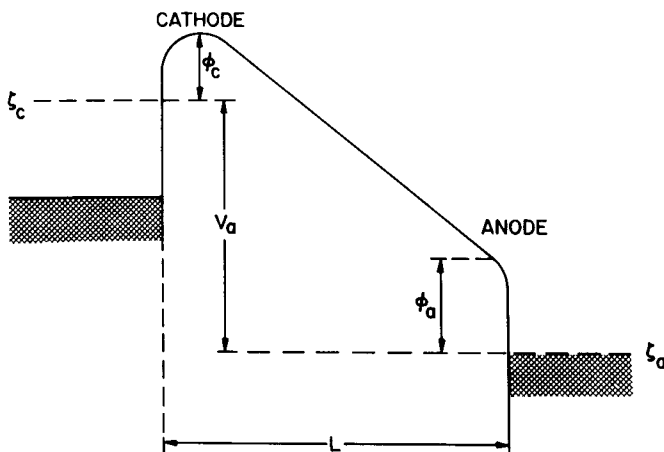


Figure 6. Potential Distribution in a Diode (no space charge)

Fig. 6 gives a potential-energy diagram for an electron in a plane-parallel diode, in which the anode is held positive with respect to the cathode by  $V_a$  volts. It is assumed that the electron-charge density in the cathode-anode space is negligible. The diagram shows the surface barriers,  $\phi_a$  and  $\phi_c$ , and the Fermi levels of the two electrodes. The electric field in the cathode-anode space is given by

$$[V_a - (\phi_a - \phi_c)]/L$$

where  $L$  is the cathode-anode spacing.

The difference between the anode and cathode work-functions,  $\phi_a - \phi_c = V_c$ , is called the contact difference in potential, and must be taken into account when the voltages applied to the diode are small. The actual potential difference across the vacuum gap for an applied voltage of  $V_a$  is  $V_a - V_c$ .

If the cathode coating has an appreciable resistance  $R_k$ , a potential difference  $R_k i_k$  is formed across it by the cathode current  $i_k$ . The vacuum gap potential difference then becomes

$$V_a - V_c - R_k i_k \quad (6)$$

The electrons within the cathode-anode space of the plane-parallel diode must obey the usual laws of mechanics and electrostatics. Therefore,

$$\nabla \cdot \vec{D} = \rho \quad \frac{mv^2}{2} = \frac{mv_0^2}{2} + q\psi$$

$$\vec{j} = nqv \quad \vec{D} = \epsilon_0 \vec{E}$$

$D$  is the electric displacement,  $\rho$  the charge density,  $v$  the velocity of an electron at the potential  $\psi$ ,  $v_0$  the velocity of an electron at zero potential,  $\vec{j}$  the current density,  $n$  the density of electrons in the vacuum space,  $\epsilon_0$  the permittivity of free space, and  $\vec{E}$  the electric field. If it is assumed that the initial electron velocity is zero, these equations may be combined to yield the following expression for the cathode current density,  $j_1$ :

$$j_1 = \frac{4\epsilon_0}{9} \sqrt{\frac{2q}{m}} \frac{V^{3/2}}{L^2} \quad (7)$$

Eq. (7) is the familiar space-charge relationship.

The above equation is, of course, somewhat idealized; a much more complete analysis is given by Nottingham.<sup>11</sup> A sketch of the actual potential distribution between the cathode and anode, neglecting  $V_c$ , is given in Fig. 7. The equations which describe the current density  $j_2$  are as follows:

$$j_2 = j_0 e^{-qV_s/kT} \quad (8)$$

$$j_2 = \frac{4\epsilon_0}{9} \sqrt{\frac{2q}{m}} \frac{(V + V_s)^{3/2}}{(L - l)} \quad (9)$$

$V_s$  is the height of the potential barrier due to space charge (see Fig. 7), and  $l$  is the distance of the top of the barrier from the cathode surface.

If the applied voltage is varied, the potential distribution changes, as shown in Curves B and C of Fig. 7. As  $V$  is made more positive, the potential barrier becomes smaller and moves toward the cathode. At a critical voltage, the field at the cathode is zero,  $V_s$  and  $l$  are zero, and  $j_2 = j_0$ , which is the current described by Richardson's equation. One important method of determining emission, which will be described later, involves a technique for increasing  $V$  until  $j_2 = j_0$ .

In the introduction to this paragraph, an idealized theory was described as a simple explanation for the current-voltage curve of a diode. The subsequent discussion has shown some of the fallacies in the simple explanation. In reality, the characteristic curves look more like those shown in Fig. 8. Curve A shows the case when the cathode resistance is negligible, curve B when appreciable resistance is present. The theory of Eqs. (8) and (9) is meaningful when the cathode current is limited by space charge, that is, when the

applied voltage is rather low. Eq. (7) applies only when the field at the surface of the cathode is exactly zero, which occurs only at a single current value for any given diode. As the voltage applied to the diode is gradually raised, a semi-saturation of current is reached as shown in curve A of Fig. 8. In this region, called the Schottky region, additional theory is required for explanation.

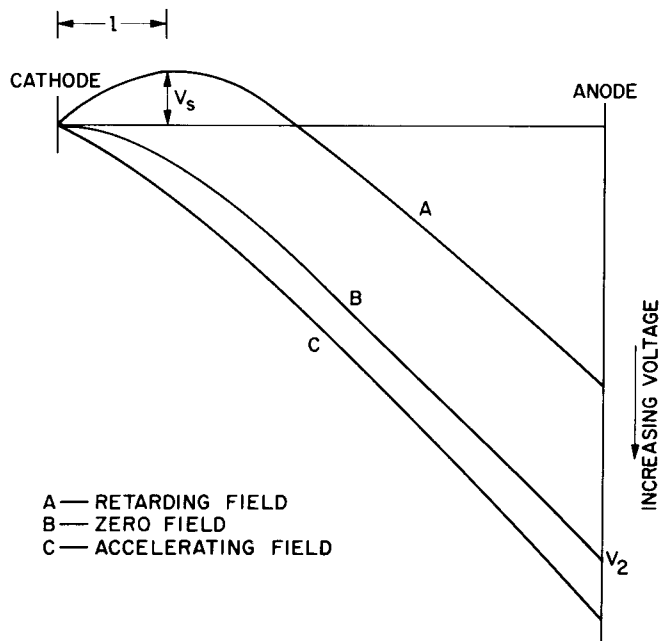


Figure 7. Potential Distribution in a Diode (space charge): curve A, retarding field; curve B, zero field; curve C, accelerating field

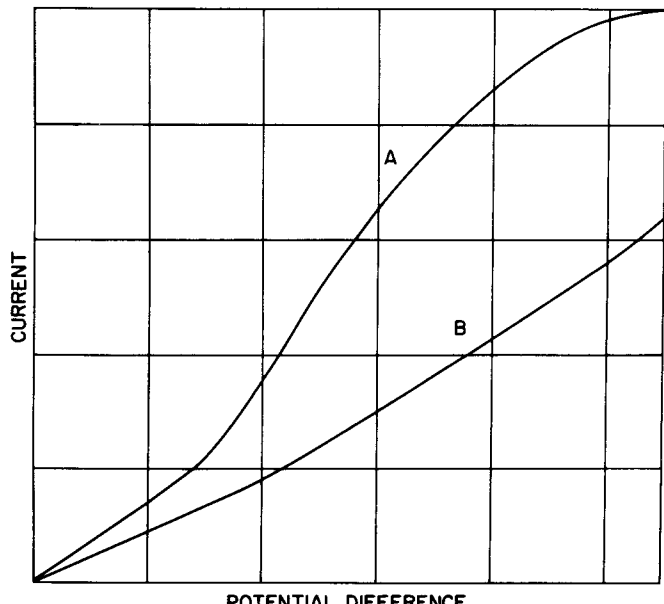


Figure 8. Current versus Voltage Characteristics for a Diode: curve A, zero cathode resistance; curve B, appreciable cathode resistance

As shown in Fig. 7, diode voltages beyond the space-charge region cause an accelerating field at the surface of the cathode. This accelerating field lowers the surface barrier ( $\chi$  in Fig. 4), and allows electrons of lower-than-usual energy to be emitted. The calculation of the amount by which the barrier is lowered was first made by Schottky<sup>13</sup>, who made the assumption that the force exerted by the emitter on an emitted electron is the familiar image force. The theory is, therefore, accurate only when the electron is at some distance from the emitter. The lowering of the work-function barrier is given by

$$\Delta \phi = \sqrt{\frac{qE}{4\pi\epsilon_0}} \quad , \text{ where } E \text{ is the field}$$

at the surface of the cathode

The current density for the accelerating condition is, therefore

$$j_3 = j_0 e^{q\Delta\phi/kT} \quad (10)$$

For any diode,  $E$  is proportional to  $V$ ; therefore, a plot of  $\ln j_3$  versus  $\sqrt{V}$  should give a straight line having an intercept  $\ln j_0$ . This method is sometimes used for the determination of the field-free current.

It is important that the condition of the cathode remain constant during measurement. Any poisoning will cause  $\phi_0$  to increase and  $N_b$  to decrease. Because  $j_0$  is more sensitive to  $\phi_0$  than to the other variables, the net effect of the poisoning is a lowering of emission. There are three factors most important to cathode poisoning.

1. Even for well-processed tubes, excessive heating of the anode causes a tube to become gassy. The effect can be minimized if the anode power is kept to a minimum. The two requirements of low anode power and zero-field current tend to work in opposite directions. If zero-field current is drawn under dc conditions, it is usually necessary to reduce the cathode temperature. For temperatures nearer the operating range, the anode power may be kept low by the application of voltage in microsecond pulses.
2. Any cathode (and in particular an oxide-coated cathode) evaporates material to the anode during life. These evaporated materials, frequently oxides, can be decomposed by electrons having more than about 10 volts of energy. The decomposition products are able to poison the cathode.
3. Poisoning effects act much more strongly as the cathode temperature is lowered.

In addition to the effects discussed above, which apply to all cathodes, there are some special effects which are characteristic especially of oxide-coated cathodes. These effects result from the semiconductor nature of these emitters. In the section on thermionic emission theory, it was noted that the emission from semiconductors was due to the presence of donor levels. The donors are mobile at the temperature of operation, and are moved toward the base material by the electric field which is present during the drawing of current. Two of the effects of donor mobility which are applicable to

this discussion are:

1. Pulse emission for oxide cathodes is from 10 to 100 times as large as dc emission.
2. The Schottky theory of Eq. (10) may not hold. If emission data are plotted as  $\ln j_3$  versus  $\sqrt{V}$ , the slope of the curve for a plane-parallel diode is as follows.

$$\frac{d}{dV^{1/2}} \ln j_3 = \frac{q}{kT} \left( \frac{q}{4\pi\epsilon_0 L} \right)^{1/2}$$

Similar equations are found for tube geometries other than plane-parallel. Metallic emitters and emitters such as thoriated tungsten perform as predicted by Eq. (10), but oxide-coated cathodes show an anomalously high slope (3 to 4 times that expected). This effect casts doubt on the validity of using a Schottky plot for the determination of field-free emission for oxide-coated cathodes.

On the basis of the above discussion, the most satisfactory simple way to properly measure the thermionic emission of an oxide-coated cathode is:

1. Apply voltages to the diode-connected tube. Draw currents within, and slightly above, the space-charge region.
2. Make a plot of the current to the  $2/3$  power versus the applied voltage. (Eq. 7).
3. Correct the plot for cathode-coating resistance. This correction may frequently be made by a determination of what coating resistance must be assumed in order that the space-charge current satisfies geometric considerations.
4. Find the field-free emission current at the point where the plot of the measured current departs from the space-charge line.

It is tedious to make the space-charge plot point-by-point, and it is impossible in production. The next best expedient is to make a single pulsed-emission measurement at a voltage sufficiently high that the current does not change too rapidly with voltage. The emission so measured will be several times higher than the field-free value.

The least satisfactory method of all is to measure current with a moderate voltage applied to the collector. The accuracy of such a measurement depends primarily on geometry and on the resistance of the cathode. Since Eqs. (4) and (5) show that both the emission and the resistance vary with cathode activity, the current will be some measure of the activity of the cathode if the geometry can be assumed constant from tube to tube.

#### DYNAMIC EQUILIBRIUM AND POISONING

Although the previous paragraphs have discussed separately the various mechanisms occurring in oxide cathodes, the condition of the cathode at any time is determined by a dynamic equilibrium of all the mechanisms in progress. It is convenient to classify the mechanisms as follows:

#### Activating Mechanisms

1. Migration of reducing agents through base metal.

2. Reducing action between the oxide coating and various reducing agents present.
3. Diffusion of the activating centers throughout the oxide coating.
4. Reduction by electrolysis.

#### De-Activating Mechanisms

1. Evaporation of activating centers.
2. Oxidation of the coating by undesirable impurities such as oxygen, water vapor, and chlorides.
3. The evolution of gases from tube parts.
4. The reduction of compounds on electrode surfaces by electron bombardment.

#### Destruction of Barium, Strontium, or Calcium Oxides

1. Reaction with materials such as water vapor, chlorides, and carbon dioxide.
2. Destruction by ion bombardment.
3. Evaporation of the coating.

The cathode will become useless for emission if any of the activating mechanisms is interrupted unduly, or if the undesirable reactions are present to any extent. According to the discussion following Eq. (4), a well-activated cathode has an activator concentration of about  $10^{23}$  centers per cubic meter. Referred to BaO, the activator concentration is thus a few parts per million. Concentrations of impurities as high as 0.001 per cent by weight will not seriously affect the cathode performance. As a rule of thumb, 1 microgram of poisoning material for every milligram of cathode coating may be considered to be enough to destroy cathode emission. These figures emphasize the necessity for great cleanliness, not only in the cathode materials, but in every part that enters the finished tube.

Every tube type must be considered as an individual within a species. Schedules for baking, evacuation, activation, and aging cannot usually be taken over bodily from one tube type to the next. Proper procedures for any new type must, therefore, be developed experimentally, and frequently with considerable difficulty.

#### CONCLUSIONS

In the field of oxide cathodes, perhaps more than in any other field, it is difficult to make many specific recommendations that will apply to all situations. Accordingly, the author has attempted to generalize and to present a broad picture of theory and practice. It is hoped that the presentation is broad enough to permit the reader to particularize according to his own needs.

#### LIST OF SYMBOLS

- $n_c$  = density of electrons in the conduction band.  
 $N_c$  = density of available states in the conduction band.  
 $q$  = electron charge.  
 $\xi$  = energy of the Fermi-level measured from the bottom of the conduction band.  
 $k$  = Boltzmann's constant.

$T$	= absolute temperature.
$h$	= Planck's constant.
$m$	= mass of an electron.
$N_i$	= density of states at the energy $E_i$
$E_i$	= energy of a state in the forbidden band (measured from the bottom of the conduction band).
$n_{oi}$	= the density of the electrons in the $i^{\text{th}}$ state at a temperature of absolute zero.
$\sigma$	= electrical conductivity of the oxide coating.
$\mu$	= mobility of the electron in the conduction band.
$j_0$	= thermionic emission current density with zero-field at the cathode surface.
$\chi$	= electron affinity of the oxide-coated cathode.
$N_b$	= density of impurity levels in the cathode coating.
$E_b$	= energy of the impurity level (measured from the bottom of the conduction band).
$\phi_0$	= work-function of the cathode (as expressed in Richardson's equation).
$V_a$	= anode voltage.
$R_k$	= cathode coating resistance.
$i_k$	= cathode current
$\phi_a$	= anode work-function
$\phi_c$	= cathode work-function
$L$	= anode-cathode spacing.
$D$	= electric displacement.
$\rho$	= charge density.
$v$	= velocity of the electron at the potential $\psi$ .
$\psi$	= potential within the cathode-anode space.
$v_0$	= velocity of the electron at zero potential.
$\vec{j}$	= electron current density (vector).
$n$	= density of the electrons in the cathode-anode space.
$\vec{v}$	= velocity of an electron in the cathode-anode space
$\epsilon_0$	= permittivity of free space.
$\vec{E}$	= electric field
$j_1$	= current density under idealized space-charge theory.
$j_2$	= current density under practical space-charge conditions
$V_s$	= height of the space charge barrier.
$l$	= distance of the top of the space charge barrier from the cathode surface.

$V$	= vacuum gap potential.
$j$	= electron current density (scalar).
$E$	= the electric field at the surface of the cathode.
$j_3$	= current density under accelerating conditions.

## REFERENCES

1. Wehnelt, A., S. -B. physik. -med. Soz., Erlangen, 95, 115, 1903
2. Wehnelt, A., Verh. Dtsch. physik., Ges., 5, 346, 1903
3. Wehnelt, A., Ann. Physik 14, 425, "On the Emergence of Negative Ions from Hot Metallic Compounds", 1904
4. Wilson, H. A., Proc. Roy. Soc., Lond., A134, 277-287, 1931
5. Wagener, S. and G. Hermann, The Oxide Cathode, Vols. I and II "The Oxide-Coated Cathode," Chapman and Hall, 1951
6. Rittner, E. S., "A Theoretical Study of the Chemistry of the Oxide Cathode," Philips Research Reports, 8, 184, 1953
7. Becker, J. A., "Phenomena in Oxide-Coated Filaments," Phys. Rev., 34, 1323, 1929
8. Nergaard, L. S., "Studies of the Oxide Cathode," RCA Review, 13, 464, 1952
9. Plumlee, R. H., "The Electron Donor Centers in the Oxide Cathode," RCA Review, 17, 231, 1956
10. Private Communication
11. Nottingham, W. B., "Thermionic Emission," Handbuch der physik, Vol. XXI, Springer, Berlin, 1959, Academic Press, New York, 1948
12. Eisenstein, A. S., "Oxide-Coated Cathodes," Advances in Electronics, Vol. 1, p. 1, 1948
13. Schottky, W., Physik Z., 15, 872, 1914
14. Benjamin, M., and H. P. Rooksby, "Emission from Oxide-Coated Cathodes," Phil. Mag., 15, 810, 1933
15. R. Loosjes and H. J. Vink, "The Conduction Mechanism in Oxide-Coated Cathodes," Philips Res. Rep., 4, 449, 1949

# Electron-Emission Coating for the Oxide Cathode

C. H. Meltzer and E. G. Widell

Harrison

## BASIC CONSIDERATIONS FOR THE EMISSION COATING

The oxide-coated cathode is a system for producing efficient emission of electrons by the application of thermal energy to a material having a low work function. The system uses a nickel alloy for the cathode substrate metal upon which the oxide coating derived from alkaline-earth carbonates is formed. The presence of an activated oxide coating lowers the work function of the substrate nickel core metal. The low work function of the system permits operation at the relatively low temperature of 1025 K, and copious electron emission at low heater-wattage input. Electron emission is influenced by the effects of the low work function as well as by the electron transfer efficiency involved in the porous nature of the emission-oxide matrix coating.

### Work Function

The work function  $\phi$ , or the total amount of work necessary to free an electron from a solid, is measured in electron-volts (ev) and is temperature dependent. The temperature dependence may be produced either by the work function of the base metal, or by absorbed layers of atomic films. In general, the work function increases with the decrease in atomic volume or lattice spacing, i.e., the work function increases with the increasing electron affinity by reason of increasing electrical forces of attraction to the nucleus with decreasing distance, as shown in Fig. 1. When atoms of a lower work function are adsorbed onto the surface of a higher work function metal, the work function of the substrate metal is reduced by the potential barrier at the surface of the metal. For example, when a monolayer of barium ( $\phi = 2.52$  ev) is vaporized onto the surface of nickel ( $\phi = 4.96$  ev), the resultant adsorption layer, barium-oxygen-nickel, has a work function of 0.9 ev.<sup>1</sup>

Although large lattice spacings in a solid contribute to a low work function, they are also associated with low melting points and low boiling points. Therefore, the usefulness of materials having large lattice spacings is limited by their high rate of evaporation, which tends to shorten the life of a system under vacuum tube conditions as well as to contaminate adjoining electrode surfaces. A balance of the two factors—work function and rate of evaporation—is desired in an oxide-cathode system. The barium/barium oxide system

has the lowest usable work function consistent with minimum rate of evaporation and long life at the operating temperature of the tube. Fig. 2 illustrates the relative emission capability of the oxide, tungsten, and thoriated-tungsten cathode systems.

The work function of a metal not only involves the particular substrate metal but also involves the type of crystal surface that is being measured. In some cases, preferred orientation occurs and it is found that the work functions of different faces of the metal lattice will vary with the plane of the lattice that is exposed.<sup>2,3</sup> However, for practical purposes, the values of the work function assigned to those materials used for cathode systems apply to polycrystalline surfaces with random orientation such that average effects are created.

### Semiconductor Plus "Electron-Pore Gas" Conductivity

The activated alkaline-earth oxide coating on a cathode nickel base metal lowers the work function of the system by modifying the surface-energy potential barrier of the substrate metal so that electrons are transferred copiously at a relatively low operating temperature. In addition to creating a low work function system, which can be obtained by a thin film of oxide coating, a relatively thick oxide coating (0.75 to 3.5 mils) introduces a factor of coating porosity that allows an "electron pore gas"<sup>4,5,6</sup> effect to operate in conjunction with the basic semiconductor mechanism of electron transfer.<sup>7,8,9</sup> Normally, pure oxide coating has a resistance of  $10^{12}$  ohms. The activating process causes the oxide to act as a semiconductor by a process of physical-chemical reactions which are believed to lead to the formation of barium and associated donor sites in the oxide lattice. In addition to this semiconductor property of electron transfer, there exists a phenomenon of electron transfer through an "electron pore gas" in the interstices between the macroscopic crystal particles of the oxide matrix at temperatures above 575 K. Although the electron gas, i.e., a cloud of electrons which is considered in terms of kinetic theory of gases, does not reduce the work function of the system, it does increase the efficiency of emission by increasing the conductivity of the system, as shown in Fig. 3.<sup>10</sup> A higher level of emission performance is possible at the operating temperature of 1025 K because there is a greater net voltage applied between cathode and plate as a result of the lower voltage drop across the oxide coating, i.e., the depth of the poten-

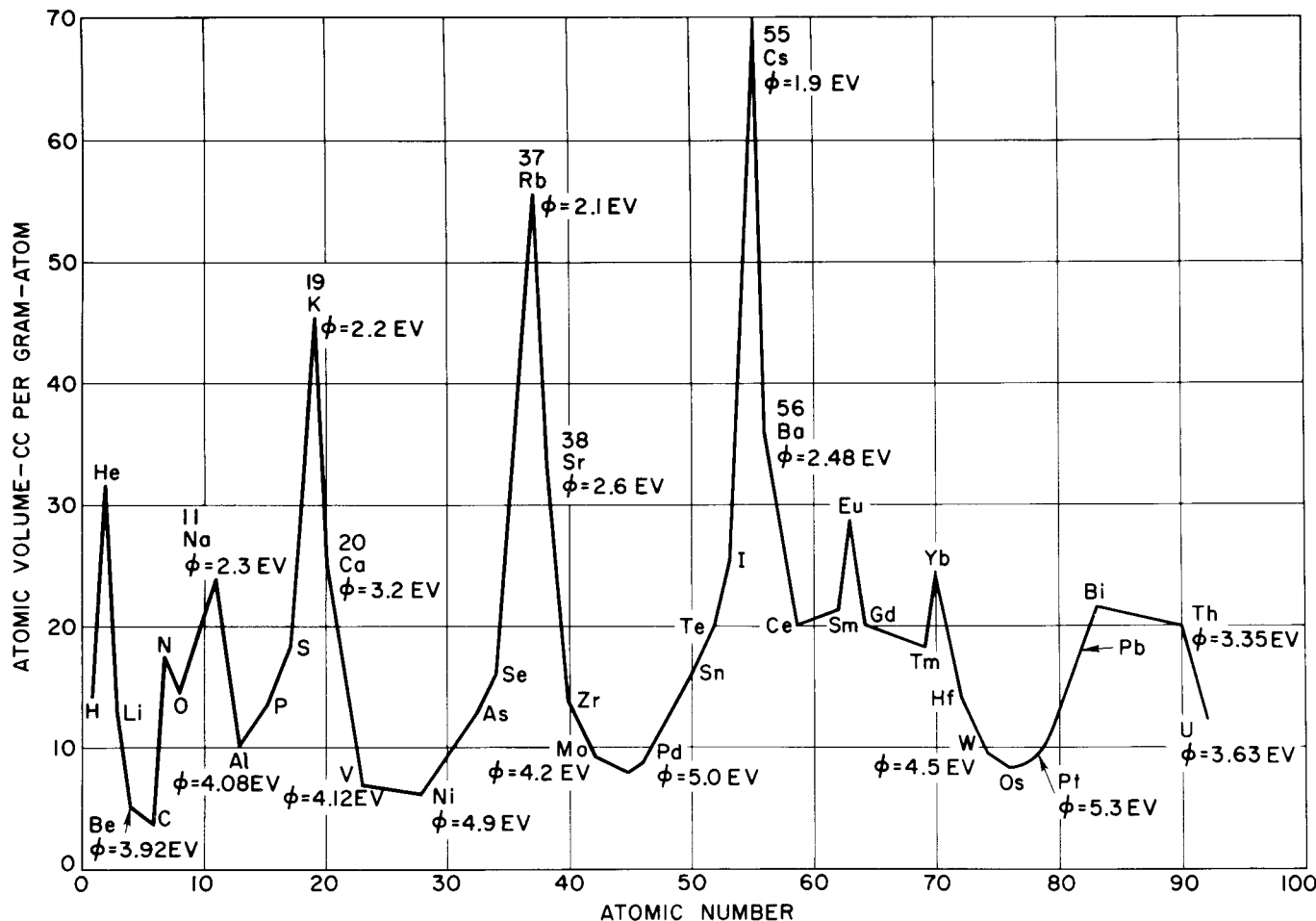


Figure 1. Atomic Number Versus Atomic Volume for Elements with Various Work Functions ( $\phi$ )

tial minimum, as well as its distance from the surface of the cathode, is decreased to permit more of the electrons to reach the plate. A relatively thick porous oxide coating, in addition to contributing a higher conductivity by reason of the electron pore gas effect, contributes to long life performance because the matrix of barium oxide in the coating is a reservoir for active barium sites in the system by reason of the chemical reduction processes induced by the active reducing agents of the nickel base metal.

#### Activation of the Oxide-Cathode System

Barium and associated donor centers are produced by chemical reduction of the barium oxide by reducing agents in the cathode nickel-alloy base metal. Barium oxide plus metal yields the metal oxide plus barium. Barium oxide can not be decomposed to barium and oxygen within the temperature limitations of the vacuum tube. The temperature required to decompose barium oxide would be close to 3000 K at a vacuum of  $10^{-5}$  millimeters of mercury. Electrolytic dissociation of barium oxide yields only about two per cent of the available barium centers. Electrolysis of barium oxide occurs upon passage of current through the coating whereupon the barium ion is transported toward the base me-

tal to be reduced to free barium by acquiring two electrons. The oxygen ion forms atomic oxygen yielding two electrons in the process.<sup>11</sup> Oxygen ultimately leaves the oxide coating to enter the vacuum space where, in time, it is removed from the vapor phase by combining with the getter flash material. As soon as barium has been created and donor sites have been established in the oxide matrix, the oxide coating is capable of transferring high emission current. Electrolysis does not activate an oxide system as readily as chemical reduction by certain alloying metals in commercial cathode nickel. The time for activation by electrolysis is measured in tens of hours for a pure platinum cathode in contrast to a time of minutes for activation by chemical reduction, as shown in Fig. 4.

#### Electrical Importance of the Substrate Metal and Emission Coating

The reducing-element content of the cathode nickel base metal creates and replenishes the supply of barium centers which maintain the low work function of the system and the basic semiconductor method of electron transfer. The operating characteristics of the cathode with respect to other tube electrodes are determined by composition, purity, and particle size of

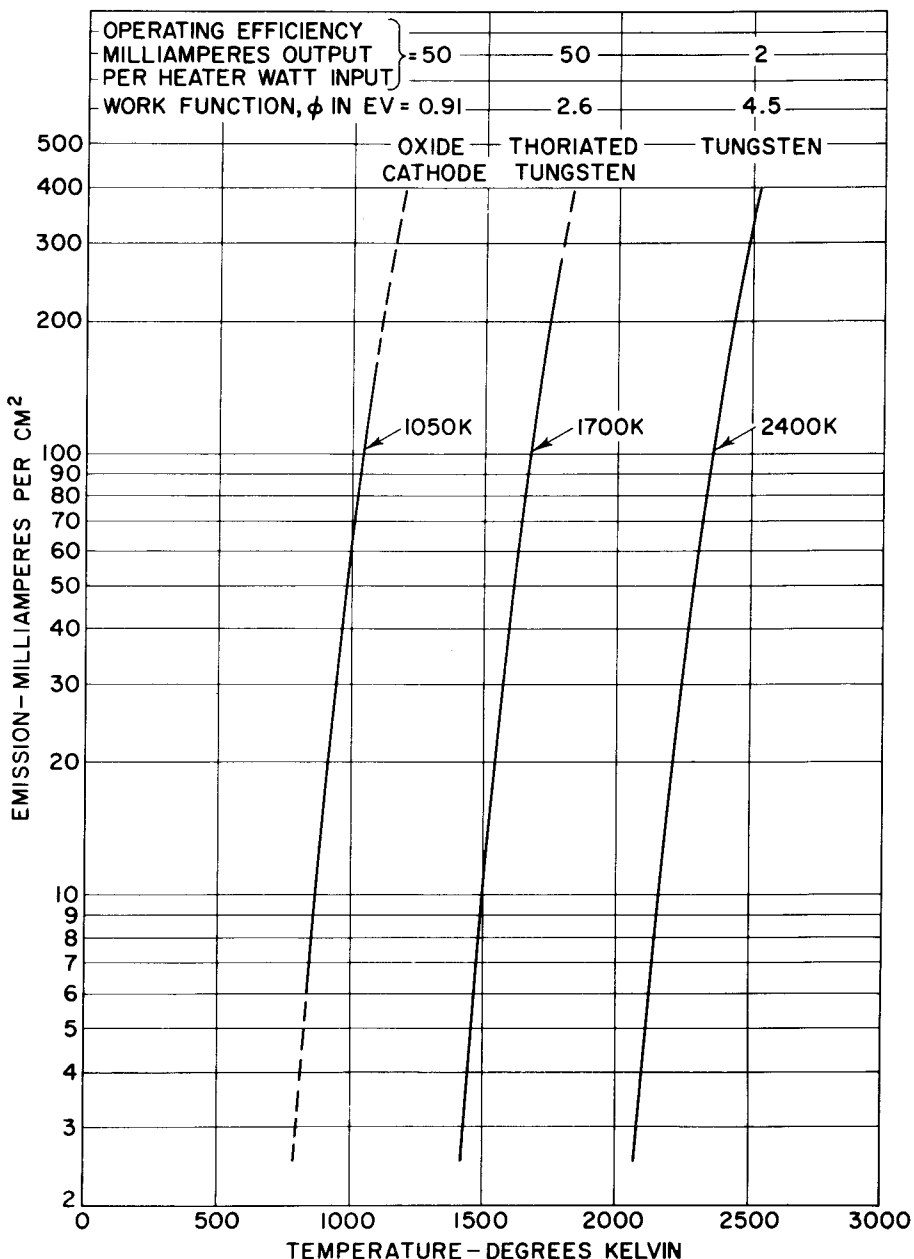


Figure 2. Average Value of DC Emission Current from Different Cathode Systems

the emission carbonates; the technique of coating the cathode metal; the conversion of the carbonates to the oxide-matrix crystal structure; the rate of thermal diffusion of barium through the coating; the rate of electrolytic transport of the barium ion; the rate of evaporation of barium/barium oxide; 12, 13, 14 and the concurrent formation of surface films on adjoining elements. The location of the active barium donor sites—whether in, on, or around the crystal lattice of the alkaline-earth oxide—is not known with certainty. The electrical importance of the crystal structure of the oxide lattice is related to the degree of porosity, which determines the effectiveness of the electron pore gas in decreasing the resistance of the coating at the operating temperature of 1025 K as shown in Fig. 5.

#### Equilibrium Systems and Interactions

In addition to the variable factors noted above, further variations on the physical-chemical equilibria which influence the micro-chemical actions occurring in the oxide coating are induced by the effects of temperature, time for decomposition of the carbonate to the oxide, coating weight, particle size, and density. Evaporation of certain condensable metals from the cathode base metal, as well as from the oxide coating, tends to contaminate insulating mica spacers as well as the heater insulation coatings. The effect of temperature, time, and partial pressure of carbon dioxide and carbon monoxide gases influences the porosity of the coating in terms of sintering and fusion of the coating. Elec-

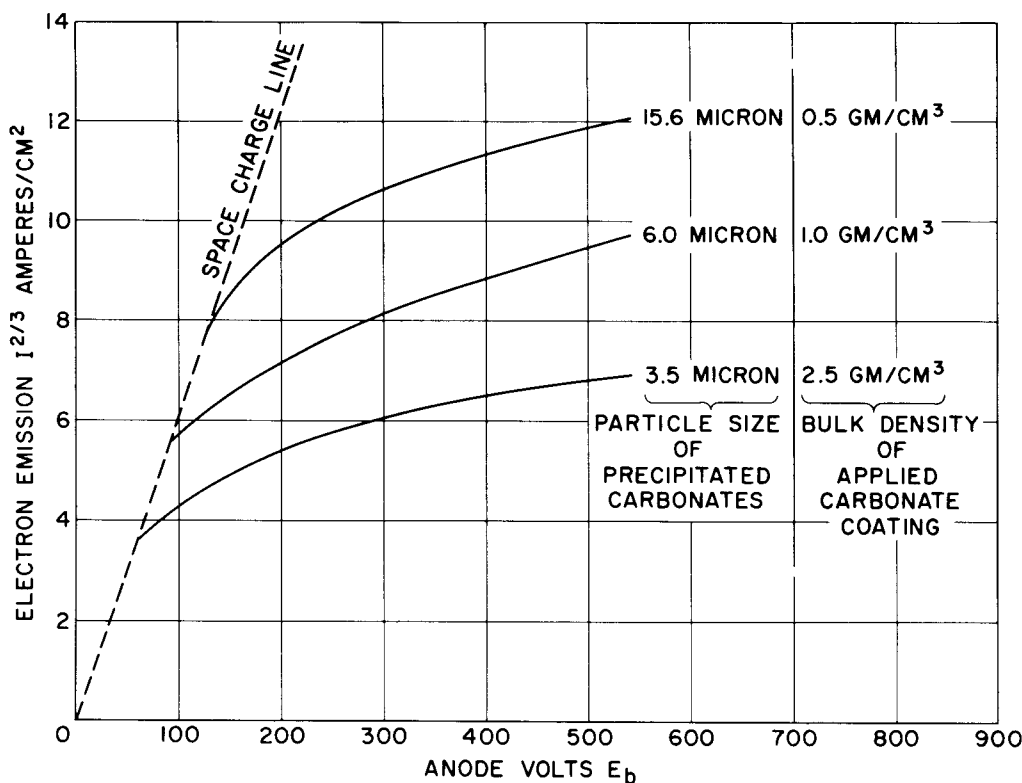


Figure 3. Pulse-Emission Performance from Oxide-Coated Cathodes Using the Same Cathode Base-Metal Nickel Alloy, but with Oxide Coatings Derived from Carbonates of Different Particle Size as Originally Precipitated. Particle-size determination by the Andreasen pipette sedimentation method. Type 1-v tube with  $E_f = 5.5$  volts; plate voltage of one-microsecond duration at a pulsed repetition frequency of 1000 cycles per second.

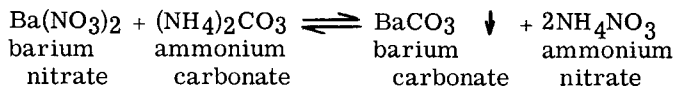
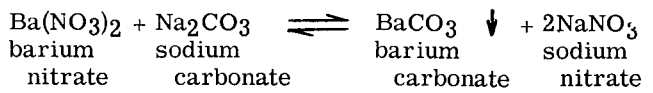
tron bombardment of electrode surfaces and glass walls of the tube releases gaseous products that interact with the active barium centers of the coating causing a reduction of emission; positive-ion bombardment can disrupt surface layers of the oxide cathode to cause an increase in the work function of the system. In view of the varied factors and phenomena involved,<sup>15, 16</sup> it may be concluded that all equilibria in the oxide cathode are in delicate balance with each other in the sequence of activation and regeneration during the life of the tube. These equilibria are dependent upon the non-injurious nature of the environmental vapor phase for the best electron-transfer performance and long life.

#### PREPARATION OF THE EMISSION COATING

##### The Carbonate Form

The preparation of the alkaline-earth emission carbonates is a critical operation in terms of maintaining purity, uniformity, particle size, and chemical composition. The carbonates are formed by precipitation in which a solution of sodium and/or ammonium carbonate is added to a solution of alkaline-earth nitrates. The solutions are made under controlled conditions using distilled water and are filtered before being mixed together in the reaction. The reaction is of the double decomposition type in which the equilibrium is shifted in the forward direction because of the insolubility of the alkaline-earth carbonate which precipitates out of sol-

ution. For example,



Various precipitation methods can be used, but to obtain reproducible uniform particle size distribution all methods must adhere to standardized control procedures with respect to concentration of reacting solutions, temperatures, rate of addition, rate of mixing, and pH of the reacting media. The carbonates that are used for emission purposes are usually the coprecipitated double carbonate of barium and strontium in 50/50 mole per cent composition (57/43 weight per cent) or the coprecipitated triple carbonate of barium, strontium, and calcium in 57/39/4 weight per cent composition. The carbonates may be made as the needle form (orthorhombic crystal lattice) or the spherulite form (rhombohedral crystal lattice) depending upon the temperature, composition, and concentration of the reactant solutions. The carbonate particles as precipitated in needle or spherulite form are composed of crystallites representing a lattice arrangement. The carbonate crystal particles are from 1 to 25 microns long, and from 1 to 4 microns in diameter. Crystallite sizes are from

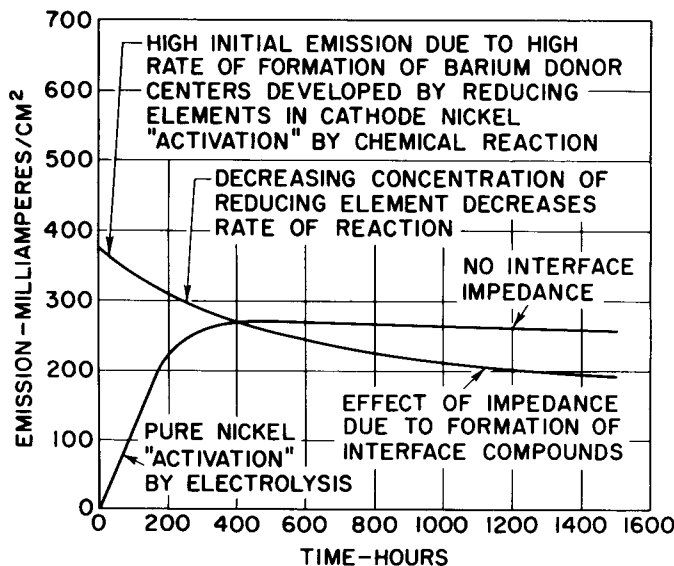


Figure 4. Difference in Level of Emission Obtained from Oxide-Coated Cathodes Using the Same Oxide Coating but Different Cathode Base-Metal Alloys: (1) a reducing-element-bearing nickel alloy having a high rate of initial activation by chemical-reduction processes, but also, having increased impedance effects due to interface-compound formation; (2) a pure nickel alloy having a slow rate of activation by means of electrolysis action, but then maintaining a relatively stable level of performance on life.

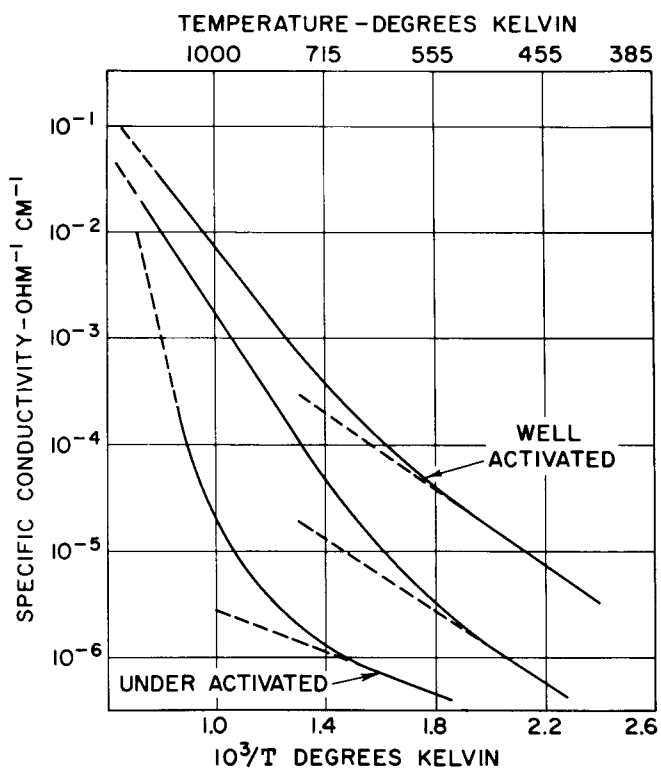


Figure 5. Conductivity of Oxide Coatings as a Function of Temperature for Different Degrees of Activation and Pore-Gas Conduction

100 to 1000 angstroms. Figs. 6 and 7 show representative needle shaped crystal of triple carbonates precipitated by sodium and ammonium reagents.

The methods of precipitation are essentially straightforward. However, because purity of the product is essential to emission performance, the effects of adsorption and entrapment of foreign ions are minimized by the use of proper sequences of precipitation and washing operations. There are two precipitation methods: (1) a batch method wherein one reagent solution is added to the other reagent solution and (2) a continuous flow method wherein both reagent solutions are brought confluently into a reaction zone.<sup>17</sup> In the batch method, the addition of alkali carbonate solution to the alkaline-earth nitrate solution is preferred to the addition of the nitrate solution to the carbonate solution because the former procedure insures the production of a chemically pure product with a smaller amount of contamination from the alkali ions and salts. In the second method, the simultaneous addition of equimolar proportions of alkaline-earth nitrates and alkali carbonates minimizes the impurity content of the adsorbed alkali nitrate ions because the concentration of the alkali nitrate ions is at a minimum at the time of the formation of the alkaline-earth carbonate crystal. Another important feature of continuous flow methods of precipitation is the greater uniformity of the precipitated particle size than that obtained by the batch process. The continuous-flow reaction approaches one of constant-volume constant-con-

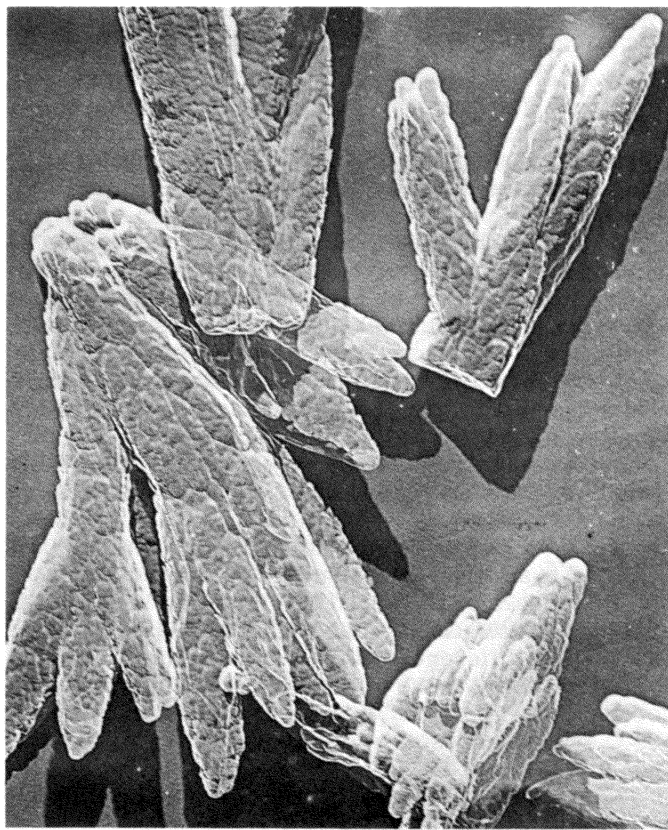


Figure 6. Sodium-Precipitated Triple Carbonate Photographed by Carbon-Replica Technique (electron-microscope magnification  $\times 50,000$ ; courtesy Dr. E.P. Bertin)

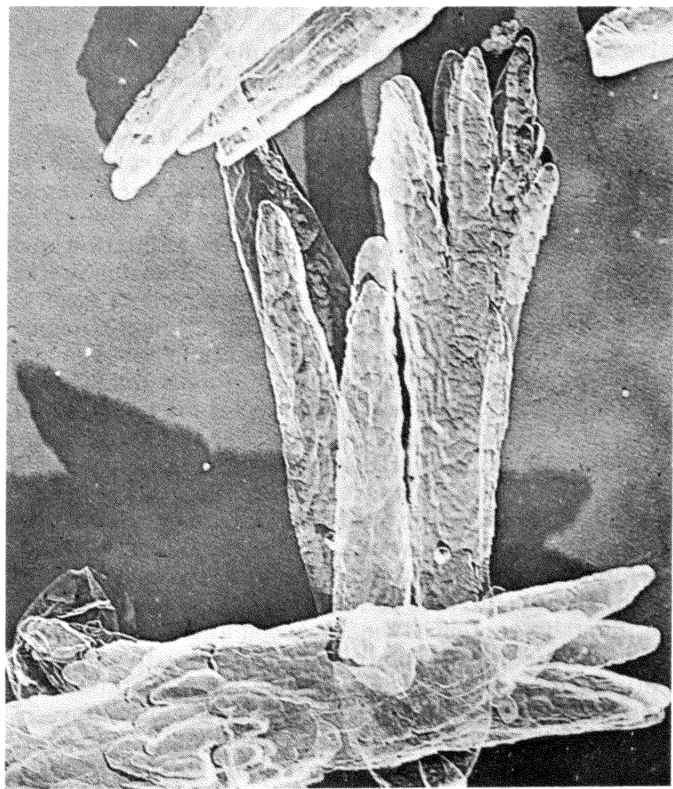


Figure 7. Ammonium-Precipitated Triple Carbonate Photographed by Carbon-Replica Technique (electron-microscope magnification  $\times 50,000$ ; courtesy Dr. E. P. Bertin)

centration during precipitation instead of undergoing dilution as does the batch type of reaction.

Emission carbonates precipitated by the addition of sodium carbonate differ from those prepared by ammonium carbonate reaction in particle size and residual impurity content of the alkali salt.<sup>18</sup> Under equivalent conditions, the "ammonium" type of emission carbonate will tend to be about 10 per cent larger than the corresponding "sodium" type of emission carbonate when precipitated in the temperature range above 80 C. The difference of impurity content between "ammonium" and "sodium" types of emission carbonates is that the former is ammonium nitrate and the latter is sodium nitrate. Both ammonium nitrate and sodium nitrate are adsorbed to an equal extent onto the surfaces of the carbonate crystals or entrapped within the crystals. Both nitrates are washed from these carbonates to the same extent. The difference between ammonium nitrate and sodium nitrate is in the difference in melting points and decomposition products. Ammonium nitrate melts at 169 C and decomposes into gaseous nitrogen, oxygen, and water vapor at 210 C; whereas, sodium nitrate melts at 308 C and decomposes into sodium oxide, nitrous oxide, and oxygen at 380 C. Thus, when the residual impurity is trace amounts of ammonium nitrate, it is lost during bakeout or sealing-in operations. During decomposition from the carbonate, the emission oxide coating is not contaminated with any low-melting-point

substances that might cause excessive sintering and fusing of the coating. Where the impurity is sodium nitrate, the higher melting point and decomposition temperature contribute to side effects in the early decomposition stages of the carbonates leaving a residue of sodium oxides which sublimes at temperatures above 800 C. The low melting point of the sodium salts contributes to the inherent melt condition of the eutectic of barium carbonate (2BaCO<sub>3</sub>:1BaO) which melts at 1030 C. The over-all effect is to increase the tendency toward fused oxide coatings under high speed sealex operation where both the heater wattage and induction heating by RF coils are high, and vacuum pumping efficiency is low.

The particle size of the precipitated emission carbonate and the particle-size distribution of the carbonate are of importance in determining the ultimate porosity of the oxide coating. It is this porosity that contributes to the electron pore gas effect in decreasing the electrical resistance of the coating.<sup>19, 20, 21</sup> Within the limits of the controlling factors of concentration, temperature, pH, and rate of input mixing of the confluent reagent solutions, the method of continuous flow precipitation can give a narrower distribution of particle size range about a given desired particle size than the batch method.

The factors of temperature and concentration, pH of the reacting media, and rate of mixing of the reagent solutions are major determinants of the shape and size of the precipitated carbonate crystals. The crystals are produced as relatively large needles in the temperature range about 80 C. A mixture of crystal forms, varying from spatulate clusters of needles to spherulite forms, are obtained in the mid-temperature range from 50 to 75 C. Spherulite formation is predominant at temperatures below 50 C. All crystal forms within the composition ranges that are used for emission purposes are of the orthorhombic type of lattice formation. Particle size varies directly with temperature and inversely with concentration of the reacting solutions, i.e., needle size increases with increasing temperature; needle size decreases with increase of concentration, provided the temperature is constant. When the pH of the reacting media is below 7, the precipitated carbonate crystals are larger than those precipitated from a reaction medium above pH 7. The rate of addition of the reagent solutions to each other influences the particle size; rapid addition causes small particle-size formation, whereas slow addition causes large particle-size formation. The rate of mixing, the shape of the impeller blade, and the turbulent currents produced in the reactor vessel also influence the crystal habit of nucleation and growth. Manufacturing practice has resulted in the standardization of processes designed to control all these factors to the high degree necessary for the production of uniform, chemically pure, ultrafine quality emission carbonates.

The relationship between the size and shape of the emission carbonate particle as precipitated and the emission performance of an oxide coating is complex.<sup>22, 23</sup> In general, carbonate particle sizes within the limits of 2 to 18 microns in length and 2 microns in diameter yield an oxide coating capable of a higher level of emission than can be obtained from carbonates

which are originally precipitated larger than 25 microns long or smaller than 2 microns long. Emission carbonate crystals that are precipitated either too large or too small yield oxide coatings that are not capable of good emission performance. Ideally, the larger the carbonate-particle size, the higher would be the level of emission obtainable from the oxide coating from these carbonates by reason of the greater degree of porosity. The deviation from this effect in the instance of very large precipitated particles results from three factors.

First, the growth of large carbonate crystals is brought about by long contact with the mother liquor wherein small crystals are solubilized and redeposited onto larger crystals. Such large crystals contain many crevices and cavities enclosing mother liquor solution. These occluded impurities are entrapped by a bridging of the fissure at the surface of the crystal. As a result, it is difficult to remove the impurities by washing. Coarse crystalline material can be much more heavily contaminated than the same material in a finer state of subdivision. However, when the particle size is too small, the effects of adsorption onto the increased surface area also creates a high degree of impurity which is very difficult to remove. Thus, a balance point in terms of optimum particle size must be made between too large or too small a particle size.

Second, large crystals require a longer or harder ball-milling to grind the particle down to dimensions usable for coating techniques calling for smoothness and density needed for close-spaced tube design or high voltage gradient characteristics. The prolonged milling necessary to reach a fine state of subdivision builds up the abrasive content from the ball-mill pebbles (a potassium aluminum silicate clay complex) and, thus, tends to increase the electrical resistance of the coating.

Third, the more porous type of emission coating derived from carbonates of large particle size is capable of being decomposed to the oxide more readily and at somewhat lower temperatures. However, the very porosity of the crystalline matrix subjects it to more extensive sintering from unfavorable gas equilibrium conditions that lead to eutectic-melt formation.

In contrast to these effects of large particle size carbonates, when the carbonate powders are precipitated as very small particles, they are difficult to process and handle in centrifugal washing and filtering operations; the adsorption effects resulting from the increased surface area of matter in a finer state of subdivision increases the impurity content of absorbed alkali salts; and the denser type of emission coating derived from small particle size carbonates are more difficult to decompose on sealex processes and yield a lower level of emission performance due to the increased resistance of the coating that results from the much reduced porosity. Fig. 3 shows that the level of emission performance for the less porous type of coating is definitely lower because of the decreased conductivity of the coating. The denser type of coating, however, is more resistant to "poisoning actions" that tend to decrease the amount of active barium centers of the oxide matrix. The denser type of oxide coating offers

more dimensional stability with respect to grid-to-cathode spacing and, because of the decrease of surface area within the bulk of the less porous oxide matrix, less barium/barium oxide evaporates to contaminate adjoining tube electrodes. In production practice, a balance of factors including particle size and porosity, decomposition characteristics, resistance to poisoning, and level of emission performance determines the final selection of the optimum type of carbonate material to be used.

After precipitation, the carbonates are collected in a centrifuge, washed, reslurried in fresh distilled water, centrifuged, and reashed to free the crystals of residual mother liquor salts and impurities. Next, the carbonate powder is dried to a very low moisture content, blended, and analyzed for purity and composition. Acceptable bulk powder is then stored as approved lots. Carbonate powder is withdrawn from stock upon demand, redried to insure a moisture content of less than 0.10 per cent, and then ball-milled. The technique of application and the end use of the carbonate coating dictate the ball-milling time, selection of binder, and solvents. The number, weight, and size of the ball-milling pebbles, the quantity of carbonate powder and binder solution, the speed of milling in terms of revolutions per minute and peripheral speed, and the viscosity of the charge are maintained at standard conditions to insure reproducibility and uniformity of the emission carbonate coating.

The emission performance of the oxide coating is influenced by the texture and porosity of the emission carbonate coating. The physical properties of texture and porosity of the carbonate coating are transferred to the oxide form despite the conversion from the orthorhombic lattice of the carbonate to the cubic lattice of the oxide crystals. When the emission coating is deposited onto the base metal, the solvents evaporate and leave the carbonates mechanically bonded to the metal with the nitrocellulose or methyl methacrylate binder. The proportion of the weight of the coating to its thickness depends upon the type of cathode and the tube type. The weight and thickness of the coating (i. e., the packing density) must be uniform and reproducible. This uniformity is especially important for maintaining uniform transconductance values.

The type of solvents used in the carbonate-spray formulations influences the bulk density (porosity) of the emission coating as it is applied to the base metal. Solvents having a high vapor pressure (low boiling point) evaporate rapidly and produce a porous, fluffy coating. Solvents having a low vapor pressure (high boiling point) evaporate slowly to leave a smooth, dense coating.

The spray-gun aperture settings control the amount of material deposited per application, whereas, spray-gun air pressure and distance from the cathode control the degree of porosity of the applied coating. High air pressures tend to deposit dry, fluffy coatings; low air pressures tend to deposit wetter, more dense coatings. A dry, porous coating is deposited onto the cathode when the cathode is further away from the gun nozzle; a denser deposit of coating material is obtained when the cathode base metal is closer to the gun nozzle.

Low humidity and high temperature increase the rate of evaporation of the solvents and produce a more porous coating. On the other hand, high humidity causes the nitrocellulose binder to set in a brittle fashion and thus contributes to imperfect adherence of the coating to the base metal. The emission coating is applied in an air conditioned environment at 50 per cent relative humidity and at a temperature of 72 F to insure uniform spray application. The dew point of the water vapor in the compressed air is maintained at minus 40 F to minimize the effects of moisture on the setting of the nitrocellulose binder. The rate of air flow through the spray booth is kept constant to maintain a constant rate of solvent evaporation in order to obtain uniform deposition of the coating. The ratio of solids to solvents and the viscosity of the coating formulation are maintained within close limits. Low specific gravity formulations tend to deposit a wet, dense coating; high specific gravity formulations tend to deposit a dry, porous coating.

Whereas the true density of the triple-carbonate emission powder used in production is about 4.0 grams per cubic centimeter, the range of apparent density of the coatings of emission carbonates as normally deposited onto the cathodes is 0.50 to 2.0. Thus, the porosity of the carbonate coatings ranges from 87.5 to 50 per cent. The range of weight distribution of the carbonate coatings is 3.5 to 8.0 milligrams per square centimeter. A coating that is packed too densely has a lower level of emission performance than a fluffy, porous coating; however, when the coating is too fluffy, its mechanical adherence to the base metal is poor and the coating tends to powder. The standardizing notices show representative curves for weight, outside diameter, and apparent densities that can be used as a guide for design purposes. Ref. 24 describes coatings for oxide cathodes. The character of the spray is classified into three grades — wet, medium, and dry. In general, the adherence of the sprayed coating increases with the wetness of the spray during application. A wet spray produces a smooth, hard coating that is strongly adherent to the base metal and is difficult to damage in handling. A medium spray produces a coating that is visibly rough and which adheres firmly enough to withstand normal handling. A dry spray produces a coating that is decidedly rough and which must be handled carefully because of its fragility.

The use of the tube should determine the density of the coating. Close-spaced rectifiers, where arcing is a factor, require a high-density, smooth coating, as do cathode ray tubes and tubes with very close spacing. High emission performance can be better obtained with low-density porous coatings but only at the cost of lower resistance to poisoning and greater instability in performance. High-density coatings are more stable but have a lower level of emission performance; the quantity-rate of evaporation of barium/barium oxide is reduced to a minimum and grid contamination is less critical. In practice, compromises in coating weights and densities are required to obtain the desired tube characteristics under sealex conditions consistent with the base metal reducing activity and the temperature-time-pressure equilibrium during the decomposition of the carbonate coating.

## The Oxide Form

Oxide-coated cathodes are used under a wide variety of conditions, and some of the requirements which come first to mind include such objectives as: low cost of preparation, high heater efficiency, long life at a continuous emission level of 80 to 130 milliamperes per square centimeter (Fig. 8), and reliable performance under pulse conditions of 40 to 80 amperes<sup>25, 26, 27</sup> per square centimeter (Fig. 9).<sup>28</sup> Tubes can be designed and built with oxide-coated cathodes to last more than 100,000 hours (about 10 years) by operating the cathodes at reduced temperatures. However, the lower the cathode temperature, the more likely is the oxide coating to yield lower emission due to the effects of gaseous residues in the tube. This tendency of the oxide-coated cathode to "slump" under low temperature conditions results from the decrease in the rate of chemical reaction between the reducing element content of the base metal and the oxide. Sufficient active barium centers are not produced to offset the inactivation effects of those physical-chemical reactions from the environmental gas and vapor phase that tend to decrease the amount of active barium donors in the oxide matrix. When the oxide cathode is examined in terms of economy, ease of preparation and fabrication, relative mechanical stability, ease of activation, and relative low rate of evaporation consistent with long life, it is apparent that the alkaline-earth oxides have the lowest usable work function consistent with the objectives stated at the beginning of this paragraph.

Numerous methods are used for the application of the alkaline-earth compounds to the cathode base-metal.

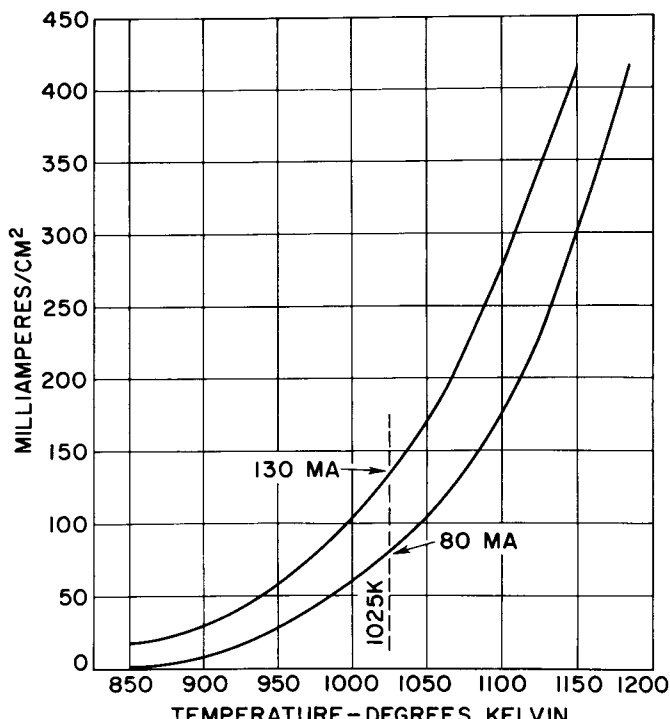


Figure 8. Permissible Direct-Current Density (ma/cm<sup>2</sup>) for Long Life Performance for Average Oxide-Coated Cathodes

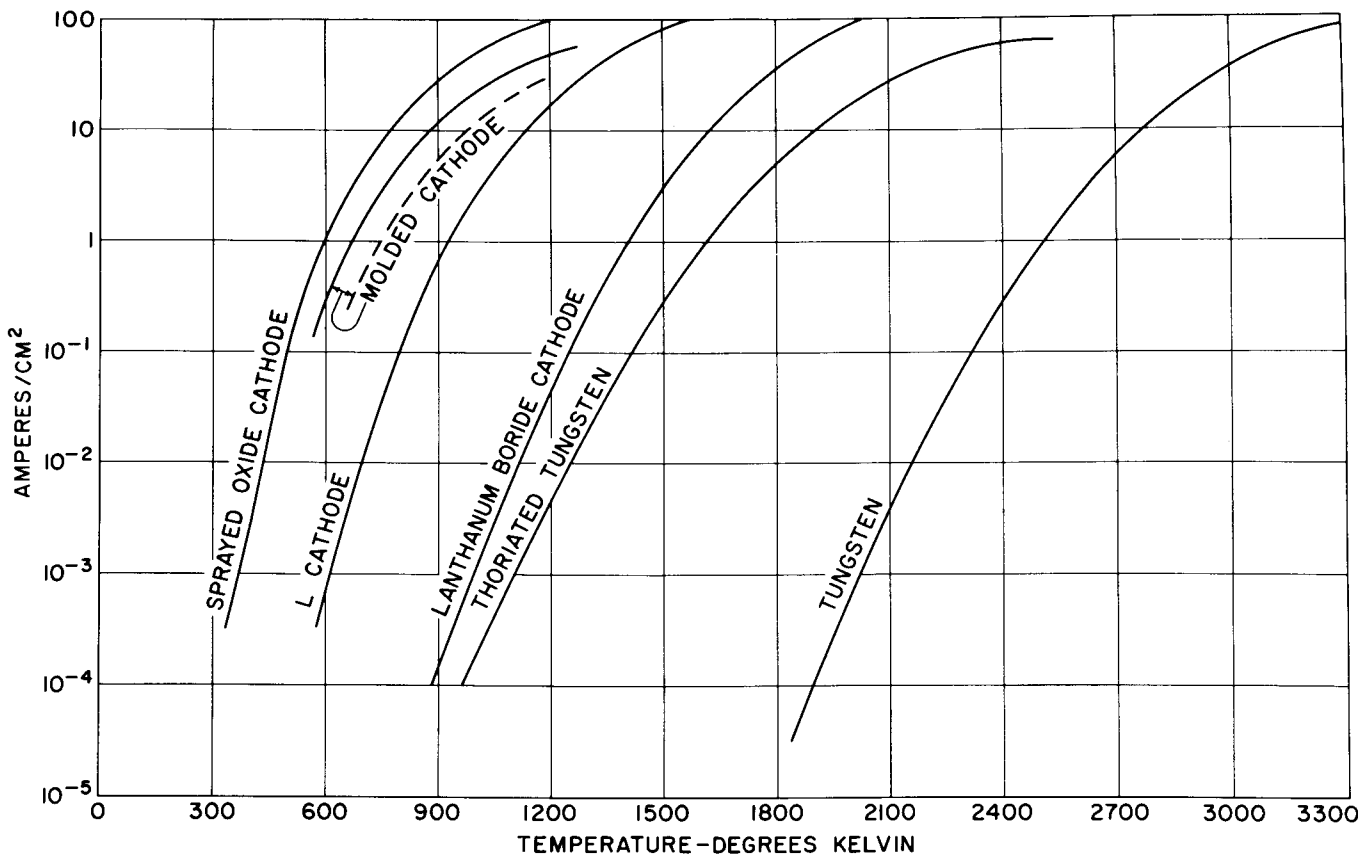
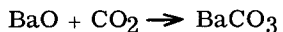
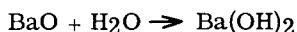
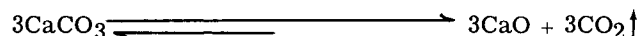
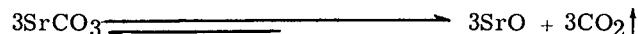
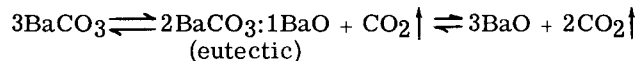


Figure 9. Pulsed-Emission Levels of Cathode Systems<sup>28</sup>

The emission coating can not be applied directly in the form of the oxide during the manufacturing operation because it reacts with water vapor and carbon dioxide in the air to form the hydroxide and carbonate compounds.



Therefore, some barium compound that is stable under atmospheric conditions, pure, and easily convertible to the oxide under vacuum conditions is required for coating the cathode base metal. The alkaline-earth carbonates have this required stability, purity, and convertibility. Although the system barium/barium oxide has the lowest usable work function of the family group (barium, strontium, calcium) at the operating temperature (the work function, in electron volts, for Ba/BaO on nickel is 1.1 at 1025 K; for Sr/SrO on nickel, it is 1.4 at 1175 K; for Ca/CaO, it is 1.9 at 1300 K), the barium/barium oxide system is not useful as an emission coating when used alone, because, as shown in Fig. 10, it inherently passes through a comparatively low-melting eutectic phase while being decomposed from the barium carbonate to the barium oxide.<sup>29, 30</sup> However, the strontium and calcium systems do not pass through such a eutectic phase during the conversion from the carbonate to the oxide form at these temperatures:



The melt condition of the eutectic phase of barium carbonate/barium oxide,  $2\text{BaCO}_3 : 1\text{BaO}$ , (melting point 1300 K) compared to that of barium oxide, BaO, (melting point 2170 K) causes the emission coating that is formed from barium carbonate alone to sinter to a great degree under certain conditions of temperature and carbon dioxide gas equilibrium pressure encountered during sealex operation. In practice, decreased porosity (i.e., fusion) and varying degrees of poor coating adherence to the base metal, in terms of brittleness, result from a greater cohesion for itself as a melt than adhesion to the base metal where the coating is of some thickness other than that of a thin film. The level of emission is reduced in a sintered oxide coating because of the decrease of porosity and increase in the size of the crystallite lattice. The conductivity of such a fused coating is decreased as the effect of the electron pore gas type of electron transfer is diminished. Consequently, the coprecipitated double carbonate of barium-strontium (50/50 mole per cent) composition was used because it minimized the eutectic melt formation of the barium carbonate component as a result of the diluent effect exerted by the strontium carbonate at

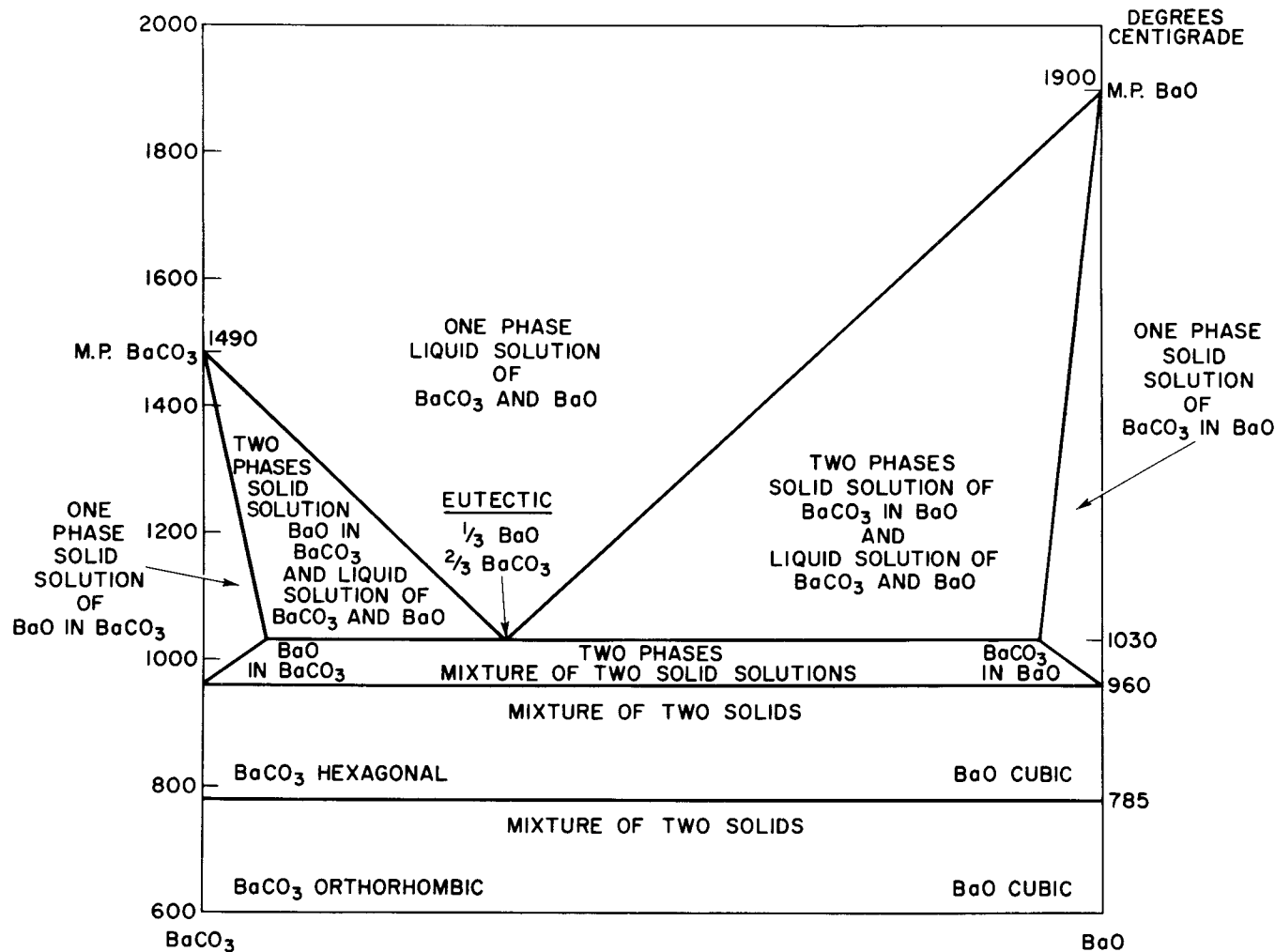


Figure 10. Phase Diagram for Barium Carbonate-Barium Oxide

the temperatures of processing and operation. In addition, the coprecipitated double carbonate, (BaSr)CO<sub>3</sub>, yields larger crystals than the single barium or strontium carbonate under the same conditions of precipitation, i.e., standard temperature, concentration, and rate of reaction. The increased size of the precipitated particles, as carbonates, decreases the ultimate packing density of the emission oxide coating. Similarly, the use of the coprecipitated triple carbonates of barium, strontium, and calcium, (BaSrCa)CO<sub>3</sub> of 57/39/4 weight per cent composition, yields a still larger particle-size formation under the same conditions of precipitation. Figs. 6 and 7 show the large-size needle form of the crystal structure obtained for the triple carbonate. The conductivity of the oxide coatings derived from such carbonates is maintained at a higher level by virtue of the increased mean free path of the electron pore gas associated with increased porosity. The level of emission performance is consequently higher because of the lower voltage drop across the coating.

The complex changes that occur when the carbonate is converted to the oxide have been under investigation by many laboratories. The use of X-ray powder pat-

terns as well as Geiger-counter display on graph recorders has shown that the crystallographic transformations that occur during the decomposition and subsequent heat treatment of the oxide are critical in determining the emission activity of the oxide coating. X-ray data have shown that for the coprecipitated crystal of barium-strontium carbonate (BaSr)CO<sub>3</sub>,<sup>31</sup> there exists a range of lattice constants which vary continuously and linearly with composition indicating that true single-phase solid solution exists through the entire composition range. Similar studies on the triple carbonates (BaSrCa)CO<sub>3</sub><sup>32, 33, 34</sup> indicate that true solid solution can exist for the three component system; it is only when the calcium component is less than 10 mole per cent or 6 weight per cent of the composition ratio, as shown in Fig. 11, that true single-phase solid-solution exists.\*

X-ray investigation of the internal crystallite formation of carbonate particles, by Eisenstein<sup>35</sup> has

\* Bertin, E. P., C. H. Meltzer, and E. G. Widell, X-ray Study of the Triple Carbonates (unpublished)

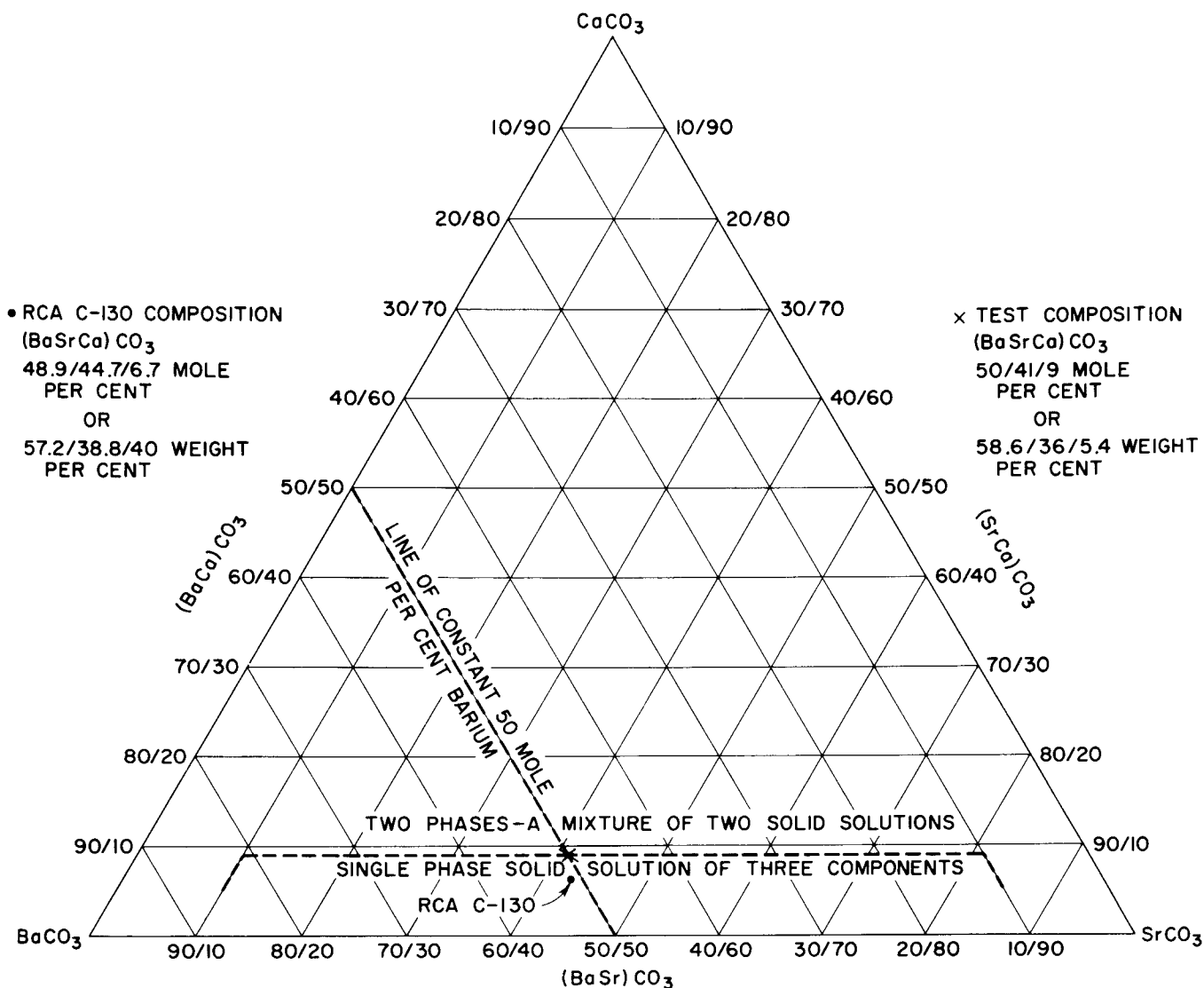
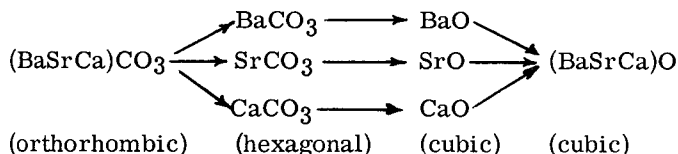


Figure 11. Ternary Diagram for Three-Component Solid-Solution Phase Systems of Barium-Strontium-Calcium Carbonates

contributed an important observation of the decomposition of the emission carbonates. It was noted that in the decomposition of the single-phase solid-solution double carbonate  $(\text{BaSr})\text{CO}_3$  crystals, the strontium carbonate component is converted to the oxide first; the barium carbonate component remaining in the lattice is converted some time later. When the decomposition is completed, the two oxides,  $\text{SrO}$  plus  $\text{BaO}$ , exist as separate phases; crystals of single-phase solid-solution  $(\text{BaSr})\text{O}$  are obtained only after further heat treatment;<sup>36</sup> the critical temperature for this final transformation is about 1050 C. Similar decomposition phenomena occur for the triple carbonates of coprecipitated barium-strontium-calcium  $(\text{BaSrCa})\text{CO}_3$  within a limited range of composition when the calcium component is less than 6 weight per cent.



The important insight into this complex transformation is the fact that single-phase solid-solution carbonates ultimately yield oxides having small crystallite units of 150 angstroms, whereas, mixtures of the single carbonates,  $\text{BaCO}_3$ ,  $\text{SrCO}_3$ , and  $\text{CaCO}_3$ , yield oxides having crystallite units of 250 to 300 angstroms, because of the higher temperature needed on heat treatment to create the single-phase solid-solution oxide from the separate, mechanically mixed, single carbonates.<sup>35, 37, 38, 39</sup> The single-phase solid-solution double carbonate  $(\text{BaSr})\text{CO}_3$  is of larger particle size than either of the separate single carbonates; the single-phase triple component solid-solution  $(\text{BaSrCa})\text{CO}_3$  (where calcium is less than 6 weight per cent) is larger than the comparable double carbonate when made under the same conditions. The coincidence of the resultant smaller crystallite formation in the oxide form with the porosity of the oxide coating derived from the larger-particle-size double or triple carbonate is related by a minimum fusion effect in explaining the higher emission. In a later paper, Eisenstein<sup>40</sup> concluded that the barium oxide molecules move to the surface of the coating by

diffusion to form crystallites and that the crystallites were the source of the low-work-function points from which emission can occur.

The electron-emission performance of the oxide coating derived from the carbonates of barium, strontium, and calcium is primarily correlated with the low work function of the system and its increased electrical conductivity as contributed in part by the porosity of the oxide matrix and the electron pore gas. The system barium/barium oxide has the lowest usable work function for emission purposes in vacuum tubes consistent with ease of activation and relative low rate of evaporation for long life. The presence of the strontium and calcium components in the triple carbonate composition contributes:

1. a diluent effect to offset the low-melting eutectic phase of the barium carbonate-to-barium oxide conversion.
2. a crystal habit of large particle growth of the carbonate form that determines the extent of the porosity of the oxide-matrix emission coating that is obtained.

The single-phase two-component solid-solution-oxide lattice exists for the double oxides  $(\text{BaSr})\text{O}$  and  $(\text{SrCa})\text{O}$  but not for barium and calcium because of the disparity of the size of their ions, i. e., barium possesses an ion radius of 1.35 angstroms, strontium has an ion radius of 1.13 angstroms, and calcium has an ion radius of 0.99 angstrom. The difference between the ion radii of barium and strontium is 16.3 per cent; whereas, the difference between the ion radii of barium and calcium is 26.7 per cent. Solid solution formation in the oxide form can exist only when differences between ion radii are within 17 per cent. X-ray data indicate that all the alkaline-earth-carbonate crystals that are made by coprecipitation to form  $(\text{BaSr})\text{CO}_3$ ,  $(\text{SrCa})\text{CO}_3$  and  $(\text{BaCa})\text{CO}_3$  consist of solid solutions throughout the range of composition (although not always single-phase solid solutions). However, only the oxides  $(\text{BaSr})\text{O}$  and  $(\text{SrCa})\text{O}$  become solid solutions upon conversion from the carbonates. The decomposition of  $(\text{BaCa})\text{CO}_3$  results in a matrix of a microcrystalline mechanical mixture of  $\text{BaO}$  plus  $\text{CaO}$  forms. In terms of significance of the effect of solid solution upon a favorable level of emission, the absence of the solid-solution formation for the  $\text{BaO}$  plus  $\text{CaO}$  matrix is important in the considerations to be given to too high a calcium content in the triple-component-oxide system that is derived from a triple carbonate orthorhombic (needle form) lattice structure.

Under standard conditions of preparation in which concentration, temperature, pH, rate of addition and rate of mixing are held constant, a series of double carbonates of barium and strontium compositions show an increase in the particle size of the precipitated carbonate crystal from 100 per cent barium to 75/25 mole per cent  $(\text{BaSr})\text{CO}_3$ ; the particle-size range and distribution remain essentially constant through the composition range from 75/25 to 25/75 mole per cent  $(\text{BaSr})\text{CO}_3$ ; as the composition ratio becomes richer in the strontium component the particle size decreases from the composition ratios 25/75 mole per cent

$(\text{BaSr})\text{CO}_3$  to 100 per cent strontium carbonate. Commercial practice undertook the preparation and use of the 50/50 mole per cent barium-strontium composition and controlled the particle-size range and distribution in order to influence the porosity of the final oxide-coating form that was used on the cathode base metal. The use of the 50 mole per cent barium component was undertaken for reasons of useful long life performance in terms of sufficient active barium in the emission coating for self-gettering, minimum contamination of adjoining electrodes due to evaporation of barium/barium oxide, and the above-mentioned porosity factor that controlled the conductivity of the oxide coating and, thus, influenced the level of emission performance of the tube.

The use of the coprecipitated triple carbonate of barium, strontium, and calcium was in commercial production in the early 1930 period. At RCA, the composition change was made by the addition of the calcium component at the expense of the strontium component while keeping the barium component constant in the system. Thus, the use of the former double carbonate of 50/50 mole per cent, or 57.2/42.8 weight per cent,  $(\text{BaSr})\text{CO}_3$  was discontinued in favor of the triple carbonate of 57.2/38.8/4.0 weight per cent  $(\text{BaSrCa})\text{CO}_3$  because of the increased level of emission performance that was obtainable from the use of such triple carbonates as they were of larger particle size than the double carbonates when made under the same standard conditions of manufacture.

In discussing particle-size range and distribution of the emission carbonates, comparisons are made within a given series of compositions that are produced under standard conditions. Thus, in terms of tube performance as influenced by the porosity of the oxide coating, i. e., its conductivity, it is recognized that the greater porosity made possible by a change in the precipitation process (use of more dilute reactant solutions, or use of a slower rate of addition) is equally effective as the same degree of porosity achieved at a different concentration of reactants and with a change of component composition provided that the amount of the barium component remains at a value that is useful for tube performance. Precipitated carbonates can be made with the same particle-size range and distribution at two entirely different compositions provided suitable adjustments are made in the precipitating technique. For example, initial levels of performance are the same for double carbonates of 70/30, 50/50, and 30/70 mole per cent barium and strontium when their particle size is the same. Similarly, triple carbonate compositions of 57/39/4, 44/50/6, 49/45/6,<sup>20</sup> and 56/38/6 weight per cent<sup>41</sup> yield initial levels of emission that are equal when they are precipitated with the same particle size and are given equal treatment of ball milling and spray formulation to yield the same weight, diameter, and density of emission coating. The final choice of a composition ratio, or particle-size range and distribution or both for an emission carbonate is based on standardized practices of manufacturing the carbonate, the sealing procedures, and life performance of the tubes under the environmental conditions, i. e., materials of construction, processing methods for preparing these materials for use in the tube, and duty cycle requirements in the application of the tube in the circuit.

Under standard conditions of manufacture, composition ratios of double carbonates ranging from 70/30 to 30/70 mole per cent  $(\text{BaSr})\text{CO}_3$  yield the same particle size. The particle size of the triple carbonate  $(\text{BaSrCa})\text{CO}_3$  i.e., the calcium component is 4 weight per cent, within the same composition range when precipitated under the same standard conditions is larger than the particle size of the corresponding double carbonate with the same barium content. The crystal structure of the barium-strontium-calcium triple carbonates and the emission performance of the corresponding triple-oxide systems have been investigated by the laboratories at RCA, Harrison. It has been observed that a large sub-central area in the three-component phase-diagram system is capable of yielding higher emission performance than can be obtained from the two-component barium-strontium phase system, i.e., larger particle size for the triple carbonate as a single-phase three-component solid-solution carbonate providing that the calcium component is less than 6 weight per cent. For purposes of such comparison, it is necessary to prepare the carbonates under standard conditions. It is known that the oxide coating derived from a solid solution double-carbonate  $(\text{BaSr})\text{CO}_3$  system yields higher emission than one from an oxide coating derived from a mechanical mixture of  $\text{BaCO}_3$  plus  $\text{SrCO}_3$ . For a given heat treatment (temperature and time), a solid solution of the oxide  $(\text{BaSr})\text{O}$  forms more readily at a lower temperature from the solid solution  $(\text{BaSr})\text{CO}_3$  than from the mixed single phases of the mechanical mixture. Part of the explanation for the higher emission from the solid-solution  $(\text{BaSr})\text{CO}_3$  to  $(\text{BaSr})\text{O}$  can be explained by the larger particle size of the carbonate crystal and the resultant greater porosity (increased conductivity) of the oxide coating. Nonetheless, it is important to take into account the lower temperature of 1325 K versus 1400 K at which solid solution phase formation occurs together with the smaller internal crystallite growth as a contributory factor to the higher conductivity of the oxide coating. These considerations apply equally as well to the three-component single-phase oxide of barium, strontium, and calcium derived from the single-phase three-component solid-solution triple carbonate  $(\text{BaSrCa})\text{CO}_3$ . It is interpreted that the presence of the calcium oxide component serves to complex the oxide phase by reason of the smaller ion radius of the calcium compared to the radii of barium and strontium which would tend to yield a distorted crystallite lattice. The three-component triple oxide tends to possess the smallest parameter crystallite lattice of the three systems  $(\text{BaO}$ ,  $(\text{BaSr})\text{O}$ , and  $(\text{BaSrCa})\text{O}$ )<sup>38, 39</sup> and tends to form the single-phase solid-solution oxide with the minimum effects of fusion at the relatively low temperature of 1275 K.

The crystallite formation in the oxide form is determined to some extent by the composition of the carbonate form in that the eutectic melt formation of the barium carbonate component is minimized by the presence of strontium and/or calcium components. Once this eutectic form has been minimized, the interdependence of temperature, time, and carbon dioxide gas equilibrium pressure on the decomposition of the carbonates affects the crystallite growth of the oxide coating. Because the surface energy forces are greater for a fused condition, i.e., the packing density in the lattice struc-

ture is greater, the work function of such crystallite systems is higher than that of a system where the melt formation is at a minimum. Measurement of crystallite growth is a measure of the degree of fusion; crystallite growth is more rapid in the melt condition. Investigations<sup>37, 38, 39</sup> indicate that the growth of crystallites in the oxide form is more rapid from the single barium carbonate (eutectic melt condition is pronounced), less rapid from the double carbonate, and least rapid from the triple carbonate. This effect is observed for emission coatings made from single barium carbonate in which the work function is about 1.25 ev as contrasted with the work function of 1.0 ev for the emission coatings derived from the double and triple carbonates. It is noted that at temperatures below 1070 K the reducing agent activity of the cathode base metal is the dominant factor for obtaining high emission from the oxide coating, but at temperatures above 1200 K, heating effects of high temperatures cause rapid growth of crystallites, i.e., fusion, to become the dominant factor for causing low emission performance. Thus, the higher emission that is obtained from coatings derived from the double and triple carbonates over that of the single barium carbonate occurs by reason of the greater conductivity of the oxide coatings derived from the double and triple carbonates. The increased porosity of the oxide coating derived from double and triple carbonates as well as the smaller crystallite growth in the oxide form contributes to this higher conductivity. The higher conductivity of the triple oxide derived from triple carbonates of the same particle size as equivalent compositions of the double carbonate is due to the still smaller growth of crystallites and slightly better conductivity of the oxide coating.

Thus, the use of the coprecipitated triple carbonate of barium, strontium, and calcium contributed several advantages in terms of tube manufacture and tube performance.

1. The particle size of the triple carbonate within the composition range in use as precipitated under standard conditions is larger than the particle size of the corresponding double carbonate of the same barium content.
2. The thermal decomposition characteristics of the triple carbonate are slightly faster and more uniform than those of the corresponding double carbonate by reason of the larger particle size and the earlier decomposition of the calcium carbonate component, provided that the calcium carbonate content does not exceed six weight per cent.
3. The oxide phase resulting from the conversion of the triple carbonate tends to possess the smallest parameter crystallite lattice structure which contributes to the higher conductivity of the coating; the formation of small crystallites in the oxide crystal phase is indicative of minimum fusion or crystal growth, i.e., a greater degree of porosity is retained in the oxide coating.

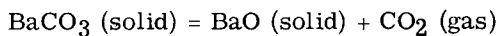
It is evident in the case of the double carbonate system that a series of solid solutions of  $(\text{BaSr})\text{CO}_3$  could be made throughout the composition range and that the series of solid solutions could be maintained in the oxide phase  $(\text{BaSr})\text{O}$  upon conversion of the carbonates to the oxide. However, in the case of the triple carbonate

(BaSrCa)CO<sub>3</sub> it is not possible to attain the solid-solution single-phase triple oxide when the calcium carbonate content is in excess of six weight per cent. In the final analysis, since it is desirable to maintain single-phase solid-solution formation of small crystallite size in the oxide form, it is not essential to increase the calcium content beyond the present composition ratio: (BaSrCa)CO<sub>3</sub> 57/39/4 weight per cent. The qualities of long life, resistance to poisoning effects (optimum porosity, not maximum porosity) under manufacturing conditions, stability, and minimum quantity-rate of evaporation of barium/barium oxide onto adjoining electrodes are important criteria rather than maximum emission under ideal vacuum tube conditions. Thus, the manufacturing, sealex, and stabilizing schedules would determine the optimum composition and particle size (for a given manufacturing schedule) as the time schedule and heat treatment cycle would determine the single-phase solid-solution oxide form that contributes to high emission performance.

## THERMODYNAMIC CONSIDERATIONS OF OXIDE-CATHODE SYSTEMS

In any considerations of the chemical and physical processes that go on during the conversion of the emission carbonates to activated oxide coatings, much thought must be given to a time-temperature-pressure sequence of equilibria reactions. The processes that occur during the decomposition of the carbonates and the subsequent activation of the oxide form influence the properties of the oxide cathode system to a great degree.

Thermodynamic considerations indicate that barium can not be derived from thermal decomposition of the barium oxide nor from the reduction of the barium oxide by the nickel of the cathode base metal. The change in the Gibbs free energy  $\Delta F$  accompanying a change in the state of matter is expressed as  $\Delta F = \Delta H + T(\Delta S)$ , where the symbols H and S represent the heat content (enthalpy) and the entropy respectively, and T is the temperature in degrees Kelvin. For a given chemical reaction, if  $\Delta F$  is negative, the reaction is thermodynamically possible; whereas, if  $\Delta F$  is positive, the reaction does not take place. Where  $\Delta F$  is zero, chemical equilibria exists. For purposes of calculation, the relationship of a substance in its standard state (at a temperature of 298 K and at a pressure of 760 millimeters of mercury) between the standard free energy change  $\Delta F^{\circ}$  for the given reaction at the temperature T is  $\Delta F_p^{\circ} = -2.3 RT \log K_p$ , where  $\Delta F^{\circ}$  is the free energy for the reaction in calories at a temperature T in degrees Kelvin, and R is the molar gas constant equal to 1.987 calories/mole/degree Kelvin. K is the equilibrium constant for the reaction



and 
$$K = \frac{\text{Conc. BaO} \times \text{Conc. CO}_2}{\text{Conc. BaCO}_3}$$

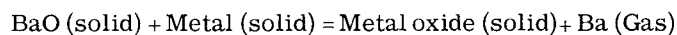
or, in terms of partial pressures (assuming that solids do not possess vapor pressures), the equilibrium constant  $K' = P_{\text{CO}_2}$  (partial pressure of CO<sub>2</sub>). The free

energy change for the transfer of reactants at arbitrary partial pressures to products at arbitrary pressures is given by the equation

$$\Delta F = 2.3 RT \log K' - 2.3 RT \Sigma n \log p$$

$$\text{or, } \Delta F = \Delta F_p^{\circ} + 2.3 RT \Sigma n \log p$$

where  $\Sigma n \log p$  represents the algebraic sum of all the  $n \log p$  terms, those for products being taken as positive and for reactants as negative. The equilibrium constant K' is related to the equilibrium of all partial pressures of all gaseous reactants and products by the rule of mass action and can be applied to the chemical reduction of barium oxide,



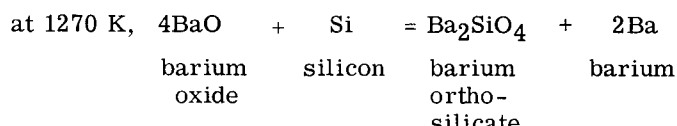
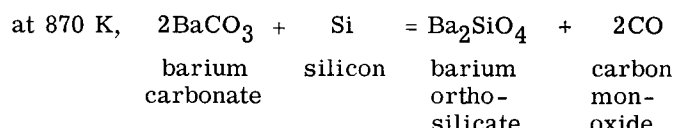
and, therefore, K' is equal to the partial pressure of barium. Heat and entropy data are usually referred to the reference standard temperature of 298 K; therefore, in order to compute  $\Delta F$  at a new temperature of 1050 K, it is necessary to obtain data referring to the variation of H and S with temperature in terms of heat capacity data, such that

$$\Delta F_T^{\circ} = \Delta H_{T_0} + T \Delta S_{T_0} + f(\Delta C_p, T)$$

The factor f depends upon the difference in heat capacity  $\Delta C_p$  between products and reactants and upon temperature T. White<sup>42</sup> and Rittner<sup>43</sup> have indicated the value of such thermodynamic calculations in discussing the rate processes and reactions that occur in the oxide cathode.

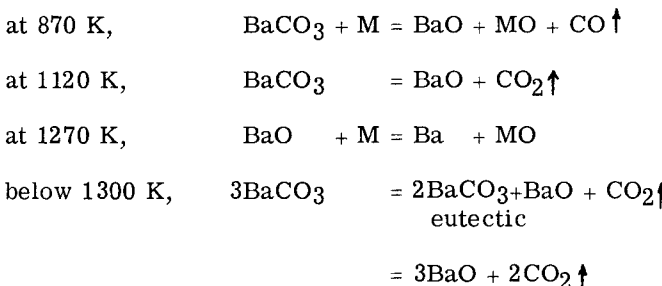
Where gaseous products of reactions are formed, the equilibrium pressures impose an upper limit on the rate of reaction, and also on the rate at which these gas products can be removed. It has been indicated that the diffusion process of the reducing agents in the cathode base metal limits the rate of reaction because the reactants can not be brought together fast enough. The following metals can react with barium oxide to yield an equilibrium pressure of barium above barium oxide: Mg, Si, Zr, Al, and W; the following metals are inert in the presence of barium oxide: Ni, Co, Cu, Pb, Au, Pd, and Pt.

The reduction of barium carbonate by metals to yield carbon monoxide is thermodynamically more favorable than the corresponding reduction of barium oxide. For example, the oxidation of silicon or tungsten by barium carbonate will occur preferentially at the lower temperature of 870 K before the reduction of barium oxide by the silicon or tungsten can occur at 1270 K.<sup>44, 45</sup>



Thus, there can be no effective yield of barium released by introducing reducing agents into the carbonate coating. Barium hydroxide and barium nitrate are prone to oxidize nickel and the reducing metals and are not used in emission coatings. Nickel oxide as an interface compound is highly undesirable because it can act as a "sink" for barium as well as being conducive to poor coating adherence. In some instances, a solid solution of  $\text{NiO}:\text{NiO}_2$  can form in the presence of  $\text{BaCO}_3$  to yield a blue-black barium nickelite,  $\text{BaNi}_2\text{O}_5$ .

The decomposition of the carbonate coating is a critical step in the processing schedule. It is during this time that the carbonate may oxidize the surface layers of reducing elements in the base metal and form oxide or interface compounds prematurely along with the release of carbon monoxide. The time for decomposition must be short and is determined in practice by the pumping characteristics of the sealex system and by the temperature of processing. If, however, the time of decomposition is too fast in terms of pumping efficiency, the partial pressure of carbon dioxide will accelerate a melt situation due to the presence of the  $2\text{BaCO}_3:1\text{BaO}$  eutectic phase, leading to large crystallite growth and fusion effects. Thus, at the time of decomposition, there are several reaction-rate processes occurring, two of which are competitive for the reducing action of the base metal alloy. For example.



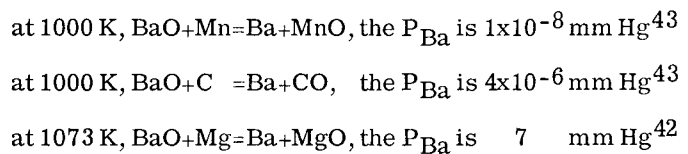
Thus, under conditions of thermal decomposition of the carbonates, wherein the removal of the carbon dioxide gas is too slow, the undesirable side-reactions leading to the reaction of the carbonate with the reducing element of the cathode base metal at the lower temperature of 870 K, and the concurrent reaction of eutectic melt formation, cause low emission and slumping performance on two counts. The side-reaction with the carbonate uses the surface concentration of reducing elements of the nickel alloy so that the rate of replenishment of barium by the main reaction with barium oxide is slowed down to produce a slumping emission with respect to the normal rate of recovery from gas poisoning actions in the tube after processing and aging. Where the interface compound is formed prematurely, an impedance exists that further lowers the emission performance. The eutectic melt formation tends toward a fusion of the oxide coating, decreasing its porosity, and thus increasing its bulk electrical resistance which lowers the level of emission by reason of the decrease of the cathode to anode voltage.

The activation reaction yielding the barium and associated donor sites in the oxide coating is a "reaction-rate" process defined by the temperature and the following physical-chemical kinetics:

1. Concentration of the effective reducing element in the cathode base metal
2. Lattice structure of the base metal and distribution of grain boundary lines
3. Rate of diffusion of the reducing elements along grain boundary lines in the base metal to the interface surface region<sup>46, 47, 48</sup>
4. Rate of chemical reaction of the reducing element with the barium oxide to form barium and the interface compounds
5. Rate of diffusion of barium through the oxide matrix and rate of diffusion of gaseous barium into the oxide lattice involving equilibrium pressures of barium (solid) to barium (gas) to barium (ion)
6. Rate of electrolytic transport of barium ions to the cathode-metal interface region where it is reduced to the barium
7. Rate of diffusion of barium to the surface of the oxide coating
8. Rate of evaporation of barium/barium oxide from the surface of the coating leaving a layer deficient in barium oxide about  $10^{-4}$  centimeters thick<sup>1</sup>

In order to obtain an appreciable solubility of barium in barium oxide, the vapor pressure of barium must be maintained at a rather high level. It is considered that the barium generated at the interface region is transported through the barium oxide matrix of crystals by a volume-diffusion process termed Knudsen flow, or free molecule diffusion.<sup>43</sup> The Knudsen flow effect postulates that the flow of gas through a long tube (pore space) takes place at a pressure such that the mean free path is much greater than the radius of the tube. Rittner calculates that since the barium can penetrate into the barium oxide particle a maximum distance of  $4 \times 10^{-4}$  centimeters, the oxide coating must be a porous mass containing relatively fine particles in order to account for the rate of evaporation of barium, e.g., the rate of evaporation of barium is four micrograms per square centimeter per hour at a temperature of 1225 K for an oxide coating on a nickel base metal alloy containing 0.12 weight per cent Mg.<sup>43</sup>

As previously stated, a reaction is thermodynamically possible in terms of Gibbs free energy change during any change of a state of matter such that the  $\Delta F$  is negative. And since the standard free energy  $\Delta F^\circ$  is related to the equilibrium pressure through the relation  $\Delta F^\circ = 2.3 \text{ RT} \log K'$ , where  $K'$  varies directly with the partial pressure of the barium gas, the relative activity of the reducing element content of the base metal can be estimated in terms of the partial pressure of barium generated by the molecular reaction of  $\text{BaO}$  with the element, e.g.,



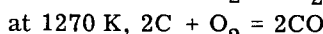
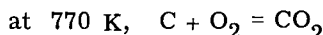
The thermodynamic lower limit for the equilibrium Ba pressure is that partial pressure of Ba produced by the thermal dissociation of  $\text{BaO}$ , i.e.,  $8 \times 10^{-16} \text{ mm Hg}$ ; the thermodynamic upper limit for the equilibrium Ba pressure is the partial pressure of Ba above a  $\text{BaO}$

phase saturated with excess barium which is estimated to be about  $1 \times 10^{-2}$  mm Hg (this limit is somewhat lower than the vapor pressure of pure Ba). Thus, where high pressures are found for active reducing agents, e.g., Mg, it is only because the postulated reaction involving the gaseous Ba phase does not represent the lowest energy state of the system. The calculation does indicate the relative activity of the several reducing elements.

In practice, where the reduction of barium oxide is to be accomplished by a reducing element that is present in very minute concentrations in the nickel base metal alloy, instead of molecular amounts in intimate contact with each other, this type of calculation can not be applied as readily. In order to be able to solve this problem and predict the behavior of the cathode system, it is necessary to have a knowledge of the phase diagram of such dilute-solid-solution alloys, the effective concentration of the reducing element and its rate of diffusion in the alloy; in addition, the free energy of formation of the intermetallic compounds such as Mg<sub>2</sub>C<sub>2</sub>, Mg<sub>2</sub>C<sub>3</sub>, SiC, Al<sub>2</sub>C<sub>6</sub>, WC, Ni<sub>2</sub>Mg, Ni<sub>3</sub>Si, and Ni<sub>4</sub>W must be known before predictions can be calculated.

The reactions between the barium carbonate and the barium oxide forms with the reducing elements in the nickel base metal and with the residual gases in the tube are shown in Table I.

The reactions and equilibria involving carbon monoxide and carbon dioxide are of considerable importance in vacuum tube technology. Around 770 K, carbon (in excess) in an atmosphere of oxygen yields carbon dioxide, but at 1270 K, the reaction of oxygen with excess carbon yields almost pure carbon monoxide:



It follows that the equilibrium between CO<sub>2</sub> and CO at the higher temperature will be toward the formation of carbon monoxide, i.e., C + CO<sub>2</sub> = 2CO, in the presence of excess carbon. It is only at temperatures above 2400 K that carbon dioxide is appreciably dissociated to carbon monoxide: 2CO<sub>2</sub> = 2CO + O<sub>2</sub>. Where excess oxygen is present, both carbon and carbon monoxide are oxidized to carbon dioxide: 2CO + O<sub>2</sub> = 2CO<sub>2</sub>. At

870 K, carbon plus water vapor yield carbon monoxide and hydrogen: C + H<sub>2</sub>O = CO + H<sub>2</sub>; and CO + H<sub>2</sub>O = CO<sub>2</sub> + H<sub>2</sub> occurs at lower temperatures.

Trace reactions can account for methane, alcohol, and even benzene, as follows: CO + 3H<sub>2</sub> = CH<sub>4</sub> + H<sub>2</sub>O; CO + 2H<sub>2</sub> = CH<sub>3</sub>OH; 12CO + 3H<sub>2</sub> = C<sub>6</sub>H<sub>6</sub> + 6CO<sub>2</sub>.

The reactions of methane with barium oxide at high temperatures are really the reactions of carbon and hydrogen, as the methane decomposes quite readily. Thus, CH<sub>4</sub> = C + 2H<sub>2</sub>, then BaO + C = CO + Ba and 2BaO + 2H<sub>2</sub> = 2H<sub>2</sub>O + 2Ba. The reaction of methane with barium oxide gives rise to a high concentration of barium but results in low emission, nonetheless, because the carbon deposits onto the coating to yield a dark surface with a resultant low operating temperature, i.e., with black body radiation.

## DECOMPOSITION OF THE EMISSION COATING

The decomposition of the carbonate coating is a critical step in the processing of an oxide cathode system. In the decomposition process, the carbon dioxide gas is in equilibrium with the barium carbonate and barium oxide phases at definite dissociation pressures with temperature. Because the dissociation pressure for barium carbonate is the lowest of the three component carbonates, it is the determining factor in the selection of the temperature for decomposition. It is during the time that the carbonate is being converted to the oxide that the competitive reactions of the reducing elements with barium carbonate and barium oxide make it mandatory to convert to the oxide phase as quickly as possible in order not to deplete the surface concentration of reducing elements in the base metal before they can react with the barium oxide to yield the active barium. The time for decomposition should be short and is determined in practice by the pumping characteristics of the system and by the temperature. However, when the time for decomposition is too short relative to the pumping efficiency of the system at the surface of the coating, the partial pressure build-up of carbon dioxide gas will repress the decomposition of the carbonates long enough to allow for the direct oxidation reaction of the carbonates with the reducing elements, and also, will create the eutectic melt phase that produces large crystallite growth and fusion effects. If silicon

Table I

Chemical Reactions of BaCO<sub>3</sub> — BaO with Some Reducing Elements

Reducing Element	Temperature	
	870 K	1270 K
carbon	BaCO <sub>3</sub> + C = BaO + 2CO	BaO + C = Ba + CO
magnesium	BaCO <sub>3</sub> + Mg = BaO + MgO + CO	BaO + Mg = Ba + MgO
manganese	BaCO <sub>3</sub> + Mn = BaO + MnO + CO	BaO + Mn = Ba + MnO
silicon	2BaCO <sub>3</sub> + Si = Ba <sub>2</sub> SiO <sub>4</sub> + 2CO	4BaO + Si = Ba <sub>2</sub> SiO <sub>4</sub> + 2Ba
tungsten	3BaCO <sub>3</sub> + W = Ba <sub>3</sub> WO <sub>6</sub> + 3CO	6BaO + W = Ba <sub>3</sub> WO <sub>6</sub> + 3Ba
carbon monoxide	-----	
hydrogen	BaCO <sub>3</sub> + H <sub>2</sub> = BaO + CO + H <sub>2</sub> O	BaO + CO = CO <sub>2</sub> + Ba
		BaO + H <sub>2</sub> = H <sub>2</sub> O + Ba

or tungsten are involved as reducing agents, premature formation of the interface impedance may occur due to the formation of the barium orthosilicate or barium tungstate to yield the consequent lower emission performance. Thus, the sealex operation becomes a complex sequence of events related by the factors of time, temperature, and pressure during the decomposition of the carbonate coating, as shown in Fig. 12,<sup>49</sup> and the diffusion-rate-reaction process of the reducing-element content of the cathode base metal together with the interrelated gas and vapor reactions from adjoining tube elements.

The partial pressure of carbon dioxide gas in the tube during decomposition of the coating on the sealex is determined not only by the size of the cathode and the weight, density, and particle size of the carbonate coating, but also by the rate of exhaust, and the pumping efficiency. The factor of pumping efficiency is influenced by the time, temperature of decomposition, volume of the tube, gas content of the tube, diameter of the tubulation, and the bore size of the plumbing. The vacuum during the decomposition of the carbonates is about  $10^{-3}$  millimeters of mercury on sealex so that a breakdown temperature of 1273 K would be sufficient, provided that the time for decomposition were of the order of tens of seconds. However, production sealex speeds of 1000 units per hour allow only about 2.4 seconds per position and 1.2 seconds for indexing to the next position. Thus, temperatures for initial decomposition of the carbonate coating actually range about 1473 K in order to bring about rapid breakdown of the carbonate coating in the first few positions. X-ray analysis shows that the single-phase solid-solution oxide form occurs about 1350 K; correlating data indicate that the high emission is obtainable from such a small-crystallite solid-solution oxide matrix. Therefore, it is desirable to attain a high temperature for some short period of time in order to obtain good emission per-

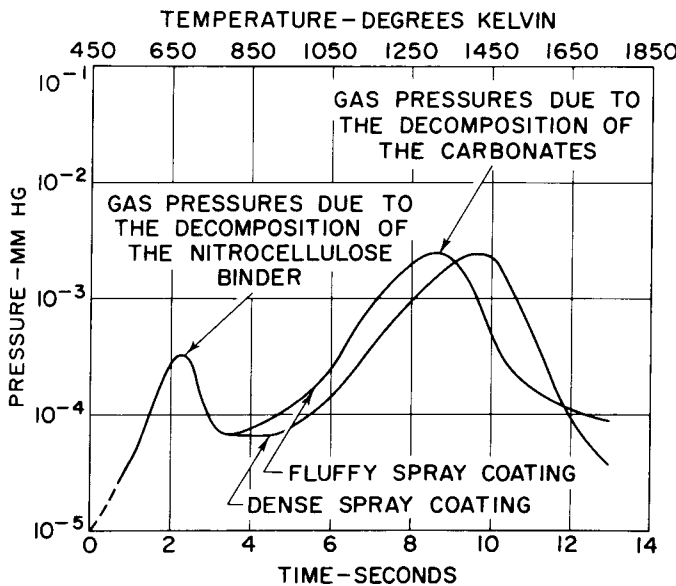


Figure 12. Pressure-Time-Temperature Interdependence on Decomposition of the Emission Carbonates<sup>49</sup>

formance. This result can be achieved by heating the cathode to a high temperature provided certain side-effects do not overshadow the desired goal of a good activated oxide cathode in a tube possessing good operating characteristics. At high temperatures, the following side-effects must be taken into consideration:

1. The more volatile barium/barium oxide can evaporate preferentially from the triple-oxide matrix to an excessive degree, as shown in Fig. 13<sup>50</sup> and Fig. 14<sup>51</sup> and contaminate adjoining grid electrodes and thus tend to introduce effects of primary grid emission, contact potential shifts, and even secondary emission from other electrodes.
2. The crystallite structure of the oxide coating can grow too large and fuse to reduce the conductivity of the coating, and thus, lower the level of emission performance.
3. The evaporation of the more volatile chemical reducing agents alloyed with the cathode nickel, as shown in Fig. 15,<sup>52</sup> e.g., Mg, Mn, can cause leakage paths across adjoining surfaces which would tend to produce feedback, rf noise, and lower transconductance.
4. The nickel cathode base metal (melting point 1450 C) can be softened, i.e., lose hot bend strength, to create bowing of the cathode and misalignment.
5. The tungsten heaters may become embrittled by excessive crystallization and burn out; the insulation

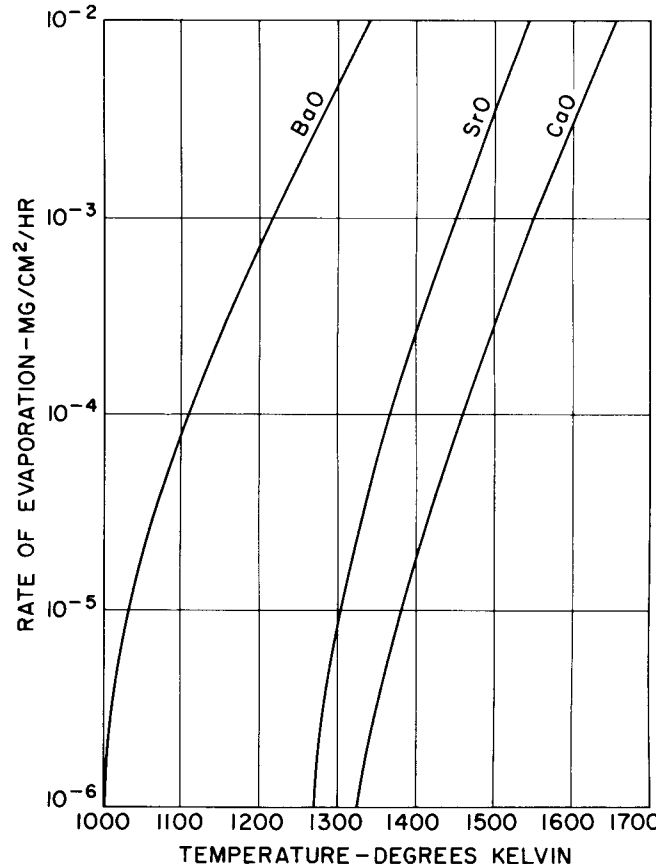


Figure 13. Rate of Evaporation of Alkaline-Earth Oxides<sup>50</sup>

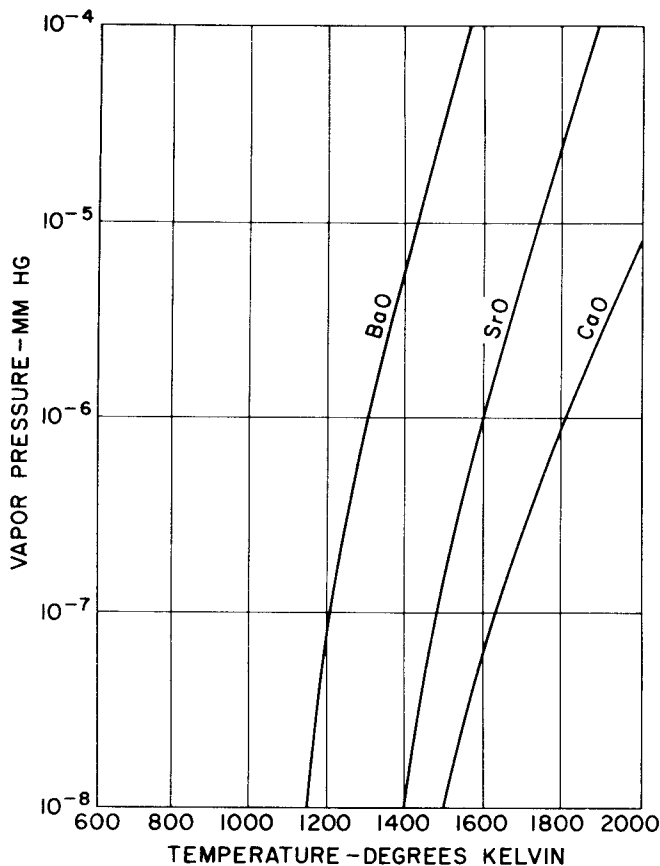


Figure 14. Vapor Pressure of Alkaline-Earth Oxides<sup>51</sup>

coating can become impaired and create heater-cathode leakage effects.

Hence, in practice, there will be an optimum temperature for decomposition; this temperature determines the minimum time for the decomposition of the carbonate coating, provided that the partial pressure of carbon dioxide gas is not excessive.

It can be observed from the curves of the dissociation pressures of the alkaline-earth carbonates, as shown in Fig. 16, that barium carbonate is very difficult to decompose because of the low equilibrium pressure of carbon dioxide that exists at the lower temperatures. The reaction can be driven to completion only by rapid removal of the gas under vacuum pumping conditions. The decomposition of the carbonate coating is primarily a problem of gas evolution-gas removal at the surface of the coating at a given temperature regardless of the vacuum pressure in the tube as a unit that is measured at some distance from the cathode surface. If the condition of temperature and pressure of carbon dioxide gas at the surface of the coating places the system to the right of the equilibrium pressure curves, the carbonates will decompose without giving evidence of pitting or fusion, i.e., the eutectic low melting point phase of the barium carbonate will not have been formed to an appreciable extent. Should the temperature-pressure equilibrium that exists at the surface of the coating place the system to

the left of the equilibrium curve, the barium carbonate component will not decompose quickly enough to avoid formation of the eutectic phase. The entire sequence of events is transient in time (fractions of seconds) such that the pumping efficiency, tubulation bore size, gas content and surface areas of the anodes, and the amount and density of carbonate coating are in critical balance with sealex speed, heater current, and rf induction heating.

After decomposition of the carbonate coating has been accomplished during the early stages of sealexing, the envelope and electrode parts of the tube are further degassed in successive stages of induction heating while the cathode is kept hot by means of the lighted heater. When the cathode coating is in the oxide form, it is vulnerable to the poisoning actions of gases and water vapor that would tend to change it back to the hydroxide or carbonate. After degassing, the tube is "gettered" (the getter is flashed) to absorb residual gases, and then is sealed off. Usually, there has been sufficient chemical reducing activity to create the necessary barium phases in the oxide coating by the reaction of the barium oxide with the reducing agent. A high emission current can be obtained immediately after decomposition of the coating; however, it is often necessary to activate the oxide coating still further after the tube has been sealed off because the amount of barium and associated active donor sites are depleted by reaction with the gases coming from the adjoining electrode surfaces upon electron bombardment during the passage of current in the tube.

Thus, after gettering and sealing off, the tube is usually heated to a high temperature by the use of one and one-half times the rated heater voltage in order to create additional active barium centers by chemical reducing action of the cathode base metal alloy on the oxide coating. Then the residual gases must be removed from the adjoining tube electrodes. This is accomplished by applying positive voltages to grid and anode and drawing current. The electrodes are bombarded by electrons and heated so that their gases are driven off to be absorbed by the getter and by the activated cathode coating. During such treatment, the emission current passes through a minimum and then increases to a higher value as the gases are absorbed by the getter and cathode coating. During this "aging" schedule, the rates of diffusion of reducing elements in the base metals are stabilized and active barium centers in the coating are well distributed by electrolysis and chemical reducing activity. Details of an activation schedule will vary with the tube type and kind of material used in construction. The size and configuration of the electrodes, the properties of the materials, degree of preparation by washing and hydrogen firing, type and position of the getter, cathode base metal alloy (active or passive), coating weight and density, and the efficiency of the original sealex degassing and pumping will determine the activation schedule.

## AMMONIUM-PRECIPITATED CARBONATES

The porosity of the oxide coating, i.e., the degree of fusion and crystallite growth, is adversely affected by low-melting impurity salts that may be present in

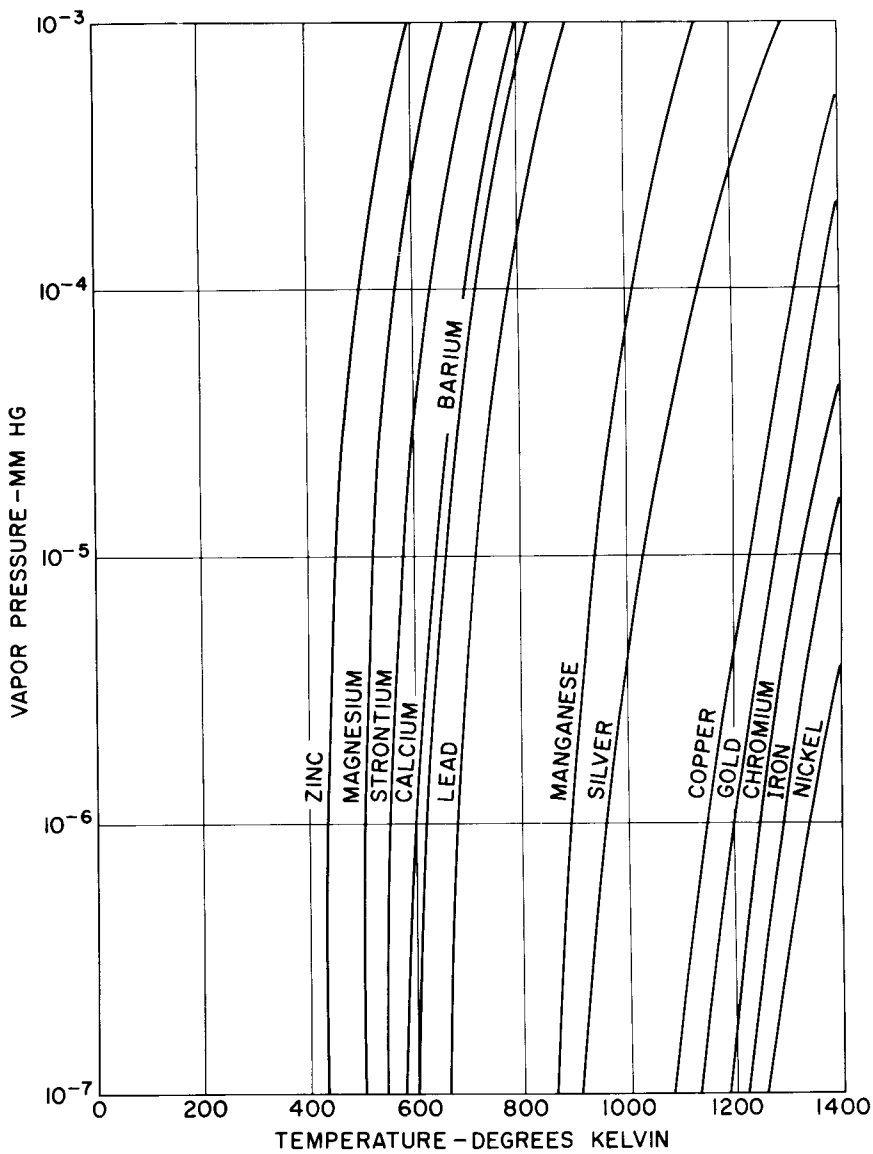


Figure 15. Vapor-Pressure Curves for Some Elements<sup>52</sup>

the emission-carbonate form. As far as can be determined, the presence of low-melting sodium-salt compounds as an absorbed layer at the crystal surfaces of the carbonate causes excessive sintering action between adjoining crystals during the low temperature range (500 to 750 K) of decomposition. Later in the time sequence (measured in milliseconds), the internal content of sodium salts that is released upon complete decomposition of the carbonates contributes to the low-melting condition of the barium carbonate eutectic phase at the higher temperature range of 1000 to 1270 K. Furthermore, it is at this temperature range in the decomposition process that the more volatile sodium/sodium oxide molecules are deposited upon adjoining electrode surfaces. Thus, this volatile sodium contaminant contributes to excessive leakage and RF noise effects beyond the normal level that is ordinarily contributed by deposits of barium/barium oxide.

The ammonium-precipitated type of emission carbonate is purer than the emission carbonate prepared

by use of sodium carbonate reagents because any ammonium salts left in the emission carbonate, after precipitation and washing, vaporize completely as gases. Thus, the oxide coating is purer than the parent ammonium precipitated emission carbonate. Because the oxide coating derived from ammonium-precipitated carbonates contains no contaminant with a low melting point (the eutectic phase is the sole inherent melt condition), it does not sinter and contract in dimensions to the same extent as oxide coatings containing sodium salt impurities. The spacing between cathode and grid does not change as drastically because the sintering action is at a minimum so that transconductance decreases less on life.

In general, the contamination of grid wire surfaces is the result of barium/barium oxide evaporating from the oxide coating. This normal form of contaminant is more stable than where the more volatile sodium/sodium oxide forms are present so that the tube perfor-

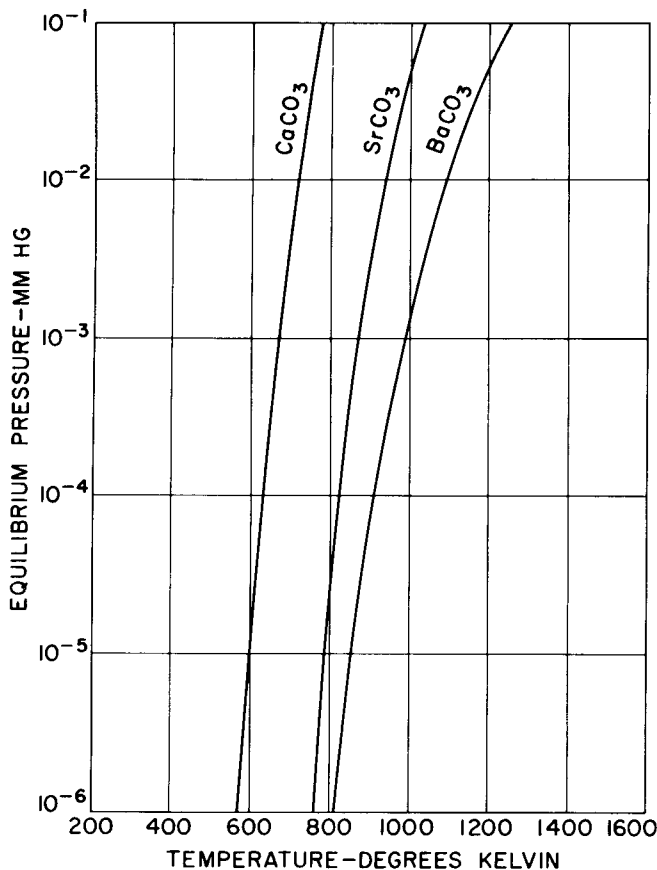


Figure 16. Equilibrium Pressures of the Alkaline-Earth Carbonates

mance slumps less over the life period as the contact potential difference between cathode and grid is more constant. The more stable type of contaminant of barium/barium oxide, ordinarily arrived at by the use of slightly higher controlled hot shot schedules during aging, can not be usefully obtained when using carbonates having sodium-salt impurity content because of the excessive leakage effects induced by the presence of the more volatile sodium/sodium oxide contaminant on grid and mica surfaces.

Compared to the oxide coating derived from sodium-precipitated emission carbonates, the oxide coating derived from ammonium-precipitated emission carbonates is more porous. As such, the latter form reacts more quickly to the poisoning actions of gases in the tube. However, when the tube has been properly degassed, the very porosity of the oxide coating derived from ammonium-precipitated carbonates offers higher conductivity across the coating by reason of the electron-pore gas effect. An improved level of emission performance can be obtained, with more stable contact potentials, minimum screen-grid emission, and minimum decrease of transconductance on life. The important corollary to gas poisoning actions on the oxide coating is the need for proper parts, properly pre-processed. In order to manufacture tubes of good quality, and with minimum shrinkage due to poisoning effects, the proper selection of materials of construct-

ion for anodes, i.e., low gas content together with good heat dissipation capability, or, better parts processing in terms of hydrogen firing and sealex degassing would be required.

## LIFE ASPECTS OF THE OXIDE-COATED CATHODE

The oxide cathode is usually spoken of as an electrode in the vacuum tube. Actually, it is a complex system of interacting phase changes between the nickel base metal and the oxide coating derived from alkaline-earth carbonates. Specific alloys of nickel containing controlled trace amounts of several metallic agents of magnesium, silicon, manganese, tungsten, and even carbon are used to obtain the desired degree of activity from the cathode system. These reducing elements react with the barium oxide to yield barium and associated active donor sites in the oxide lattice at a replenishing rate during the life of the system. The rate of diffusion of these reducing elements is the controlling factor in determining the activity and recuperative power of the cathode during the life of the tube.

The emission carbonates from which the oxide coating is derived has been developed along a range of composition ratios with respect to barium, strontium, and calcium. These carbonates are carefully controlled with respect to size, shape and purity. Moderate bulk density, needleform carbonates are used for most of the applications where high level emission performance is necessary; high density, spherulite forms of carbonates are used for emission coatings where the requirements demand smooth, dense coatings for close-space, high-voltage gradient rectifier service.

After being applied to the cathode by suitable means of spray coating or electrophoretic techniques, the emission coatings are held in place by the binder of nitrocellulose or methyl methacrylate (Lucite) that was present in the carbonate coating suspension. After the coated cathodes have been assembled and mounted in the tubes, the carbonates are converted to the oxide by a combination of heating and vacuum pumping to form an adherent coating of oxide crystals on the cathode base metal; carbon dioxide and carbon monoxide gases, along with other tube gases, are removed by vacuum pumping. Nitrocellulose is oxidized to several forms of nitrous oxides, water vapor, carbon dioxide, and light organic fractions of ethylene at 200 C; where methyl methacrylate is used as the binder, it sublimes as the monomer gas phase at 300 C. A carefully controlled schedule of high-temperature filament heating of the cathode and rf-induction heating of the metallic parts is performed on the sealex. Further high temperature treatment is performed on the cathode, and actual current passage is accomplished during the aging-stabilization step to bring the cathode system to a reasonably high level of emission activity.

The mechanism of electron transfer through the oxide-coated cathode has not been completely detailed in all its phases. There exists a basic semiconductor mechanism for electron transfer coupled with an electron pore gas path of transfer which improves the conductivity of the system. The equilibria phases of barium (solid) to barium (gas) to barium (ion) are involved such

that a large excess of barium vapor phase is required to maintain a threshold content of active donor sites in the oxide lattice. Changes occur in the surface layers of the oxide matrix due to the preferential rate of evaporation of barium/barium oxide from the external surfaces. Strontium and calcium oxides which have lower vapor pressures than barium oxide at the operating temperatures of the cathode system remain after the outer surface is free of barium oxide. Electron-diffraction techniques confirm the fact that for equimolar barium-strontium oxide, the surface layer is almost pure strontium oxide. Eisenstein was able to calculate from X-ray scattering patterns that the surface composition differed from the bulk composition of the oxide.<sup>1</sup> In 115 hours, the surface layers containing less than 10 mole per cent of barium oxide were about  $10^{-5}$  centimeters thick; at 1205 hours, the layer that was deficient in barium oxide was about  $3 \times 10^{-4}$  centimeters thick. In this instance, the cathode coating that was being observed was heated but no current was drawn. Because the physical nature of the external surface of the oxide matrix is independent of the bulk oxide composition, electron affinity for such surfaces would appear to be the same regardless of the bulk composition. In practice, a range of bulk compositions exists that yield the same emission performance when due regard is given to the carbonate particle size and the resultant porosity-conductivity of the oxide coating.

When the emission obtained from an oxide coating is decreased by gases or other foreign material, the term "poisoning" is used to denote a series of physical-chemical reactions that tend to deplete the amount of active donor centers in the oxide lattice as well as to bring about physical changes in the coating that causes its bulk resistance to increase. The poisoning of the oxide coating is most likely to occur at low operating temperatures of the cathode wherein the forward equilibrium reactions creating the active barium centers are slowed down to the extent that the reverse physical-chemical phenomena of depleting the active barium donor content override it.

These "poison" gases or vapors may be given off by the nickel base metal, by the micas, by the heaters, by the anodes, and by the glass envelopes.<sup>53, 54</sup> Water vapor combines with barium oxide or barium to form barium hydroxide which, as a low-melting compound, induces excessive sintering and fusion of the cathode coating.<sup>55</sup> Chlorides and fluorides form low-melting compounds with barium, too. Fused coatings have a minimum porosity such that the conductivity of the coating is decreased, i.e., bulk electrical resistance is increased. Gas poisoning due to carbon dioxide, carbon monoxide, and oxygen are, in effect, the result of harmful equilibrium pressures of these gases that tend to extend the low-melting actions of the eutectic phase of barium carbonate. Where the barium phases are depleted due to the interaction with these gases, the cathode system can bring about a recovery from the effect by the replenishment of the barium by means of the reducing activity of the agents in the nickel alloy. Where the malfunction has been brought about by sintering of the coating, no recovery can be obtained; further processing by activation-aging schedules only worsens the melt situation and increases the bulk resistance of the coating.

The pulse operation of the oxide-cathode system can give initial high currents of 50 to 100 amperes per square centimeter during one or two microsecond intervals provided that the duty cycle (repetition rate) is not excessive. The initial high level of current may decay swiftly due to impedance effects of four basic phenomena:

1. Surface layer "skin resistance" at the oxide-coating-to-vacuum interface. This impedance is thought to be caused by a depletion of active emission centers by reason of a depletion of barium ions which are rapidly transported away from the surface by the large electrolysis effects of high current densities. The removal of positively charged barium ions from the surface layers would leave a relatively high negative field at this surface for the transient one- or two-microsecond interval. Correspondingly, the excessive loss of electrons from the surface during the high-current passage exerts a cooling effect greater than the Joule heating effect in the bulk of the oxide matrix such that the surface layer is at a lower temperature and therefore maintains a high impedance.<sup>27</sup>
2. Interface resistance due to the formation of barium orthosilicate by the chemical reaction of silicon with barium oxide. This type of interface compound, where it exists, offers impedances of 50 to 200 ohms which introduces a large voltage drop — cathode to anode—during large current passage.<sup>56, 57</sup>
3. Insufficient plate-dissipation capability causes gases to be evolved upon electron bombardment of the anode. These gases can react with and deplete the active donor centers of the oxide coating to reduce the conductivity of the coating so that the emission level of performance will be decreased.
4. Blocking action due to the formation of the equivalence of an electron space charge effect in the pore spaces. The large micro-second surge of pore-gas electrons, including high ratio secondary electrons, actually builds up rapidly to exert a space-charge limiting effect within the pore volume to throttle itself back and thus create the decay effect. Thus, rapid cascading avalanche type of secondary electron build-up may be applicable in the instance of the oxide cathode under pulsed conditions.<sup>6</sup>

Normal tube life expectancy is temperature limited. The lower limit of temperature is determined by the level of emission desired and the reserve capacity required to resist poisoning actions; the effects of poisoning increase with decreasing temperature of cathode operation. The upper limit of temperature is limited by several factors, i.e., evaporation of barium/barium oxide, sublimation of base metal reducing elements, sintering of the coating, and interface formation and growth. It has been calculated that 50 per cent of the barium oxide content of the coating would evaporate within 1500 hours at 1200 K, whereas, only 83 per cent of the barium oxide would evaporate within 1,000,000 hours at 1000 K.<sup>51</sup>

The requirements of reliability, stability, and long life from vacuum tubes involve two major areas of tube technology, i.e., the tube-manufacturing operation and the application of the product in electronic circuitry.

## The Manufacturing Operation

From the manufacturing point of view, the problems involved include mechanical failure and electrical failure induced by physical-chemical phenomena. Gross mechanical errors of misalignment, short circuits, vibration hazards and glass breakage, and mechanical failures due to burn-out of heaters, bowing of cathodes and thermal shock can all be minimized by correct design and by the use of selected materials of construction. Electrical failure, on the other hand, that is induced by gaseous products of evaporation and chemical interaction across electrode surfaces is mainly involved in the manufacturing operation of preparation of parts, of maintenance of efficiency and cleanliness of sealex equipment, of the mounting operation, and of observance of the limitations of the materials of construction, e.g., in the use of copper-clad side rods for cooling effect on the grid laterals; one must be aware of the relatively high vapor pressure of copper and its evaporation under too high a setting of the rf induction-heating equipment used for degassing the metal parts.

The physical chemistry of the oxide cathode has been discussed in some detail. The recognition and understanding of the reactions and interactions are important in order to establish a suitable manufacturing process. Controlled purity of the cathode nickel alloy and of the emission carbonates is necessary in order to obtain reproducible results and maintain a manufacturing schedule. The cathode nickel alloy, in terms of its reducing element content and diffusion rate processes, controls initial-life as well as long-life characteristics of the cathode system by its ability to contribute a replenishment rate of supply of active barium emission centers. The oxide coating, in terms of matrix resistance, space geometry, and porosity of structure, effectively controls the level of emission and transconductance values.

These factors are interdependent and are acted upon by the environmental gas and vapor phases in the tube at the time of decomposition of the coating. The geometry of the tube and the sealex speed required for optimum production define the temperature limits for the decomposition of the coating consistent with pumping efficiency and gas removal; these limits, in turn, determine the requirements of weight, outside diameter, and density of the emission carbonate coating. The equilibrium-gas pressures at the transient port and index times on the sealex influence the direction and relative speed of chemical reactions necessary for good activation and for proper porosity structure within the oxide coating. The gas content of the other electrodes in the tube will influence the partial pressures of carbon dioxide and carbon monoxide gases, which, in turn, will affect the decomposition characteristics of the carbonate coating. The optimum conditions for the proper sequential processing of tubes in the manufacturing operation (provided all component parts are properly cleaned and prepared) should consider the following:

1. Glass envelopes should be baked out just prior to use (preferably during the process) to remove much of the air and water vapor that are absorbed in the glass. The release of such gases and water vapor

during tube processing and life poisons the activated oxide coating by reacting with and depleting the active barium centers as well as accelerating sintering of the coating.

2. Sealing-in flames should be adjusted, and the mechanical alignment of the cathode within the tube should be arranged so that the coating is not subjected to temperatures greater than 200 C. The nitro-cellulose binder volatilizes while being oxidized at 200 C leaving the residual carbonate coating poorly adherent to the base prior to decomposition. The result is an incomplete bonding of the coating to the base metal such that peeling of coating can occur initially as well as later on in life. Moreover, when such a poor interface bond exists, proper activation of the coating can not be achieved since good paths for the diffusion of the reducing elements from the base metal do not exist.

3. The "breakdown positions" — i.e., normally, No. 5 and No. 6 in a 16-head sealex operation — should be adjusted for heater lighting and rf-induction heating such that there is a relatively rapid decomposition of the carbonate coating to the oxide form. This cycle is admittedly the result of a balance of many factors among which are the size, weight, and density of the carbonate coating, the total gas content of the adjoining metal electrodes, the warm-up time of the heaters and the orientation of the rf coil for optimum induction heating. The controlling mechanical feature (all other things being equal) is the bore size of the tubulation which determines the efficient removal of the gases by the pumping system. The complex state of affairs that must be balanced is the effect of the relative carbon dioxide gas pressure at the time of breakdown. Where the time-temperature-pressure ratio results in a high relative pressure of the gas, the eutectic melt phase of the carbonate is prolonged to the extent that the resultant oxide coating has a lesser porosity and in extreme cases may be fused. The relatively high partial pressure of carbon dioxide gas at the time of decomposition of the carbonate coating accelerates the oxidation of the reducing element content at the surface of the base metal without creating active barium centers in the coating. The net effect is premature heavy interface formation, low emission, and early life slumping which will require a longer and harder aging schedule to bring the cathode system and tube to a good level of emission performance.

4. The position of the getter in the tube and the position setting of the getter flash coil are of critical importance in creating a good tube. The position of the getter should be such as to eliminate a line of sight path to the cathode in order to prevent poisoning of the coating by the deposition of metallic elements from the getter channel or the getter compound itself. Deposits of getter material onto the insulating surfaces of micas and electrode supports create leakage effects. The use of metal or mica shields can minimize such effects. The getter flashing coil on the sealex should be positioned such that no extensive heating of the anode metal surfaces occur to release gases onto the oxide coating. In this position in the sealex sequence, the oxide coating is not being kept hot while heater lighting is not being applied so that the coating is vulnerable to the poisoning effects of

the oxygen and water vapor that are being released from the glass walls and the metal parts.

The production of a uniform highly reliable tube product is dependent upon parts preparation and processing. Uniformity of cathode-base-metal structure and effective reducing element content (vacuum-melt alloys); uniformity in carbonate-coating weight, density, and outside diameter; well degassed or essentially gas-free parts; and stable line voltages to maintain uniform heater-lighting and rf-induction heating schedules would contribute to this uniformity and reliability. It was indicated earlier that activation can be achieved by chemical reducing activity to create barium centers without the passage of current. Many tube types come off the sealex in an active condition solely by means of thermal action on chemical activity. The use of the aging schedule, after sealex processing, is mainly for the purpose of stabilization and gas clean-up of metal parts by electron bombardment during the passage of current. Correct settings will yield uniform and reliable results: meters should be calibrated; panel wiring, resistors, and ballast lamps should be operative and at rated dissipation wattage. Correct wattages and time sequences will insure reproducible results. In general, hot shot treatments (high heater wattage application without current passage to activate the coating by thermal chemical means) should be at relatively lower filament voltages and longer time sequences rather than at higher filament voltages and shorter time sequences in order to avoid fusion of the coating, excessive rates of evaporation and sublimation from the cathode system that causes leakage, and bowed cathodes.

#### Application End Use

From the operational point of view, the problems involved in insuring tube reliability and long life require consideration of the limitations of materials of construction based on the recognition of the dynamic equilibrium of the physical-chemical processes involved in creating electron emission. Tube design and tube application should take into consideration the following basic ideas.

1. Cathode systems should be designed to operate at the relatively low temperature of 1000 K for long life. The cathode system should be operated within  $\pm 5$  per cent of this rated value in order to obtain optimum life performance.

At operating temperatures above 1050 K, the evaporation of barium/barium oxide is accelerated so that cathode life expectancy is decreased. Deposition of such barium/barium oxide onto adjoining insulating support surfaces creates leakage paths and results in variable frequency response. Deposits of such material onto grid Laterial wires give rise to primary grid emission, reverse grid current which changes the bias, rf noise, shifts in contact potential, and even blocking-action effects.

At operating temperatures below 950 K, the emission level will decrease due to the slower rate of diffusion of the reducing element content of the base metal required to maintain the replenishment rate of

active barium centers needed to compensate for the poisoning action of the normal tube vapor phase. Sparking and arc-over may result due to the high voltage gradient with respect to local hot spots. Cold starting, i.e., application of anode voltage before the cathode has reached operating temperature, should be avoided where possible because positive-ion bombardment will damage the cathode system to the extent of rupturing the oxide-coated surface. Normally, the effects of positive-ion bombardment are minimized because the space cloud of electrons (surrounding the heated cathode system) cushions and neutralizes the velocity of these positive ions.

2. Envelope temperatures should be maintained at reasonably low levels. Glass and metal surfaces adsorb and absorb quite an amount of water vapor and gases; such surfaces, upon being warmed, release these materials as vapors which poison the cathode in the extreme case, and cause slumping performance, grid current flow, and back-bombardment effects in general. For similar reasons, the plate dissipation capability should be adequate to minimize excessive gas release with the wattage required to be handled. The designed factor of safety may be nullified if the ambient temperature of the tube is elevated above that expected in normal tube application. It should be noted that a deposit of getter-flash material on the sidewalls of the tube, where it opposes the radiation characteristics of the anode, can actually reflect 80 per cent of the heat that would have passed through the glass. Therefore, tube and application design should make provision for proper ventilation in order to maintain a low ambient temperature. Where the application requirements demand a higher rating, either a redesign of the tube structure is indicated, or a change in the materials of construction within the same tube design, e.g., substitution of a copper-core, iron-clad, aluminum-clad anode metal for a nickel-clad-iron metal.

3. The maximum tube ratings are limits below which the tube must be operated in order to obtain good performance. In applying ratings of a tube, the equipment designer must take into account the effects of longer duty cycles or higher operating frequencies. Longer duty cycles can impose heavy current demands on the cathode coatings which can cause it to become heated excessively and cause it to sinter. High frequencies can increase tube losses which decrease the output of the tube and reduce its efficiency.

4. Tube characteristics do change on life due to the chemical-physical nature of electron emission that is a function of coating porosity, i.e., characteristics can be changed by sintering of the coating which lowers the conductivity or increases the bulk electrical resistance and also increases the spacing between cathode and grid,<sup>58</sup> by decrease in the effective reducing-element content of the base metal, by decrease in the effectiveness of the getter, and by electrolysis effects on glass which release gas. Thus, circuits should be designed to operate over a rather wide range of tube characteristics. A range of  $\pm 20$  per cent of published values is a commonly used criterion. Acceptable life performance can be extended in many instances if a wider range of plate current and transconductance values can be tolerated. This statement is not intended to imply a looseness in rating which

permits nonuniformity of characteristics; what is intended is that the circuit application of a specific tube be evaluated on the merits of the tube design rather than on the requirements of the circuit. If the circuit requirements are mandatory, a tube of the proper design should be used that can meet the requirements. Some application problems originate from lack of consideration of the limitations of the tube rather than from the defects of its design or manufacture.

5. Formation of interface impedance formerly interfered with standby and cutoff type of operation. The use of high silicon (0.08 per cent) nickel alloy as a cathode base metal would normally create the interface compound, barium orthosilicate, to an excessive extent. The problem is not as extensive today as formerly because most present-day cathodes are of the low (0.02 per cent) silicon type. However, where this problem can still cause malfunctioning because the circuit is operated most of the time well-biased below cutoff, reduction of the heater voltage during periods of cutoff or standby operation will minimize the growth of the interface compound.

6. The problem of grid contamination by evaporation of barium/barium oxide from the cathode system is essentially due to the intensity of the processing technique (high temperature) rather than the cumulative effect during life.<sup>59</sup> The problems of contact potential, grid emission, and developed bias readings are discussed more thoroughly under their specific chapters.<sup>60</sup> However, where negative grid currents may be due to primary grid emission, ionization of residual gases, or leakage currents across micas, high values of grid resistors increase the susceptibility of the circuit to develop a runaway condition. In some instances, the proper choice of a grid resistor of slightly lower value (if it did not change the circuit condition) made the difference between a good tube and a bad one assuming no excessively contaminated grid surface or gas content in the tube.

7. The problem of noise and hum has become more severe in today's high-frequency tubes having closely spaced elements. Noise may be attributed to each of the following: emission coating and gas ionization, as well as electromagnetic, contaminating, and mechanical sources.

a. Shot effect is the noise derived from random bursts of electrons propagated under conditions of temperature-limited emission. The shot effect arises from the discreteness of the electron; the effect has the same intensity at all frequencies.<sup>61</sup> A reduced shot effect is experienced under space-charge limited conditions; the noise is due primarily to velocity variations of the electrons in the potential minimum region.

b. Flicker effect<sup>62,63</sup> is propagated by variations in the activity of the emitting surface of the oxide coating. This effect is essentially a low-frequency variation rather small for space-charge limited conditions but large for temperature-limited conditions. The flicker noise effect is induced by the passage of varying velocity electrons across the charged layer set up on the surface of the oxide coating. Pore gas electrons have different escape velocities induced by them by the effects of elec-

trostatic gradients through the bulk of the oxide matrix. The surface dipole layer comes into existence due to the electrolytic transport of active donor centers back to the cathode and the escape of electrons into the vacuum space during the passage of current. The consequence of the passage of varying electron current across a charged layer is to induce an amplitude-modulated signal of rather low frequency variation. This effect can be minimized to some extent by the use of high-density coatings which result in a reduced porosity of the coating, thus lowering the velocity of these electrons. The use of an oxide coating with decreased porosity reduces the level of emission as rated by the d. c. diode emission test, but there is still sufficient current for normal space-charge limited conditions.

c. Gas ionization effects are induced by variable positive-ion gas currents in the grid circuit. The effects of this noise are not appreciable unless the positive-ion current is greater than 0.02 microampere and its frequency is below 10 megacycles.

d. Electromagnetic induced noise at frequencies above 30 megacycles result from induced voltage variation in the grid circuit due to stray electromagnetic fields; these grid-voltage changes cause the plate current to vary.

e. Reverse grid current noise is induced by negative grid currents, created by positive-ion bombardment or primary grid emission, across composition resistors in the grid-leak circuit.

f. Leakage noise arises from the variable leakage currents along mica insulators and glass due to the contaminants evaporated from the cathode base metal and the oxide coating, e.g., Mg or Mn from the nickel cathode, Ba/BaO from the oxide coating. The phenomenon is closely related to the manufacturing operation, the materials of construction, and the circuit application. Excessive heater wattage during sealex and aging schedules will accelerate the volatile elements (Mg, Mn) out of the base metal along with amounts of Ba/BaO from the coating. The choice of base metal with respect to a low content of Mg or Mn will determine whether a given heat treatment for activation is or is not excessive with respect to the metal. The density of the oxide coating will influence the quantity-rate of evaporation of Ba/BaO. The choice of mica coating or glass surface can determine whether leakage can become a factor as a consequence of processing temperatures. The end application wherein a 12-volt tube is required to pass a 16-volt filament life test, will determine the original choice of material to an even lower content of volatile-reducing-agent content in the nickel base metal, or to a more dense oxide coating.

g. Mechanically induced noise results from heater hum from the use of non-inductive heater windings; this noise may be cancelled out by proper design and choice of winding, i.e., the use of double-helical-wound heater types will cancel out 60-cycle variations in magnetic fields. Noise currents due to heater-cathode leakage effects resulting from alkali impurities in the heater coating can be minimized by the use of pure heater coating material or improved heat transfer characteristics at lower

operating temperatures for the same wattage input. h. Poor mica insulation can allow more than normal leakage currents to flow because its surface is more conductive, or the condition of the mica coating did not provide sufficient roughness to interrupt the continuity of the leakage paths. This effect can be minimized to some extent by the proper choice of mica coating or texture of coating applied to the mica surface.

i. Vibration can cause noise currents to flow. When the vibration is due to loose fit of the cathode within the mica (ballistic microphonics), it is detected when, with no signal input to the stage, a rise in output current results from tapping the tube. This type of vibration effect is rarely caused by original hole-insert diameters but can be due to the enlargement of the opening by excessive heat treatment of the cathode or a life-cycle requirement of the cathode such that the opening in the mica is enlarged by "puffing" of the mica. Vibration itself can also release small amounts of gas from the puffed mica. This gas can contribute a variable-positive-ion gas current in the grid circuit and, so, create a noise effect.

## CONCLUSION

It is apparent that the emission obtainable from an alkaline-earth-oxide film on a nickel-alloy base metal is of the same order of magnitude as that obtained from a cathode system made from a relatively thick coating of oxide. The work functions are essentially the same but the efficiency in terms of milliamperes output per watt input is higher for the thick oxide coating by reason of the porosity factor. The thick oxide matrix coating acts as a reservoir for a replenishment rate of supply of active barium centers by reason of the chemical reducing activity of the base metal to offset the evaporation of barium/barium oxide. The several instances of pulse-emission decay and diminishing performance capability with life are only manifestations of the dynamic equilibria existent in the several physical-chemical processes that exist in the cathode system. The effects of vapor phase interaction and deposition of material onto electrodes in the tube system create unwanted side-reactions. Nonetheless, the oxide-coated cathode is an efficient, consistent performer within those limitations and can be made more stable in operation when due considerations are given to chemical purity in parts processing and sealex operation, temperature limitations, and duty cycle in the end-use application.

Theories of the mechanism of electron emission from a hot metal surface offer an explanation in terms of a kinetic velocity distribution of electrons from the "free mobile" electrons from the valence band into the conduction band. However, a mechanism for transferring electrons through the coating of an oxide cathode is not as yet fully described. The complex nature of the composite surface that is deficient in barium/barium oxide offers a reduced surface-energy-potential barrier and, as such, lowers the work function of the system. In addition to the distribution of barium donor equivalents through the bulk oxide causing the coating to have a high conductivity as a semiconductor material, the porosity of the oxide matrix introduces a factor of elec-

tron pore gas that increases the conductivity to a still greater degree, thereby, yielding the high emission performance. The complete mechanism will, ultimately, include the several rate processes, both chemical and physical,<sup>64, 65, 66, 67</sup> that are involved: rate of diffusion of reducing elements in the nickel base metal; rate of reaction with the oxide coating; rate of thermal diffusion of barium; rate of electrolytic transport; and the equilibrium phases of barium (solid) to barium (gas) to barium (ion) forms.

## REFERENCES

1. Eisenstein, A. S., Oxide Coated Cathodes, Advances in Electronics, Vol. I, 1948
2. Nichols, M. H., "Thermionic Constants of Tungsten as a Function of Crystallographic Direction," Phys. Rev., Vol. 57, p. 297, 1940
3. Pearson, R. F., "Production of Single Crystal Nickel with Faces Parallel to the Desired Plane," Brit. Jour. Appl. Phys., Vol. 4, p. 342, 1953
4. Loosjes, R., and H. J. Vink, "Properties of Pore Conductors," Philips Research Rpt., Vol. 4, p. 449, 1949
5. Loosjes, R., and C. G. Jansen, "Abnormal Distribution of Velocities of Electrons in Oxide Cathodes During Pulse Emission," Le Vide, Vol. 7, p. 1131, 1952
6. Jansen, C. G., R. Loosjes, and K. Compaan, "Velocity Distribution of Electrons of Pulsed Thermionic Emitters," Philips Research Rpt., Vol. 9, p. 241, 1954
7. Nergaard, L. S., "Studies of the Oxide Cathode," RCA Review, Vol. 13, p. 464, 1952
8. Nergaard, L. S., "Physics of the Cathode," RCA Review, Vol. 18, p. 486, 1957
9. Nergaard, L. S., "Thermionic Emitters," RCA Review, Vol. 20, p. 191, 1959
10. Code R1
11. Plumlee, R. H., "Electrolytic Transport Phenomena in the Oxide Cathode," RCA Review, Vol. 17, p. 190, 1956
12. Plumlee, R. H., and L. P. Smith, "Study of the Sublimation Characteristics of Oxide Cathode Material by Mass Spectrography," Jour. Appl. Phys., Vol. 21, p. 811, 1950
13. Aldritch, L. T., "Study of the Evaporation Products of Barium Oxide from Various Base Metals by Mass Spectrography," Jour. Appl. Phys., Vol. 22, p. 1168, 1951
14. Pelchowitch, I., "Mass Spectrometric Analysis of Evaporation Products of Alkaline Earth Oxides," Philips Research Rpt., Vol. 9, p. 42, 1954
15. Metson, G. H., Electrical Life of an Oxide Cathode Tube Advances in Electronics and Electron Physics, Vol. 8, 1956
16. Wright, D. A., "Survey of Current Knowledge of Thermionic Emitters," Proc. IEE, Vol. 100, III, p. 125, 1953
17. Code R2
18. Code R3
19. Hensley, E. B., "Conduction Mechanism in Oxide Cathodes," Jour. Appl. Phys., Vol. 23, p. 1122, 1952
20. Young, J. R., "Electrical Conductivity and Thermo-electric Power of Oxide Cathodes," Jour. Appl. Phys., Vol. 23, p. 1129, 1952

21. Forman, R., "Measurement and Theoretical Study of Electrical Conductivity and the Hall Effect in Oxide Cathodes," Phys. Rev., Vol. 96, p. 1479, 1954
22. Biguet, C., and C. Mano, "Emission Carbonates for Vacuum Tube Cathodes," Le Vide, Vol. 1, p. 137, 1946
23. Violet, F., and J. Riethmueller, "A Study of the Oxide Coated Cathode," Annales de Radio-electricity, Vol. 4, p. 184, 1949
24. Code R4
25. Sproull, R. L., "An Investigation of Short Time Thermionic Emission from Oxide Cathodes," Phys. Rev., Vol. 67, p. 166, 1945
26. Coomes, E. A., "The Pulsed Properties of Oxide Cathodes," Jour. Appl. Phys., Vol. 17, p. 647, 1946
27. Matheson, R. M., and L. S. Nergaard, "The Decay and Recovery of the Pulsed Emission of Oxide Coated Cathodes," Jour. Appl. Phys., Vol. 23, p. 869, 1952
28. Hannay, N. B., D. MacNair, and A. H. White, "Pulsed Emission Levels of Cathode Systems," Jour. Appl. Phys., Vol. 24, p. 1335, 1953
29. Lander, J. J., "The Phase System: Barium Carbonate - Barium Oxide," Jour. Amer. Chem. Soc., Vol. 73, p. 5893, 1951
30. Lander, J. J., "Experimental Heat Contents for BaO, SrO, and CaO," Jour. Amer. Chem. Soc., Vol. 73, p. 5794, 1951
31. Huber, H., and S. Wagener, "The Crystallographic Structure of Alkaline Earth Oxide Emission Mixtures," Zeit. fur Tech. Physik, Vol. 23, p. 1, 1942
32. Terada, J., "Crystal Structure of the Barium, Strontium, Calcium Triple Carbonate," Jour. Phys. Soc. Jap., Vol. 8, p. 158, 1953
33. Terada, J., "X-ray Study of the Ba-Sr-Ca Triple Oxide," Jour. Phys. Soc. Jap., Vol. 10, p. 555, 1955
34. Ostapchenko, E. P., "X-ray Investigation of the System of Double and Triple Carbonates and Oxides of the Alkaline Earth Metals," Izvest. Akad. Nauk. S.S.R., Ser. z 20, 755, 1105, 1956
35. Eisenstein, A. S., "Study of the Oxide Cathode by X-ray Diffraction," Jour. Appl. Phys., Vol. 17, pp. 434, 654, 1946
36. Faivre, R., and G. Chandron, "X-ray Study of the Structure and Thermodynamic Decomposition of the Mixed Carbonates of Barium, Strontium, and Calcium," Compt. Rend., Vol. 226, p. 249, 1948
37. Shimaza, J., "Emission and Crystal Size of the Oxide Coated Cathode," Jour. Phys. Soc. Jap., Vol. 6, p. 479, 1951
38. Yamaka, E., "X-ray Diffraction Study of Oxide Cathodes," Jour. Appl. Phys., Vol. 22, p. 1087, 1951
39. Yamaka, E., "X-ray Diffraction Studies of Oxide Cathodes," Jour. Appl. Phys., Vol. 23, pp. 498, 937, 1952
40. Eisenstein, A. S., and P. N. Russel, "Thermionic Emission and Electron Diffraction from Thin Films of Barium Oxide," Jour. Appl. Phys., Vol. 25, p. 954, 1954
41. Grey, L. E., "Pulsed Emission from the System (BaSrCa)O," Nature, Vol. 167, p. 522, 1951
42. White, A. H., "Application of Thermodynamics to Chemical Problems Involving the Oxide Cathode," Jour. Appl. Phys., Vol. 20, p. 856, 1949
43. Rittner, E. S., "Theoretical Study of the Chemistry of Oxide Cathodes," Philips Research Rpt., Vol. 8, p. 184, 1953
44. Hughes, R. C., P. P. Coppola, and H. T. Evans, "Chemical Reactions in Barium Oxide and Tungsten Emitters," Jour. Appl. Phys., Vol. 23, p. 635, 1952
45. Cayless, M. A., and B. N. Watts, "Reactions Occurring During the Decomposition of Alkaline Earth Carbonates," Brit. Jour. Appl. Phys., Vol. 7, No. 10, p. 351, 1956
46. Hoffman, R. E., F. W. Pikus, and R. A. Ward, "Self Diffusion in Solid Nickel," J. Metals, Vol. 8, No. 5, p. 483, 1956
47. Swalin, R. A., and A. Martin, "Solute Diffusion In Nickel Base Substitutional Solid Solutions," J. Metals, Vol. 8, No. 5, p. 567, 1956
48. Peterson, R. W., D. E. Anderson, and W. G. Shepherd, "Influence of the Cathode Base Metal on the Chemical Activation of Oxide Cathodes," Jour. Appl. Phys., Vol. 28, p. 22, 1957
49. Wolk, B., and J. G. Buck, "The Relationship Between Thermal Decomposition in Vacuum and Macrostructure of the Alkaline Earth Carbonates," The Electrochemical Society, p. 190, 1957
50. Claassen, A., and C. F. Veeneman, "Rate of Evaporation of the Alkaline Earth Oxides," Z. Phyzik, Vol. 80, p. 342, 1933
51. Herman, G., and S. Wagener, The Oxide Coated Cathode, Barth, Leipzig, 1943
52. Honig, R. E., "Vapor Pressure Curves for Some Elements," RCA Review, Vol. 18, p. 195, 1957
53. Higginson, G. S., "The Effect of Sulfur and Oxygen on the Electrical Properties of the Oxide Cathode," Jour. Appl. Phys., Vol. 8, No. 4, p. 148, 1957
54. Grattidge, W., and H. John, "Electronic Properties of Barium Sulfide," Jour. Appl. Phys., Vol. 23, No. 10, p. 1145, 1952
55. Code R5
56. Wright, D. A., "The Effect of Coating Core Interface on Conductivity and Emission of Oxide Cathodes," Proc. Phys. Soc. Lond., Vol. A190, p. 394, 1947
57. Eisenstein, A. S., "Properties of the Barium Orthosilicate Interface," Jour. Appl. Phys., Vol. 20, p. 776, 1949
58. Code R6
59. Haas, G. A., and J. T. Jensen, "Preconversion of Oxide Cathodes," Naval Research Lab. Bul. No. 5275, PB151442, Office of Technical Services, Dept. of Commerce, Washington 25, D. C., 1959
60. Schrader, E. R., "Survey of Methods Used to Determine Contact Potential," RCA Review, Vol. 18, p. 243, 1957
61. Thompson, B. J., D. O. North, and W. A. Harris, "Fluctuations in Space Charge Limited Currents at Moderately High Frequencies," RCA Review, Vol. V, No. 3, p. 269, 1940; Vol. V, No. 2, p. 244, 1940; and Vol. V, No. 1, p. 115, 1941
62. Tomlinson, T. B., "Partition Components of Flicker Noise," Jour. Brit. Inst. Radio Eng., Vol. 14, No. 11, p. 515, 1954
63. Schwantes, R., H. J. Hannan, and A. Van der

- Ziel, "Flicker Noise in Secondary Emission Tubes and Multiplier Photo Tubes," Jour. Appl. Phys., Vol. 27, p. 573, 1956
64. Peterson, R. W., D. E. Anderson, and W. G. Shepherd, "Influence of the Cathode Base on the Chemical Activation of Oxide Cathodes," Jour. Appl. Phys., Vol. 28, pp. 22-31, 1956
65. Noelcke, C. L., "Deterioration Mechanisms in Electron Tubes," ARINC Research Monograph No. 6, Publication No. 101-4-127, 1958
66. Code R7
67. Code R8

such as ammonium dichromate (in older literature it is often called bichromate), is added to the polyvinyl alcohol (PVA) while it is in solution, the resultant dried film may be made insoluble in water by exposure of the film to ultraviolet radiation. Actually, the photosensitivity extends over quite a wide range as shown in Fig. 4.

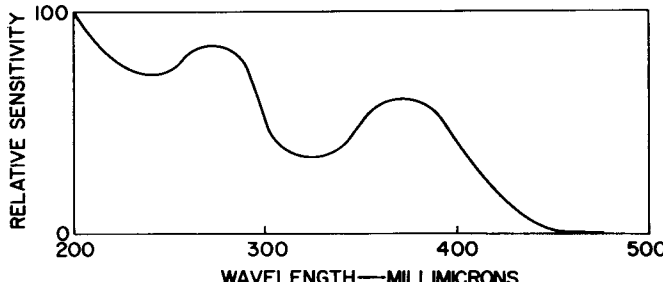


Figure 4. Photosensitivity of PVA-Ammonium Dichromate Film

If only selected portions of the film are exposed to ultraviolet radiation, only those areas become insoluble (other terms are insolubilized, hardened, tanned); the remaining unexposed areas are still water soluble and may be removed by washing them away.

#### EXPOSURE SYSTEM

A high-pressure, mercury-capillary-type, quartz-envelope lamp is a suitable source for an exposure unit (lighthouse). Its spectrum is typical of that of a high-pressure mercury arc. If a suitable orange filter is placed over the light source, beam landing may be checked with a screened faceplate panel without affecting the photobinder. Although dichromated PVA has very low photosensitivity as compared to that of a silver halide photographic emulsion, it must be handled under a safety light which is yellow to orange. White incandescent lamps, fluorescent lamps, or natural daylight are all capable of fogging dichromated PVA films.

#### DEVELOPING

Water is the developer for dichromated PVA. The water is sprayed onto the screen uniformly with considerable force (20 to 30 pounds per square inch). The water pressure and duration of development are adjusted to give good clean-up, i. e., complete removal of unexposed and unwanted areas with as little harm as possible to the desired screen areas.

The basic elements of photodeposition, phosphor application, photobinder application, exposure, and developing, have been combined in many ways to yield the following systems:

1. One-Step Slurry. Phosphor is mixed with phosphor binder and applied to tube face panel as a slurry.
2. Two-Step Slurry, or Tacky Film. Clear photobinder is applied by spinning. Dried film is exposed and developed. Phosphor slurry in unsensitized PVA is applied by spinning and is then dried and redeveloped.
3. Dusting. Clear photobinder is applied by spray-

ing. While film is still wet, dry phosphor powder is air-settled onto wet film. After the phosphor-photobinder layer is dried, it is exposed and developed.

4. Water Settling. Phosphor powder is applied to panel by conventional water settling. Clear photobinder is applied to dry screen by swirling. After photobinder has soaked into settled screen and dried, the screen is exposed and developed.

All four methods are capable of producing high-quality screens. The one-step slurry method has reached the highest degree of perfection. The two-step slurry method is capable of giving the finest elemental screen area definition (since exposure is made without the presence of light-scattering phosphor crystals). The dusting method can yield screens with the optical characteristics of water-settled screens (high contrast, low optical contact). The water-settling method is the easiest way to make a few screens for experimental purposes.

#### ONE-STEP SLURRY PROCESS

The principal steps in screening faceplate panels by the slurry process are given in Fig. 5. Each color phosphor is made into a suitable slurry in its own special way. In order to conserve space, only the preparation of the green slurry will be presented as representative of a currently used typical procedure and compositions. The phosphor powder is ball milled in water for one and one-half to three hours. Following the milling, PVA is added from a 10 per cent stock solution to yield a concentration of 38 per cent phosphor, 3.6 per cent PVA, 58 per cent water. This mixture is rolled in the ball mill an additional one and one-half hours to ensure good mixing. After the mill charge is transferred to a portable mixing vat, a final adjustment of slurry viscosity is made by adding more water. A few hours before the slurry is to be used, it is sensitized with ammonium dichromate from a 10 per cent stock solution.

The final slurry composition, as presently delivered to the factory, is 38 per cent phosphor, 3.6 per cent PVA, 6 per cent ammonium dichromate (based on weight of PVA) and 58 per cent water. The slurry is kept in constant agitation until used. It is applied to the faceplate panel by a combination spinning and tilting cycle. The panel is positioned at 15°, open end up. About 180 milliliters of slurry are added to form a puddle near the center of the panel. The puddle is worked out to the edge and spread over the entire faceplate area by spinning and tilting. The wet phosphor slurry film covering the panel is kept in position by additional spinning until it is dry.

The amount of PVA used in the slurry controls the viscosity, which is adjusted to give the best application characteristics. The amount of phosphor in the slurry is essentially the greatest amount that can readily be held in good suspension. This amount, in turn, is controlled by the amount of PVA present. The concentration of ammonium dichromate is not critical. The exposure time decreases with increasing dichromate concentration, but dot quality and slurry shelf-life are poor at very high dichromate concentrations. The effect of dichromate concentration on exposure time is shown in Fig. 6.

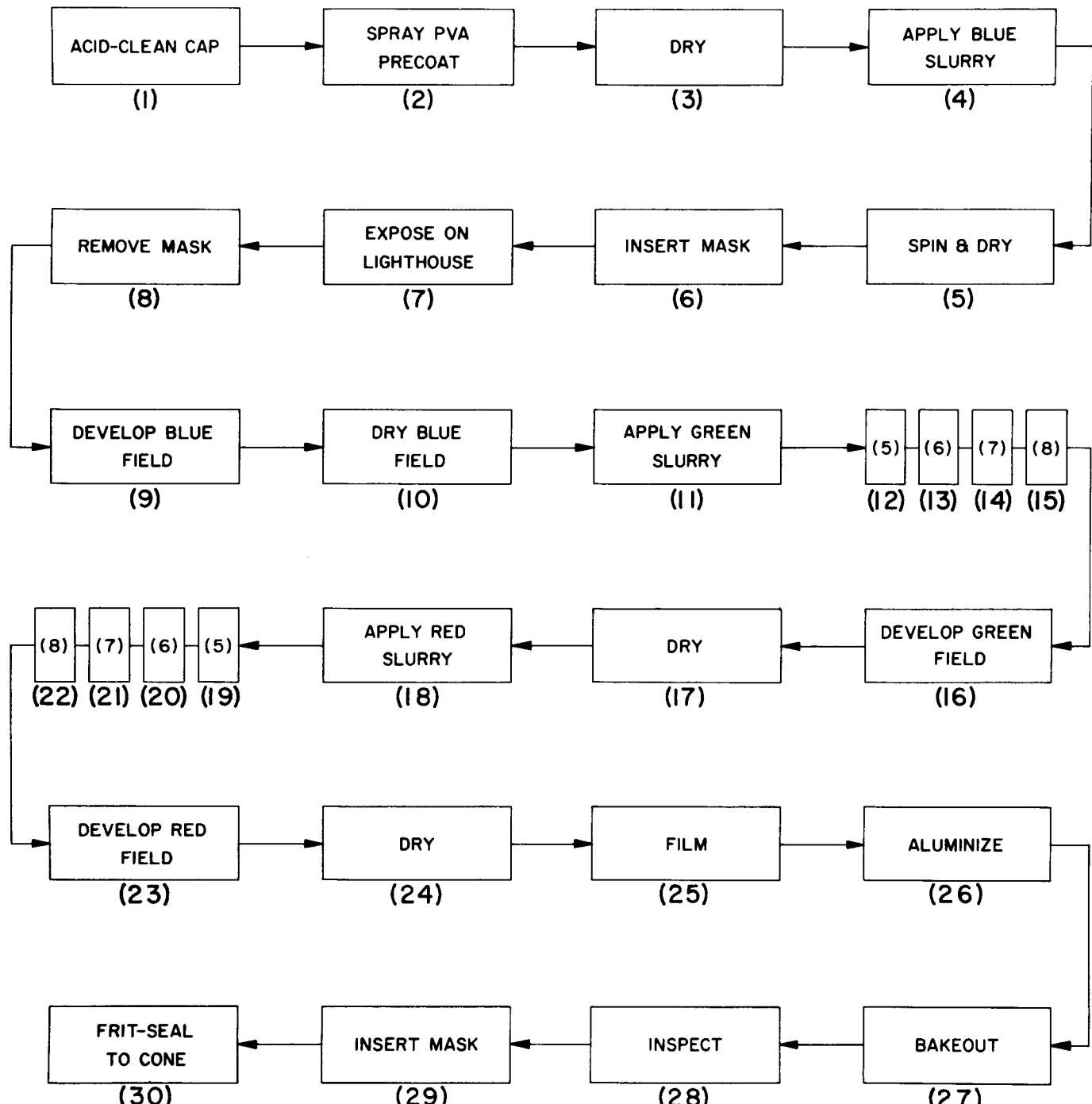


Figure 5. Principal Steps in Screening Face-Plate Panels by the Slurry Process

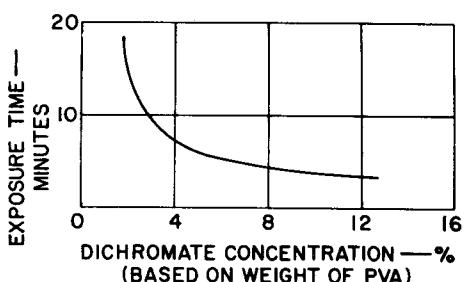


Figure 6. The Effect of Dichromate Concentration on Exposure Time

Phosphor-dot size is dependent, not only on light-source and mask-hole sizes, but also on exposure time. An empirical relationship of exposure time versus hole size is shown in Fig. 7. Final dot size is also dependent to some extent on the pH of the developing water (low pH produces small dots) and the vigor with which the screen is developed. Due to the intensity distribution of light within the light-spot image (see Fig. 8), the core of the phosphor dot is more completely hardened than the edge. In some instances the edge of the dot is not hardened all the way through to the glass substrate and, as a result, the edge, while still wet, is seen to float like a skirt

surrounding the central core. Very hard development will completely break off this skirt, leaving an undersized dot. Prolonged exposure will result in good adherence of this skirt to the glass, giving an oversize dot with poorly defined edges.

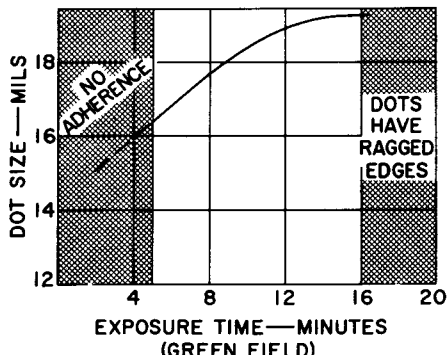


Figure 7. Effect of Exposure Time on Dot Size

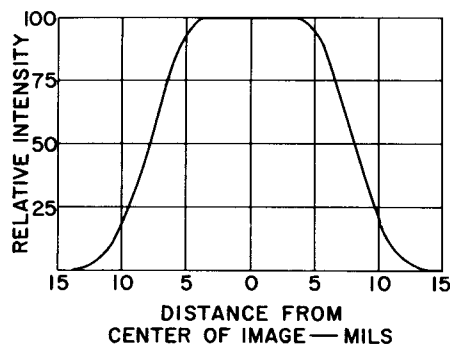


Figure 8. Light Distribution Across an Aperture Image

## SCREEN DEFECTS

### Cross-Contamination

One of the common problems in making the phosphor screen for a color picture tube is the presence of wrong-color phosphor particles on dots of the desired color. Because phosphor dots are coarse and rough on a microscopic scale, there is a tendency for the phosphors that are deposited on dots already formed, to be trapped mechanically. Insufficient development will result in a high level of this kind of contamination, called "cross-contamination."

In addition to mechanical trapping, some phosphors seem to have a natural affinity for one another. The present sequence of depositing the phosphors, i. e., blue, green, and red, results in the least cross-contamination.

### White Nonuniformity

The production of a white field requires that the three color fields be excited simultaneously by their respective guns, and that the beam current for each color be adjusted to give the proper balance for white. If the light output of any field varies over the field, the over-

all color balance will also vary to produce different whites. Thus, a section of the white field may appear pink relative to the rest of the field.

The causes of white nonuniformity include: (1) mechanical causes (misregistry, dented masks, small dots, overlapping dots, missing dots); (2) electrical causes (stray electron excitation); (3) chemical causes (phosphor deterioration or poisoning); (4) physical causes (variation in screen weight per square centimeter).

Phosphor light output is a function of coating thickness or screen weight per unit area as shown in Fig. 9. As a result, screen weight per square centimeter within a field must be held within a certain range if the light output is to remain essentially constant. Although variations in coating weight per square centimeter in excess of twice this range will affect light output to the extent of only 5 to 10 per cent, this variation may degrade white uniformity.

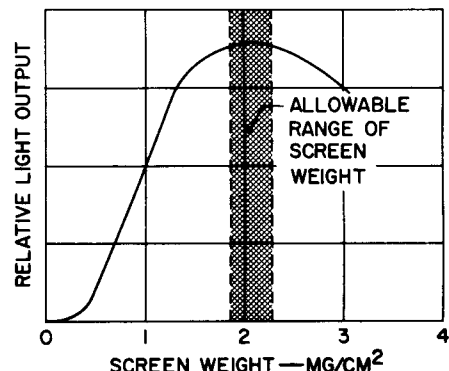


Figure 9. Light Output as a Function of Screen Weight

### Blue-Phosphor Breakdown

No discussion of color tube screen defects would be complete without a brief mention of the long-standing problem of blue-phosphor breakdown. The blue phosphor, silver-activated zinc sulfide, is very susceptible to contamination by copper (0.01 parts per million is detectable).

If the blue-screen phosphor becomes contaminated with copper before the screen-baking stage, the baking will cause activation of the zinc sulfide by the copper and a resultant color change from blue to green. Most screens will have a few sections, perhaps only a dot or two, where copper particles have affected the coating. The principal source of copper is the atmosphere. Accordingly, elaborate filtering of the air is required in the screen-processing areas.

## FILMING AND ALUMINIZING OF COLOR-TUBE SCREENS

Until very recently color screens were filmed in the same general way as black-and-white screens. However, a new filming technique, known as emulsion filming is now available. The emulsion is similar in principle to latex water-base paints wherein an organic film

former is dispersed in water. After the emulsion is applied by a slurry technique, it is allowed to dry while spinning is continued. As the water evaporates, the organic molecules get closer together until finally they coalesce and form a true organic film. Emulsion filming, particularly for a separate faceplate panel, is cheaper, safer, and more readily automated than conventional spray filming.

The process of aluminizing color screens is similar to that employed for black-and-white screens. Because the evaporator does not have to be inserted through the neck of the color tube, four widely spaced evaporators are used. The use of several evaporators is particularly fortunate because they facilitate obtaining a thick aluminum film. The aluminum thickness in the color tube is in the range of 3000 to 4000 angstroms which is about two times as great as that for black-and-white tubes. This very thick aluminum is needed to absorb low-velocity secondary electrons and to attenuate high-velocity scattered primary electrons, which, if they reached the phosphor screen, would degrade field purity and white uniformity.

## SCREEN BAKEOUT

The final step in the processing of color-tube screens is screen baking. The screened, filmed, and aluminized panels are placed on a flat horizontal wire-mesh conveyor belt which carries the panels through a six-zone lehr oven. Fig. 10 is a plot of a typical oven temperature calibration run and shows the temperature in each zone.

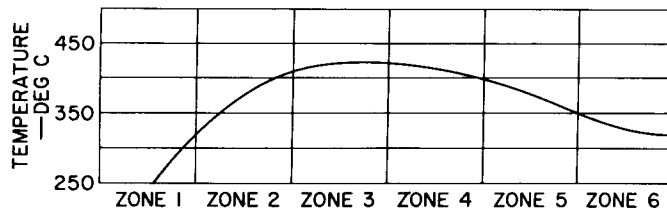


Figure 10. Typical Oven-Temperature Calibration Chart

During the lehr-oven bakeout, the PVA and filming lacquer are removed by decomposition, combustion, evaporation, and sublimation. All of the organic material must be removed if a good vacuum is to be maintained in the finished tube. All of the organic material removed by the baking must pass through the many pinholes normally present in the aluminum film. Filming and aluminizing techniques which do not result in adequate aluminum-film porosity result in blistering of the aluminum.

Recent radiotracer studies give quantitative data, Fig. 11, on the effectiveness of time and temperature in removing the PVA.

## PHOTOMETRY OF PHOSPHOR SCREENS

Seeing is such a subjective act that countless systems of light units and definitions have come into existence. It is helpful to go back to the old concept of a single candle

placed at the center of a sphere having a radius of one foot. By agreement, let the candle have an intensity of one candle.

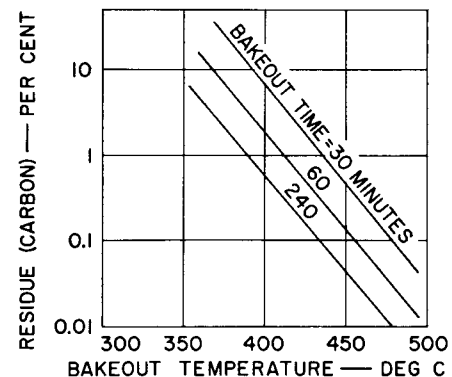


Figure 11. The Effect of Time and Temperature on the Removal of PVA

Further assume that the candle emits uniformly in all directions. It is then convenient to divide space surrounding the candle into unit solid angles with their apices at the candle. The unit solid angle used is the steradian. The candle flame is surrounded by  $4\pi$  lumens.

A one-square-foot section of the sphere with a radius of one foot subtends a solid angle of exactly one steradian. It follows that the illumination on the one square foot is one lumen. By definition, one lumen per square foot is equivalent to an illumination of one foot candle. If the illuminated surface is fully diffusing without absorption or specular reflection, it will have a brightness of one foot lambert. If the surface absorbs one-half of the incident flux, its brightness will be one-half foot lambert.

An extended light source, such as a cathode-ray-tube screen, has a candle-power equivalent. A phosphor screen is essentially a Lambertian emitter: its candle power intensity varies with the cosine of the angle of view. As a result, a one-candle extended source emits a total of only  $\pi$  lumens on one side.

For example: In Fig. 12, S is a phosphor screen.  $I_0$  is the candle power of the screen, measured on its axis at a distance from S.

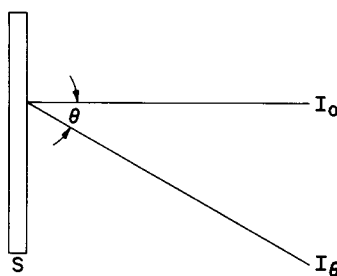


Figure 12. Derivation of Observed Brightness of an Extended Source

Candle power at an angle  $\theta$  from the axis is:

$$I_0 = I_\theta \cos \theta$$

and the apparent brightness of  $S$  is:

$$B = \frac{I}{S}$$

$$\text{but, } I = I_0 \cos \theta$$

$$\text{and } S = S_0 \cos \theta$$

$$\text{Therefore, } B = \frac{I_0 \cos \theta}{S_0 \cos \theta} = B_0$$

and the observed screen brightness is independent of direction of view.

The basic equations for the cathode-ray-tube-screen light source are as follows:

$$\text{One candlepower (Cp) (extended source)} = \pi \text{ lumens (on one side)} \quad (1)$$

$$\text{One Cp/ft}^2 = \pi \text{ lumens/ft}^2 = \pi \text{ foot lamberts} \quad (2)$$

$$\text{The candlepower} = \frac{\text{area (ft}^2\text{)}}{\pi} \text{ foot lamberts} \quad (3)$$

$$\text{or, foot lamberts} = \frac{\text{Cp } \pi}{\text{area (ft}^2\text{)}} \quad (4)$$

For example:

A color tube which has a screen area of 250 square inches (1.735 square feet) with a brightness of 8 foot lamberts, has a candle power equivalent of:

$$Cp = \frac{1.735 \times 8}{\pi} = 4.42$$

and emits  $4.42 \times \pi = 13.9$  lumens.

If the tube operates at a voltage of 25,000 volts and 400 microamperes ( $25,000 \times 400 \times 10^{-6} = 10$  watts), the efficiency of the screen itself as a light source under these conditions is  $13.9/10 = 1.39$  lumens per watt.

## MEASURING INSTRUMENTS

The most widely used device for measuring screen brightness is a photovoltaic cell equipped with a correction filter to simulate the color sensitivity of an average eye. This type of instrument is usually calibrated in terms of illumination from an incandescent lamp which has been calibrated by the National Bureau of Standards.

If the photocell unit is used at distances which are large compared to the size of the phosphor screen, readings are obtained in foot candles, and reliable values for screen brightness may be calculated. The general practice, however, is to place the cell on the tube face and, under this condition, brightness is supposedly measured directly. However, the large ac component in the photocell current due to raster scanning and light losses resulting from rays reaching the photocell face at oblique angles can introduce very large errors.

An early subjective instrument used for illumination measurements is the MacBeth illuminometer. This instrument requires matching the brightness of a built-in incandescent lamp with the brightness of the phosphor screen. Because the color of the phosphor light and that of the lamp are quite different in most cases, much experience is required for the proper use of this instrument. Another instrument, known as the Spectra Spot Brightness Meter, uses a lens system and a multiplier phototube. It reads directly in foot lamberts and can measure areas as small as 0.030 inch in diameter. This instrument also presents problems in reading the absolute brightness of a phosphor.

It is recommended that all photometers for measuring color television screens be calibrated with the standard diffuse sources available from the National Bureau of Standards (NBS). NBS is preparing a new diffuse source for measurement of black-and-white screens to replace the original standard which is no longer available.

Measurements made with an eye-corrected photovoltaic cell, Weston Model 759, calibrated on the NBS color primary standards at a distance from the source of three times the source diameter, gave the basic efficiencies shown in Table III.

Table III

Tube Type	Screen Phosphor Number	Phosphor	Efficiency lumens/watt
Display Storage Tube	P20	ZnCdS:Ag	60
21CEP4	P4	ZnS:Ag + ZnCdS:Ag	36
5ABP1	P1	Zn <sub>2</sub> SiO <sub>4</sub> :Mn	30
21CYP22	P22	Blue-ZnS:Ag Green-Zn <sub>2</sub> SiO <sub>4</sub> :Mn Red-Zn <sub>3</sub> (PO <sub>4</sub> ) <sub>2</sub> :Mn	{ 1.39 7.3*
5WP11	P11	ZnS:Ag	27
5WP15	P15	ZnO:(Zn)	18
5ZP16	P16	CaMgSiO <sub>3</sub> :Ce (ultraviolet)	0.09

\*Corrected for mask loss.

## COLOR MEASUREMENT AND SPECIFICATION

The basic instrument for measuring color of phosphor screens is a spectroradiometer. This instrument determines the emission intensity of a source as a function of wavelength over a certain wavelength interval. It is often confused with a spectrophotometer which usually can only measure the fraction of incident light that is transmitted or is reflected by a substance. Curves obtained with a spectroradiometer are called spectral-energy-distribution curves (S.E.D. curves).

Because colors are not uniquely determined by S.E.D. curves, such curves have limited direct value. However, starting with the S.E.D. data, it is possible to convert to an objective color specification system such as the C.I.E. (Commission Internationale de L'Eclair-

age) color system—formerly I. C. I. (International Commission on Illumination). In this system, every color is uniquely determined by a set of x, y, and z coordinates. Because x, y, and z are coefficients which add up to one (see below), only two are required to define a color. By convention, x and y are used.

The C.I.E. color system cannot be discussed in detail here; however, the following defining equations are vital to the use of the system:

$$x = \frac{X}{X + Y + Z} \quad (5)$$

$$y = \frac{Y}{X + Y + Z} \quad (6)$$

$$z = \frac{Z}{X + Y + Z} \quad (7)$$

from the preceding equations

$$\frac{X}{x} = X + Y + Z \quad (8a)$$

$$\frac{Y}{y} = X + Y + Z \quad (8b)$$

$$\frac{Z}{z} = X + Y + Z \quad (8c)$$

where x, y, and z are the trichromatic coefficients

X, Y, and Z are the tristimulus values

The conversion from the S.E.D. data to the x and y coordinates is accomplished by a set of three integrations where, in effect, the source is resolved into the relative amounts of the C.I.E. primaries required to color-match the source.

A plot of the x and y coordinates for the pure-spectrum locus produces a horseshoe-shaped locus in Cartesian coordinates. This locus with a straight line joining the ends is called the color mixture diagram. All colors will have coordinates lying within this area.

A very useful characteristic which applies to the mixing of phosphor colors (a color-addition process) is the fact that a straight line joining two phosphor points represents all the intermediate colors that can be obtained from mixtures of these two phosphors. For example, it can be seen in Fig. 13 that combining a blue phosphor and a yellow phosphor in the proper proportions will produce white. It is this principle that is used in the making of screens for black-and-white picture tubes. Color mixture problems may be solved by considering them as moment arms. The two colors have a certain intrinsic colorimetric weight, called stimulability, which must balance around the mixture point as a fulcrum. Stimulability is defined as luminous efficiency Y (lumens per watt) divided by y.  $S = Y/y$

It has been shown that  $Y/y$  is equal to  $X + Y + Z$  which are the actual amounts of the C.I.E. primaries required to match the unknown source in color and intensity.

## APPLICATION OF C.I.E. COLOR SYSTEM TO BLACK-AND-WHITE SCREENS

The development of an all-sulfide black-and-white screen requires the making of a series of silver-activated zinc-cadmium sulfide phosphors. The series should run from 100 per cent zinc to 30 per cent zinc (the balance cadmium sulfide) in steps of approximately 10 per cent. The color of each phosphor is measured and plotted on the C.I.E. mixture diagram. A line through these points is the color locus of the zinc-cadmium sulfide system and is shown in Fig. 14. In addition to color, the visual efficiency must be measured—at least on a relative scale—and the stimulabilities calculated. Plots of relative visual efficiency and relative stimulability are shown in Figs. 15 and 16.

Neglecting certain secondary effects, such as the body color of the yellow phosphor, it is now possible to pick a pair of phosphors which produce a given shade of white with maximum light output. In referring to white light, it is convenient to describe it in terms of the nearest equivalent black-body temperature. Charts are available for the center section of the C.I.E. diagram which show the black-body color locus, isothermal lines across this screen, and a minimum perceptible color difference scale (M.P.C.D.) along the isothermal lines.

Assuming the 10,000 degrees Kelvin at +20 M.P.C.D.'s (above the black-body line) is a desirable white, it can be seen from Fig. 17 that a number of straight lines can be drawn through this point, each of which will intersect the phosphor color locus at two places.

The choice of the phosphor pair depends simply on which pair produces the greatest light output.

The screen brightness  $Y_{Sc}$  of a television tube is related to the intrinsic brightness of the phosphors by the relationship:

$$Y_{Sc} = \alpha Y_y + \beta Y_b \quad (9)$$

where  $Y_y$  and  $Y_b$  are the luminosities of the yellow and blue phosphors, respectively, and  $\alpha$  and  $\beta$  are the relative amounts used in the blend. Since  $Y_y$  is usually about ten times as great as  $Y_b$  and  $\alpha$  and  $\beta$  are nearly equal, most of the visual efficiency of a television screen is due to the yellow phosphor.

The approximate amounts of blue and yellow phosphor needed to make the 10,000-degree Kelvin white light are given by the following equation:

$$\alpha = \frac{(100 - \alpha) S_B \cdot L_B}{S_y \cdot L_y} \quad (10)$$

where,

$\alpha$  = per cent yellow to be used

$S_y$  = relative stimulability of the yellow phosphor

$L_y$  = linear distance from the 10,000-degree Kelvin point to the yellow end of the color line

$S_B$  = relative stimulability of the blue phosphor

$L_B$  = linear distance from the 10,000-degree Kelvin point to the blue end of the color line

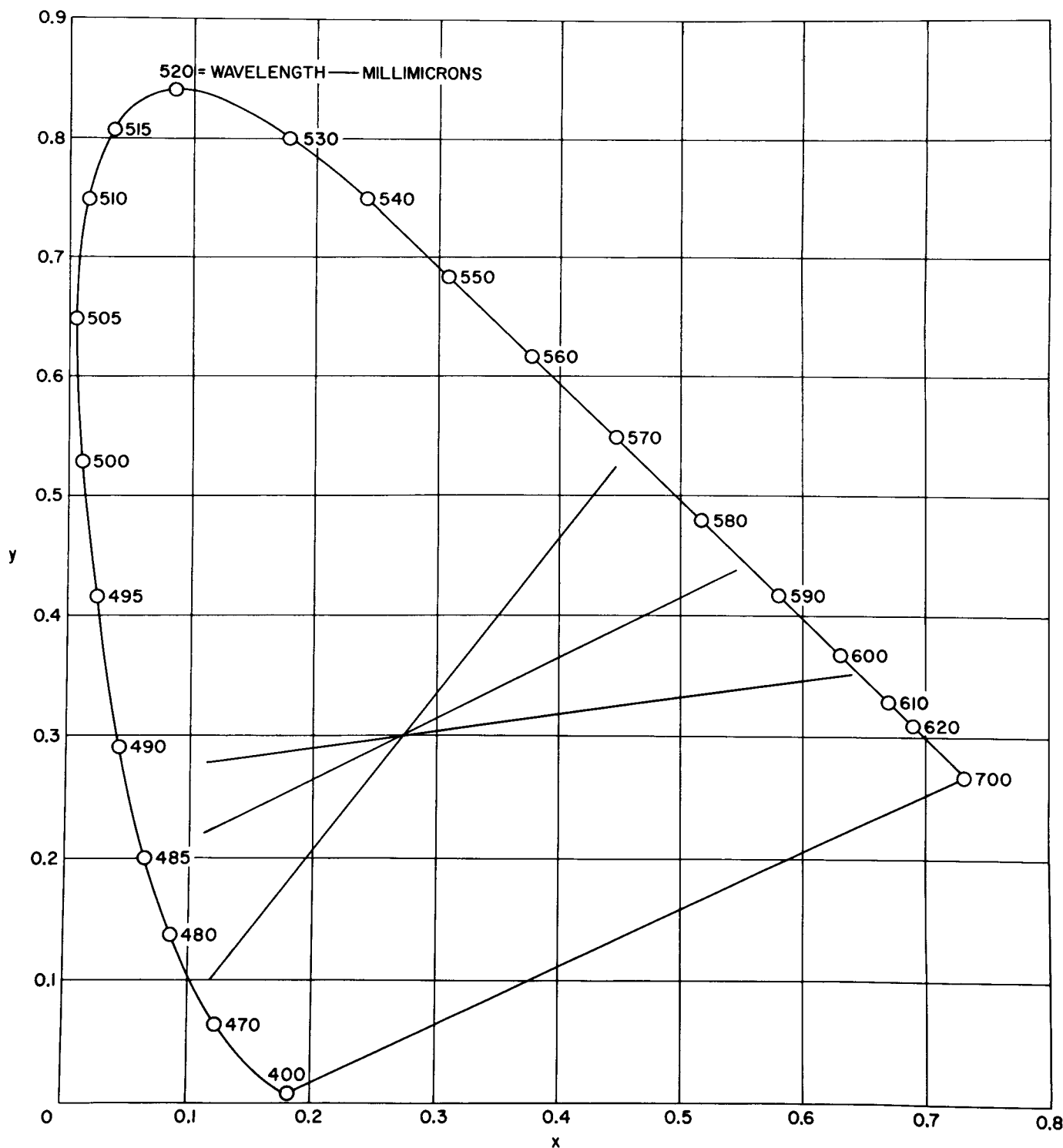


Figure 13. Three Complementary Phosphor Pairs which will Produce White

A pair of phosphors for optimum efficiency may be picked from among the three pairs shown in Fig. 17 by means of Eqs. (9) and (10).

Table IV shows that phosphor pair number one will produce a brighter 10,000-degree Kelvin white than any of the others.

Table IV

Phosphor Pair	Per Cent Yellow to Make 10,000° Kelvin White	Relative Screen Brightness
1	61.80	100.00
2	30.53	57.90
3	26.27	41.60

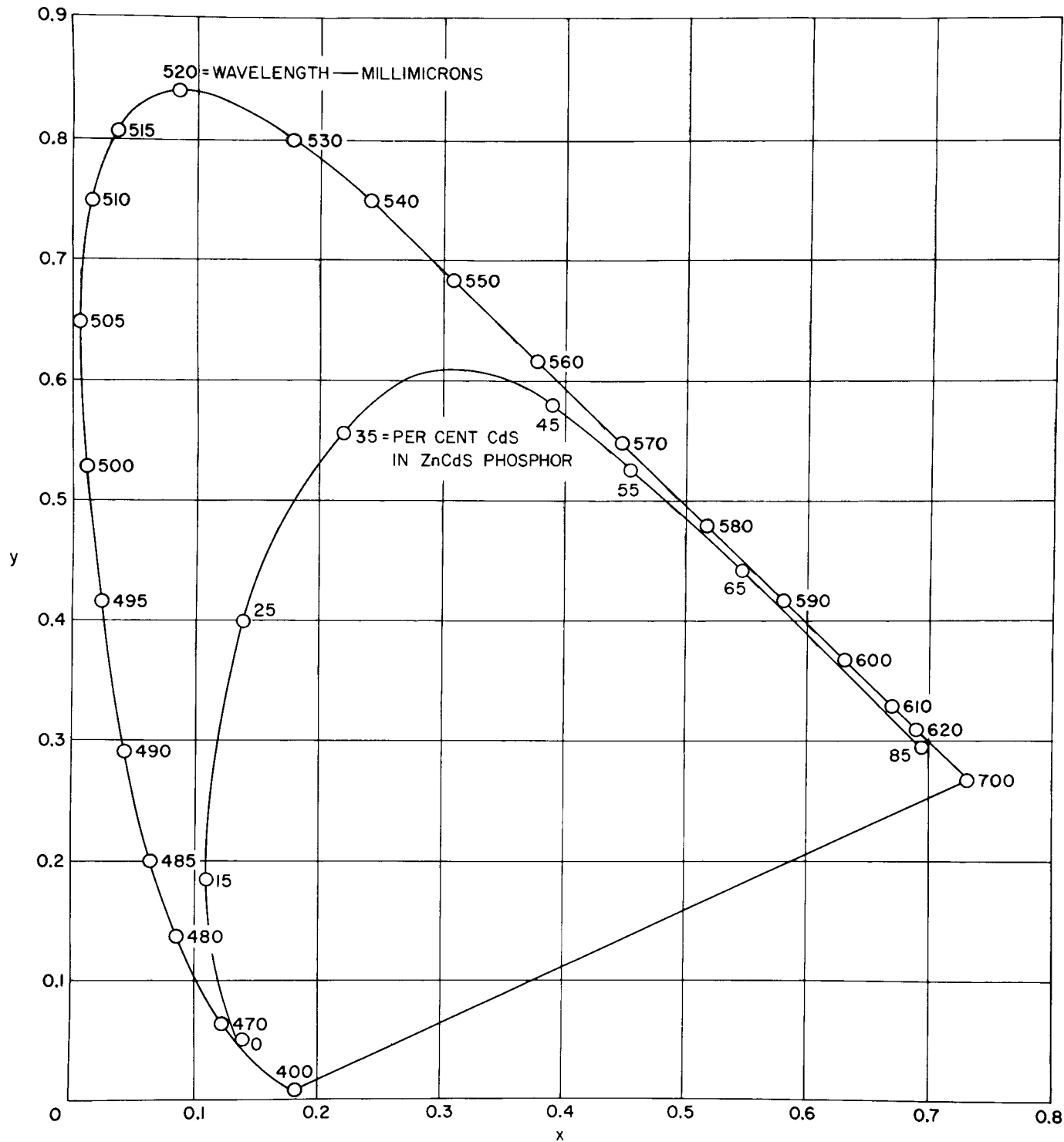


Figure 14. Phosphor Locus of the Zinc-Cadmium Sulfide Silver-Activated System

Calculating a 10,000-degree Kelvin white on paper is simple and direct. Achieving it in a finished tube is very difficult. Factors such as body color, screen weight, particle size, and operating conditions all affect the final result.

#### APPLICATION OF C.I.E. COLOR SYSTEM TO COLOR TELEVISION SCREENS

Much of what has been said about photometry, color-

imetry, and the use of the C. I. E. system for screens for black-and-white tubes also applies to color screens for tubes. Early in the development of color television the National Television Standard Committee (NTSC) proposed the three phosphor primaries and described them in terms of their C. I. E. coordinates. (See Table V.)

The C. I. E. diagram has been used often to show how the fidelity of color television pictures compares with

other color media such as color photography and color printing. Fig. 18 compares the color gamut of the color television phosphors with the color gamut of printing inks.

Table V

Color	NTSC PROPOSAL	
	C. I. E. X	Coordinates Y
Red	0.670	0.330
Green	0.210	0.710
Blue	0.140	0.080

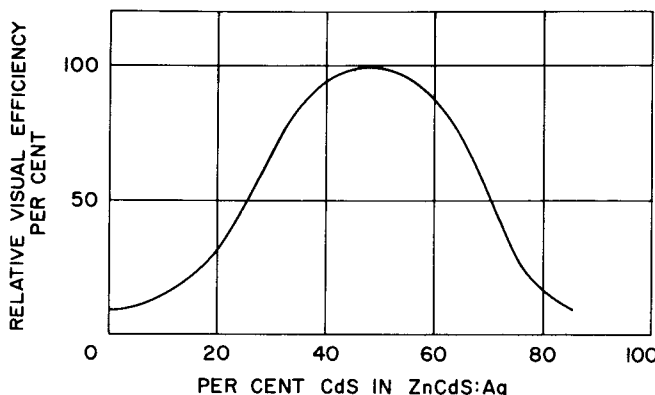


Figure 15. Relative Efficiency of a Phosphor

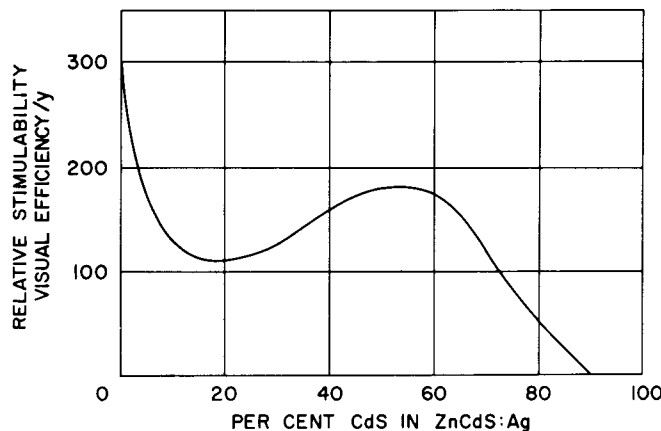


Figure 16. Relative Stimulability of a Phosphor

The laws of color addition may be used to determine the ratios of beam current for the red, blue, and green guns to produce any color, including white, within the phosphor triangle. These same principles may be used to determine the magnitude of color change when changes are made in the beam-current ratios for the three guns.

It is also possible to calculate the relative and absolute currents for each gun to produce any color point within the color triangle by means of Grassmann's equations. Simply stated, these equations say that the X, Y, and Z, which are the C.I.E. tristimulus values of a color mixture, are equal to the sum of X, Y, and Z of the component colors.

Applying these equations to the problem of finding the gun currents which will yield 8500-degree Kelvin white gives:

$$X_{8500} = I_R X_R + I_B X_B + I_G X_G \quad (11)$$

$$Y_{8500} = I_R Y_R + I_B Y_B + I_G Y_G \quad (12)$$

$$Z_{8500} = I_R Z_R + I_B Z_B + I_G Z_G \quad (13)$$

where  $I_R$ ,  $I_B$ ,  $I_G$  are the relative red, blue, and green gun currents

and,  $X_R$ ,  $Y_R$ ,  $Z_R$

$X_B$ ,  $Y_B$ ,  $Z_B$

$X_G$ ,  $Y_G$ ,  $Z_G$

are the C.I.E. tristimulus values of the red, blue, and green phosphors.

and,  $X_{8500}$ ,  $Y_{8500}$ , and  $Z_{8500}$  are the tristimulus values for the 8500-degree Kelvin white point.

The following data for the three phosphors are sufficient to make the calculation as outlined:

	x*	y*	z*	X <sup>‡</sup>	Y <sup>‡</sup>	Z <sup>‡</sup>
Red	0.670	0.330	0.000	4	2	0
Blue	0.140	0.080	0.780	3.5	2	20
Green	0.210	0.710	0.080	2	8	1
8500° Kelvin White	0.287	0.316	0.397	-	-	-

\*Value calculated from the spectral-energy distribution curves.

†Value measured with eye-corrected photocell.

‡Value calculated from Eqs. (5), (6), and (7).

Using these data:

$$x = 0.287 = \frac{4I_R + 3.5I_B + 2I_G}{6I_R + 25.5I_B + 11I_G}$$

$$y = 0.316 = \frac{2I_R + 2I_B + 8I_G}{6I_R + 25.5I_B + 11I_G}$$

$$z = 0.397 = \frac{20I_B + I_G}{6I_R + 25.5I_B + 11I_G}$$

Solving these equations gives the following current relationships:

	Per Cent Calculated	Per Cent Measured
$I_G$ =	28	30
$I_B$ =	22	20
$I_R$ =	50	50

The final step is to calculate the absolute currents for a given light level.

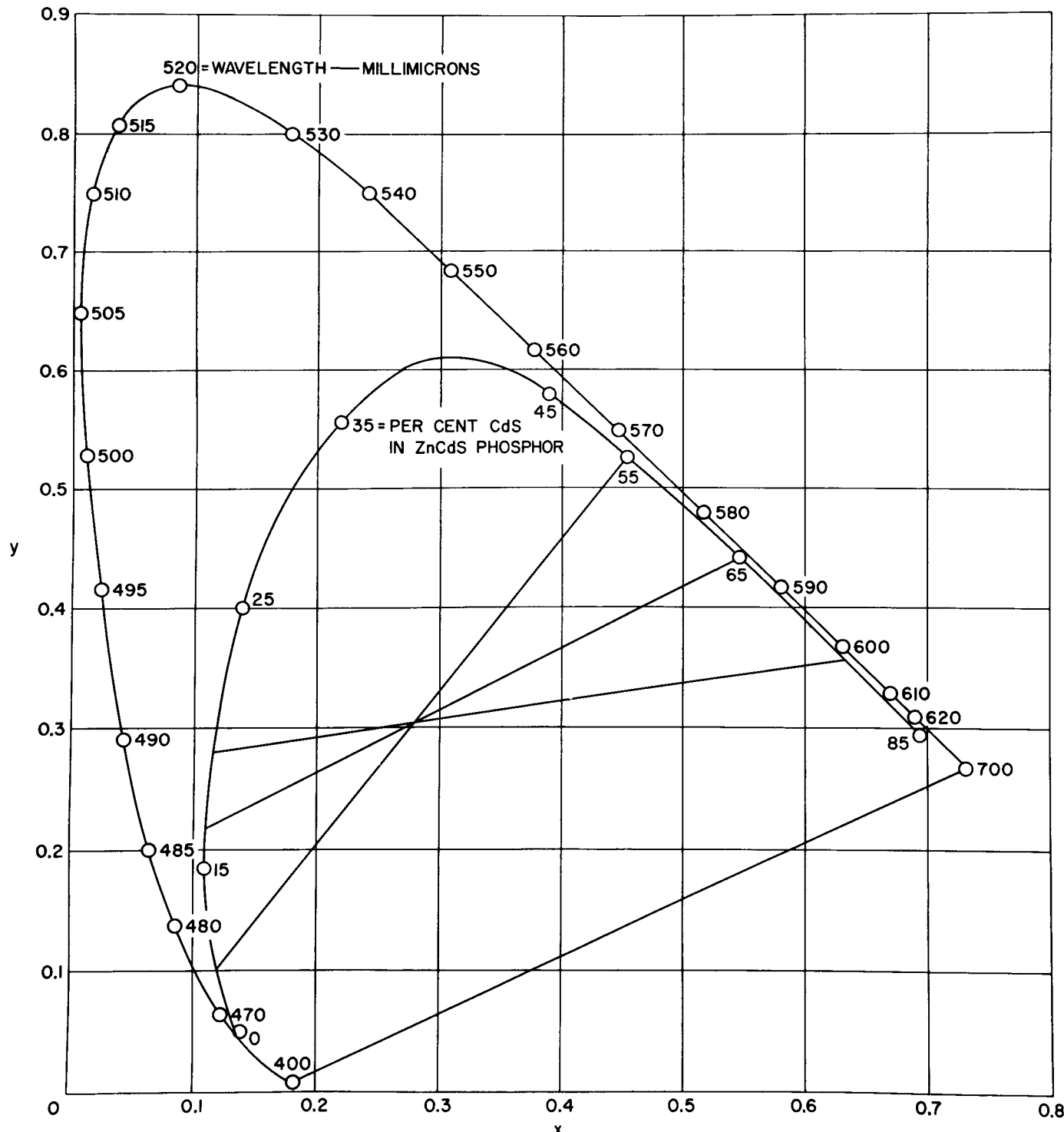


Figure 17. Locus of Zinc-Cadmium Sulfide Phosphor System and Three Complementary Phosphor Pairs for Producing White Light

Assume:

8 footlamberts brightness required

Screen area = 250 sq. in.

Ultor voltage = 25,000 volts

Candle Power = 4.4 [See Eq. (3)]

$Y_{8500}$  = 3.7 cp/w [See Eq. (12)]

Beam Watts  $\frac{4.4}{3.7} = 1.2$

and

Beam Current  $= \frac{4.4 \times 10^{-6}}{25000} = 480 \mu \text{a}$

The principles of photometry and colorimetry are relatively simple and straightforward. However, the practical difficulties of making precise measurements are enormous and have yet to be fully resolved. An accuracy of  $\pm 10$  per cent on measurement of absolute screen brightness or gun current to produce a given brightness is quite good.

An accuracy of  $\pm 0.005$  in x- and y- C.I.E. units would also be quite good; even this level is reached with considerable difficulty.

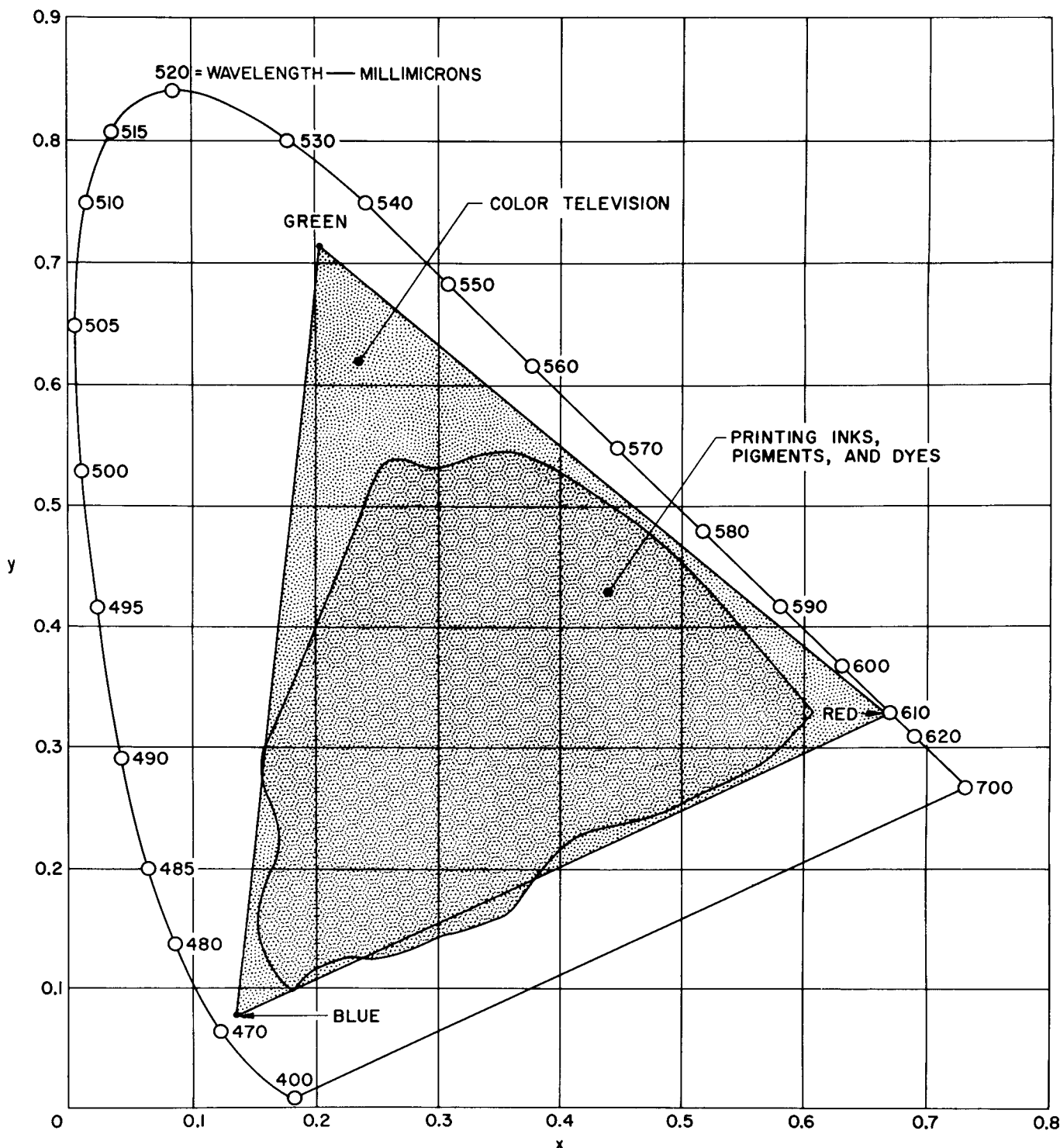


Figure 18. Color Gamut of Color-Television Phosphors Compared with Pigments, Dyes, and Inks

#### REFERENCES

1. Hardy, A. E., Handbook of Colorimetry, Technology Press, Cambridge, 1936
2. Nottingham, W. B., "Notes on Photometry, Colorimetry and Centibel Scale," Radiation Laboratory Report 804, M. I. T., 1945
3. Judd, D. B., "Equivalent Color Temperatures," J. O. S. A., 26, pp 421-426, 1936
4. Leverenz, H. W., Luminescence of Solids, Wiley, New York, 1950
5. Judd, D. B., Color in Business, Science, and Industry, Wiley, New York, 1952

6. Gibson, K. C., "Spectrophotometry," National Bureau of Standards, Circular 484, September 15, 1949
7. Hardy, A. E., "A Combination Phosphorometer and Spectroradiometer for Luminescent Materials", Jour. Electrochem. Soc., Vol 91, pp 127-146, 1947
8. Hardy, A. E., "Application of I. C. J. Color System to Development of All-Sulfide White Television Screen," RCA Review, Vol. VIII, No. 3, September 1947
9. Epstein, D. W., "Photometry in Television Engineering," Electronics, pp 1-5, July, 1948
10. "Optical Characteristic of Cathode Ray Tube Screens," Report No. J6-C3-1, October 1, 1959 (Available from E.I.A. Standards Laboratory, 32 Green Street, Newark, New Jersey)

# Calculation of Fields and Currents

L. C. Scholz

Harrison

## ELECTROSTATIC FIELDS

This chapter discusses the basic relations and laws governing electrostatic fields and currents. The laws are presented axiomatically; for rigor and further clarification, the standard literature<sup>1, 2, 3</sup> should be consulted.

In a static field, the electric field intensity  $\vec{E}$  (a vector quantity) may be expressed as the gradient of a scalar potential as follows:

$$\vec{E} = -\text{grad } V = -\Delta V, \quad (1)$$

or

$$\vec{E} = -\left(\vec{i} \frac{\delta V}{\delta x} + \vec{j} \frac{\delta V}{\delta y} + \vec{k} \frac{\delta V}{\delta z}\right) \quad (1a)$$

where  $\vec{i}$ ,  $\vec{j}$ , and  $\vec{k}$  are unit vectors in the x, y, and z directions, respectively. The gradient at a point in space is the maximum space variation of the potential and is defined at that point.

Gauss's law, which expresses a further relation between the electric flux and its source charge, states that the total flux through the surface of a body is equal to the total charge enclosed. This relationship may be written in terms of the flux density  $\vec{D}$  (known as the displacement) and the charge density  $\rho$  as follows:

$$\iint \vec{D} d\vec{s} = \iiint \rho d\sigma, \quad (2)$$

or rephrased in differential form.

$$\frac{\delta D_x}{\delta x} + \frac{\delta D_y}{\delta y} + \frac{\delta D_z}{\delta z} = \rho \quad (3)$$

From the identity  $\vec{D} = \epsilon \vec{E}$  and a combination of Eqs. (1) and (3), Poisson's equation (in rectangular coordinates) is obtained as follows:

$$\frac{\delta^2 V}{\delta x^2} + \frac{\delta^2 V}{\delta y^2} + \frac{\delta^2 V}{\delta z^2} = -\rho/\epsilon \quad (4)$$

This equation is the basis of the present analysis of electrostatic problems.

A similar result, for cylindrical coordinates, is expressed as follows:

$$\frac{1}{r} \frac{\delta}{\delta r} \left( r \frac{\delta V}{\delta r} \right) + \frac{1}{r^2} \left( \frac{\delta^2 V}{\delta \theta^2} \right) + \frac{\delta^2 V}{\delta z^2} = -\frac{\rho}{\epsilon} \quad (5)$$

## SOLUTIONS FOR SIMPLE GEOMETRIES

In the absence of space charge, Eq. (4) has the form known as Laplace's equation and may be used for analytic solutions of simple geometries. Although two cases presented below are extremely simple, they provide basic required analysis information.

### Infinite Parallel Planes

The potential  $V$  at any point  $z$  between two parallel planes held at potentials  $V_1$  and  $V_2$ , and distance  $d$  apart is given as:

$$V = V_1 + \frac{V_2 - V_1}{d} z, \quad (6)$$

a linear variation  $E_z$  is expressed as:

$$E_z = -\text{grad } V = -\left(\frac{V_2 - V_1}{d}\right) \quad (7)$$

### Concentric Cylinders

For concentric cylindrical planes, the basic equation has the following form:

$$V = V_1 + (V_2 - V_1) \frac{\ln r/R_1}{\ln R_2/R_1}, \quad (8)$$

and the linear variation is written as

$$E_r = -\frac{V_2 - V_1}{r \ln R_2/R_1} \quad (9)$$

Although analytic solutions are possible for certain other simple geometric configurations, the approximation methods discussed below are generally used.

## THE THERMIONIC DIODE

The analysis of the electrical field of a diode differs from the previous problems in electrostatics only in that electrons flow through the interelectrode space. The presence of these electrons results in a charge

(treated as being continuous) which interacts with the total field distribution. In the analysis procedure, Poisson's equation, written with the charge expressed in terms of the current and tube geometry, is integrated over the proper limits.

Before attempting the solution of the equation, however, the more general problem of a current injected into the region between two infinite parallel planes<sup>4, 5, 6</sup> (these planes may be physical electrodes or imaginary in space) must be considered briefly. In the absence of charge, the potential variation, plotted from Eq. (6), is a straight line. As electrons enter the interelectrode space, the potential is everywhere depressed by the field resulting from the charge.

Two possible conditions may exist as the electrons enter the interelectrode space:

(1) an accelerating field may be present as a result of a higher potential on the second plane, as shown in Fig. 1, or, of current.

(2) a retarding field may exist as a result of a higher potential on the first plane, as shown in Fig. 2.

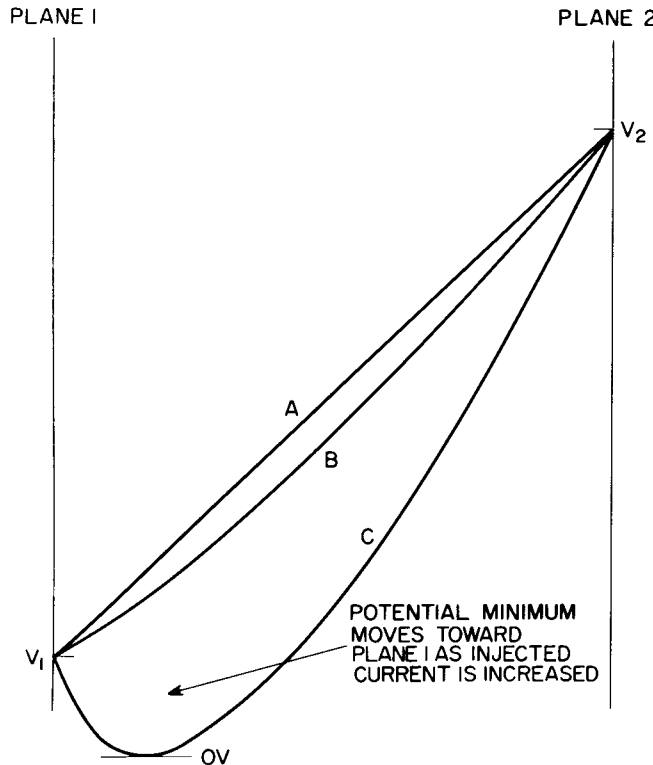


Figure 1. Typical Accelerating Potential Distributions

As the current is increased, a potential minimum is formed; as the current is further increased, the potential at the minimum is lowered to a critical current value at which a transition takes place and a virtual cathode is formed.

In Figs. 1 and 2, curves (A) show the charge-free variation, curves (B) show the effect of a small charge,

and curves (C) show the formation of potential minimum.

The concept of self regulation of current, the so-called space-charge-limited current flow, is essential to a clear understanding of the physical processes within an electron tube. Although the idea of a potential minimum is also fundamental and has a physical basis, the sudden transition of potential distribution is less easily visualized and is best explained mathematically. The following analysis of the current flow between two infinite-parallel planes provides a basis for the solution of some of the more important problems of electron-tube design.

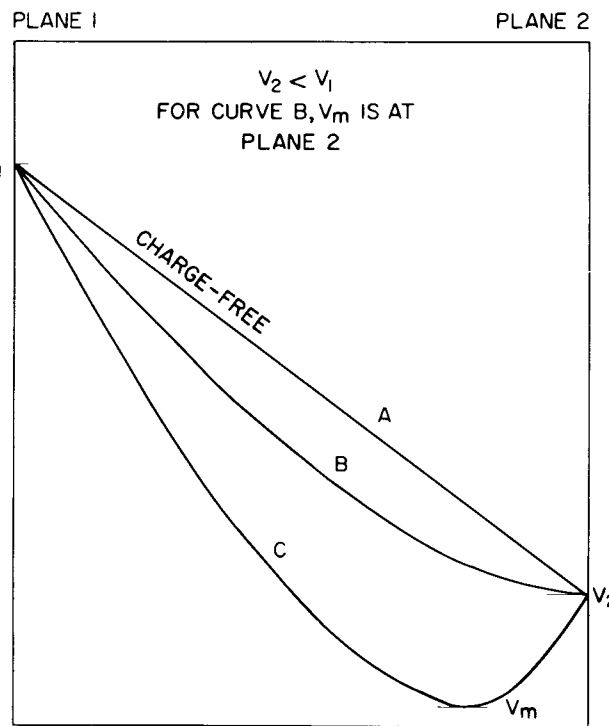


Figure 2. Typical Retarding Potential Distributions

In an infinite-parallel plane geometry,\* when a current which has originated at a point of zero potential flows in a Z direction, the velocity in any plane perpendicular to the Z axis is a constant. This condition defines a single-velocity beam. The total current flowing  $\vec{J}$  is the sum of the conduction and displacement currents.

$$\vec{J} = \rho \vec{u} + \frac{\epsilon_0 \delta \vec{E}}{\delta t} \quad (10)$$

It can be shown that

$$J = \epsilon_0 \frac{dE}{dt} \quad (11)$$

and this expression leads to the following three equations:

\*The assumptions inherent in an ideal infinite-parallel plane configuration are outlined in the following section.

$$E = \frac{J}{\epsilon_0} T + E_0 \quad (12)$$

$$U = \frac{e}{m} \frac{J}{\epsilon_0} \frac{T^2}{2} + \frac{e}{m} E_0 T + U_0 \quad (13)$$

$$Z = \frac{e}{m} \frac{J}{\epsilon_0} \frac{T^3}{6} + \frac{e}{m} E_0 \frac{T^2}{2} + U_0 T \quad (14)$$

where  $E_0$  and  $U_0$  are the values at  $Z = 0$ , and  $T$  is the time of flight of the electrons. These equations may be solved for  $T$  by assuming that the value of  $U_0$  is known.

$$T^3 \left( \frac{e}{m} \frac{J}{\epsilon_0} \frac{12}{12} \right) - \frac{U + U_0}{2} T + Z = 0 \quad (15)$$

Physically realizable solutions for  $T$  are positive real values. At most,  $T$  has two such roots if the following condition holds true:

$$\frac{1}{12} \frac{e J}{m \epsilon_0} \leq \frac{1}{54} \frac{(U + U_0)^3}{Z^2}$$

Therefore, the current may have a maximum value

$$J_{\max} = \frac{2}{9} \epsilon_0 \frac{m}{e} \frac{(U + U_0)^3}{Z^2} \quad (16)$$

and for this value of current

$$T = \frac{3}{2} \left( \frac{2Z}{U + U_0} \right) \quad (17)$$

The transit time for zero current is given as:

$$T_0 = \frac{2Z}{U + U_0} \quad (18)$$

and

$$T = \frac{3}{2} T_0 \quad (19)$$

Values of current greater than  $J_{\max}$  result in negative solutions for  $T$  because above the value  $J_{\max}$ , current flow is not stable. Therefore, the equation does not apply above this value. Attempts to increase the current result in changes in the field that turn part of the current back to the source. This effect and related phenomena are observed in pentodes and beam power tubes.

Further discussion of the thermionic diode requires an investigation of the effects of velocity distribution on the equation for space-charge flow. In practical electron tubes, the electrons are initially derived from a heated cathode of metal or some oxide mixture. Thermally emitted electrons travel in a direction perpendicular to the emitting plane at velocities ranging from zero to infinity according to the following Maxwellian distribution function.

$$dN_u = N \frac{m u_1}{K T} \exp(-mu_1/2KT) du \quad (20)$$

Where  $dN_u$  is the number of electrons emitted per second having velocities between  $u$  and  $u+du$ , and  $N$  is the total number of electrons emitted. This plot of distribution, which has the form shown in Fig. 3, applies to metal emitters as well as the more usual oxide-coated emitter. This spread in velocities contradicts the assumption of a single velocity made above, but for the diode (or grid-cathode region of other tubes), it is possible to compensate for this change by deducing the type of potential distribution that exists in the real diode.

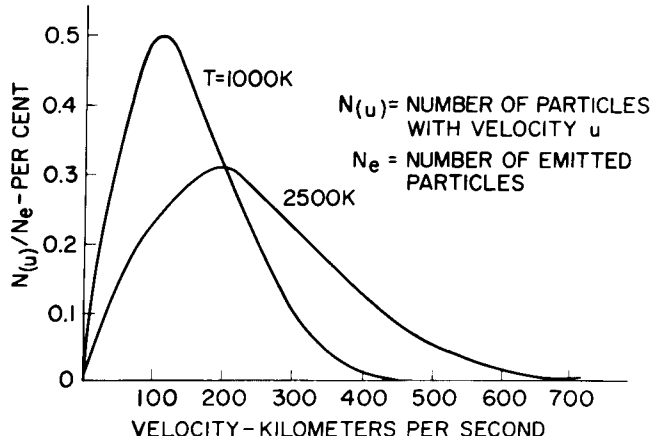


Figure 3. Form of the Normally-Directed Maxwellian Velocity Distribution

In the presence of an accelerating field, a large current can flow in a charge-free tube. The current depresses the potential until a retarding field is formed at the cathode. The retarding field, in turn, limits the current because only electrons having sufficient energy can pass the potential minimum. If enough electrons are available, a limiting condition is established and only a portion of the available electrons reach the anode. This condition is known as space-charge-limited operation. If the current is not sufficient to form a potential minimum, all the available electrons reach the plate, as shown in curve A of Fig. 4. This condition is known as temperature-limited operation. Because all the electrons have energies greater than zero, even zero field at the cathode surface (potential minimum at the cathode surface) permits all the available electrons to flow. These conditions distinguish the boundary between temperature-limited and space-charge limited operation. As the anode potential is reduced, the current is reduced, and the potential minimum moves towards the anode, as shown in curve B of Fig. 4. At some given current, the potential minimum is at the anode surface, as shown in curve C of Fig. 4. A lower current level results in operation in the region of the retarding field. One additional case must be considered: that of electrons emitted with zero energy. If the electrons emitted have zero velocity (energy), the potential minimum must fall on the cathode surface. An accelerating field would cause full current flow and a retarding field would permit no current flow.

#### THE IDEAL INFINITE PARALLEL-PLANE DIODE

The preceding section presented some of the general

concepts and theory pertaining to the flow of charge between two electrodes. The following is a specific solution for the ideal infinite parallel-plane diode. Because of mathematical complexity, this discussion is restricted to ideal cases. However, experience has shown that these solutions are generally applicable and may be used as a basis for most design problems.

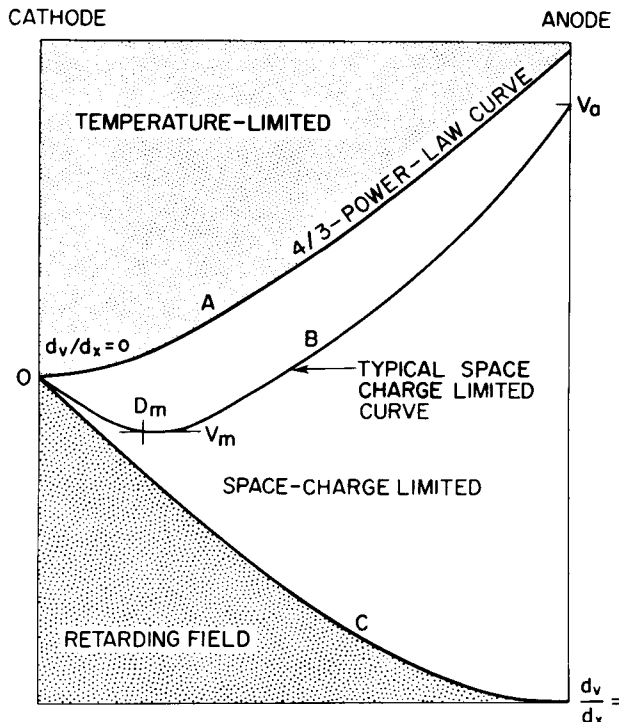


Figure 4. Boundary Potentials Defining Mode of Operation in Diode

The configuration treated here consists of two perfectly parallel uniformly spaced planes infinite in extent. This configuration eliminates the field variation in the directions along the plane and permits a mathematically simple solution. In actual tubes, that are of course finite in extent, end effects must be neglected or some empirical correction must be made. Tubes that have small interelectrode spacing compared to the other dimensions have very small fringe effects. Curved electrode systems may be treated as planes if the spacing is small compared to the curvature.

The method described here is annotated derivation which provides, at each step, the reasons and justification for all assumptions. The discussion is maintained on a general level so that the results may be used as take-off points for less restrictive analyses. It is also very important that the designer realize the limitations and assumptions inherent in the analysis.

Poisson's equation in one rectangular coordinate  $z$  is used as the starting point of the analysis.

$$\frac{d^2V}{dz^2} = -\rho(z)/\epsilon_0 \quad (21)$$

where  $(z)$  is a function of  $z$ .

Because there are no sources of current in the tube

except the cathode, the current must be constant through the tube; the current and space charge density may be related as follows:

$$\rho = J/u \quad (22)$$

When the principle of conservation of energy is applied to the electrons in an electrostatic field the following relationship between velocity and potential is obtained:

$$U = \left( U_0^2 + \frac{2e}{m} V \right)^{1/2} \quad (23)$$

where  $U_0$  is the initial  $z$ -directed velocity of the electrons as they leave the cathode. Because a distribution function for  $U_0$  leads to a multivalued  $U(z)$  that is difficult to manipulate, that case must be treated differently. However, if it is assumed that  $U_0$  is single-valued (zero) and the equation is solved for  $J$ , the result is generally useful.

### Initial Velocity - Zero

In the most direct analysis procedure,  $J/u$  is substituted for  $\rho$  in Eq. (21).

$$\frac{d^2V}{dz^2} = \frac{J}{\epsilon_0} \left( \frac{m}{2e} \right)^{1/2} V^{-1/2} \quad (24)$$

Integration from 0 to  $z$  yields

$$E^2 - E_0^2 = \frac{4J}{\epsilon_0} \left( \frac{m}{2e} \right)^{1/2} \left( V^{1/2} - V_0^{1/2} \right) \quad (25)$$

The boundary conditions must also be defined:  $E_0$  is zero because it has been assumed that  $U_0$  is zero, and the cathode potential  $V_0$  can also be assigned a zero value with no loss in generality. Therefore,

$$E = \frac{dV}{dz} = \left( \frac{4J}{\epsilon_0} \right)^{1/2} \left( \frac{m}{2e} \right)^{1/2} V^{1/2} \quad (25a)$$

A second integration from 0 to  $d$  and 0 to  $V_a$  yields

$$\frac{4}{3} V_a^{3/4} = \left( \frac{4J}{\epsilon_0} \right)^{1/2} \left( \frac{m}{2e} \right)^{1/4} d \quad (26)$$

The significant results, first derived by Langmuir<sup>8</sup> and Childs<sup>9</sup>, are as follows:

$$J = 2.336 \times 10^{-6} \frac{V_a^{3/2}}{d^2} \text{ amp per square meter} \quad (27)$$

$$V = 5.68 \times 10^4 J^{2/3} z^{4/3} \text{ volts} \quad (28)$$

$$E = \frac{4}{3} \times 5.68 \times 10^4 J^{2/3} z^{1/3} \text{ volts per meter} \quad (29)$$

by simple substitution,

$$E/\text{anode} = \frac{4}{3} \frac{V_a}{d} \quad (30)$$

This result shows that the electric-field intensity is increased at the anode under space charge conditions because the negative electrons depress the potential (except at the electrodes) and increase the gradient.

The simple relationship shown in Eqs. (27), (28), and (29) is the basis of all tube design. Although a more sophisticated analysis is presented below, much of the work rests on these equations. The three-halves power law is quite general and holds for all geometries (Langmuir<sup>8</sup> and Ivey<sup>10</sup>). The equations may be used to initiate changes in existing tube design or to give a first approximate answer before proceeding with a more refined design.

### Initial Velocities - Maxwellian

The distribution of the normally-directed velocities of the emitted electrons is given by the following Maxwellian distribution function:

$$dN_u = \frac{Nmu_1}{KT} \exp(-mu_1/2KT) du_1$$

A distribution of velocities results in the formation of a potential in front of the cathode, which has a position  $dm$  and a magnitude  $V_m$ , a negative number. On the anode side of the potential minimum, all electrons move towards the anode and have energies greater than  $V_m$  electron volts; on the cathode side, electrons move in both directions. The total emitted electrons ( $N$ ) move towards the minimum; those with energies less than  $V_m$  are returned to the cathode. However, the total current through any plane in the interelectrode space must be a constant. As the electron stream approaches the minimum, the slower electrons are continuously returned, and the faster electrons slowed down. Because the average velocity is constant (Langmuir,<sup>12</sup> p. 423), the following expressions may be used to define the space charge.

On the cathode side of the potential minimum,  $0 \leq z \leq dm$ .

$$\rho(z) = -e \left[ \int_{(-2 \frac{e}{m} V_m)^{1/2}}^{\infty} \frac{dN_u}{u} + 2 \int_{(2 \frac{e}{m} V)^{1/2}}^{(-2 \frac{e}{m} V_m)^{1/2}} \frac{dN_u}{u} \right] \quad (31)$$

where  $V$  is the potential at  $z$ , and  $u$  the velocity at  $z$  is defined by

$$U^2 = U_1^2 + 2eV/m \quad (32)$$

On the anode side of the potential minimum,  $dm \leq z \leq d$

$$\rho(z) = -e \int_{(-2 \frac{e}{m} V_m)^{1/2}}^{\infty} \frac{dN_u}{u} \quad (33)$$

Under these conditions, the current is determined by the value of the potential minimum and is given by the following expression:<sup>7</sup>

$$J = J_o e + \frac{eV_m}{KT} \quad (34)$$

where  $J_o$  is the total thermionic current available and the exponential  $e$  is the electronic charge. This equation is generally used to determine  $V_m$  by assuming the values of  $J_o$  and  $J$  to be known.

A single integration of Poisson's equation gives the following relationship:

$$\left( \frac{dV}{dz} \right)^2 - \left( \frac{dV}{dz} \right)_{dm}^2 = -\frac{2}{\epsilon_0} \int_{V_m}^V \rho(z) dz \quad (35)$$

where  $V$  equals  $V_m$  and  $dV/dz$  is equal to 0 when  $z$  is equal to  $dm$ .

The integration of  $\rho(z)dz$  results in the combination of some error functions, but a second integration is required to complete the solution. This procedure requires the numerical integration of a new function. Langmuir simplified this evaluation by introducing the following normalizations to give pure numbers.

$$\eta = \frac{e(V - V_m)}{KT} = \frac{11,605 (V - V_m)}{T} \quad (36)$$

$$\xi = \frac{(2m\pi)^{1/4}}{(2KT)^{3/4}} \left( \frac{eJ}{\epsilon_0} \right)^{1/2} (z - dm) = 9.186 \times 10^5 T^{-3/4} J^{1/2} (z - dm) \quad (37)$$

Then

$$\left( \frac{dV}{dz} \right)^2 = \left( \frac{2\xi KT}{e(z - dm)} \right)^2 \left[ e^{\eta - 1} \pm e^{\eta} \operatorname{erf}(\eta^{1/2}) \mp 2 \left( \frac{\eta}{\pi} \right)^{1/2} \right] \quad (38)$$

The upper signs apply in the cathode region, and the lower signs in the anode region;

$$\operatorname{erf}(\eta^{1/2}) = \frac{2}{\sqrt{\pi}} \int_0^{\eta^{1/2}} e^{-u^2} du$$

this expression may be integrated to yield

$$\xi = \int_0^{\eta} \frac{d\eta}{\left[ e^{\eta - 1} \pm e^{\eta} \operatorname{erf}(\eta^{1/2}) \mp 2 \left( \frac{\eta}{\pi} \right)^{1/2} \right]} \quad (39)$$

This expression has been evaluated numerically by Kleynen.<sup>14</sup>

### Discussion

The preceding analysis is applied to actual design problems through the use of implicit solutions for  $J$ . Graphical solutions further facilitate design procedures and aid in the visualization of the effect of the initial velocity on the current.

Under the assumption of zero initial velocity, the current depends on the voltage and spacing only. In the actual case, current is a function of voltage, spacing, cathode temperature, and available cathode current because the position and magnitude of the potential minimum are functions of these variables. Therefore, an adequate analysis must define the effects of these parameters on the current so that a tube may be designed for a given current under a given set of conditions for the greatest utility; this information should be in graphical or tabular form.

The definition of the three important variables  $\eta$ ,  $\xi$ , and  $V_m$ :

$$\eta = \frac{V - V_m}{T} = 11,605 \quad (40)$$

$$\xi = 9.186 \times 10^5 \quad (41)$$

$$V_m = \frac{kT}{e} \ln \frac{J_s}{J} = V_T \ln \frac{J_s}{J} \quad (42)$$

By insertion of the proper values for  $Z$  and  $V$ , the following results are obtained for the cathode and plate:

$$\eta_K = \frac{e}{kT} V_m = \ln \frac{J_s}{J} \quad (43)$$

$$V_m = \eta_K V_T = \eta_K \frac{T}{11,605} \quad (44)$$

$$\eta_a = \frac{V_a + V_m}{V_T} = \frac{V_a}{V_T} + \eta_K \quad (45)$$

$$V_a = (\eta_a - \eta_K) \frac{T}{11,605} \quad (46)$$

$$\xi_K = 9.186 \times 10^5 T^{-3/4} J^{1/2} dm \quad (47)$$

$$dm = \xi_K T^{3/4} / 9.186 \times 10^5 J^{1/2} \quad (48)$$

$$\xi_a = 9.186 \times 10^5 T^{-3/4} J^{1/2} (d - dm) \quad (49)$$

$$\xi_a = 9.186 \times 10^5 T^{-3/4} J^{1/2} d - \xi_K \quad (49a)$$

Figs. 5, 6, and 7 may be used to determine  $\eta_K$ ,  $\xi_K$  and  $\xi_a$  directly.

These formulas are used, as follows, to design a diode with current density  $J$  and voltage drop  $V$ :

- (1) Assume values for  $J_s$  and  $T_K$ . (1 to 10 amperes per square centimeter for  $J_s$  and 1100 deg K for  $T_K$  are practical values for the oxide cathode.)
- (2) Calculate (in order)  $\eta_K$ ,  $V_m$ , and  $\eta_a$ .

- (3) Determine from tables or graphs  $\xi_K$  and  $\xi_a$ .
- (4) Calculate  $d$  from Eq. (49a).

For example, if  $J = 40$  ma/cm<sup>2</sup> and  $V = 1.0$  volts ( $J_s = 1000$  ma/cm<sup>2</sup>).

$$1. \quad \eta_K = \ln \frac{1000}{40} = 3.22$$

$$V_m = \ln 25 (1.1/11.6) = 0.306 \text{ volts}$$

$$\eta_a = \frac{1.0}{0.095} + 3.22 = 13.72$$

$$2. \quad \xi_K = 2.26, \xi_a = 18 \text{ (from Fig. 6)}$$

$$3. \quad d = (\xi_a + \xi_K) T^{3/4} / 9.186 \times 10^5 J^{1/2} = 0.2 \text{ millimeters or 0.008 inch}$$

(note that  $J$  must be in amperes)

This procedure may be varied to accomodate various combinations of given and desired tube parameters. Some of the actual calculations required in this solution may be eliminated by using the plot of position and magnitude of the potential minimum given in Figs. 8 and 9.

A completely explicit design procedure would provide the current density directly as a function of voltage and spacing; such a plot may be found in Liebermann.<sup>15</sup> A more useful form results through the following normalization.<sup>16</sup> If the current density equals  $J_1$  when the potential minimum falls on the anode surface,  $J_1$  is the transition value as the current density changes from the retarding-field to space-charge-limited mode. If  $V_1$  is that value of anode voltage that gives  $J_1$ ,  $J_1$  and  $V_1$  are functions of cathode temperature ( $T_{1C}$ ) and saturation-current density ( $J_s$ ), but are only slightly dependent on  $J_s$  if the ratio  $J_s/J_1$  is very large. Because the ratio is usually large,  $J_s$  is assumed infinite and  $J_1$  is designated  $J_\infty$ . The purpose of this normalization is evident from an examination of a complete potential cross section of a diode, as shown in Fig. 10. The diagram shows that the effective potentials include the work functions of the surfaces. However, because these work functions are not known until after the tube is made, it is necessary to measure or eliminate them. Therefore, after a tube is designed and constructed,  $J_1$  and  $V_1$  are measured and the values are used as a basis for other measurements. If  $J_1$  is not within design limits, something is wrong with the tube. Because the measured values of  $V_1$  include the effect of contact potential,  $J_\infty$  is introduced to eliminate contact potential voltages from the measurements. The value of  $J_1$  may be determined from Fig. 11 by letting  $dm$  equal  $d$ .

An equation for one additional tube parameter, the conductance, is required.

Differentiation of Eq. (27) provides

$$G = \frac{3}{2} \times 2.336 \frac{V^{1/2}}{d^2} \text{ micromhos per square centimeter} \quad (50)$$

and

$$\frac{G}{J} = \frac{3}{2} V \frac{\text{mhos}}{\text{ampere}} \quad (51)$$

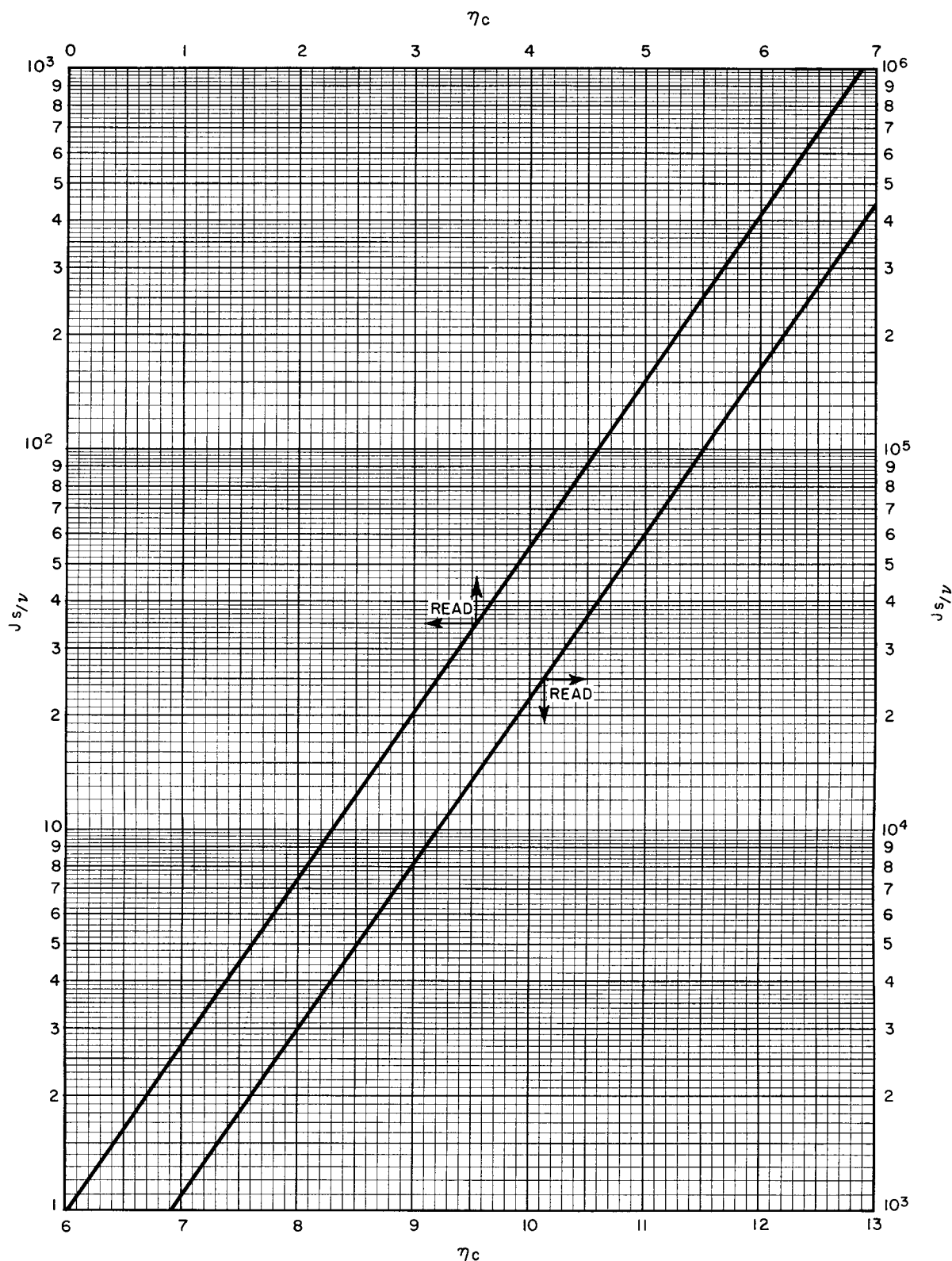


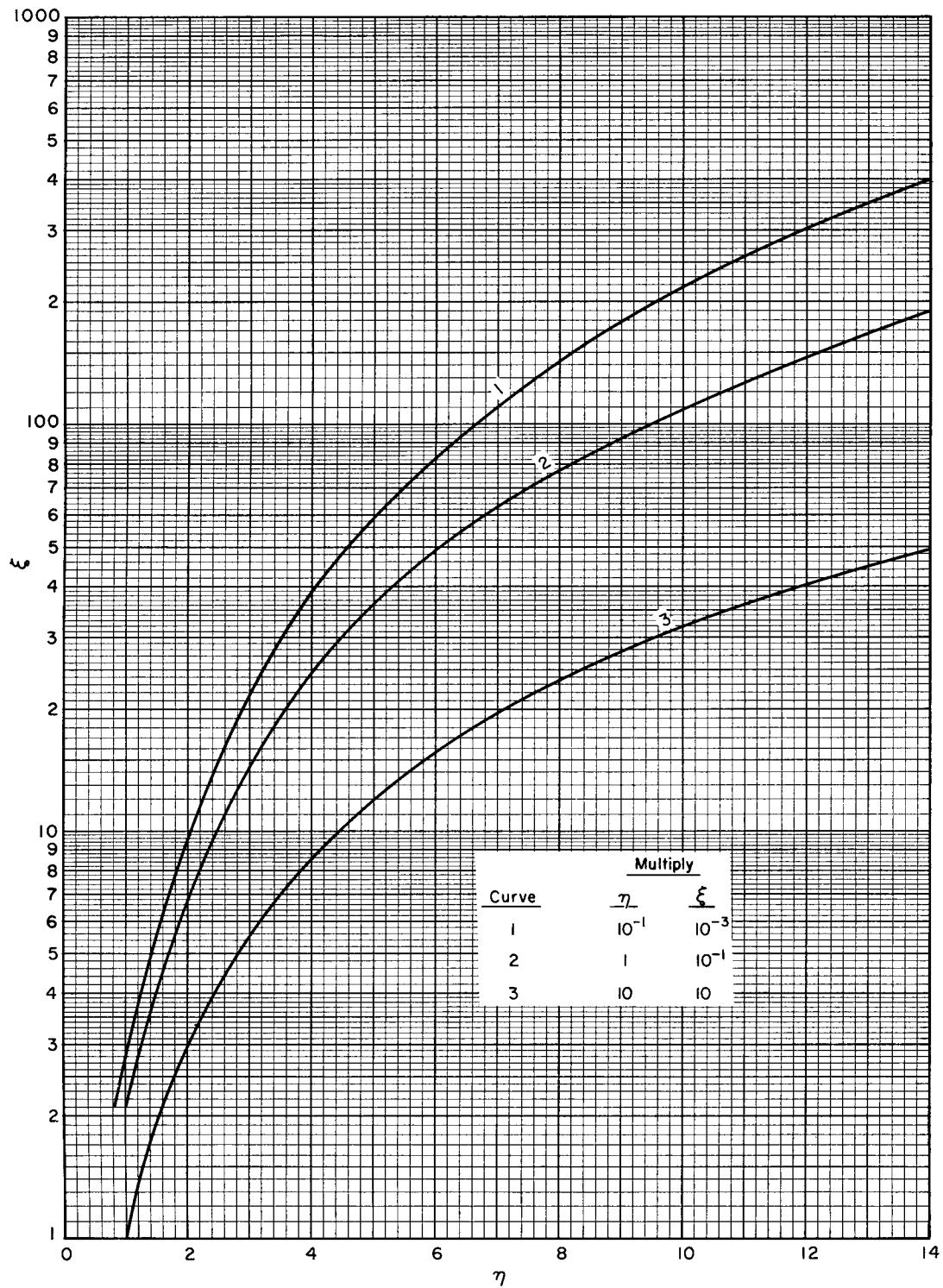
Figure 5.  $\eta_c$  as a Function of the Ratio  $J_s/v$

for the case of zero initial velocity. In the exact case, graphical differentiation of the J-V plot is the simplest method, but in the retarding field region

$$J = J_s \exp (eVr/KT) \quad (52) \quad \text{and}$$

Therefore,

$$G = \frac{e}{KT} J_s \exp (eVr/KT) \quad (53)$$

Figure 6.  $\xi_a$  as a Function of  $\eta$ 

$$\frac{G}{J} = \frac{e}{KT} \quad (53a)$$

Fig. 12 shows the relationship of  $J$ ,  $G$ , and  $dm$  at various temperatures and current densities. The set of lines marked (1) is a plot of  $G$  as a function of  $J$ , when  $J$  is less than  $J_1$  (retarding field mode). Set (2)

is a plot of  $dm$  as a function of  $J$  and set (3) is  $G$  as a function of  $J$ , when  $J$  is greater than  $J_1$  and has the specific value of 2 mils.

The figure is used as follows: If a diode has a spacing of  $X$  mils,  $J_1$  is found by letting  $dm$  equal  $X$ . The intersection of line 2 and  $dm = X$  yields  $J_1$ . Project this to line 1. To the left ( $J < J_1$ ),  $G = RJ/KT$  may be found

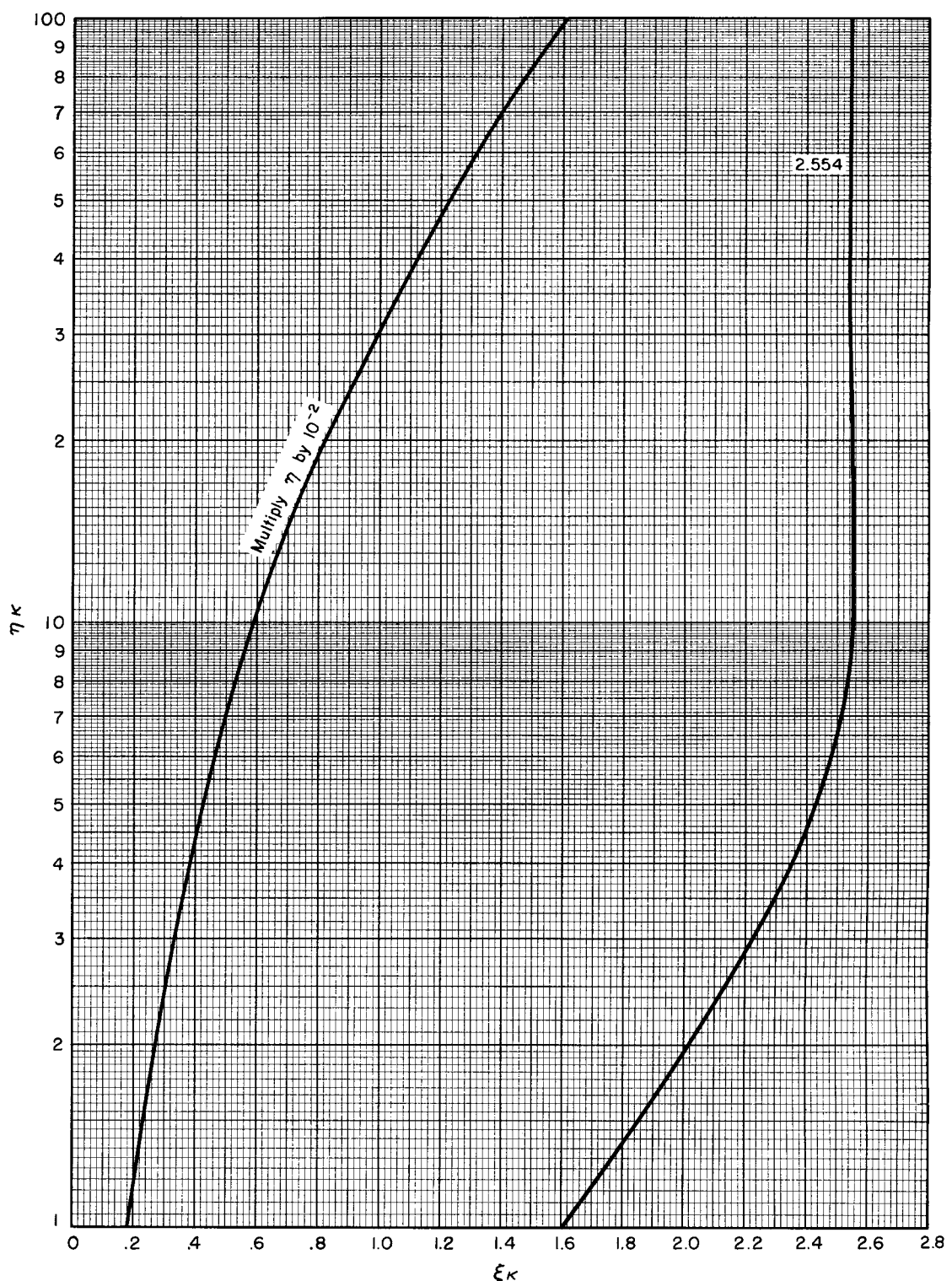


Figure 7.  $\eta_K$  as a Function of  $\xi_K$

from line 1; to the right ( $J > J_1$ ), it may be found by graphical differentiation, but the construction of a line parallel to 3 is usually sufficient. The result is a complete plot of  $G$  as a function of  $J$ ;  $J$  as a function of  $V$  may be calculated. (The designer will probably find it convenient to use universal plots for actual design work.)

The term  $\xi$  can be series expanded as shown by Beck,<sup>7</sup> and approximate solutions for  $J$  can be obtained.

When only the first term is used,

$$J = \frac{2.336 \times 10^{-6} (V - V_m)^{3/2}}{(d - d_m)^2} a / m^2 \quad (54)$$

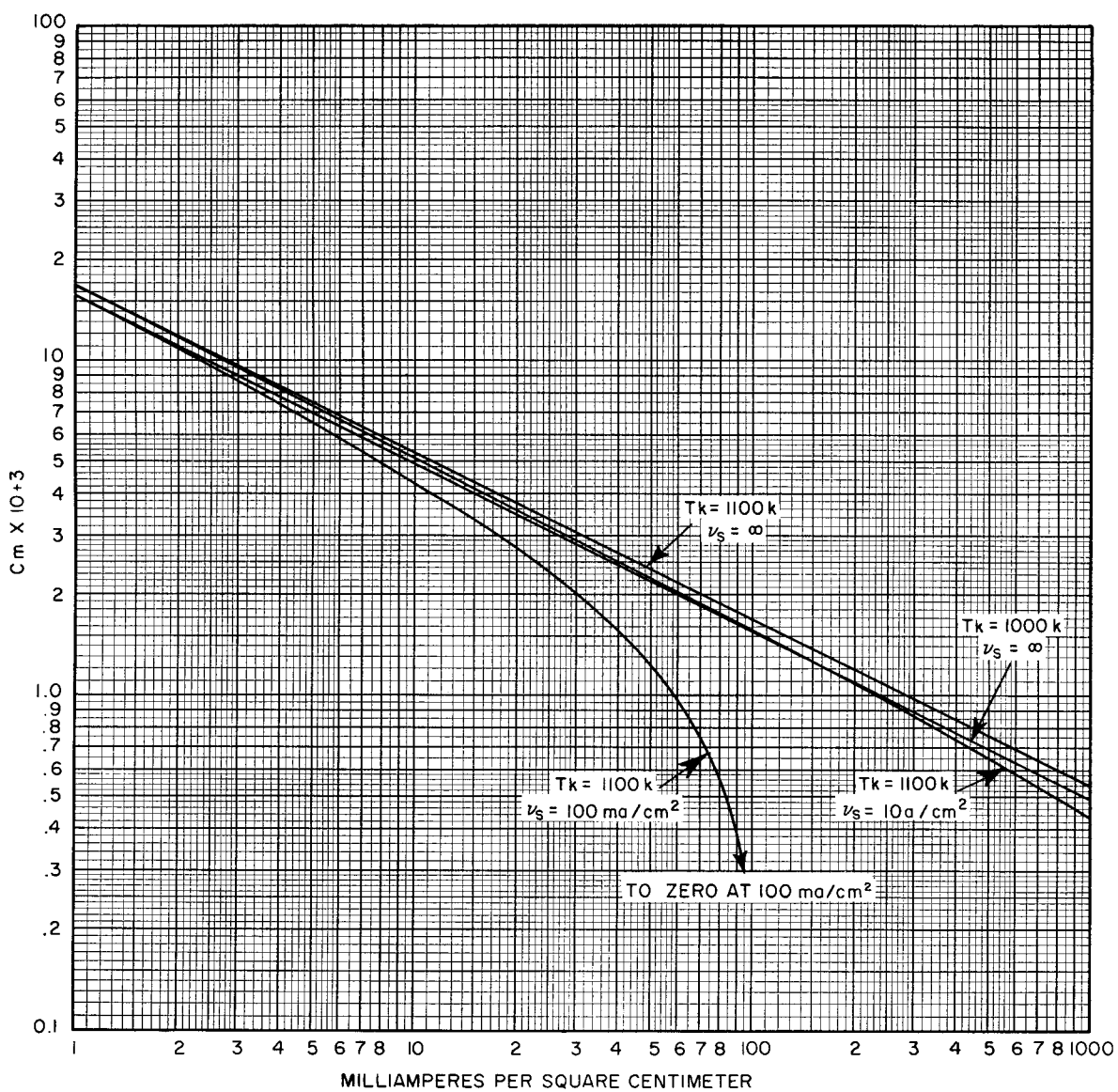


Figure 8. Position of Potential Minimum as a Function of Current Density

When the first two terms are used,

$$J = \frac{2.336 \times 10^{-6} (V - V_m)^{3/2}}{(d - d_m)^2} \left[ 1 + \frac{2.66}{\sqrt{\eta}} \right] \quad (55)$$

The potentials used must include the effects of contact potential.

#### THE IDEAL CYLINDRICAL DIODE

The following discussion covers only the basic formulation and the results in the analysis of an ideal cylindrical diode because more rigorous examination is not required for the present analysis.

#### Initial Velocities - Zero

For a given cathode length  $L$ ,

$$\frac{\delta}{\delta r} \left( r \frac{\delta V}{\delta r} \right) = \frac{I}{2 \pi r \epsilon_0 L} \left( \frac{mV}{2e} \right)^{1/2} \quad (56)$$

The solution found by Langmuir<sup>8, 13, 17</sup> is

$$I = \frac{14.66 \times 10^{-6} L V^{3/2}}{r_a \beta^2} \quad (57)$$

$$\text{or } I = \frac{2.336 \times 10^{-6} A V^{3/2}}{r_a r_K \beta^2} \quad (57a)$$

where  $\beta^2$  is a function of  $r_a/r_K$  or  $r_K/r_a$  only.

Similar solutions are available for the spherical diode. A spherical diode forms the basis of many convergent electron-gun designs.

#### Initial Velocity - Maxwellian

The solution to this problem is complicated by the effects of the nonnormal velocities (tangential veloci-

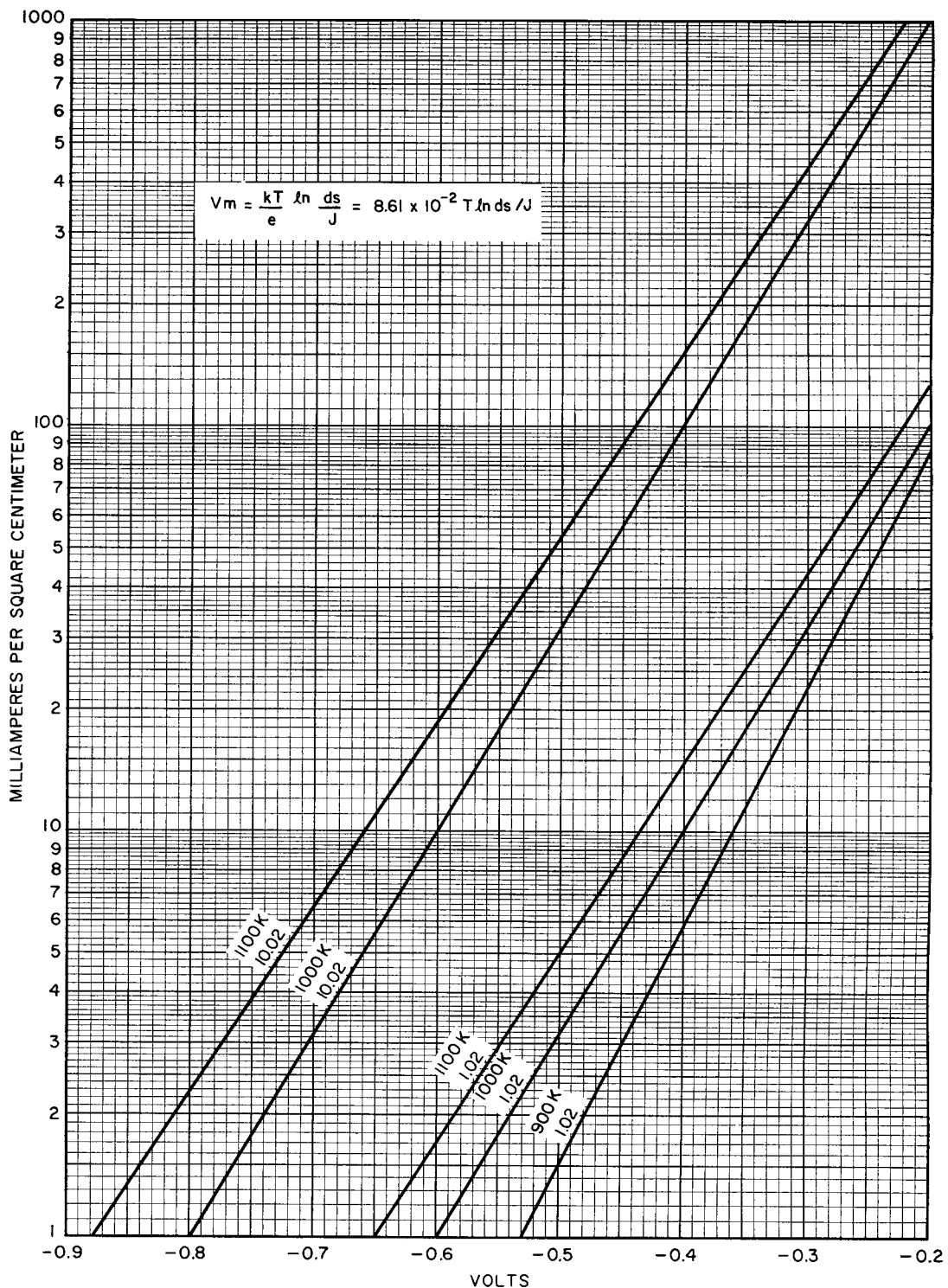


Figure 9. Magnitude of Potential Minimum as a Function of Current Density

ties) on the space-charge distribution, although various approximations have been found.<sup>13, 17</sup> The correction to the three-halves power law is smaller for cylindrical geometry than for the parallel planes. The approximate solution found by including the change in space-charge near the anode is as follows:

$$I = \frac{14.66 \times 10^{-6} L}{\beta^2 r_a} \left[ V - V_m + \frac{V_o}{4} \left( \ln \frac{V}{\lambda V_o} \right)^2 \right]^{3/2} \quad (58)$$

where

$V$  = the effective voltage

$$V_0 = \frac{3}{2} \frac{KT}{e} = \frac{T}{7733} \text{ volts}$$

(The average radial component of initial velocity due to actual radial velocity  $KT$  and tangential velocity  $1/2 KT$ .)

$V_m$  = the value of the potential minimum

$r_a$  = anode radius

$\lambda$  = a number between 1 and 2

The position of the minimum does not enter into the equation because it effects only the effective cathode radius which does not enter the equation. Although beta should be determined on the basis of the radius of the potential minimum, such a refinement is not warranted by this approximate solution.

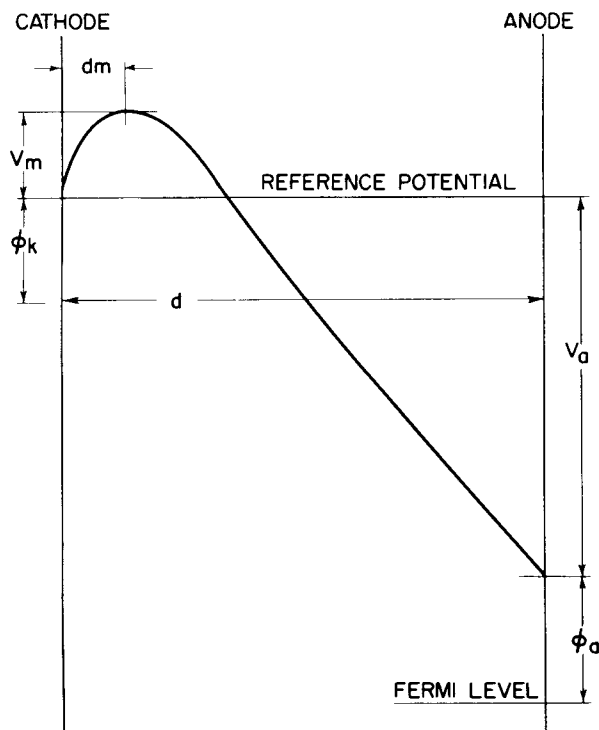


Figure 10. Potential Cross Section of a Thermionic Diode

## Discussion

Little need has been found for these formulas, because most close-spaced tubes approximate parallel-plane geometry sufficiently well to justify their use. However, these results can provide the initial steps for the design of electron gun or other such specialized configurations. Fig. 12 shows a graphic solution of Eq. (57) supplied by A. Kauzmann.

## THE EXTENSION OF DIODE THEORY TO TRIODES

An analytic solution for the field distribution in a triode is complex, but not impossible if the geometry meets the right criteria. Such a solution is not attempted here because it is not generally useful, but the principle involved in arriving at such a solution will be discussed.

The field distribution around an array of very fine wire was first described by Maxwell<sup>18</sup> (p. 310). If the anode and cathode are not close to the grid, and if the wires are small, this solution may be used for the triode. More involved methods are required to compute the field distribution of a real grid which has wires that are large in diameter compared to their spacing and is close to the cathode and/or anode. In general, these methods involve the replacement of the grid wire by an infinite set of charges, usually a set of multipoles (see Stratton, <sup>3</sup> p. 176). Because of the difficulty in summing the contributions of an infinity of charges, approximations must be used and the solution for the field distribution used indirectly. The quantity wanted is a solution for current flow through the tube with given electrode potentials and geometry. The "equivalent diode" method used is simple, direct, and yields the correct value for the current. It consists of replacing the values of the triode with those of a diode in which anode-cathode voltage and spacing are functions of the geometry and electrode voltages of the triode. The current calculated for the diode is the current for the triode. This method requires that the potential minima (in volts) be the same in each case. Through a unique theorem this may be related to the field intensity (gradient) at various points in the tube.

## The Shielding Effect of a Grid

The properties of the field between two electrodes have been discussed in some detail for various geometries, but what are the effects of an array of wires (a grid) placed between the two electrodes? Although a quantitative answer can not be given without reference to a particular geometry, some general results can be discussed by first defining the following parameters:

- a - the spacing of the grid wires (for a helical grid the spacing is equal to the pitch)
- b - the spacing from the grid to the cathode
- c - the spacing from the grid to the plate
- r - the radius of the wire

All spacings are measured to the center of the grid wires. The following terms are also used: coverage ratio ( $2r/a$ ) and window factor ( $a/b$  and  $a/c$ ).

If the cathode and plate are arranged in some arbitrary geometry and have a potential difference of  $V$  volts, a flux  $\phi$  exists between them, and field intensities  $E_1$  and  $E_2$  are present at the surface of the cathode and plate, respectively. The potential, flux density, and field intensity at each point in space are known, or can be calculated, and a capacitance coefficient is assigned to the two electrodes. If a third electrode (say a grid) is placed in the field, it intercepts some of the flux and alters the field distribution. If it is initially charged, its field interacts with the field of the other electrodes, and the gradient, flux density, and potential at each point in space are no longer the same. The magnitude of the change depends on the shape of the third electrode and how and where it is placed in the field. An interposed electrode that physically shields one element from the other has a greater effect than one placed near the edge of the field. The quantity  $\mu$  defines the shielding effect of a grid in an electron tube.

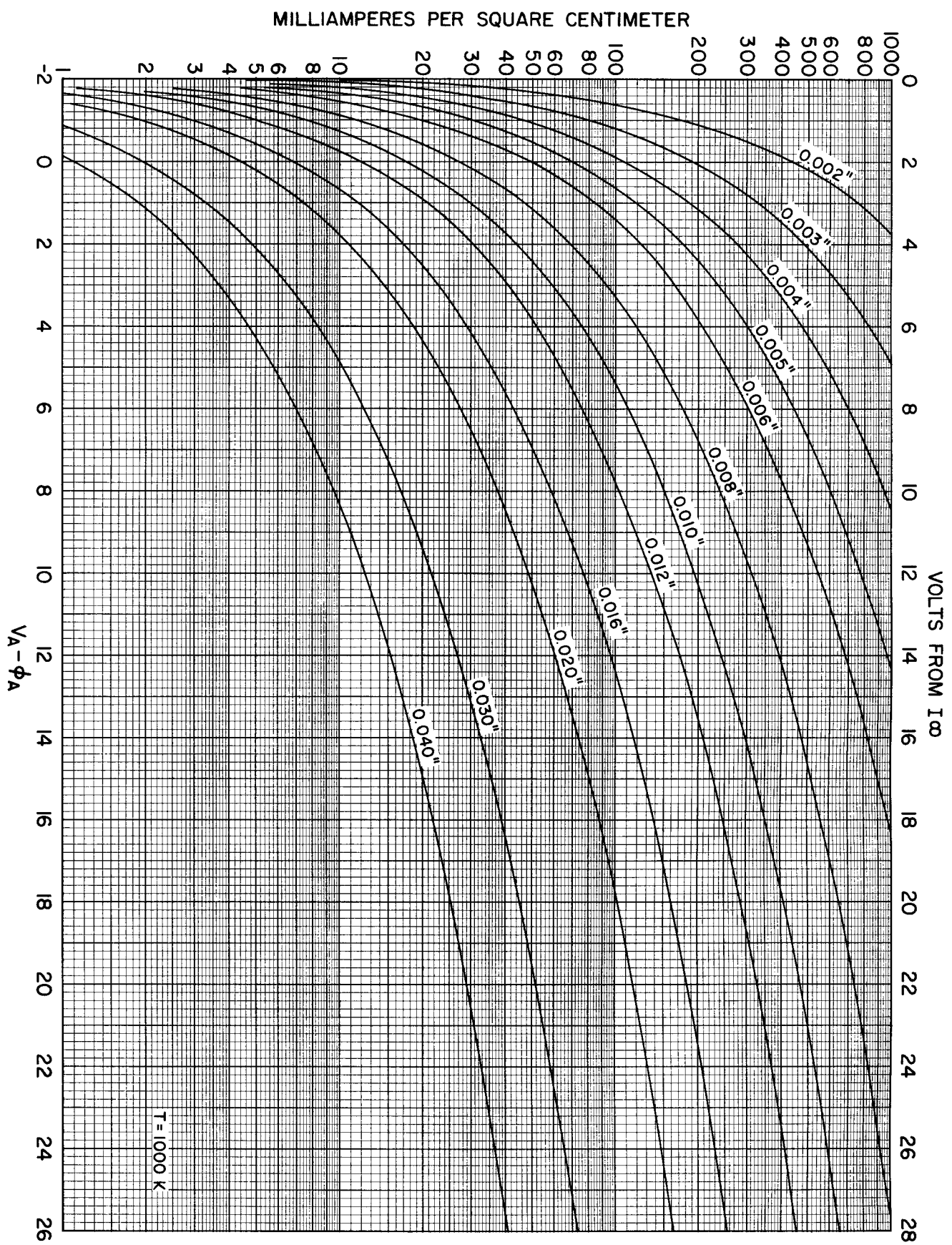


Figure 11. Plot of  $J$  vs.  $V$  with  $d$  as a Parameter

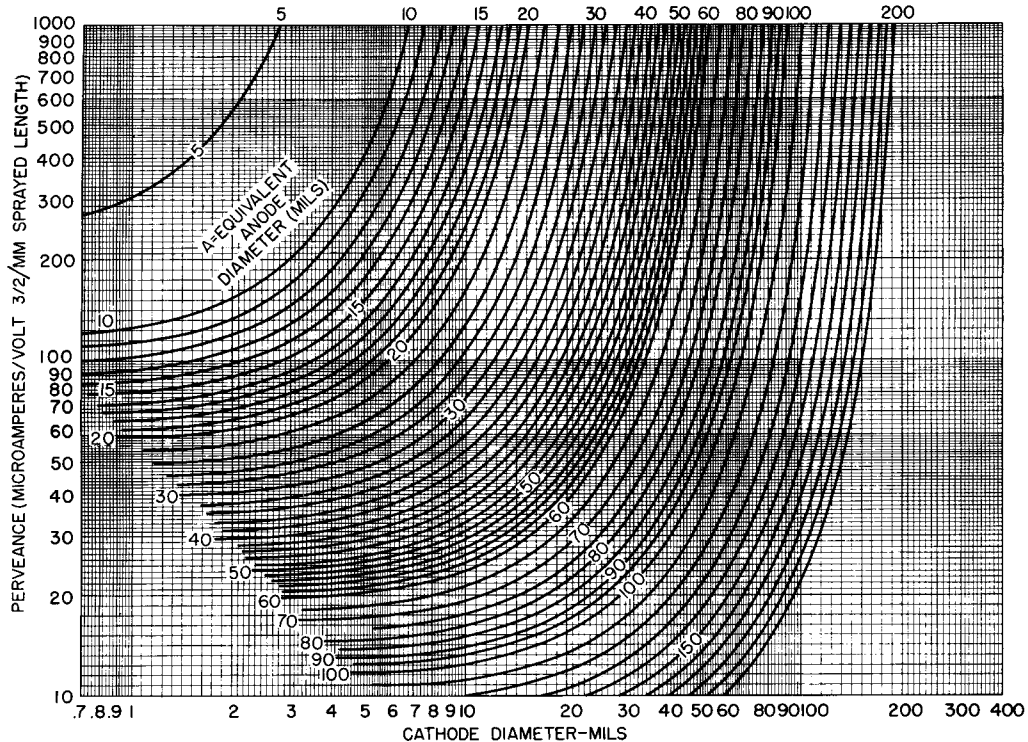


Figure 12. Universal Plane-Parallel Diode Design Curves

The following definitions of  $\mu$  represent two separate points of view, but give the same result.

From the user's viewpoint, the tube is considered as a device (a three-terminal network), of which the internal workings are not known, and  $\mu$  is defined as "the limit of the ratio of the change in anode voltage to the change in grid voltage with the anode current held constant." This relationship is expressed as follows:

$$\mu = \left. \frac{\delta V_a}{\delta V_g} \right|_{I_a = \text{constant}} \quad (59)$$

From the designer's point of view, the tube is considered as a problem in electrostatics. The fields due to the three electrodes are considered, and  $\mu$  is defined as "the limit of the change in the cathode-surface charge density due to a change in grid voltage to the change in cathode-surface charge density due to a change in anode voltage." This relationship may be expressed mathematically as follows:

$$\text{LIMIT } \frac{\Delta \sigma_K / \Delta V_g}{\Delta \sigma_K / \Delta V_a} = \mu \quad (60)$$

At the boundary of a conductor

$$\sigma_K = E \text{ normal}$$

This term may be substituted in Eq. (60) as follows:

$$\text{LIMIT } \frac{\Delta E_{NK} / \Delta V_g}{\Delta E_{NK} / \Delta V_a} = \mu \quad (60a)$$

and reduced to

$$\mu = \left. \frac{\sigma V_a}{\sigma V_g} \right|_{\delta K = E_{NK} = \text{constant}} \quad (60b)$$

Although this is an electrostatic definition, it can also be applied when space charge is present. The equivalency of the two definitions may be shown from an examination of the field in a diode having a flow of electrons which have initial velocities; a discrete value for the gradient is present at the cathode surface for each value of current. Hence, the current is maintained constant by maintaining the off-cathode field constant. It should be understood that in defining  $\mu$  (electrostatically) it is not necessary to refer to the cathode surface; any point in space may be used. The cathode was used in this case to illustrate the equivalency of the two definitions. In addition, it is not necessary to take the limit in the electrostatic case, because the mathematics is linear and finite deviations may be used. In the space-charge-considered case, because the current is not a linear function of voltage, the limiting value must be used.

The two charts shown in Figs. 13 and 14 may be used to calculate the penetration factor (Durchgriff) of any grid in a plane parallel geometry. Penetration factor is the inverse of  $\mu$  and is sometimes given as a percentage. These charts are from an article by Kleijnen.<sup>19</sup> An additional chart with somewhat more limited range is shown in Figs. 15 and 16. This chart is useful in calculating  $\mu$  for tubes having cylindrical geometry. Various methods are discussed below for measuring  $\mu$  of odd structures by analog methods. The results of a set of such measurements made by Hsu and Horton<sup>20</sup>

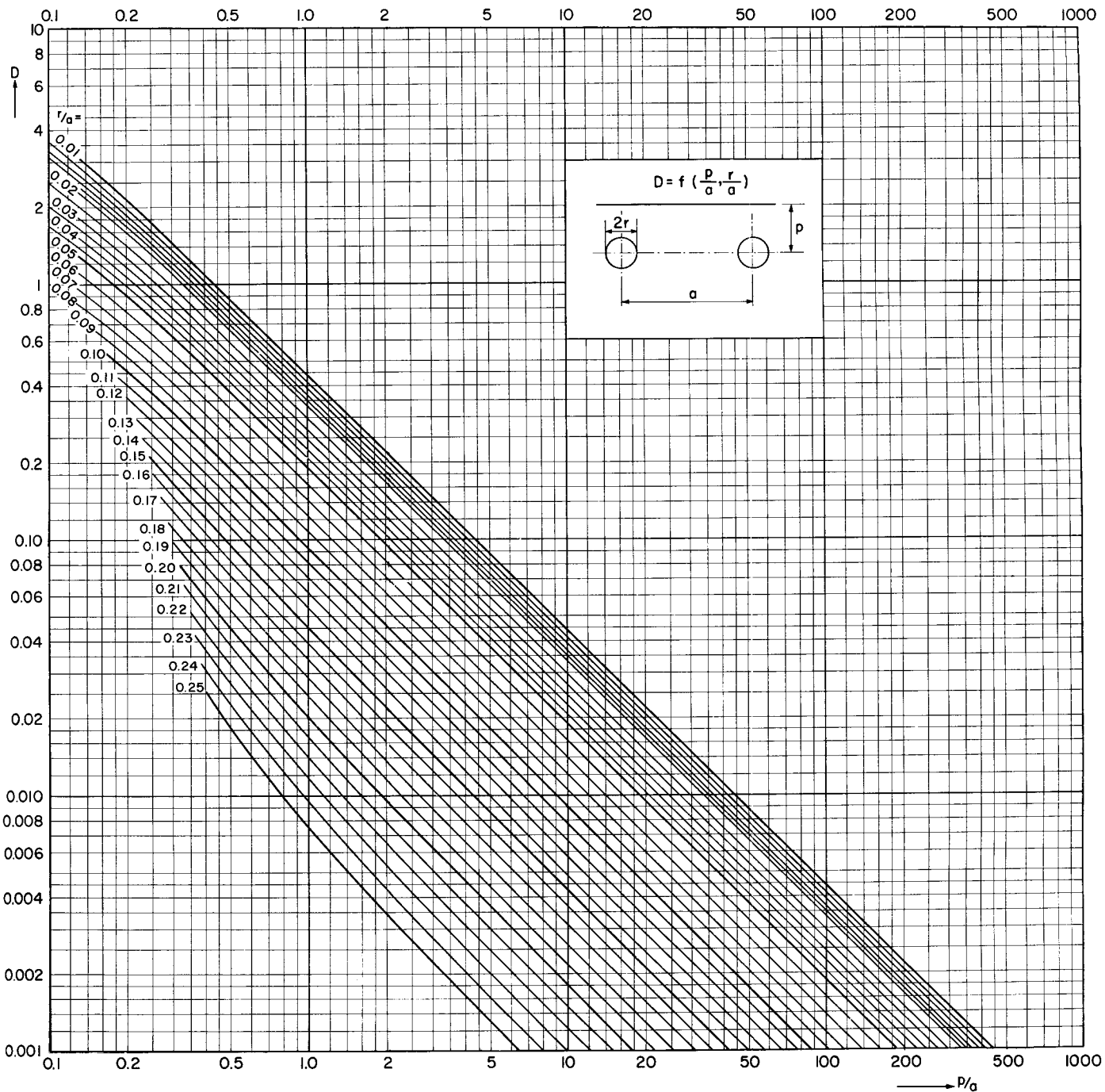


Figure 13. Design Data for Cylindrical Diodes

are shown in Fig. 17. These measurements may be used to determine the  $\mu$  of various mesh grids.

Various calculations have been made of  $\mu$ ; Maxwell<sup>18</sup> probably made the first such calculation. His results may be used for grids which have small wires and are placed far from any other electrode. The method replaces the grid with an array of infinitesimal line charges which have potential lines that are circles near the charge. The charges are chosen such that the resultant potential lines fit the grid wires. Farther from the charges, the potential contours become cardioidal and can no longer be fitted to a round grid wire.

Vodges and Elder<sup>21</sup> overcame this difficulty by replacing the simple line charge with a dipole. This method resulted in a better fit for wire diameters up to 16 per cent of the grid to cathode spacing. Herne<sup>22</sup> replaced the round grid wire with a wire having a polygon cross section and used a Schwartz-Christofel transformation to obtain results that are valid for cases in which the anode is close to the grid plane. Ollendorf<sup>23</sup> proceeded further, and he obtained a multiplicity of charges by taking successive approximations that included more and more terms. His third and fourth approximations are useful for large grid wires up to  $0.72 \frac{2r}{a}$ , but not for closely-spaced anodes. Kleijnen replaced each grid

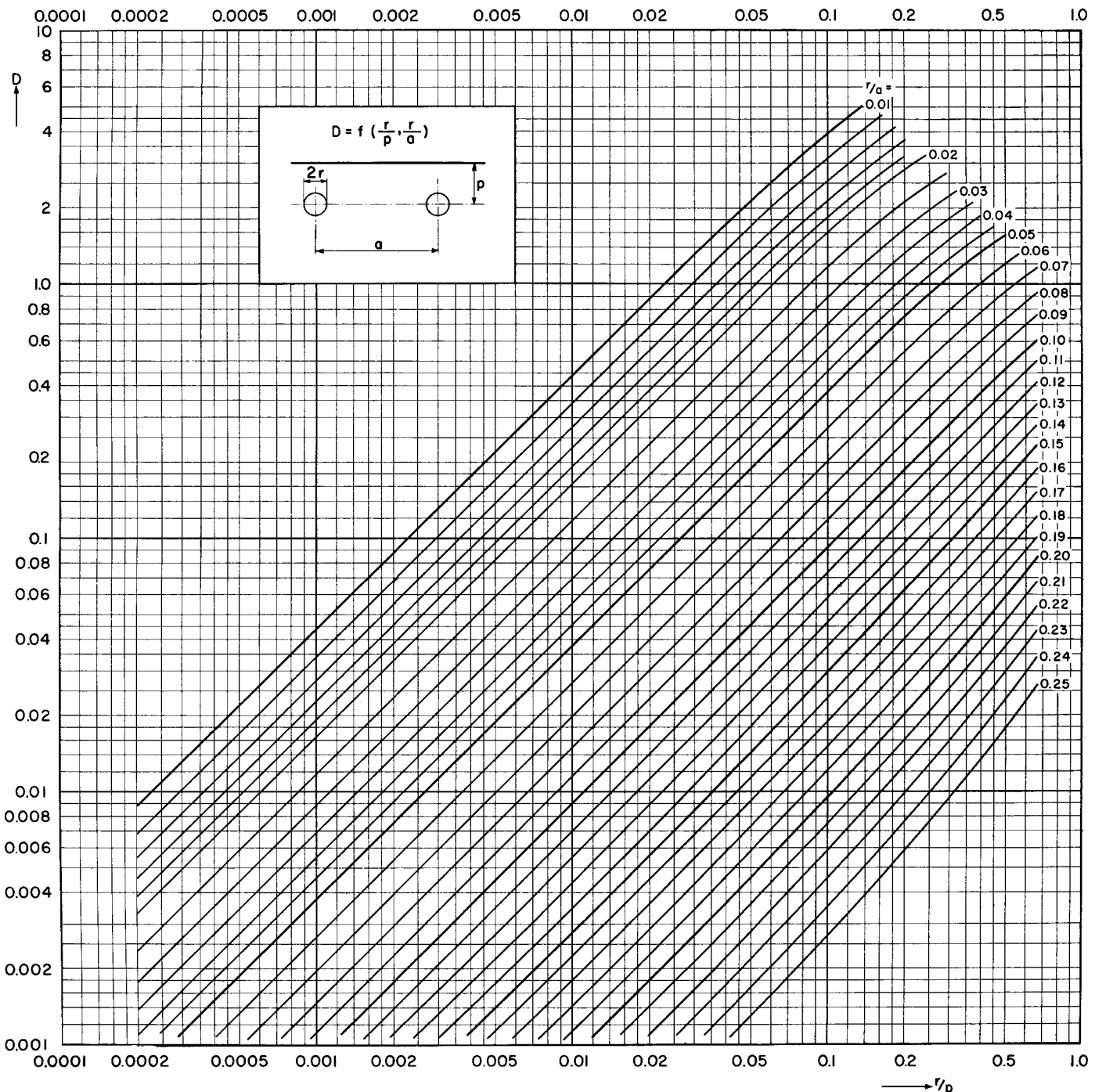


Figure 14. Penetration Factor (Kleijnen)

wire by a series of  $n$ -pole charges where  $n$  varies from one to infinity. His results, presented below, are theoretically good for all coverage ratios and for all grid-anode spacings up to the limiting values of  $2r = a$  and  $s = a$ ;  $s$  is the grid-anode spacing. The results discussed above are not valid for tubes in which the pitch is large compared to the grid-cathode spacing. This mathematically special case (which includes most modern high-performance tubes) is discussed below. Under these conditions, the field at the cathode surface is not smooth (i.e., it varies from a minimum at a point under a grid wire to a maximum at a point between grid wires)

and, as a result, the current density is not uniformly distributed. The present discussion is restricted to the case in which the grid-cathode spacing is larger than the pitch.

#### Calculation of Equivalent Potentials

The importance of a unified approach to the electronics of a vacuum tube is most important at high frequencies when the tube capacitance and inductance are a significant part of the circuit. The interelectrode capacitances of a tube, however, are not constant, but

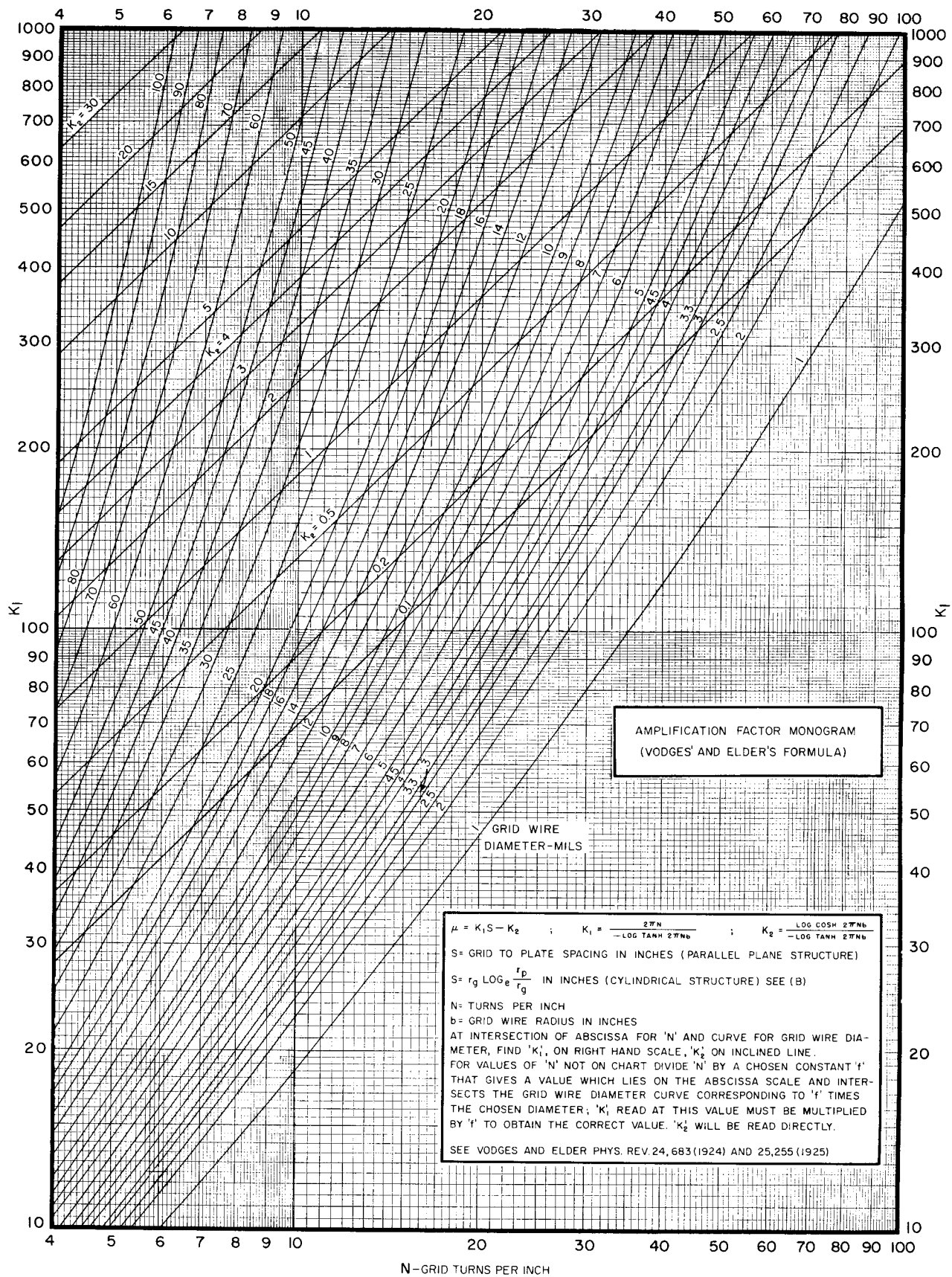


Figure 15. Penetration Factor (Kleijnen)

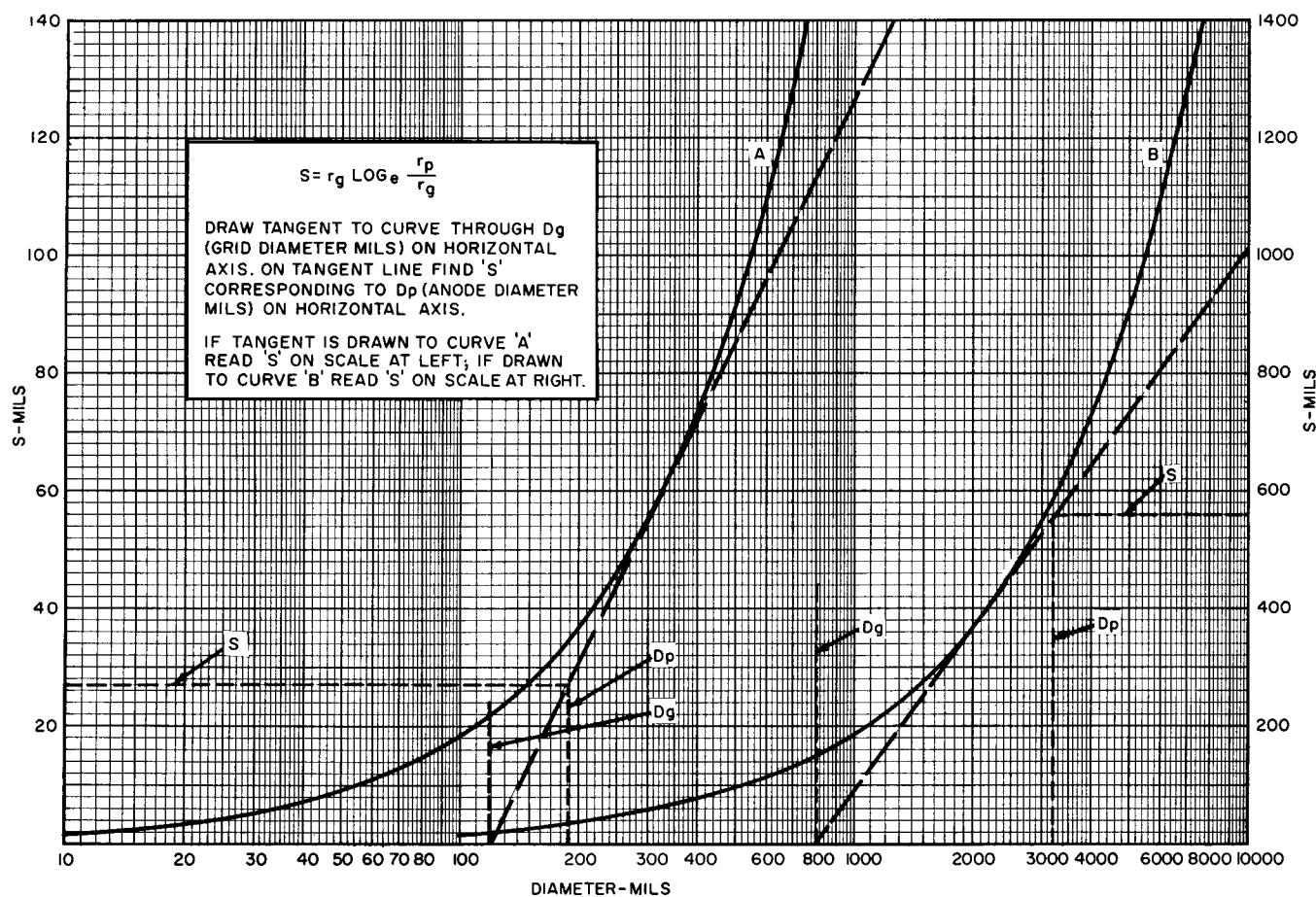


Figure 16. Amplification Factor Nomogram (Vodges & Elder Formula)

vary with the amount of space charge present. At high frequencies, electrons take an appreciable part of a cycle to cross the grid-cathode space and hence do not encounter a static conservative field. At these high frequencies, the electrons absorb energy, manifested as a power requirement for the grid drive. An effective design procedure for these tubes must treat the tube and circuit together as has been done in more recent years by Llewellyn and Peterson.<sup>27</sup> The earlier approach is more simple, but less accurate.

The most simple approach to the calculation of equivalent diodes<sup>24, 25, 26</sup> is purely electrostatic and only charge-free regions are considered. The first refinement, a correction for space charge in the grid-cathode region, is commonly used. Space charge in the grid-anode region is very rarely considered because it leads to undue difficulty. However, because even small amounts of space charge may have large effects, an analysis has been made, as a second order correction, that includes some effects of space charge in the anode region, but not the space charge itself. This approach, although similar to the Llewellyn-Peterson approach, includes only the dc terms.

The Simple Charge-Free Model is a basic analysis approach which leads to the standard form for the equiv-

alent-diode voltage. Although the result is widely used, it is not accurate for high-frequency or low-voltage tubes (i. e., those having a large transit time).

The tube is replaced by the electrostatic capacitances between elements (these capacitances cannot be measured because they include only those active portions of the electrodes that actually carry current), see Fig. 18. This delta or pi network is transformed to a tee, by the ordinary rules of circuit analysis. The transformation equations are as follows:

$$C_A = P/C_{GK} \quad (61a)$$

$$C_G = P/C_{AK} \quad (61b)$$

$$C_K = P/C_{GA} \quad (61c)$$

$$\text{where } P = C_{GK} C_{AK} + C_{GA} C_{AK} + C_{GA} C_{GK}$$

It is assumed that there is an imaginary plane in the tube at the mode (n) for which potential  $v$  is determined.

The equation  $VC = Q$  relates the charge on the electrodes to the potential difference between them. In addition, because the plane at n is in space and no real

net charge may exist there, the charge at n has the following identity:

$$0 = (V_g - V) C_g + (V_a - V) C_a + (V_K - V) C_K,$$

$V$  may be found to be

$$V = \frac{V_g C_g + V_a C_a + V_K C_K}{C_g + C_a + C_K} \quad (62)$$

$$V = \frac{\frac{V_g}{C_g} + \frac{V_a}{C_g} + \frac{V_K}{C_g}}{1 + \frac{C_a}{C_g} + \frac{C_K}{C_g}} \quad (63)$$

From Eq. (61),

$$C_a/C_g = C_{aK}/C_{gK}, \text{ and } C_K/C_g = C_{aK}/C_{ga}$$

This relationship indicates that the imaginary plane is situated in the plane of the actual grid. From our definition of  $\mu$ , Eq. (60), the relationship between the capacitances is expressed as follows:

$$C_g/C_a = \mu_{ga}, \quad (64)$$

and

$$C_g/C_K = \mu_{gK} \quad (65)$$

Eq. (63) may be rewritten as follows:

$$V = \frac{\frac{V_g}{1 + \frac{1}{\mu(g-a)}} + \frac{V_a}{\mu(g-a)} + \frac{V_K}{\mu(g-K)}}{1 + \frac{1}{\mu(g-a)} + \frac{1}{\mu(g-K)}} \quad (66a)$$

The  $\mu$  of a helical grid is a function of wire size, pitch, and spacing to the plane under consideration. For a grid between two planes, as in a triode (with  $V_K = 0$ ), the relationship is expressed as follows:

$$V = \frac{\frac{V_g}{1 + \frac{1}{\mu(1 + \frac{s}{b})}} + \frac{V_a}{\mu}}{1 + \frac{1}{\mu(1 + \frac{s}{b})}} \quad (66b)$$

where  $\mu = \mu_{ag}$ ,  $b = g-K$  spacing, and  $s = g-a$  spacing.

The preceding discussion has been limited to the charge-free case. The following correction considers the charge in the cathode-grid region (called space 1), but neglects the grid-anode region (space 2). If it is again assumed that the simplified case is based on a cathode that emits an infinity of electrons at zero velocity, we may express the gradient on the cathode side of the grid plane as follows:

$$E_{g1} = \frac{4}{3} \frac{V}{b} \quad (67)$$

This value is  $4/3$  of the gradient in the charge-free model. The same gradient is achieved in the model

and the actual tube by reducing the spacing in the model to  $3/4b$ . This reduces the gradients the same but also reduces the reverse  $\mu$  to  $3/4$  of its calculated value. Therefore, Eq. (66) may be rewritten as follows:

$$V = \frac{\frac{V_g}{1 + \frac{4}{3} \frac{s}{b}} + \frac{V_a}{\mu}}{1 + \frac{1}{\mu} (1 + \frac{4}{3} \frac{s}{b})} \quad (68)$$

This equation represents the charge-free model with a first-order correction for charge in the cathode space.

The simplified two-space analysis of a triode attempts to include the effects of space charge in both spaces. The final result includes the effect of the finite transit time, but neglects the space charge itself. First, an expression for the field in a gap with current flowing is obtained which is then applied to the various regions in the triode. The essential steps of the procedure are presented below. Space 1 is the grid-cathode region and space 2 is the grid-anode region. A zero subscript refers to charge-free values. The analysis applies to a single-velocity current flow.

The electric-field intensity at the entrance plane is expressed as follows:

$$E_1 = \frac{V_2 - V_1}{Z_2 - Z_1} \cdot \frac{T_0}{T} - \frac{J}{2\epsilon_0} T \quad (69)$$

and at the exit plane is expressed as:

$$E_2 = \frac{V_2 - V_1}{Z_2 - Z_1} \cdot \frac{T_0}{T} + \frac{J}{2\epsilon_0} T \quad (70)$$

These values are the linear gradients modified by a space-charge factor.

This general result may be applied to a triode by evaluating the gradients at each electrode in each space. Space 1 is the  $g-K$  gap and space 2 is the  $g-a$  gap. The grid is a common element and has a gradient on each side. The numerical subscripts refer to the space and the zero indicates no space charge.

In the grid-cathode space:

$$E_K = 0 \quad (71)$$

$$E_{g1} = \frac{4}{3} \frac{V}{b} \quad (72)$$

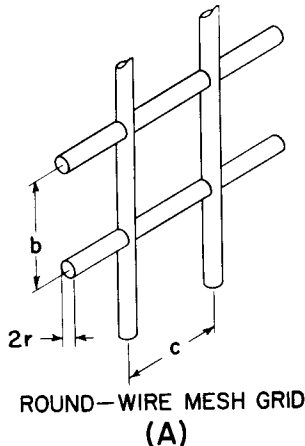
$$T_1 = \frac{4}{3} \frac{\epsilon_0}{J} \frac{V}{b} \quad (73)$$

These expressions have been previously derived.

In the grid-anode space:

$$E_a = \frac{V_a - V}{s} \frac{T_{20}}{T_2} + \frac{2}{3} \frac{V}{b} \frac{T_{20}}{T_2} \cdot \frac{T_2}{T_{20}} \quad (74)$$

$$E_{g2} = \frac{V_a - V}{s} \frac{T_{20}}{T_2} - \frac{2}{3} \frac{V}{b} \frac{T_{20}}{T_2} \cdot \frac{T_2}{T_{20}} \quad (75)$$



ROUND-WIRE MESH GRID  
(A)

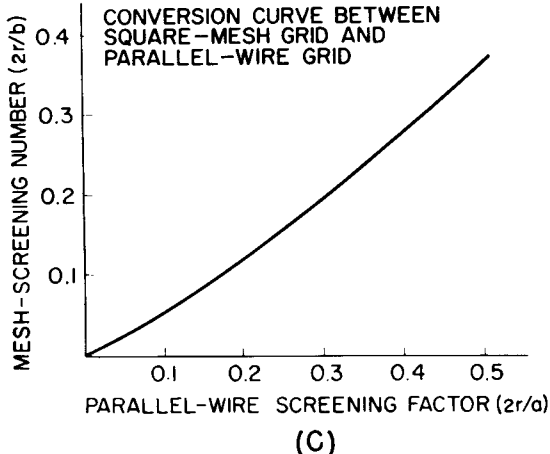
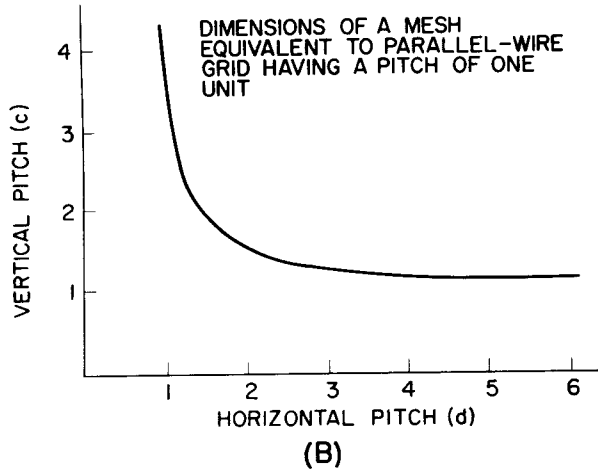


Figure 17. Relations between Helical and Mesh Grids:  
(A) Round-wire mesh grid; (B) Horizontal pitch (d);  
(C) Parallel-wire screening factor (2r/a)

These expressions can be used by evaluating the transit time ratios as follows:

$$\frac{T_{20}}{T_1} = \frac{2}{3} \frac{s}{b} \frac{V_a^{1/2}}{V_a^{1/2} + V_s^{1/2}} \quad (76)$$

$$\frac{T_2}{T_{20}} = \left(1 + \frac{4}{27} \frac{J}{J_s}\right) \quad (77)$$

An expression for the equivalent voltage  $V$  is obtained from these equations as follows:

$$V = \frac{V_g + V_a / \mu'}{1 + \frac{1}{\mu'} \left[ 1 + \frac{4}{3} \frac{s}{b} \frac{T_2}{T_{20}} \left( 1 + \frac{1}{2} \frac{T_2}{T_1} \right) \right]} \quad (78)$$

where

$$\mu' = \mu \frac{T_2}{T_{20}}$$

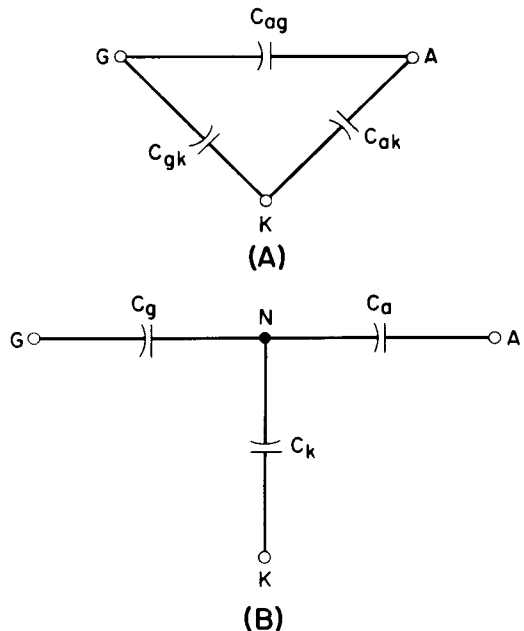


Figure 18. Electrostatic (Capacitance) Representation of a Triode: (A) Delta representation of interelectrode capacitances; (B) Tee representation of interelectrode capacitances (transformed from Delta)

If  $T_2$  is zero and  $T_2/T_{20}$  approaches 1, the expression can be reduced to the previous result [Eq. (68)]. However, if  $T_2/T_{20}$  approaches 1 when  $T_2$  is not zero, the result is a solution which may be said to be a first-order correction for space charge in the anode space. It simply takes into account the finite transit times of the electrons and adds a small correction to the field due to the accumulated charge.

As a final result,

$$V = \frac{V_g + V_a / \mu}{1 + \frac{1}{\mu} \left[ 1 + \frac{4}{3} \frac{s}{b} \left( 1 + \frac{1}{2} \frac{T_{20}}{T_1} \right) \right]} \quad (79)$$

and

$$G_m = \frac{G}{1 + \frac{1}{\mu} \left[ 1 + \frac{4}{3} \frac{s}{b} \left( \frac{2}{3} + \frac{1}{2} \frac{T_{20}}{T_1} \frac{V^{1/2} + 3/2 V_a^{1/2}}{V^{1/2} + V_a^{1/2}} \right) \right]} \quad (80)$$

The ratio  $T_{20}/T_1$  may be evaluated from Eq. (81) by assuming some small value for  $V$  consistent with the known requirements of the design.

### Interpretation

This quasi-static representation for an ideal triode, which includes at least first order corrections for the space charge in both the cathode and anode spaces, can be used for design or analysis. For accurate calculations, the contact potentials, potential minimum, and the electrode potentials must be included. Because the determination of the contact potential is difficult and accurate prediction of current is almost impossible, the design of electron tubes is somewhat empirical. Any methods of analysis should consider information on the accuracy of design, an estimate of degradation in performance from imperfect grids and parts, and information about the contact potential. This information may be used to determine: (1) errors in parts and spacing, (2) the actual electrode voltages required to obtain a desired current level, and (3) any improvements which may be effected by changes in grid design.

An analysis procedure for triodes (and multigrid tubes) is derived from that previously discussed for the diode. The following tests\* may be performed on a General Radio vacuum-tube parameter bridge.

Normally, for any finite grid-wire size, the cathode current is bunched toward the center of the grid aperture (see Fig. 19); a diode of similar dimensions would have laminar flow. Diode conditions may be duplicated by adjusting the electrode voltages until laminar flow results. Under these conditions, the grid intercepts  $2r/a$  per cent of the cathode current and the space around it must be at the same potential;\*\* no change would result if the grid were removed. The grid is said to be at natural or space-charge potential.

In the actual case, shown in Fig. 19D, the potential line that is at grid potential just grazes the lower edge of the grid wires. The diode spacing in this case is  $(b-r)$  rather than  $b$ .

\*This procedure was first described by O. H. Schade, Sr.

\*\*This statement is not strictly true. For any wire of finite radius, the equipotential lines must bend around the wires in the vicinity of the wires. Laminar flow is probably established when the field has the shape shown in Fig. 17D, rather than in Fig. 17C.

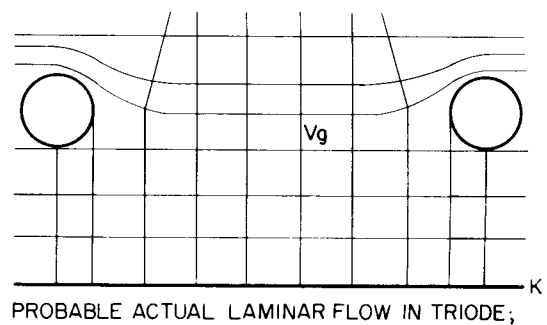
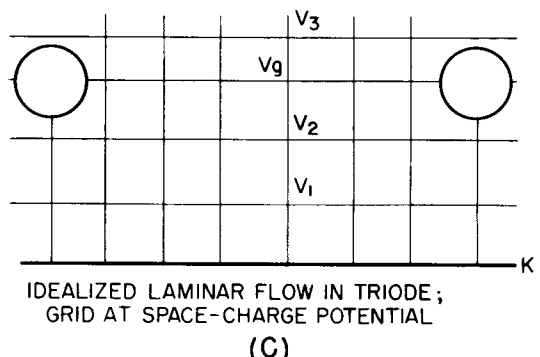
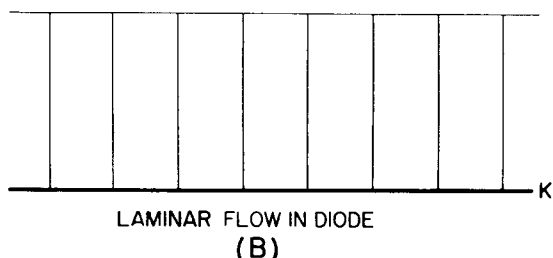
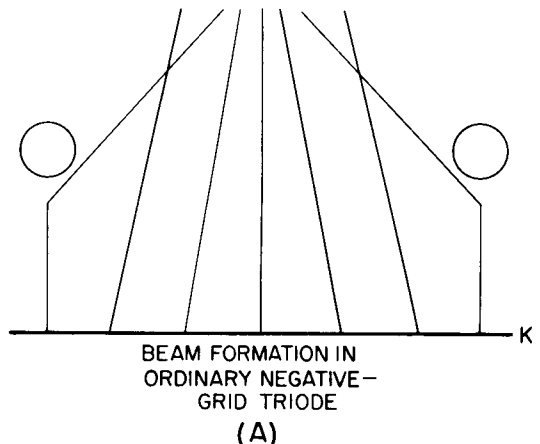


Figure 19. Electron Flow Patterns in Diodes and Triodes

## Procedure for Analysis\*

(1) Read  $I_K$  and  $\hat{g_m}$  as a function of  $V_g$  with the ratio  $I_g/I_K$  equal to  $2r/a$ . The term  $\hat{g_m}$  is defined as the transconductance read with the grid at space charge potential and should be read at the cathode lead to include all the current,  $I_K = I_g + I_a$ .

(2) At a constant bias (e.g., -0.6 to -1.0 volts) or constant grid current (e.g., 0.1 microamp) read  $g_m$  as a function of  $I_b$  by varying  $E_b$ .

(3) Plot  $\log I_K$  and  $\hat{g_m}$  as functions of  $V_g$ . On the same graph plot  $g$  as a function of  $V_g$ . The diode conductance  $g$  may be obtained by graphical differentiation of the  $I_K$  curve. On the same sheet plot  $g_m$  as a function of  $I_b$ ; use the  $I_K$  curve as an axis, as shown in Fig. 20. The diode conductance  $g$  is the theoretically obtainable conductance for the tube structure under analysis. The term  $\hat{g_m}$ , the maximum transconductance obtainable for the triode structure, is less than  $g$  by the factor of the denominator of Eq. (80). The term  $g_m$ , the actual transconductance available, which is less than  $\hat{g_m}$  because of field nonuniformities may be increased (theoretically up to the value of  $\hat{g_m}$ ) by using more ideal grids. The break point of the  $I_K$  curve is used to determine  $I_\infty$ .

The design of triodes is similar to the design of diodes except that the design  $G$  must be greater than the desired  $g_m$  by two factors: (1) the denominator of Eq. (80) and (2) a factor of 2 or 3 for field roughness.

The capacitances may be estimated from field plots for the active portion of the structure. The total capacitance is the sum of these estimates plus the capacitances of the stem, support members, etc. The optimum triodes require the finest wire and highest pitch grids commensurate with the attainable interelectrode spacings, manufacturing techniques, and tolerances. The capacitances of the nonactive structure must be kept to a minimum.

## TETRODES AND PENTODES

This section discusses multigrid tubes, especially the tetrode and pentode; the analysis may be extended to other multigrid tubes. 28, 29, 30, 34 In this basic approach, equivalent potentials for the various grids are calculated, and ultimately, the structure is reduced to an equivalent diode. Because of the additional electrodes at positive potentials, an additional factor, current distribution, must be examined. It has been shown that the space charge has a marked effect on the current distribution, plate resistance, and overall simplification factor.

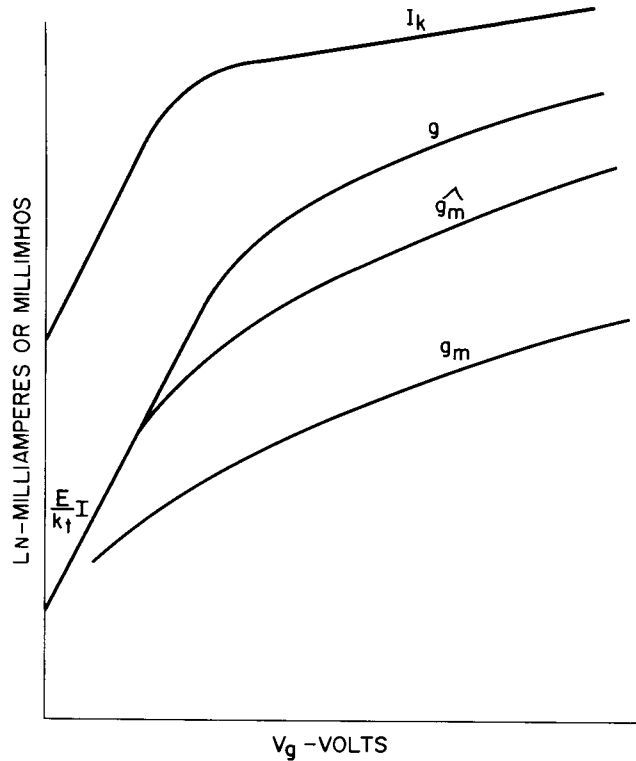


Figure 20. Typical Plot  $g$ ,  $\hat{g_m}$ ,  $g_m$ , and  $I_K$  vs.  $V_g$

The tetrode, which was originally designed to reduce the grid-anode capacitance of the triode, has found wide use because of the form of the plate current-anode voltage characteristic. Although the triode is limited in that the voltage available for accelerating the electrons varies with the plate voltage swing, the tetrode has a fixed voltage available (the screen-grid voltage) which makes it especially useful when power output or a large voltage swing is required. However, the tetrode still finds widest use when low grid-anode capacitance is a requirement.

Early tetrodes were limited by the characteristic dip resulting from secondary emission from the plate. In the pentode, a third grid was introduced to suppress these secondary emissions. However, other means of suppression are used, and many tetrodes are still designed. The beam power tetrode, an important subgroup, is discussed separately in the article, "Beam Power Tube Design Considerations" by O. H. Shade, Jr., in this book. The design of pentodes and tetrodes depends mainly on the proper designing of the suppression mechanism (sometimes referred to as back-end design). The front end (cathode, grid No. 1, and grid No. 2) may be designed using triode principles. Many modern pentodes for wide-band amplifier service are essentially tetrodes which use a suppressor grid or beam plate only to reduce interelectrode capacitances.

## Equivalent Potentials

The equivalent potentials for the pentode  $V_{eqv}$  (see Fig. 21) are derived from the basic equation

$$V_{eqv} = \frac{V_1 D_{12} + V_2 + V_3 D_{32}}{D_{12} + 1 + D_{32}}$$

\*This analysis is an attempt to provide a more exact and scientific means of evaluating tubes, but does not include a good deal of subsequent work. The author suggests referring to Dingwall<sup>67</sup> and the article in this book by O. H. Schade, Sr. for a description of the latest work on this subject.

From this equation, the equivalent potentials for each of the grids may be written directly as follows:

$$V_1 = \frac{D_{21} V_2 + V_g}{1 + D_{21} + D_{01}} \quad (81)$$

$$V_2 = \frac{D_{12} V_1 + V_s + D_{32} V_3}{1 + D_{12} + D_{32}} \quad (82)$$

$$V_3 = \frac{D_{23} V_2 + V_{sp} + D_{43} V_p}{1 + D_{23} + D_{43}} \quad (83)$$

$D_{ij}$  is the penetration factor element  $i$  to element  $j$ .

$V_i$  is the equivalent voltage of element  $i$  (numbered outward from  $K$ ;  $K = 0$ )

where

$V_p$  = plate voltage (applied)

$V_g$  = grid voltage (applied)

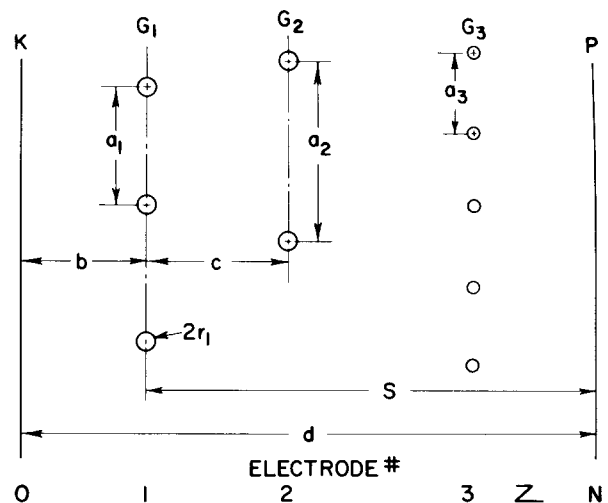
$V_s$  = screen voltage (applied)

$V_{sp}$  = suppressor voltage (applied)

These equations could be combined to give a single expression for  $V_1$ . A more sensible approach is to eliminate the negligible factors and compute  $V_2$  and  $V_3$  and then  $V_1$ . These equations may be used for tetrodes by setting  $V_3$  equal to  $V_p$ . The following procedure may be used:

- (1) Calculate  $V_3$ , let  $V_2 = V_s$ .
- (2) Calculate  $V_2$ , let  $V_1 = 0$ ; use  $V_3$  as calculated above.
- (3) Calculate  $V_1$ ; use  $V_2$  as calculated above.

In the tetrode, the situation is more complex. There is generally a potential minimum between screen and plate, but the calculation of its position and magnitude is among the more difficult problems. In beam power tubes, it is generally assumed that the potential in the plane of the beam plate is zero. Just how important these inaccuracies are is a matter of conjecture. Usually the results will be close enough for the first trial and a small amount of empirical work will finish the design. When the equivalent diode has been determined, the cathode current and triode  $gm$  may be calculated. Because not all of the current reaches the plate, the front end must be over-designed. Because the screen is a grid, the field is not uniform in the plane of the screen. This condition contributes to the degradation of the theoretical transconductance ( $gm$ ) in the same manner as control grid field roughness. When the cathode current and triode  $gm$  have been calculated, the ratio  $I_a/I_s$ , the plate resistance  $r_p$ , and the knee voltage (and suppression which is intimately connected with the knee voltage) may be determined as discussed below.



$a_n$  = PITCH OF  $N$ TH ELECTRODE

$r_n$  = RADIUS OF GRID WIRE OF  $N$ TH GRID

$b$  = GRID 1 - CATHODE SPACING

$S$  = GRID 1 - ANODE SPACING

$c$  = GRID 1 - GRID 1 SPACING

$d$  = CATHODE - ANODE SPACING

Figure 21. Cross Section of Multigrid Tube Giving Nomenclature for the Various Spacings

#### The Effect of Space Charge in the Anode Region

Because a mathematical analysis of the space-charge effects has been described elsewhere and is somewhat involved, this section is restricted to a discussion of some of the ramifications of the analysis.

Qualitative Discussion. It is assumed that the initial velocity for the emitted electrons is zero and that any point in the beam up to the screen grid has a single velocity. The electrons are assumed to travel in straight parallel paths as they approach the screen. These assumptions are also generally used in mathematical treatments. Based on the above assumptions, as the beam passes through the screen, a small portion of the current is directly intercepted, and the remainder continues on towards the plate. If space charge is neglected (or is very small) the electrons reach the plate even if the plate potential is zero because they originated at zero potential. However, we know that for reasonable current densities the space charge becomes important, and the potential variation is such that, for low plate voltages, some of the current is turned back (thermal velocity spread must then be considered). There is a critical value of plate voltage, the knee voltage, above which all the injected current is collected. The knee voltage is not generally precise or sharply defined because the electrons passing near the wires of the screen grid are deflected laterally. This effect gives the beam a lateral spread and introduces a velocity spread. The electrons having the greatest entrance angles require the highest voltages to be collected and, as a result, the knee is rounded. In an actual tube, the electrons approaching the screen usually have a considerable angular spread which causes further rounding of the knee.

Mathematical Solution-References. The mathematical analysis of the problem has been carried out in great detail by Fay, et al<sup>5</sup> and Salzberg and Haeff.<sup>4</sup> Both papers give graphical data that may be used to compute the form and magnitude of the potential distribution. Such factors as the knee voltage, the voltage available for suppression, and maximum current may be calculated. Such anomalies must be expected; the mathematics is not always single-valued and hysteresis effects have been predicted and observed. The geometry in a real tube deviates widely from the ideal and this, of course, gives additional errors.

Screen-Grid Current. The calculation of screen-grid current is always difficult. The directly intercepted current may be estimated, but the current returned from the plate space may make many excursions through the screen plane before it is collected. This makes accurate calculation of screen current difficult. Some work has been done on this problem.<sup>31, 32, 33, 35</sup> Low screen current is important in power output tubes to provide high efficiency and safe screen temperatures. In rf amplifier tubes, screen current causes noise (partition noise) and low screen current is desirable. For power output tubes, the control and screen grids are aligned to provide focusing. Because wide-band amplifiers have low-pitch control grids and higher values of  $\mu$ , it is not generally possible to line up the grids. Low screen current may be achieved by careful design of the back end or by special construction (i. e., shielding the screen grid with a third grid run at zero potential). This has been used in the past, but generally requires high voltages or complicated structures and is only economical in extraordinary circumstances.

Plate Resistance.<sup>36</sup> Very little can be said about this calculation of plate resistance, other than that it is largely controlled by the space charge in the anode region. We know that the  $\mu$  is affected by space charge (the cathode space in the triode analysis), but there are also further complications such as secondary emission and reflected electrons returned to the screen grid.

## VARIABLE MU EFFECTS

### The Concept of Variable Mu

The preceding sections considered only ideal tube structures; this section discusses some deviations from the ideal. The ideal triode is assumed to have a perfect grid that controls the field at the cathode without intercepting or deflecting the electrons. The electric field intensity at the cathode will then be a constant along the cathode in either of the two dimensions. Such an ideal structure has a constant  $\mu$  that is not attainable in practice. Nonconstant or variable  $\mu$  introduces nonlinearity into the characteristics of the tube (over and above the basic nonlinear 3/2-power relation). This additional variation may or may not be desirable. For radio and television systems, a wide range of signal amplitudes is handled without distortion by tubes having a remote cutoff characteristic. On the other hand, because variable-mu tubes suffer some degradation in gm and performance, it is desirable to eliminate any unwanted variation to maximize gain.

Variable  $\mu$  effects may be categorized as (1) designed effects, which result from variable-pitch grids and other methods, and (2) accidental effects, which result from nonideal grids, variable spacing, or statistical variations (in electrode dimensions). This section describes an approximate method of design for variable pitch grids and discusses the accidental variations.

### Design of Variable-Mu Tubes

A  $\mu$  variation is used to extend the grid base (remote cutoff) and provide large signal handling capacity.

In an ideal tube, having a grid voltage for cutoff of  $E_{bb}/\mu$ , the cutoff may be extended by winding the grid so that the main section has low pitch and high  $\mu$ , and one or more sections of lower  $\mu$ . The various sections of the grid cut off at different values of grid voltage, and, at low bias, the characteristic is a composite (see Fig. 22). If the characteristics of the individual sections could be computed, the overall characteristics could be drawn. Fig. 22 shows idealized linear approximations; before attempting to calculate actual characteristics, some general aspects of the problem will be discussed.

CURVE	GRID SECTION
1.	HIGH- $\mu$
2.	MEDIUM- $\mu$
3.	LOW- $\mu$

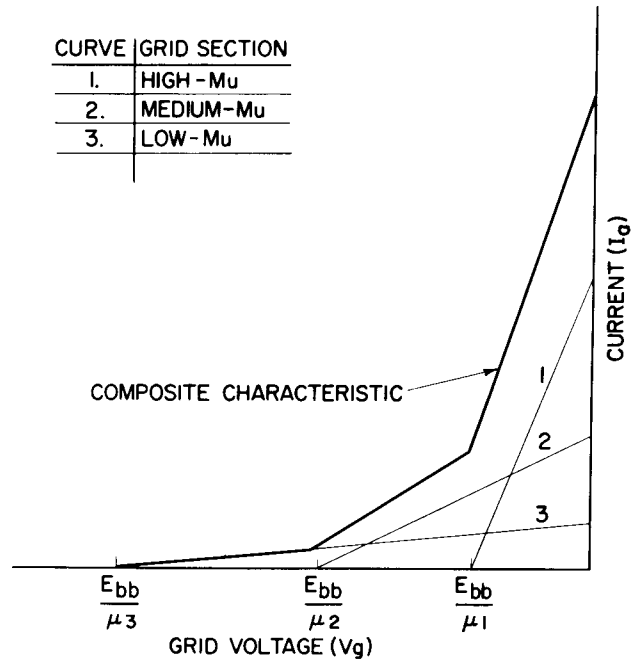


Figure 22. Composite Transfer Characteristic for Variable Mu Tube

The lowest value of  $\mu$  is governed by the cutoff bias desired for the tube. The area of this section (i. e., number of turns) is, in turn, governed by the gm and/or current desired at some bias less than the cutoff value. The intermediate sections are determined by the curvature desired in the transfer characteristic. The main section is determined by the gm and current required near zero bias. In practice, the various sections of the grid are chosen and the composite curve computed. The design is varied until the desired composite curve is achieved.

This section describes how the contribution of the individual sections may be combined to give the composite characteristic. It should be realized that the following discussion is general and does not refer to variable-pitch-grid tubes only, but to any combination of nonuniform tubes. In fact, it applies to the present case only insofar as the sections are separate and distinct. Any interaction between sections would somewhat invalidate these results.\*

The total plate current  $I$  is the sum of the currents through each section of the grid.

$$I = i_1 + i_2 + i_3 + \dots + i_n \quad (84)$$

Differentiation with respect to  $V_g$  gives

$$\frac{\delta I}{\delta V_g} = \frac{\delta i_1}{\delta V_g} + \frac{\delta i_2}{\delta V_g} + \frac{\delta i_3}{\delta V_g} + \dots + \frac{\delta i_n}{\delta V_g} \quad (85)$$

or

$$Gm = glm + g2m + g3m + \dots + gnm \quad (85a)$$

Differentiation with respect to  $V_a$  gives

$$\frac{\delta I}{\delta V_a} = \frac{\delta i_1}{\delta V_a} + \frac{\delta i_2}{\delta V_a} + \frac{\delta i_3}{\delta V_a} + \dots + \frac{\delta i_n}{\delta V_a} \quad (86)$$

or

$$Ga = g1a + g2a + g3a + \dots + gna \quad (86a)$$

The composite transconductance and plate conductance are the sums of the individual conductances because the tubes are in parallel. The composite mu is determined from the following expression for current:<sup>67</sup>

$$I = \frac{KA}{B^2} (DV_a + V_g)^{3/2} \cdot F \quad (87)$$

$$B = b - dm, \quad V_a = V_a - V_m - \phi_K + \phi_a$$

$$F = \phi(\eta^+), \quad V_g = V_g - V_m - \phi_K + \phi_g$$

If this expression holds, with the appropriate values, for both the composite tube and the individual sections, the expression may be written as follows:

$$\frac{KA}{B^2} (DV_a + V_g)^{3/2} F = \sum_{i=1}^N \frac{KA_i}{B_i^2} (D_i V_a + V_g)^{3/2} F_i \quad (88)$$

The values for the composite tube are average values, as discussed below. This equation may be solved for the composite Durchgriff  $D$  as follows:

\*The mu of individual sections of a variable pitch grid may be difficult to determine accurately. The formulas presented apply to an infinite array of wires equally spaced. For short sections of the grid where the wire spacing changes abruptly the calculation is likely to be in error.

$$D = \frac{1}{V_a} \left\{ \left[ \sum_{i=1}^N \frac{a_i}{b_i^2} f_i (D_i V_a + V_g)^{3/2} \right]^{2/3} - V_g \right\} \quad (89)$$

$$\text{where } a_i = \frac{A_i}{A}, \quad b_i^2 = \frac{B_i^2}{B^2}, \quad f_i = \frac{F_i}{F}$$

Some approximations must be made when applying these results.

The grid-cathode spacing may vary if the actual geometry varies or if the potential minimum position varies because of varying current density. The average value used to compute the composite current is taken as the mean-square average of the individual spacings.

$$B = \sqrt{\frac{\sum B_i^2}{\eta}}$$

The values of  $F$ ,  $V_m$ ,  $\phi_K$ ,  $\phi_a$ , and  $\phi_g$  should be average values for the composite structure. Eq. (89) may be used to compute the Durchgriff for variable pitch grid, variable spacing, or even varying work functions. For a quick check on variable-pitch tubes, the refinements may be dropped and the simpler Child's formula may be used as in the following example of the 6FW8 variable-pitch grid tube shown in Table I.

#### Mu Variations from Nonideal Grids

There are many mathematical formulations for the mu of a helical grid between two plane electrodes. This calculated mu and its subsequent application in the calculation of equivalent diodes is usually limited to the case where  $b > a$  and  $r \ll a$ . Very few modern tubes meet these criteria and most are characterized by the existence of a phenomenon known as inselbildung or shadow effect (see Fig. 23). Under these conditions, the field strength and current density at the cathode surface are not constant. Depending upon the operating condition, some areas of the cathode may be cut off before others. Measurement of mu as a function of grid voltage shows a decrease with increasing bias, as shown in the published data sheets for any modern tube. This variation has two effects which must be considered:

- (1) the normal tailing-off of the transfer curve and the reduction in gm resulting from nonuniformity
- (2) cathode current may be less than predicted from theoretical mu values, because some areas of the cathode may be cut off.

An estimate of these effects requires some idea of the magnitude of the variation of mu and current density. This variation has been determined empirically and mathematically by Fremlin,<sup>68, 69</sup> mathematically by Bennett and Peterson,<sup>37</sup> and Dahlke,<sup>38</sup> on the analog field plotter by Napiorski, Schade, and Scholz,<sup>39</sup> and numerically by Harris and Kirk<sup>40</sup> on a digital computer. The data are conflicting even for the simple cases considered. The actual situation is greatly modified by the space charge, and, to our knowledge,

Table I  
Calculation for Mu of 6FW8

Section	Length	Pitch	r/a	Da	ai	
1	0.2056	0.0022	0.091	0.025	0.745	S = 0.008
2	0.0500	0.0025	0.080	0.032	0.181	D <sub>avg</sub> = 0.0287
3	0.0168	0.0028	0.071	0.042	0.061	
4	0.0032	0.0032	0.062	0.059	0.016	Mu = 34.8

The computed average of 34.8 compares favorably with the measured value of 33.

the complete solution has not yet been obtained. The results obtained by Bennett and Peterson, shown in Fig. 24, are valid only for small grid wires. The results obtained by Napiorski, et al are presented for comparison (Figs. 25 thru 28). Any work of this sort must be considered as a first approximation and interpreted in the light of the assumptions that were made in its derivation. The numerical solutions<sup>40</sup> are probably the most accurate, but have not yet been made generally available; a portion of this data is included in Fig. 29.

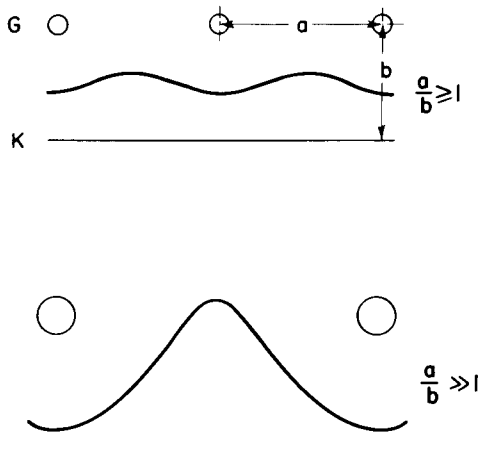


Figure 23. Current Flow Patterns Showing Inselbildung

#### Variable Spacing and Statistical Variations

The problem of variable or nonuniform spacing may be handled in the same manner as the variable-pitch grid, but requires more accurate analysis to obtain useful results. There is evidence that for variations in grid-cathode spacing inselbildung effects may outweigh other effects and make analysis difficult.

Statistical variations in grid pitch or tube interelectrode spacing also lead to variable mu and degradation of tube performance. The difference between statistical variations and shifted parts is one of degree and may be handled in a similar manner except that statistical methods must be used. This problem has been treated theoretically by Dahlke.<sup>41</sup>

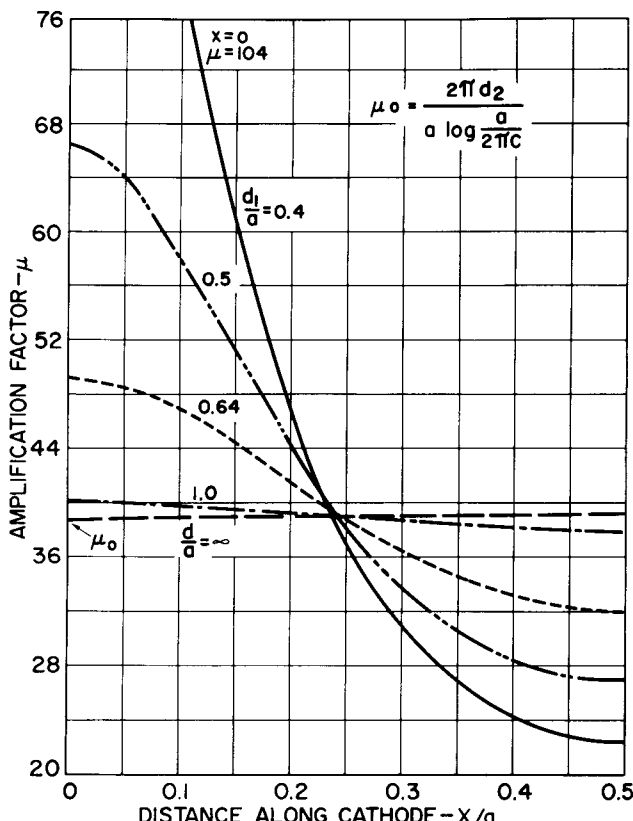


Figure 24. Inselbildung Effects in Triodes - Bennett and Peterson: (A) Variation of mu along cathode surface of triode;

#### FIELD PLOTTING

The previous sections derived current-voltage relations for common geometries without explicit calculation of the electric fields. However, it is sometimes necessary or desirable to actually plot the field for electron trajectory problems, estimation of capacitance or the determination of points of high field for voltage-breakdown consideration.

#### Mathematical Plotting Methods

Direct Solution of the LaPlace Equation. Direct solution of the LaPlace equation is possible only for simple geometrical configurations, and, therefore, the direct application of this method to electron tubes

is limited. However, small sections of the complex tube structure may be successfully investigated by this method.<sup>42</sup>

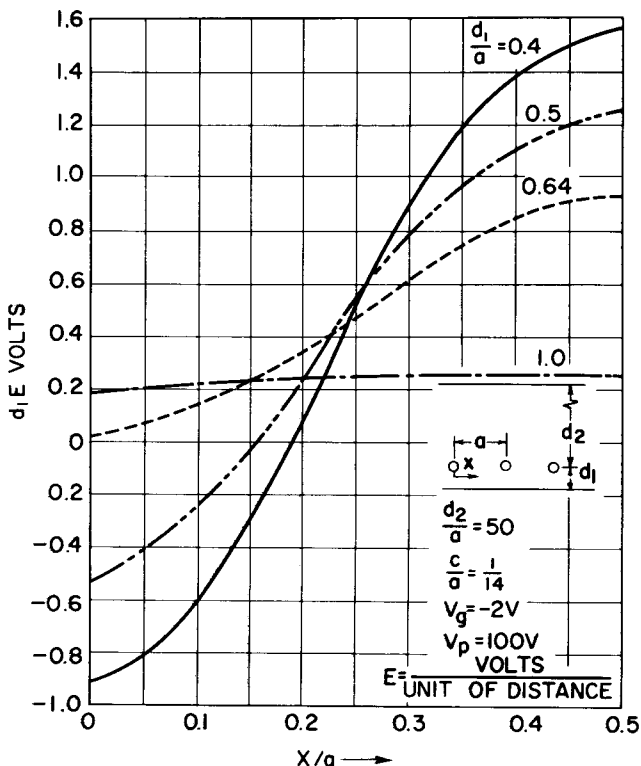


Figure 24(B). Variation of field strength along cathode surface of triode

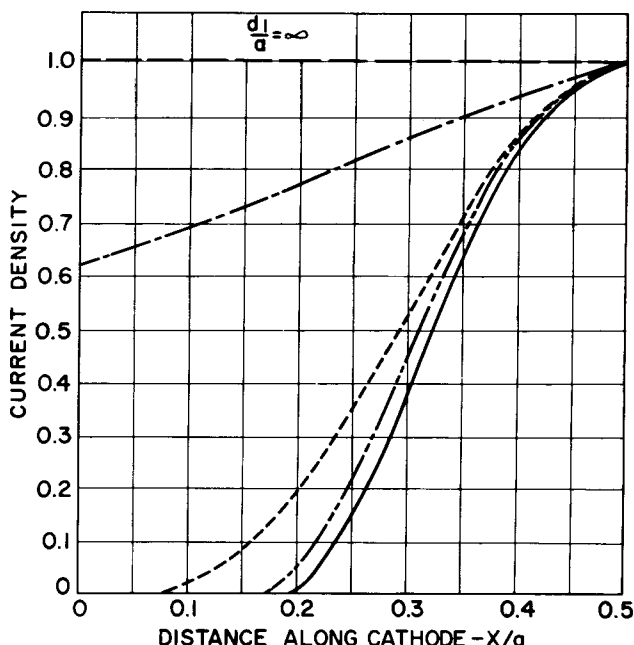


Figure 24(C). Variation of current density along cathode surface of triode

Conformal Mapping. In a conformal map, orthogonal functions retain their orthogonality when mapped.\* As a result, it is possible to map a complex geometry and transform (warp) it into a simpler one for which a solution is obtainable. This method has many applications and has often been used (e.g., Vodges and Elder<sup>21</sup> and Herne<sup>22</sup>). A collection of conformal mapping functions have been made by Kober<sup>43</sup> and Breckenback.<sup>44</sup>

Numerical Solutions. Many highly sophisticated numerical methods for the solution of partial differential equations may be found in the literature.<sup>45, 46</sup> However, some relatively simple approximation methods are also available. Consider a subdivided region having an electric field as a function of the potential; if the divisions are fine enough, a linear approximation of the derivatives may be used, as follows. (See Fig. 30.)

$$\left. \frac{\delta V_a}{\delta x} \right|_a = \frac{V_i - V_o}{\delta} \quad \& \quad \left. \frac{\delta V_b}{\delta x} \right|_b = \frac{V_o - V_2}{\delta} \quad (90)$$

In the center at point 0, the second derivatives are evaluated and the substitution is made in the LaPlace equation.

$$\frac{\delta^2 V_o}{\delta x^2} + \frac{\delta^2 V_o}{\delta y^2} = 0$$

$$\frac{\delta^2 V_o}{\delta x^2} = \left( \frac{\delta V_a}{\delta x} - \frac{\delta V_b}{\delta x} \right) \frac{1}{\delta} = \frac{1}{\delta^2} (V_1 + V_2 - 2V_o) \quad (91)$$

A similar result is found for  $\delta^2 V_o / \delta y^2$  and LaPlace's equation is found to be equivalent to  $V_o = 1/4 (V_1 + V_2 + V_3 + V_4)$ .

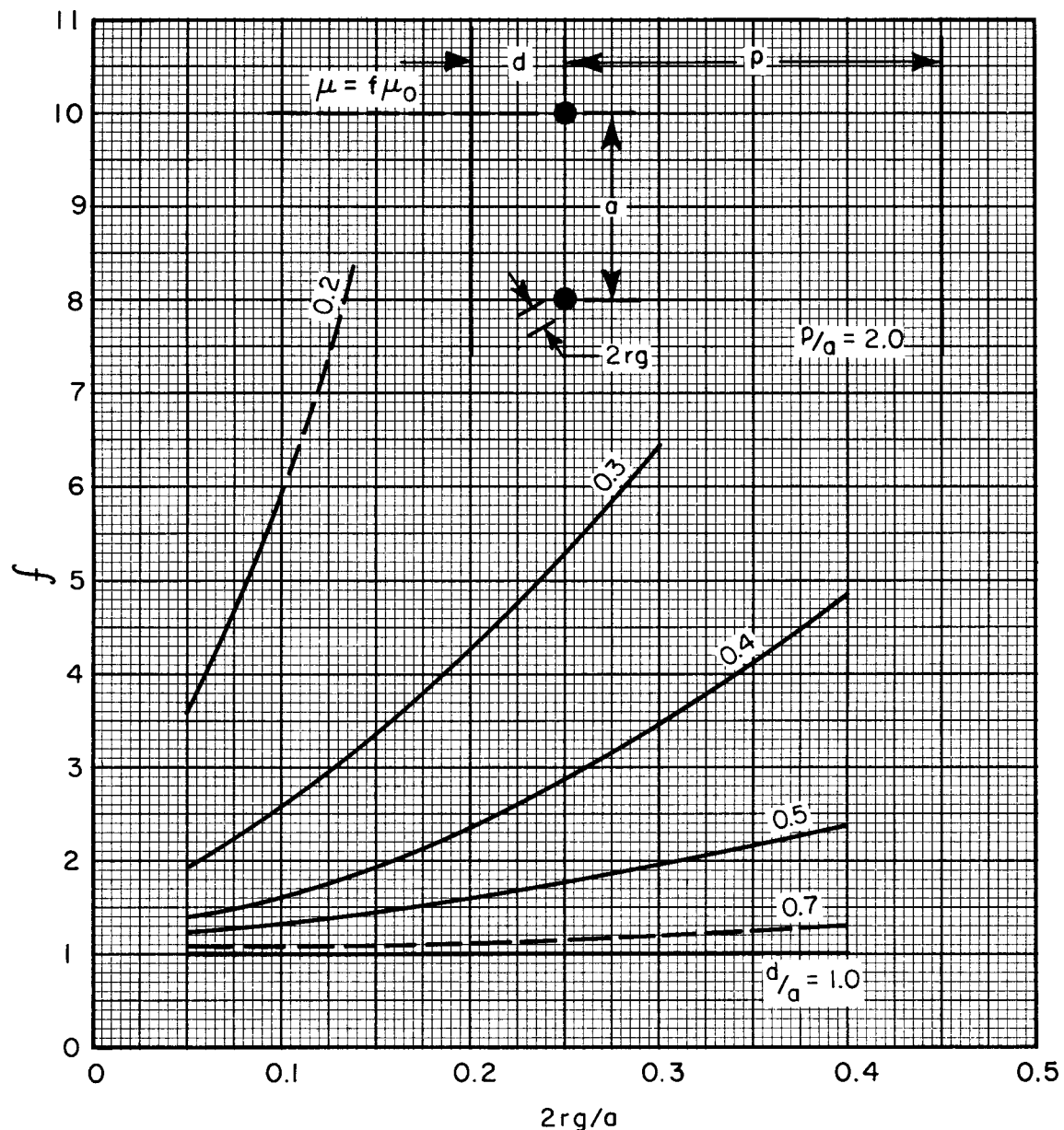
For small subdivisions, the center potential is just the average of the four surrounding potentials. This relationship is the basis of the relaxation net or point net methods in which the region around a set of electrodes is subdivided and potentials are assigned arbitrarily to the intersections. The assigning of the potentials makes full use of known boundaries and symmetry planes.

The assigned potentials are used to calculate a new set of potentials which, in turn, is used to recalculate the initial values. The process is repeated until the values show a minimum change with each new determination. The solution of the problem is facilitated if values that show excessive change are adjusted before recalculating. Southwell has formalized a somewhat modified procedure.<sup>47, 48</sup> (See Fig. 31.)

#### Analog Plotting Methods<sup>49</sup>

There are three well-known analogs: (1) the resistance paper or electrolytic tank,<sup>50, 51</sup> (2) the rubber sheet,<sup>52, 56</sup> and (3) the resistor net.<sup>53, 54, 55</sup> In each of these systems, two quantities may be found that are related, in the first order, by the LaPlace equation. These quantities are generally easier to measure than

\*Equipotential and flux lines retain their relationship.

Figure 25. Increase of  $\mu$  Directly behind a Grid Wire

electrostatic flux and/or potential. The rubber sheet analog has been little used in recent years and is not discussed here.

The Resistance-Paper or Electrolytic-Tank Method. In these analogs, flux is equated to current and potential difference is equated to voltage difference. A model of the device to be mapped is made on either special conducting paper or in an electrolytic tank (the paper and the tank may be considered the same except that the tank is sometimes more versatile). Maximum use must be made of the boundaries and symmetry to simplify the model. The problem is considered in only two dimensions. The actual device is reduced to two dimensions either by assumption or by using sections and making a series of plots. The basic concepts of field plotting are shown in Figs. 32 thru 38.<sup>57</sup>

The following conditions must be considered when making a field plot:

- (1) Lines of symmetry are flux lines in an actual field.
- (2) Current flow must follow the edges of the paper, therefore, the edge of the paper is a flux line. (The paper may be cut to a special shape.)
- (3) If the edges of the paper are not used as a boundary, the plot must be kept away from the edges to limit the perturbation of the field.
- (4) Periodic structures may be represented by a single section by using the edges of the paper as a "reflecting" boundary.<sup>20, 51</sup>
- (5) Sections of a tube in which the grid wires represent circles present no special problems, but sec-

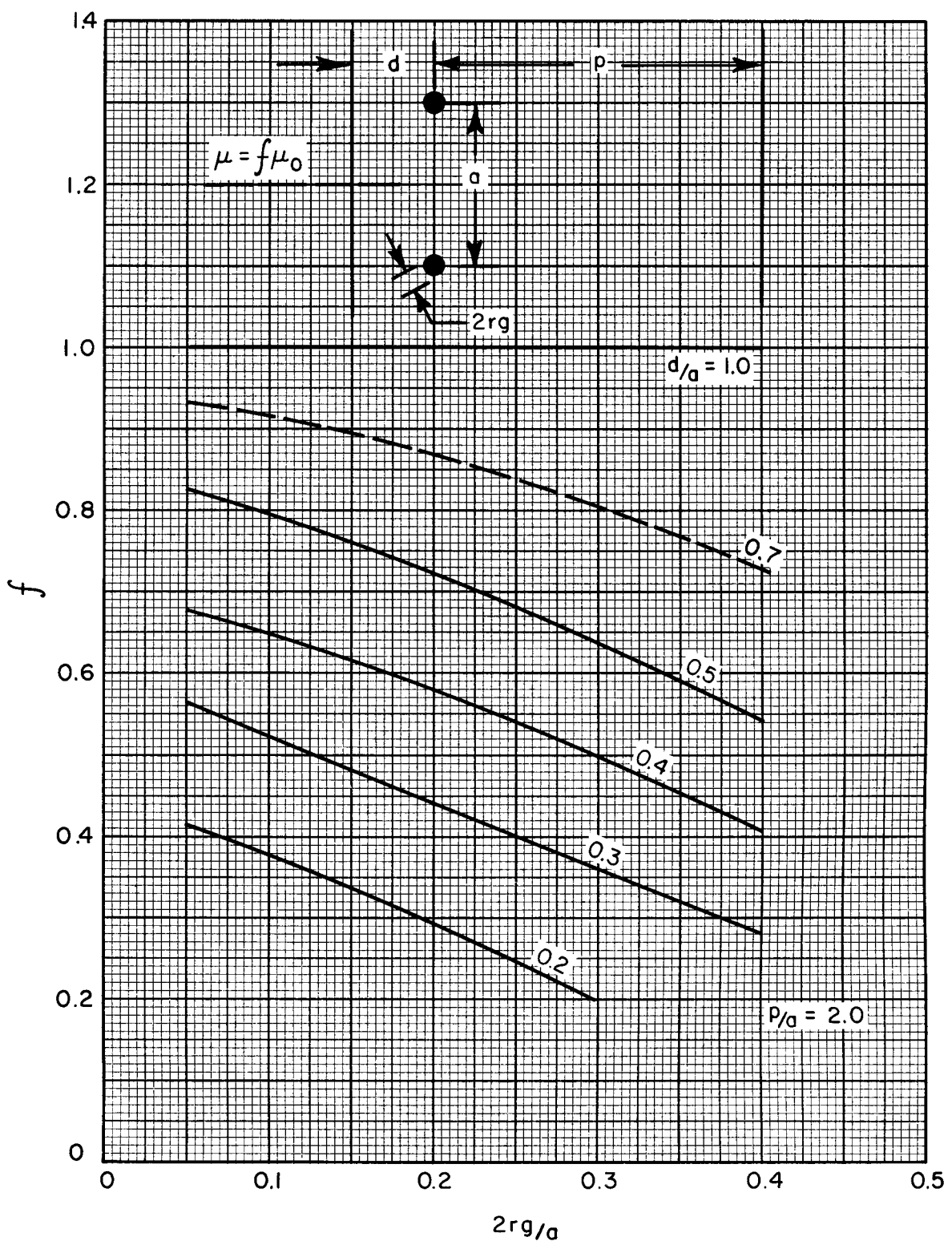


Figure 26. Decrease of  $\mu$  at the Center of the Aperture

tions in the other direction may be difficult to represent, for you must either go through a grid wire or between the wires. Either choice is essentially wrong. It is sometimes better to establish an equivalent potential in that plane by means of a fine-wire low-pitch grid of equivalent  $\mu$ , as shown in Fig. 39.

- (6) Space charge is normally neglected.
- (7) Before making a plot, decide exactly what it is you will learn from the plot.
- (8) The accuracy of the plot is affected by the variations of the paper, the accuracy of the model, and the degree to which measurements can be made without

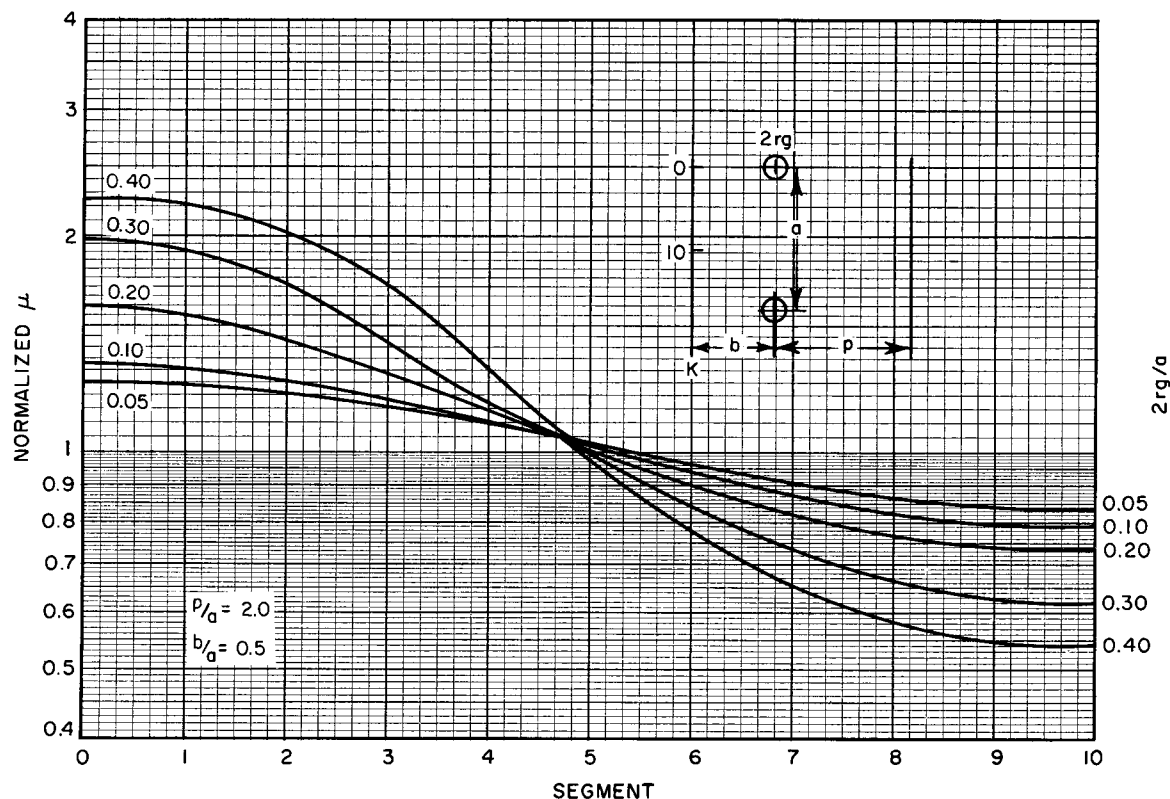


Figure 27. *Mu* Variation along Cathode  $2r/a$  as a Parameter (Scholz, et al data)

disturbing the current. The electrolytic tank probably has a greater accuracy.<sup>58</sup>

(9) By tilting the electrolytic tank, one may represent a wedge of a cylinder or various squares or polygons.<sup>20, 51</sup>

(10) Methods are available for simulating space charge by injecting current into the tank or resistor wedge.<sup>59</sup> This technique does not apply to the paper method.

(11) Theoretically, the scale has no effect on the solution, but, in general, the larger the scale the greater the relative precision possible in the model.

(12) It is possible to make three-dimensional models in the tank and, by probing at various depths with an insulated fine probe, to make a three-dimensional plot.

**The Resistor Net.** The resistor-net method is essentially a lumped parameter or discrete approximation of the paper or tank, representing either rectangular or cylindrical geometry. Space charge may be represented by successive approximations. The data is available in digital form and lends itself to automatic plotting of trajectories.<sup>60, 65</sup> This method is especially well-suited to cylindrical beam problems.

#### Field Sketching

This method, although it gives only approximate results, requires a firm understanding of the basic relations of electrostatics. A sketch is made of the probable field configuration based on simple structures and the basic relations, as shown in Fig. 40. A curvilinear

square is formed by the intersection of four curved lines; the intersections are perpendicular and the figure tends to become a square as it is subdivided. Sketching flux and potential lines and forming curvilinear squares results in an acceptable plot from which trajectories, gradients, and capacitances can be estimated. Capacitance may be estimated as shown in Fig. 40. The capacity  $C$  is, by definition, equal to  $\phi/V$ , where  $\phi$  is the total flux and  $V$  is the potential difference. For a square of width  $d$ , the gradient  $E$  is  $V/d$  and the flux density  $D$  is  $\epsilon E$ . Multiplication by the area provides the following relationship for a one-meter length:

$$\phi = \epsilon E d = \frac{\epsilon V}{d} d \quad (93)$$

and, therefore,

$$C = \epsilon \text{ farads/meter} \quad (93a)$$

Because the voltage across a square and the flux through it is the same for all squares, we find the total capacitance to be

$$C = \frac{P}{Q} \epsilon \text{ farads/meter} \quad (94)$$

where  $P$  is the number of squares around one of the electrodes and  $Q$  is the number between them. In the example of Fig. 40,  $P = 18$ ,  $Q = 4$ ,  $\epsilon = 1/36\pi \times 10^{-9}$ , and  $C = 29.8$  picofarads/meter.

#### Electrode Fitting

Generally, the electrode configuration is given and

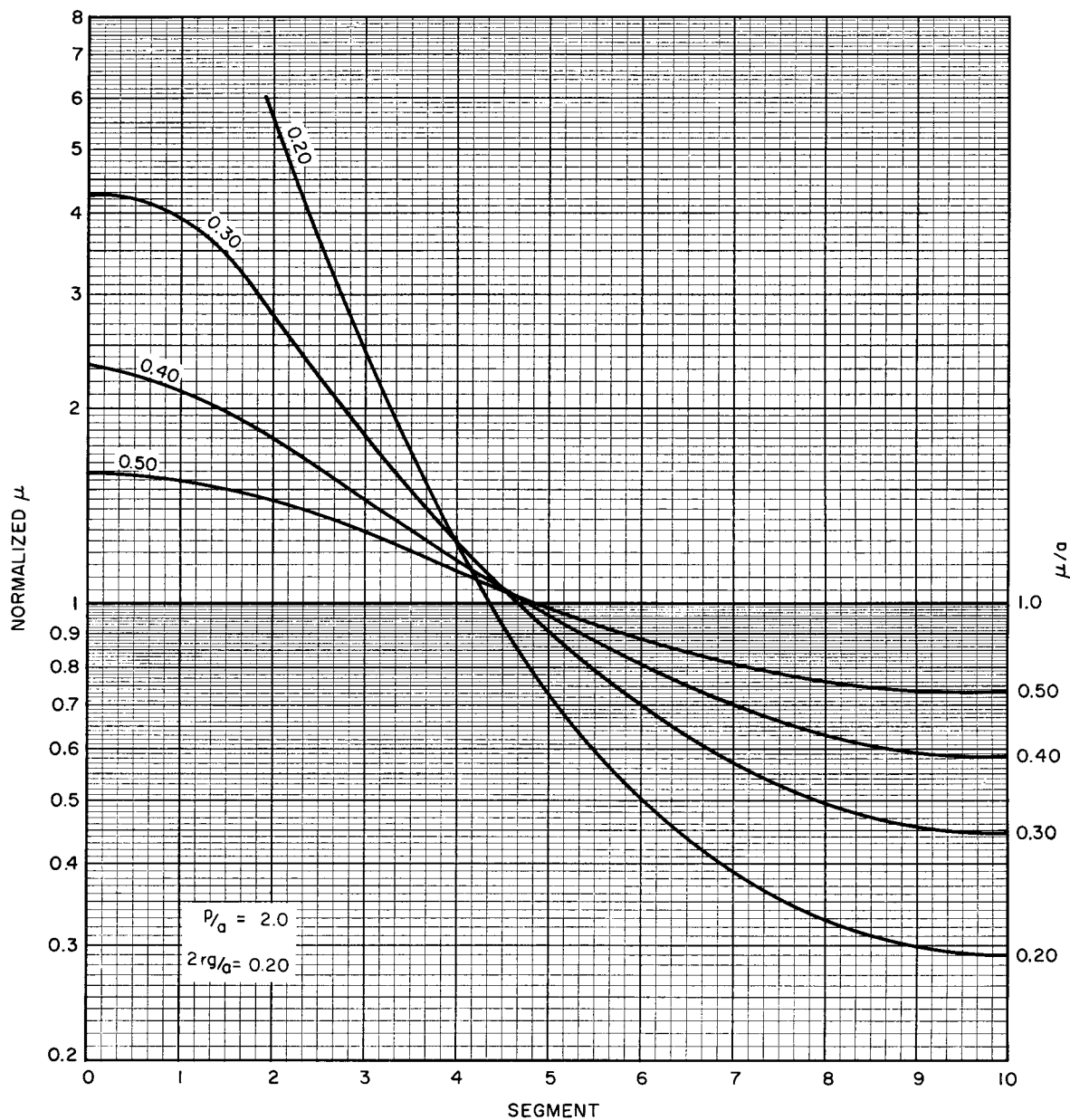


Figure 28. *Mu* Variation along Cathode  $b/a$  as a Parameter (Scholz, et al data)

the field distribution must be determined. In electron beam devices, the beam boundaries are usually specified, the field required to hold the beam within these boundaries is calculated, and then a set of electrodes and potentials are designed which provide the required field. The field requirements are generally in the form of required potentials along the edge of the beam. The determination of these potentials is exceedingly difficult. Although there is only one field configuration for each set of electrodes, and only one field configuration that will give the proper beam, many sets of electrodes will give approximately the proper field along the beam edge. Therefore, the set of electrodes is most easily found empirically (e.g., by an analog plot). This method simulates the edge of the required beam by shaping the paper or providing a dielectric boundary in the tank. A set of electrodes is tried and then the shape

or relative potentials are adjusted until a fit is reached. This technique can be made almost automatic by switching back and forth between the field map and a reference voltage and adjusting the electrodes for minimum error.<sup>61, 62</sup>

#### TRAJECTORY TRACING

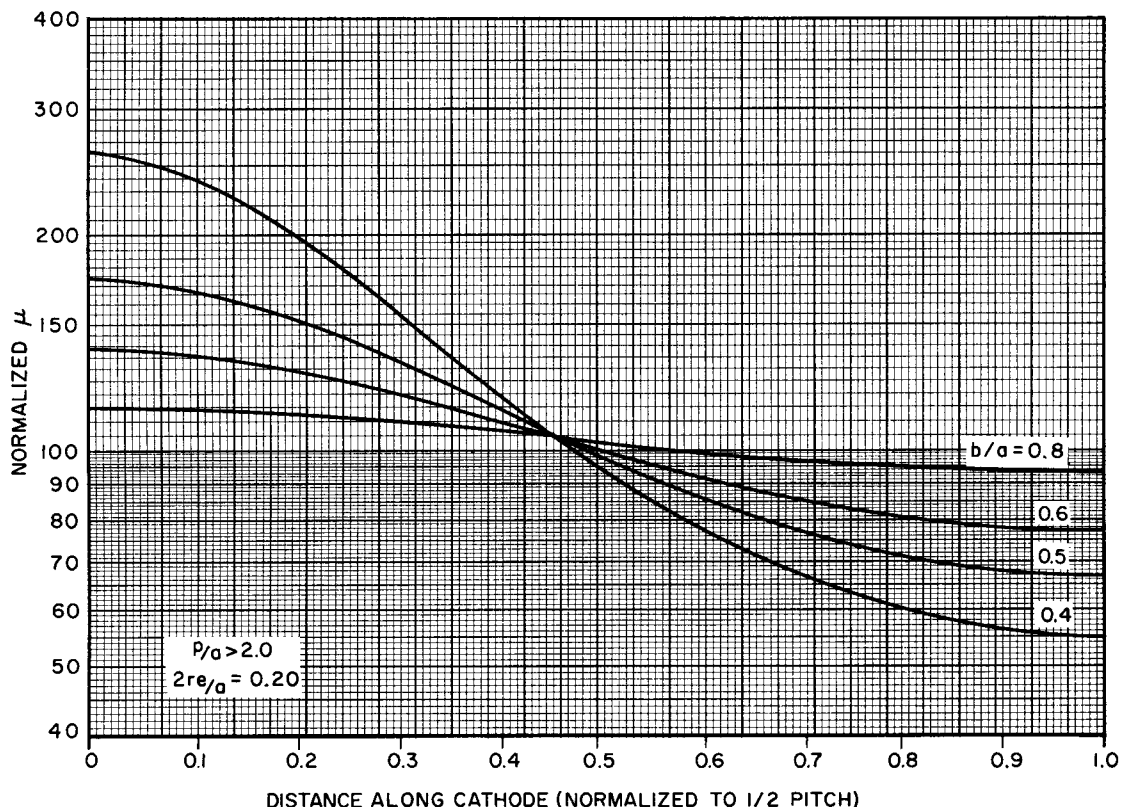
##### General Equations of Motion<sup>64</sup>

In an electrostatic field, the force on an electron is represented as follows:

$$\mathbf{F} = -e\mathbf{E} = e \nabla V \quad (95)$$

and the general equation of motion is

$$\mathbf{MS} = \nabla V \quad (96)$$

Figure 29. *Mu Variation along Cathode (Harris-Kirk data)*

In rectangular coordinates:

$$m\ddot{x} = e \frac{\delta V}{\delta x} \quad (97a)$$

$$m\ddot{y} = e \frac{\delta V}{\delta y} \quad (97b)$$

$$m\ddot{z} = e \frac{\delta V}{\delta z} \quad (97c)$$

$$m = \frac{M_0}{\sqrt{1 - V^2/C^2}} \quad (98)$$

If the velocity is less than  $0.1C$  ( $3 \times 10^7$  meters per second), the correction may be neglected. Because the electrostatic field is conservative, the following expression may be applied:

$$\frac{1}{2}mu^2 = eV \quad (99)$$

For an electron that starts at rest from a source at zero potential,

$$u = \sqrt{\frac{2e}{m}} V^{1/2} \quad (100)$$

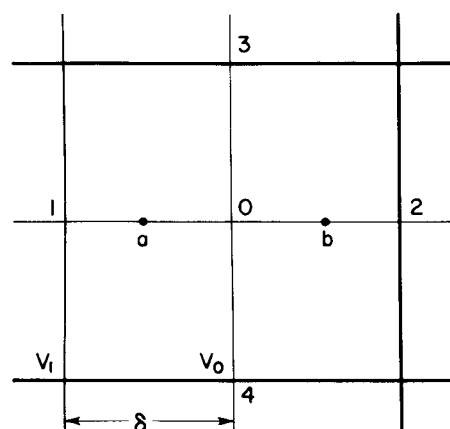
or  $u = 5.95 \times 10^5 V^{1/2}$  meters per second,  $u = 6 \times 10^7$  meters per second corresponds to a potential difference of approximately 10 kilovolts and is important only for kinescopes or special high-voltage types.

#### General Projectry in Two Dimensions

By eliminating time in the force equations it is possible to obtain the general trajectory equation.

$$2 \frac{d^2y}{dx^2} = \left[ Ex \frac{dy}{dx} - Ey \right] \left[ 1 + \left( \frac{dy}{dx} \right)^2 \right] \quad (101)$$

This equation is not suitable for direct solution, but may be numerically integrated, especially if the potential is available as point-by-point numerical data.

Figure 30. *Subregion for Net-Point Analysis*

These nonrelativistic equations apply as long as the mass of the electron is constant. The motional mass of an electron is related to the rest mass by the following transformation:

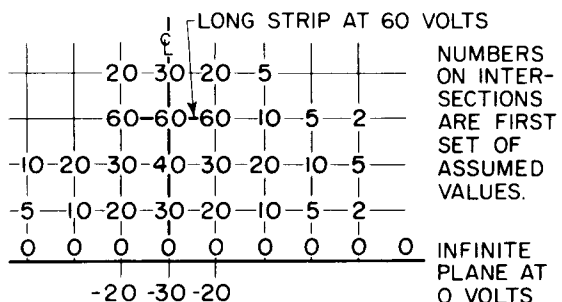


Figure 31. Sample Problem Point-Net Method

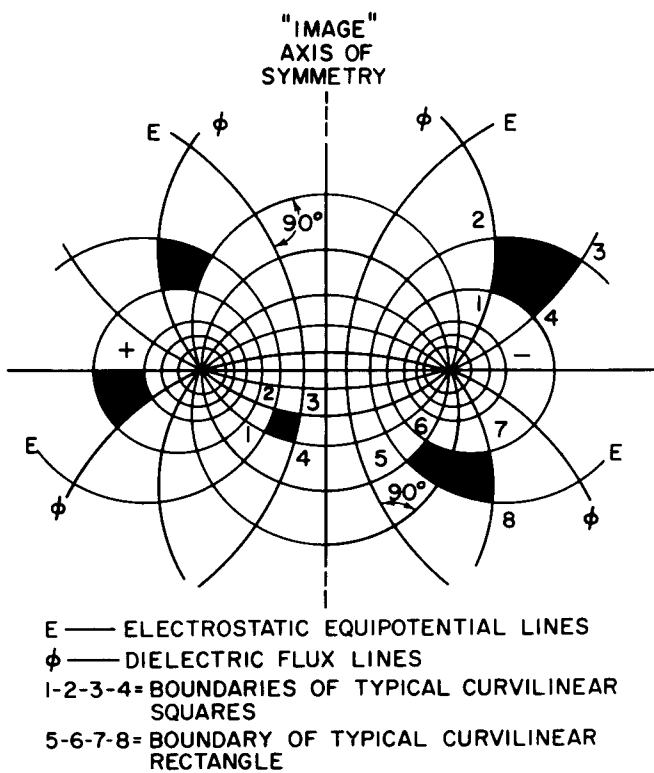


Figure 32. Basic Orthogonal Field Concept

Solutions for specific electrode configurations are not generally available, but the following general conclusions drawn from the above result are given by Harman:<sup>63</sup>

- (1) The path does not depend on the mass or charge and is the same for all particles.
- (2) The velocity at which the particle moves depends on the charge-to-mass ratio.

(3) The path does not depend on the magnitude of the field (potential), but only on the configuration (gradient), and if the potential is everywhere multiplied by a factor  $K$  the path will be unchanged, but the time required to transverse the path is reduced by a factor  $1/K$ .

(4) The path is unchanged if all the dimensions are scaled by a constant factor.

(5) The trajectory is not a function of the direction of travel.

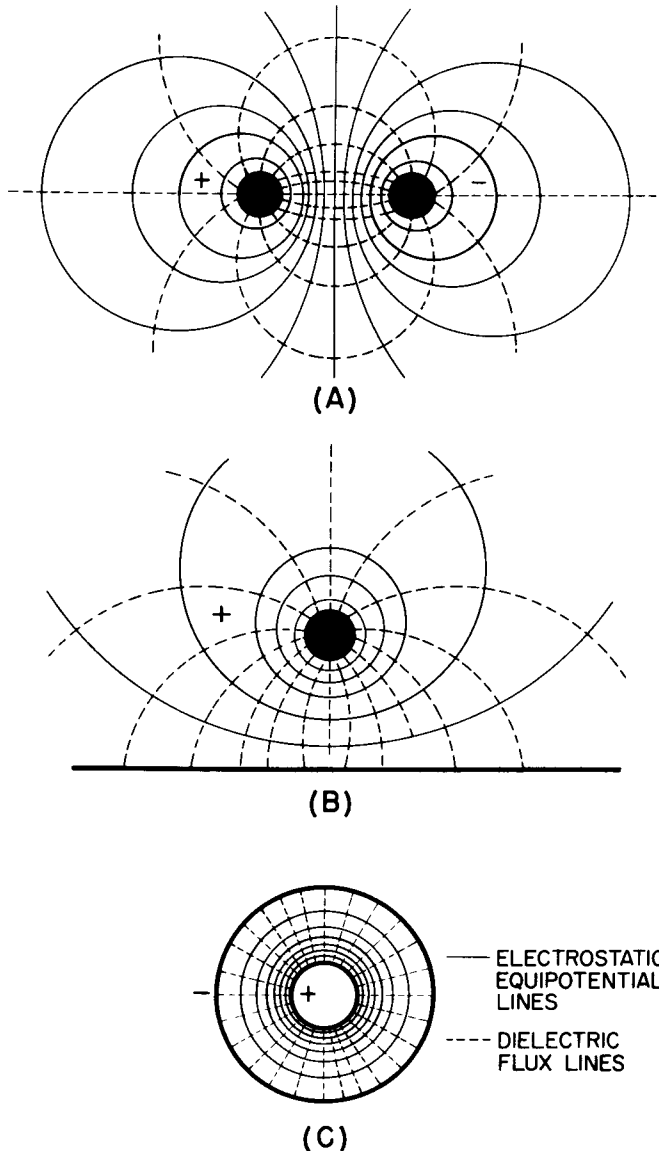


Figure 33. Fundamental Field Patterns: (A) Electrostatic field pattern between two oppositely charged parallel cylinders; (B) Electrostatic field pattern between oppositely charged plane and cylinder; (C) Electrostatic field pattern between oppositely charged concentric cylinders

#### Electron Motion in a Uniform Electric Field

In this simple case, the field is in only one direction  $y$ , the motion is described by the following equation:

$$M \frac{d^2 y}{dt^2} = eE_y$$

For the general case of an electron injected with a velocity  $U_0$  at an angle of  $\sigma$  with the field (see Fig. 41), the following expression is obtained for  $y$  (a parabola):

$$y = x \tan \sigma - x^2 \frac{E_y}{4V_0 \cos^2 \sigma} \quad (103)$$

At a time expressed as

$$t_1 = \sqrt{\frac{2mV_0}{e}} \frac{\sin \sigma}{E_y} \quad (104)$$

the electron reaches its maximum penetration into the field.

$$y_m = \frac{V_0}{E_y} \sin^2 \sigma \quad (105)$$

and at a time  $2t_1$  the electron has returned to the initial potential and crosses the  $x$  axis at the value

$$x_m = \frac{4V_0}{E_y} \sin \sigma \cos \sigma \quad (106)$$

By dividing the field into small sections, each essentially uniform, parabolic path segment may be calculated and the trajectory constructed. This is the basis for O. H. Schade's method with preplotted parabolas, explained below. Two methods of plotting trajectories are discussed below.

### Snell's Law

Segmented Straight-Line Trajectories. Many of the laws of ordinary geometrical optics have analogies in electron optics.

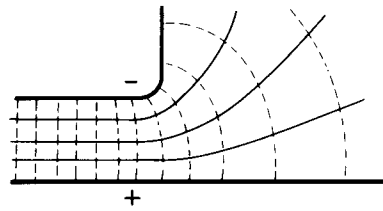
$$\frac{\sin \alpha}{\sin \beta} = \frac{\eta_2}{\eta_1} \quad (107)$$

The familiar Snell's law for a light wave traversing the boundary between two media can be extended to electronics for an electron traversing the boundary between two uniform electrostatic fields.

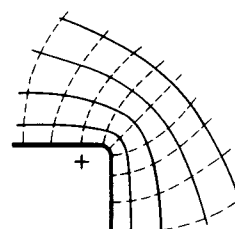
$$\frac{\sin \alpha}{\sin \beta} = \frac{u_2}{u_1} = \sqrt{\frac{V_2}{V_1}} \quad (108)$$

Where  $\alpha$  and  $\beta$  are the entrant and emergent angles, and  $\eta_1$  and  $\eta_2$  are the indices of refraction; the other symbols have the standard meaning. The application of this law is straightforward and simple.

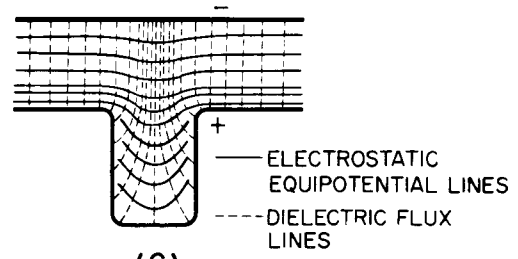
Mechanics of Trajectory Tracing. The equipotential lines must be plotted at an interval small enough to allow the assumption of uniform fields between the equipotential lines. The trajectory is constructed of straight line segments as follows (see Fig. 42).



(A)



(B)



(C)

Figure 34. Typical Field Patterns: (A) Electrostatic field between oppositely charged corner and plane; (B) Electrostatic field at a charged corner (all other charges assumed at "infinite" distance away); (C) Electrostatic field between oppositely charged slot and plane

- (1) Draw the average potential line for region I.\*
- (2) Construct a normal to this line.
- (3) Measure the angle between the path and the normal (the entrant angle).
- (4) Calculate the average potentials for the two regions.
- (5) Compute the new angle ( $\beta$ ).
- (6) Draw the segment of the trajectory for region II.
- (7) Repeat for the other sections.

Segmented Parabolic Trajectories. A series of universal parabolas (Fig. 43), constructed by O. H. Schade, Sr., provide a method of constructing electron trajectories which is relatively easy to apply. This method is most generally used and probably gives the best results. Construction of the parabolas depends on the fact that the volt velocity of an electron is given by the potential value of its position,\*\* regardless of the electron direction.

\*An average potential line determines the average angle for a region. The average line is constructed, by eye, to fit midway between the known potential lines.

\*\*Neglecting the velocity of emission and transit-time effects.

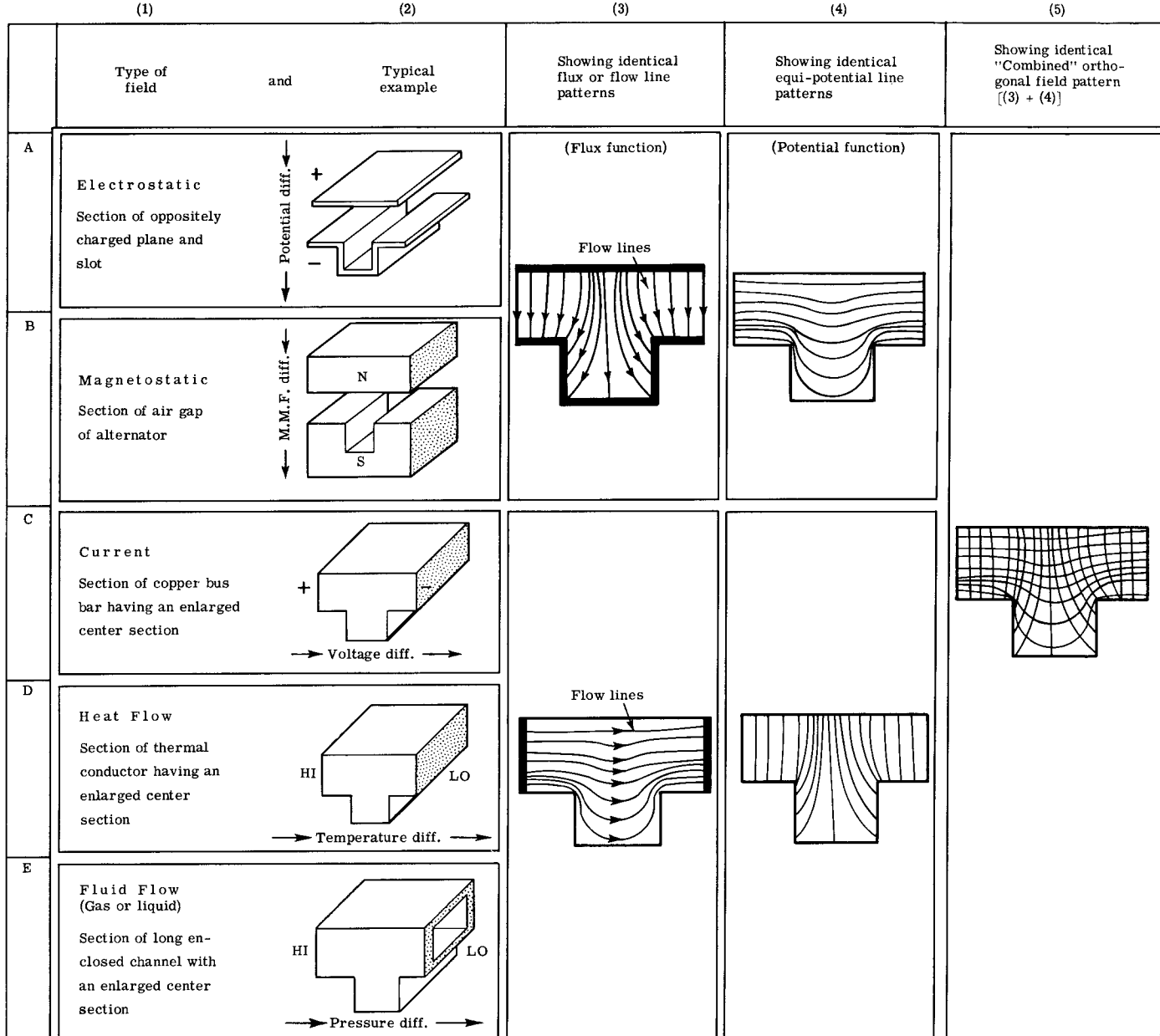


Figure 35. Analogies between Various Types of Fields

Construction is simplified by making the initial volt velocity of the electron  $V_0$ , when it leaves the potential line  $V_0$ , the unit in which the potential is measured (i.e.,  $V_0 = x_0$ ). If the electron leaves at an angle of 90 degrees with respect to the direction of the potential gradient, the electron path is given by the equation

$$y = 2 \sqrt{x}$$

with  $x$  having the direction of the gradient in a right-angle coordinate system. (See Fig. 43 insert.) Both  $x$  and  $y$  are measured in units equal to  $V_0$  (for the insert,  $V_0$  is five divisions). The value of  $y_0$  was made equal to  $2V_0$  to simplify drawing. Assigning the unit  $V_0$  various values results in the family of electron paths shown in Fig. 43.

Due to the fact that the electron volt velocity is equal to the value of the intersected potential line, the intersection of any electron path with a given potential line may be considered as the starting point of an electron with the velocity leaving at the angle shown. This type of plot results in a general family of curves showing the accurate path in a limen field for all electrons of all velocities leaving at all angles within the scale limits of the drawing.

The angle of incidence or slope of any curve is

$$\tan \alpha = \frac{dy}{dx} = \frac{1}{\sqrt{x}}$$

Thus, as the dimensions  $x_0$ ,  $y_0$ ,  $x$ , and  $y$  have the

same ratios for all points of equal slope due to the method of drawing, all points of equal slope are intersected by a straight line drawn through  $x_0 = y_0 = 0$ . Fig. 43 shows that any one of these lines is divided into equal sections by electron trajectories having equal increments of  $V$ , thus permitting correct interpolation of trajectories. The dotted line is a curved scale of points through which the slope indicating lines are to be drawn for the zero point. The 45-degree line is drawn as an example.

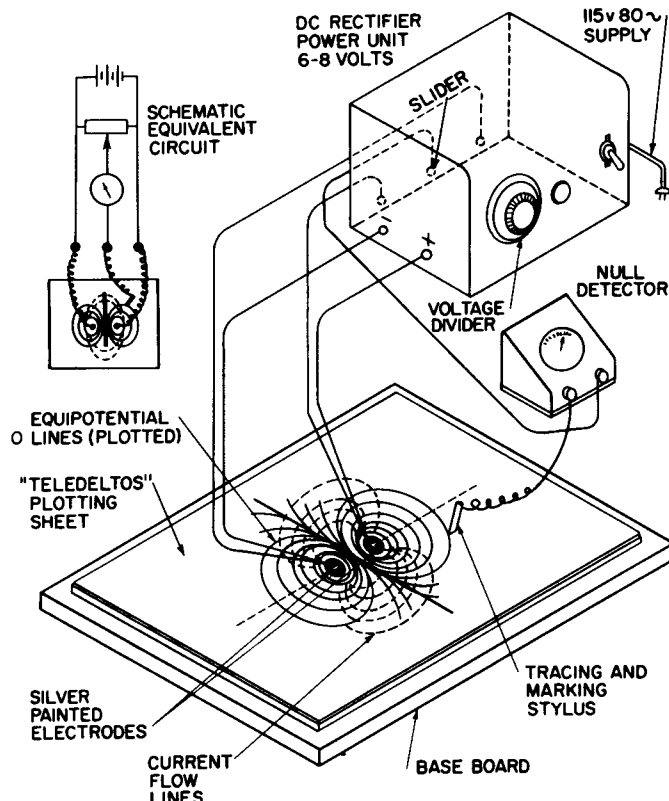


Figure 36. Components and Schematic Circuit of Analog Field Plotter

The use of the curves for tracing electron paths in field plots is illustrated in Fig. 44A. The path of an electron entering a linear field section at 30 volts with the angle shown is to be traced to the 80-volt potential line. The first step is to determine the location of the 0 potential line of this field. It is located at the distance  $d_1 = (E_L/E_H - E_L)d_2$  if the linear field section is continued with the same gradient. The sketch is then placed over the family of curves of Fig. 43 with the 30-volt line at the distance  $d_1$  from 0 and then shifted parallel to the potential lines until the angle of incidence of the electron matches one of the curves. The curve, which is then traced, represents the correct electron path.

If the equipotential lines are not straight and parallel (Fig. 44B) the parabolas may still be used; however, the field lines should first be adjusted. In many cases it is not advisable to subdivide the actual potential field into very short sections. For the case shown, the error of electron position is quite small if the average values of potential line direction and gradient between the

limits A and B are used. Too fine a subdivision can cause cumulative matching errors unless it is done on a large scale and with great precision. Then again, if small differences of electron angles cause large computational deviations, the physical structure is very likely just as much affected by mechanical inaccuracies and requires high precision in manufacture to obtain optimum results.

## Discussion

Trajectory tracing is a simple and mechanical, though tedious, procedure which can be handled most satisfactorily by digital computers if the volume of work warrants their use. Generally, in receiving-tube design, trajectories are a secondary consideration and are usually computed by hand. Special purpose analog computers have been built to plot trajectories directly in an electrolytic tank. The technique of rolling steel balls on a rubber sheet may also be used.<sup>64, 65</sup>

In any focused-beam device, the space-charge density may be quite large and greatly affect the trajectories. The solution is compensated, in these cases, by an integration procedure.

- Plot the field.
- Trace the beam.
- Recalculate the field from the knowledge of the approximate beam shape.
- Trace the new beam shape density, etc.
- Repeat as often as necessary to obtain the desired accuracy.

There is extensive literature on electron optics, beam devices, etc. This has originated in the fields where it is of primary concern and should be consulted.

## Nomographs for the Rapid Modification of Electron-Tube Characteristics

In the design and production of electron tubes, it is often necessary to modify internal tube dimensions to bring about desired changes in electrical characteristics. Three nomographs have been developed which make it possible to determine quickly the physical tube dimensions required to provide certain electrical characteristics, provided the dimensions and electrical characteristics of a tube of the same general class are already known. For instance, the tube design engineer can determine the internal spacings for a new amplifier tube which is to have higher transconductance than an existing type provided the dimensions and electrical characteristics of the existing type are known. In a similar manner, those engaged in electron-tube production could rapidly calculate the construction changes necessary to center various "off bogey" characteristics.

## Theoretical Basis for Nomographs

It is assumed that the current in a diode is given by the simple Child-Langmuir law.

\*The nomographs and the essential details of this section were supplied by Mr. R. D. Reichert of RCA Laboratories. See Ref. 66

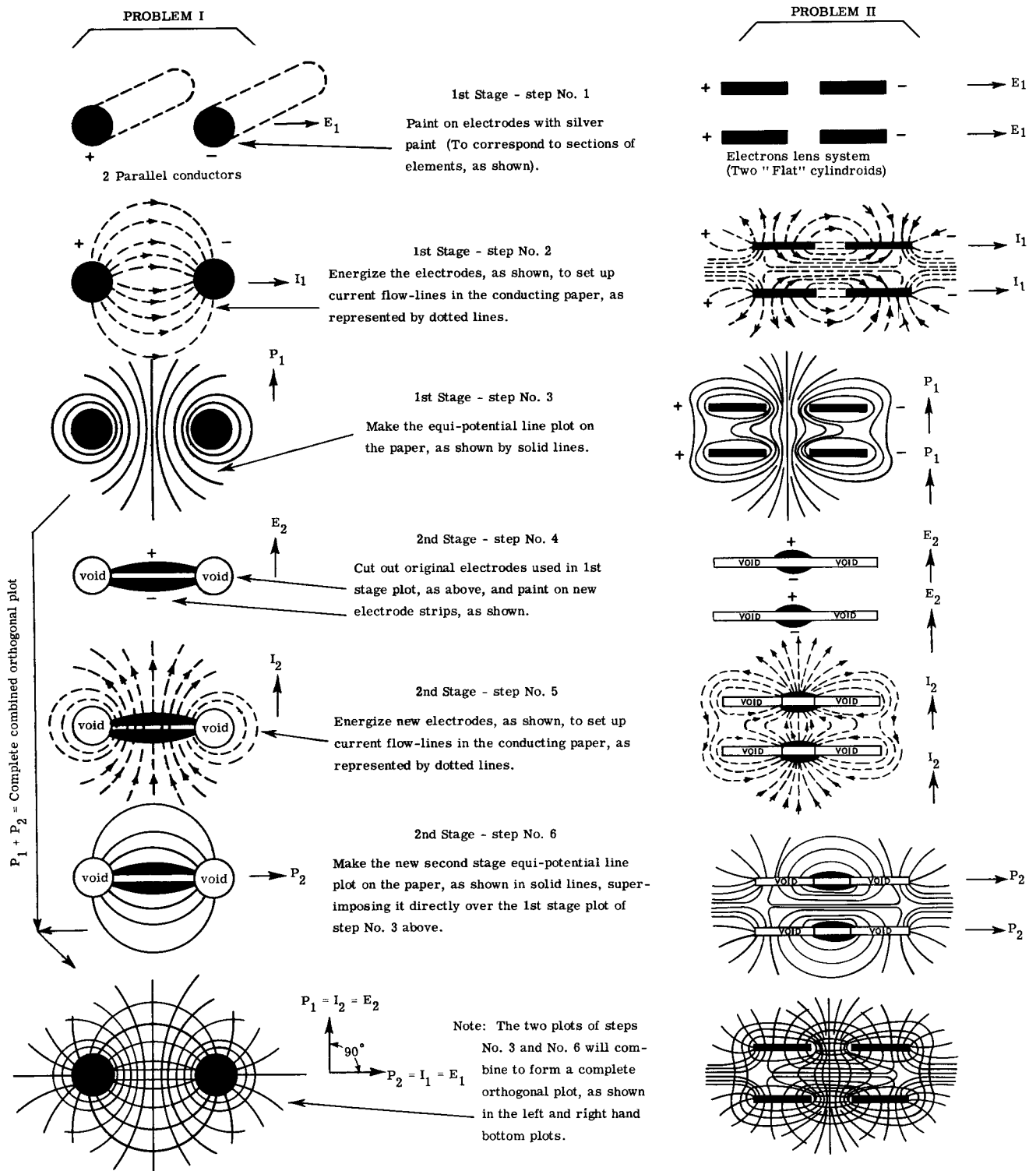


Figure 37. Illustrations of "Two-Stage" Plotting Method

$$I = \frac{KA}{d^2} E_a^{3/2} \quad (109)$$

This equation is extended to triodes by using a simple equivalent diode, as follows:

$$I = \frac{KA}{b^2} (E_a/\mu + E_c)^{3/2} \quad (110)$$

and the gm is assumed to be given by the following expression:

$$gm = \frac{3}{2} \frac{KA}{b^2} (E_a/\mu + E_c)^{1/2} \quad (111)$$

Empirical data has shown that the mu of a helical grid is given by the following law:

$$\mu = CN^2 rs \quad (112)$$

where  $C$  is a constant and  $N$  is the number of turns per inch of the lateral wire. For pentodes and tetrodes, if it is assumed that the anode voltage has a negligible effect, Eq. (110) may be rewritten using  $E_s$  and  $\mu_{12}$ .

$$I_K = \frac{KA}{b^2} \left( \frac{E_s}{\mu_{12}} + E_c \right)^{3/2} \quad (113)$$

The term  $\mu_{12}$  is often known as the triode mu  $T_\mu$ . Because only a portion of the cathode current reaches the anode and, in the normal operating range, the ratio is constant, the current may be expressed as:

$$I_a = \frac{K'A}{b^2} \left( \frac{E_s}{T_\mu} + E_c \right)^{3/2} \quad (114)$$

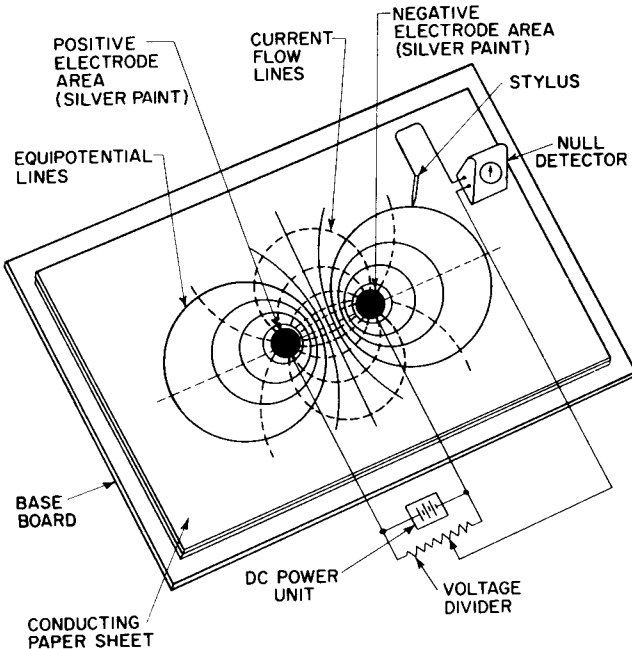


Figure 38. Typical Electrostatic Field Plot Showing Circuits, Electrodes, and Plotted Lines

The previous equations do not take into account any of the phenomena attributable to close-spaced front ends (i.e., inselbildung effects). If Eq. (111) is divided by Eq. (110), the following results:

$$\frac{gm}{I} = \frac{3}{2} \frac{1}{E_a / \mu + E_c} \quad (115)$$

This expression is not exactly true for real tubes, and the ratio varies if the ratio  $a/b$  is not held constant. Therefore, a factor is introduced which is dependent on  $a/b$  and the ratio  $gm/I$  is rewritten as follows:

$$\frac{gm}{I} = \frac{3}{2} F \frac{1}{E_a / \mu + E_c} \quad (116)$$

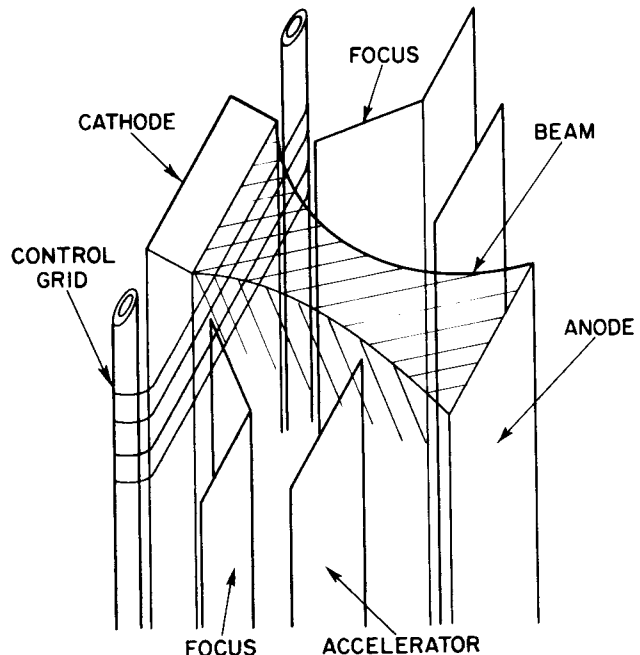


Figure 39. Method of Representing Grid for Field Plot

### Applications and Limitations of the Nomographs

The nomographs (Fig. 45) described in this paper are used to determine the changes in tube dimensions that are required to modify the characteristics  $\mu$ ,  $gm$ , and  $I_a$ . The starting point in the use of the nomographs is always the notation of data from an existing comparable type (referred to as the original tube) on the appropriate axis of the nomograph. This operation determines various tube factors and constants. The next step is the notation of the desired electrical characteristics while the factors determined by the original tube are kept constant. The intersection points on certain axes then indicate the dimensions of the desired tube. The nomographs cannot be used for changing the ratio of plate current to screen current of pentodes, modifying the suppression characteristics of pentodes, or for modifying interelectrode capacitances.

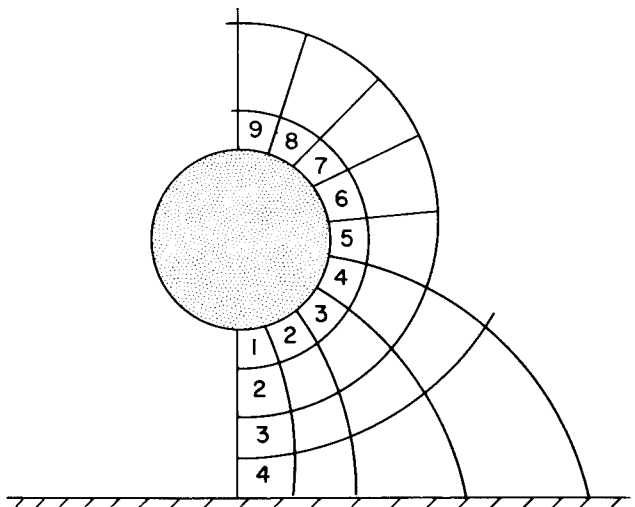


Figure 40. Field Sketching Using Curvilinear Squares

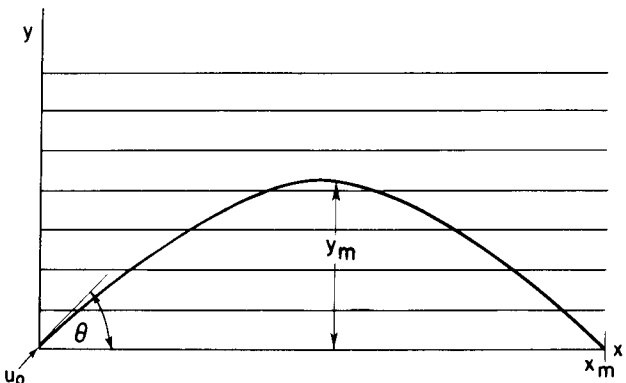
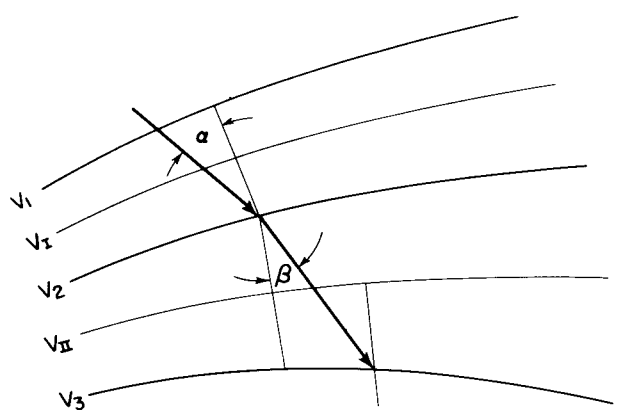


Figure 41. Electron Injection into a Uniform Field



$$V_I = \frac{V_1 + V_2}{2}$$

$$V_{II} = \frac{V_2 + V_3}{2}$$

$$\frac{\sin \alpha}{\sin \beta} = \sqrt{\frac{V_2 + V_3}{V_1 + V_2}}$$

Figure 42. Example of the Snell's Law Method of Trajectory Tracing

The use of the nomographs assumes that the factor  $F$  and the constants  $K$  and  $C$  remain constant (or vary so little that the variations may be neglected) over the range of the original tube and the desired tube.

Many of the modifications of tube characteristics may be accomplished in more than one way. For instance, diode plate current at a given plate voltage may be increased by either decreasing plate-cathode spacing or by increasing the cathode area. In all cases of multiple solutions, the nomographs provide either solution and, in addition, many solutions which represent various combinations of the two. The user of the nomographs must decide on the desired solution by considering other requirements such as interelectrode capacitances, available heater input power, and the ease with which either change can be made (an important factor when the tube being modified is in production).

The nomographs (and the equations upon which they are based) are valid only over a limited range. Although extreme solutions may be obtained which appear mathematically correct, it is impractical or impossible to construct a useful vacuum tube based on these extreme solutions. In general, if the grid-cathode spacing factor  $a/b$  and the screening factor  $2r/a$  of the desired tube are kept similar to the corresponding factors of the original tube, the solution obtained is valid.

In triodes and pentodes, the designer does not have complete freedom in the choice of  $I_a$ ,  $gm$ , and triode  $\mu$ . Eq. (115) shows that for a given set of applied voltages, two of the three above characteristics may be chosen but the third characteristic is then dependent. When solving triode and pentode problems, by using the nomographs, no attempt should be made to modify  $I_a$ ,  $gm$ , and triode  $\mu$  simultaneously. Instead, two of these characteristics should be modified and the problem solved with the nomographs to see where the third characteristic falls. If the third characteristic is a value which is other than that desired, the problem becomes one of an advanced nature and requires a significant modification of the grid-cathode spacing factor  $a/b$  which, in turn, will modify the  $F$  factor.

In the nomographs, straight lines are drawn intersecting three axes at a time. The axes marked "bend" indicate turning points. In the case of diode problems, it is only necessary to use axes  $V$  through  $XI$  of nomograph (B). It is not always possible to work across from left to right. For some problems, the user has to start at both ends independently; however, a continuous line bent at the "bend" axes should be the final result.

The basic steps for using the nomographs are as follows:

- (1) Enter into the nomographs the known characteristics and dimensions of a tube which is in the same general class as the desired tube.
- (2) Keep  $F$  and  $K$  constant (i.e., passing through the same intersection points on the  $F$  and  $K$  axes); enter the desired electrical characteristics of the new tube.
- (3) Read the dimensions of the new tube; obtain practical solutions when more than one solution is possible.

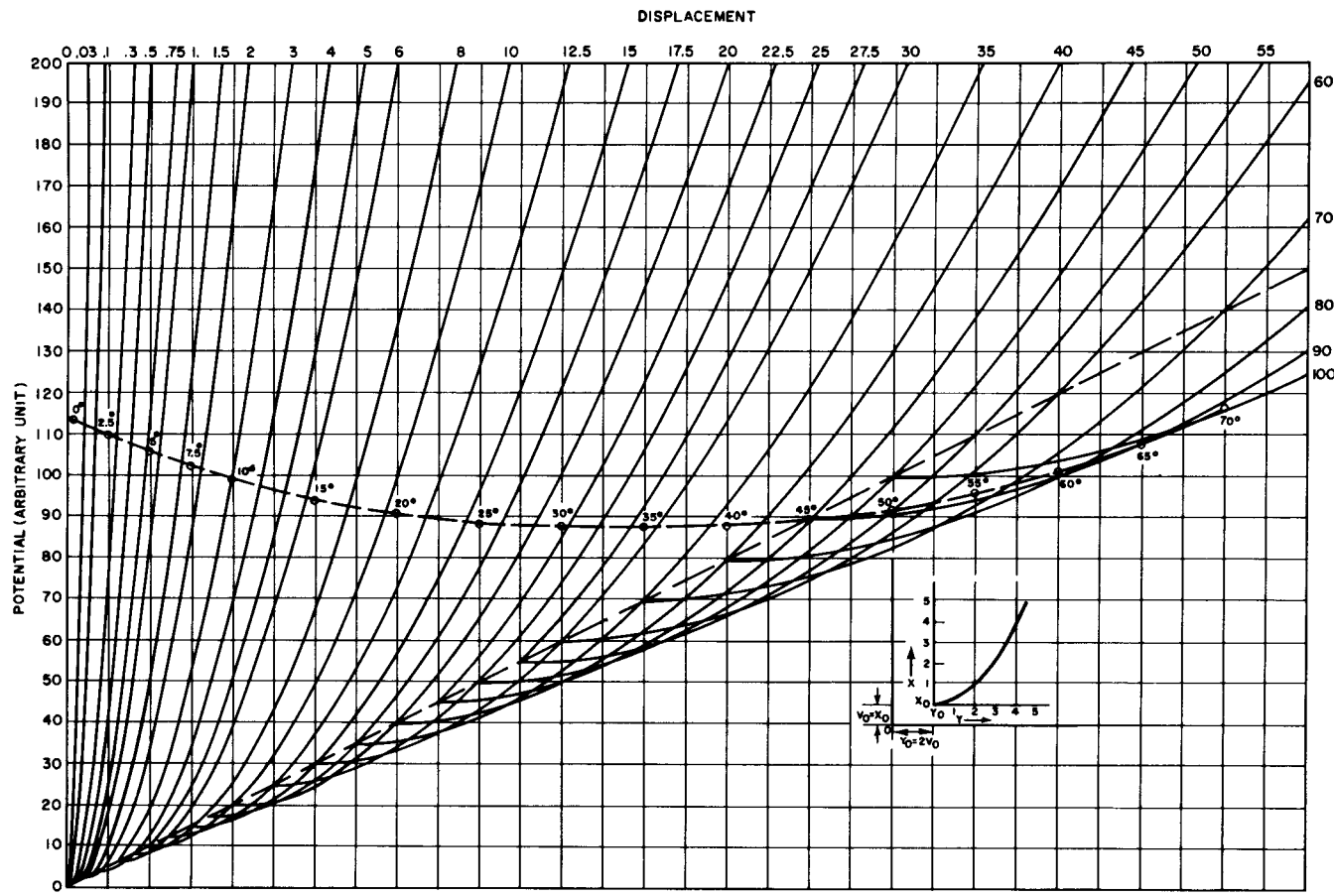


Figure 43. O. H. Schade's Parabolas

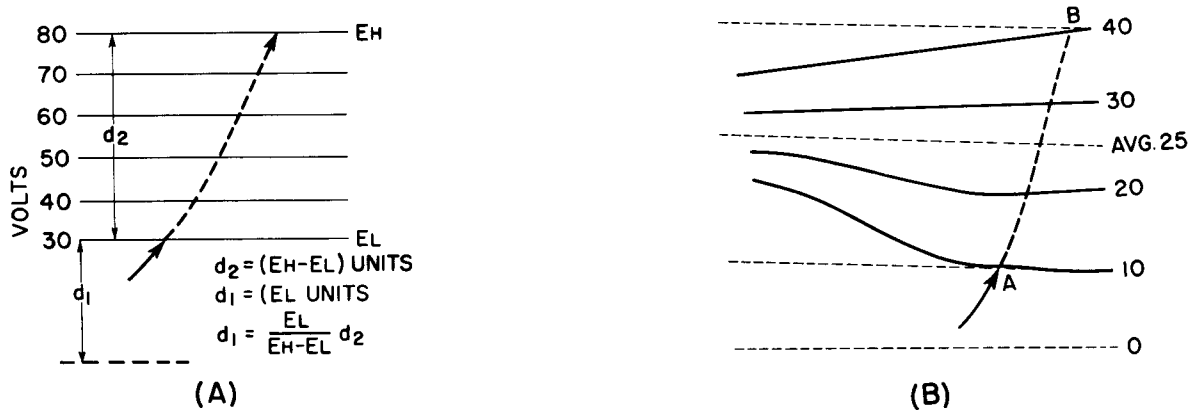


Figure 44. Example of the Piece-Wise Parabolic Method of Trajectory Tracing: (A) Plot of electron path in linear field; (B) Plot of electron path in nonlinear field

### Use of Multiplying Factors on Nomographs

Any of the scales on nomographs (B) and (C) may be multiplied by any factor provided the same factor is used throughout the entire problem. The multiplication of any axis, or combinations of axes, by any factors does not require the correction of other axes.

In the case of nomograph (A), however, it is not pos-

sible to apply multiplying factors to the various scales. If a particular problem involves values which are beyond the scales of nomograph (A), the value of  $(E_a/M) + E$  can be calculated arithmetically and inserted in nomograph (B).

### REFERENCES

1. Kellogg, O. D., Foundations of Potential Theory, Julius Springer, Berlin, 1929

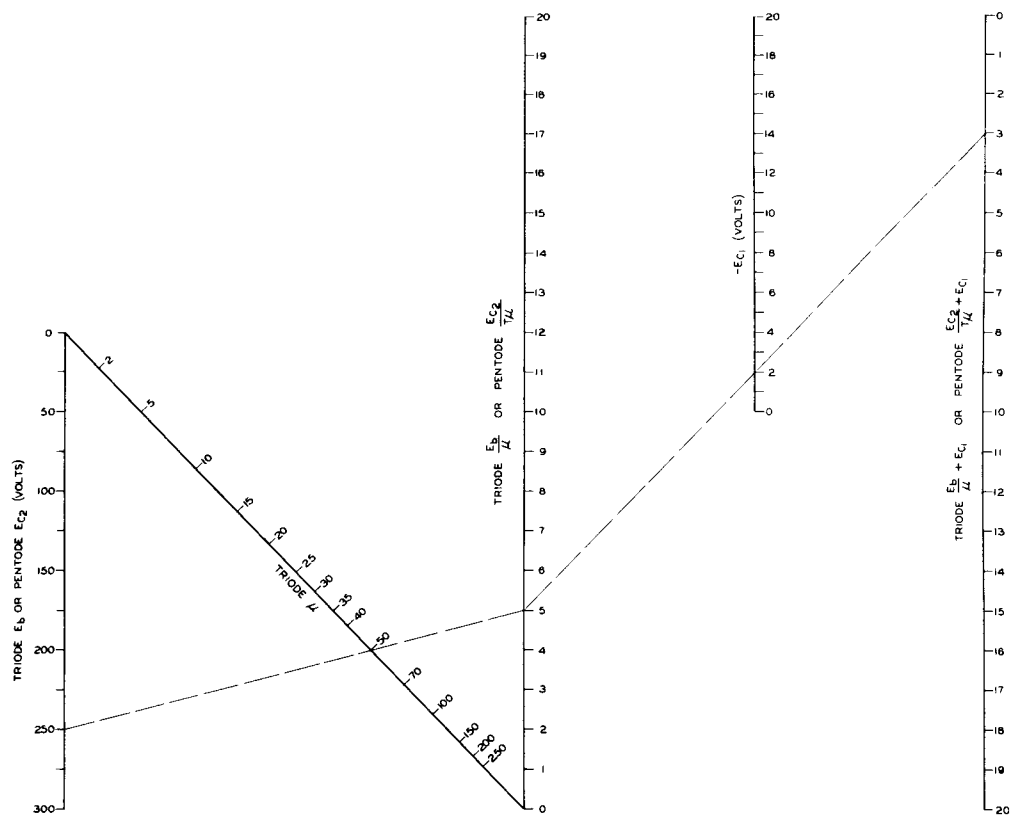


Figure 45A. Nomograph for the Rapid Adjustment of Tube Characteristics

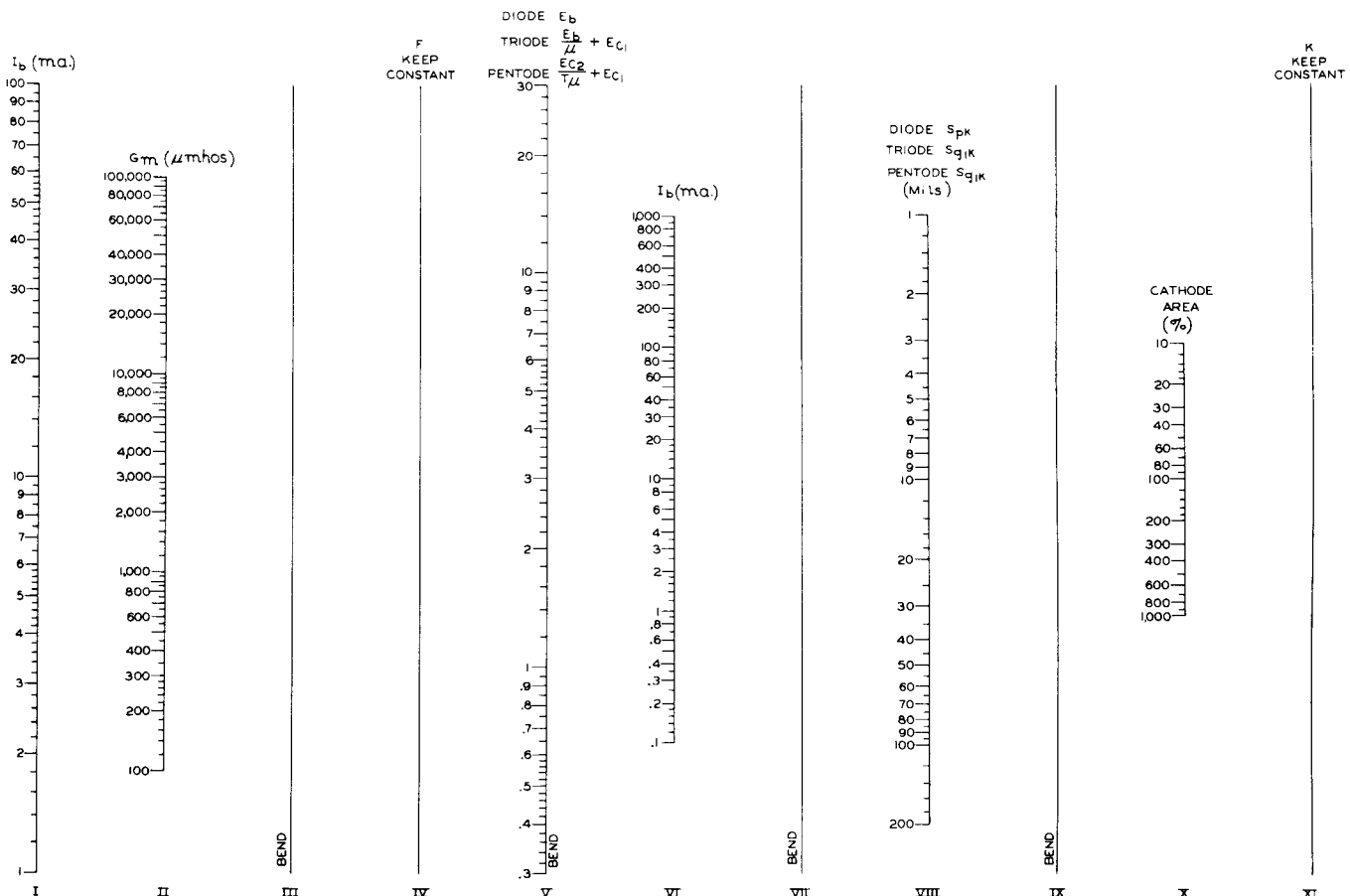


Figure 45B. Nomograph for the Rapid Adjustment of Tube Characteristics

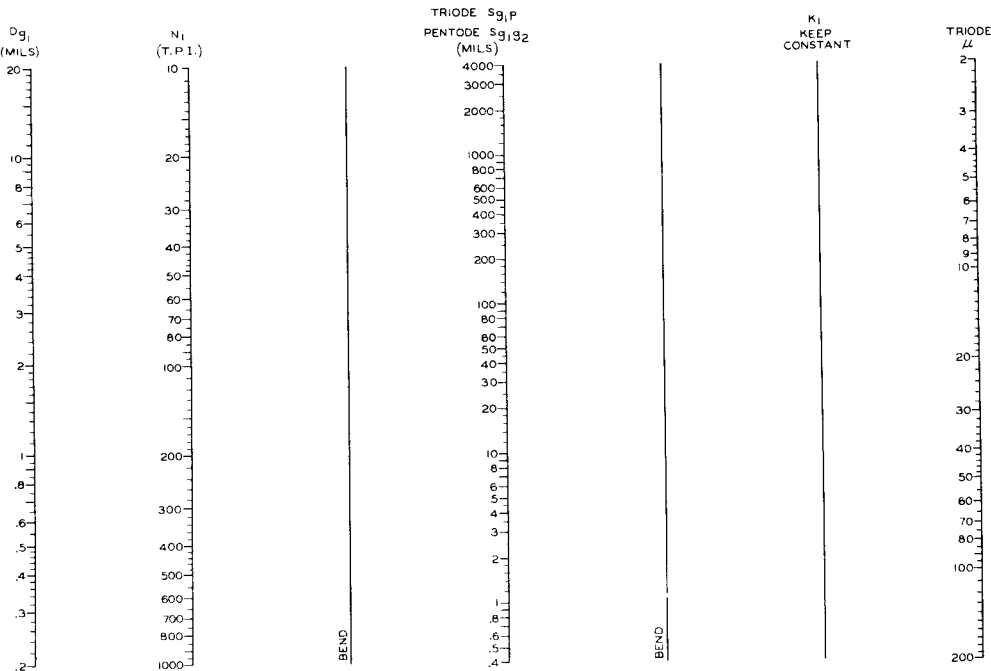


Figure 45C. Nomograph for the Rapid Adjustment of Tube Characteristics

2. Ramo, S., and J. R. Whinnery, Fields and Waves in Modern Radio, John Wiley and Sons, 2nd Edition, 1953
3. Stratton, J. A., Electromagnetic Theory, McGraw-Hill, 1941
4. Salzberg, B., and A. V. Haeff, "Effects of Space Charge in the Grid-Anode Region of Vacuum Tubes," RCA Review, Vol. 2, pp. 336-374, 1938
5. Fay, C. E., A. L. Samuel, and W. Shockley, "On the Theory of Space Charge Between Parallel Plane Electrodes," Bell Syst. Tech. Jour., Vol. 17, pp. 49-79, January 1938
6. Ramberg, E. G., and L. Malter, "Potential Distribution for Space-Charge-Limited Current Between a Plane Accelerating Grid and Parallel Anode," Jour. Appl. Phys., Vol. 23, pp. 1333-1335, December 1952
7. Beck, A. H. W., Thermionic Valves, Cambridge Univ. Press, 1953
8. Langmuir, I., "The Effects of Space Charge and Residual Gases on Thermionic Currents in High Vacuum," Phys. Rev., Vol. 2, pp. 450-486, 1913
9. Childs, C. D., Phys. Rev., Vol. 32, p. 492, 1911
10. Ivey, H. F., "Space Charge Limited Currents," Advances in Electronics and Electron Physics, Vol. VI, pp. 137-256 (contains 215 refs.), 1954
11. Millman, J., and S. Seely, Electronics, McGraw-Hill, 2nd Edition, 1951
12. Langmuir, I., "The Effect of Space Charge and Initial Velocities on the Potential Distribution and Thermionic Current Between Parallel Plane Electrodes," Phys. Rev., Vol. 21, p. 419, 1923
13. Langmuir, I., and K. T. Compton, "Electrical Discharges in Gases," Part II, Rev. of Mod. Phys., Vol. 3, p. 191, 1931
14. Kleijnen (Kleijnen), P. H. J. A., "Extension of

- Langmuir's ( $\xi, \eta$ ) Tables for a Plane Diode with a Maxwellian Distribution of the Electrons," Philips Res. Rpt., Vol. 1, pp. 81-96, 1945
15. Lieberman, G., "The Calculation of Amplifier Valve Characteristics," Jour. IEE, Part III, Vol. 93, pp. 138-153, 1946
16. Ferris, W. R., "Some Characteristics of Diodes with Oxide Coated Cathodes," RCA Review, Vol. 10, p. 134, 1949
17. Langmuir, I., and K. B. Blodgett, "Currents Limited by Space Charge Between Coaxial Cylinders," Phys. Rev., Vol. 22, p. 347, 1923
18. Maxwell, J. C., A Treatise on Electricity and Magnetism, 2 Vols., Oxford, 3rd Edition, 1904
19. Kleijnen, P. H. J. A., "The Penetration Factor and the Potential Field of a Planar Triode," Philips Res. Rpt., Vol. 6, pp. 15-33, February 1951
20. Hsu, H., and C. E. Horton, "Electrolytic Tank Measurements of Mesh Grid Characteristics," IRE Nat. Convention Rec., Part 3, Vol. 5, pp. 114-119, 1957
21. Vodges, F. B., and F. R. Elder, "Formulas for Amplification Factors for Three Element Tubes," Phys. Rev., Vol. 24, pp. 283-289, Dec. 1924
22. Herne, H., "Valve Amplification Factors," Wireless Eng., Vol. 21, pp. 59-64, February 1944
23. Ollandorff, F., "Calculation of Controllance Due to a Fine-Mesh Grid," Electrotechnik und Maschinenbau, Vol. 52, pp. 585-591, 1934
24. Thompson, B. J., "Space Current Flow in Vacuum Tube Structures," Proc. IRE, Vol. 31, pp. 485-491, September 1943
25. Walker, G. B., "Theory of Equivalent Diode," Wireless Eng., Vol. 24, pp. 5-7, 1947
26. Telegren, B. D. H., "De Grootte van de Emisistroom in een Triode," Physica, Vol. 5, pp. 301-315, 1925

27. Llewelyn, F. B., and L. C. Peterson, "Vacuum-Tube Networks," Proc. IRE, Vol. 32, pp. 144-166, 1944
28. Strutt, M. J. O., Elektronenröhren, Springer-Verlag, Berlin, 1957
29. Schade, O. H., "Beam Power Tubes," Proc. IRE, Vol. 26, pp. 137-180, 1938
30. Rothe, H., and W. Kleen, Hochvacuum-Elektronen-Röhren, Band 1, Physikalische Grundlagen, Akademische Verlagsgesellschaft M. B. H., Frankfurt a.m., 1955
31. Jonker, J. L. A., and B. D. H. Tellegren, "The Current to a Positive Grid in Electron Tubes," Philips Res. Rpt., Vol. 1, pp. 13-32, 1945
32. Jonker, J. L. A., "The Control of the Current Distribution in Electron Tubes," Philips Res. Rpt., Vol. 1, pp. 331-338, November 1946
33. Deb, S., "Current Distribution in Plane Positive-Grid Triodes," Indian Jour. Phys., Vol. 26, pp. 337-392, August 1952
34. Spangenberg, K. R., Vacuum Tubes, 1st Edition, McGraw-Hill, 1948
35. Spangenberg, K., "Current Division in Plane Electrode Triodes," Proc. IRE, Vol. 28, pp. 226-236, May 1940
36. Jonker, J. L. H., and Z. van Gelder, "The Internal Resistance of a Radio-Frequency Pentode," Philips Res. Rpt., Vol. 12, pp. 141-175, April 1957
37. Bennett, W. R., and L. C. Peterson, "The Electrostatic Field in Vacuum Tubes with Arbitrarily Spaced Elements," Bell Syst. Tech. Jour., Vol. 28, pp. 303-314, 1949
38. Dahlke, W., "Gittereffektivpotential und Kathodenstromdichte einer Ebenen Triode unter Berücksichtigung der Inselbildung," Telefunken Zeit., Vol. 24, pp. 213-222, December 1951
39. Napiorski, F. R., O. H. Schade, Jr., and L. C. Scholz, Unpublished work
40. Harris, W. A., and H. W. Kirk, Unpublished work
41. Dahlke, W. A., "Statische Kennwerte der Nicht-idealen Triode," Telefunken Zeit., Vol. 27, pp. 172-187, September 1954
42. Weber, E., "Mapping of Fields," Electromagnetic Fields, Vol. I, John Wiley and Sons, 1950
43. Kober, H., Dictionary of Conformal Representations, Dover Publications, 1952
44. Breckenback, E. F. (ed), "Constructions and Applications of Conformal Maps," Nat. Bur. of Standards, Appl. Math Series, Vol. 18, 1952
45. Ince, E. L., Ordinary Differential Equations, 4th Edition, Dover Publications
46. Bateman, H., Partial Differential Equations, Cambridge University Press, 1932
47. Southwell, R. V., Relaxation Methods in Engineering Science, Oxford University Press, 1940
48. Southwell, R. V., Relaxation Methods in Theoretical Physics, 2 Vols., Oxford University Press, 1946, 1956
49. Liebmann, G., "Electrical Analogies," Brit. Jour. Appl. Phys., Vol. 4, p. 193, 1953
50. Harries, J. H. O., "The Rubber Membrane and Resistance Paper Analogies," Proc. IRE, Vol. 44, pp. 236-248, February 1956
51. Kennedy, P. A., and G. Kent, "Electrolytic Tank, Design and Applications," Rev. of Sci. Inst., Vol. 27, p. 916, November 1956
52. Kleynen, P. H. J. A., "The Motion of an Electron in Two-Dimensional Electrostatic Fields," Philips Tech. Rev., Vol. 2, pp. 338-345, 1937
53. Code W1
54. Code W2
55. Francken, J. C., "The Resistance Network, a Simple and Accurate Aid to the Solution of Potential Problems," Philips Tech. Rev., Vol. 21, pp. 10-23, 1959-1960
56. Alma, G. A., G. Diemser, and H. Groenijk, "A Rubber Membrane Model for Tracing Electron Paths in Space Charge Fields," Philips Tech. Rev., Vol. 14, pp. 336-343, 1953
57. Sunshine Scientific Co., "Use and Theory of the Analog Field Plotter," Instruction Manual for Apparatus Manufactured by the Sunshine Co.
58. Einstein, P. A., "Factors Limiting the Accuracy of the Electrolytic Plotting Tank," Brit. Jour. Appl. Phys., Vol. 2, p. 49, 1951
59. VanDuzer, T., and G. R. Brewer, "Space-Charge Simulation in an Electrolytic Tank," Jour. Appl. Phys., Vol. 30, pp. 291-301, March 1959
60. Code W3
61. Stanford Electronics Laboratories, "Electron Devices Research," Consolidated Quarterly Report No. 10, April 1-June 30, 1959, pp. 45-47, Project 314T, Electrolytic Tank Studies, Contract No. DO36(039)SC73178
62. Pierce, J. R., Theory and Design of Electron Beams, D. Van Nostrand and Co., Inc., 1954
63. Harman, W. W., Fundamentals of Electron Motion, McGraw-Hill, 1953
64. Klemperer, O., Electron Optics, Cambridge University Press, 1939
65. Liebmann, G., "Field Plotting and Ray Tracing in Electron Optics. A Review of Numerical Methods," Advances in Electronics, Vol. II, pp. 101-149, Academic Press, 1950
66. Code W4
67. Dingwall, A. G. F., "The Mathematical Basis for the Computer Program," Appendix B, Quarterly Reports 1 and 2, "A Study of Electron Tube Deterioration Utilizing Kinetic Theory," Contract No. NObsr-77637. (This is a discussion of the generalized Child-Langmuir equation referred to above. The derivation of the correction factor ( $\theta\eta$ ) and of the general form of the equations was done by A. G. F. Dingwall, Jr., but has not yet been published.)
68. Fremlin, J., "Calculation of Triode Constants," Elec. Communications, Vol. 18, pp. 33-49, July 1939
69. Fremlin, J. H., R. N. Hall, and P. A. Shatford, "Triode Amplification Factors," Elec. Communications, Vol. 23, pp. 426-435, Dec. 1946
70. Rothe, R. (ed), F. Ollendorff, and K. Pohlhausen (trans. A. Herzenberg), Theory of Functions, As Applied to Engineering Problems, Technology Press, MIT, 1933
71. Richardson, O. W., The Emission of Electricity from Hot Bodies, Longmans Green, 2nd Edition, 1921

# Design and Processing of Microwave Magnetrons

F. E. Vaccaro and D. E. Nelson

Princeton

A magnetron has been defined as a diode immersed in a magnetic field; however, two additions should be made to this definition. First, the dc electric field and magnetic field must be at right angles to each other. The relationship is often expressed by calling the magnetron a crossed-field device. Second, electron movement occurs in such a way that the potential energy due to the dc electric field is converted to rf energy.

The magnetron generally consists of a cylindrical cathode surrounded by a cylindrical anode that may be divided into segments and requires for its operation a magnetic field parallel to the cathode. The rf circuits are connected either between the cathode and anode or between the segments of the anode. The region between the cathode and the anode is called the interaction space. In this region, the electrons interact with the rf field, and the energy gained from the dc field applied between anode and cathode is converted into rf energy.

In the analysis of the operating principles of a magnetron, it is desirable to first consider the case involving only dc operation (no rf voltage applied). An electron emitted from the cathode is acted upon by two radial forces, as shown in Fig. 1. The force,  $F_1$ , due to the dc electric field is directed toward the anode and is equal to  $eE$ , where  $e$  is the charge of the electron and  $E$  is the intensity of the electric field. The force,  $F_2$ , due to the magnetic field is directed toward the cathode and is equal to  $e[v_e \times B]$ , where  $[v_e \times B]$  is the vector cross-product of electron velocity and magnetic-field density.

When the two forces,  $F_1$  and  $F_2$ , are equal and opposite, the electron travels in a circular path around the cathode. In this "equilibrium" condition, therefore, a cloud of electrons circling the cathode extends to a certain radius. Beyond this radius there is no electron space charge. If this radius is less than the anode radius the magnetron is said to be "cutoff", i. e., no electrons can reach the anode. However, if the anode voltage is raised, the radius of the space-charge cloud increases and electrons reach the anode.

A simple, or cyclotron-frequency, magnetron oscillator results if a circuit that is resonant at the cyclotron frequency of the electrons is connected between the anode and cathode of the dc magnetron. The electrons flow from the cathode toward the anode and then MKS units are used throughout this article except where specified otherwise in the text.

back toward the cathode (at the cyclotron frequency). This type of magnetron is very inefficient and is rarely used.

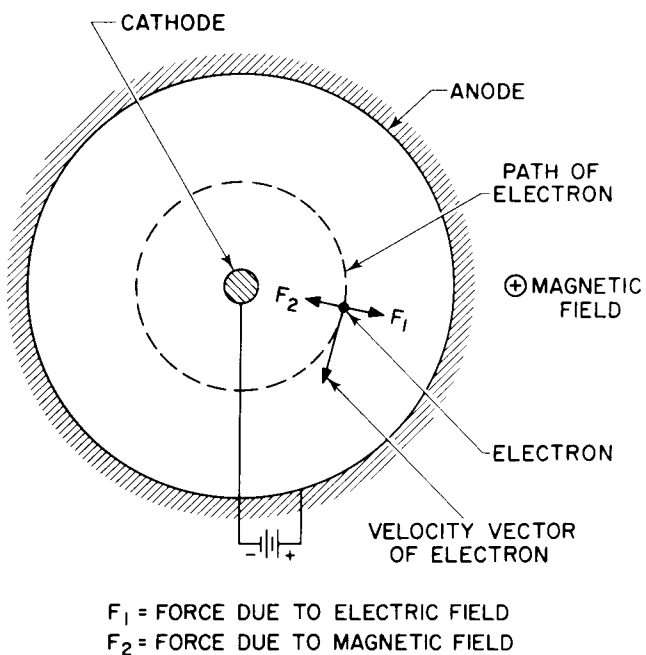


Figure 1. Electron Motion in a DC Magnetron  
(no rf voltage applied)

Of much greater importance is the traveling-wave type of magnetron. This type is often called a cavity magnetron although it does not necessarily employ cavities, i. e., the circuit could consist of lumped parameter elements or resonant sections of transmission lines. The term cavity magnetron came into use because the first traveling-wave magnetrons of practical importance were made with rf circuits which were resonant cavities.

Fig. 2 shows some typical unstrapped-resonant-systems for traveling-wave types of magnetron oscillators. The anode may be considered as a series of  $N$  quarter-wave transmission lines which act as resonators. A system of  $N$  coupled resonators can be shown to have  $N$  resonant frequencies called "modes," each of which has a different electric field distribution. At these resonant frequencies standing waves can be excited. These

standing waves can be resolved into oppositely directed traveling waves; if the electrons rotate in synchronism with one of these waves, interaction will take place to transfer energy from the electrons to the wave.

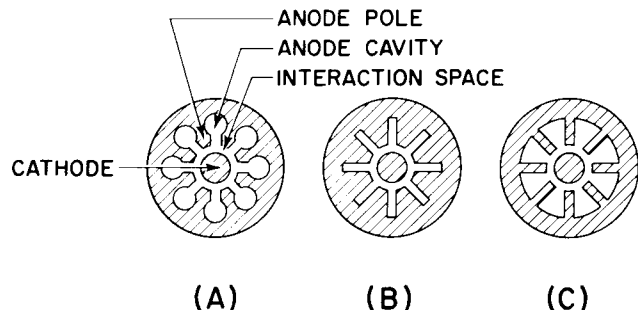


Figure 2. Typical Unstrapped Resonant Systems for Traveling-Wave Magnetron Oscillators: (A) With hole-and-slot-type side resonators, (B) With slot-type side resonators, (C) With vane-type side resonators

Fig. 3 shows a linear form of the traveling-wave magnetron illustrating some of the basic principles. An rf wave is shown traveling to the right. If an electron travels with the same velocity as the waves and in the proper phase, it will continuously lose energy over a number of cycles. The magnetron, therefore, is independent of transit time; i. e., the electrons will continue to lose energy even though their transit time is a number of cycles. If the linear magnetron structure of Fig. 3 is rolled up it assumes the more usual circular reentrant form.

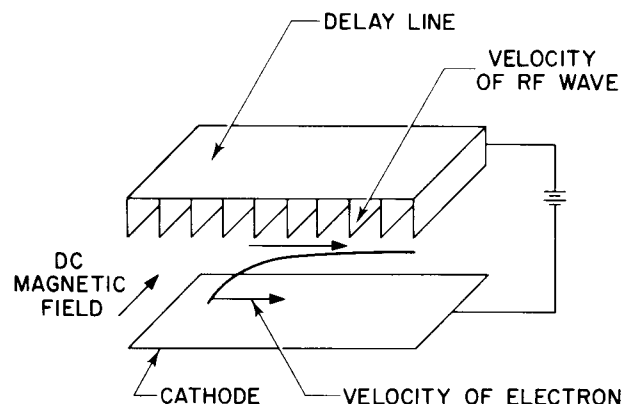


Figure 3. Interaction of Electron with RF Wave in Traveling-Wave Magnetron

Some of the paths of electrons in a traveling-wave magnetron are shown in Fig. 4. The electrons travel in cycloidal paths; however, the design equations ignore the cycloidal motion and deal only with the average paths of the electrons. Electrons out of phase with the radio frequency fields are quickly returned to the cathode. This action is one reason for the high efficiency of the magnetron. A second reason for the high efficiency, mentioned previously, is that the potential energy of the electrons is converted to rf energy so that the velocity remains constant and the electrons, therefore, tend to stay in proper phase. A third reason for high effi-

ciency is the phase-focusing effect which keeps the electrons in the proper phase. Fig. 5 shows a plot of lines of electric force on an electron (drawn for the plane case) for the fundamental of the  $\pi$  mode. The plane of maximum opposing force on the electron intersects that of the figure along the line M. The arrow shown above the line M indicates the direction of electron motion. The force on the electron due to the dc electric field is directed from cathode to anode. The force lines shown may be considered to be those of the total field component at the instant the rf field is maximum. An electron which lags behind the rf field, say at point P, "sees" a radial component of the rf field which adds to the radial electric field divided by the magnetic field; this increased electric field accelerates the electron until it is in the correct phase to give up energy to the field. Similarly, electrons which get ahead of the rf field are slowed down.

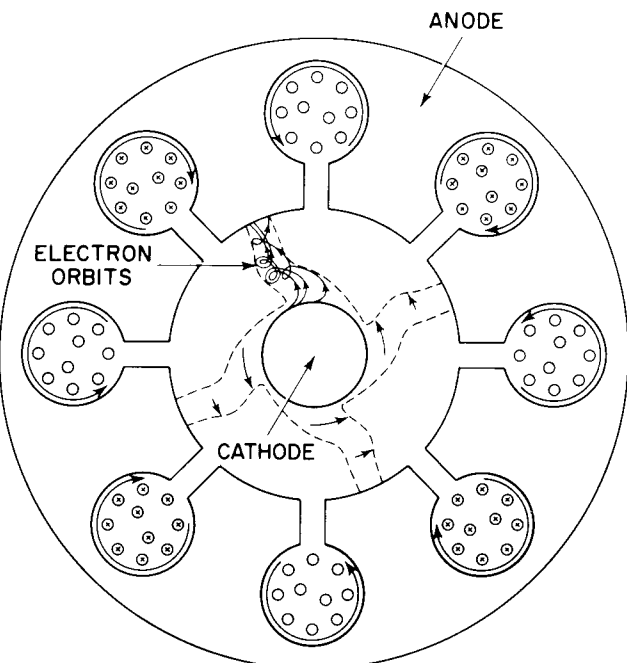


Figure 4. Space Charge in Oscillating Magnetron

It should be realized that the traveling-wave magnetron and the traveling-wave tube are very closely related. Both tubes require a structure to slow down the rf wave so that the electrons can have approximately the same velocity as the rf wave and can continuously lose energy to the rf field. In both types of tubes the electrons may interact with forward waves or backward waves. Both types may serve as amplifiers or oscillators. The basic difference between the two tube types is that, in the case of the magnetron, potential energy is converted to rf energy while, in the case of the traveling-wave tube, kinetic energy is converted to rf energy.

The most important use of the magnetron is as a self-excited oscillator in pulsed radar systems. In the more sophisticated radar systems now being developed, the magnetron oscillator is being replaced by amplifier tubes of the magnetron, traveling-wave, or klystron type. Probably the most important future applications

of magnetrons will be in lightweight radars and in the field of dielectric heating where an efficient source of high-frequency power is all important. At present, magnetrons are being used in electronic ovens and diathermy devices. Other magnetron applications include frequency-modulation communication, weather radar, and radar countermeasures. A typical magnetron for use in pulsed radar is shown in Fig. 6.

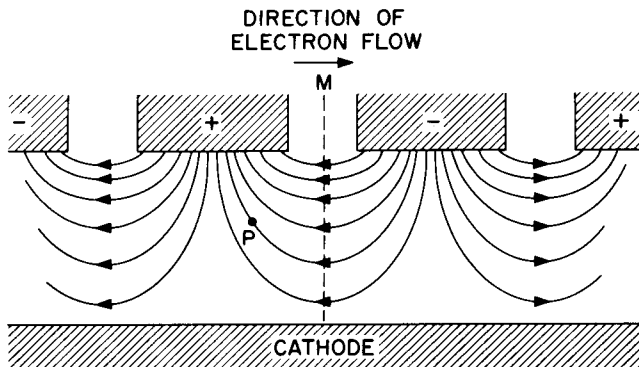


Figure 5. Phase-Focusing Effect in a Traveling-Wave Magnetron

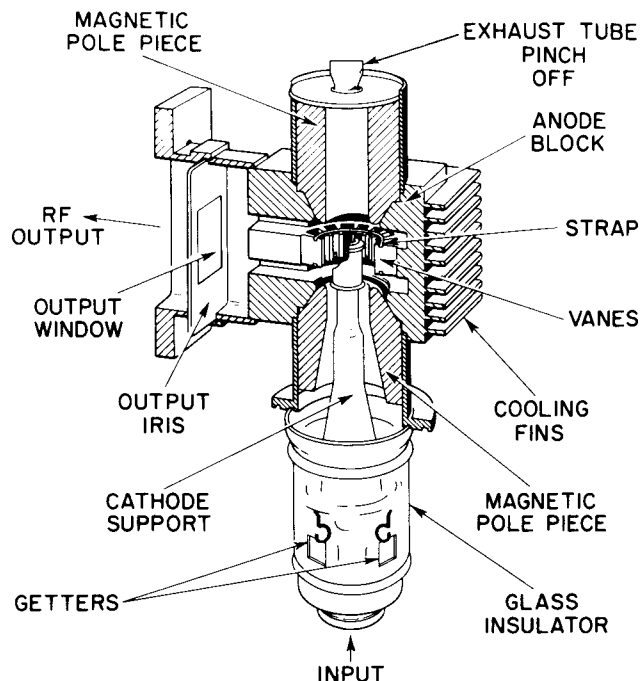


Figure 6. Cutaway View of RCA-6521 Magnetron

## DESIGN OF THE MAGNETRON INTERACTION SPACE

### Interdependence of Magnetron Components

The components of the magnetron are so interdependent that no one component can be designed independently of the others. The basic problem is, given a set of requisite parameters by the magnetron user, to determine a design for each component meeting these parameters which is also consistent with the design adopted

for the other components. Fig. 7 is a chart showing an analysis of the various factors in magnetron design. At the left are the parameters specified by the equipment designer. The relative importance of these parameters may assume equal or greater importance in special applications; for example, frequency stability may be especially important in beacon applications, or weight may be important in airborne equipment.

The four components of the magnetron are indicated in heavily lined blocks, namely, interaction space, resonant system, cathode, and magnetic circuit. The output circuit is considered to be a part of the resonant circuit in the chart although it might have been considered as a separate component. The arrangement of the chart indicates the usual method of magnetron design, i. e., a trial design of the interaction space is determined which satisfies the required parameters. This design establishes a set of specifications for the remaining components. Then it must be decided whether or not each of the remaining components can be designed to meet these specifications. Thus, the specified parameters plus the interaction space design impose sets of conditions upon the remaining elements.

### Modes of the Magnetron

In a circular system of  $N$  resonators, the phase difference between adjacent resonators may assume values  $2\pi n/N$ , where  $n$  represents the integers 0, 1, 2, ...,  $N/2$ . The variation of potential from one segment to the next depends upon the mode of oscillation of the whole system of resonators. The mode number  $n$  denotes the number of complete waves of potential around the anode. Magnetrons are normally operated in the  $n = N/2$  or  $\pi$  mode. These anode potential waves may be either standing waves or waves traveling around the anode structure with angular velocity  $2\pi f/n$  radians per second, where  $f$  is the frequency of the particular mode  $n$ . For the two modes in which adjacent resonators are in phase (when  $n = 0$ ), or  $\pi$  radians out of phase (when  $n = N/2$ ), only standing waves are possible. These modes are a property of the resonant circuit.

An electron traveling around the interaction space can continue to lose energy to one of the modes if it crosses each anode gap in the proper phase. If the time to reach the next gap is  $(|q| + 1/2)T$ , the electron will cross the next gap when the rf phase is the same as when it crossed the previous gap. The letter  $q$  is any integer. It can be shown that this action will occur if the angular velocity of the electron is  $2\pi f/|k|$ , where  $k = n + qN$ . The number  $k$  is the Hartree mode number and is equal to both the number of rf cycles required for the electron to move once around the interaction space and the number of spokes in the space-charge cloud. If  $|k| = n$ , the electronic interaction is said to be with the fundamental Hartree component of the rf field. If  $|k| \neq n$ , the electronic interaction is said to be with a Hartree harmonic. Fig. 8 is a  $\pi$ -mode potential plot showing the Hartree fundamental and several harmonics.

Magnetrons are usually designed for operation in the fundamental component and the  $\pi$  mode. The use of the  $\pi$  mode is indicated by its greater mode separation (for

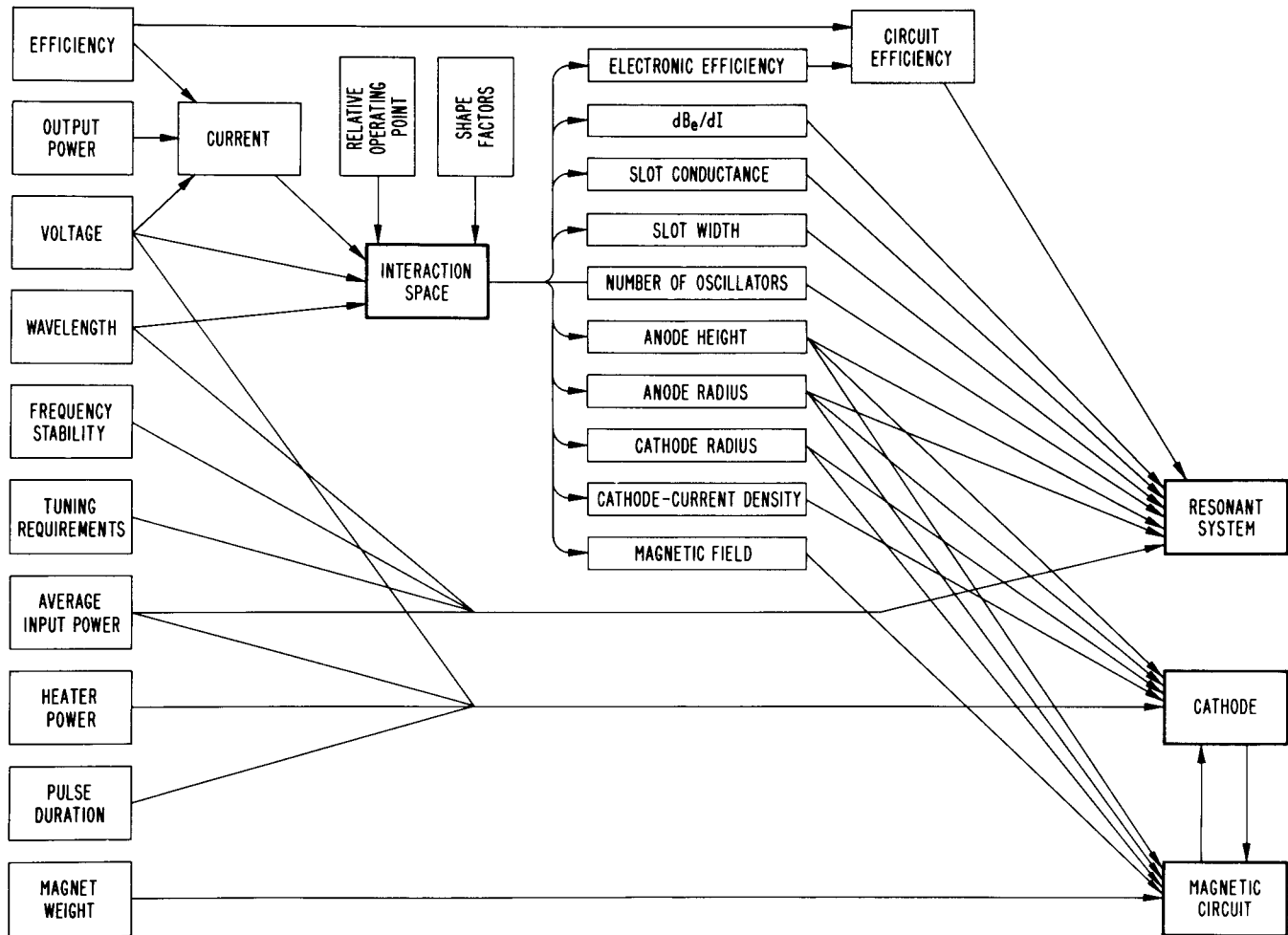


Figure 7. Principal Factors in Analysis of Magnetron Design

a strapped or rising-sun system). The use of the fundamental component gives the most efficient interaction of electrons with the rf field.

#### The Equations of Cross-Field Interaction

The relationship between the magnetic field  $B$  and the voltage at which an electron just grazes the anode of a cylindrical magnetron (with no rf fields present) is given by the Hull cutoff relation:<sup>1</sup>

$$V_c = \frac{eB^2 r_a^2}{8m} \left[ 1 - \left( \frac{r_c}{r_a} \right)^2 \right]^2 \quad (1)$$

Here  $e/m$  is the ratio of electronic charge to mass, and  $r_a$  and  $r_c$  are the anode and cathode radii, respectively. At voltages below the Hull cutoff voltage  $V_c$  no current reaches the anode in the ideal case.

Langmuir's<sup>2</sup> relation for space-charge-limited current flowing between coaxial cylinders in the absence of a magnetic field is:

$$\frac{I}{h} = \frac{8\epsilon_0 \sqrt{2}}{9\beta^2} \pi \sqrt{\frac{e}{m}} \frac{V^{3/2}}{r_a} \quad (2)$$

where  $h$  is the height of the cylinders,  $V$  is the volt-

age between the cylinders, and  $\beta$  is a dimensionless function of  $r_a/r_c$  tabulated by Langmuir.

The current  $I_c$  which flows when the voltage just exceeds the cutoff voltage given in Eq. (1) is shown by Allis<sup>3</sup> to be:

$$\frac{I_c}{h} = \frac{\pi \epsilon_0 a_1}{4} \left( \frac{e}{m} \right)^2 r_c^2 \left( \frac{r_a}{r_c} - 1 \right) B^3 \quad (3)$$

where  $a_1$  is a function of  $r_a/r_c$  (Fig. 9) approximately equal to one.

Eqs. (1), (2) and (3) apply to the dc magnetron.

One equation is of paramount importance for the oscillating magnetron — the Hartree relation. Hartree<sup>4</sup> has shown that there is a critical relation between  $B$  and  $V$  which establishes a value of  $V$  below which oscillation cannot be expected to start. If  $V$  is lower than the value specified by Eq. (4), no electrons can reach the anode with an infinitesimal amplitude of rf voltage on the anode; a finite amplitude is required and there is no way for this amplitude to be generated.

$$V = \pi c \frac{Br_a^2}{|k|\lambda} \left[ 1 - \left( \frac{r_c}{r_a} \right)^2 \right] - \frac{m}{2e} r_a^2 \left( \frac{2\pi c}{k\lambda} \right)^2 \quad (4)$$

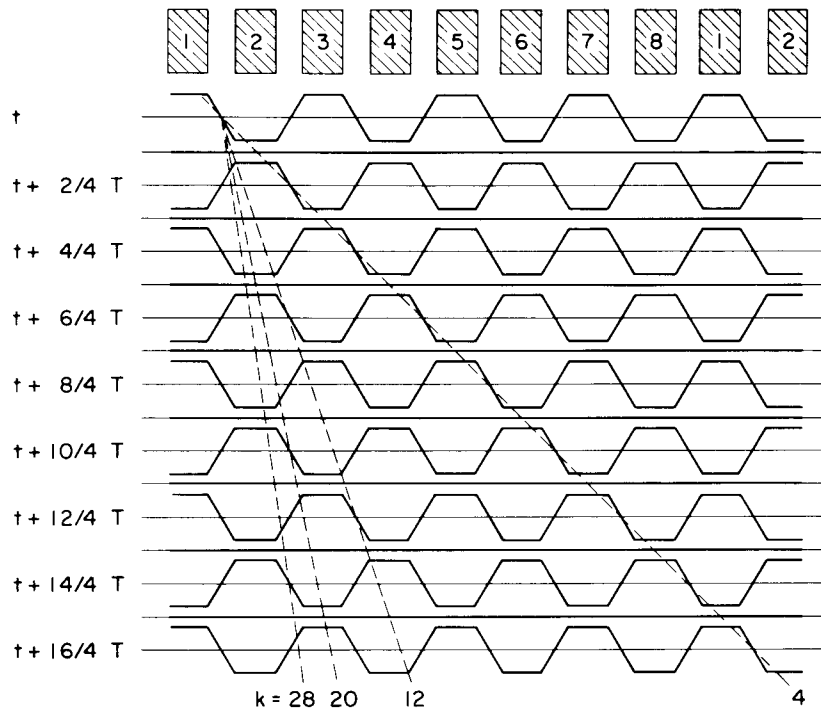


Figure 8. Plot Showing  $\pi$ -Mode Anode Potential Wave at Several Instants in an 8-Resonator Magnetron

Note that this relation depends on  $|k| \lambda$ , the product of the Hartree mode number and the wave length. The value of anode voltage  $V$  given by Eq. (4) is called the Hartree voltage.

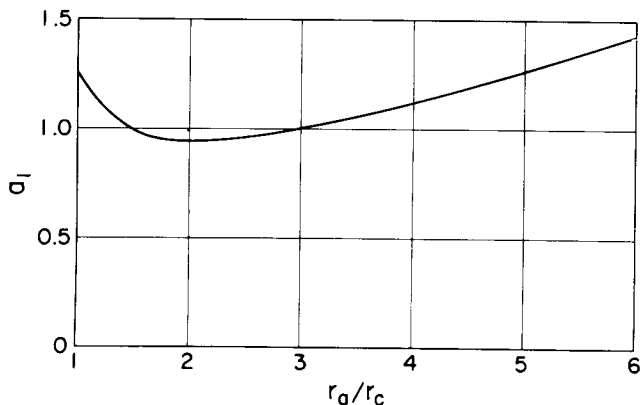


Figure 9. Plot of  $a_1$  as a Function of  $r_a/r_c$

Fig. 10 shows the current vs. voltage characteristic of a magnetron for a fixed magnetic field. The solid line represents the ideal dc case; the current is zero until the Hull cutoff voltage, Eq. (1), is reached. The current then jumps to the Allis current, Eq. (3). As the voltage is increased above the cutoff voltage, the current increases and approaches the Langmuir diode current, Eq. (2). The dashed curve shows the practical dc case. The current begins to flow below cutoff. No satisfactory explanation of the "leakage" current has been made. Initial velocities of electrons and tube asymmetries are not sufficient to explain the effect.

The long-dash line shows the current for an oscillating tube. When the voltage reaches the Hartree voltage, Eq. (4), oscillation begins and the current increases above the dc leakage current. It continues to increase above the dc value until the voltage nearby reaches the cutoff value, at which point oscillation ceases. The value of current at this point is empirically given as one-half the Allis current. This value is not very accurate, however, as most tubes cease oscillating at current values considerably below that of half of the Allis current.

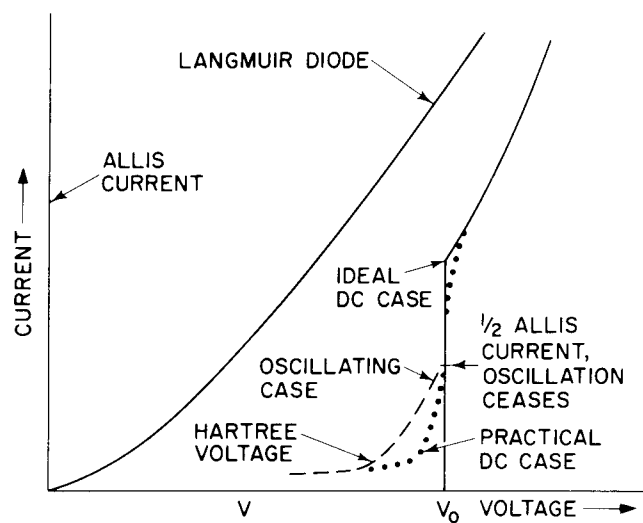


Figure 10. Current-vs.-Voltage Characteristic of a Magnetron for a Fixed Magnetic Field

The Hartree voltage for the various magnetron modes is often plotted against magnetic field. Such a Hartree diagram for an 8-resonator magnetron is given in Fig. 11. This Hartree diagram shows the voltages at which oscillation in the different magnetron modes can start. It is most useful in determining the mode in which the magnetron is operating. The line representing the voltage for a particular mode is termed the Hartree line for that mode. The Hartree mode lines  $k = n = 4, 3, \text{ and } 2$  are tangent to the Hull cutoff curve. The line for  $n = 4$  gives the voltage at which oscillation starts for the  $\pi$  mode. As the current is increased the voltage rises above the line for  $n = 4$  as indicated by the two lines shown in dashes. As the magnetic field is decreased, the electronic efficiency decreases until it reaches zero at the intersection of the line for  $n = 4$ , as indicated by the two lines shown in dashes. As the magnetic field is decreased, the electronic efficiency decreases until it reaches zero at the intersection of the line for  $n = 4$  and the Hull cutoff curve. The value of  $B$  and  $V$  at this intersection,  $\mathcal{B}$ , the characteristic magnetic field, and  $\mathcal{V}$ , the characteristic voltage, are of importance in scaling. Fig. 12 shows a three-dimensional plot of current and voltage vs. magnetic field, combining the information Figs. 10 and 11.

#### Interaction-Space Design Equations

There are two basic ways to design the interaction space of a magnetron: (1) calculate the design from the basic design equations, or (2) derive a new design from an existing magnetron design in one of several different ways. If a design is available which does not differ too greatly from the desired design, the second method is usually preferable. However, it is often worthwhile to check the design by applying the basic design equations.

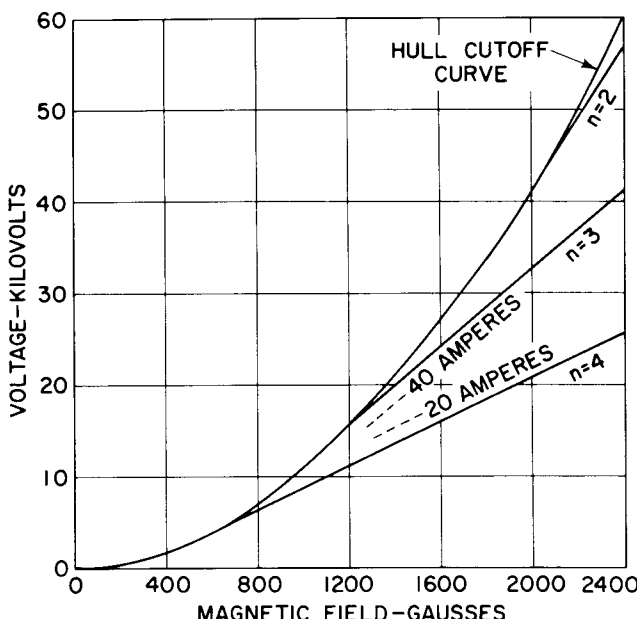


Figure 11. Hartree Diagram for an 8-Resonator Magnetron

First, the basic equations involved in method 1 will be presented; several ways of applying method 2 will be covered later.

The use of the characteristics scale factors,  $^* \mathcal{B}$ ,  $\mathcal{V}$ ,  $\mathcal{P}$ , and  $\mathcal{G}$ , is valuable in both methods. In general, these factors depend upon the Hartree mode number  $k$ . For each mode, there are different values of the scale factors. In the design of magnetrons, the  $\pi$  mode values  $k = n = N/2$  are usually desired; therefore, in the equation  $n$  will be used instead of  $|K|$ .

The characteristic magnetic field  $\mathcal{B}$  is the magnetic field at the intersection of the Hartree line and the cutoff curve (see Fig. 11) and is given by:

$$\mathcal{B} = 2 \frac{m}{e} \frac{2\pi c}{n \lambda} \frac{1}{1 - \left(\frac{r_c}{r_a}\right)^2} \quad (5)$$

or, if  $\mathcal{B}$  is in gauss and  $\lambda$  in centimeters

$$B = \frac{21200}{n \lambda \left[1 - \left(\frac{r_c}{r_a}\right)^2\right]} \text{ gauss} \quad (5a)$$

Similarly, the characteristic voltage  $\mathcal{V}$  is the voltage at the intersection of the Hartree mode line and the cutoff curve:

$$\mathcal{V} = \frac{1}{2} \frac{m}{e} \left[ \frac{2\pi c}{n \lambda} \right]^2 r_a^2 \quad (6)$$

or

$$\mathcal{V} = 253,000 \left( \frac{2\pi r_a}{n \lambda} \right)^2 \quad (6a)$$

The magnetron efficiency is zero at the point  $\mathcal{V}$ ,  $\mathcal{B}$  and increases as the operating point moves out along the mode line, i.e., as  $V$  and  $B$  are increased. The characteristic current  $\mathcal{J}$  is the current flowing when  $B$  equals  $\mathcal{B}$  and  $V$  is just greater than  $\mathcal{V}$ , with no rf voltage present.

$$\mathcal{J} = \frac{2\pi a_1}{\left[1 - \left(\frac{r_c}{r_a}\right)^2\right] \left[\frac{r_a}{r_c} + 1\right]} \frac{m}{e} \left( \frac{2\pi c}{n \lambda} \right)^3 r_a^2 \epsilon_0 h \quad (7)$$

or

$$\mathcal{J} = \frac{8440 a_1}{\left[1 - \left(\frac{r_c}{r_a}\right)^2\right] \left[\frac{r_a}{r_c} + 1\right]} \left( \frac{2\pi r_a}{n \lambda} \right)^3 \frac{h}{r_a} \text{ amperes} \quad (7a)$$

where  $a_1$  is a function of  $r_a/r_c$  (see Fig. 9)

$\mathcal{P}$  is the characteristic power:

$$\mathcal{P} = \mathcal{J} \mathcal{V} \quad (8)$$

The characteristic conductance  $\mathcal{G}$  is

$$\mathcal{G} = \mathcal{J} \mathcal{V} \quad (9)$$

There are a number of ways of applying these equations to the design of the interaction space. The method given here starts with the specification of the dc magnetic field  $B$ . (Alternative methods will be found in

\*Page 416 of reference 5.

section 10 of Ref. 5) The method is as follows:

Step 1: Specify values of  $\lambda$ ,  $V$ , and  $P_o$ . Assume a value of  $B$  which can reasonably be obtained. Estimates of the anode height and radius will have to be made to judge what value is reasonable.

Step 2: Assume a value of  $N$ . Calculate  $r_a/r_c$  from

$$\sigma = \frac{r_a}{r_c} = \frac{N - 4}{N + 4} \quad (10)$$

Step 3: Calculate  $\mathcal{B}$  from Eq. (5a).

Step 4: Calculate  $V$  from Eq. (4), Hartree relation, which can be rewritten in terms of  $V$  and  $\mathcal{B}$  as

$$\frac{V}{V} = 2 \frac{B}{\mathcal{B}} - 1 \quad (4a)$$

Step 5: Calculate  $r_a$  from Eq. (6a). Check to see that  $2r_a/\lambda < 0.3$  for a strapped tube or  $< 0.6$  for the rising-sun type.

(This inequality must be satisfied to insure adequate mode separation.)

Step 6: Check the value of electronic efficiency by means of Slater's equation:

$$\eta_e = 1 - \left( \frac{B}{B} \right)^2 \frac{V}{V} \quad (11)$$

If  $\eta_e$  is low, a larger value of  $N$  or a higher value of  $B$  must be used. (Because this equa-

tion is based on very simple assumptions, it may give inaccurate results. This is a disadvantage of this method compared to scaling from a known tube.)

Step 7: Assume a reasonable value for the circuit efficiency  $\eta_c$  and calculate  $I$  from

$$I = \frac{P_o}{V \eta_e \eta_c} \quad (12)$$

Step 8: Assume a value of anode height  $h$ , keeping in mind the problem of attaining the required magnetic field and the restriction that  $h/\lambda < 0.3$  for a strapped tube or  $< 0.6$  for a rising-sun type (to insure adequate mode separation). Calculate the cathode current density  $J_c$  from

$$J_c = \frac{I}{2 \pi r_c h} \quad (13)$$

If  $J_c$  is higher than the proposed cathode can provide, a larger value of  $h$  or of  $N$  must be used.

Step 9: Select a value of  $\mu$  (the relative slot width) in the range  $0.5 > \mu > 0.3$

$$\mu = \frac{W}{2 \pi r_c h} \quad (14)$$

Satisfying this condition insures a good rf field pattern in the interaction space. Fac-

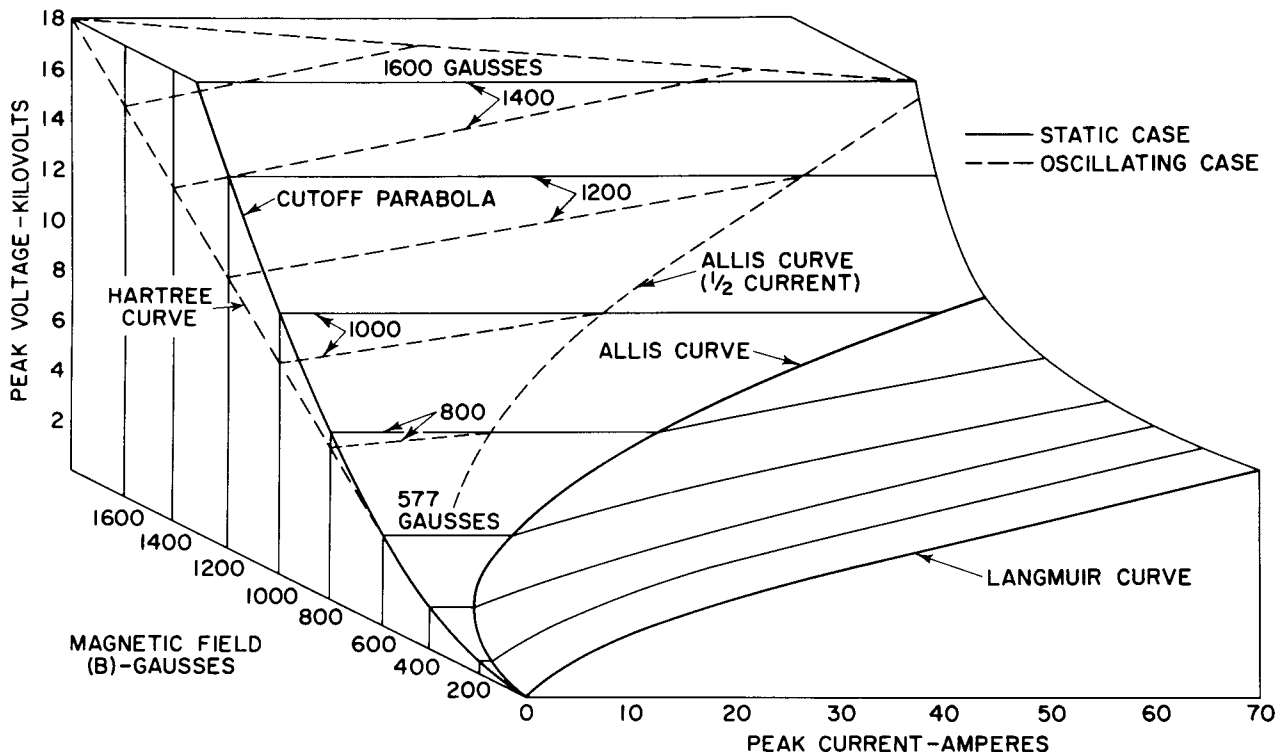


Figure 12. Three-Dimensional Plot of Current vs. Voltage vs. Magnetic Field for a Magnetron

tors to be considered in choosing  $\mu$  are thermal dissipation, mechanical strength, and its effect on the resonant circuit and on the slot conductance.

Two factors remain undetermined, the slot conductance  $G_1$  and the ratio of load conductance to maximum power load conductance  $g/g_0$ . The slot conductance is a characteristic of the resonant circuit. Methods of calculating  $G_1$  are given in chapter 4 of Ref. 5. However, the difficulty of accurately calculating  $G_1$  is such that the usual practice is to ignore it in the design of magnetrons. Fortunately, the operation is not critical with respect to  $G_1$ ; for a particular design, the electronic efficiency varies from 50 to 60 per cent and back down to 50 per cent, as  $G_1$  is varied over a 5 to 1 range. The ratio  $g/g_0$  indicates at what fraction of the load for maximum power the magnetron operates and, therefore, is part of the output circuit problem.

The resonator impedance (which is a function of  $G_1$  and the other resonator characteristics) and the value of  $g/g_0$  are important in magnetrons designed for very high power output. It is also important that the rf voltage be kept as low as possible in the design of very high power tubes, in order that the electrons may interact efficiently and, in addition, so that arcing between the vane tips and between the straps is prevented. The impedance appearing at the vane tips should, therefore, be made as low as possible.

### Magnetron Scaling

Given the interaction-space design of a magnetron of known characteristics, the design of a magnetron of different characteristics but with the same electronic efficiency can be obtained by using scaling equations. This method was originated before the design equations discussed earlier were developed to their present state and is still used because of its convenience. It should be emphasized that the application of the scaling equations gives a design for a new magnetron of the same electronic efficiency as the original magnetron. Thus, if a magnetron for long wave length is scaled to provide a shorter-wave length magnetron, the over-all efficiency will usually decrease because the resonant circuit for the short wave length will usually have a lower circuit efficiency than that for the long wave length.

The scaling equations given below derive directly from the equations for the characteristic scale factors given previously. This derivation is equivalent to requiring that the ratio of the time required for an electron to move between two points in the original magnetron to the time required for an electron to move between corresponding points in the new magnetron should be proportional to the ratio of the wave lengths. It also requires that the electron execute the same number of convolutions in moving between the two points in each case. This requirement insures that the electronic efficiency remains constant. In earlier scaling equations,<sup>6</sup> this requirement was not included and the electronic efficiency, therefore, could change considerably if a large change in  $N$  were made. If  $N$  is the same for both designs, the equations reduce to the original scal-

ing equations derived by Clogston<sup>7</sup> as shown in the forthcoming paragraphs.

Eq. (10) for the ratio of cathode radius to anode radius is often ignored so that the cathode can be made larger to obtain improved mode stability (at the cost of reduced electronic efficiency). For this reason, the equations are given in terms of  $r_c$  and  $r_a$  instead of  $N$ , so that they may easily be applied even if Eq. (10) is not satisfied.

Define the following ratios where the subscript 1 refers to the original magnetron and the subscript 2 refers to the new magnetron.

$$\alpha = \frac{r_{a2}}{r_{a1}} \quad \theta = \frac{N_2}{N_1}$$

$$M = \frac{\lambda_2}{\lambda_1} \quad \phi = \frac{h_2}{h_1}$$

$$\delta = \left( \frac{N_2 - 4}{N_2 + 4} \right) \left( \frac{N_1 + 4}{N_1 - 4} \right)$$

if Eq. (10) is satisfied, the cathode radius is given by:

$$r_{c2} = \alpha \delta r_{c1} \quad (15)$$

If Eq. (10) is ignored,  $r_{c2}$  may be arbitrarily chosen; its value may be as large, perhaps, as 10 per cent higher than  $r_{a2} (N_2 - 4)/(N_2 + 4)$ .

The operating voltage of the new tube is

$$V_2 = V_1 \left( \frac{\alpha^2}{\theta^2 M^2} \right) \quad (16)$$

and the magnetic field of the new tube is given by

$$B_2 = B_1 \left( \frac{1}{\theta M} \right) \frac{\left( \frac{r_{c1}}{r_{a1}} \right)^2}{1 - \left( \frac{r_{c2}}{r_{a2}} \right)^2} \quad (17)$$

The current of the new tube corresponding to current  $I_1$  of the original tube is

$$I_2 = I_1 \left( \frac{a_{1,2}}{a_{1,1}} \right) \left( \frac{\alpha^2 \phi}{\theta^3 M^3} \right) \left[ \frac{1 - \left( \frac{r_{c1}}{r_{a1}} \right)^2}{1 - \left( \frac{r_{c2}}{r_{a2}} \right)^2} \right]^2 \left\{ \frac{r_{a1}}{1 + \frac{r_{a1}}{r_{c1}}} \right\}^2 \left\{ \frac{r_{a2}}{1 + \frac{r_{a2}}{r_{c2}}} \right\}^2 \quad (18)$$

and the corresponding cathode current density is

$$J_{c2} = J_{c1} \left( \frac{a_{1,2}}{a_{1,1}} \right) \left( \frac{\alpha^3}{\theta^3 M^3} \right) \frac{\left[ 1 - \left( \frac{r_{c1}}{r_{a1}} \right)^2 \right]^2}{\left[ 1 - \left( \frac{r_{c2}}{r_{a2}} \right)^2 \right]^2} \left( \frac{r_{c1} + r_{a1}}{r_{c2} + r_{a2}} \right) \quad (19)$$

The generated power  $P_2$  of the new tube corresponding to the generated power  $P_1$  of the original tube is given by

$$P_2 = P_1 \left( \frac{a_{1,2}}{a_{1,1}} \right) \left( \frac{\alpha^4 \phi}{\theta^5 M^5} \right) \frac{\left[ 1 - \left( \frac{r_{c1}}{r_{a1}} \right)^2 \right]^2}{\left[ 1 - \left( \frac{r_{c2}}{r_{a2}} \right)^2 \right]^2} \left\{ \frac{1 + \frac{r_{a1}}{r_{c1}}}{1 + \frac{r_{a2}}{r_{c2}}} \right\} \quad (20)$$

and the power output is

$$P_{02} = P_2 \eta_e \eta_{c2} \quad (21)$$

If  $N_2 = N_1$ , the equations are much simpler and are identical to those derived by Clogston,<sup>7</sup> i. e.,

$$\begin{aligned} V_2 &= V_1 \left( \frac{\alpha}{M} \right)^2 & r_{c2} &= r_{c1} \alpha \\ B_2 &= B_1 / M & J_{c2} &= J_{c1} \frac{\alpha}{M^3} \\ I_2 &= I_1 \frac{\alpha^2 \phi}{M^3} & P_2 &= P_1 \frac{\alpha^4 \phi}{M^5} \end{aligned} \quad (22)$$

The application of the equations is straightforward although it involves a cut-and-try procedure to obtain the desired characteristic of the new magnetron.

### Reduced-Performance Charts; Generalized Hartree Diagrams

A plot of contours of magnetic field, power output, efficiency, and sometimes frequency, in the voltage-current plane for a particular magnetron is known as its performance chart. Fig. 13 shows a performance chart of a typical pulse magnetron. The performance chart applies to a particular tube geometry (specified by  $N$ ,  $\mu$ ,  $r_c$ , and  $r_a$ ) operating with a particular loading, i. e., a specific resonant circuit and output circuit connected to a specific load, usually a matched load.

The preceding explanation has shown that from a given magnetron, operating at a particular operating point on the performance chart, the application of the scaling equations will give the characteristics of a new magnetron operating at a corresponding operating point. If a number of operating points on the performance chart of the original magnetron are all scaled to a new magnetron of a particular geometry and loading, the performance chart of the new magnetron may be predicted. It should be noted that  $\mu$  is not involved in the design equations or the scaling equations. Therefore, if

the results are to be absolutely accurate,  $\mu$  must be the same in both the original and the new magnetrons.

Calculation of the new performance chart can be simplified by plotting the universal or reduced-performance chart of the original tube. Fig. 14 shows the reduced performance chart of the type 2J32 magnetron whose conventional performance chart was given in Fig. 13. In Fig. 14, the reduced magnetic field, power output, and efficiency are plotted on the reduced voltage-current plane. The reduced or dimensionless variables are given by

$$\begin{aligned} b &= \frac{B}{B} & i &= \frac{I}{I} \\ v &= \frac{V}{V} & p &= \frac{P}{P} \end{aligned} \quad (23)$$

where  $B$ ,  $V$ ,  $I$ , and  $P$  are the magnetic field, voltage, current, and power generated, measured experimentally, while  $B$ ,  $V$ ,  $I$ , and  $P$  are the characteristic magnetic field, voltage, current, and power calculated from Eqs. (5, 6, 7, and 8).

Having derived this reduced-performance chart, the performance chart of any new magnetron may be obtained by calculating the characteristic factors  $B$ ,  $V$ ,  $I$ , and  $P$  and reapplying the above equations to obtain  $B$ ,  $V$ ,  $I$ , and  $P$  for the new tube. The electronic efficiency remains unchanged, provided the original and the new tube have the same  $\mu$  and loading. Therefore, the power output of the new tube is  $P \eta_c$ .

This reduced-performance chart represents all magnetrons having the same  $\mu$  and loading as the original tube for which it was plotted. That is to say, that if the effect of changes in  $\mu$  or in the loading are ignored, then one reduced-performance chart represents all magnetrons of the traveling-wave type. The performance chart for any new magnetron may be obtained from it by calculating the characteristic factors, multiplying them by the reduced variables, and taking into account the circuit efficiency in calculating the power output and over-all efficiency.

A Universal or Generalized Hartree Diagram is shown in Fig. 15; this diagram is useful in determining whether a tube is operating in the  $\pi$  mode. The diagram is plotted on a reduced-voltage-vs. -reduced-magnetic field plane so that it may be applied to tubes of any wave length and anode geometry. The operating point of a tube should lie just above the mode-number line  $k$  of the mode in which the tube is operating. Thus, for a tube operating in the  $\pi$  mode, the operating point should lie just above the line  $k = N/2$ .

The Generalized Hartree Diagram may also be used for designing a magnetron by a cut-and-try method. If values of  $N$ ,  $\lambda$ ,  $B$ ,  $r_c$ , and  $r_a$  are assumed, the normalized variables may be calculated and the operating voltage obtained from the chart by the use of the proper mode line,  $k = N/2$ . Operation at points near the Hull cutoff curve must be avoided because the efficiency in this region will be very low. For good electronic efficiency, operating points to the right of the dotted curve should be selected.

## MAGNETRON RESONANT CIRCUITS

Types of Resonant Circuits

For the magnetron to generate rf power, there must be an rf field with which the electrons in the space charge can interact. This field must be of the desired frequency and of the proper configuration for efficient generation of rf power. The resonant circuit provides this field by storing a quantity of energy, obtained over a number of rf cycles. The resonant circuit must be a stable frequency-determining element and must provide fields extending into the interaction space, where the electrons can interact with them.

The resonant circuit of a magnetron oscillator may be thought of as a filter circuit with a narrow pass band which permits only the desired frequency component in the electron stream to build up. As the magnetron starts oscillation, the resonant circuit absorbs and stores energy at this frequency. This storage results in increased rf electric field with which the electrons interact. The rf field, in turn, causes the electrons to bunch in such a way that their energy in the desired frequency component is increased. Thus, the resonant system can absorb more energy, present still higher fields to the electrons, etc. The start of oscillations is, as in the case of other oscillators, due to random fluctuations.

There are two major types of resonant circuits used in traveling-wave magnetrons. The strapped system, shown in Fig. 16, consists of a number of cavities having the same resonant frequency and having the front of alternate segments connected by straps to increase the frequency separation of the desired  $\pi$  mode from the other modes. The purpose of using many cavities is to reduce the required magnetic field and voltage for a given frequency and anode diameter. The cavities effectively operate in parallel and the frequency of the system is approximately that of a single cavity. The equivalent circuit of the strapped anode is shown in Fig. 17.

The second major type of resonant circuit for traveling-wave magnetrons is the rising-sun type shown in Fig. 18. The rising-sun system consists of  $N$  resonant cavities of two different frequencies. The large and small cavities alternate around the anode; their frequencies are so chosen to give optimum mode separation without the necessity of strapping. The rising-sun system has the advantage of permitting twice as large an anode diameter and anode length as the strapped anode, before other modes become troublesome. It is therefore used for very high-frequency and/or high-power tubes.

Because the strapped resonator system is the more common type, a method of design for this type follows.

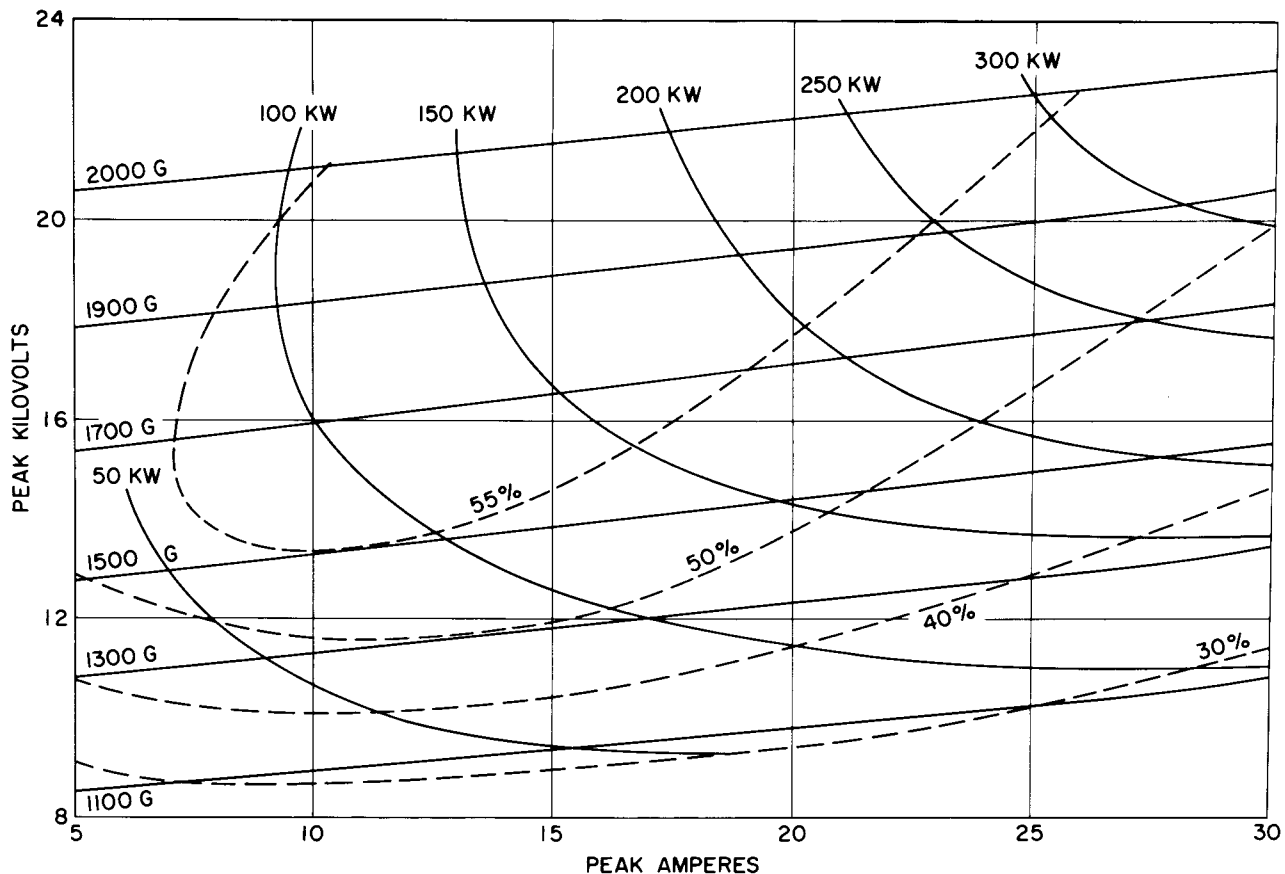


Figure 13. Performance Chart of a Typical Pulse Magnetron (Type 2J32) (frequency, 2800 Mc; pulse duration, 1  $\mu$ sec; prr, 1000 pps; pulling figure, 12 Mc)

Design information on rising-sun systems may be found on page 470 of Ref. 5.

### Design of Strapped-Resonator Systems

The basic requirement to be satisfied in designing the resonator system is to obtain values compatible with the interaction space design for the following four characteristics:  $\mu$ , the relative slot width;  $G_1$ , the slot conductance;  $Q_0$ , the unloaded  $Q$ , and  $\lambda$ , the resonant wave length. The handling of  $\mu$  and  $G_1$  was discussed earlier.  $Q_0$  should, of course, be as high as possible to give the maximum circuit efficiency (for a given  $Q_{ext}$  or output loading).  $Q_0$  increases with wave length and varies inversely as the number of resonators. It also varies inversely as the relative slot width and the slot conductance. In general, therefore, there is but a limited control over the value of  $Q_0$  because the range of these parameters is limited by other considerations. Approximate formulas for the calculation of  $Q_0$  for strapped anodes is given on page 466 of Ref. 5.

The most important resonator characteristic, the resonant wave length, is now to be determined. The basic method for determining the wave length is to solve Maxwell's equations in the resonator region. Because the boundary conditions at the junctions with the interaction space and the end space regions are complicated and require approximations, the effort of solving Maxwell's equations usually is not justified. Instead, it is normal practice to use approximate formulas to deter-

mine the wave length. The results are then verified by constructing a model anode whose frequency can be measured by cold test methods (See Chapter 18, Ref. 2). The approximation which follows is due to W. V. Smith (Ref. 3) and is accurate to within 5 per cent.

The equivalent circuit of a magnetron operating in the  $\pi$  mode can be represented by a simple parallel circuit of inductance  $L$  and capacitance  $C$ , whose values may be calculated from the tube geometry. If the magnetron is strapped, an additional shunt capacitance  $C_s$  is added which may be calculated from the strap geometry. The wave length  $\lambda$  is then obtained from:

$$\lambda = \sqrt{0.0355 L (C + C_s)} \quad (24)$$

where  $L$  is in micromicrohenries and  $C$  in micro-micromicrofarads.

Values of  $L$  and  $C$  may be obtained by constructing a scale drawing of the cavity, as shown in Fig. 19. The area of the cavity is divided into two areas:  $A_2$ , the area from the vane tips to a distance  $s/3$ , and  $A_1$ , the remaining area. Angles  $\theta_1$  and  $\theta_2$  are also constructed and measured.  $C$  and  $L$  are then obtained from:

$$C = 0.090 N (0.8 + 0.7 \operatorname{Cot} \theta_2 + 0.2 \operatorname{Cot} \theta_1 + 0.02 s/w) \quad (25a)$$

$$(h + 0.3 w) \text{ micromicrofarads}$$

$$L = \left( \frac{12,600}{N} \right) \left( \frac{A_1 + 0.3 A_2}{h + s/3} \right) \quad (25b)$$

$$\text{micromicrohenries}$$

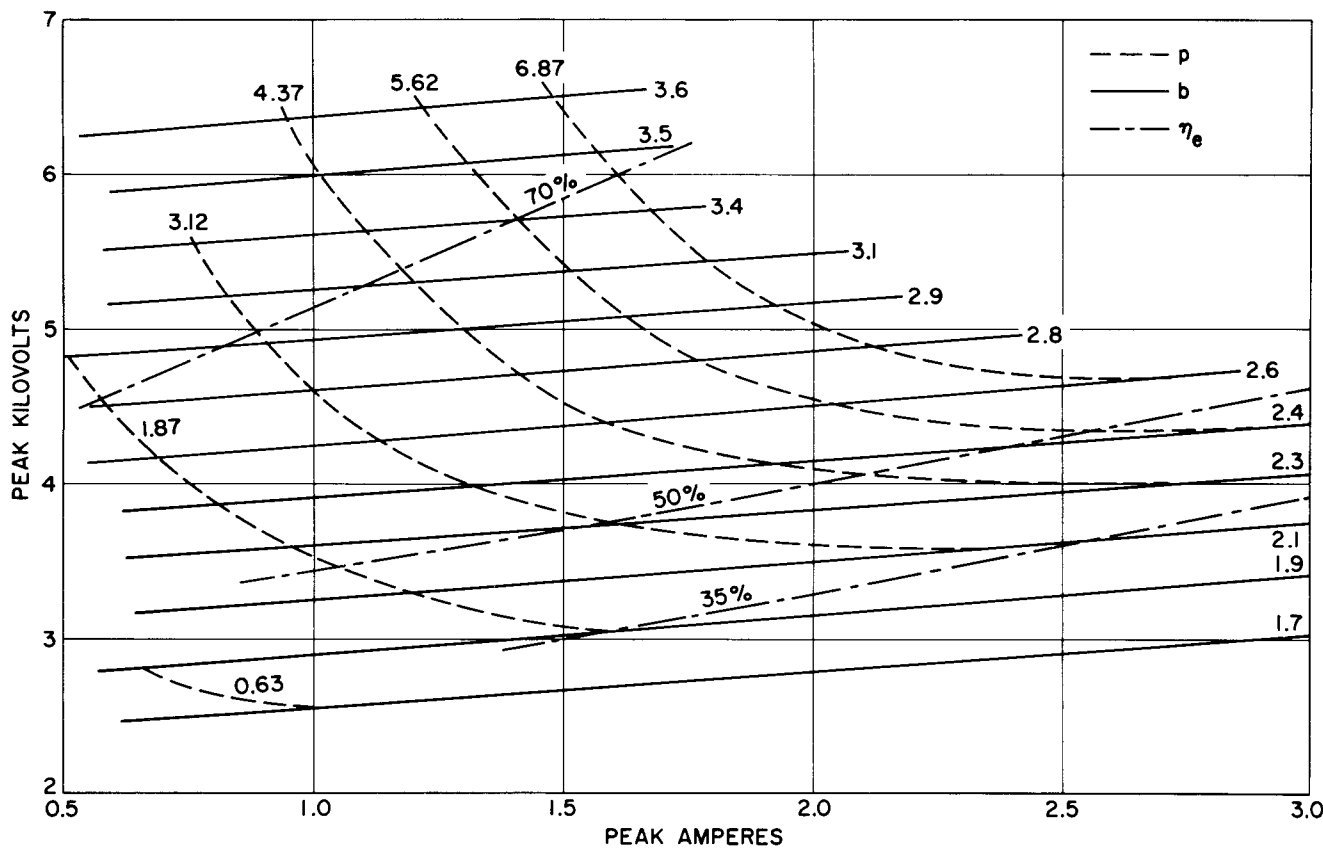


Figure 14. Reduced Performance Chart of Type 2J32 Magnetron ( $N = 8$ ;  $\sigma = 0.38$ ;  $\mu = 0.37$ ;  $g = 0.51$ )

where  $h$  is the axial height of the resonator.

The strap capacitance is calculated by using standard capacitance formulas. For double-ring strapping, the capacitance value will include the capacitance between the two straps (multiplied by two if there is a set of straps at each end of the anode) and the capacitance between each strap and the vanes which are not connected to the strap. Formulas for standard resonator geometries (for calculating  $C$  and  $L$ ), as well as formulas for some of the more common strap geometries, are given in Ref. 8.

## MAGNETRON TUNING

### Single Tuning Cavity

The most direct method of mechanically tuning<sup>9</sup> the frequency of a magnetron is to change the inductance or capacitance of its anode resonators. Fig. 20A illus-

trates two conventional methods used for this purpose. The "crown-of-thorns" method utilizes a number of pins that can be inserted into the back part of the magnetron resonators; these pins decrease the inductance of the resonant system and thereby tune the tube to a higher frequency. Magnetrons of this type are capable of producing a plate power output of approximately 500 kilowatts at a duty factor of 0.001 and can be tuned over a frequency range of 10 per cent within the X-band. Figure 20B illustrates the technique used to change the effective capacitance of the anode resonator. The bottom end of the "cookie-cutter" tuner is made to penetrate between the strap rings of the magnetron. By this method, the effective strap spacing is decreased; the accompanying increase in capacitance results in a lower resonant frequency. Although these methods can provide satisfactory tuning ranges, other performance characteristics, such as stability, may be adversely affected.

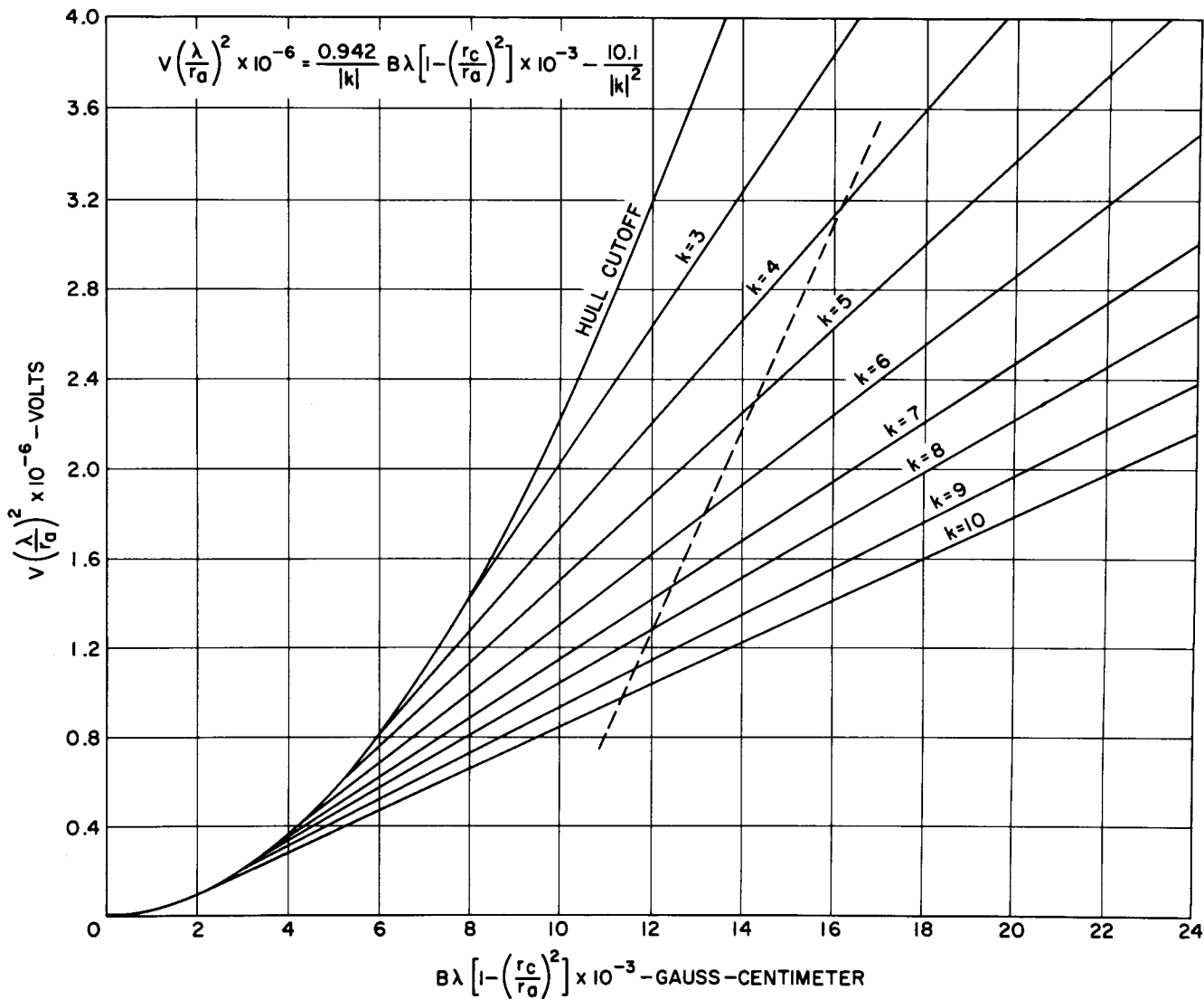


Figure 15. Universal (Generalized) Hartree Diagram

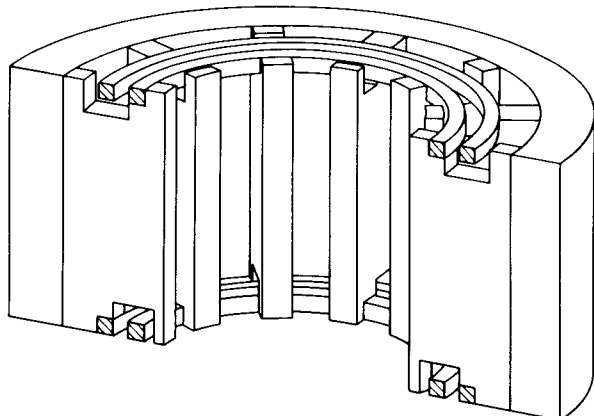
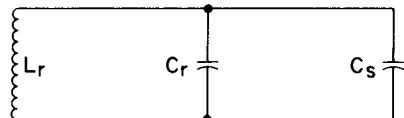


Figure 16. Double-Ring Strapped-Anode Block (Section)



$L_r$  = RESONATOR INDUCTANCE  
 $C_r$  = RESONATOR CAPACITANCE +  
 FRINGING CAPACITANCE  
 $C_s$  = STRAP CAPACITANCE

Figure 17. Equivalent Circuit of Strapped Anode

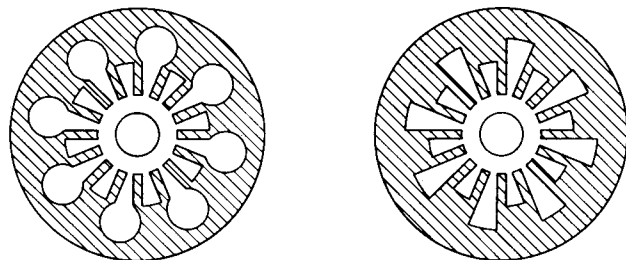


Figure 18. Rising-Sun Types of Anodes

Another method of changing the frequency of a magnetron is to vary the reactance coupled into the anode circuit by means of one or more external tuning cavities connected to anode resonators. This method is well suited for high-power tubes because it does not restrict anode cooling or require small dimensions which can lead to voltage breakdown problems. A commercial, high-power, X-band magnetron tuned in this manner has demonstrated nearly constant power output over a wide tuning range with simultaneous attainment of low thermal drift, good spectrum shape, and excellent mode stability even at high rates of voltage rise.

Tuning ranges slightly greater than the frequency separation between the  $\pi$  mode and the  $(N/2)-1$  mode have been obtained at high peak power output by use of four tuning cavities symmetrically arranged with respect to the anode, i. e., 90 degrees between adjacent tuning cavities. The use of four cavities reduces field

pattern distortion and improves mode stability. High-power tubes tuned with a single external cavity seem to be limited to bandwidths of the order of one-fourth the mode separation between the  $\pi$  mode and the  $(N/2)-1$  mode. This approximate limit is set by a decrease in electronic efficiency, increased heating of the cathode by back-bombardment, and moding — mostly as a result of field pattern distortion. However, certain continuous-wave (CW) magnetrons operating at a relatively low current level and power output, successfully use single-cavity tuning to cover a frequency range almost as great as the frequency separation between the  $\pi$  mode and  $(N/2)-1$  mode. Performance charts for single-cavity, high-power, pulsed tubes also confirm that much wider tuning can be obtained with good electronic efficiency when the power output is relatively low.

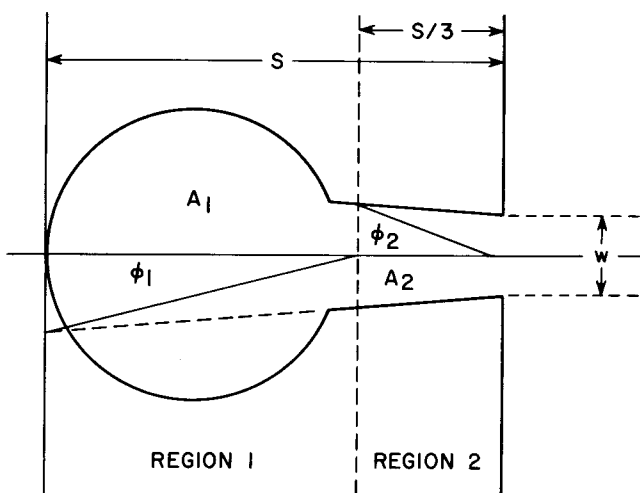


Figure 19. Resonator Geometry as Drawn for Calculation of Frequency

An important feature of cavity-tuned magnetrons is their relatively small thermal frequency drift when the tuner position or the input power is changed. These magnetrons usually have thermal characteristics superior to magnetrons which are tuned by elements having small clearance to the anode, because cavity tuners dissipate little energy and the consequent heating causes little movement of the tuner parts. Because the field configuration in the cavity is well understood, it is relatively easy to avoid extraneous tuner resonances and the associated problems of heating and drop in output power.

Description. Although the use of a single coupled cavity<sup>9, 10, 11, 12</sup> has given large tuning ranges only at relatively low power, a study of its characteristics is important because it helps in understanding some of the general considerations applicable to the design of multiple-cavity tubes.

Consider the magnetron anode and tuning arrangement shown in Fig. 20C. The double-strapped vane-type magnetron is coupled to a ridged wave guide tuning cavity through a slot in the resonator diametrically opposite to the output transformer. This cavity has the

desirable features of low characteristic impedance, wide band-width free from higher mode interference, and an adequately high  $Q$ . It can be constructed with the width of the ridge equal to the anode height, thereby permitting the use of a thin coupling iris which is relatively broadband. Because most of the energy in the cavity is in the region between the ridges, a movable short circuit between them provides a simple and effective tuner.

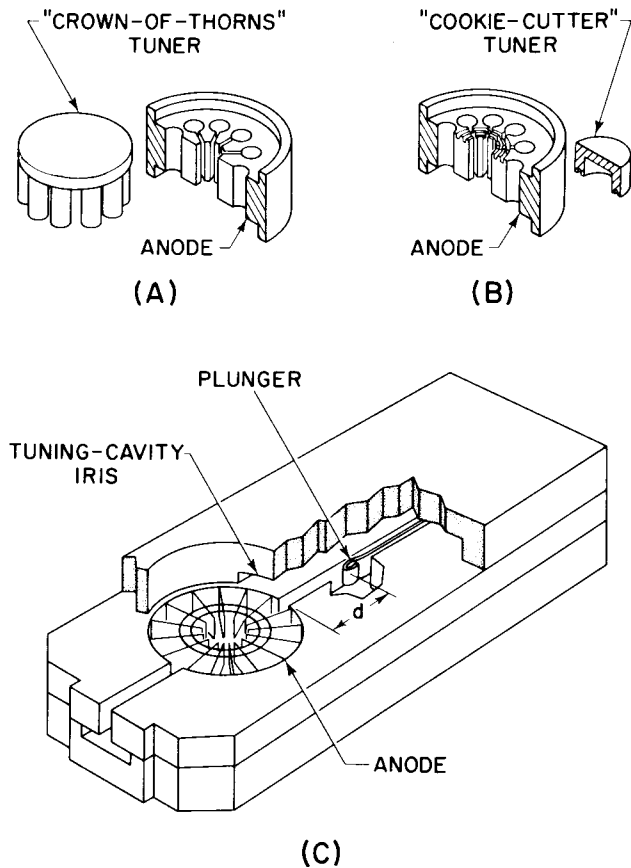


Figure 20. Magnetron Tuning: (A) Crown-of-thorns inductive tuning element and anode; (B) Cookie-cutter capacitive tuning element and strapped anode; (C) Single-cavity tunable magnetron

**Equivalent Circuit.** Microwave devices such as tunable magnetrons are usually large compared to the free-space wave length at which they operate and therefore involve parameters of a distributed nature. An equivalent circuit with lumped constants and having the same admittance or impedance function as the device can be synthesized according to network theory, but the usefulness of the circuit is restricted unless it has physically realizable parameters that can be directly related to parts of the device. Fortunately, for the case of the single-cavity tunable magnetron, there is a good equivalent circuit which is relatively simple.

An equivalent circuit, neglecting losses, for the single-cavity tunable magnetron is shown in Fig. 21. This circuit is an extension of one used previously by M. A. Herlin<sup>10</sup> and is valid over a much broader frequency range because all anode modes can be taken into

account, each mode being represented by one branch of a series inductance-capacitance (LC) circuit. The iris between anode and tuning cavity can be represented by a parallel combination of  $L$  and  $C$ ; if, however, the iris is resonant far from the frequency range of interest, a single shunt-reactance element is a good approximation. The ridge wave guide tuning cavity is represented by a section of wave guide terminated in a movable short circuit and having a characteristic admittance  $Y_0$ .

Derivation of an equation relating plunger position  $d$  to the resonant frequency of the system, now that the equivalent circuit has been established, is a straightforward network problem using the following relation which applies at resonance.

$$B_m + B_i + B_c = 0 \quad (26)$$

$B_m$ ,  $B_i$ , and  $B_c$  are, respectively, the susceptances of the magnetron anode, coupling iris, and a length  $d$  of tuning cavity terminated in a short circuit. These susceptances are given by:

$$B_m = \sum_{m=1}^{N/2} \frac{\sqrt{\frac{C_m}{L_m}}}{\lambda / \lambda_m - \lambda_m / \lambda} \quad (27)$$

$$B_i = \sqrt{\frac{C_i}{L_i}} (\lambda_i / \lambda - \lambda / \lambda_i) \quad (28)$$

$$B_c = -Y_0 \cot \left( \frac{2\pi d}{\lambda_g} \right) \quad (29)$$

$$\lambda_m = 2\pi c \sqrt{L_m C_m} \quad (30)$$

$$\lambda_i = 2\pi c \sqrt{L_i C_i} \quad (31)$$

where

$\lambda$  = free-space wave length

$Y_0$  = characteristic susceptance of tuning cavity

$\lambda_g$  = guide wave length in tuning cavity

$c$  = velocity of light

Substituting Eqs. (27), (28), and (29) into Eq. 26 and solving for  $d$  gives

$$d = \frac{\lambda_g}{2\pi} \cot^{-1} \left[ \sum_{m=1}^{N/2} \frac{\frac{1}{Y_0} \sqrt{\frac{C_m}{L_m}}}{\lambda / \lambda_m - \lambda_m / \lambda} \right] + \frac{n\lambda_g}{2} \quad (32)$$

where  $n = 0$ , or a positive integer

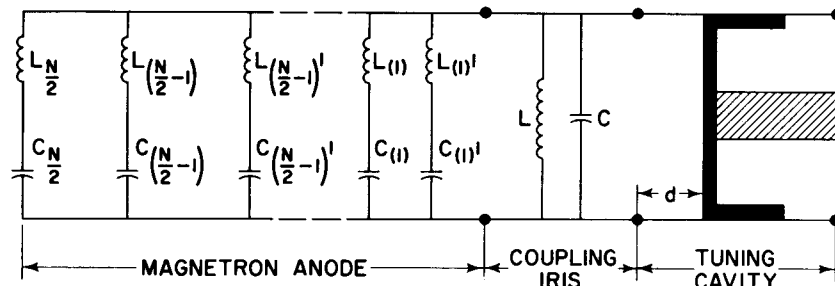


Figure 21. Equivalent Circuit for a Single-Cavity Tunable Magnetron

Using reasonable values for the parameters in Eq. (32) leads to curves of  $d$  vs.  $\lambda$  of the type shown in Fig. 22. These curves are commonly referred to as tuning curves.

Tuning Curves. Slater<sup>13</sup> has derived, by the solution of field equations, an expression similar to Eq. (32) for the tuning of a single multiple-resonant cavity tuned by a coupled wave guide with a movable short circuit. Because the magnetron anode can be considered as a multimode cavity, the general observations regarding the tuning curves for the magnetron and the multimode cavity are the same. As in the case of the multimode tunable cavity, a valuable insight into the characteristics of the tunable magnetron can be obtained from these curves.

From Fig. 22 it is seen that, when the plunger is at  $d = n\lambda_g/2$ , the resonant wave lengths of the circuit are those of the anode alone, the curves being continuous between adjacent anode modes and progressing from one mode to the next as the plunger is moved a distance  $\lambda_g/2$ . If the field pattern of an anode block is observed as the tube is tuned from the point B to the point C, the pattern will initially be that of the  $\pi$  mode, changing continuously as  $d$  is decreased, and finally assuming the pattern of the  $(N/2)-1$  mode. Thus, the field patterns become distorted when a mode is tuned; the amount of distortion is related to the mode separation and amount of tuning. Because field distortion is one of the main limitations on single-cavity-tuned tubes, the widest tuning ranges are obtained by operating about the  $\pi$ -mode resonance and by using a structure having a large mode separation. It also follows that expressing the tuning range as a percentage of the mode separation is meaningful, because it permits a better comparison of the performance of tubes operating at different frequencies and with different mode separations.

It is important to know the distribution of stored energy in the resonant system (as will be discussed later) in order to determine in which of several possible modes of oscillation a tunable magnetron will operate. An estimate of this stored energy can be obtained from the slope of the tuning curves. If most of the energy is in the tuning cavity, the tuning curves will be steep because a perturbation of the boundary (such as a slight motion of the plunger in a part of the system that contains a considerable portion of the energy) will cause a large change in frequency. On the other hand, the nearly horizontal parts of the tuning curves like those

shown at the  $(N/2)-1$  and  $(N/2)-2$  modes, indicate that nearly all of the energy is in the anode rather than in the tuning cavity.

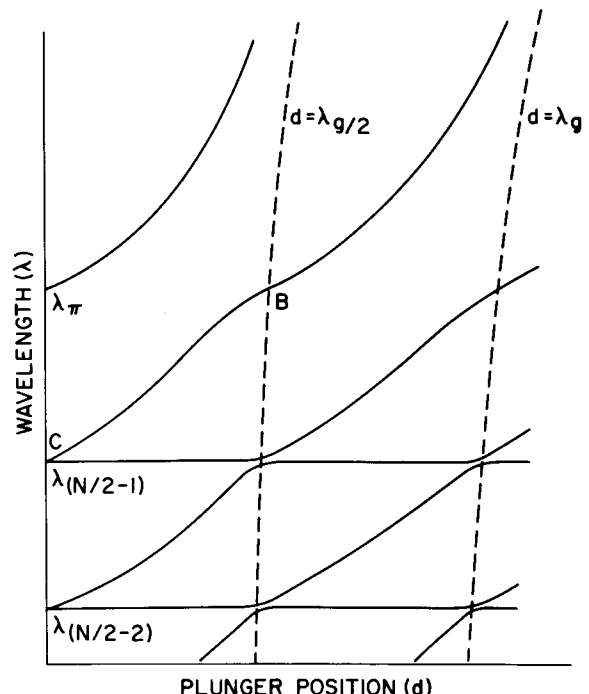


Figure 22. Tuning Curves of a Magnetron with a Single Coupled Tuning Cavity

Another quantity closely related to the distribution of energy is the degree of coupling of the anode to the tuning cavity for different modes. The degree is indicated by the slope of the tuning curves at wave lengths corresponding to anode resonances and by the value of  $(1/Y_0) \sqrt{L_m/C_m}$  in Eq. (32). Denoting this term by  $1/Q_{ext}\ m$ , it is seen that in this form  $Y_0$  appears as the loading on the series resonant circuit formed by  $L_m$  and  $C_m$ , the inductance and the capacitance of the magnetron anode. Resonances that do not tune will have a very high  $Q_{ext}\ m$  indicating, as it should, a very light coupling of the mode to the tuning cavity.

From Eq. (32) it should be noted that, at an anode resonance, the term  $B_1$  is negligible compared to the term  $B_m$ . Although the iris does not affect the shape of the tuning curves in this immediate frequency range, it is important at frequencies far removed from an anode

resonance. In these regions, an inductive iris will displace the curves to the right while one that introduces a shunt capacitance will displace the curves to the left.

To obtain precise values of the parameters for the equivalent circuit of a particular tunable magnetron, it is necessary to use information from its experimental tuning curves. From these values, the anode resonant frequencies and the slope of the curves at the resonances can be obtained. Differentiating Eq. (32) with respect to  $\lambda$  and evaluating at the anode resonances gives

$$\left( \frac{dd}{d\lambda} \right)_{\lambda=\lambda_m} = \frac{\lambda_{gm}}{\lambda_m} \left[ \frac{Y_0}{\pi} \sqrt{\frac{L_m}{C_m}} + \frac{n}{2} \left( \frac{\lambda_{gm}}{\lambda_m} \right)^2 \right] \quad (33)$$

where  $\lambda_{gm}$  is the guide wave length evaluated at  $\lambda = \lambda_m$ .

Substituting the measured value of slope and the  $Y_0$  computed from the dimensions of the cavity into Eq. (33), permits the evaluation of  $L_m/C_m$ . Therefore,  $L_m$  and  $C_m$  can be determined because their product is known from the anode resonant frequency. The parameters of the iris can be obtained from its dimensions or they can be determined with the aid of additional points on the tuning curves, preferably at frequencies far removed from that of an anode resonance. Tuning curves computed from equivalent circuits give excellent agreement with experimental results.

Stabilization Factor. The energy stored in the tuning cavity of a magnetron partially stabilizes it against frequency changes resulting from variations in rf load and input conditions and is an important consideration that must be taken into account to arrive at a wide-tuning-range design. The division of stored energy in the system is given by the stabilization factor  $S$ ,<sup>14</sup> which is defined as the ratio of the total energy stored in the magnetron anode, coupling iris, and tuning cavity to that stored in the magnetron anode alone.

$$S = \frac{W_m + W_i + W_c}{W_m} \quad (34)$$

An expression for this quantity in terms of the parameters of the equivalent circuit can be obtained by use of circuit theory. The theory states that in a resonant system the stored energy is equal to the peak instantaneous energy in either the electromagnetic field or the electrostatic fields. At a frequency other than resonance, these energies are not equal; the stored energy in the system is always the smaller of the two. It has also been shown<sup>15</sup> that, in general,

$$B_s = \frac{2 (W_e - W_h) \omega}{|E|^2} \quad (35)$$

$$\frac{dB_s}{d\omega} = \frac{2(W_e - W_h)}{|E|^2} \quad (36)$$

where  $B_s$  is the shunt susceptance,  $E$  is the terminal

voltage, and  $W_e$  and  $W_h$  are the peak instantaneous stored electric and magnetic energies in the system.

Solving Eqs. (35) and (36) for  $W_e$  and  $W_h$  and taking the smaller value to be the stored energy  $W_s$  gives

$$W_s = \frac{|E|^2}{4} \left( \frac{dB_s}{d\omega} - \left| \frac{B_s}{\omega} \right| \right) \quad (37)$$

Combining Eqs. (34) and (37) gives

$$S = 1 + \frac{\left[ \frac{dB_c}{d\omega} + \frac{dB_i}{d\omega} \right] - \left[ \left| \frac{B_c}{\omega} \right| - \left| \frac{B_i}{\omega} \right| \right]}{\frac{dB_m}{d\omega} - \left| \frac{B_m}{\omega} \right|} \quad (38)$$

This expression is valid for computing stabilization at all values of  $\lambda$  except at  $\lambda = \lambda_m$ , where  $B_m$  and  $B_c$  go to infinity.

An expression for  $S$  valid at  $\lambda = \lambda_m$  can be obtained from the following general network relations:<sup>15</sup>

$$X = \frac{2 (W_h - W_e) \omega}{|I|^2} \quad (39)$$

$$\frac{dX}{d\omega} = \frac{2 (W_h - W_e)}{|I|^2} \quad (40)$$

where  $X$  is the series reactance and  $I$  is the terminal current.

Solving for  $W_h$  or  $W_e$  and evaluating at resonance gives the stored energy. Substituting this value of stored energy into Eq. (34) gives the following expression for  $S$  which is valid  $\lambda = \lambda_m$

$$S_{\lambda=\lambda_m} = 1 + \frac{\frac{dX_c}{d\omega} \Big|_{\lambda=\lambda_m}}{\frac{dX_m}{d\omega} \Big|_{\lambda=\lambda_m}} \quad (41)$$

The stabilization factor can be computed at any point on the tuning curves by use of Eqs. (38) and (41) and the expressions for  $B_m$ ,  $B_i$ , and  $B_c$ .

It has been shown that the speed of starting in a particular mode of oscillation varies inversely with the degree of stabilization of the mode.<sup>16</sup> Therefore, if it is desired to have a broadband tunable design which will operate at fast rates of voltage rise and without the added complexities of damping the interfering modes, it is necessary that the stabilization factor be small. Furthermore, from considerations of Eqs. (32), (38), and (41), it can be shown that, once the maximum value of stabilization factor has been fixed, the greatest tuning

range of a particular mode is obtained by a tight coupling between anode and tuning cavity.

Mode Selection Criterion. It would be very desirable to have a criterion that would enable one to predict the exact operating frequency range of a tunable magnetron. This range, however, is difficult to establish because mode selection is a very complicated process involving many variables. Some of these variables include power supply impedance, cathode size and emission, field pattern distortion, voltage pulse rate of rise, mode separation, stabilization factor, and rf load.

An approximate criterion useful for maximizing the tuning range can be established<sup>17</sup> from the principle of minimum dissipation proposed by B. Von der Pol.<sup>18</sup> This principle states that if a self-oscillatory system has more than one possible mode of operation, it will operate in the mode requiring a minimum dissipation from the power sources present in the system. It follows that a magnetron will tend to operate in the mode that has the greatest ratio of energy stored in the magnetron anode to the total energy dissipated, i. e., it will tend to operate in the mode with the highest value of  $Q_L/S$ .

That this ratio is not the only factor that determines the mode selection is evident from an inspection of the tuning curves shown in Fig. 22. Here it is seen that one of the  $(N/2)-1$  modes does not tune and therefore has a stabilization factor approximately equal to unity. Furthermore, because this mode has two-fold symmetry, the weak coupling to the tuning cavity indicates that it will also be lightly coupled to the output by a transformer diametrically opposite the tuning cavity. Even though this mode has a high value of  $Q_L/S$ , tubes operate in the  $\pi$  mode with relatively little mode interference over at least a part of this region. However, it is known that this non-tunable mode does cause serious interference in some regions and that decreasing its  $Q_L/S$  decreases the interference.

## Four-Cavity Tunable Magnetrons<sup>19</sup>

The advantages accrued by coupling tuning cavities to resonators (see Fig. 23) can be explained by showing how this arrangement overcomes the limitations encountered with single-cavity tuning. It is evident from the symmetry and number of tuning cavities that the field pattern will be less distorted. The tuning curve that passes through the  $\pi$ -mode wave length at  $d = \lambda_g/2$  will also pass through the  $(N/2)-2$  mode wave length at  $d = 0$ ; the result is a relatively large frequency range over which the  $\pi$ -mode configuration is only slightly distorted. Tests on a pulsed, high-power, X-band tube have shown that there is no appreciable degradation in performance from pattern distortion for an 18 per cent frequency band, this percentage being 1.2 times the separation between the  $\pi$  mode and the  $(N/2)-1$  mode. The uniformity of output coupling as a function of frequency is also improved, because the impedance of the output resonator remains more nearly constant. No compensation for changes in coupling is required when the tube is tuned.

Single-cavity tunable tubes, as shown in Fig. 20, have

one  $(N/2)-1$  mode that does not couple to the tuning cavity and output wave guide. As indicated previously, this fact establishes a favorable condition for oscillation in this mode. A magnetron with four cavities equally tuned and symmetrically arranged with respect to the anode does not have this difficulty. Both  $(N/2)-1$  modes have high tuning rates because their doublet nature requires that they have positions for maximum coupling at resonators separated spatially by 90 degrees. In fact, for a tube with 16 resonators as shown in Fig. 23, both doublets of all odd-numbered modes will tune. Furthermore, the loading of the  $(N/2)-1$  modes by the output can be approximately equalized over a wide frequency range by locating the output at 45 degrees with respect to the tuning cavities and by tuning two diametrically opposite cavities so that they are slightly longer than the other two cavities. This arrangement introduces a discontinuity which orients the  $(N/2)-1$  modes for equal coupling to the output resonator. Thus, the  $Q_L/S$  ratio can be made much more favorable for the desired mode with four-cavity tuning than by use of a single-cavity tuning. It is also evident that a minimum of four cavities must be tuned to satisfy the symmetry requirement and provide, at the same time, tuning curves with favorable  $Q_L/S$  ratios.

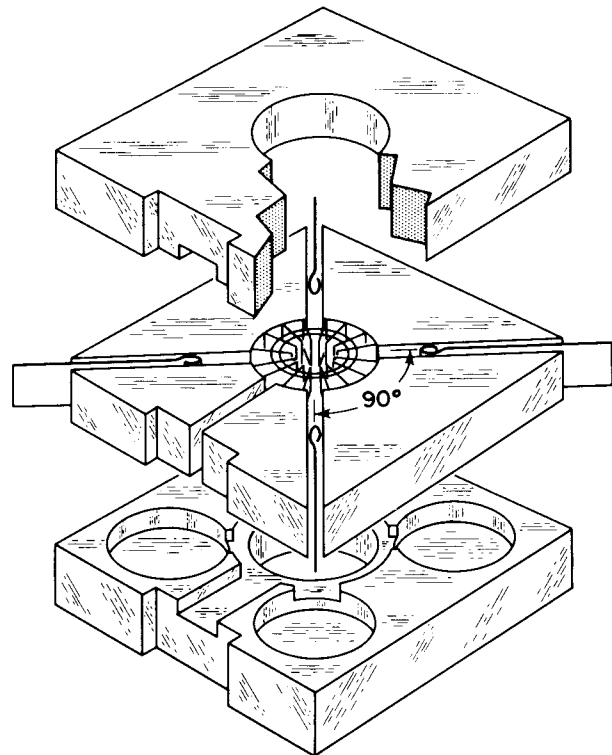


Figure 23. Magnetron with Four Tuning Cavities

Four-cavity X-band pulsed magnetrons of the type shown in Figs. 23 and 24 give tuning ranges of 1100 megacycles or greater (as compared to 300 megacycles for single-cavity tuned tubes).

## MAGNETRON CATHODES

The cathode is subject to a number of stringent conditions which must be met for proper magnetron operation.

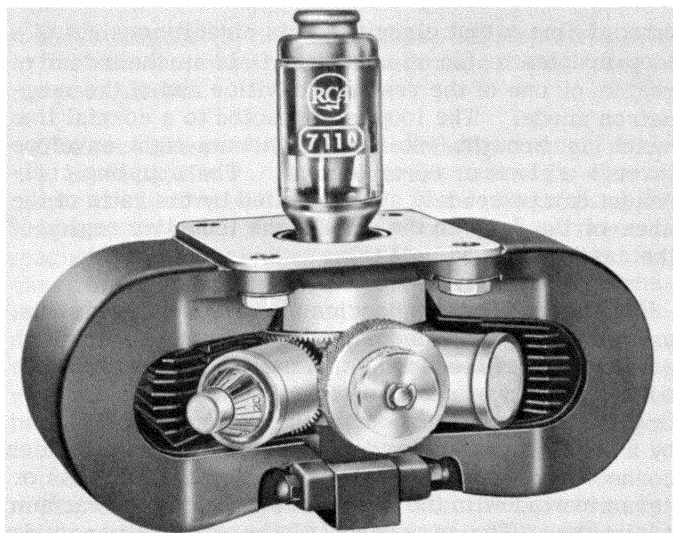


Figure 24. Tunable Magnetron, RCA-7110

First, the cathode must furnish a large current density without sparking or becoming temperature limited to an extent that sufficient change in potential distribution occurs to cause moding or even a decrease in efficiency. Pulsed tubes usually operate at current densities of 25 amperes per square centimeter and values as high as 100 have been attained.

Second, the cathode must withstand bombardment by returned electrons and ions and must have sufficient thermal capacity and cooling to dissipate the back bombardment energy without overheating. Often it is necessary to decrease the heater power to zero when a magnetron is oscillating. The cathode diameter for a given anode design is limited by the decrease in electronic efficiency which occurs if the cathode is made too large.

Third, the cathode must provide an axial boundary to electron flow. The magnetron operates at a voltage several times that of a tube with similar geometry but with no magnetic field. The resulting high space-charge repulsion forces would cause an excessive axial current from the ends of the interaction space if no boundary were provided.

In view of these conditions, it is not surprising that the cathode is usually the element responsible for determining the end of life of the magnetron. As a corollary, it follows that the design of a long-life magnetron requires a massive cathode and operation of it at low current density and at a low temperature. This design has been used in the case of the type 6521 magnetron (used in commercial airline weather radar) to give tubes with a mean life of 6000 hours as compared to the life of 250 to 500 hours for magnetrons less conservatively designed.

The large current density required from a pulsed magnetron cathode is not such a problem as it might initially appear. First, pulsed magnetrons are normally operated at short pulse lengths — a few microseconds, or even less, for high-frequency tubes. The

peak pulse emission which can be drawn from a cathode is many times the steady-state emission. In addition, because most cathodes are reasonably good secondary emitters, the back-bombarding electrons knock out secondaries which add to the primary emission.

The cathode thermal dissipation problem is more serious. Three to ten per cent of the input power may be expected to appear as cathode back-bombardment power. Maintaining a reasonable cathode temperature often requires the use of heavy support structures and large radiating surfaces to increase the thermal dissipation. The extension above the top end hat of the center cathode in Fig. 25 is designed to increase the area available for thermal radiation. The roughening of surface areas of the cathode support by sand blasting or spraying with molybdenum powder is a means of increasing thermal dissipation.

The increased thermal dissipation required to compensate for back bombardment introduces the additional problem of heater life. The available space for the heater is very limited and, therefore, magnetron heaters often must be operated at temperatures far higher than those employed in other tube types. The high temperatures complicate the task of insulating the heater; consequently, heater shorts due to the failure of the alumina oxide insulation are a problem. Additions of small amounts of titanium dioxide and chromium to the coating are sometimes made to increase the thermal emissivity of the heater so that its temperature for a given amount of heat radiated is decreased. In some instances, a molybdenum powder coating is sintered to the heater before coating it with insulation to increase the adherence of the insulating coating. Quality control measures are also indicated; the cycling of sample heaters out of each coated lot in dummy cathodes is frequently done before the lot is approved for use.

The normal method of providing axial boundaries to the space charge is by the use of enlarged diameters of the cathode support at each end of the cathode. These supports are called end hats or end shields. Here again, another difficulty is introduced by this solution. If the end hats have large electron emission, either primary or secondary, they are useless. The most effective techniques for reducing end-hat emission are the prevention of contamination by the emission material and the design of the cathode structure to provide low end-hat temperatures by isolation of the end hats, or by other means. In some cases, these methods are not adequate and it is therefore necessary to reduce end-hat emission by chromizing (diffusion of chromium into molybdenum end hats and then oxidation of the material) or by coating with zirconium powder. Both of these techniques reduce the end-hat temperature by increasing radiation; their effectiveness is partly due to this reduction.

Several typical magnetron cathodes are shown in Fig. 25. The left cathode, of the thoria-dispenser type, is for a 200-watt X-band CW tube. The outer sleeve is made of molybdenum and has a number of 0.010-inch holes drilled in it. The inside of the cylinder is packed with thoria, some of which reduces to thorium and migrates through the holes to the outside

of the cathode. The cathode operates at a temperature of 1300 to 1400°C and gives a CW current density of 1.5 amperes per square centimeter. Its life is relatively short (a few hundred hours) due to the high operating temperature and the small size which results in a mechanically weak structure. Larger cathodes of this type give lives of a thousand hours or more at similar current density and temperatures.

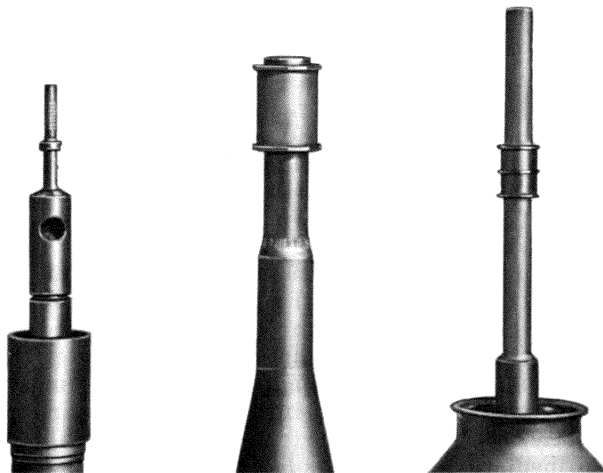


Figure 25. Typical Magnetron Cathodes

The cathode in the center is for the type 6521, an 80-kilowatt pulsed C-band magnetron which was designed specifically for long life. It is of the sintered nickel type. A layer of fine nickel (0.030-inch thick) powder is pressed on the inner molybdenum sleeve and sintered in a hydrogen furnace. A barium carbonate emission mixture is cataphoretically coated on the sintered nickel, filling the pores to a considerable depth. The nickel is then compacted in a press to the final cathode size. This cathode operates at a temperature of about 850°C at a current density of 5 amperes per square centimeter for pulsed conditions and gives a mean life in excess of 6000 hours.

The cathode on the right in Fig. 25 is used in the 7008/7010/7111 series of tunable 200-kilowatt X-band magnetrons, one of which is shown in Fig. 24. This cathode has an active surface of type-A barium aluminate impregnated tungsten. It consists of a sleeve of porous tungsten impregnated with barium aluminate and brazed to the molybdenum supporting structure. The end hats are chromized to prevent emission. The cathode operates at a temperature of 800 to 900°C and a current density of 27 amperes per square centimeter. The life is of the order of 1000 hours. These results demonstrate the value of the impregnated-tungsten cathodes because the untuned version of this tube (4J50) which used a sintered nickel cathode had a life of only about 250 to 500 hours.

#### OUTPUT CIRCUITS

Most magnetrons employ one of two major types of output circuits. At frequencies below 400 megacycles, low- and moderate-power magnetrons usually have a

coaxial-line output circuit. This circuit consists of a loop coupled to the rf magnetic field in the inductive region of one of the resonant cavities and of the magnetron anode. The loop is connected to a coaxial line which is brought outside the vacuum-tight envelope through a glass or ceramic seal. The coupling coefficient can be crudely approximated by the ratio of the area of the loop to the area of the inductive region of the cavity (Ref. 5, p. 191).

Magnetrons for frequencies above 4000 megacycles, as well as magnetrons designed to operate at very high power at lower frequencies, usually have a wave guide output. This type of output normally consists of a coupling slot in the back of one of the resonators, followed by a  $\lambda/4$ -ridge-wave guide matching transformer which connects to a standard wave guide. A matched glass or ceramic window in the wave guide provides the vacuum enclosure. The impedance of the ridged-wave guide matching section is the geometric mean between the impedance at the back of the resonator and the impedance of the standard wave guide. Because the impedance at the back of the resonator is normally in the range of a fraction of an ohm to a few ohms, the matching section impedance is roughly 40 ohms to give a match to the 377-ohm standard wave guide impedance. The length of the matching section must be near enough to  $\lambda/4$  so that an excessive amount of reactance is not coupled into the tube. Other than causing a frequency change, the detrimental effect of coupling reactance into the tube is one of pattern distortion of the rf field patterns around the anode. The usual criterion for coupled reactance is that it does not have a value in excess of the coupled resistance. This requirement is not a stringent; the simple  $\lambda/4$  transformer satisfies it over a wide enough bandwidth for even the widest-tuning-range tunable magnetrons.

The degree of coupling of the magnetron to the load is indicated by the external  $Q$  which is defined as the energy stored in the resonant circuit per cycle divided by the power to the load.  $Q_{ext}$  may be measured by cold impedance measurements or may be calculated approximately.<sup>5</sup> The pulling figure of the magnetron is defined as the maximum frequency change occurring when a load having a voltage standing-wave ratio of 1.5 is varied through all phases. As  $Q_{ext}$  is decreased, the circuit efficiency and the pulling figure increase. The value of  $Q_{ext}$ , therefore, is a compromise between optimum efficiency and the value of pulling figure which can be tolerated. A high pulling figure may cause long-life effects or it may cause the magnetron to mode.

The Rieke Diagram<sup>5</sup> shows the performance of the magnetron with constant input conditions but with varying load. It consists of contours of constant frequency, power output, and voltage (taken at constant anode current) plotted on the Smith impedance chart.

#### THE MAGNETIC CIRCUIT

There are two aspects to the design of magnetic circuits for magnetrons: (1) the design of the pole-piece geometry to give the desired shape of magnetic field in the interaction space, and (2) the design of the per-

structure. The propagation constant can be calculated or experimentally determined for any type of slow-wave structure.

#### MATHEMATICAL DESCRIPTION OF A WAVE ON A SLOW-WAVE STRUCTURE IN THE PRESENCE OF AN ELECTRON BEAM

When an electron beam interacts with the wave on a slow-wave structure, the propagation constant of the structure  $\Gamma_1$ , is modified by the presence of the beam and may be denoted as  $\Gamma$ . Thus, the equation for the wave on the slow-wave structure in the presence of the electron beam becomes

$$V(z, t) = V_1 e^{i\omega t - \Gamma z} \quad (5)$$

This new propagation constant  $\Gamma$  fully describes the amplitude and velocity of the rf signal at any given time and place in the slow-wave structure of an operating traveling-wave tube. Once  $\Gamma$  is determined, the relative signal amplitudes at the input and output of a traveling wave tube can be compared, and the gain calculated.

#### THE DETERMINATION OF $\Gamma$

The development of the equation describing  $\Gamma$  is basically the same as that for the interaction between the wave and the electron of transmission line down which the wave is propagated and that a nearby electron beam has a velocity close to the phase velocity of the wave on the transmission line. A small ac or rf signal is assumed to be on the transmission line and the effect of this signal on the electron beam is calculated. Then it is assumed that a small ac signal is on the electron beam (effectively a small amount of bunching or rf modulation) and the effect that this modulation on the electron beam has on the transmission line is calculated. The two relationships are equated and the resulting transcendental equation defines  $\Gamma$  in terms of the propagation constant of the slow-wave structure and the parameters of the beam.

$$\frac{i K I_0 \beta_e \Gamma^2 \Gamma_1}{2 V_0 (\Gamma_1^2 - \Gamma) (i \beta_e - \Gamma)} = 1 \quad (6)$$

where

$$\Gamma_1 = -i \frac{\omega}{v_p} \quad (\text{it is assumed that the slow-wave structure is lossless})$$

$$\beta_e = \frac{\omega}{u_0} \quad (\text{where } u_0 \text{ is the velocity of the electron beam})$$

$K$  is the impedance of the slow-wave structure encountered by the beam and may be calculated or determined experimentally;

$I_0$  is the beam current;

$V_0$  is the beam voltage.

It is further assumed that  $v_p$  is not too different from  $u_0$  and that  $\Gamma$  is not too different from  $\Gamma_1$ . The number of symbols may be reduced by defining  $C^3$  as follows:

$$C^3 = \frac{K I_0}{4 V_0} \quad (7)$$

The determinantal equation for  $\Gamma$  may then be expressed as follows:

$$\frac{2i C^3 \Gamma^2 \Gamma_1}{(\Gamma_1^2 - \Gamma^2)(i \beta_e - \Gamma^2)} = 1 \quad (8)$$

This equation is in the fourth power of  $\Gamma$  and has four possible solutions. The solution is simplified by further assuming that the electron velocity is equal to the cold-phase velocity of the structure; i.e.,  $-\Gamma_1 = i \beta_e$ .

The solution has the following form:

$$\Gamma = i \beta_e - \delta \beta_e C \quad (9)$$

where

$$\delta_1 = \frac{\sqrt{3}}{2} - \frac{i}{2}$$

$$\delta_2 = -\frac{\sqrt{3}}{2} - \frac{i}{2}$$

$$\delta_3 = -i$$

The fourth solution describes the wave traveling in a direction opposite to the beam, but not interacting with the beam. This solution is lost in making the approximation required to arrive at the other three solutions.

The propagation constant  $\Gamma$  in terms of  $\beta_e$  and Pierce's gain parameter  $C$  can be substituted into Eq. (5) to calculate the gain of a traveling-wave tube.

#### CALCULATION OF GAIN

When the three solutions for  $\Gamma$  are substituted into the wave equation [Eq. (5)], the following equations result:

$$V(z, t) = V_1 e^{i \left[ \omega t - \left( \frac{\omega}{u_0} + \frac{\omega}{2u_0} C \right) z \right]} e^{\frac{\sqrt{3}}{2} \beta_e C z} \quad (10)$$

$$V(z, t) = V_1 e^{i \left[ \omega t - \left( \frac{\omega}{u_0} + \frac{\omega}{2u_0} C \right) z \right]} e^{-\frac{\sqrt{3}}{2} \beta_e C z} \quad (11)$$

$$V(z, t) = V_1 e^{i \left[ \omega t - \left( \frac{\omega}{u_0} - \frac{\omega}{u_0} C \right) z \right]} \quad (12)$$

The first of these three equations describes a wave traveling at a velocity slower than the beam velocity and increasing exponentially in amplitude. The second equation describes a wave again traveling slower than the beam velocity, but with an amplitude which is decreasing exponentially with distance. The third equation shows a wave traveling faster than the beam velocity, but not changing in amplitude.

An input signal which is fed onto the slow-wave structure is divided equally among these three waves. After

traveling only a short distance down the slow-wave structure, the increasing amplitude of the first wave very quickly swamps out the effect of the other two waves which then have an increasingly negligible amplitude compared to the first wave. Thus, the voltage at the output is

$$V_{\text{out}} = \frac{V_{\text{in}}}{3} e^{\frac{\sqrt{3}}{2} \beta_e C l} \quad (13)$$

where  $\sqrt{3}/2 \beta_e C$  is the attenuation constant from Eq. (10),  $l$  is the length of the slow-wave structure and the  $1/3$  term comes from the input signal being divided equally between the three waves. The power gain in db can now be written

$$G = 20 \log \frac{V_{\text{out}}}{V_{\text{in}}} = 20 \log \frac{1}{3} + 20 \log_e \frac{\sqrt{3}/2 \beta_e C l}{\lambda} \quad (14)$$

or

$$G = -9.54 + 47.3 C N \quad (15)$$

where  $N$ , the number of wavelengths in the slow-wave structure, is equal to

$$\frac{1 \beta_e}{2 \pi}$$

Eq. (15) was derived with certain simplifying assumptions: a lossless slow-wave structure, a beam velocity equal to the phase velocity of the slow-wave structure, and no space charge parameter. Practical tubes do not satisfy these assumptions, and the gain equation must be modified to take into account the following effects:

1. Lumped attenuation, which is usually introduced to prevent the tube from oscillating.
2. An arbitrary electron velocity.
3. The passive or higher order mode parameter  $Q$ .

The more complete gain equation is now written as follows:

$$G = A + B C N - L_{\text{att}} \quad (16)$$

where  $L_{\text{att}}$  is the loss due to the lumped attenuation. The initial loss parameter  $A$  and the growing-wave parameter  $B$  become functions of the distributed loss, the electron velocity, and the space-charge parameter  $Q C$ . The passive-mode parameter  $Q$  may be found from Fig. 5, where it is plotted as a function of  $\gamma_a$  for different values of beam-to-circuit diameter. The function  $\gamma_a$ , the radial propagation constant, which is the argument for the Bessel functions which describe the fields in the interaction region, are described under SLOW-WAVE STRUCTURES. The function may be defined as follows:

$$\gamma_a = \frac{\omega}{u_0} = \frac{2 \pi a}{\eta_g} \quad (17)$$

Although not exact, this function is a close approximation for tubes operating below 10,000 volts.

Figs. 6 and 7 show the dependence of  $A$ , the initial-

loss parameter, and  $B$ , the growing-wave parameter on the parameter  $Q C$ . Fig. 8 shows the attenuation or loss of gain which is to be expected with the introduction of the lumped attenuator. This curve is based on the assumption that the slow-wave circuit is severed and a drift tube of length measured by  $C N$  is substituted for the circuit, as is very nearly the case when a lumped attenuator with a loss in the order of 20 db per wavelength or more is used. The wave beyond the drift tube has a level with respect to the incident wave shown by the ordinate.

Almost all the information required to calculate the gain of the traveling-wave tube is now available. The initial loss  $A$ , the growing-wave parameter  $B$ , and the loss due to the attenuator can be obtained from Figs. 5 through 8. The length of the tube  $N$  in helix or slow-wave wavelengths can be readily calculated from the following equation:

$$N = \frac{1 \beta_e}{2 \pi} = \frac{1.506}{\lambda \sqrt{V_o}} \quad (18)$$

The only factor remaining to be determined is the impedance parameter  $K$ , which is included in the expression for the gain parameter  $C$ . How this parameter is determined is described under Helix and Other Slow-Wave Structures because  $K$  is necessarily a function of the slow-wave circuit used.

## FORWARD-WAVE AMPLIFIER DESIGN

This section deals with the actual design of the forward-wave traveling-wave tube amplifier, specifically, the helix and other types of slow-wave structures, the electron gun, the focusing structure, the couplers, the attenuator, and the collector.

## THE HELIX AS A SLOW-WAVE STRUCTURE

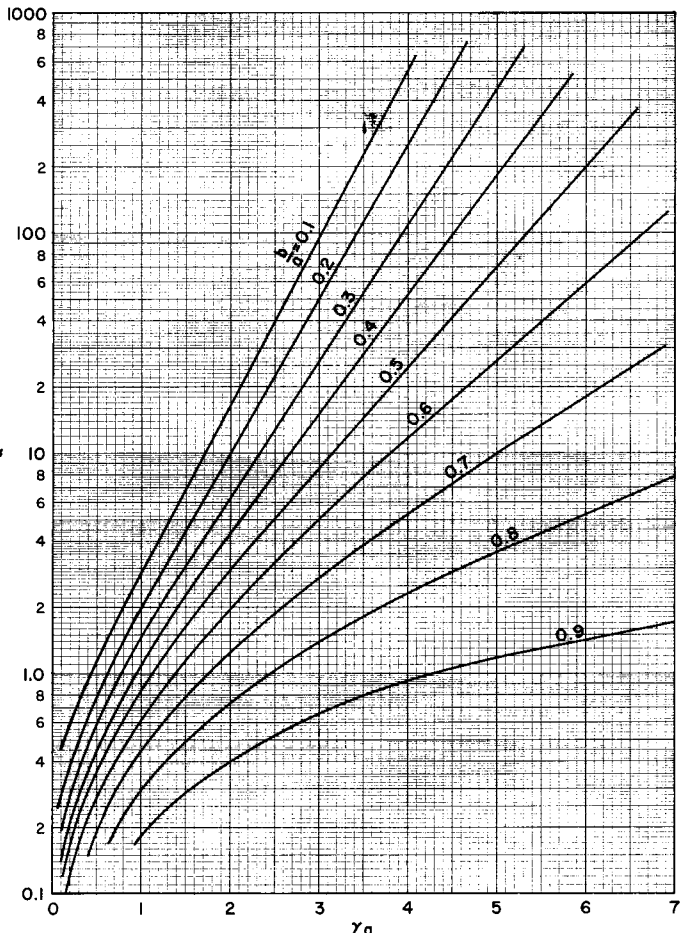
Previously, the expression for the gain of the traveling-wave tube was derived in terms of the initial loss factor  $A$ , the slow-wave parameter  $B$ , the length of the tube  $N$ , and the impedance parameter  $C$ . The expressions for the first three of these terms were derived exclusive of the type of circuit used, but the determination of  $C$  can be made only from an examination of the slow-wave structure.

Any circuit capable of propagating an rf wave at velocities about one-tenth the speed of light and allowing interaction with an electron beam may be used for the slow-wave structure of a traveling-wave tube. The helix is very nearly ideal for this purpose because it is easy to construct, has a nearly constant phase velocity over a wide frequency range, and can be readily coupled.

The following parameters are used frequently during this discussion:

$$\gamma \approx \beta = \frac{\omega}{v} \approx \frac{\omega}{v_p} \quad (19)$$

where  $\gamma$  is the radial-phase constant,  $\beta$  is the axial-phase constant,  $v$  is the phase velocity of the wave in



the presence of the beam and  $v_p$  is the phase velocity of the wave on the circuit in the absence of the beam.

$$\beta_0 = \frac{\omega}{C} = k \quad (20)$$

which is the free-space phase constant.

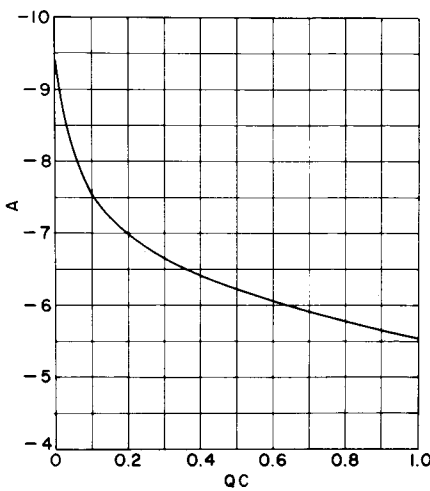


Figure 6. The Initial-Loss Parameter A as a Function of the Space-Charge Parameter QC

The fields inside and outside the helix vary as certain Bessel functions, the argument of which is normally  $\gamma_a$  or  $\gamma_r$ , where  $r$  is the radial distance from

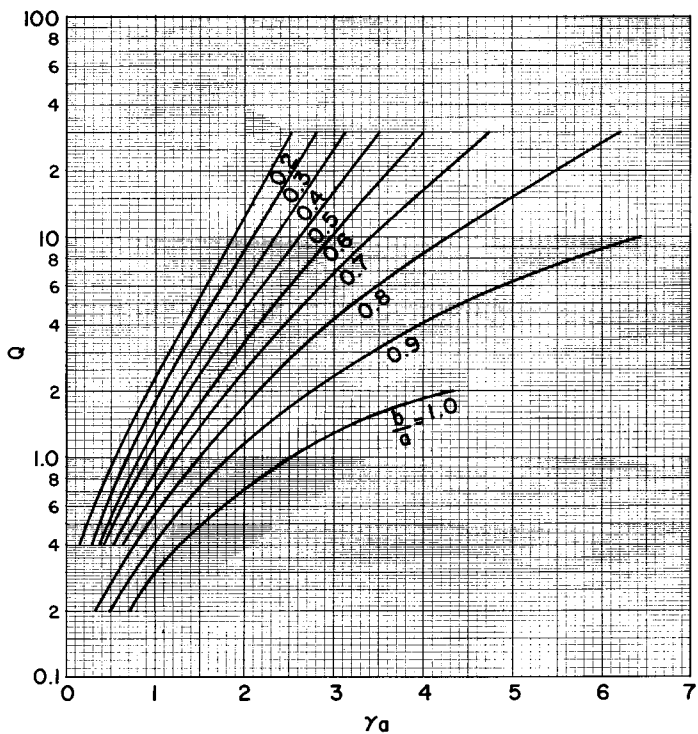


Figure 5. Family of Curves Showing the Passive-Mode Parameter Q as a Function of  $\gamma_a$  for Different Ratios of the Radius of the Electron Beam to the Radius of the Slow-Wave Circuit ( $b/a$ ): (A) For a solid beam; (B) For a hollow beam

the axis of the helix and  $a$  is the mean radius of the helix. Fig. 9 shows various parameters which describe the helix.

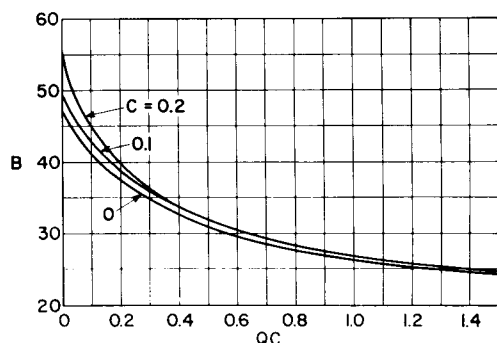


Figure 7. The Growing-Wave Parameter B as a Function of the Space-Charge Parameter QC

#### Helix Phase Velocity

Fig. 10 shows the axial phase velocity of the helix  $v_p/c$  as a function of  $ka$  for various pitch angles.

For values of  $\gamma_a$  greater than 1.5, the phase velocity approaches sine  $\psi$  and

$$\frac{v_p}{c} = \frac{P}{2\pi a} \quad (21)$$

At lower values of  $\gamma_a$ , the phase velocity varies rapidly with frequency (under this condition the helix is

said to be dispersive), and the proper pitch angle for a reciprocal velocity may be determined from Fig. 10.

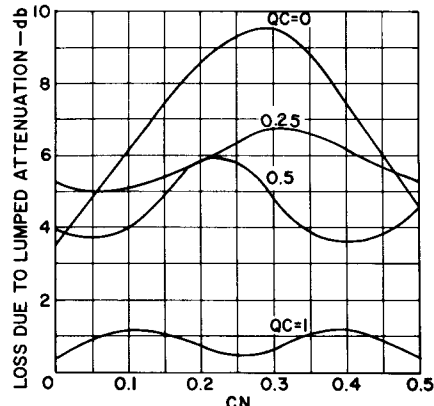


*Figure 8. Loss of Gain Resulting from the Use of a Lumped Attenuator for Different Values of the Space-Charge Parameter  $QC$  as a Function of the Drift-Tube Length  $CN$*

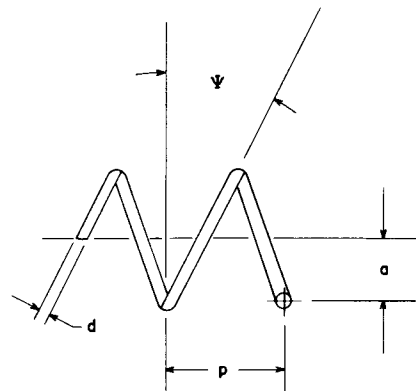


Figure 9. Parameters which Define the Geometry of a Helix

The means by which the helix is supported also affects the phase velocity. The dielectric loading factor DLF is defined as

$$DLF = \frac{\text{Phase velocity of the helix in the dielectric}}{\text{Phase velocity of the helix in free space}} \quad (22)$$

The DLF for various types of helix supports can vary from 0.7 to 0.9 depending upon the geometrical configuration and material used. Fig. 11 shows the approximate values of DLF obtained for some typical configurations.

Some reduction in dispersion is obtained from the dielectric supports because the DLF is normally not constant with frequency. At higher frequencies, because the fields are closer to the helix and interact less with the dielectric, the DLF decreases, as shown by the typical dispersion curve in Fig. 12. In this case, the small-fluted tubing used to support the helix produced a dielectric loading factor of 0.9 at the high-frequency end and 0.85 at the low-frequency end of the slow-wave structure. As shown in Figure, the config-

uration resulted in a considerable decrease in dispersion. An equivalent decrease in dispersion with the other types of supports would require a large mass of dielectric near the helix and result in a much greater value of DLF, and would have a detrimental effect on the helix impedance and gain.

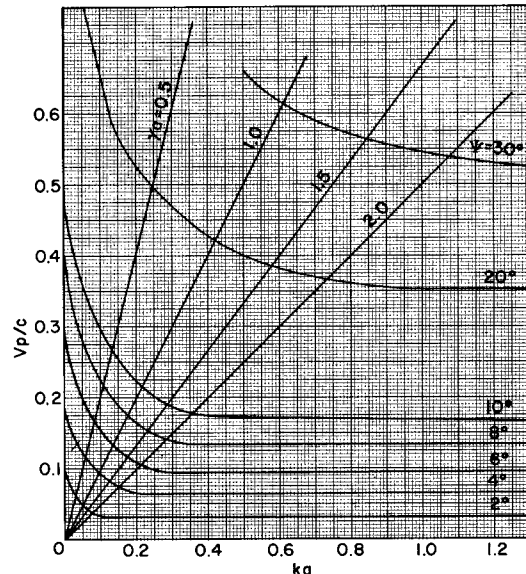


Figure 10. Family of Curves Showing the Phase Velocity of the Helix  $v_p/c$  as a Function of  $ka$  for Several Values of the Helix Pitch Angle  $\psi$ . Lines of Constant  $\gamma_a$  are Included for Reference.

<u>TYPE OF SUPPORT</u>	<u>DIELECTRIC LOADING FACTOR</u>
SOLID GLASS TUBING	0.70 - 0.80
FLUTED GLASS TUBING; SMALL FLUTES SMALL CERAMIC RODS	0.85 - 0.90
FLUTED GLASS TUBING; LARGE FLUTES LARGE CERAMIC RODS	0.75 - 0.85

Figure 11. Range of Dielectric Loading Factor for Three Types of Helix Support Structures

A conducting shield around the helix may also be used to decrease the dispersion as shown in Fig. 13. Reference 2 fully describes the effect of various size shields on dispersion and on impedance.

## Helix Impedance

The axial component of the electric field on the axis

of the helix has an amplitude which varies with  $\gamma_a$ , as shown in Fig. 14A. The impedance  $K$ , which is required to determine the gain parameter  $C$  [See Eq. (7)], is a function of the axial electric field  $E_z$  and of the phase constant  $1/\gamma$ . High impedance is desirable for two reasons: first, it enables a higher gain per unit length; and second, it is essential for high efficiency. In general, it has been empirically found that the efficiency  $\eta$  is approximately equal to  $2 \times C$ . As shown in Fig. 14A, the electric field on the axis of the helix falls off rapidly at higher frequencies, and thus, the impedance is a rapidly decreasing function of frequency. The impedance parameter  $F(\gamma_a)$  is given as a function of  $\gamma_a$  in Fig. 15 where

$$K = \frac{[F(\gamma_a)]^3 C}{2 v} \quad (23)$$

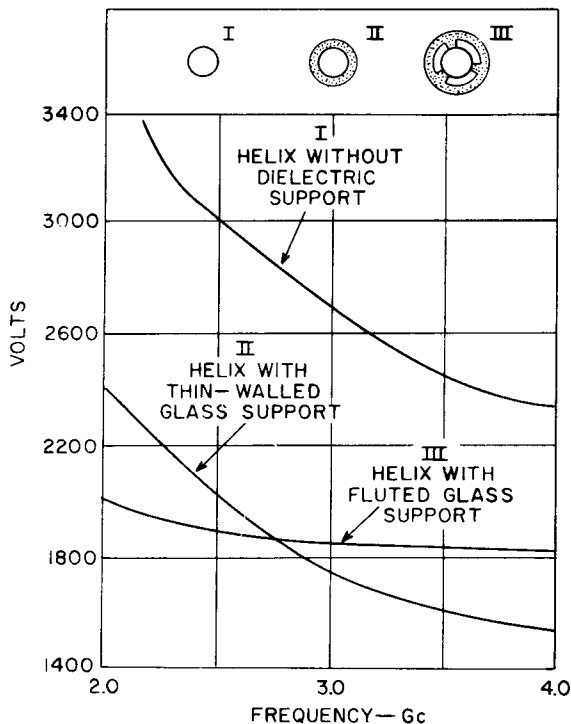


Figure 12. Effect of the Dielectric Loading on Helix Dispersion Resulting from Different Types of Support Structures

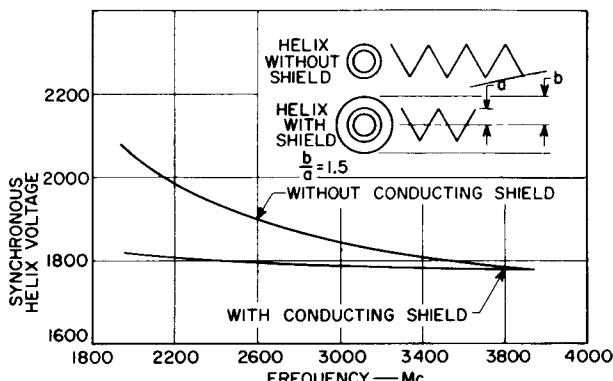


Figure 13. Curves Showing how the Use of a Conducting Shield over the Helix Reduces Dispersion

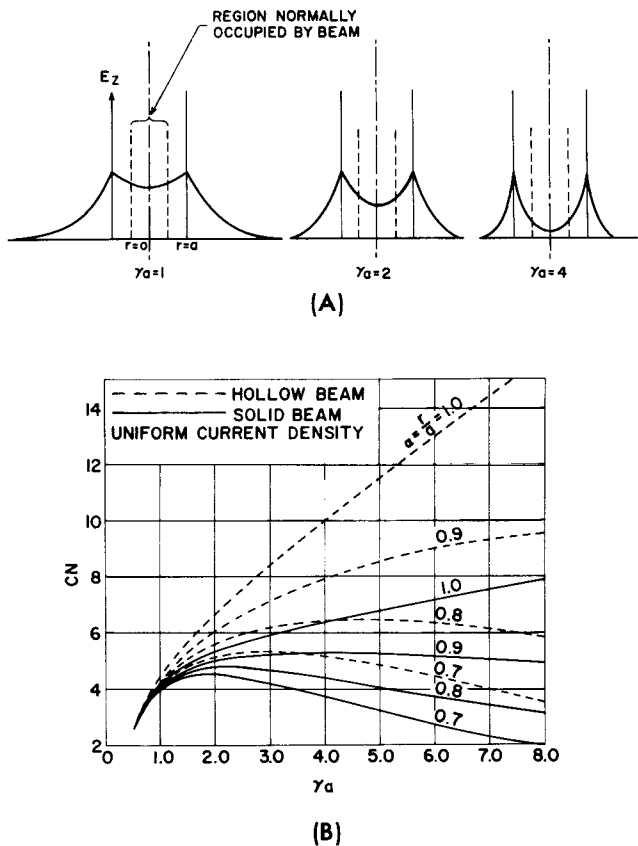


Figure 14. Effect of Beam Size and  $\gamma_a$  on Beam Impedance: (A) Showing that the amplitude of the axial component of the electric field on the axis of the helix ( $E_z$ ) varies as a function of  $\gamma_a$ ; (B)  $CN$  as a function of  $\gamma_a$  for several solid and hollow beams of different radii.  $CN$  is very nearly proportional to gain; thus, the curves show the variation of gain with frequency.

At normal ratios of beam-to-helix diameters of about 0.5 to 0.7, the impedance falls off at the higher frequencies while the number of helix wavelengths  $N$ , becomes smaller at lower frequencies. A plot of  $CN$ , which is roughly proportional to the gain [See Eq. (15)], as a function of  $\gamma_a$  for several beam diameters is shown in Fig. 14B.

If the tube is operated at a frequency at which  $\gamma_a$  is less than 1.0, the beam-field interaction is very efficient (high  $C$ ), but the helix becomes dispersive and the beam and wave fall out of synchronism over a relatively narrow frequency range. For this reason, only narrow-band operation is obtainable at low values of  $\gamma_a$ .

A helix designed for wideband operation is a compromise between low  $\gamma_a$ , where the helix is a high impedance circuit, but dispersive and high  $\gamma_a$ , where the helix is less dispersive, but has a low impedance. Experience indicates that for most applications, a value of  $\gamma_a$  of 1.5 at the center frequency is a good compromise between efficiency and broadband operation.

Fig. 14 shows that at a high value of  $\gamma_a$ , the amount of the electric field interacting with the beam is highly

dependent on the ratio of the beam diameter to the helix diameter. Thus, for the typical beam diameter shown, a much larger proportion of the electric field inside the helix is interacting with the beam when  $\gamma_a$  is equal to 1 than when  $\gamma_a$  is equal to 4. However, if the beam diameter is increased, the impedance at high values of  $\gamma_a$  increases rapidly. This effect is shown quantitatively in Fig. 16 for solid and hollow beams. When this factor is included, the impedance becomes:

$$K = \frac{[F \gamma_a]^3 [IRF]^3 c}{2} \quad (24)$$

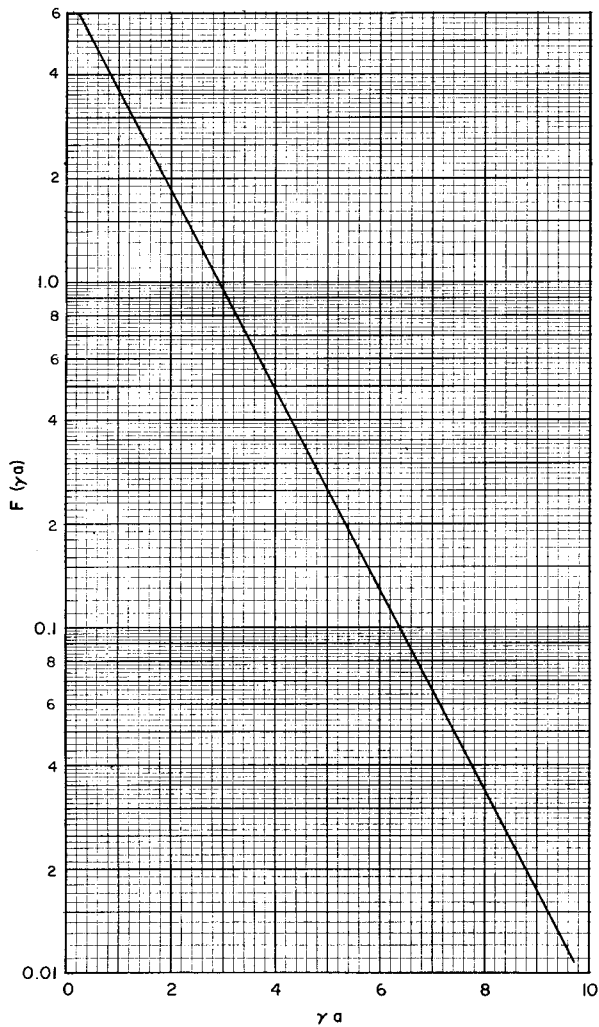


Figure 15. The Impedance Parameter  $F(\gamma_a)$  as a Function of  $\gamma_a$ . The impedance on the axis of the helix is obtained from  $F(\gamma_a)$ .

The final correction factor to be introduced is Tien's impedance factor  $F$ , which describes the reduction in the electric field inside the helix as a result of the dielectric loading factor. In addition, the curve for  $F(\gamma_a)$  was derived for a sheath helix and Tien's factor includes the impedance reduction resulting from the use of tape or wire instead of a conducting sheath. This factor is plotted in Fig. 17 as a function of  $ka$  for varying values of DLF. Thus, the final expression for  $K$  is written as follows:

$$K = \frac{[F \gamma_a]^3 [IRF]^3 F c}{2} \quad (25)$$

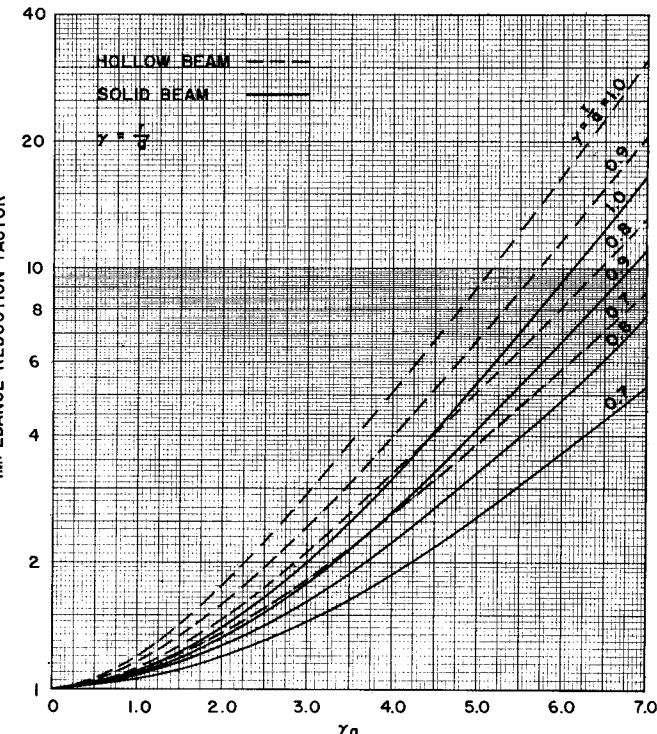


Figure 16. Family of Curves Relating the Impedance-Reduction Factor to  $\gamma_a$  for Several Hollow and Solid Beams with Different Radii. This factor is used to modify the impedance on the axis for solid or hollow electron beams.

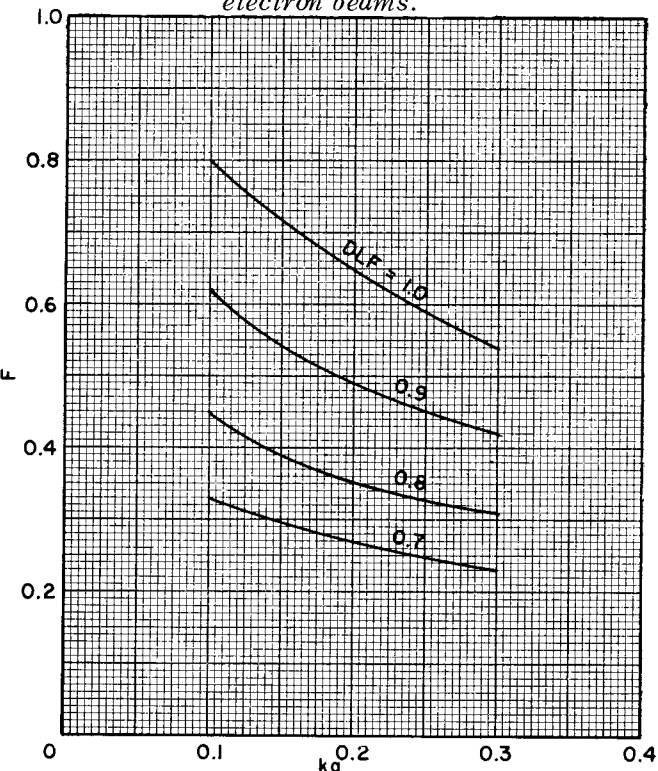


Figure 17. Curves Showing the Impedance-Reduction Factor  $F$  as a Function of  $ka$  for Several Values of the Dielectric Loading Factor

### Limitation of the Helix

The helix, although simple to make and having excellent rf characteristics, is normally limited in use to the lower power level traveling-wave tubes for several reasons.

First, the helix has rather poor power-handling characteristics. The structure is inherently light and skimpy; at higher frequencies it is small and difficult to cool. This factor primarily limits the cw capabilities of a helix-type traveling-wave tube, as shown in Fig. 18. The upper regions of this range are reached only by providing some sort of liquid cooling to the dielectric supporting the helix or to the helix itself. However, as efforts in this direction are increased, dielectric loading and the complexity of the structure increase to the point where other types of circuits are preferable.

Second, the use of helices for high-power traveling-wave tubes is limited by the interference of other space harmonics. Two effects are felt: first, a reduction of impedance in the desired space harmonic and, second, the occurrence of backward-wave oscillations at a frequency near the operating frequency of the tube.

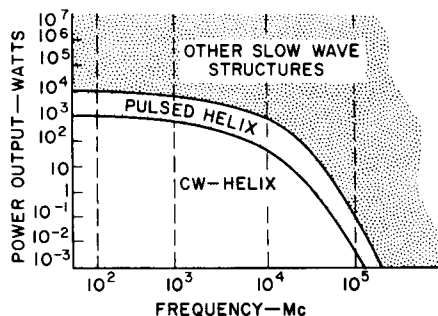


Figure 18. Power Limitations on Traveling-Wave Tubes Using the Helix Type of Slow-Wave Circuit

As described earlier,  $\gamma_a$  for a traveling-wave tube must be between 1.0 and 1.6 to maintain both efficiency and bandwidth. Thus, as the voltage is increased to obtain higher power levels,  $\gamma_a$  remains fixed and  $ka$ , which is  $\gamma_a \frac{v}{c}$  increases. Fig. 17 shows that Tien's factor decreases with increasing  $ka$ , thus decreasing the impedance at higher helix voltages. Fig. 19 is a plot of helix voltage as a function of  $ka$  for both the forward- and backward-wave space harmonics of a helix. At the point where  $ka$  is 0.5, the phase velocity of both space harmonics is the same. The tube can act as a backward-wave oscillator at the frequency defined by a  $ka$  of 0.5 while operating as a forward-wave amplifier at some lower frequency. If the normal operating range of the tube is as high as  $ka$  equal to 0.4, then it may be difficult to suppress the backward-wave oscillation without affecting operation in the desired band. This condition normally occurs when the helix voltage is about 10,000 volts or greater or at lower voltages if the current is high or the tube is long and thus limits the maximum peak power available from the helix type traveling-wave tube.

### OTHER SLOW-WAVE STRUCTURES

Many structures have been devised which in whole or

part circumvent the limitations of the helix at high-power levels. In general, these structures have a considerable amount of stored energy which cannot interact with the beam and a much narrower bandwidth than the helix. Typical of such structures is the folded waveguide which was shown in Fig. 4. In this structure, the wave follows the waveguide at a phase velocity determined by the frequency and the dimensions of the waveguide, while the electron beam, following a more direct path, travels at a velocity determined by the beam voltage. By properly arranging the length of the path in the waveguide, the arrival of the wave at each point where the beam crosses the waveguide can be made to coincide with the same electrons which the wave met at the previous crossing point. In this way, the beam and wave are in synchronism down the length of the structure and interaction takes place.

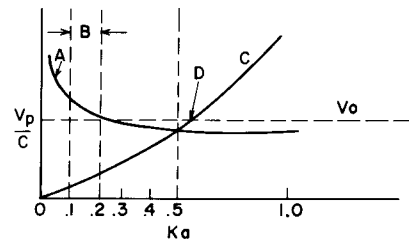


Figure 19. Phase Velocity  $v_p/c$  as a Function of  $ka$  for Both the Forward and the Backward Space Harmonic of the Wave on the Helix

A single cell of a practical structure is pictured in Fig. 20. The folds of the waveguide are brought together to a common wall and coupling from cell to cell is accomplished through the coupling slot. This is a very rugged and massive structure compared to the helix and is able to handle considerably higher average-power levels. The useful space harmonics of this structure are at high values of  $ka$ . This permits operation at voltages well above the 10-kilovolt limit of helices.

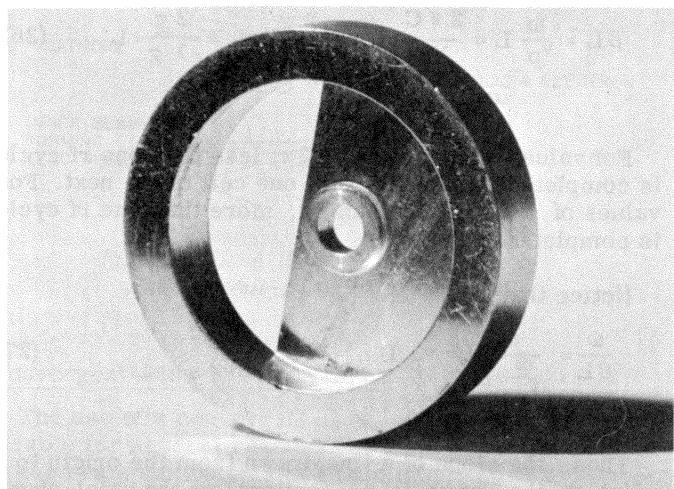


Figure 20. Single Cell of the Folded-Waveguide Type of Slow-Wave Structure

An excellent survey of many other types of slow-wave structures is given in an article by Nalos<sup>3</sup> which describes some of the types that are in use and the features that are desirable for specific applications. A

more detailed description of the characteristics of some slow-wave structures is given by Belohoubek.<sup>4</sup> The reader is referred to these and other references for the actual choosing and design of structures for high-powered traveling-wave tubes. However, as an introduction to these papers, a brief description of how these slow-wave structures are measured and compared is given below.

The characteristics of these structures is usually described by a Brillouin diagram, which relates the phase shift per cell to the frequency. A typical Brillouin diagram for the folded waveguide is shown in Fig. 21. The phase shift per cell is the amount of phase shift in the rf wave at a given instant in the distance from one interaction region to the next. This phase shift is usually given in terms of  $\beta L$ , where  $\beta = \omega/v_p$  and  $L$  is the period of the structure.  $\beta L$  is equal to  $2\pi$  or a 360-degree phase shift for that value of frequency at which the guide wavelength  $\lambda_g$  is equal to the period of the structure.

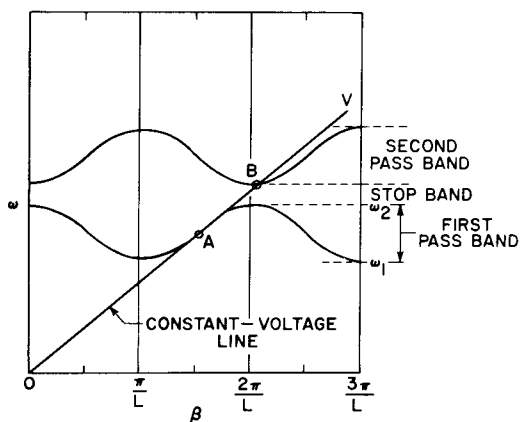


Figure 21.  $\omega - \beta$  Diagram for the Folded-Waveguide Slow-Wave Structure

$$\beta L = \frac{\omega}{v_p} L = \frac{2\pi C}{\lambda_0} L = \frac{2\pi}{\lambda_0} \frac{v_p}{C} L = \frac{2\pi}{\lambda_g} L \quad (26)$$

For values of  $\beta L$  less than  $2\pi$ , less than one rf cycle is completed in passing from one cell to the next. For values of  $\beta L$  greater than  $2\pi$ , more than one rf cycle is completed.

Notice that

$$\frac{\omega}{\beta L} = \frac{\omega}{\frac{\omega}{v_p} L} = v_p L \quad (27)$$

Thus, the slope of a line drawn from the origin to a point on the curve is proportional to the axial-phase velocity at that point. The slope of the curve itself is related to the group velocity of the wave which indicates the direction of power flow in the structure. Therefore, in the region where  $\pi < \beta L < 2\pi$  the phase and group velocity are nearly equal and in the same direction. In addition, the phase velocity is nearly constant over the available frequency band from  $\omega_1$  to  $\omega_2$  and indicates

little dispersion and, consequently, good forward-wave interaction over most of the available bandwidth. The constant voltage line intersects the second pass band at point B, however, which would indicate interference from possible oscillations at that frequency.

Also of interest is the region where  $0 < \beta L < \pi$  in which the phase velocity is still positive, but the group velocity is still positive, indicating power flow in a direction opposite to that of the phase velocity. Note that for a given voltage there is only one frequency at which interaction can take place; thus, this is a backward-wave device, voltage-tunable over the pass band.

The determination of the  $\omega - \beta$  diagram is important in the design and evaluation of slow-wave structures because it gives information on the bandwidth, voltage, and possible interference from other modes. The technique used is to take a short length of the slow-wave structure, usually about 5 cells, short the ends of the structure and determine the resonant frequencies. These resonant frequencies can then be related to certain phase shifts per cell and plotted to form the  $\omega - \beta$  diagram.

The impedance of such structures can be obtained from perturbation of the fields on the axis of the shorted structure by means of small dielectric beads. The impedance can then be calculated from measurements of the frequency change due to the introduction of the dielectric. A detailed description of these measurements is too complicated to be included here, but several good descriptions of techniques are available in literature.<sup>5</sup>

Figs. 22 and 23 show, respectively, a cross-section drawing of a structure designed for 1-kilowatt peak power over a 20 per cent bandwidth at S-band and the  $\omega - \beta$  diagram plotted for the same structure. This structure may be scaled to other frequencies, with the voltage constant, by scaling all dimensions to the change in wavelength. The voltage is changed by scaling the period only by the square root of the voltage. Variations of dimension "w" will vary the bandwidth. A larger coupling slot will increase the bandwidth but decrease the impedance.

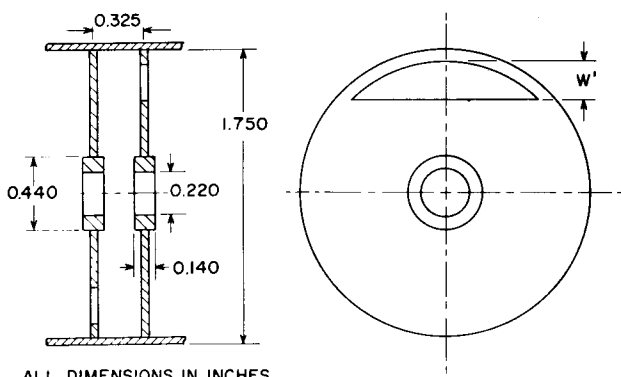


Figure 22. Cross-Sectional Drawings of a Folded-Waveguide Slow-Wave Structure Designed for S-Band Operation at 1 Kilowatt of Peak Power over a 20 Per Cent Bandwidth

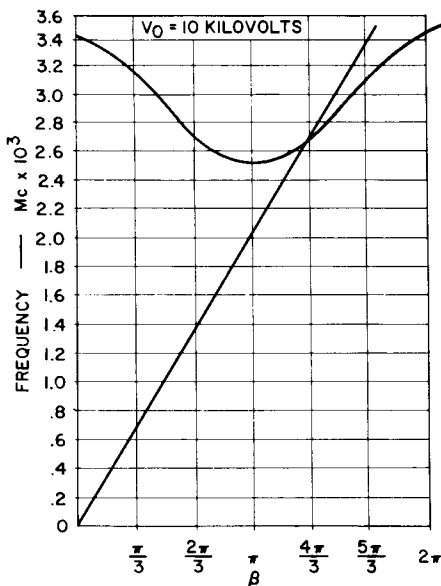


Figure 23.  $\omega - \beta$  Diagram for the Folded-Waveguide Structure Shown in Fig. 22

### ELECTRON GUN

The design of the electron gun can be extremely critical in the ultimate performance of a traveling-wave tube. The formation of a well-defined beam of correct diameter is important in obtaining the proper rf characteristics of a tube. A gun producing a beam smaller than required for a given helix or slow-wave structure lowers the interaction impedance, particularly at the high-frequency end of the band. Conversely, a beam too large or not well defined is difficult to focus. In high-power tubes in which interception on the slow-wave structure can be sufficient to cause severe thermal problems, a well-defined beam of the proper diameter is vital to the successful operation of the tube.

Many different types of electron guns are in use on traveling-wave tubes. One of the most common types is the convergent-flow gun shown in Fig. 24. A related gun, the parallel-flow type, is shown in Fig. 25. Fig. 26 is a hollow-beam parallel-flow gun. Fig. 27 is a convergent-flow hollow-beam gun. Fig. 28 is a magnetron injection gun. A typical low-noise gun is shown in Fig. 29. Each of these types has a specific application. The most commonly used is the convergent-flow solid-beam electron gun. Because of the widespread use of this particular gun, the following description is fairly detailed, and some design procedures are also discussed. For the other types of guns, only the operation and literature references for design are given.

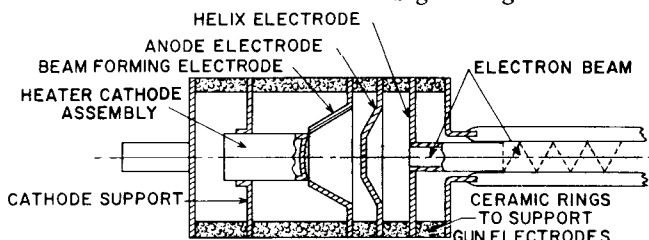


Figure 24. Cross Section of the Convergent-Flow Electron Gun

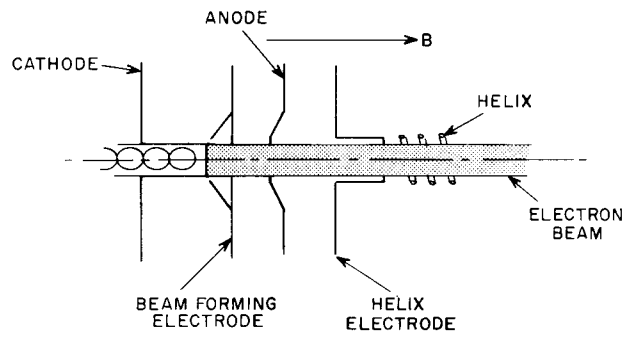


Figure 25. Schematic Diagram of a Parallel-Flow Electron Gun

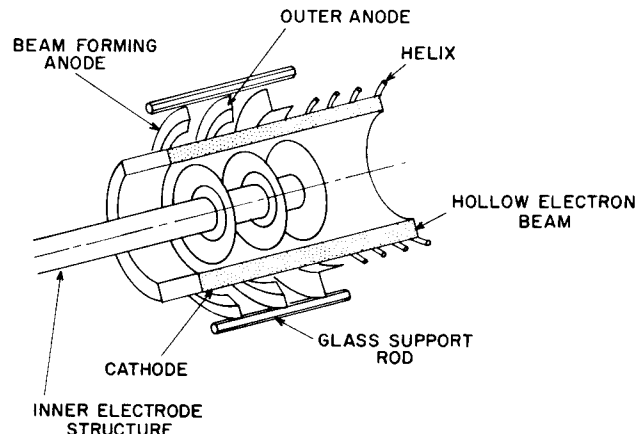


Figure 26. A Hollow-Beam Type of Parallel-Flow Electron Gun

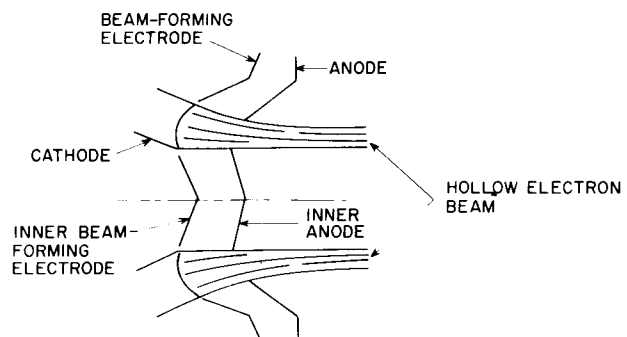


Figure 27. A Hollow-Beam Type of Convergent-Flow Electron Gun

### Convergent-Flow Electron Gun

The use of a convergent-flow, solid-beam gun is desirable for several reasons. A higher current density in the beam can be obtained than is normally available from a cathode surface by converging the beam in the gun region. Convergence ratios of 2:1 to 10:1 are readily available and provide extremely high beam-current densities in the interaction region of the tube. An initially convergent beam is necessary for several of the focusing schemes, described later, in which the gun region must be shielded from the magnetic field and the beam must enter the magnetic field with parallel elec-

tron trajectories. From the parallel-flow gun the beam would normally be divergent as it leaves the anode of the gun. However, with a convergent-flow gun, a beam minimum occurs some distance from the anode, at which point the electron trajectories are parallel, the radial velocities of the beam are at a minimum, and the magnetic field can be introduced.

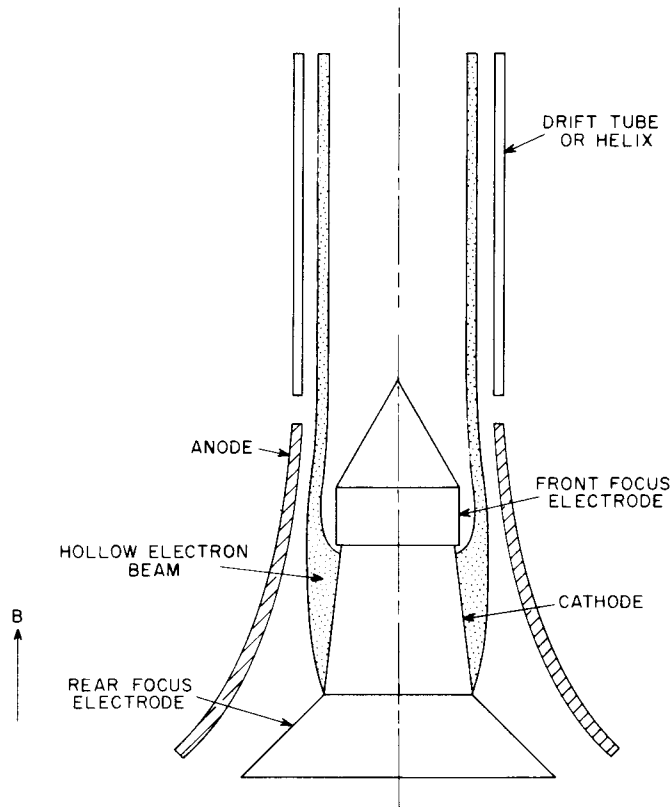


Figure 28. Cross Section of a Magnetron-Injection Electron Gun

Considerable analytical background is available which makes it possible to design a convergent-flow electron gun having a micropervaneance of less than one, where pervaneance  $p$  is equal to  $I/V^3/2$ . A particularly good reference by Danielson, Rosenfeld, and Saloom<sup>6</sup> is found in the Bell System Technical Journal. The general approach to the analytical method is as follows: It is assumed that in two concentric spheres, the inner surface of the outer sphere emits electrons to the inner sphere. By the law of minimum astonishment, the electrons all travel in a straight line from the outer sphere to the inner sphere, with none of their paths crossing. The object in designing an electron gun is to cut out a segment of these spheres and form a potential along the boundary of the beam so that the cut out portion of the beam is not affected by the missing portion of the spheres. Presumably, the electrons travel in smooth laminar paths from the cathode to an anode. Reference 6 provides the correction required for the hole in the anode and also includes the effect of the thermal velocities of the electrons.

For a pervaneance greater than one, the design curves break down because the hole in the anode through which

the beam must pass becomes quite large compared to the spacing between the anode and the cathode. Two methods are available when designing a gun having a pervaneance greater than one. The first method involves setting up the boundary conditions for the beam in an electrolytic tank and experimentally determining the shape of the electrodes which produce the proper electric field along the edge of the beam. The second is to scale from an existing gun. The first of these methods has been adequately described in the literature.<sup>7, 8</sup>

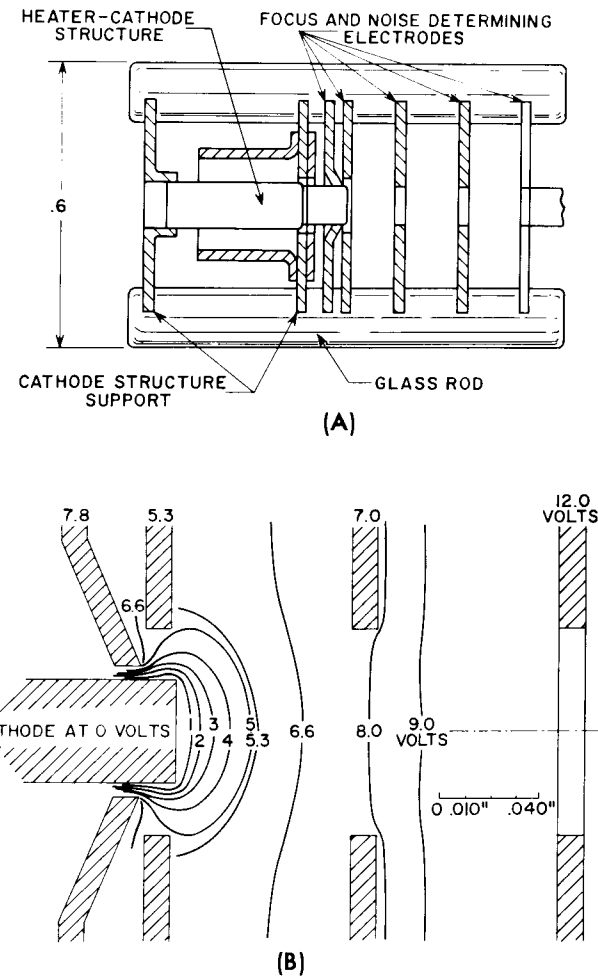


Figure 29. A Typical Low-Noise Electron Gun:  
(A) Cross section of the gun structure;  
(B) Electrode arrangement and distribution of the equipotential lines in the gun

An electron gun, the dimensions of which were empirically determined by Siekanowitz in 1954 and which has been modified to produce beams with a pervaneance ranging from 0.5 to 1.7 at a convergence ratio of 4 to 1, does provide an excellent starting point for scaling of a gun design. The critical dimensions of this gun are shown in Fig. 30; the minimum beam diameter has been normalized to unity. This gun, operated at a pervaneance of 1.25, produces a minimum beam diameter of 0.110, from a cathode diameter of 0.400 with the beam minimum located 0.550 inch from the anode aperture. The original and scaled models of the gun have been used in several tubes and have provided excellent focusing at very nearly the minimum theoretical value of the mag-

netic field. Figs. 30B, C, and D, show how the various parameters of this gun were modified in order to vary the perveance from 0.5 to 1.75. In each case, the cathode diameter remained the same and the beam-minimum diameter remained the same within about 10 per cent.

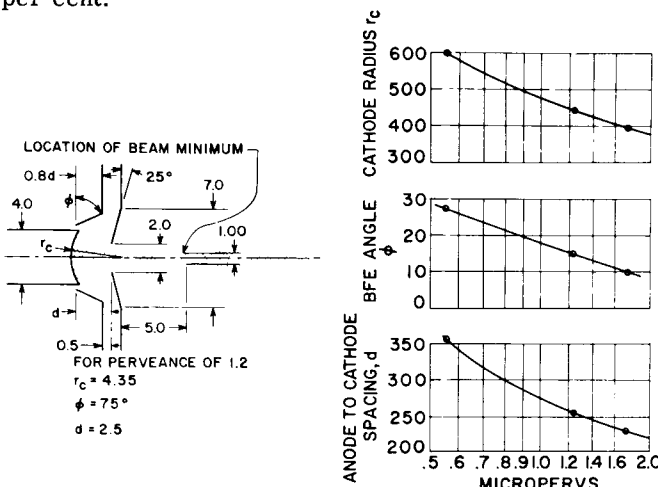


Figure 30. Schematic Diagram Showing the Electrode Dimensions and Spacings of a Modified Siekanowitz Electron Gun. Graphical data show how the parameters of this gun may be modified to vary the perveance over the range of 0.5 to 1.75 micropervs.

The performance of this gun has been consistently excellent. For example, in one tube, a 100 milliamper beam current at a beam voltage of 2000 volts can be focused through a 0.175-inch I. D. helix with only 1 per cent interception at a peak magnetic field of 350 gauss in a periodic permanent-magnet structure. In another case, a 50-milliamper beam at 1100 volts was focused with 3 per cent interception through a helix with an I. D. of 0.130 inch at a peak magnetic field of 450 gauss. In both cases, the peak magnetic field is very near the minimum theoretical value. Such good focusing can only be obtained with a beam generated from a gun having few aberrations.

#### Parallel-Flow Gun

When the magnetic field is permitted to thread through the cathode itself and the current density in the beam is not too great, a parallel-flow gun may be used. The derivation of the analytical approach for this gun is similar to that of the convergent-flow electron gun except that instead of two concentric spheres there are two infinite planes, one of which emits electrons to the other. In this case, the electric field along the beam in the gun region is a simple function of the distance between the planes and can be readily duplicated with electrodes by following the procedure of Pierce.<sup>7</sup> However, because of the hole in the anode, the beam diverges as it leaves the gun and, therefore, this gun is practical only in cases where the magnetic field threads through the gun region. The disadvantages of this type of focusing will be explained later.

#### Hollow-Beam Parallel-Flow Gun

The hollow-beam parallel-flow gun is essentially

similar to the parallel-flow gun, except that instead of producing a solid circular beam, a long thin ribbon beam is formed which is folded back upon itself to form a hollow beam. This type of gun is extremely useful in cases where the electron beam must be very near the interaction structure for good performance. As discussed earlier, it is particularly useful to maintain high impedance when operating at high values of  $\gamma_a$ .

In this type of gun, extremely high perveances may be obtained. For instance, if the circular cathode is spread out in a straight line and then divided up into squares, the perveance of each square is limited to about one, as described above for the convergent-flow gun. However, with a sufficiently large length-to-width ratio, there may be 10 to 100 such squares. Therefore, the total perveance of the gun as a whole can be 10 to 100 times the perveance of a single square; it is not unusual to have a perveance of 10 to 100.

#### Convergent-Flow Hollow-Beam Gun

The convergent-flow hollow-beam gun has been rarely used in experimental tubes. As shown in Fig. 27, the inherent difficulty of obtaining a well-defined beam from a hollow convergent cathode and properly directing the beam down the axis of the tube is so formidable that no clear-cut analytical method has been found to describe it. The experimental results to date, which have not been very encouraging, are included in the references.<sup>9, 10</sup>

#### Magnetron-Injection Gun

The magnetron-injection type of gun has received increasing attention in recent years because of its extremely high convergence ratio and the fact that the beam can be readily focused in a uniform magnetic field. As shown in Fig. 30, the electrons are drawn away from the cathode by a slight positive potential on  $G_1$ , but are constrained to move in an axial direction because of the magnetic field. In this way, a rather well-defined hollow beam of very high current density (compared to the current density of the cathode) can be formed. Because no flux actually passes through the cathode surface, the electrons leaving the gun have a rotational velocity which aids focusing. The design procedure for this type of gun is given in reference 11.

#### Low-Noise Gun

Special design problems exist in the development of electron guns for low-noise traveling-wave tubes because, in these tubes, the gun serves a dual function: not only is the electron beam generated and defined by the gun, but the gun must also maintain the proper beam-entrance conditions for minimum noise at the point of entry into the rf interaction region.

Modern theory considers two essentially uncorrelated sources of noise: velocity fluctuations and current fluctuations of the electrons leaving the cathode. The beam can be considered as a propagating medium for these noise waves and an analogy has been constructed between the beam viewed as a space-charge-

wave transmission medium and the familiar transmission line. The gun may be considered to act as a transducer which must be carefully designed to match the impedance (ratio of voltage or velocity fluctuations to current fluctuations) at the cathode plane to the desired impedance at the helix. Several of the familiar transmission-line transformers can be used as models. The exponential transformer comes closest to fulfilling the requirements of the low-noise gun. The RCA "three-region gun" is a transformer of this type.

A discussion of design of low-noise guns can be found in a thorough study by R. W. Peter in reference 12. The theory of low-noise guns is presently confused and the design parameters in the region of the cathode are now undergoing constant revision. At the time of publication, no survey article has appeared which covers the developments of the past few years since Peter's article was written.

## FOCUSING

Many schemes have been devised for focusing the beam in a traveling-wave tube. Most efforts have been directed at reducing the size and the weight of the focusing structure. Several of the better-known types of focusing which have actually been put into use in production or developmental tubes are described below. In most cases, the more esoteric forms of focusing are some modification or combination of these focusing methods.

### Magnetic Focusing

Magnetic focusing was the first method used to confine the beam in the interaction region of traveling-wave tubes. After fifteen years, magnetic focusing is still used in over 95 per cent of traveling-wave tubes. During that time, the techniques and the means of supplying the field have become increasingly refined.

Basically, there are two types of magnetic focusing. The first and most commonly used in the earlier days of the industry is magnetically confined flow, otherwise known as the "brute force" method. The second and more commonly used method today is magnetically focused flow, frequently called Brillouin flow.

Confined Flow. When a strong magnetic field is directed along the axis of the tube so that the flux is threaded through both the cathode and the interaction region, the magnetic field constrains the electrons to follow a relatively straight path from the cathode down the length of the tube. If the beam is not well focused, the magnetic field is merely increased until it reaches a value sufficient to provide the desired beam transmission.

Radial forces on the electrons come from the space-charge forces generated by the mutual repulsion of the electrons; thus, the higher the current density in the beam, the stronger the magnetic field required. The path of an individual electron is shown in Fig. 31. Space-charge forces produce a small radial component in the electron velocity which, under the action of the magnetic field, results in a circular motion of the elec-

tron when viewed from the end. In traveling down the tube, the electron follows a helical path. The strength of the magnetic field determines the diameter of the circle described by the electrons and thus determines the definition of the beam. For beams of moderate current density such as in a ten-watt S-band tube, about 500 to 600 gauss is adequate for focusing.

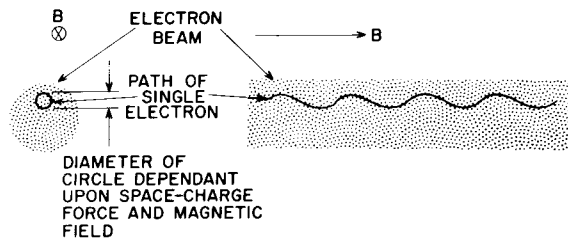


Figure 31. Path Traced by an Individual Electron in Confined Magnetic Flow

A parallel-flow gun must be used with this type of focusing because the electrons are under the influence of the magnetic field from the time they leave the cathode surface. Use of any of the convergent-type guns would involve cutting lines of flux during the convergence of the beam and, consequently, destroying the action of the gun. In the parallel-flow gun, both the action of the electrostatic lens in the gun and the magnetic field tend to keep the electrons moving in a straight line.

With the exception of its use in low-noise tubes where the magnetic field requirements are determined more by the noise-figure properties than by the density of the beam, this type of focusing is not generally in widespread use because it requires a stronger magnetic field than focused flow.

Focused Flow. Focused flow is considerably more sophisticated and requires less magnetic field and a smaller size magnet than confined flow. The most common type of focused flow, known as Brillouin flow, in which two counterbalancing forces on the electrons in the beam tend to keep the beam on the desired path. The electron beam is generated, usually by a convergent-flow gun, and the magnetic field starts abruptly at the point at which the beam reaches its minimum diameter and the radial velocities are at a minimum. Bush's theorem states that upon entering the magnetic field the electrons begin to rotate about the axis with a rotational velocity which is proportional to the distance of each electron from the axis of the beam and the strength of the magnetic field. Thus, we have set up the conditions shown in Fig. 32; an electron beam travels through the interaction region with each electron following a helical path about the axis of the tube at a constant radius.

Under the ideal conditions, three forces act on each electron. First, there are the normal space-charge forces which tend to increase the radius of the electron path. Second, there is the centrifugal force, outward, of the spiraling electrons which also tends to increase the radius. Third, the spiraling electrons are cutting lines of flux and experience an inward Lorentz force. When the conditions for Brillouin flow have been satis-

fied, these forces balance out to zero and the electrons are focused down the length of the tube. The conditions for Brillouin flow  $B_0$  are shown by the following equation:

$$B_0 = \frac{326 I^{1/2}}{V^{1/4} a} \text{ gauss} \quad (28)$$

where  $I$  is the beam current in amperes,  $V$  is the beam voltage in volts, and  $a$  is the radius of the beam in inches. In practice, the actual field required is frequently about 1.3 times the value obtained from this equation.

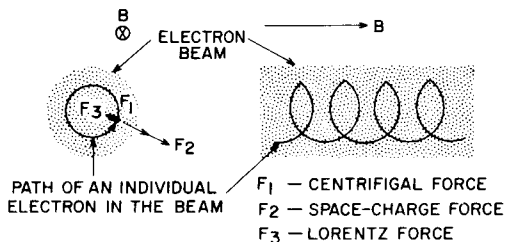


Figure 32. Path Traced by an Individual Electron in Focused Magnetic Flow

If an electron is perturbed slightly, either by entering the magnetic field with an initially slight radial velocity or as a result of some perturbation during transit, there are forces which tend to restore the electron to its original orbit. A force diagram of the relative forces on a given electron having an initial radius  $r_0$  is shown in Fig. 33. As the orbital diameter of the electron becomes larger, greater force tending to decrease the diameter is created because more flux lines are cut. At the same time, the centrifugal and the space-charge forces decrease. On the other hand, if the diameter of the electron path becomes smaller, the space-charge force and the centrifugal force increase and the magnetic force decreases, tending to push the electron out to its original path. Thus, a potential valley is formed with a minimum at the equilibrium radius. The steepness of the walls of this potential valley determine the stiffness of the focusing. Actually, if electrons are displaced at any time, an oscillatory motion takes place in the diameter of the beam as a whole, and results in beam scalloping about the initial radius  $r_0$ .

This type of focusing requires less field than confined flow, but also requires a certain optimum field. In other words, unlike confined flow in which the magnetic field is merely increased to improve the beam definition and transmission, increasing the magnetic field results in a severe inward scalloping of the beam and a reduction in the average beam diameter which can be detrimental to the rf performance of the tube.

**Sources of Magnetic Field.** Generating the magnetic field for focusing traveling-wave tubes has been considerably advanced in recent years. Initially, the solenoid was used to generate a uniform magnetic field because performance was easily predicted and the magnetic field could be readily varied to find the optimum field for best focusing. However, as traveling-wave tube requirements become more stringent, especially

in airborne applications where power consumption and weight were extremely important, solenoids were replaced with various types of permanent magnets.

**Solenoids.** Solenoids are still frequently used today in special applications such as low-noise tubes in which the magnetic field must be carefully controlled and transverse fields held to a minimum, and in tubes for high-temperature service, in which the commonly-used magnetic materials cannot be used. Improvements in the insulating materials for magnet wires will eventually permit the use of solenoids in ambient temperatures up to several hundred degrees centigrade.

**Permanent Magnets.** Permanent magnets, although weighing as much or more than a well-designed solenoid, have the advantage of requiring no power to maintain the magnetic field. Although largely superseded by periodic magnet focusing, which requires considerably less magnetic material, the straight-field permanent magnets still are useful in focusing very-low-noise traveling-wave tubes and tubes requiring a very high magnetic field for a relatively short distance. In the latter case, the present material limitations prevent the use of periodic permanent magnetics. The design procedure for the straight-field permanent magnet has been described by Glass<sup>13</sup> and Schindler<sup>14</sup>. These magnets can be used for either confined flow with the flux threading the cathode or Brillouin flow with the gun suitably shielded from the magnetic field.

**Periodic Permanent Magnets.** Periodic permanent-magnet focusing was the first major breakthrough in making the traveling-wave tube a light-weight portable device. As mentioned under "Brillouin Flow," the centrifugal and space-charge forces on the electron are counterbalanced by the magnetic field. However, in the equation describing this relationship, the magnetic field term appears as  $B_0^2$ . Therefore, the sign or polarity of the magnetic field can be neglected. Thus, if the magnetic field changes polarity periodically down the length of the tube, focusing is unaffected.

The arrangement of a periodic permanent-magnet focusing stack is shown in Fig. 34. The magnetic material is in the form of rings of high-coercive-force material, usually a barium ferrite, and the shims are formed of magnetically soft iron, usually Armco iron. The ring magnets are alternately magnetized so that they oppose each other and form the indicated magnetic field along the axis.

In a periodic permanent magnet, the stray external fields tend to cancel each other and thus produce a much greater percentage of the usable field in the center of the magnet stack, where it can be efficiently used to focus the beam. In general, as the length over which a magnetic field is to be maintained is halved, the weight of the magnet required to maintain that field is reduced by a factor of 8. Thus, if a single permanent magnet is replaced by a periodic permanent magnet having some ten periods, there will be a theoretical reduction of weight of 100 to 1. While this is not normally obtained in practice because of the greater demagnetizing forces in a periodic permanent magnet, a normal re-

duction of greater than 10 to 1 in the weight of a focusing structure is readily obtainable.

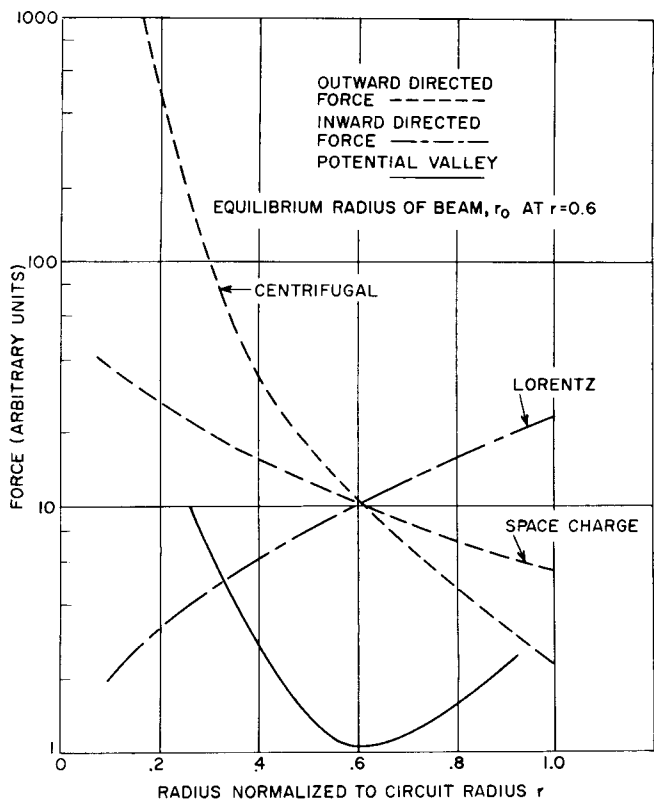


Figure 33. Diagram of the Forces Acting on a Single Electron in a Brillouin-Flow Beam

Many design procedures have been devised to calculate the magnet dimensions required to provide the given magnetic field on the axis for a given period. The most recent, by Schindler,<sup>15</sup> includes probably the most accurate and certainly the fastest available designing for these magnets.

Two conditions must be met to obtain satisfactory focusing with periodic permanent magnets: the proper rms magnetic field must be obtained and the periodicity of the focusing structure must be within certain limits. Because the magnetic field along the axis is sinusoidal, the Brillouin field  $B_0$  must be multiplied by a factor of 1.4 to obtain the peak magnetic field  $B_m$ . The proper magnetic field results in the same type of focusing discussed under Focused Flow.

The periodic nature of the magnetic field imposes a limit on the allowable period of the magnet structure. The rising and falling of the magnetic field along the axis of the beam causes a scalloping of the beam in which the scallops have the same period as that of the magnet stack. As in Brillouin flow, a focused electron beam also has another scallop having a periodicity related to the restoring forces on the electrons. If the scallops from the periodicity of the magnetic field and the scallops from the restoring forces have approximately the same frequency, the beam tends to expand rapidly. The condition which sets the allowable limits of the period of the magnet structure is expressed by the following equation:

$$L = C \frac{V^{1/2}}{B_m} \quad (29)$$

where  $L$  is the period in inches,  $V$  is the beam voltage in volts,  $B_m$  is the peak magnetic field in gauss, and  $C$  is a constant between 0 and 16. If  $C$  is maintained below 16, the scallops are not amplified and the beam is stable. In actual practice, the value of  $C$  ranges from 8 to 10. Above 10, the scalloping is excessive, and below 8, the demagnetizing forces encountered in the periodic stack are so high that the required magnet stack is difficult to construct or too great in weight.

Fig. 35 shows two typical helix-type traveling-wave tubes focused with periodic permanent magnet stacks. For the tube using helical couplers in which the input and output lines are of relatively small diameter coaxial cable, the line can be brought up directly through a hole drilled in either the magnet or the shim. In general, cutting through the magnet is best, because it causes less interference with the magnet circuit and is less likely to introduce transverse fields on the axis. In the case of the waveguide coupler, the waveguide is made as narrow as possible and is placed between two magnets. This interruption of the magnetic field does not seem to affect the focusing appreciably.

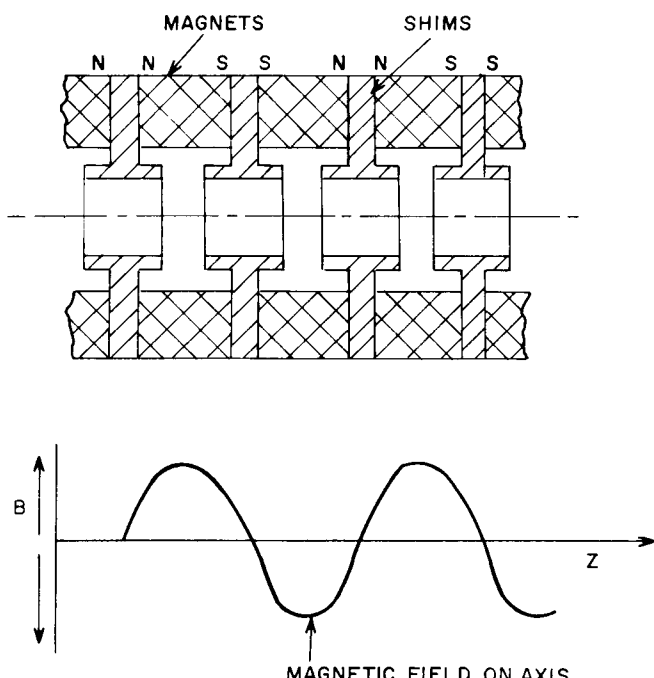


Figure 34. Cross-Sectional Diagram of a Typical Periodic-Permanent-Magnet Focusing Stack and the Distribution of the Magnetic Field along its Axis

Fig. 36 shows how a periodic permanent-magnet structure is built into a folded-waveguide slow-wave structure. The walls of the cavity and the drift tubes are made of soft magnetic material, and the outside vacuum-envelope ring is made of copper. The soft iron extends out beyond the interaction space and the mag-

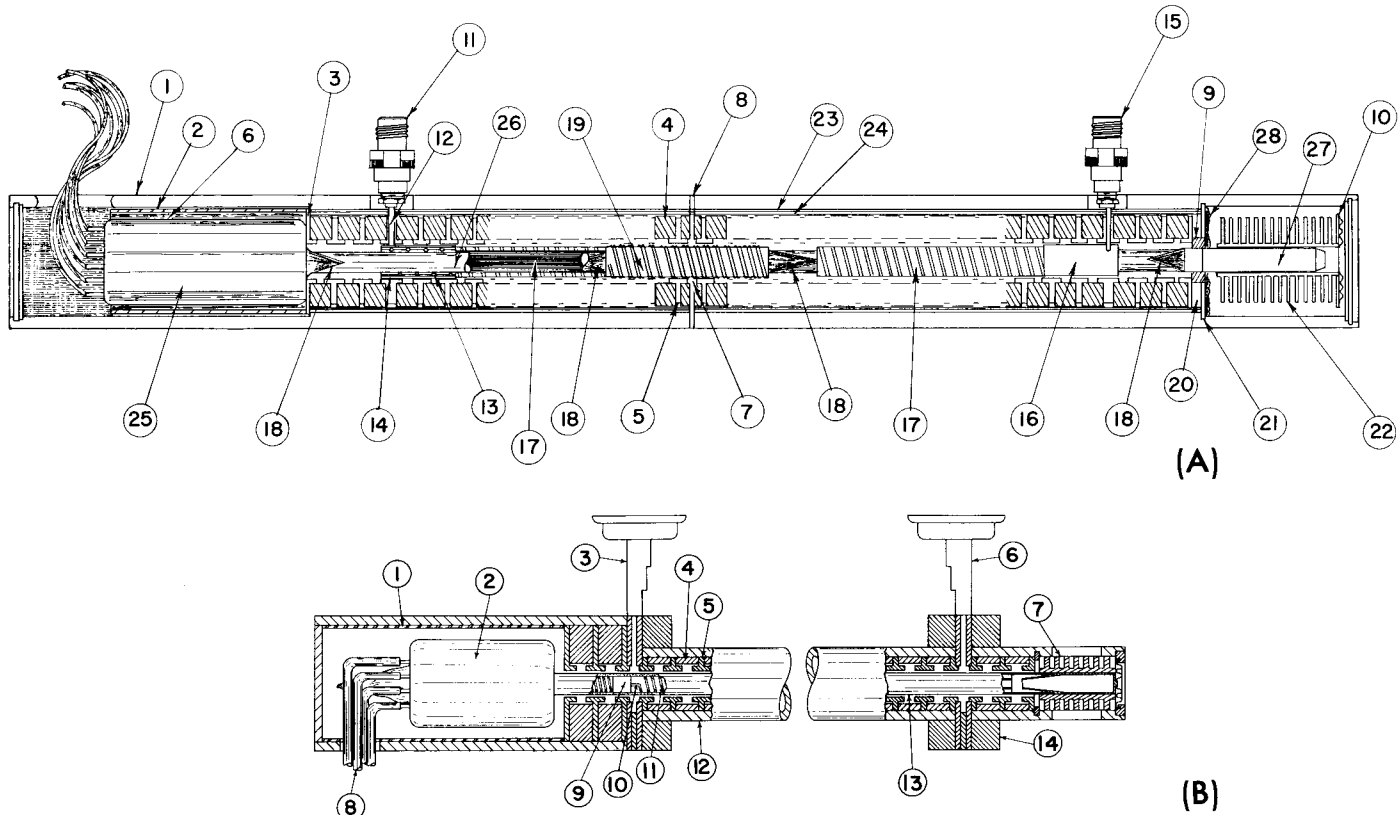


Figure 35. Cross-Sectional Drawings Showing the Arrangement of a PPM Stack in a Helix-Type Traveling-Wave Tube: (A) Tube using helical couplers; (B) Tube using waveguide couplers

nets, which are split for ease of assembly and are then placed between the shims. This type of construction has made possible X-band folded-waveguide traveling-wave tubes of relatively small size and weight with peak powers of 15 to 500 kilowatts and average powers up to 1000 watts.

Lens (Fig. 37) or (2) the radial electric field generated between two concentric cylinders. In addition, combinations of these two methods with magnetic fields can achieve greater stability of electron flow.

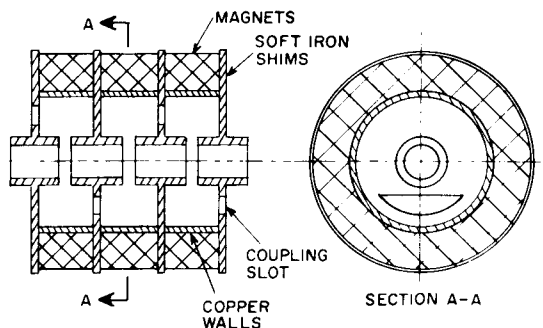


Figure 36. Arrangement of a PPM Stack Using a Folded-Waveguide Slow-Wave Structure

#### Electrostatic Focusing

Because of the need for small and light traveling-wave tubes for airborne equipment, missiles, and satellites, light-weight electrostatic focusing has been used to eliminate the magnet or solenoid entirely. Two major types of electrostatic focusing are used: (1) spatially alternating electric fields such as the Einzel

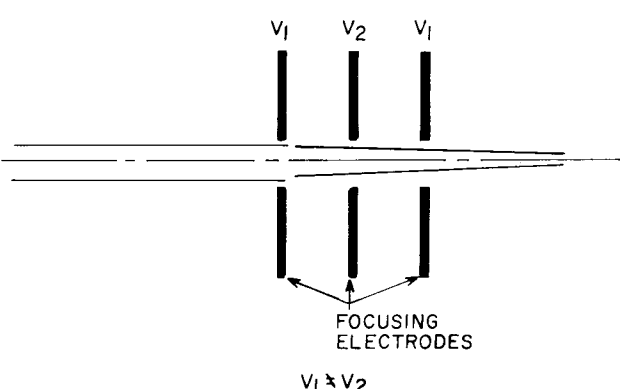


Figure 37. An Einzel-Lens Electrostatic Focusing Arrangement

Spacially Alternating Electrostatic Fields - Bifilar Helices. A bifilar helix (such as that shown in Fig. 38) having two different potentials applied to the two windings, has a net focusing force similar to that obtained with an Einzel lens. As an electron passes alternately high- and low-voltage helix wires, there is a net inwardly-directed force on the electron which is balanced

only by the space-charge forces of the electron beam. The force diagram, shown in Fig. 39, shows the relative amplitude of these forces on an electron placed at a distance  $r_0$  from the axis in a helix with a mean radius of  $a$ . This form of focusing is not very rigid because no strong forces tend to keep an electron exactly in its original path. The inward-directing forces from the bifilar helix fall off very rapidly from the helix and the outward space-charge force is relatively weak. The forces in this diagram indicate considerably less stiffness than those of Fig. 33, which show Brillouin flow. Because the electrostatic force falls off so rapidly from the helix, it is generally believed that the beam becomes partially hollow as it passes through the helix and becomes essentially a "dirty" hollow beam. Because of the lack of rigidity, the maximum permeance which can be focused with a 3:1 ratio of the two helix voltages is about one.

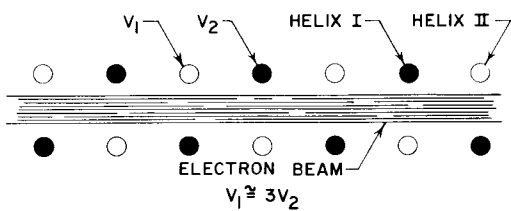


Figure 38. A Bifilar-Helix Electrostatic Focusing Arrangement

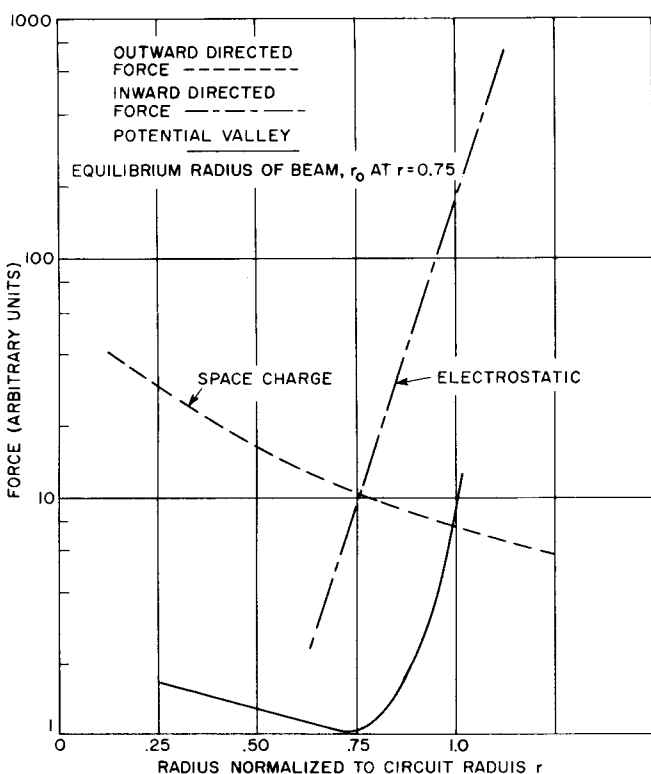


Figure 39. The Relative Amplitudes of the Forces Acting on an Electron at a Given Distance from the Beam Axis in the Bifilar-Helix Electrostatic-Focusing Arrangement

The chart by Blattner and Vaccaro shown in Fig. 40 relates the ratio of beam-to-helix diameters, the helix-voltage ratio, and the maximum permeance which can be focused. The second helix wire in the bifilar helix does not affect the rf characteristics of the helix, and both the phase velocity and impedance are unchanged from that of a unifilar helix having the same pitch angle and diameter.

The original form of electrostatic focusing by means of bifilar helices employed a stiffer form of focusing than that which has just been described. The gun region of the tube was immersed in a magnetic field which was abruptly terminated as the electron beam entered the bifilar helix region. By Bush's theorem, this caused the beam to rotate rapidly about the axis as it left the magnetic field and produced outward forces based on both centrifugal forces and space-charge forces. These forces were then counterbalanced by the inwardly-directed force from the electric field of the bifilar helix. The force diagram shown in Fig. 41 indicates that this arrangement provides a stiffer form of focusing which tends to keep each electron on its original radius. This type of focusing was demonstrated by Chang.<sup>16</sup>

Another scheme proposed and demonstrated by Chang<sup>17</sup> to improve the stiffness of purely electrostatic focusing is the use of an inner bifilar helix concentric with the outer one, but having nonpropagating characteristics; a hollow beam is directed between the two pairs of helices. The force diagram shown in Fig. 42 indicates the resulting forces on the electrons. As seen from this figure, this is a very stiff form of focusing in that the restoring forces are large. Relatively high permeances per square can be focused with good beam definition. Because of the complexity of the device and because of the poor heat dissipation properties of the inner helix, this has only been used on one experimental tube.

**Folded-Waveguide Structure.** Fig. 43 shows a typical cross section of a folded-waveguide slow-wave circuit in which focusing spades have been inserted between the drift tubes of the slow-wave circuit. By isolating these focusing spades from the body of the tube and applying a potential either lower or higher than the body potential with a ratio between the two voltages of about 3:1, a 2.5 micro-permeance beam can be focused. One such tube has produced 10 kilowatts of peak power at X-band. Details of the design and construction of this tube are given in several papers by Siekanowitz and Vaccaro<sup>18</sup> and Belohoubek<sup>19</sup>.

The basic philosophy of this design is similar to that of the parallel-flow gun in that the spades and drift tubes, which are shaped to provide the proper potential along the beam boundary, simulate the flow of electrons between two infinite planes. Fig. 44 compares the voltage shape actually obtained with the ideal.

**Radial Electric Field.** In Harris flow is an example of focusing with radial electrostatic fields; a cylinder or wire is placed coaxially inside the slow-wave structure and a hollow beam is shot between the cylinders from a gun immersed in a magnetic field. The mag-

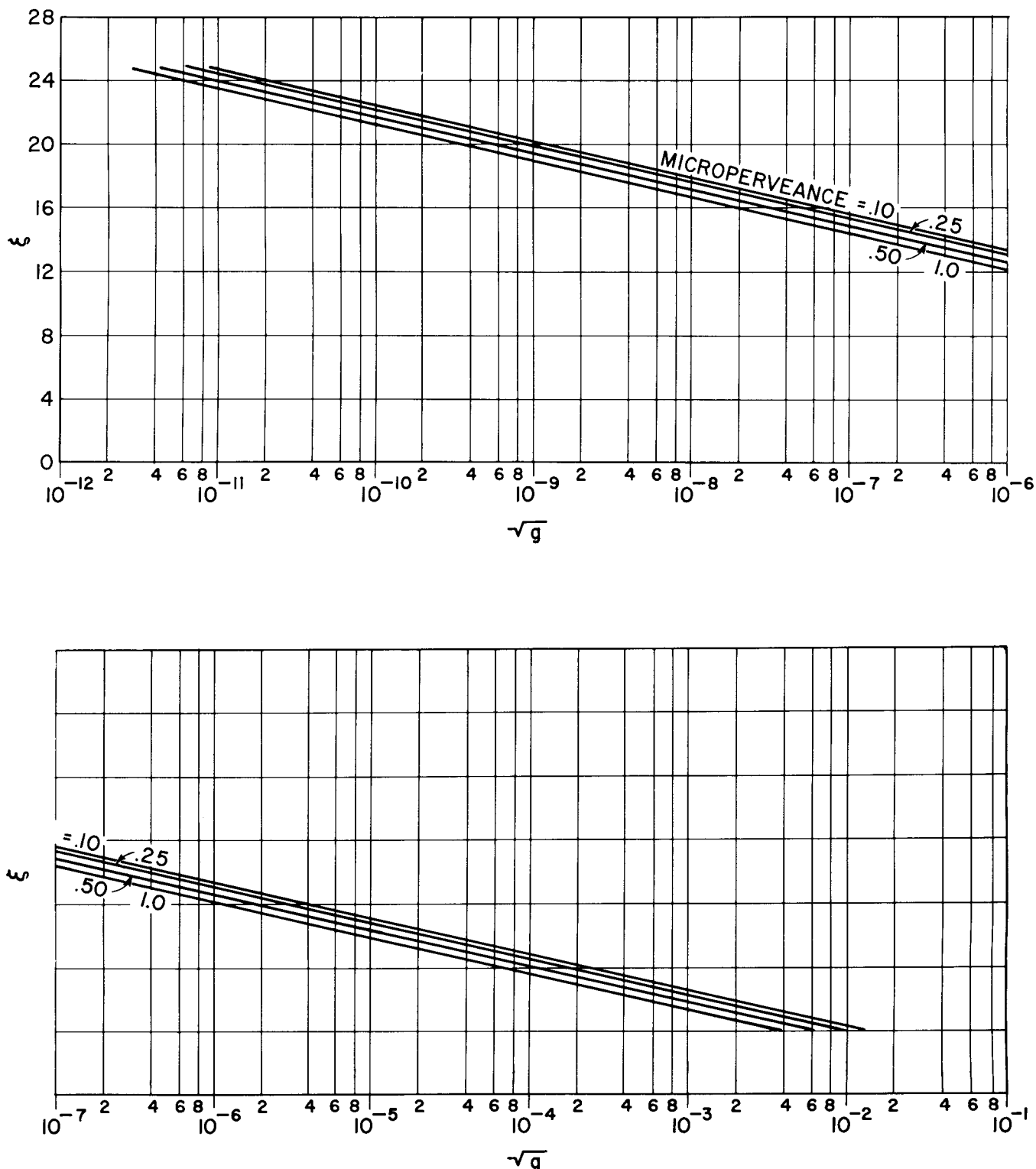


Figure 40. Design Chart for the Bifilar-Helix Electrostatic Focusing Structure

netic field is abruptly terminated as the electrons leave the gun region and enter the radial electrostatic field region. By Bush's theorem, the beam begins to rotate

about the axis with a certain angular velocity with the result that there are two forces tending to push the beam outward: the centrifugal force of the rotating

electrons, and the space-charge forces in the beam itself. These outward forces are counteracted by the radial electric field produced by operating the inner cylinder at a higher potential than the outer cylinder, as shown in a cross section of a typical Harris flow traveling-wave tube in Fig. 45; Fig. 46 shows the resulting force diagram. Because there is less radial dependence of the inward electrostatic force than there is for the inward magnetic force in the case of Brillouin flow, Harris flow is not as stiff and stable as Brillouin flow. Only a few experimental tubes have been made using this focusing scheme, because of the dissipation problems on the inner cylinder and the problem of generating a magnetic field in the gun region and cutting it off sharply as the interaction region is reached.

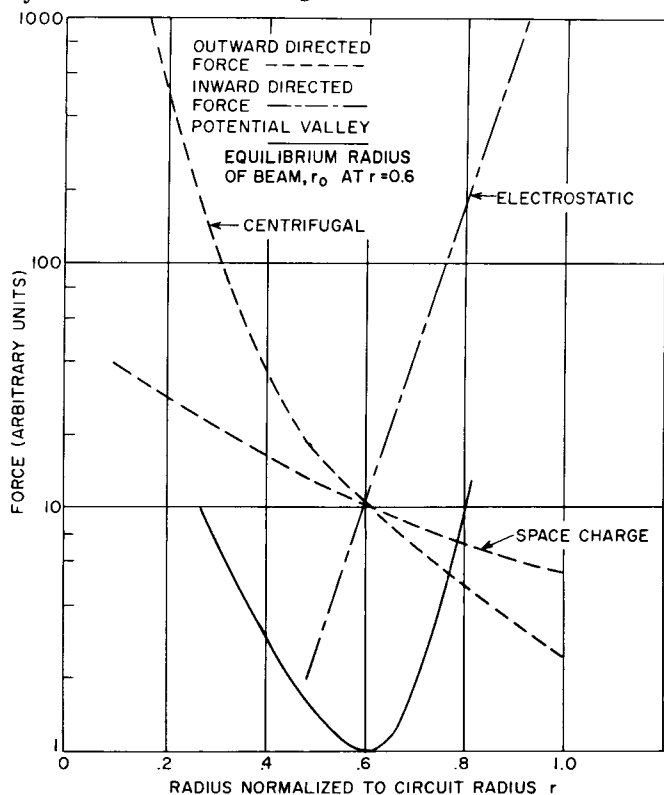


Figure 41. Diagram of the Forces Acting on the Electron Beam in the Bifilar-Helix Electrostatic Focusing Arrangement when the Electron Gun is Immersed in a Magnetic Field that is abruptly Terminated at the Entrance to the Helix Region

## COUPLERS

The rf couplers of a traveling-wave tube are probably the nearest thing to a necessary evil on a traveling-wave tube. They frequently take up space urgently needed for the magnetic focusing, limit the bandwidth of the tube, or require extra seals which are likely to develop leaks. The basic function of the coupler is to provide a means for passing rf energy from an external line to the slow-wave structure and then from the slow-wave structure back to the output line. In doing so, the impedances of the input and output lines must be matched to the impedance of the slow-wave structure.

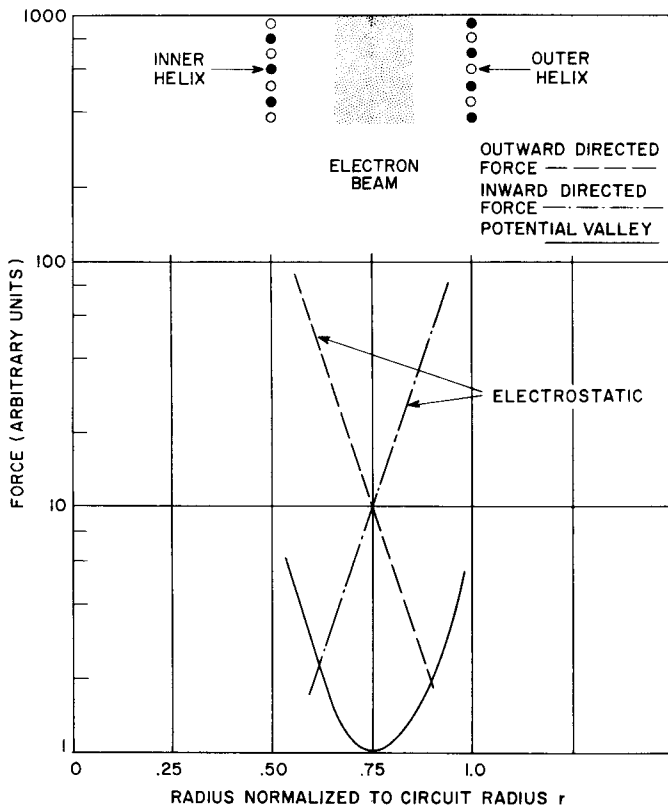


Figure 42. Diagram of the Forces Acting on an Electron in a Hollow Beam Propagating the Annular Space between two Concentric Bifilar Helices

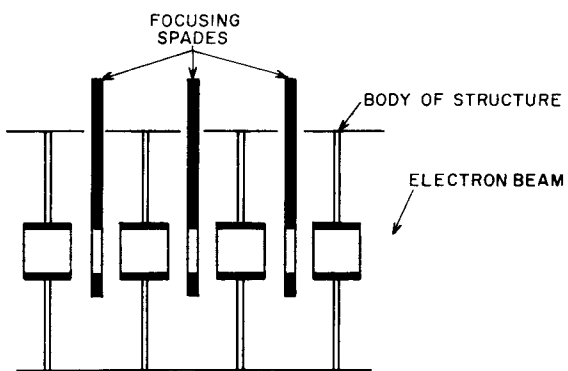


Figure 43. Cross Section of an Electrostatically-Focused Folded-Waveguide Slow-Wave Circuit

## Coupling to Helices

Direct Connector. The simplest and most direct way of coupling the rf energy into and out of the helix is by means of a direct connection to a coaxial line, as shown in Fig. 47. The impedance from the helix to the coaxial line is matched by tapering the entrance of the helix and providing a close shield about the helix. This type of match is very broadband and usually a VSWR of less than two can be maintained over a band of an octave or more. However, it is fairly difficult to construct because a wire must pass through the envelope of the tube and some form of tuning device is needed to

improve the impedance match. A very low VSWR, e.g., below 1.2:1, is difficult to achieve either over a wide frequency range or at one specific frequency. However, in certain types of tubes, specifically backward-wave amplifiers or oscillators, in which coupling is difficult because of the type of propagating mode set up on the helix, this method of coupling is still in wide use.

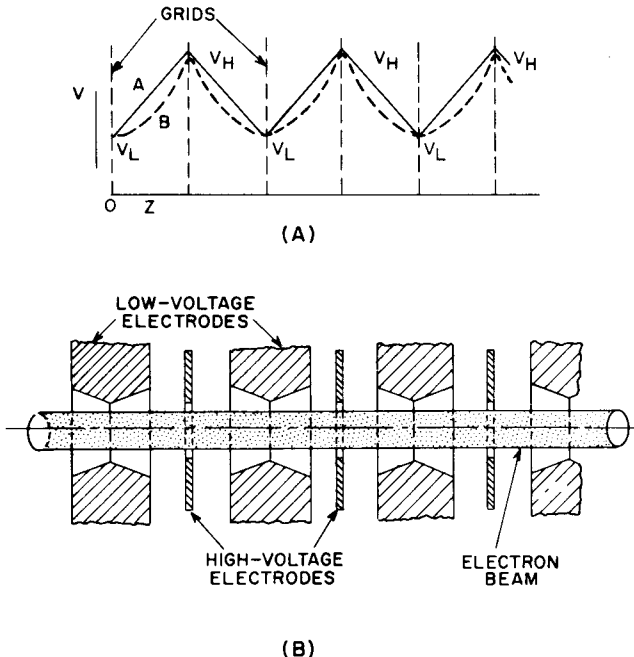


Figure 44. Electrostatically-Focused Folded-Waveguide Slow-Wave Structure: (A) Comparison of the ideal and actual shape of the focusing field; (B) Cross section of the structure

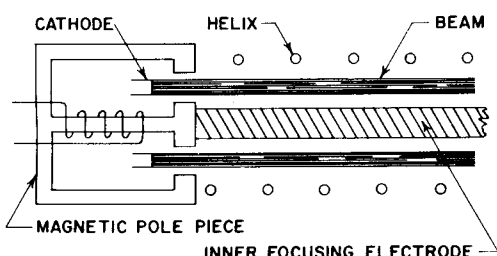


Figure 45. Cross Section of the Electron-Gun and Helix Regions of a Typical Harris-Flow-Focused Traveling-Wave Tube

**Cavity Coupler.** The cavity coupler, because of its large size and relatively narrow bandwidth, is not consistent with today's small light-weight broadband traveling-wave tubes. However, it still has some limited use in specific applications such as narrow-band low-noise traveling-wave tubes in which the coupler loss must be reduced to a bare minimum. Fig. 48 shows the cavity coupler used on the RCA-6861 low-noise traveling-wave tube. The pertinent dimensions are shown on the drawing; for design purposes, it is recommended that dimensions be scaled to other frequencies from the dimensions given in the drawing.

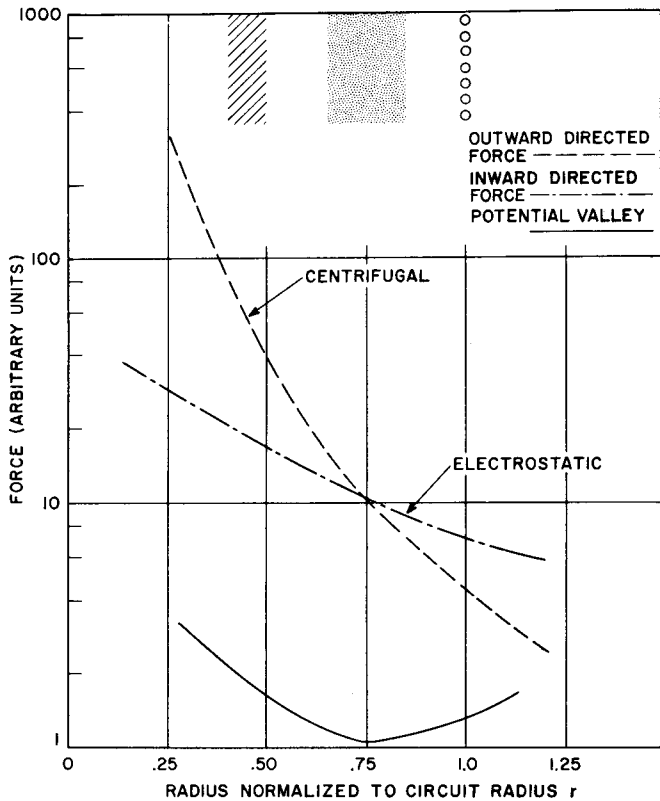


Figure 46. The Focusing Forces Acting on the Electron Beam in a Harris-Flow-Focused Traveling-Wave Tube

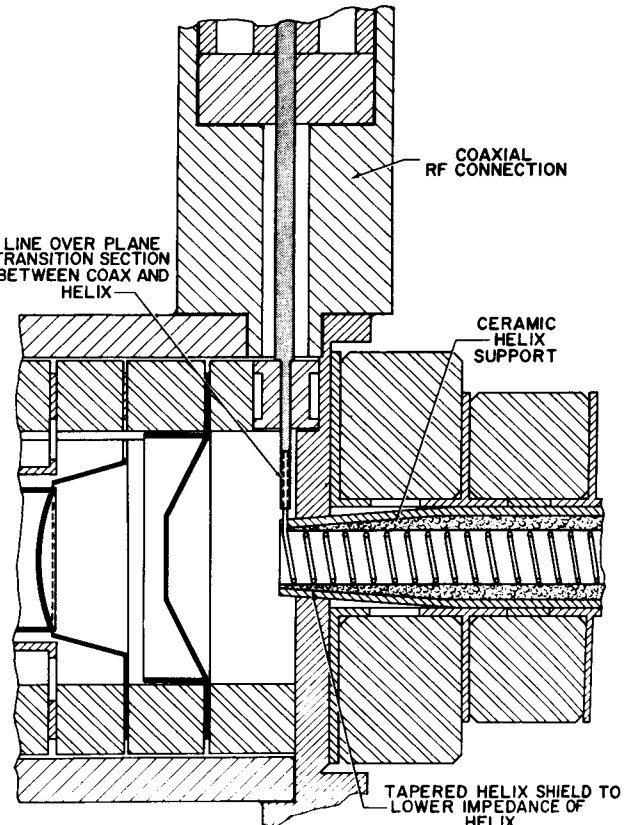


Figure 47. Cross-Sectional Diagram Showing the Direct-Coupling Method of Coupling RF Energy to the Helix

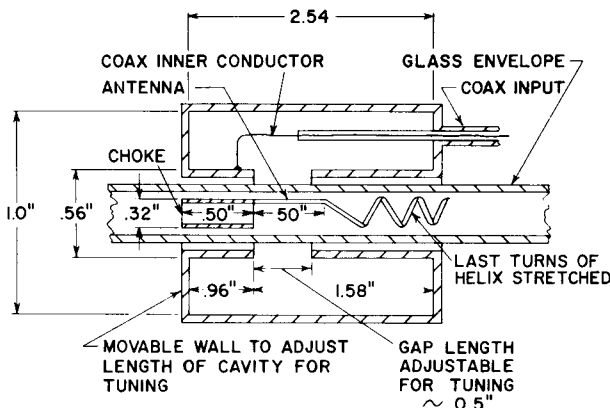


Figure 48. Cross Section of the Cavity Coupler Used in the RCA-6861 Traveling-Wave Tube

In this type of coupling, the helix is terminated by a short antenna followed by a choke section. The last three or four turns of the helix are stretched to provide a smooth transition into the antenna. Surrounding the antenna is an open portion of a fairly broadband and low-Q cavity. The transition of the cavity to a coaxial line is made as shown in Fig. 48.

Several adjustments can be made to achieve the lowest possible coupler loss over a specific frequency range; for example, the width of the gap of the cavity or the over-all length of the cavity can be changed. Over relatively narrow frequency ranges of 400 to 500 megacycles at S-band, a very low VSWR in the order of 1.1:1 can be regularly achieved.

**Waveguide Couplers.** In the waveguide method of coupling, the helix is terminated in exactly the same manner as in the helical-coupler method with several stretched turns, an antenna, and a choke section. The impedance of the helix is matched by making the waveguide thinner by a factor of 3 or 4, either by a smooth transition or by a multiple-step transition. A hole cut through the waveguide, as shown in Fig. 49, is placed over the antenna. One end of the waveguide is terminated with an adjustable short and the other end goes through the transition to the standard-height waveguide. Bandwidths of more than one-half octave have been obtained with this type of coupling, with a VSWR of less than 2:1. Over narrow-frequency ranges, by adjusting the position of the short and adding additional tuning screws, low values of VSWR of less than 1.1:1 can be maintained. Fig. 50 shows the dimensions of a typical waveguide coupler for an X-band traveling-wave tube; couplers for other frequency bands can be scaled from these dimensions.

Waveguide-type couplers are most commonly used in the frequency ranges of C-band, X-band, and above for two reasons. First, at the lower frequencies, the waveguide is large and bulky (frequently much larger than the tube itself). In such cases, some form of coaxial coupling is preferred. Second, at C-band and X-band, where the helices are very small and supported on ceramic rods, the diameter of the envelope of the tube can be several times the diameter of the helix. Under these conditions, the more commonly used heli-

cal couplers, to be described later, cannot be used, and waveguide couplers are the preferred alternative. At any frequency, where very high cw or pulsed power is generated, the low-loss waveguide is preferred to coaxial types.

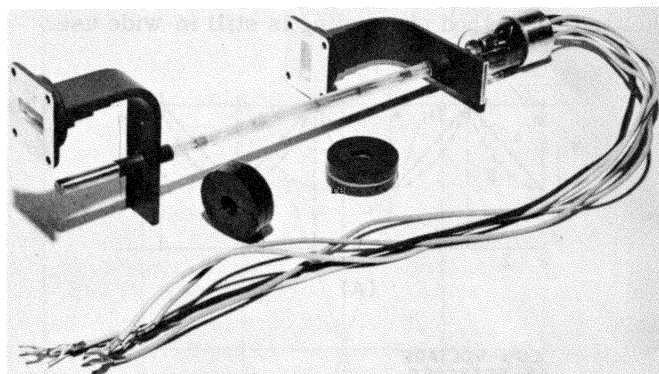


Figure 49. Arrangement Used in the Waveguide Method of Coupling Energy into and out of the Helix

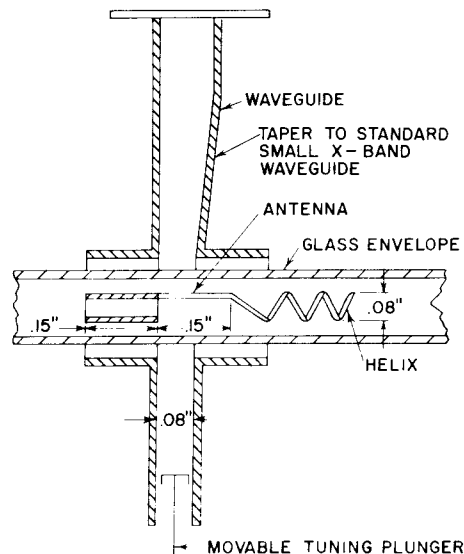


Figure 50. Cross Section of a Typical Waveguide Coupler for an X-Band Traveling-Wave Tube

**Helical Couplers.** In recent years, most of the tubes designed and in production employ helical couplers. The helical coupler is extremely broadband; excellent coupling can be obtained over more than an octave of bandwidth. They take up little space and can be easily built inside a periodic permanent magnet stack. Unlike the direct connection, which has a roughly equivalent bandwidth, the coupled-helix coupler does not require a break in the vacuum envelope.

The bandwidth of the coupled-helix coupler is much wider than that obtained with a cavity coupler or with a waveguide coupler and is comparable to that obtained with a direct connection. The helical coupler can be made with a lower VSWR than the direct connection, typically less than 1.5:1 over an octave. But the helical

coupler will add several inches to the length of the tube.

The helical coupler occupies less volume than other types and thus causes little interference with the location and operation of the focusing magnets. In addition, the helical coupler can couple to the bifilar helix used in electrostatic focusing without coming in direct contact with either of the helices. This can be very important in electrostatic focusing where the helices can have a potential difference of several thousand volts.

The theory and design of coupled-helix couplers has been thoroughly treated by Cook, Kompfner, and Quate.<sup>20</sup> Only the basic theory and some construction details are presented here. The theory of operation is simple, as shown in Fig. 51. Two helices having different diameters are wound concentrically with one wound in the opposite direction to the other. If an rf signal is introduced on the helix at the left-hand side, the signal propagates down the helix in the right-hand direction. Because the field of the helix extends into the region occupied by the other helix, some of the energy is transferred to the other helix. If the phase velocity of the two helices are the same and have the proper diameter ratio, a beating phenomenon occurs which is similar to the mechanical analog of the coupled pendulum. After traveling a short distance, the energy, which is initially all in the outer helix, is transferred entirely to the inner helix. At a later point, it is transferred back entirely to the outer helix. If, however, the outer helix is terminated at the point at which all the energy is on the inner helix, the energy is, in effect, transferred or coupled from a coupling helix to the tube helix. If the process is reversed, an output coupler for a traveling-wave tube is formed.

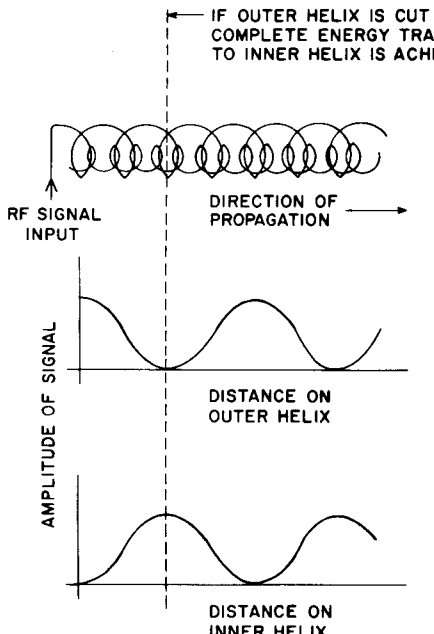


Figure 51. Diagram of the Interaction in the Coupled-Helix Coupler

Typical construction of such a coupler is shown in Fig. 52. A 50-ohm coaxial line having a center conductor wound into the form of a helix which is sur-

rounded by a close-spaced metal shield. With the proper spacing between this metal shield and the coupling helix, the impedance of the line-over-plane formed by the coupling helix in the shield can be made to match that of the coaxial line, and no impedance mismatch occurs at the transition. The coupling helix then couples with the tube helix as described previously. From the referenced article, it is possible to find the optimum diameter ratio for the two helices for a given frequency range and calculate the length of the coupled helix. However, in practice, the length of the coupling helix is normally one to two times the calculated value. The easiest means to determine the actual length is to make an overlength coupler and then gradually cut off turns until the minimum VSWR is achieved.

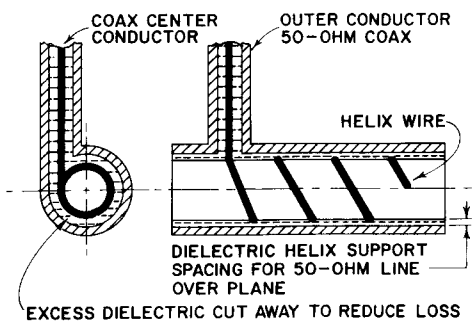


Figure 52. Cross Section of a Coupled-Helix Coupler

The optimum spacing ratio between the inner and outer helices for broadband operation is about 1.6:1. At higher or lower ratios, the bandwidth of the coupler becomes more restricted. At higher ratios, e.g., 2:1, the length of the coupler required for complete transfer of energy may become excessive. For this reason, in C-band and X-band tubes in which the relatively small fragile helix is supported on three ceramic rods and the outside of the tube envelope may be several times the helix diameter, helical couplers are not generally used. However, at low C-band, S-band, and L-band using larger and more physically rugged helices, which can be held in precision glass or imbedded in fluted glass, the outer diameter of the envelope may be only 1.3 times the helix diameter and helical couplers may be used.

#### Coupling to Other Types of Slow-Wave Structures

Means of coupling to other types of slow-wave structures are nearly as numerous as the types of slow-wave structures. In the case of a coupled-cavity or folded-waveguide structure, the last cavity opens up into a waveguide, usually of reduced height, which is then tapered to the size of a standard waveguide, as shown in the cross section in Fig. 53. In the general design procedure, a waveguide is tapered down to the size of the final cavity and the impedance presented to the waveguide is measured at various frequencies across the passband of the slow-wave structure. This data is then plotted on a Smith Chart and the required amount of added inductance or capacitance is determined. Normally, the addition of an inductance, as shown in Fig. 53, is required as an inductive post where the waveguide joins the first cell of the structure.

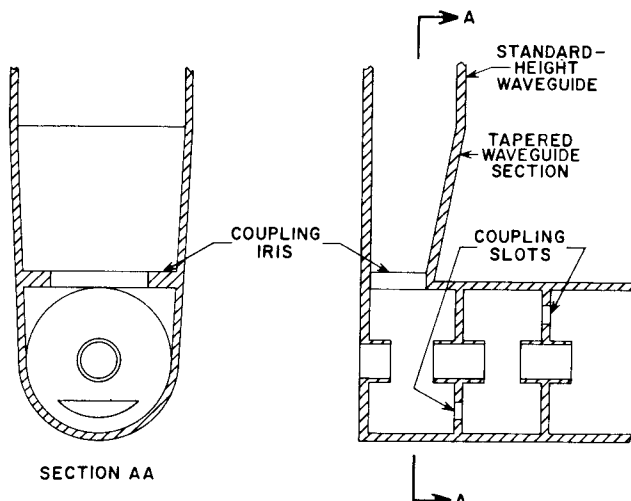


Figure 53. Method Used for Coupling Energy into a Folded-Waveguide Slow-Wave Structure

## ATTENUATORS

The first traveling-wave tube, built by R. Kompfner<sup>21</sup> in England, did not have an attenuator and, consequently, was an extremely unstable device. Reflections from the output or from the load could be reflected back through the tube, be re-reflected from the input or the generator, reamplified in the tube and, depending upon whether in or out of phase with the original signal, could either cause oscillations at some frequencies or cancellation of output at other frequencies. It remained for Pierce and Field<sup>22</sup> in this country to add an attenuator in the center of the tube to isolate the input section from the output section and create a stable high-gain wide-band amplifier. For stability, the value of the attenuation should be about 10 db greater than the gain of the tube.

In the same way that lack of an attenuator can cause oscillations, reflections from the attenuator itself can produce the same effect. For instance, in the output section of a traveling-wave tube, the gain may be as great as 30 db. If a mismatch exists in the output coupler or in the load with a VSWR of 2:1, the power reflected back down the helix from the mismatch is 10 db less than the output signal. If the match at the input of the attenuator has a 2:1 VSWR, the power being re-reflected from the attenuator is 20 db less than the output signal. However, because the gain of the output section is 30 db, the signal reflected from the attenuator is amplified and emerges from the tube at a greater amplitude than the original signal. This condition leads to unwanted oscillation.

Many parameters control the placement, the amount, and the type of attenuation used. Among these are the amount of power handled by the attenuator, the efficiency required from the tube, how the output power is to vary with the input power near the saturation region, and the type of slow-wave structure used. These parameters are discussed below in connection with the various types of attenuators.

### Attenuators for Helices

In helix-type traveling-wave tubes, the design of the

attenuator frequently depends on the type of helix support used. For tubes having rod-supported helices, the attenuation must be applied inside the vacuum envelope, usually on the rods. Helices supported directly inside a glass envelope may use an attenuator external to the vacuum envelope in the form of a coupled-helix attenuator or lossy material painted on the outside of the glass envelope.

Attenuators on Rod-Supported Helices. In tubes having rod-supported helices, a carbon suspension, Aquadag, can be sprayed on the rods at the proper location to supply the desired attenuation. (Usually, at the ends of the attenuator, the amount of carbon sprayed on is tapered in density or geometrically shaped to provide a good match looking into the attenuator.) An excellent discussion of the techniques used in applying attenuation to rod-supported helices is given in an article by Laico, McDowell, and Master.<sup>23</sup>

This type of attenuation is usually limited to low average-power traveling-wave tubes because reflected power absorbed by the attenuator is dissipated inside the vacuum envelope and can cause overheating or outgassing of the rods or the helix. One drawback to this form of attenuator is the lack of adjustment to either the placement or the amount of the attenuation after the tube has been constructed and processed. Particular difficulty results in cases in which the processing of the attenuation is not closely controlled, and drastic changes in the amount of attenuation occur during tube processing.

The primary advantage to this type of attenuation is its effectiveness over a broad frequency range, usually extending for an octave above and below the operating range of the tube. This wide range can be particularly important in suppressing certain out-of-band oscillations, especially those of the backward-wave type which may occur at nearly twice the highest operating frequency of the tube. This type of compensation is frequently not possible with other types of attenuators.

Coupled-Helix Attenuators. One means of overcoming the power handling problems inherent in an internal attenuator is to use a coupling helix (described previously) to extract the energy from the tube helix to a point outside the tube envelope. Two types of coupled helix attenuators are commonly used — a lossy-wire coupling helix or a lossless-wire coupling helix imbedded in a lossy dielectric.

The lossy-wire coupling helix is made by winding a coupling helix of Karma or Baker alloy wire having a diameter of 0.0005 inch. The helix is held in shape by winding the wire on a cellophane-tape mandrel and then covering it with another layer of cellophane tape. If the tube must operate at high temperatures, Teflon tape is substituted for the cellophane tape. This type of attenuator is quite effective and 10 to 20 db of loss per wavelength can be obtained. The number of turns per inch and the diameter of the coupling helix are determined as described under COUPLERS.

The second method, having much greater power-handling capability, uses a relatively lossless coupling

helix wound with 0.005 to 0.010 inch tungsten wire for rigidity. This coupling helix is then placed on a cylinder of material having a loss of about 2000 ohms/centimeter. The cylinder with the coupling helix is then placed over the precision glass supporting the tube helix.

The lossy cylinder is usually a porous ceramic (Alsimag 222) impregnated with carbon by either the methane cracking process or by soaking the ceramic in a 10:1 water-sugar solution and firing in hydrogen to reduce the sugar to carbon. Because it is of metal-ceramic construction and located outside the tube envelope, this type of attenuator can handle many watts of reflected power without damaging the tube.

Both these types of coupled helix attenuators have high reflection coefficients. A mismatch of 1.5:1 or 2:1 VSWR at the input of this type of attenuator is not uncommon. Some type of buffer attenuation must be provided at both ends of the attenuator to reduce reflections. This is generally provided by painting an Aquadag arrow on the outside of the helix bulb or by pasting on arrows cut from carbon-impregnated paper. A typical coupled-helix attenuator with Aquadag arrows is shown in Fig. 54.

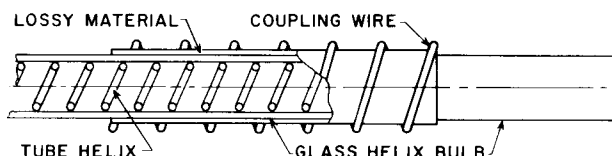


Figure 54. Cross Section of a Typical Coupled-Helix Attenuator

Coupled-helix attenuators are especially useful on bifilar-helix electrostatically-focused traveling-wave tubes. Aquadag-coated rod attenuation would short out the helices, but the coupled helix attenuator, which makes no physical contact cannot cause shorting.

Severed Helix. In general, the attenuator must be at least 2 or 3 wavelengths long to provide the usually required attenuation of 50 to 60 db. At normal frequencies (S-band and above), the length involved is relatively short, especially in low-voltage tubes. However, for high-voltage tubes at S-band and for tubes in the lower frequency ranges, three or four helix wavelengths can require several inches of length and in some high-power low-frequency tubes, the attenuator may add as much as a foot to the over-all length of the tube. In these cases, it is frequently desirable to sever the helix in the center, usually by inserting a drift tube between the input and output section of helix, and terminate the helices at the drift tube with just sufficient attenuation to prevent reflections from the short caused by the drift tube. In this way, 60 to 90 db of attenuation can be provided over shorter distances.

#### Attenuators for Other Types of Slow-Wave Structures

The problems involved in the design of attenuators for high-power tubes are even more complex than those involved in the helix-type tube. For optimum efficiency, the attenuator should be as short as possible. In

the case of the folded-waveguide or other types of coupled-cavity structure, it is desirable that not more than one or two cells be used for the attenuator. The circuit is severed at the point where the attenuation is desired by sealing off the coupling slots between the cavities. This effectively prevents the propagation of the wave in either direction past this point and immediately introduces an isolation in the order of 50 to 60 db.

A lossy substance introduced into the cavities on each side of the break provides a good match and absorbs the incident power. The material used is a porous ceramic described above. Generally, the lossy material almost entirely fills the cavity, although the exact shape must be determined experimentally to find the configuration which provides the lowest VSWR.

When the power is so great that it cannot be handled by an internal attenuator, waveguide couplers are used on either side of the break to take the reflected rf power out of the tube when it may be dissipated in an external load. To reduce the VSWR presented to these attenuators, several cavities (before and after the attenuator) are lightly sprayed with Aquadag to provide some buffer attenuation.

Attenuators for other types of slow-wave structures follow essentially the same general design as for the helix or for the folded waveguide. Some lossy material, either Aquadag or ceramic impregnated with carbon, is placed on or near the slow-wave structure and some form of taper is provided to maintain a good match at the input of the attenuator.

#### COLLECTOR

In many low-power traveling-wave tubes, almost any piece of copper is satisfactory as a collector if operated about 100 volts above the helix potential to prevent secondary electrons from returning to the helix from the collector. However, for tubes above the one-watt level, the collector design must be more carefully considered. The power which the collector must dissipate may be considerable because of the low efficiency of most traveling-wave tubes. In a 100-watt tube, the beam power can range from 500 to 1000 watts.

#### Depressed-Collector Operation

Because of the low-helix interception, nearly all the dc power in the tube is dissipated at the collector. Thus, any reduction in the collector potential at which the beam is collected can materially increase the operating efficiency of the tube.

One of the primary disadvantages of traveling-wave tubes, particularly in the high-power ranges, has been their relatively low efficiency compared to crossed-field or "M"-type devices. Thus, traveling-wave tubes have been used only when equipment designers were forced to use them because of their tremendous bandwidth. As the techniques of collector depression become more advanced and more widely used, the traveling-wave tube, operating at efficiencies of 40 to 50 per cent, will be suitable for many equipments where amplitrons and other crossed-field devices are presently used.

The efficiency of an intermediate power tube such as a 100-watt traveling-wave tube, which would normally operate at about 10 per cent efficiency, can be doubled or tripled simply by reducing the collector voltage and collecting the spent electron beam at voltages far below the helix voltage. However, several factors have to be considered before this type of operation is readily possible. For instance, when the collector is operated at a much lower potential than the helix, secondary electrons generated by the beam striking the collector, are drained from the collector to the helix or slow-wave structure, and cause local overheating. Another limit to the lowest value at which the collector can be operated is set by the space-charge depression in the center of the beam. The effects of space-charge depression and its limitation on the amount by which the collector can be depressed have been discussed in an article by Wolkstein.<sup>24</sup> The limit is dependent on the amount of beam current and on the ratio of the beam diameter to the inner diameter of the collector. For example, a 0.25-ampere beam in a collector with a diameter twice the beam diameter, can be depressed no lower than 550 volts. Fig. 55 is a design chart from which the space charge depression of any beam can be determined.

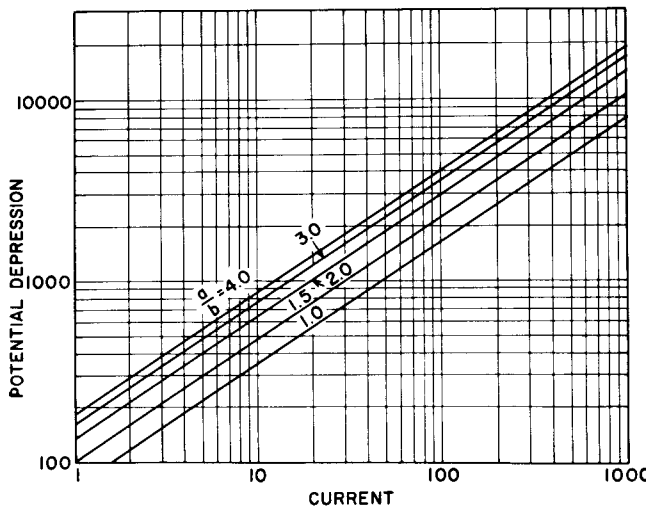


Figure 55. Design Chart Used to Determine the Space-Charge Depression of an Electron Beam

### Two-Stage Depressed Collector

An additional factor which determines the minimum potential to which the collector may be depressed is the velocity spread of the electrons after they have given up their energy to the rf field. Because the rf energy comes from the kinetic energy of the electrons, the beam is slowed down and a higher potential must be used to collect the electrons. Not all electrons are slowed down by the same amount and, as a result, there is a considerable velocity spread in the electron beam. An article by F. Sterzer<sup>25</sup> describes this effect in detail. His solution to the problem of optimum collector depression is to divide the collector into two segments as shown in Fig. 56. In this way, the few electrons which have given up the most energy to the rf wave and, therefore, require a higher collector voltage are collected on the first segment. The remainder of electrons are

then collected on the second segment which collects the bulk of the beam at a much lower voltage. With this approach, he was able to obtain an efficiency of over 45 per cent in a 100-watt S-band traveling-wave tube in which the efficiency would otherwise be only 15 per cent.

### Secondary-Emission Suppression

The secondary electron emission from the collector to the helix may be reduced by reducing the emission coefficient of the collector. A second and more efficient means is to trap the secondary electrons in the collector by making a small entrance to a large collector — essentially a sort of Faraday Cage. The magnetic field must be terminated at the entrance of the collector to prevent the secondary electrons from following the lines of flux back into the helix region. Fig. 57 shows a collector of this type which has been used on several traveling-wave tubes with a very small number of returned electrons, even with the collector depressed to near the theoretical limit.

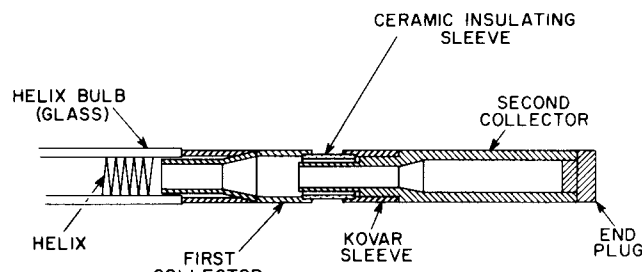


Figure 56. Cross Section of a Two-Stage Collector Assembly

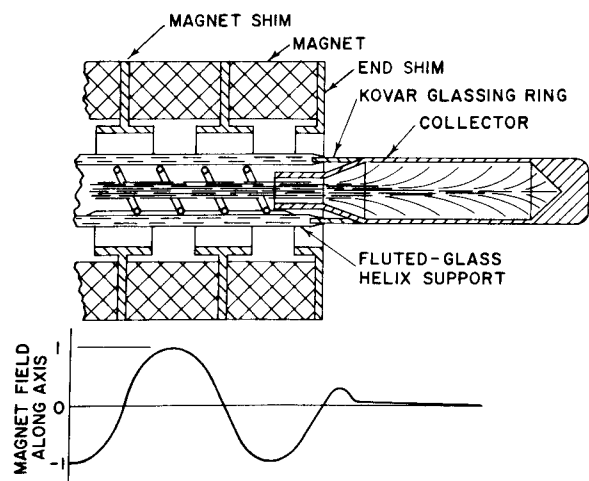


Figure 57. Cross Section of a Magnetically-Shielded Collector Assembly

### Collector Cooling

Cooling of the collector is handled by relatively conventional means — either by heat transfer to nearby massive objects, by forced air cooling, or by some form of liquid cooling.

## APPENDIX

## DESIGN PROCEDURE FOR TRAVELING-WAVE TUBES

As an illustrative example of the procedures followed in the design of a traveling-wave tube, let us assume that a customer has requested an amplifier having the following characteristics:

Frequency range	2.0-4.0 Gc
Power output	1.0 kilowatts
Duty cycle	0.01
Gain (at 1.0 kw)	33 db

The broad bandwidth requires a helix type circuit. With the low duty cycle resulting in an average power of 10 watts, the helix is sufficiently robust to handle the power. Focusing will be supplied by periodic permanent magnets. Because the customer did not specify the voltage, we will calculate tube designs for a range of voltages and then interpolate between these to determine the optimum design based on available electron guns, magnetic field, and size of the tube.

The items given above, which include the midband frequency of 3.0 Gc, are normally specified by the customer and thus are not under the control of the designer.

The following three parameters do not change appreciably from tube to tube and for a first approximation may be chosen as follows:

Efficiency	15 per cent
Dielectric Loading Factor	0.85
$\gamma_a$	1.5

The efficiency is roughly equal to  $2C$  (where  $C$  is Pierce's gain parameter) and the validity of the original assumption can be checked later in the calculation when  $C$  is determined. The dielectric loading factor can be estimated depending upon the type of helix support to be used but cannot be checked until a helix assembly has been constructed and tested. The midband value of  $\gamma_a$  was chosen because of the wide bandwidth required.

The following two items are entirely at the discretion of the designer:

Helix phase velocity, $v_p$	3.0 kilovolts
	5.0
	8.0

Ratio of beam to helix diameter 0.5

The effect of the beam-helix diameter was discussed in the text while the effect of the various helix voltages will be noted as a result of the calculations.

In the following discussion, the terms voltage and velocity will be used interchangeably. They are related by the equation

$$\frac{v}{c} = \frac{\sqrt{V}}{506}$$

where  $v$  is the velocity,  $V$  is the voltage, and  $c$  is the speed of light.

## GENERAL TUBE DESIGN

Parameter	Units	Design 1	Design 2	Design 3
Midband frequency	Gc	3.0	3.0	3.0
Wavelength	centimeters	10.0	10.0	10.0
Helix phase voltage, $V_p$	volts	3000	5000	8000
Helix phase velocity $v_p/c$		0.1085	0.140	0.1755
Beam current				
$I_o = \frac{P_{out}}{\eta V_p}$	amperes	2.22	1.33	0.835

The space charge potential depression is the difference between the voltage applied to the helix and the actual velocity of the electrons. This difference is caused by the negative charge of the electrons as explained in the text.

Parameter	Units	Design 1	Design 2	Design 3
Space charge potential depression (See Fig. 55)	volts	2300	1650	1200

In order for the electrons to give up energy to the rf wave, the electrons must travel faster than the cold phase velocity of the helix. This difference is approximately equal to  $3/4$  of the space charge potential depression.

Parameter	Units	Design 1	Design 2	Design 3
Difference between $v_p$ and $u_0$	volts	1700	1250	900
Voltage corresponding to electron velocity, $V_o$	volts	4700	6250	8900
Power supply voltage, $V_{ps}$ (electron velocity plus space charge depression voltage)	volts	7000	7900	10100

The proper voltage (i.e.,  $V_p$ ,  $V_o$ , or  $V_{ps}$  and the corresponding phase velocities) must be used at the appropriate occasions below as noted.

Parameter	Units	Design 1	Design 2	Design 3
$\gamma_a = \frac{2\pi a}{\lambda} \frac{506}{\sqrt{V_p}}$ [See Eq. (17)]		1.5	1.5	1.5
$k_a = \frac{2\pi a}{\lambda}$		0.163	0.21	0.263
Helix radius, $a$ (Calculated from equation for $\gamma_a$ )	inches	0.102	0.132	0.165
$F(\gamma_a)$ (See Fig. 15)		2.62	2.62	2.62
IRF (See Fig. 16)		1.075	1.075	1.075

Parameter	Units	Design 1	Design 2	Design 3
F [See Fig. 17)]		0.45	0.42	0.38
K - use $V_p$ [See Eq. (25)]	ohms	43.2	31.3	22.5
C - use $V_o$ [See Eq. (7)]		0.172	0.118	0.081

At this point we can calculate the efficiency and check the beam current which was calculated earlier using the approximate efficiency. The efficiency will be twice the value of C but reaches a limit about 0.2. The voltage corresponding to the electron velocity,  $V_o$ , should be used, and the power output should be about 1.5 times the minimum required to allow for the drop in power near the ends of the frequency band.

Parameter	Units	Design 1	Design 2	Design 3
$\eta$		0.20	0.20	0.16
$I_o$	amperes	1.6	1.2	1.0

Using these new values of current, the electron velocity and power supply voltage can be recalculated and the value of C recalculated. The helix impedance K will not change because the phase velocity does not change.

Parameter	Units	Design 1	Design 2	Design 3
Space charge potential depression	volts	1850	1500	1350
Difference between $v_p$ and $u_o$	volts	1400	1100	1000
$V_o$	volts	4400	6100	9000
$V_{ps}$	volts	6250	7500	10350
C		0.158	0.115	0.085

We can now recalculate the beam current using the same assumptions as before.

Parameter	Units	Design 1	Design 2	Design 3
$\eta$		0.2	0.2	0.17
$I_o$	amperes	1.70	1.23	0.98

These values of beam current are sufficiently close to the previous set that no further recalculation is required.

Parameter	Units	Design 1	Design 2	Design 3
Q (See Fig. 5A)		1.6	1.6	1.6
QC		0.272	0.197	0.157
B (See Fig. 7)		36	38	39
A (See Fig. 6)		-6.75	-7.0	-7.2
$L_{att}$		6.0	6.0	6.0

The loss introduced by the attenuator can be read from Fig. 8 assuming the attenuator is a sever in the circuit and the length is known. However, because the attenuator is composed of a finite amount of loss which is tapered at each end, the first assumption is not entirely valid and the exact length is difficult to determine. Thus, an estimate of 6 db attenuation is a reasonable average.

The next step is the determination of the active length of helix required to obtain 33 db gain at a power output of 1.0 kilowatt. It should be noted that the traveling-wave tube equations apply to small signal conditions only in which the rf power output is about 10 per cent or less of the saturated power output. The gain at saturation is normally about 6 db less than the gain under small signal conditions. Thus, in determining the length of the circuit as a function of gain, the small signal gain, 39 db, should be used.

Parameter	Units	Design 1	Design 2	Design 3
$N$ , active length of circuit in helix wavelengths - See Eq. (16)		9.1	11.9	15.7
$l$ , active length of circuit - use $V_o$ - See Eq. (18)	inches	4.7	7.25	11.6
Coupler length	inches	1.2	1.8	2.9
Attenuator length	inches	1.4	2.2	3.9
Gun and collector length	inches	6.0	6.0	6.0
Total tube length		13.5	17.25	24.4

The attenuator length must be about one-third the active length of the circuit to obtain the required attenuation.

The combined length of the input and output helical couplers will normally be about one-fourth of the active length required to obtain 30 to 40 db of gain.

Parameter	Units	Design 1	Design 2	Design 3
$r_o$ , beam radius	inches	0.051	0.066	0.082
$B_m$ , $1.4 B_o$ - use $V_o$ [See Eq. (28)]	gauss	1450	880	572
$L$ , magnet period for $C = 8$ [See Eq. (29)]	inches	0.367	0.710	1.33
Gun perveance - Use $V_{ps}$	$\mu$ pervs	3.4	1.9	0.81

The power supply helix voltage is used for the gun perveance because we would like the anode to operate at the helix potential.

Some of the more important parameters which have been calculated for the three designs are plotted in Fig. A1 as a function of helix diameter. The only parameter which is limiting is the gun perveance. At

the present time, we do not have a gun with good performance above a perveance of 2.0 and, thus, the smallest helix diameter which could be used is 0.260 inch. A smaller diameter would be attractive because of the shorter length tube which would then be possible as well as the lower operating voltage which is always desirable to the equipment manufacturer. For this tube, however, the present state of the art of the electron gun sets the limit of the design. Tubes at other power levels and other frequencies may be limited by other factors than the gun such as the magnetic field which can be generated by present-day magnet materials.

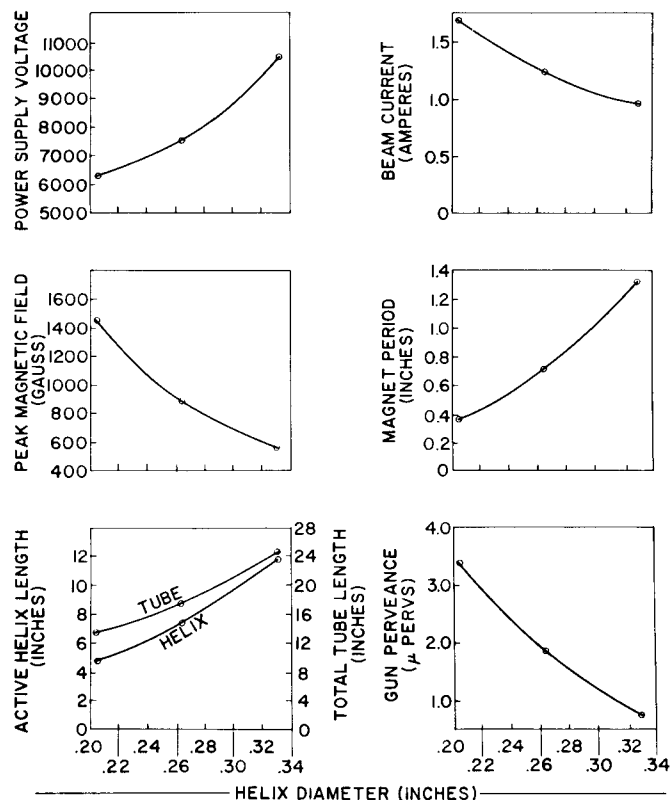


Figure A1. Design Parameters as Functions of Helix Diameter

At this point, the tube design is essentially complete. The major parameters are tabulated below:

Power supply voltage	7400
Beam current	1.25 amperes
Helix diameter	0.260 inch
Peak magnetic field	900 gauss
Magnet period	0.70 inch
Active length of helix	7.0 inches
Total length of tube	17 inches
Electron gun perveance	1.9 $\mu$ pervs
Phase velocity of helix	5000 volts
Electron velocity	6100 volts
C	0.115

In order to verify that the performance will be uniform across the band, the calculations made above should now be repeated varying the frequency instead of the helix diameter or voltage. The frequencies chosen

might be 1.5, 2.0, 2.5, 3.0, 3.5, 4.0, and 4.5 Gc. An effort should be made to estimate the correct phase velocity at each frequency, as shown in Fig. 10, and modified by the dielectric loading factor. To calculate the gain, start with the helix diameter, the phase velocity, and the current at each frequency and compute the electron velocity, the helix impedance  $C$ , and then the gain. The results of this calculation will show if the center frequency of the tube corresponds with the required center frequency. If not,  $\gamma_a$ , or the beam-helix diameter ratio, is adjusted and the procedure repeated.

## SYMBOLS

- A - Initial loss
- a - Mean helix radius
- B - Growing wave parameter (Fig. 7)
- $B_m$  - Peak magnetic field in a periodic permanent magnet assembly
- $B_0$  - Brillouin magnetic field
- b - Beam radius; also  $r_0$
- r - Shield radius
- C - Pierce's gain parameter  $C^3 = KI_0/4 V_0$
- Constant determining allowable period of periodic permanent magnet stack
- c - Speed of light
- d - Helix wire thickness
- DLF - Dielectric loading factor
- F - Impedance reduction due to DLF (Fig. 17)
- f - Frequency
- $I, I_0$  - Beam current
- i - Square root of -1
- IRF - Impedance reduction factor, actually an increase of helix impedance due to finite size of electron beam (Fig. 16)
- K - Helix impedance
- k - Free space wave constant  $k = \omega/c$
- L - Period of loaded waveguide slow-wave structure
- Period of periodic permanent magnet assembly
- Loss on helix or other type circuit
- l - Length of circuit
- Latt - Loss due to lumped attenuator (Fig. 8)
- N - Length of circuit in guide wavelength  $N = 1/\lambda_g$
- P - Helix pitch
- Perveance,  $p = I_0/V^{3/2}$
- Q - Pierce's passive mode parameter
- r - Radial distance from axis of beam, helix, or other slow-wave circuit
- $r_0$  - Beam radius; also b
- $u_0$  - Velocity of electron beam
- V - Voltage
- $V_0$  - Voltage corresponding to velocity of electron beam
- $V_{ps}$  - Voltage applied to helix or other slow-wave structures from power supply
- v - Velocity of growing wave
- $v_p$  - Phase velocity of circuit in absence of electron beam
- $\alpha$  - Attenuation constant
- $\beta$  - Growing wave phase constant,  $\omega/v$
- $\beta_e$  - Electron beam phase constant  $\omega/u_0$
- $\beta_0$  - Free space phase constant,  $\omega/c$
- $\Gamma$  - Propagation constant of growing wave

- $\Gamma_1$  - Propagation constant of slow-wave structure  
 $\eta$  - Efficiency  
 $\gamma$  -  $\frac{2\pi a}{\lambda_0} \frac{c}{v}$ , radial phase constant  
 $\lambda_g$  - Circuit wavelength,  $\lambda_0 \frac{u_0}{c}$   
 $\lambda_0$  - Free space wavelength  
 $\psi$  - Helix pitch angle,  $\tan \psi = \frac{P}{2\pi a}$   
 $\omega$  - Angular frequency,  $\omega = 2\pi f$

## REFERENCES

1. Pierce, J. R., Traveling Wave Tubes, D. Van Nostrand Co., Inc., New York, 1950
2. Poschl, Van Kalus, "Wellenfortpflanzung langs einer Wendel mit zylindrischem Außenleiter," A. E. U., Vol. 7, pp. 518-522, 1953
3. Nalos, E.J., "Present State of Art in High-Power Traveling-Wave Tubes," Microwave Jour., Vol. 2, No. 12, p. 31, Dec. 1959; Vol. 3, No. 1, p. 46, Jan. 1960
4. Belohoubek, E., "Propagation Characteristics of Slow-Wave Structures Derived from Coupled Resonators," RCA Review, Vol. 19, No. 2, pp. 283-310, June 1958
5. Nalos, E.J., "Measurement of Circuit Impedance of Periodically Loaded Structures by Frequency Perturbation," Proc. IRE, Vol. 42, No. 10, pp. 1508-1511, October 1954
6. Danielson, W. E., J. L. Rosenfeld, and J. A. Saloom, "A Detailed Analysis of Beam Formation with Electron Guns of the Pierce Type," Bell Syst. Tech. Jour., Vol. 35, No. 2, pp. 375-420, March 1956
7. Pierce, J. R., Theory and Design of Electron Beams, D. Van Nostrand Co., Inc., New York, 1949
8. Helm, R., K. Spangenberg, and L. M. Field, "Cathode Design Procedure for Electron Beam Tubes," Electrical Communications, Vol. 24, p. 105, March 1947
9. Samuel, A. L., "On the Theory of Axially Symmetric Electron Beams in an Axial Magnetic Field," Proc. IRE, Vol. 37, No. 10, pp. 1252-1258, Nov. 1949
10. Susskind, C., "A Convergent Hollow Beam Elec-
- tron Gun for Microwave Tubes," Stanford Electronics Labs and Microwave Labs, Stanford Univ., Stanford, Calif., Tech. Report No. 450-1, June 29, 1956
11. Kino, G. S. and J. J. Taylor, "The Design and Performance of a Magnetron Inspection Gun," IRE Trans. on Electron Devices, Vol. ED-9, No. 1, pp. 1-11, January 1962
12. Smullin, L., Noise in Electron Devices, John Wiley, 1959
13. Glass, M.S., "Straight Field Permanent Magnets of Minimum Weight for TWT Focusing-Design and Graphic Aids in Design," Proc. IRE, Vol. 45, No. 8, pp. 1100-1105
14. Code Z1
15. Code Z2
16. Chang, K. K. N., "Confined Electron Flow in Periodic Electrostatic Fields of Very Short Periods," Proc. IRE, Vol. 45, No. 1, pp. 66-73, Jan. 1957
17. Chang, K. K. N., "Biperiodic Electrostatic Focusing for High-Density Electron Beams," Proc. IRE, Vol. 45, No. 11, pp. 1522-1527
18. Siekanowitz, W.W. and F.E. Vaccaro, "Periodic Electrostatic Focusing of Laminar Parallel-Flow Electron Beams," Proc. IRE, Vol. 47, No. 3, pp. 451-452, March 1959
19. Belohoubek, E. F., "Slow-Wave Structures for Electrostatically-Focused High-Power Traveling-Wave Tubes," RCA Review, Vol. 21, No. 3, pp. 377-388, Sept. 1960
20. Cook, J. S., R. Kompfner, and C. F. Quate, "Coupled Helices," Bell Syst. Tech. Jour., Vol. 35, No. 1, pp. 127-178, January 1956
21. Kompfner, R., "Traveling Wave Valve-New Amplifier for Centimetric Wavelengths," Wireless World, Vol. 52, pp. 369-372, Nov. 1946
22. Based on work done by J. R. Pierce and L. M. Field
23. Laico, J.P., H. L. McDowell, and C. R. Master, "A Medium-Power Traveling-Wave Tube for 6,000 Mc Radio Relay," Bell Syst. Tech. Jour., Vol. 35, No. 6, pp. 1285-1346, Nov. 1956
24. Wolkstein, H. J., "Effect of Collector Potential on the Efficiency of Traveling-Wave Tubes," RCA Review, Vol. 19, No. 2, June 1958
25. Sterzer, F., "Improvement of Traveling-Wave Tube Efficiency through Collector Potential Depression," IRE Trans. on Electron Devices, Vol. ED-5, No. 4, October 1958

# Article Outlines

## Emitters and Photoconductors

<b>Fundamentals of Electron Emission</b>	
L. S. Nergaard	
ELEMENTARY CONSIDERATIONS.....	1
The Dual Nature of Particles	
Quantization of Energy	
Quantum Statistics	
Fermi-Dirac Statistics	
Bose-Einstein Statistics	
ELEMENTARY SOLID-STATE PHYSICS.....	2
Some Properties of Solids	
Electronic Properties of Solids	
Band Structure	
Conductivity	
Diffusion	
Donors, Acceptors, and Traps	
Conclusion	
EMISSION MECHANISMS.....	8
Thermionic Emission	
Field Emission	
Photoemission	
Secondary Emission	
THE PHYSICS OF THE OXIDE CATHODE .....	15
Emission-Current Density	
Model of the Oxide Cathode	
Cathode Conductivity	
Pulse Operation of Oxide Cathodes	
Donors and Their Formation	
APPENDIX A.	
THE "WAVE EQUATION" FOR ELECTRONS, AND THE DENSITY OF STATES .....	23
The Wave Equation	
A Simple Case of Quantization	
The Density of States for a Free Electron	
APPENDIX B.	
FERMI-DIRAC STATISTICS.....	25
The Transitions Between Two "States"	
Transitions to "Free" Energy States	
LIST OF SYMBOLS.....	26
REFERENCES.....	27
 <b>Oxide-Coated Emitters</b>	
C. P. Hadley	
GENERAL DESCRIPTION.....	28
THE CATHODE COATING.....	28
THE BASE MATERIAL .....	29
DECOMPOSITION OF BINDER AND CARBONATES.....	30
ACTIVATION.....	30
MECHANISM OF OPERATION .....	31
THE MEASUREMENT OF THERMIONIC EMISSION .....	32
DYNAMIC EQUILIBRIUM AND POISONING.....	35
Activating Mechanisms	
De-Activating Mechanisms	
Destruction of Barium, Strontium, or Calcium Oxides	
CONCLUSIONS .....	35
LIST OF SYMBOLS.....	35
REFERENCES .....	36
 <b>Electron-Emission Coating for the Oxide Cathode</b>	
C. H. Meltzer and E. G. Widell	
BASIC CONSIDERATIONS FOR THE EMISSION COATING .....	37
Work Function	
Semiconductor Plus "Electron-Pore Gas" Conductivity	
Activation of the Oxide-Cathode System	
Electrical Importance of the Substrate Metal and Emission Coating	
Equilibrium Systems and Interactions	
PREPARATION OF THE EMISSION COATING.....	40
The Carbonate Form	
The Oxide Form	
THERMODYNAMIC CONSIDERATIONS OF OXIDE-CATHODE SYSTEMS .....	50
DECOMPOSITION OF THE EMISSION COATING .....	52
AMMONIUM-PRECIPITATED CARBONATES .....	54
LIFE ASPECTS OF THE OXIDE-COATED CATHODE....	56
The Manufacturing Operation	
Application End Use	
CONCLUSION.....	61
REFERENCES.....	61
 <b>Nickel Base Metal for the Oxide Cathode</b>	
C. H. Meltzer and E. G. Widell	
NICKEL .....	64
REQUIREMENTS OF NICKEL ALLOYS FOR CATHODE BASE MATERIAL .....	64
METALLURGY OF NICKEL AND ITS ALLOYS.....	65
Air-Melt Process	
Vacuum-Melt Process	
EFFECTS OF REDUCING AGENTS ON HOT STRENGTH AND HOT RESISTIVITY .....	68
EFFECTS OF REDUCING AGENTS ON CATHODE ACTIVITY AND REACTIONS.....	70
Barium Vapor Pressure and Diffusion Rates	
Sublimation Effects	
REVIEW OF SPECIFIC REDUCING AGENTS.....	72
Carbon in Pure Nickel—N81	
Carburized N18 Cathodes	
Carbon and Magnesium	
Magnesium	
Silicon	
Aluminum	
Tungsten	
Titanium	
Manganese	
Calcium	
Boron	
CHARACTERISTICS OF SELECTED CATHODE ALLOYS..	75
REFERENCES.....	75

## The Interface and Other Oxide-Cathode Impedances

E. J. Hannig

CATHODE SLEEVE ACTIVITY .....	77
CATHODE ACTIVATION .....	78
CATHODE IMPEDANCES .....	79
EQUIVALENT CIRCUIT OF CATHODE IMPEDANCES .....	80
DECAY CHARACTERISTICS .....	82
EFFECT OF ALLOY ON CATHODE IMPEDANCE .....	83
OPERATIONAL CAUSES OF INTERFACE IMPEDANCE .....	83
COATING ADHERENCE .....	84
CATHODE IMPEDANCE EVALUATION .....	84
Sine-Wave Methods	
Square-Wave Methods	
Pulse Method	
REFERENCES .....	87

## Tungsten, Thoriated-Tungsten, and Thoria Emitters

W. E. Harbaugh

PURE-TUNGSTEN EMITTERS .....	90
Preparation of Tungsten Filaments	
Properties of Tungsten Emitters	
Present Uses	
THORIATED-TUNGSTEN EMITTERS .....	91
Preparation	
Reasons for Carburization	
The Carburization Process	
End-Loss Correction	
Preferred Carburization	
Some Precautions for Carburization	
Quality Control	
THORIA EMITTERS .....	96
SUMMARY .....	98
REFERENCES .....	98

## Photoelectric and Secondary-Electron Emission

A. H. Sommer

### PHOTOELECTRIC EMISSION

GENERAL CONSIDERATIONS .....	99
METALLIC PHOTOEMITTERS .....	99

SEMICONDUCING PHOTOEMITTERS .....	100
PRACTICAL PHOTOCATHODES .....	101

The Antimony-Cesium (Sb-Cs) Cathode	
Formation	
Properties	
Miscellaneous Cathodes of the Sb-Cs Type	
Multi-Alkali Cathodes	
The Silver-Oxygen-Cesium (Ag-O-Cs) Cathode	
Formation	
Properties	
The Bismuth-Silver-Oxygen-Cesium (Bi-Ag-O-Cs) Cathode	
Formation	
Properties	
Matching of Photocathode and Light Source	

### SECONDARY-ELECTRIC EMISSION

GENERAL CONSIDERATIONS .....	105
PARAMETERS OF SECONDARY-ELECTRON EMISSION ..	105
Gain Factor $\delta$ as a Function of Primary Energy	
Energy Distribution of Secondary Electrons	
Gain Factor $\delta$ as a Function of Angle of Incidence	
PRACTICAL SECONDARY EMITTERS .....	106
Secondary-Emitting Photocathodes	
Silver-Magnesium-Oxygen (Ag-Mg-O)	
Copper-Beryllium-Oxygen (Cu-Be-O)	
REFERENCES .....	106

## Photoconductors for Camera Tubes

C. W. Rector

BASIC THEORY .....	108
APPLICATIONS .....	112
Germanium	
Cadmium Sulfide	
Microcrystalline Photoconductors	
Amorphous Photoconductors	
PHOTOCONDUCTORS FOR THE VIDICON .....	115
Antimony Trisulfide Photosurfaces	
Effects of Pressure	
Effects of Photolayer Thickness	
Effects of the Substrate	
Effects of Modifications of the Basic Photoconductor	
Miscellaneous Evaporation Parameters	
FACTORS INFLUENCING SELECTION OF PHOTOCONDUCTORS FOR THE VIDICON .....	122
General Requirements of Photoconductors for the Vidicon	
Spectral Photoconductive Response	
COMPOSITION GRADED PHOTOSURFACES .....	126
REFERENCES .....	127

## Phosphors

### Cathodoluminescent Materials

R. N. Summergrad

THE CATHODOLUMINESCENT PROCESS .....	128
PREPARATION OF PHOSPHORS .....	129
PHOSPHOR RESEARCH .....	131
PHOSPHOR CHARACTERISTICS .....	133

Phosphor Efficiency	
Decay Characteristics of Phosphors	
The Variation of Light Output with Accelerating Potential and with Current Density	
Accelerating Potential	
Current Density	
Temperature: Its Effect on Luminescence	
REFERENCES .....	136

## Application and Colorimetry of Phosphor Screens

A. E. Hardy

SCREEN APPLICATION TECHNIQUES.....	138
APPLYING PHOSPHOR SCREENS FOR BLACK-AND-WHITE PICTURE TUBES AND OSCILLOSCOPE TUBES.....	138
STOKE'S LAW.....	139
SCREEN ADHERENCE .....	139
FILMING AND ALUMINIZING BLACK-AND-WHITE SCREENS.....	139
SCREENS FOR COLOR TUBES .....	140
EXPOSURE SYSTEM.....	141
DEVELOPING .....	141
ONE-STEP SLURRY PROCESS .....	141
SCREEN DEFECTS .....	143
Cross-Contamination	
White Nonuniformity	
Blue-Phosphor Breakdown	
FILMING AND ALUMINIZING OF COLOR-TUBE SCREENS.....	143
SCREEN BAKEOUT.....	144

PHOTOMETRY OF PHOSPHOR SCREENS.....	144
MEASURING INSTRUMENTS .....	145
COLOR MEASUREMENT AND SPECIFICATION.....	145
APPLICATION OF C.I.E. COLOR SYSTEM TO BLACK-AND-WHITE SCREENS.....	146
APPLICATION OF C.I.E. COLOR SYSTEM TO COLOR TELEVISION SCREENS.....	148
REFERENCES.....	151
<b>Manufacture of Cathodoluminescent Materials</b>	
J. A. Markoski	
SULFIDE PHOSPHORS .....	153
Preparation of Stock Solutions	
Precipitation	
Neutralization and Washing	
Drying	
Activation and Fluxing	
Firing and Coating	
OXYGEN-DOMINATED PHOSPHORS .....	157
Zinc Orthosilicate: Manganese Activated	
Zinc Orthophosphate: Manganese Activated	
REFERENCE .....	158

## Space Current

### Calculation of Fields and Currents

L. C. Scholz

ELECTROSTATIC FIELDS.....	159
SOLUTIONS FOR SIMPLE GEOMETRIES .....	159
Infinite Parallel Planes	
Concentric Cylinders	
THE THERMIONIC DIODE.....	159
THE IDEAL INFINITE PARALLEL-PLANE DIODE....	161
Initial Velocity - Zero	
Initial Velocities - Maxwellian	
Discussion	
THE IDEAL CYLINDRICAL DIODE .....	168
Initial Velocities - Zero	
Initial Velocity - Maxwellian	
Discussion	
THE EXTENSION OF DIODE THEORY TO TRIODES ..	170
The Shielding Effect of a Grid	
Calculation of Equivalent Potentials	
Interpretation	
Procedure for Analysis	
TETRODES AND PENTODES .....	180
Equivalent Potentials	
The Effect of Space Charge in the Anode Region	
Qualitative Discussion	
Mathematical Solution-References	
Screen-Grid Current	
Plate Resistance	
VARIABLE MU EFFECTS.....	182
The Concept of Variable Mu	
Design of Variable-Mu Tubes	
Mu Variations from Nonideal Grids	
Variable Spacing and Statistical Variations	
FIELD PLOTTING.....	184
Mathematical Plotting Methods	
Direct Solution of the LaPlace Equation	

Conformal Mapping	
Numerical Solutions	
Analog Plotting Methods	
The Resistance-Paper or Electrolytic-Tank Method	
The Resistor Net	
Field Sketching	
Electrode Fitting	
TRAJECTORY TRACING.....	189
General Equations of Motion	
General Projectory in Two Dimensions	
Electron Motion in a Uniform Electric Field	
Snell's Law	
Segmented Straight-Line Trajectories	
Mechanics of Trajectory Tracing	
Segmented Parabolic Trajectories	
Discussion	
Nomographs for the Rapid Modification of Electron-Tube Characteristics	
Theoretical Basis for Nomographs	
Applications and Limitations of the Nomographs	
Use of Multiplying Factors on Nomographs	
REFERENCES.....	198

## Space Current Flow

M. V. Hoover

THE ELECTRON .....	202
EMISSION OF ELECTRONS .....	202
Thermionic, or Primary, Emission	
Secondary Emission	
Photoelectric Emission	
High-Field Emission	
Radioactive Disintegration	
LAWS OF ELECTRONS IN MOTION .....	206
Electron Motion in a Uniform Electric Field	
Electron Motion in a Uniform Magnetic Field	
Electron Motion in Combined Electric and Magnetic Fields	

ELECTRON OPTICS .....	208	Space Charge and Electron-Beam Dispersion
Electrostatic Electron Optics		Space-Charge Waves
Magnetic Lenses		INTERACTIONS OF ELECTRONS WITH CIRCUITS....
Periodic Focusing		213
Electron Guns		Exchange of Energy Between Electron Streams
ELECTRON SPACE CHARGE .....	210	and Electric Fields
Space-Charge Effects in Diodes		Circuit Currents Induced by Electron Motion
Space-Charge Effects in Triodes		Electron-to-Circuit Energy-Exchange Systems
Effect of Space Charge on Electron Transit-Time		Electron Beams in a Nonpropagating-
Space Charge and the "Virtual" Cathode		Circuit Environment
		REFERENCES..... 214

---

## General Design Considerations for Receiving Tubes

### Heaters

A. G. F. Dingwall

#### BASIC DESIGN CONSIDERATIONS AND THEORY .....

Heater Wire Dimensions

Heater Design Temperature

Insulation Thickness

Apex Chip Size

Heater Warm-Up Time

#### HEATER TYPES .....

Folded Heaters

Double-Helical Heaters

Folded Single-Helical (Hairpin) Heaters

#### HEATER MATERIALS..... 225

Heater Wire Materials

Tungsten as a Heater Material

Downo as a Heater Material

Insulation Coating Materials for Heaters

#### APPLICATION OF HEATER COATINGS..... 228

#### HEATER BEHAVIOR ON LIFE..... 229

Failure-Rate Patterns and Heater Temperature

Heater-Cathode Bias

    Heater-Positive Biases

    Heater-Negative Biases

#### HEATER-CATHODE LEAKAGE .....

Definition and Characteristics

Decay and Polarization

Distribution of Heater-Cathode Leakage Values

Changes of Leakage after Tapping of Tube

Effect of Heater Temperature on Leakage

The Effects of Heater Size

The Mechanisms of Heater-Cathode Leakage

Factors Contributing to Heater-Cathode Leakage

Heater Hum

Aging

#### REFERENCES..... 242

### Heat Transfer in Receiving Tubes

O. H. Schade, Jr.

#### HEAT TRANSFER BY STEADY, UNIDIRECTIONAL CONDUCTION .....

244

    The Fourier Equation and Two Simple Solutions

    The Concept of Thermal Resistance

#### HEAT TRANSFER BY CONVECTION .....

245

### THE PHENOMENON OF HEAT TRANSFER BY RADIATION THROUGH NON-ABSORBING MEDIA..... 245

The Physics of Radiation

The Black-Body Concept

The Distribution of Radiation

The Gray-Body Concept

The Use of Spectral and Total Emissivities

### SOLUTIONS OF HEAT TRANSFER EQUATION FOR RADIATION THROUGH NONABSORBING MEDIA..... 247

Black-Body Radiation for Simple Geometries

The View Factor

Radiation from "Composite Surfaces"

    Radiation from a "Right-Angled" Surface  
        at Constant Temperature

    A U-Shaped Radiating Surface  
        at Constant Temperature

### THE APPLICATION OF THEORY TO HEAT TRANSFER PROBLEMS IN TUBE STRUCTURES..... 253

Heat Transfer Circuits of the Diode

Heat Transfer Circuits of the Triode

Heat Transfer by Conduction

    Through the Grid and Stem Leads

    Stem Lead to Each Siderod

    Stem Lead to Only One Siderod

Heat-Transfer Considerations for Multigrid Tubes

### EXAMPLE OF HEAT TRANSFER CALCULATIONS— THE 6L6G PLATE AND SCREEN-GRID TEMPERATURES..... 261

Solution for the Average Plate Temperature

    Solution for the Average Screen-Grid Temperature

### LIST OF SYMBOLS .....

262

### REFERENCES..... 264

### Contact Potential and Grid Currents

E. R. Schrader

#### WORK FUNCTION AND CONTACT POTENTIAL

#### WORK FUNCTION .....

266

#### CONTACT POTENTIAL .....

266

#### THREE METHODS OF MEASURING CONTACT POTENTIALS..

267

The Intersection Method for Measuring Contact  
    Difference of Potential (Method I)

    Significance of the Contact Potential Curve

    The Method of Measuring a Potential to Produce  
        an Arbitrary Reference Current (Method II)

    The Method of Measuring Potential with a Grid  
        Voltmeter (Method III)

## GRID CURRENTS

CATHODE-TO-GRID EMISSION.....	273
PRIMARY GRID EMISSION .....	274
LEAKAGE CURRENTS .....	274
GAS ION CURRENTS .....	274
THE COMPOSITE GRID CHARACTERISTIC .....	275
INTERPRETATION OF DATA .....	275
REFERENCES.....	276

## A New Approach to the Calculation of Electron Tube Characteristics

O. H. Schade, Sr.

### CLASSICAL METHOD OF ELECTRON-TUBE CALCULATION

THE PROBLEM OF ELECTRON-TUBE CALCULATION....	278
CHARACTERISTICS OF THE "PERFECT" DIODE.....	279

Work Functions ( $\psi$ ), Electron Velocities ( $V_T$ ), and Saturation Current ( $I_S$ )	
The Diode Circuit (Potentials and Operating Conditions)	
The Saturation Region	
The Space-Charge-Limited Region	
The Exponential Point	
The Exponential Region	
Effective Anode Potential $V$ and Reference Condition ( $V = 0$ )	
The Langmuir Relations	
Calculation of the Characteristic $I = f(V)$	
Calculation of the Characteristic $I = f(E_b)$	
Some Properties of the Perfect Diode	
The Barrier Potential ( $\psi_c + V_m$ )	
Exponential Region $V < 0$	
Positive-Accelerating-Potential Region ( $V > 0$ )	
Diode Conductance $g = f(T, \psi_c, d)$	

TRIODES .....	287
---------------	-----

Electrostatic Capacitances and Potentials in "Perfect" Parallel-Plane Triodes ( $\mu = \text{Constant}$ )	
Correction for the Space Charge by an Equivalent Diode Spacing ( $d_1'$ )	
Aberrations in Practical Triodes and Limitations of the Simple Theory	
The Grid at Space Potential	
The Grid Work Function $\psi_g$	
Cathode-Temperature Variations $+ \Delta T$	

## Eccentric Electrodes

Uniform Eccentricity of Grid and Cathode	
Eccentricity Caused by Grid Ellipticity	
Grid-Plate Eccentricity $\Delta d_2$	
Nonuniform Eccentricity (Tilting) of Cylindrical Electrodes	
Calculation of Vibration-Induced Modulation in Cylindrical Structures	

## A REFINED METHOD FOR CALCULATING THE SPACE CURRENT DISTRIBUTION AND CURRENT-VOLTAGE CHARACTERISTICS OF ELECTRON TUBES

A NEW APPROACH TO SPACE-CURRENT CALCULATION IN ELECTRON TUBES .....	295
The Electrostatic Field in the Cathode-Grid Space	
Amplification Factors ( $\mu$ )	
Effective Potentials and Space-Current Distribution	
THE COMPUTER PROGRAM.....	300
A. THE MACHINE PROGRAM FOR PARALLEL-PLANE TRIODES .....	300
Calculation of Electrostatic Potential Tables (Sub-Program)	
Calculation of (V,I) Characteristics (Main Program)	
Computed Data	
Computed Potentials ( $V_g, V_a$ ) and External Voltages ( $E_c, E_b$ )	
The Derivatives ( $g_m, r_p, \bar{\mu}$ )	
Input Information	
Determination of Potential Scales and Increments $\Delta V_g$ and $\Delta V_a$	
Starting Values for $V_a$ and $V_g$ and Current Cutoff	
B. ALTERNATE PATHS AND SUBROUTINES EXTENDING FLEXIBILITY AND SCOPE OF THE PROGRAM .....	307
Subroutine for a Direct Comparison of Computed Characteristics	
Subroutines for Triodes Having Cylindrical Elements	
Correction for Mesh Grids	
Nonuniform Spacings or Parameters (Segmentation Routine)	
CORRELATION OF COMPUTED AND MEASURED DATA..	311
Measurement of (V,I) Characteristics	
Analysis of Measured Characteristics	
CONCLUSIONS.....	313
ACKNOWLEDGMENTS.....	314
REFERENCES.....	314
LIST OF SYMBOLS.....	314

## Metals, Metallurgy, and Metal Fabrication

### Metals and Metallurgy

C. W. Horsting, et al

#### THE METALLIC STATE

C. W. Horsting

ATOMIC STRUCTURE .....	315
GRAIN STRUCTURE.....	316
ALLOTROPY.....	317
DUCTILE DEFORMATION.....	317
DISLOCATIONS.....	318
TENSILE TESTING.....	319
ANNEALING AND RECRYSTALLIZATION.....	319
DIFFUSION.....	320

### PHASE EQUILIBRIA IN ALLOY SYSTEMS .....

320

### PHYSICAL PROPERTIES OF ALLOYS.....

322

### HARDENING TREATMENTS.....

322

### VAPOR PRESSURE OF METALS.....

323

### REFERENCES.....

323

### METALS FOR ELECTRON TUBES

J. J. Carrona

NICKEL .....	324
IRON AND STEEL.....	326
COPPER.....	326
TUNGSTEN .....	327
MOLYBDENUM.....	328

OTHER METALS .....	329	PROPERTIES OF SOME TYPICAL PLATE MATERIALS... ..	338
Silver		BIBLIOGRAPHY .....	339
Aluminum			
Chromium			
Tantalum			
Titanium and Zirconium			
REFERENCES.....	330		
		GRIDS AND LEADS	
TESTING OF METALS		A. J. Stoeckert	
C. H. Li			
MECHANICAL TESTING.....	330	CONSTRUCTION .....	339
Tensile Tests		Materials—Lateral Wires	
Hardness Tests		Materials—Side Rods	
Stiffness Test			
Springback Test		LEADS.....	341
Ductility Test			
METALLOGRAPHIC TESTING .....	331	LIST OF MANUFACTURERS OF ALLOYS.....	344
X-RAY TESTING.....	331		
Industrial Radiography		METAL-TO-METAL JOINING	
Diffraction Study		E. S. Thall	
THERMAL TESTING .....	332		
Dilatometric Analysis		ELECTRIC WELDING .....	344
Emissivity Measurements		BRAZING AND SOLDERING .....	346
Thermal Analysis		COLD WELDING .....	348
CHEMICAL TESTING .....	332	RIVETING, FOLDING, AND NOTCHING AND PEENING ..	349
Compositions Analysis by Chemical		REFERENCE .....	349
and Spectrographic Means			
Rapid Identification of Metals		JOINING METALS TO GLASSES AND CERAMICS	
Corrosion Tests		K. Strater	
ELECTRICAL TESTING.....	332	METAL-TO-GLASS SEALS.....	350
Resistivity Checks		METAL-TO-CERAMIC SEALS.....	354
Burnout Tests		REFERENCES.....	356
MI SCLLANEOUS TESTING.....	333		
Weighing		SYSTEMATIC CHARTS OF THE PROPERTIES OF	
Powder Examination		ELECTRON TUBE METALS	
Surface Test for Identifying Metals		S. Y. Husni	
Spark Testing			
Color Comparison Test		This section contains tabular and graphic information	
		on some of the properties of metals and alloys that	
CATHODE MATERIALS FOR RECEIVING TUBES		should be of interest to the electron tube engineer.	
I. S. Solet		The following tables and charts are included:	
DIRECTLY HEATED CATHODES.....	333	Properties of Metals (Table XVIII).....	358-359
INDIRECTLY HEATED CATHODES .....	334	Properties of Alloys (Table XIX).....	360-363
GASES IN NICKEL.....	334	Coefficients of Thermal Expansion	
"IMPURITIES" IN NICKEL AND		at Elevated Temperatures (Table XX).....	364
THEIR RELATION TO EMISSION .....	334	Tensile Strengths at Elevated Temperatures	
THE FUTURE OF THE THERMIONIC CATHODE.....	335	(Table XXI).....	364
REFERENCES.....	336	Total Emissivity (Table XXII).....	365
		Thermal Conductivity at Elevated Temperatures	
PLATE MATERIALS (METALS)		(Table XXIII).....	365
H. G. Scheible and T. A. Sternberg		Charts of Vapor Pressures at	
PROPERTIES OF COMMON STRIP MATERIALS.....	336	Elevated Temperatures (Figs. 32, 33).....	366-369
Clear Nickel, Nickel-Plated Steel,			
and Nickel-Clad Steel			
Carbonized Nickel, Nickel-Plated Steel,			
and Nickel-Clad Steel			
GAS-CARBONIZED MATERIALS.....	337		
SLURRY-CARBONIZED MATERIALS.....	337		
ALUMINUM-CLAD STEEL.....	337		
ALNIFER .....	337		
COPPER-BASE AND COPPER-CORED MATERIALS .....	338		
		Metals for Vacuum Tube Construction	
		P. D. Strubhar	
		COPPER.....	370
		GLASS-SEALING METALS AND ALLOYS.....	371
		TUNGSTEN AND MOLYBDENUM .....	373
		STEEL.....	375
		OTHER METALS .....	376
		Principles of Metal Forming	
		L. S. Sloane	
		THE MECHANICAL PRESS.....	377
		PRESS OPERATIONS .....	377
		BLANKING AND PIERCING.....	377

DRAWING .....	378	Spot Welding	
Blankholding Pressure		Projection Welding	
Draw Radius		Seam Welding	
Material Reduction		ELECTROPOLISHING .....	387
Diameter Reduction		CHEMICAL BRIGHT DIPPING.....	387
Blank Diameter		PHOTOMECHANICAL ETCHING.....	387
Reverse Drawing		Sensitizing	
SIZING .....	381	Printing	
COINING .....	381	Developing	
EXTRUDING.....	381	Etching	
FORMING .....	381	ELECTROPLATING.....	389
TOOLING .....	382	Effect of Parts Design	
Tool Costs		Requirements for Nonplated Areas	
Component Costs		Requirements for No Nonplated Areas	
FOUR-SLIDE MACHINES.....	382	Cleaning for Plating	
Processes Used in Metal Parts		Striking	
Fabrication and Finishing		Plating Requirements and Costs	
H. A. Kauffman		Treatment after Plating	
RESISTANCE WELDING OF ELECTRON TUBE		Inspection of Plating	
PARTS AND ASSEMBLIES .....	385	Summary	
		REFERENCES.....	391

---

## Insulators, Envelope Materials, and Seals

### Glass for Receiving Tubes

J. Gallup

DEFINITION.....	392
COMPOSITION.....	392
PRINCIPAL PROPERTIES OF GLASS.....	393
Thermal Expansion	
Viscosity	
Strain Point	
Annealing Point	
Softening Point	
Working Point	
Annealing of Glass	
Electrical Resistivity	
PHYSICAL PROPERTIES OF LESSER INTEREST	
FOR RECEIVING TUBE MANUFACTURE .....	397
Density	
Weathering Resistance	
Dielectric Constant and Power Factor	
OPTICAL PROPERTIES — COLOR, LIGHT TRANSMISSION, LUMINESCENCE, INDEX OF REFRACTION, AND BIREFRINGENCE.....	400
Color	
Light Transmission, Luminescence, and Index of Refraction	
Birefringence under Strain	
STRENGTH, CRACKS, AND STRAIN CONTROL.....	402
THERMAL AND MECHANICAL TESTS.....	403
CHEMICAL TREATMENT OF GLASS SURFACES.....	404
SOME GENERAL CONSIDERATIONS CONCERNING GLASS-STEM, BULB, AND SEAL DESIGN AND USE.....	404
REFERENCES.....	405
Books	
Periodicals	

### Glass and Its Properties and Seals

J. C. Turnbull and G. E. Eiwen

COMPOSITION AND PROPERTIES.....	406
Compositions of Commercial Glasses	
Properties of Commercial Glasses	
Description and Application of Glasses	
Dumet-Sealing Glasses	
Chromium-Iron Alloy Sealing Glasses	
Iron-Sealing Glasses	
Kovar-Sealing Glasses	
Tungsten-Sealing Glasses	
MECHANICAL STRENGTH OF GLASS.....	411
Mechanical Strength and Fatigue of Glass	
Glass Fracture Analysis	
Measurement of Stresses in Glass	
Polariscope Estimation of Stress	
Measurement of Strains in Glass Surfaces	
Scratch Testing of Stresses in Glass	
Estimation of Stresses by Strength Testing of Glass Articles	
ELECTRICAL PROPERTIES OF GLASS.....	416
Electrical Failure of Glass	
Electrolysis Effects	
Puncture	
Ionization in Air Lines and Bubbles	
Conductive Films on Glass Surfaces	
OPTICAL PROPERTIES OF GLASS .....	418
Transmission of Light and Radiation	
X-Ray Absorption	
Glass Browning	
Fluorescence of Glass	
Homogeneity—Glasses Melted for Optical Use	
OUTGASSING, DIFFUSION, AND SUBLIMATION OF GLASS .....	420

Thermal Outgassing of Glass	
Diffusion in Glass	
Diffusion of Water in Glass	
Diffusion of Gases in Glass	
Diffusion of Ions in Glass	
Gases Dissolved in Glass	
Outgassing under Bombardment	
Sublimation from Glass Surfaces	
DEVITRIFICATION OF GLASS.....	423
THERMAL EXPANSION OF GLASS.....	423
GLASS-TO-METAL AND GLASS-TO-GLASS SEALS....	424
Nature of Sealing Problems	
Adherence of Glass Sealed to Metal	
Estimating Quality of Seals	
Commonly Used Glass-to-Metal Seal Combinations	
Sealing Methods	
Stresses in Seals	
Calculation of Stresses from Thermal-Expansion Differentials	
Measurement of Stresses in Seals	
Annealing of Seals	
Practical Annealing Schedules	
REFERENCES.....	432

## Ceramics

W. F. Lawrence

WHEN TO USE CERAMICS.....	433
THE INTERRELATIONSHIP OF FORMING METHODS AND PART DESIGN.....	434
Forming Techniques Used to Make Finished Parts	
Forming Techniques Suitable for Subsequent Machining	
Pressing Method	
Extrusion Method	
TOLERANCES.....	438
CHOICE OF MATERIAL .....	440
MECHANICAL PROPERTIES.....	441
Strength	
Impact Strength	
Specific Gravity, Porosity, and Water Absorption	
THERMAL PROPERTIES.....	442
Maximum Operating Temperature	
Thermal Conductivity	
Specific Heat	
Thermal Expansion	
Resistance to Thermal Shock	

ELECTRICAL PROPERTIES.....	449
Dielectric Constant and Loss Factor	
Resistivity	
Dielectric Strength	
REFERENCES.....	451
<b>Ceramics and Ceramic-to-Metal Seals</b>	
M. Berg	
<b>CERAMICS FOR ELECTRONIC APPLICATIONS</b>	
TYPES OF CERAMICS FOR ELECTRON-TUBE COMPONENTS .....	452
Alumina	
Stearites - Clinoenstatite Bodies	
Forsterite	
Electrical Porcelain	
Zircon Porcelain	
Beryllia	
High-Dielectric Constant Ceramics	
Other Ceramics	
APPLICATIONS AND PHYSICAL PROPERTIES .....	455
Design and Processing	
Fabrication Techniques	

## CERAMIC-TO-METAL SEALS

PROCESSES USED TO JOIN METAL TO THE CERAMIC ENVELOPE .....	458
The Sintered Metal Process	
The Active Alloy Process	
The Pressure Process	
The Glass Interlayer Process	
SEAL DESIGN .....	463
BIBLIOGRAPHY .....	464

## Design of Mica Spacers

M. Bondy and M. Jinetopoulos

MINING AND PROCESSING OF MICA.....	465
PROPERTIES OF MUSCOVITE .....	466
GRADING OF MICA .....	467
TOOLING .....	467
SPACER DESIGN .....	468
Mica Thickness	
Bridge Distances	
Minimum Hole Dimensions	
Outside Contour	
MICA COATINGS .....	469
VOLTAGE GRADIENTS .....	470
REFERENCES.....	471

## Parts Cleaning, Coating, and Basing

### Parts Cleaning and Processing

F. I. Scott

IMPORTANCE AND SCOPE OF CLEANING .....	472
Background	
General Considerations	
Classification of Contaminants	
Evolution of Gases from Parts	

Tests for Cleanliness  
Methods of Cleaning

PROCESS AND MATERIAL CONTROLS RELATED TO CLEANING .....	478
Raw Materials	
Lubricants	
Storage and Handling	
SUMMARY .....	480

ADDITIONAL CLEANING PROCESSES.....	480	EXTERNAL COATINGS .....	482
Alkaline Electrocleaning		METAL COMPONENT COATINGS.....	482
Emulsion Cleaning		PROTECTION OF SILVER-PLATED TUBES.....	483
Tumbling		BASES.....	483
REFERENCES.....	480	BASING CEMENTS.....	483
<b>Coatings, Bases, and Basing Cements</b>		REQUIREMENTS FOR GOOD BASE ADHERENCE.....	483
L. P. Fox			
INTERNAL COATINGS .....	481		

---

## Exhaust and Finishing

### High-Vacuum Technology and Equipment

W. G. Henderson and A. L. Lucarelli

WHAT IS A VACUUM? .....	485
PUMP RANGE .....	485
VACUUM CLASSIFICATION .....	485
TYPES OF FLOW AND MEAN FREE PATH.....	485
SYSTEM COMPONENTS.....	486
GETTERING.....	486
REQUIREMENTS FOR A GOOD VACUUM .....	487
MECHANICAL PUMPS .....	487
MECHANICAL-PUMP SPEEDS.....	488
EXHAUST TIME - MECHANICAL PUMP.....	488
GAS BALLAST PUMP .....	489
MECHANICAL BOOSTER PUMP.....	490
OIL-DIFFUSION PUMP.....	491
FRACTIONATING PUMP.....	491
BACKSTREAMING.....	491
PURPOSE OF CONSTRUCTION.....	492
PUMP COOLING.....	492
PUMP CURVE FEATURES.....	492
SYSTEM CURVES.....	493
VAPOR PRESSURE - PUMP MEDIUM.....	494
VAPOR PRESSURE - METALS.....	495
VAPOR PRESSURE - GASKET MATERIALS.....	495
EVAPOR-ION PUMP.....	495
MERCURY PUMP .....	496
GAUGES .....	497
SEALS .....	500
TRAPS AND BAFFLES.....	501
VALVES .....	502
FLOW OF GASES THROUGH VACUUM LINES.....	503
STARTING AND STOPPING PROCEDURE .....	503
OTHER OPERATING AND DESIGN PRECAUTIONS.....	503
TROUBLE SHOOTING .....	503
OTHER PROCESSES .....	504
Sputtering	
Vacuum Firing — AC Heating	
Vacuum Firing — RF Induction Heating	
Vacuum Firing — Electric Oven	
REFERENCES.....	505
BIBLIOGRAPHY .....	505

### Exhaust of Receiving-Type Tubes

C. J. Pearce

OBJECTIVES OF THE EXHAUST PROCESS.....	506
CATHODE BREAKDOWN AND BRIGHTNESS TEMPERATURE.....	506
TRACK LIGHTING SEQUENCE.....	506
Temperature - Time - Material Effects	
Pressure - Time Relationships	
PARTS OUTGASSING AND COLOR TEMPERATURES .....	508
Temperature - Time - Material Effects	
Parts Processing History	
Simultaneous Parts Degassing	
Interactions of Cathode Breakdown and Parts Outgassing	
VACUUM GAUGES.....	510
Absolute Gauges	
Relative Gauges	
FORMS OF RECEIVING-TYPE EXHAUST EQUIPMENT..	513
Manual Exhaust (Trolley)	
Manual Exhaust Schedule for Vacuum-Type Tubes	
Manual Exhaust for Gas-Filled Tubes	
Automatic Exhaust (Sealex)	
Sealex-Exhaust Schedules for Glass-Type Vacuum Tubes	
Sealex Exhaust of Metal-Type Vacuum Tubes	
Sealex Exhaust of Gas Tubes	
Effects of Exhaust Tubulation Size	
Other Methods of Exhaust	
REFERENCES.....	517
BIBLIOGRAPHY .....	517

### Getters

C. H. Thomas

GETTER ACTION.....	519
HISTORICAL TYPES OF GETTERS .....	519
Phosphorus	
Magnesium	
Barium Azide	
Misch Metal	
Barium	
Barium-Aluminum-Magnesium Pellet	
Barium-Aluminum Pellet	
Batalum Getter	
Kic Getter	

King Getter	General Rules of Procedure
Ring-Type Getter	Summary
Zirconium and Titanium	CIRCUITRY AND EQUIPMENT.....
Tantalum	Basic Circuits
Cer-Alloy	VARIATIONS OF TREATMENTS AND
Cerium-Thorium Alloy	SPECIAL PROCESSING.....
EFFICIENCY OF GETTERS .....	522
EFFICIENCY OF GETTER FLASH.....	524
Preflash	Elimination of Grid Step
Postflash	Special Cycling
Flashing in Argon	Problem Tube Types
DETERMINATION OF BARIUM IN GETTER FLASH....	524
REFERENCES.....	Contact Potential Control
	Parasitics
	STABILIZATION
	AREAS OF APPLICATION.....
	Passive-Type Cathodes
	Elimination of Potential Inoperatives
	CIRCUITS AND EQUIPMENT .....
	534

### Aging and Stabilization

G. Wolfe

#### AGING

BASIC CONSIDERATIONS.....	526
THE AGING PROCESS.....	527
The Hotshot Step	
The Grid Step	
The Anode (or Plate) Step	

	SUMMARY
	FACTORS AFFECTING AGING AND
	STABILIZATION SCHEDULES .....
	Relation of Aging to Exhaust
	Tube Parts and Materials
	Tube Design
	IMPORTANCE OF MEASUREMENTS .....
	BIBLIOGRAPHY .....
	536

---

## Design, Processing, and Application of Receiving-Type Tubes and Picture Tubes

### Diodes

A. P. Kauzmann

DIODE SYMBOLS.....	537
DIODE THEORY .....	537
Plane Parallel Electrodes	
Concentric Electrodes	
Perveance	
Diode-Plate Characteristic	
Dynamic and Effective Diode Resistances	
Diode with Added Series Resistance	
DIODE OPERATION INTO A SHORT-CIRCUITED LOAD....	542
BASIC RECTIFIER POWER CONVERTERS .....	542
RESISTANCE LOAD AND CHOKE-INPUT-FILTERED LOAD ..	543
TUNGSTEN-LAMP-LOADED RECTIFIER.....	548
CAPACITOR-INPUT-FILTERED LOAD.....	549
CAPACITOR-INPUT-FILTER CIRCUITS USING LARGE VALUES OF CAPACITANCE.....	552
VOLTAGE-MULTIPLYING CIRCUITS .....	569
HIGH-VOLTAGE RECTIFIER TUBE DESIGN.....	571

Potential Gradients and Field Emission	
Secondary Emission	
Potential Gradient at the Cathode	
Electrolysis	
X-Rays	
Diode Currents	

DAMPER-TUBE RECTIFIER DESIGN .....	574
REFERENCES.....	576

### Small-Signal Radio-Frequency Amplifier Tubes

W. A. Harris

TELEVISION INPUT-STAGE REQUIREMENTS.....	577
MEASUREMENTS OF OPERATING CHARACTERISTICS...	577
DEFINITIONS AND THEORY.....	578
Measurements of a Two-Port	
Three-Terminal Transducers	
Measurement of Noise	
Corrections for Lead Inductances and Capacitances	
LARGE-SIGNAL CONSIDERATIONS .....	592
TUBE DESIGN CONSIDERATIONS .....	597

### Design of Intermediate-Frequency Amplifier Tubes

M. B. Knight

GRID-TO-PLATE TRANSCONDUCTANCE.....	599
INPUT ADMITTANCE.....	600
OUTPUT ADMITTANCE.....	601
FEEDBACK CAPACITANCE .....	602
GAIN CONTROL.....	604
DISTORTION.....	604
REFERENCES.....	606

## Design of Converter and Mixer Tubes

T. J. Henry

CHARACTERISTICS OF CONVERTER AND MIXER TUBES.	607
THE DESIGN OF THE CONVERTER STAGE.....	610
Automatic Gain Control (AGC)	
Tuning	
Interaction of Signal and Oscillator Circuits	
Oscillator Strength	
Input Conductance at High Frequencies	
Noise	
Oscillator Radiation	
Frequency Drift During Warm-up of Television Receivers	
Economic Considerations	
TYPES OF MIXERS AND CONVERTERS .....	612
The Diode Mixer	
The Triode Mixer	
The Pentode Mixer	
The Outer-Grid-Injection Mixer	
The Inner-Grid-Injection Converter	
COUPLING EFFECTS.....	615
NOISE IN MIXER TUBES .....	616
DESIGN OF MIXER TUBES.....	617
Triode Mixers	
Pentode Mixers	
Outer-Grid-Injection Mixers	
Inner-Grid-Injection Converters	
Application Testing	
CURRENT CONTROL BY A CONTROL GRID FOLLOWING A POSITIVE SCREEN GRID.....	618
REFERENCES.....	620

## Design of AM and FM Detector Tubes

T. J. Henry

DETECTORS.....	622
DETECTION OF AMPLITUDE-MODULATED SIGNALS....	622
General Considerations	
The Diode Envelope Detector	
Other Envelope Detectors	
Single-Sideband and Vestigial-Sideband Modulation	
Product Detectors	
Noise Advantage of Product Detectors	
The Design of Tubes for Amplitude-Modulation Detector Circuits	
DETECTION OF FREQUENCY-MODULATED SIGNALS....	629
General Considerations	
Types of Frequency-Modulation Detection Systems	
Detection by Amplitude Variations	
Detection by Phase Variation with Frequency	
REFERENCES.....	635

## Vacuum-Tube Oscillators

W. E. Babcock

OPERATION AND ANALYSIS OF TYPICAL OSCILLATORS .	637
Oscillator Operation	
Sinusoidal Oscillators	
Oscillator Analysis by Feedback Amplifier Theory	

## Negative-Resistance Oscillators

Feedback Oscillators  
Electron-Coupled Oscillator  
Grid-Circuit Considerations

## OSCILLATOR CIRCUITS FOR SPECIAL APPLICATIONS. 644

    Crystal Oscillators  
    Magnetostriction Oscillator  
    Low-Frequency Oscillators

## NONSINUSOIDAL OSCILLATOR CIRCUITS..... 649

    Multivibrator Circuits  
    Sawtooth Generators

## TUBES FOR USE IN OSCILLATOR CIRCUITS..... 654

    Supply-Voltage Considerations  
    Power Output Considerations  
    Frequency Considerations  
    Sinusoidal and Nonsinusoidal Oscillator Considerations

## REFERENCES..... 655

## Beam Power Tube Design Considerations

O. H. Schade, Jr.

THE BEAM POWER TUBE IN CROSS SECTION.....	656
SPACE-CHARGE EFFECTS .....	657
THE ELECTRON-BEAM CHARACTERISTICS .....	660
CALCULATION OF THE APPROXIMATE BEAM SHAPE AT ZERO CONTROL-GRID POTENTIAL .....	663
DIRECTLY INTERCEPTED SCREEN-GRID CURRENT .....	664
HIGH VOLTAGE CONSIDERATIONS .....	664
Some Observations on the Breakdown Phenomena	
Considerations for Breakdown between Metal Electrodes	
Considerations for Breakdown along Insulator Surfaces	
THE MECHANICAL-THERMAL-ELECTRICAL DESIGN OF BEAM TUBES.....	667
Design Procedure for the "Optimum" Tube	
Some General Characteristics of Tube Structures	
LIST OF SYMBOLS.....	668
REFERENCES.....	668

## Audio Output, Vertical-Deflection, and Horizontal-Deflection Tubes for Receiving Applications

M. Bondy

### AUDIO OUTPUT TUBES

DESIGN OBJECTIVES.....	669
Power Output	
Power Sensitivity	
Distortion	
Plate-Circuit Efficiency	
DESIGN CONSIDERATIONS.....	669
Triodes	
Pentodes	
Beam Power Tubes	

DESIGN EXAMPLE .....	671
Objectives of Design Problem	
Analysis of Design Problem	
Possible Solutions	
Critical Design Areas	
VERTICAL-DEFLECTION TUBES	
DESIGN OBJECTIVES.....	675
DESIGN CONSIDERATIONS.....	676
Triodes	
Beam Power Tubes	
DESIGN EXAMPLE .....	676
Choice of Tube	
Critical Design Areas	
HORIZONTAL-DEFLECTION TUBES	
DESIGN OBJECTIVES.....	678
DESIGN EXAMPLE .....	679
DESIGN CONSIDERATIONS.....	679
Black-and-White Picture Tubes	
C. W. Thierfelder, et al	
ELECTRON GUN DESIGN CONSIDERATIONS	
DESCRIPTION AND OPERATION.....	682
ELECTRON LENS THEORY.....	683
DEFLECTION .....	683
TRIODE AND TETRODE CHARACTERISTICS.....	684
CUTOFF VOLTAGE.....	685
Design Parameters	
Mechanical Variations	
Practical Manufacturing Techniques	
PREFOCUSING LENS .....	686
ION TRAP LENS.....	688
FOCUSING LENSES .....	690
Magnetic Lens	
Electrostatic Acceleration Lens	
Unipotential Electrostatic Lens	
LENS ERRORS.....	691
PICTURE TUBE PERFORMANCE CHARACTERISTICS	
ELECTRON-GUN REQUIREMENTS AND FOCUS CHARACTERISTICS .....	691
PICTURE QUALITY.....	693
Subjective Evaluation of Picture Quality	
Factors Determining Picture Quality	
Objective Measurement of Picture Quality	
RELIABILITY.....	695
TRANSFER CHARACTERISTICS .....	696
GUN EFFICIENCY.....	697
TUBE DESIGN CONSIDERATIONS	
BULB DESIGN.....	698
SCREEN APPLICATION.....	701
FILMING AND ALUMINIZING .....	702
BAKEOUT AND EXHAUST.....	704
EXHAUST CONSIDERATIONS.....	704
Pressure Stability	
Residual Gas Composition	
REFERENCES .....	707

Color Picture Tube Design and Processing	
H. C. Moodey and A. M. Morrell	
OPERATIONAL PRINCIPLES OF MAJOR COLOR-TUBE TYPES.....	709
Accurate Beam Scanning	
Beam Switching Near the Phosphor Screen	
Direction-Sensitive Screen Assembly	
THE GEOMETRY OF SHADOW-MASK TUBE DESIGN.....	715
Planar Mask-Screen Assembly	
Curved Mask-Screen Assembly	
ELECTRON-OPTICAL DEVIATIONS FROM THE SIMPLE OPTICAL ANALOGY FOR SHADOW-MASK TUBES.....	717
Radial Error	
Degrouping Errors	
Ambient Magnetic Fields	
TRIPLE-BEAM GUNS.....	721
Special Requirements	
Description of Gun Types	
MECHANICAL DESIGN FEATURES OF SHADOW-MASK TUBES .....	724
The Shadow-Mask-Frame Assembly	
Bulb Design	
Gun Design	
COMPONENTS FOR SHADOW-MASK TUBES .....	728
Yoke	
Convergence Assembly	
Purifying Magnet	
Equalizers and Shielding	
OPERATIONAL CHARACTERISTICS .....	729
Drive Characteristics	
Magnetic Effects	
DESIGN EQUATIONS.....	732
Definitions	
Equations	
21CYP22 Parameters	
COLOR PICTURE TUBE PROCESSING.....	733
Panel Assembly	
Screening Operation	
Funnel	
Frit Sealing	
Gun Seal	
Exhaust	
Basing, Aging, and Testing	
REFERENCES .....	734

## Circuit Troubles Caused by Unusual Tube Effects

W. E. Babcock

SLEEPING SICKNESS.....	736
Cathode - Interface Problem	
Interface in Entertainment Tubes	
BLACKOUT .....	737
DC SHIFT .....	739
STRAY EMISSION .....	739
BULB OR MICA CHARGE .....	740
SPOOK INTERFERENCE .....	741
SNIVETS INTERFERENCE .....	741
REFERENCES .....	742

# Design, Processing, and Application of Industrial-Type Tubes

## Some Factors Affecting the Design and Application of Small Power Tubes

J. W. Gaylord

INTRODUCTION..... 743

Design of Output Section

Design of Input Section

Tube Operation

AMPLIFIER CLASSIFICATION..... 743

Current Component Ratios

Graphical Analysis of Constant-Current Curves

Fourier Analysis of Constant-Grid-Voltage Curves

Choice of Operating Point

Cathode Drive Considerations

CIRCUIT OPERATION..... 747

The Q Factor

Circuit Efficiency

Determination of  $E_p$  and  $I_p$  for Lumped Circuits

FREQUENCY EFFECTS..... 751

Distributed Circuits

Simplified Transmission-Line Theory

Stored Energy in Resonant Transmission Lines

Determination of  $E_p$  and  $I_p$  for Distributed Circuits

PHYSICAL DESIGN CONSIDERATIONS..... 754

Current Division

Empirical Data on Cathode-Current Division

Determination of Cathode Current

Thermionic Emission

Amplification of Mu Factor

Transconductance

Perveance

DEFINITIONS OF SYMBOLS USED..... 761

REFERENCES..... 762

## Large-Power-Tube Design, Processing, and Testing

W. P. Bennett

APPLICATIONS AND SERVICE..... 763

THE CONCEPTUAL DESIGN..... 763

DETERMINATION OF POWER REQUIREMENTS..... 764

DETERMINATION OF PLATE VOLTAGE ..... 764

SELECTION OF THE CATHODE ..... 765

COMPUTATION OF THE REQUIRED CATHODE AREA.... 767

CATHODE CONFIGURATION AND SUPPORT STRUCTURE ... 767

TYPE AND CONFIGURATION OF TUBE ..... 770

Frequency Effects in Control Service

Frequency Effects in RF Generator Service

Triodes

Tetrodes

Electron-Conduction Systems

Circuit Connections

Dissipation Considerations

VACUUM ENVELOPES..... 782

Electrical Properties of the Ceramic

Mechanical Properties of Ceramics and Metals

Bonding Techniques

Strain Isolation  
Surface Losses  
Assembly Process  
Voltage Standoff  
Materials

MECHANICAL ASPECTS OF TUBE DESIGN..... 785

EXHAUST AND PROCESSING..... 786

Bakeout  
Heating the Electrodes  
High-Voltage Breakdown  
Activation and Aging  
Fault Protection  
Getters and Getter Ion Pumps

TEST AND EVALUATION ..... 788

Over-all Evaluation  
Diagnostic Tests  
Mechanical Tests  
Circuit Development

REFERENCES..... 790

## Gas Tube Design

H. H. Wittenberg

PROCESSES PRIOR TO CONDUCTION..... 792

Collision  
Ionization

BREAKDOWN ..... 795

Secondary Emission at Cathode  
Paschen's Law

PROCESSES DURING CONDUCTION..... 797

Voltage vs. Current  
Voltage vs. Distance  
Sheath  
Plasma

RECTIFIERS..... 800

Anode Efficiency  
Cathode Efficiency  
Cathode Design  
Heater Design  
Gas Filling  
Anode Design  
Tube Drop  
Arcback

THYRATRONS..... 810

Control Characteristic  
Grid Current Prior to Conduction  
Grid Current During Conduction  
Design

REFERENCES..... 814

APPENDIX A. BREAKDOWN..... 816

APPENDIX B. PASCHEN'S LAW..... 816

APPENDIX C. COLLISION OF ELECTRON AND ION.. 816

APPENDIX D. BREAKDOWN OF A THYRATRON ..... 817

## Design and Processing of Oscilloscope Tubes

E. M. Smith

COMPARISON OF MAGNETIC AND ELECTROSTATIC DEFLECTION ..... 918

ELECTRON GUN DESIGN-- ELECTROSTATIC-DEFLECTION TYPES .....	820	PROCESSING OF CAMERA TUBES .....	845																																																																		
INTERELECTRODE CAPACITANCE .....	821	Common Problems																																																																			
DEFLECTING-ELECTRODE SHIELD .....	821	Materials																																																																			
DEFLECTING-ELECTRODE DESIGN .....	822	Mesh Fabrication																																																																			
Center of Deflection		Glass Target Fabrication																																																																			
Deflection Sensitivity		Photocathodes																																																																			
Electron-Beam Trajectory		REFERENCES .....	846																																																																		
POST-DEFLECTION ACCELERATION .....	823																																																																				
MAGNETIC DEFLECTION .....	824	Image-Converter Tubes																																																																			
PHOSPHOR SCREEN .....	824	R. G. Stoudenheimer																																																																			
PROCESSING .....	824	HISTORY .....	848																																																																		
BIBLIOGRAPHY .....	825	CONVERSION GAIN .....	849																																																																		
<b>Phototube Design</b>																																																																					
J. L. Weaver																																																																					
PHOTOCATHODES .....	826	SCREEN BACKGROUND .....	851																																																																		
SECONDARY-ELECTRON MULTIPLIERS .....	827	Thermionic Emission																																																																			
Multiplier Dynodes		Field Emission																																																																			
Multiplier Structures		ELECTRON LENS SYSTEMS .....	853																																																																		
PHOTOTUBE DESIGN TESTS .....	832	Uniform Electric and Magnetic Fields																																																																			
Vacuum and Gas Photodiode Tests		Short Magnetic Lens																																																																			
Multiplier Phototube Tests		The Electrostatic Lens																																																																			
REFERENCES .....	836	Lens Aberrations																																																																			
<b>Camera Tube Design and Processing</b>																																																																					
B. H. Vine																																																																					
TARGETS .....	838	REFERENCES .....	860																																																																		
Deposition of Signal Charge on the Target																																																																					
Scanning, Signal Extraction, and Erasure																																																																					
High-Velocity Scanning vs. Low-Velocity Scanning																																																																					
TARGET DESIGN .....	839	<b>Design and Processing of Storage Tubes</b>																																																																			
Target Size		M. D. Harsh																																																																			
Target Surface-Potential Swing		STORAGE TUBES AND INFORMATION PROCESSING .....	862																																																																		
Target Charge		DESCRIPTION OF RCA STORAGE TUBES .....	862																																																																		
Some Target Relationships		Oscillograph-Type Electrostatic Storage Tube																																																																			
Calculation of Capacitance Lag		Radechon																																																																			
Charge Required on an Image Orthicon Target		Graphechon																																																																			
Noise in the Image Orthicon		Display Storage Tube																																																																			
Video Amplifier Noise		THE STORAGE TARGET .....	866																																																																		
Capacitance Effects in Wide-Spaced		The Backplate - Perforated Type																																																																			
Image Orthicons		The Backplate - Continuous, Electron-																																																																			
ELECTRON OPTICS .....	842	Transparent Type		The Backplate - Continuous, Electron-Opaque Type		Focusing		Choice of the Dielectric		Deflection Aberrations		The Dielectric - Its Preparation		Beam-Landing Errors		Auxiliary Target-Assembly Elements		Limitations on Beam-Current Density		Luminescent Screens		MISCELLANEOUS SPURIOUS EFFECTS .....	844	ELECTRON-OPTICAL STRUCTURES IN STORAGE TUBES .....	872	Sticking and Burn		Electron Guns		Vertical Tilt		Collimating Systems		Flicker		Lens Raster Systems		Waterfall Effect		CONCLUSION .....	874	PERFORMANCE CHARACTERISTICS .....	844	REFERENCES .....	874	Spectral-Response Characteristic		<b>Design and Processing of Microwave Magnetrons</b>		Transfer Characteristic		F. E. Vaccaro and D. E. Nelson		Resolution		DESIGN OF THE MAGNETRON INTERACTION SPACE .....	878	Noise		Interdependence of Magnetron Components		Persistence Characteristic		Modes of the Magnetron		Sensitivity		The Equations of Cross-Field Interaction	
Transparent Type		The Backplate - Continuous, Electron-Opaque Type																																																																			
Focusing		Choice of the Dielectric																																																																			
Deflection Aberrations		The Dielectric - Its Preparation																																																																			
Beam-Landing Errors		Auxiliary Target-Assembly Elements																																																																			
Limitations on Beam-Current Density		Luminescent Screens																																																																			
MISCELLANEOUS SPURIOUS EFFECTS .....	844	ELECTRON-OPTICAL STRUCTURES IN STORAGE TUBES .....	872																																																																		
Sticking and Burn		Electron Guns																																																																			
Vertical Tilt		Collimating Systems																																																																			
Flicker		Lens Raster Systems																																																																			
Waterfall Effect		CONCLUSION .....	874																																																																		
PERFORMANCE CHARACTERISTICS .....	844	REFERENCES .....	874																																																																		
Spectral-Response Characteristic		<b>Design and Processing of Microwave Magnetrons</b>																																																																			
Transfer Characteristic		F. E. Vaccaro and D. E. Nelson																																																																			
Resolution		DESIGN OF THE MAGNETRON INTERACTION SPACE .....	878																																																																		
Noise		Interdependence of Magnetron Components																																																																			
Persistence Characteristic		Modes of the Magnetron																																																																			
Sensitivity		The Equations of Cross-Field Interaction																																																																			

MAGNETRON RESONANT CIRCUITS.....	885	FORWARD-WAVE AMPLIFIER DESIGN	
Types of Resonant Circuits		THE HELIX AS A SLOW-WAVE STRUCTURE.....	902
Design of Strapped-Resonator Systems		Helix Phase Velocity	
MAGNETRON TUNING.....	887	Helix Impedance	
Single Tuning Cavity		Limitation of the Helix	
Four-Cavity Tunable Magnetrons		OTHER SLOW-WAVE STRUCTURES .....	907
MAGNETRON CATHODES .....	892	ELECTRON GUN.....	909
OUTPUT CIRCUITS.....	894	Convergent-Flow Electron Gun	
THE MAGNETIC CIRCUIT.....	894	Parallel-Flow Gun	
CONSTRUCTION TECHNIQUES.....	895	Hollow-Beam Parallel-Flow Gun	
MAGNETRON PROCESSING.....	896	Convergent-Flow Hollow-Beam Gun	
Pre-exhaust Treatment		Magnetron-Injection Gun	
Exhaust		Low-Noise Gun	
Getters		FOCUSING .....	912
Aging		Magnetic Focusing	
LIST OF SYMBOLS .....	896	Electrostatic Focusing	
REFERENCES.....	897	COUPLERS .....	918
<b>Traveling-Wave Tube Design</b>			
E. E. Bliss			
TRAVELING-WAVE TUBE OPERATION			
FORWARD-WAVE TRAVELING-WAVE TUBE .....	898	ATTENUATORS.....	922
BACKWARD-WAVE TRAVELING-WAVE TUBE .....	899	Attenuators for Helices	
SLOW-WAVE CIRCUITS .....	900	Attenuators for Other Types of Slow-Wave Structures	
ANALYSIS OF OPERATION			
MATHEMATICAL DESCRIPTION OF A WAVE ON A SLOW-WAVE STRUCTURE.....	900	COLLECTOR.....	923
MATHEMATICAL DESCRIPTION OF A WAVE ON A SLOW-WAVE STRUCTURE IN THE PRESENCE OF AN ELECTRON BEAM.....	901	Depressed-Collector Operation	
THE DETERMINATION OF $\Gamma$ .....	901	Two-Stage Depressed Collector	
CALCULATION OF GAIN .....	901	Secondary-Emission Suppression	
APPENDIX			
DESIGN PROCEDURE FOR TRAVELING-WAVE TUBES.... 925			
GENERAL TUBE DESIGN..... 925			
SYMBOLS .....			
REFERENCES..... 928			